# New Molecular Designs for Donor-Acceptor Strapped Macromolecules and Polymers of Perylenebisimide

by

**Veer Sairam Dnyaneshwar**
**10CC17J26015**

Thesis submitted to the
Academy of Scientific & Innovative Research
for the award of the degree of
DOCTOR OF PHILOSOPHY
In SCIENCE

Under the supervision of
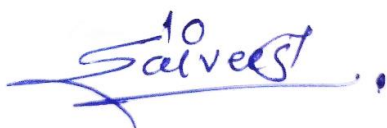**Dr. Santhosh Babu Sukumaran**



**CSIR- National Chemical Laboratory, Pune**



Academy of Scientific and Innovative Research
AcSIR Headquarters, CSIR-HRDC campus
Sector 19, Kamla Nehru Nagar,
Ghaziabad, U.P. – 201 002, India
**April, 2023**

# Certificate

This is to certify that the work incorporated in this Ph.D. thesis entitled *"New Molecular Designs for Donor-Acceptor Strapped Macromolecules and Polymers of Perylenebisimide"*, submitted by *Veer Sairam Dnyaneshwar* to the Academy of Scientific and Innovative Research (AcSIR), in partial fulfillment of the requirements for the award of the Degree of *Doctor of Philosophy in Science*, embodies original research work carried-out by the student. We, further certify that this work has not been submitted to any other University or Institution in part or full for the award of any degree or diploma. Research material(s) obtained from other source(s) and used in this research work has/have been duly acknowledged in the thesis. Image(s), illustration(s), figure(s), table(s) *etc*., used in the thesis from other source(s), have also been duly cited and acknowledged.

**Mr. Veer Sairam Dnyaneshwar**

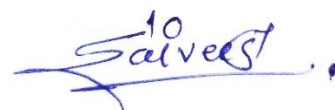Research Student

Date: 04/03/2023

**Dr. Santhosh Babu Sukumaran**

Research Supervisor

Date: 04/03/2023

# STATEMENTS OF ACADEMIC INTEGRITY

I, <u>Mr. Veer Sairam Dnyaneshwar</u>, a Ph.D. student of the Academy of Scientific and Innovative Research (AcSIR) with Registration No. <u>10CC17J26015</u> hereby undertake that, the thesis entitled <u>"New Molecular Designs for Donor-Acceptor Strapped Macromolecules and Polymers of Perylenebisimide"</u> has been prepared by me and that the document reports original work carried out by me and is free of any plagiarism in compliance with the UGC Regulations on *"Promotion of Academic Integrity and Prevention of Plagiarism in Higher Educational Institutions (2018)"* and the CSIR Guidelines for "*Ethics in Research and in Governance (2020)"*.

**Signature of the Student**
Date: 04/05/2023
Place: CSIR-NCL, Pune

It is hereby certified that the work done by the student, under my/our supervision, is plagiarism-free in accordance with the UGC Regulations on *"Promotion of Academic Integrity and Prevention of Plagiarism in Higher Educational Institutions (2018)"* and the CSIR Guidelines for "*Ethics in Research and in Governance (2020)"*.

**Signature of the Supervisor**
Name: Dr. Santhosh Babu Sukumaran
Date: 04/05/2023
Place: CSIR-NCL, Pune

# CSIR – National Chemical Laboratory

## DECLARATION

The research work embodied in this thesis has been carried out at CSIR–National Chemical Laboratory, Pune under the supervision of **Dr. Santhosh Babu Sukumaran**, Organic Chemistry Division, CSIR–National Chemical Laboratory, Pune – 411 008. This work is original and has not been submitted in part or full, for any degree or diploma of this or any other university.

4th April, 2023                                **Veer Sairam Dnyaneshwar**

CSIR–NCL, Pune                            Organic Chemistry Division

CSIR–National Chemical Laboratory

Pune–411 008

*This dissertation is dedicated to*
*-**My family, teachers and friends**-*
*Whose constant love, trust, and support*
*helped me to reach this stage of my life*

# Acknowledgement

# Acknowledgement

My special thanks to *Ravan* table members, including Dr. Milind Ahire (Master), Dr. V. Mullapudi (Babu Sir), Dr. Vivek Wakchaure, Dr. Mahesh Shinde, Dr. Pawan Dhote, Mahesh Pol, and Swapnil Halnor for the countless discussions we had over the years, I have learned so much from them and they have had a great impact on my perception towards organic synthesis and research in general. Once again I would also like to thank Dr. Mahesh Shinde and Dr. Vivek Wakchaure for supporting and encouraging me right from my bachelor's degree to introducing me to the SaBa group.

I am highly obliged to my teachers at school, college (Dr. Vijay Khanna, Dr. Shankar Thopate, Kulkarni, Deshpande, Nagawade, Rohokale, Gaikwad, Deshmukh, Kawade, Kasar, Ghumare) for their motivated teaching, advice, and encouragement.

I am lucky to have a wonderful group of friends outside the campus as a senior (Dr. Sujit (dada), Vilas, Dipak, Sunil, Rajendra, Sushil, Rohit, Dhiraj, Shailendra, Anil, and Dinesh). Master classmates like Vikas (Kalu), Shalmon, Babar, Manoj, Balasaheb, Ganesh, Gavrao (Pahilvan), and Bharti and My bachelor best buddy Dushing Vikas (Ana), Takale Mahesh (Master), Shelke Udhav (Bhau), Javle Sachin (badhree), Khomne Pratik (Balu), for energizing at the time of frustration, supporting at the time of difficulty, muttering humours at the time of leisure, and bringing full of happiness, Joy, everlasting cheerfulness in my life.

I would also like to acknowledge Dr. Sunita Barve, Mr. Gati K. Nayak, and other staff members of the library for all kinds of support and for giving access to the library.

My sincere thanks to the *Marathi@NCL* group for their support and to make my journey joyful and a memorable one.

My sincere thanks to my collaborators for their support and contributions, Dr. Sapna Ravindranathan for solving the complex macrocyclic structure NMR, Tanmoy Goswami and Prof. Hirendra N. Ghosh (INST Mohali, Punjab) for Femtosecond transient absorption spectroscopy measurements, Dr. Ruchi Dixit for their DFT calculations and Dr. Rajesh Gonnade for solving the single-crystal structure.

Special thanks must go to my colleagues from NCL Dr. Shekhar Shinde, Dr. Yogesh Marathe, Dr. Ravindar Phatake, Dr. Mote, Dr. Satish Deshmukh, Dr. Rahul Jagtap, Dnyaneshwar (Mauli), Dr. Hemant, Dr. Popat, Dr. Abdul, Dr. Amol, Dr. Bagle, Dr. Digambar, Dr. Sagar Thorat, Dr. Mahesh Pisal, Dr. Sudhakar Gaikwasd, Dr. Shrikant, Dr. Dipesh, Dr. Ashwini, Dr. Kailash, Satish, Kishor, Abha, Vibha, Sazia, Rahul (Tiger), Datta, Vishal (Jawai), Sidheshwar, Priyanka, Himanshu, Kranti, Smita, Lavanya, Prem, Manish, Pavan, Bharat, Dharmendra, Rashid, Sameer, Sachin, Nitin, Bhupendra, Christy, Ambarish, Prashant, Rohit, Anil, Sachin, Yogesh, Wale, Navnath, Uttareshwar, Ganesh, Manali, Sanket, Mayur, Bhagyashree, Apurva, Akshay, Manoj, Chaitra, Kailash, Sonu, Manoj Patil, Saroj, and Krushna.

# Acknowledgement

I would also like to thank my best friends, Mahendra Wagh, Dinesh Shinde, Bhakti Dayma, Someshwar kale, Pavan Dogapure, Ashutosh Shinde, Ranjeet Atpalkar, Dr. Balasaheb Borade, Jagjivan Sabne, and Vasudev.

I wish to convey my thanks to AcSIR coordinators Dr. B. L. V. Prasad, Dr. Mahesh Kulkarni, Dr. M. Sashidhar, Dr. Santosh Mhaske and student academic office staff, P. K. Purushothaman, Poornima Kohle, Vaishali, Komal, Vijaya, and Purnima for their help and cooperation. I also thank Mrs. Catherine and the technical team of the Organic Chemistry Division, Glass Blowing department, and DIRC, for their continuous help and support.

My family is always a source of inspiration and great moral support for me in pursuing my education. I owe a lot to my beloved family members who encouraged and helped me at every stage of my personal and academic life and longed to see this achievement come true. At this moment, I invariably feel short of words to express my sincere thanks to my father *Mr. Dnyaneshwar Gangadhar Veer*, my beloved mother *Mrs. Latabai Dnyaneshwar Veer*, my Uncle and Aunty *Bharti Nivrutti Gangadhar Veer*, *Ujwala Vasant Gangadhar Veer*, for their relentless hard work and sacrifice in bringing me up besides providing constant moral support and encouragement can hardly be acknowledged in few words. I express my deep and paramount gratitude to my brothers Mr. Manikram, Mr. Marthandaram, Mr. Chandrakant, Mr. Akshay, Mr. Dhananjay Mr. Omkar, Mr. Atharv, and all my beloved sisters like Pooja, Varsharani, Ujwala, Trupti, and Kshitija for their support in critical situations and who stood behind me throughout my Ph.D. career and became my strong moral support. I always enjoy the company of all my family members even at short stays at home and finally to the people of my village for their constant encouragement.

I am also thankful to UGC for the financial assistance in the form of a fellowship. Finally, my acknowledgment would not be complete without thanking the Almighty, for the strength and determination to put my chin up when faced with hardships in life.

I wish to thank the great scientific community whose achievements are a constant source of inspiration for me. Above all, I extend my gratitude to the Almighty God for giving me the wisdom, health, and strength to undertake this research work and enabling me to its completion.

Thank you all…!!!

Yours Sincerely

*Veer Sairam Dnyaneshwar*

# Contents:

# Contents

## Chapter-2      77-145

### Oligothiophene-Ring-Strapped Perylene Bisimides: Functionalizable Coaxial Donor-Acceptor Macrocycles

## Chapter-4, Section 2                           223-233

### Macrocycle of a Donor-Strapped Perylene Bisimide Macrocycle

**A**

| | |
|---|---|
| $\alpha$ | Alpha |
| $\text{Å}$ | Angström |
| a.u. | arbitrary unit |
| A | Acceptor (charge) |
| ACN | Acetonitrile |
| Ac | Acetyl |

**B**

| | |
|---|---|
| $\beta$ | Beta |

**C**

| | |
|---|---|
| calcd | Calculated |
| $CDCl_3$ | chloroform-d |
| CCDC | Cambridge crystallographic data center |
| CT | Charge transfer |
| CD | Circular dichroism |
| CPL | Circularly polarised luminescence |

**D**

| | |
|---|---|
| $d$ | doublet (NMR) |
| DMF | N,N-Dimethylformamide |
| DSC | Differential scanning calorimetry |
| $\delta$ | Delta chemical shift (NMR) |
| DFT | Density functional theory |
| D | Donor (charge) |
| DF | Delayed fluorescence |
| $\theta$ | Dihedral angle |

**E**

| | |
|---|---|
| ESI | Electron spray ionization |
| eV | electron-volt |
| EQE | External quantum efficiency |
| ET | Energy Transfer |
| $Et_3N$ | Triethylamine |

**F**

| | |
|---|---|
| FTIR | Fourier transform infrared |
| FRET | Förster resonance energy transfer |

**G**

| | |
|---|---|
| $T_g$ | Glass transition temperature |
| $\gamma$ | Gamma |
| G | Gauss |
| gm | Gram |

**H**

| | |
|---|---|
| h | Hour |
| $H_Z$ | Hertz |
| HRMS | High Resolution Mass Spectroscopy |

**I**

| | |
|---|---|
| ISC | Intersystem crossing |
| IC | Internal conversion |
| ICT | Intermolecular charge transfer |
| IQE | Internal quantum efficiency |

**K**

| | |
|---|---|
| K | Kelvin |

**L**

| | | | |
|---|---|---|---|
| LUMO | Lowest unoccupied molecular orbital | **S** | |
| $\lambda$ | Lambda Wavelength | s | singlet (NMR) |
| **M** | | SC | Single crystal |
| mp | Melting point | SEM | Scanning electron microscopy |
| MS | Mass spectrometry | SOC | Spin-orbit coupling |
| $T_m$ | Melting temperature | **T** | |
| MALDI-TOF MS | Matrix-assisted laser desorption ionization-time of flight mass spectrometry | t | triplet (NMR) |
| **N** | | TEM | Transmission electron microscopy |
| NIR | Near-Infrared | THF | Tetrahydrofuran |
| n-BuLi | n-butyl lithium | TGA | Thermogravimetric analysis |
| nm | Nanometer | TBAF | Tetra-*n*-butylammonium fluoride |
| NMR | Nuclear magnetic resonance | **U** | |
| **O** | | | |
| OLED | Organic light-emitting diode | UV-Vis | Ultraviolet-visible spectroscopy |
| OM | Optical Microscope | **V** | |
| OPVs | Oligo(p-phenylvinylene)s | V | Volt |
| **P** | | Vis | Visible |
| ppm | Parts per million | | |
| PL | Photoluminescence | **W** | |
| **Q** | | W | Watt |
| QY | Quantum yield | w% | Weight percentage |
| **R** | | WG | Waveguiding |
| RT | Room temperature | **X** | |
| RB | Round bottom (flask) | XRD | X-ray diffraction |

| | **Synopsis of the thesis to be submitted to the Academy of Scientific and Innovative Research for the award of the degree of Doctor of Philosophy in Sciences/ Engineering** |
|---|---|
| **Name of the Candidate** | Mr. Veer Sairam Dnyaneshwar |
| **Enrollment No. and Date** | Ph. D. in Chemical Sciences (10CC17J26015); January 2017 |
| **Title of the Thesis** | "New Molecular Designs for Donor-Acceptor Strapped Macromolecules and Polymers of Perylenebisimide" |
| **Research Supervisor** | Dr. Santhosh Babu Sukumaran (CSIR-NCL, Pune) |

1. **Introduction**: Two important classes of molecules, such as thiophene (donor) and perylene bisimide (PBIs) (acceptor), serve as the foundation for the current thesis. Perylene bisimide is one of the most extensively studied fluorescent organic dyes.[1] PBI-based materials are chemically, thermally, and photophysically stable.[2-4] The rich photo- and electrochemistry provide a wide range of features to explore, such as visible light absorption, tunable emission, and quantum yield, and characteristic long-lived excited states, as well as the ability to undergo efficient energy and electron transfer reactions, making them ideal components in synthetic donor-acceptor assemblies.[5-9] Hence, PBI-based materials, to begin with primarily used as high-quality colorants in the pigment and textile industry but recently found diverse applications in optoelectronic devices such as organic solar cells (OSCs), light-emitting diodes (OLEDs), transistors, energy storage devices, sensors, and lasers, etc.[2,6] Still there are new opportunities for PBIs to be more functional. One among them is PBI-based functionalizable macrocycles. Donor-acceptor linked $\pi$-conjugated macrocycles are inspiring as modular building blocks for the development of novel materials (1D and 2D polymers) and supramolecular structures that allow both light harvesting and excitation energy transfer and electron transfer inside the molecule's core.[10] The thesis entitled *"New Molecular Designs for Donor-Acceptor Strapped Macromolecules and Polymers of Perylenebisimide"* explores new concepts in macrocycles. The thesis is divided into four different chapters. In **chapter 1,** we describe the nature of light harvesting, facts about the excited states, and intermolecular electronic interactions. Additionally, a general overview of perylene bisimide molecules. **Chapter 2** represent, Oligothiophene-Ring-Strapped Perylene Bisimides: Functionalizable Coaxial Donor-Acceptor Macrocycles. Our macrocycle design with a supportive spatial arrangement of the donor and acceptor units will urge more complex synthetic systems with exciting electron transfer and charge separation features. In the following **Chapter 3**,

the challenge that persisted in **Chapter 2** was addressed. The design and synthesis of Donor Strapped Perylene Bisimide Macrocycle and Lemniscate Dimer with Extended Charge Separation is covered in **Chapter 3**, the new macrocycle design enables the formation of higher analogs equally capable of stabilizing the charge-separated state. In **Chapter 4**, we continue the discussion from **chapters 2** and **3** and focus on Donor-Strapped Perylene Bisimide Based Donor-Acceptor $\pi$-Conjugated Polymers and Larger Macrocycles. This chapter covers the synthesis of two new alternate donor-acceptor designs; donor-strapped acceptor polymer and a larger macrocycle of a donor-acceptor macrocycle, exhibiting high solution processability.

## 2. <u>Statement of a problem:</u>

- PBI-based $\pi$-conjugated macrocyclic compounds have been synthesized for the past few years *via* Bäuerle's[11] and Yamago's[12] approaches. Interestingly, this methodology has been utilized to create conjugated macrocycles.[13-15] However, in those cases, yield is significantly low for macrocycle formation through oligothiophenes.

- Multi-gram synthesis is not feasible.

- Würthner and co-workers reported a donor-acceptor-based perylene bisimide macrocycle containing an oligothiophene ring on the imide position that cannot be further functionalized.

- A new approach for the scalable synthesis of oligothiophene ring-strapped PBI-macrocycle is still awaiting.

## 3. <u>Objectives:</u>

- The aim of the thesis is to develop an effective method of synthesizing oligothiophene ring-strapped PBIs on the bay position to overcome the low yield via $FeCl_3$ mediated oxidative coupling reaction and Glaser-Hay coupling reaction.

- Our molecular design of the macrocycle points to the nearly orthogonal placement of donor-acceptor units, facilitating exciting electron transfer and charge separation features.

- The synthesized oligothiophene ring strapped perylene bisimide macrocycles can be further used as building blocks for the synthesis of corresponding monoimide-mono anhydride and dianhydride macrocycles, and those will serve as a precursor for the corresponding linear dimer and various 1D and 2D polymers, respectively.

> To understand the transient absorption studies of donor-acceptor-based oligothiophene strapped PBI macrocycles and their polymers.

## 4. Methodology and Results:

### Chapter 2: Oligothiophene-Ring-Strapped Perylene Bisimides: Functionalizable Coaxial Donor-Acceptor Macrocycles

Nature always inspires to draw new molecular and supramolecular designs to solve many fundamental scientific challenges. For instance, the natural photosynthetic system having long-lived charge separation (CS) is still a fascinating concept to mimic and realize in a lab. The presence of an ordered molecular unit with optimized energy leads to efficient energy, and electron-transfer (ET) processes urge the design of many synthetic analogues. A detailed understanding of the topic revealed that the preferred orientation of chromophores in donor-acceptor (D-A) assemblies support achieving long-lived CS. As a result, macrocyclic structures have gathered special attention due to their unique structure and capability to place chromophores in specific orientations, resulting in exciting optoelectronic properties. However, the synthetic challenges limit the broad exploration of such systems. Hence, we report the synthesis, crystal structure, and transient absorption of a new functionalizable macrocycle consisting of oligothiophene-ring-strapped perylene bisimide molecules **TSP1** and **TSP2**. Transient absorption features point to a sequential improvement in charge separation from the macrocycle to the corresponding dimer (**TSP1D** and **TSP2D**) and 2D-polymer (**TSP-2DP**) due to the distinct macrocycle design.



**Oligothiophene Ring Strapped Perylenebisimide Macrocycle**

$\tau_{CS}$ = 0.7 ps
$\tau_{RC}$ = 225 ps (100%)

$\tau_{CS}$ = 3.1 ps
$\tau_{RC}$ = 245 ps (100%)

$\tau_{CS}$ = 0.1 ps
$\tau_{RC}$ = 105 ps (87.9%), 840 ps (12.1%)

**Precise positioning and preferred orientation of donor and acceptor leads to ultrafast electron transfer and long lived charge separated state**
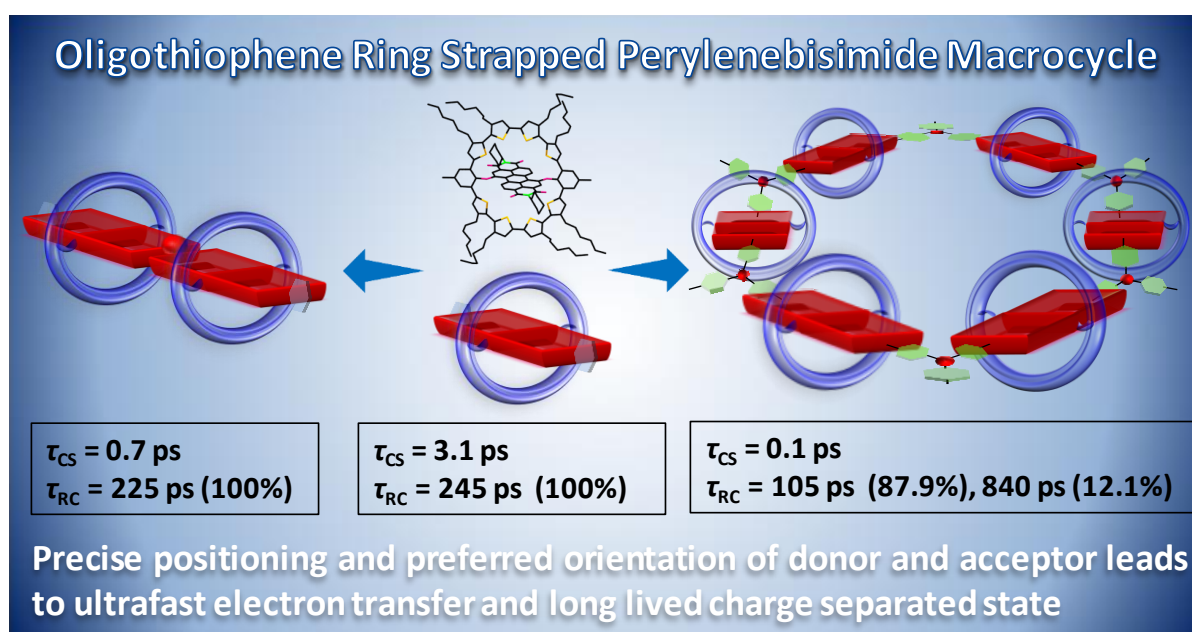
**Figure 1.** The schematic shows the correlation between the chemical structure and the TA results.

Measurements revealed that precise positioning and preferred orientation of donor-acceptor units in the three-component 2D-polymer resulted in fast charge separation ($\tau_{CS}$ ~ 0.1 ps and $k_{CS}$ ~ 10 x $10^{12}$ $S^{-1}$) and stabilized the charge-separated state ($\tau_{CR}$ ~ 105 ps (87.9 %) and 840 ps (12.1 %)) (Figure 1).

**5. <u>Summary:</u>** In conclusion, a new macrocycle with perylene bisimide perpendicular to the strapped oligothiophene ring is synthesized and studied for its ET properties by TA. A nearly orthogonal orientation of the D-A units in the macrocycle, confirmed by single-crystal X-ray analysis, results in an ultrafast ET and stabilization of the CS state for a longer duration. The unique macrocycle design achieved by the bay functionalization of PBI enabled the development of the corresponding linear dimer and 2D polymer. Precise positioning of the D-A units in the macrocycle prevents strong direct intermolecular interactions through $\pi$-$\pi$ stacking and slows down the charge recombination process. Hence, the presence of coaxial thiophene-PBI macrocycle along with a second triphenylamine donor in the three-component 2D-polymer facilitates efficient CS and its stabilization. In short, a molecular design-assisted control over the excited-state charge separation and its stabilization is demonstrated. Such a nature-inspired synthetic route toward complex structures could lead to new materials for artificial photosynthesis and organic electronics.

---------------------------------------------------------------------------------------------------------------

**Chapter 3: Donor Strapped Perylene Bisimide Macrocycle and Lemniscate Dimer with Extended Charge Separation**

Macrocyclic structures are fascinating due to their unique design and capability to place chromophores in specific orientations, resulting in exciting optoelectronic properties. However, the synthetic challenges limit the broad exploration of such systems. Herein, the continuation with chapter 2, we report a diacetylene-thiophene-ring strapped perylene bisimide macrocycles such as **SP1, SP2 and SP2D** and its notably different electron transfer features. Single-crystal analysis of the macrocycle points to the nearly orthogonal placement of donor-acceptor units, facilitating better electronic communication between them. Interestingly, introducing an alkyl substituent on the peripheral thiophene ring opened the possibility of forming a higher oligomer macrocycle consisting of multiple strapped perylene bisimide units. Diffusion and two-dimensional NMR experiments provided insight into the structure of the figure-eight-shaped lemniscate dimer. Transient absorption measurements showed faster electron transfer and extended stabilization of the charge-separated state. The

thiophene-diacetylene-based ring is a better donor unit to facilitate rapid electron transfer and long-lived charge separation in the macrocycle and its lemniscate dimer. The new macrocycle design enables the formation of higher analogs equally capable of stabilizing the charge-separated state.



**Figure 2.** Chemical structures of donor strapped perylene bisimide macrocycle

**5. <u>Summary:</u>** In conclusion, we describe the synthesis, crystal structure, and transient absorption studies of novel thiophene-diacetylene strapped perylene bisimide macrocycles. Single-crystal X-ray analysis shows the preferred perpendicular orientation of the planar perylene bisimide inside the thiophene diacetylene ring. The presence of an alkyl chain on the thiophene ring enables the formation of higher oligomers such as a dimer, trimer, and tetramer. Transient absorption studies point to the stabilization of the charge-separated states due to the unique macrocycle design. Though the placement of chromophores in the preferred orientation in macrocycles is challenging, here, it is achieved through a unique molecular design. Hence, it supports the electronic communication between the donor-acceptor units in the molecule and enables fast electron transfer. Besides, it results in the formation of a higher analog, figure-eight-shaped lemniscate dimer with similar electron transfer and stabilization of the charge-separated states. The concept of functionalizable macrocycles offers the inclusion of multiple donor-acceptor units in a single system and, at the same time, delivers exciting electron transfer features due to the unique positioning in the macrocycle. Such larger multicomponent macrocyclic systems are of fundamental importance and pave the way for futuristic applications.

**Chapter 4: Donor-Strapped Perylene Bisimide Based Donor-Acceptor $\pi$-Conjugated Polymers and Larger Macrocycles.**

Over the past decade, significant developments have been achieved in understanding the structure-function correlations determining material performance in organic electronics.[16] $\pi$-conjugated polymers and small molecules, which can be solution-processed over large-area substrates, are essential building blocks in developing printed light-harvesting technologies and mechanically conformable circuit logics.[16,17] Consequently, high-throughput processing techniques, including spin coating, inkjet printing, gravure printing, and flexographic printing, can be used to create these devices on flexible substrates.[17] Recently, optoelectronic devices based on conjugated polymers are an effective alternative to microelectronics based on inorganic materials because of their affordability, lightweight, broad absorption of light, high charge carrier advantages, mobilities, and flexibility.[18] Therefore, conjugated polymer-based organic light-emitting diodes (OLEDs), organic photovoltaic cells (OPVs), and organic field-effect transistors (OFETs) are slowly but surely making their way onto the market.[18,19] In this context, we continue with the similar molecular components from chapters 2 and 3 in the final **Chapter 4.**
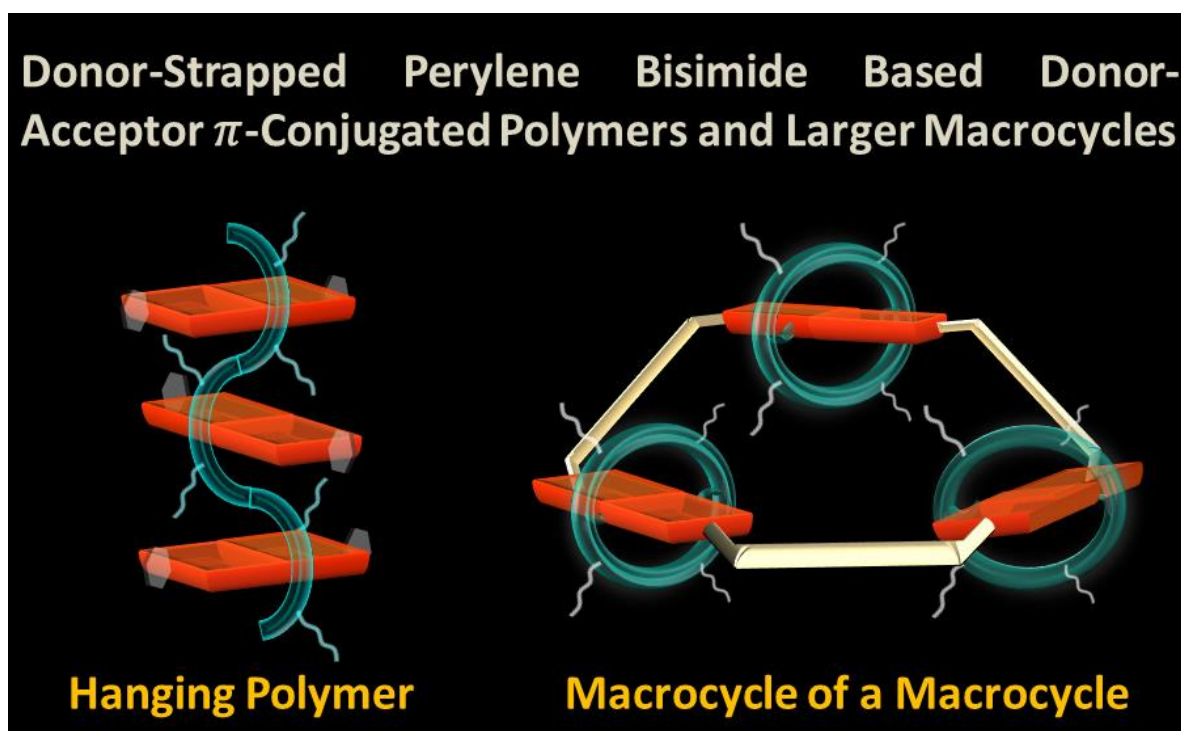


**Figure 3.** Perylene bisimide based donor-acceptor π-conjugated polymers.

In light of the above discussion, we have designed, synthesized, and characterized four novel polymers (**P1-P4**) embedding a perylene bisimides (PBIs) acceptor along with the donor

segments by changing the orientation of thiopheneacetylene and bithiophene moieties as a spacer with respective to PBIs. Our strategy synthesized a two-hanging and two-linear extended π-conjugated copolymer based on donor and accepter unit *via* Hay-Glaser and oxidative coupling reaction. For improved solubility, we have inserted a long branched alkyl chain into the PBI unit and a $C_6$ alkyl chain into the thiophene and bithiophene groups. The structural architecture allowed for easy tuning of the energy levels of the resultant polymers. All polymers exhibited excellent thermal, electrochemical, and photostabilities and high solubilities in dichlorobenzene, $CHCl_3$, THF, and chlorinated aromatic solvents. Applying these electron acceptor polymers combined with suitable donor polymers to electron mobility was also investigated.

**5. Summary:** In summary, we successfully synthesized and characterized four alternating D-A π-conjugated polymers using PBI as the "acceptor" unit and thiophene as the "donor" unit. The synthetic difficulties in developing these highly electron-deficient PBI-based polymers were successfully overcome *via* Hay-Glasear and Oxidative coupling reaction at room temperature, greatly enlarging the library of bay functionalized π-conjugated materials. All synthesized polymers are readily soluble in chloroform, THF, $CH_2Cl_2$, and chlorobenzene solvents and can readily be processed by solution-casting. These studies set molecular design guidelines for the subsequent generation of D-A conjugated polymers by illustrating clearly the connection between the polymer's backbone structure and the length of the polaron delocalization.

**6. Future directions:** Macrocycles have gathered exceptional attention due to their unique structure in which one can place chromophores in specific orientations, to achieve exciting optoelectronic properties. Such aesthetic molecular designs inspired by natural assemblies will deliver efficient donor-acceptor systems for advanced applications. Here, we desing and synthesized the Oligothiophene-Ring-Strapped Perylene Bisimides: A Functionalizable Co-axial Donor-Acceptor Macrocycle (**Chapter 2)** showed a molecular design-assisted control over the excited-state charge separation and its stabilization is demonstrated. Continution to previous chapter, we synthesized anather rigid mactrocycles. The molecular structure of the macrocycle with the diacetylene-thiophene-ring- strapped perylene bisimide is discussed here (**Chapter 3**). As a result, it facilitates electronic communication and allows fast electron transfer between the donor and acceptor units of the molecule. Such a nature-inspired synthetic route toward complex structures could produce new materials for artificial photosynthesis and organic electronics. As described in **Chapter 4**, perylene bisimide-based

donor-acceptor π-conjugated polymers have great attention because of their potential for use in low-cost, lightweight, solution-processable and flexible large-area panels. Due to this, an alternating copolymer of perylene bisimide and bithiophene building blocks will promise electron-transport materials for n-channel OFETs, organic solar cells and electron-transport materials for TA.

## 7. <u>Publications:</u>

1. K. C. Ranjeesh, R. Illathvalappil, **S. D. Veer**, J. Peter, V. C. Wakchaure, Goudappagouda, R. J. Vipin, S. Kurungot, S. S. Babu, Imidazole-Linked Crystalline Two-Dimensional Polymer with Ultrahigh Proton-Conductivity, *J. Am. Chem. Soc.* **2019**, *141*, 14950-14954.

2. V. C. Wakchaure, **S. D. Veer**, A. D. Nidhankar, Goudappagouda, R. A. Nayak, K. Asokan, S. Ravindranathan and S. S. Babu, Donor-acceptor based solvent-free organic liquid hybrids with exciplex emission and room temperature phosphorescence, *Chem. Commun.*, **2022**, *58*, 1998-2001.

3. **S. D. Veer**, V. C. Wakchaure, K. Asokan, R. Dixit, T. Goswami, R. Saha, R. Gonnade, H. N. Ghosh, S. S. Babu, Oligothiophene Ring Strapped Perylene bisimides: A Macrocycle Towards Co-axial Donor-Acceptor Design, *Angew. Chem. Int. Ed.* **2023**, e202212934.

4. **S. D. Veer**, T. Goswami, S. Ravindranathan, R. Gonnade, R. Dixit, H. N. Ghosh, S. S. Babu, Donor Strapped Perylene Bisimide Macrocycle and Lemniscate Dimer with Extended Charge Separation, *Org. Chem. Front*. **2023**, DOI: 10.1039/d3qo01060k.

5. **S. D. Veer**, V. C. Wakchaure, A. D. Nidhankar, V. Kumar, S. S. Babu, Polymerizable Solvent-free Organic Liquids: New Approach for Large Area Flexible and Foldable Luminescent Films, *Angew. Chem. Int. Ed.* **2023**, *e202307381.*

6. A. D. Nidhankar, Goudappagouda, P. Kothavade, S. D. Dongre, **S. D. Veer**, S. R. Dash, K. Rajeev, K. N. N. Unni, K. Shanmuganathan and S. S. Babu, Thermally Activated Delayed Fluorescent Solvent-free Organic Liquid Hybrids for Tunable Emission Applications, *Chem. Asian J.* **2023**, *e202300276.*

7. **S. D. Veer**, Thanasekar C, T. Goswami, H. N. Ghosh, S. S. Babu, Donor-Strapped Perylene Bisimide Based Donor-Acceptor π-Conjugated Polymers, *(Manuscript Submitted)*

8. **S. D. Veer**, T. Goswami, H. N. Ghosh, S. S. Babu, Shape Controlled Synthesis of Oligothiophene-Ring-Strapped Pyrene Macrocycles. *(Manuscript Submitted)*

## 8. References:

1. Guo, X. et. al. *Chem. Rev*. **2014**, *18*, 8943-9012.

2. Würthner, F. et. al. *Chem. Rev.* **2016**, *116,* 962-1052.

3. Würthner. F. *Chem. Commun.* **2004**, *14*, 1564-1579.

4. Spenst, P. et. al. *J. Photochem. Photobiol. C Photochem. Rev.* **2017**, *31*, 114-138.

5. Barendt, T. A.et. al. *J. Am. Chem. Soc.* **2017**, *139*, 9026-9037.

6. Huang, C. et. al. *J. Org. Chem.* **2011**, *76*, 2386-2407.

7. Schwartz, P. –O. et. al. *J. Am. Chem. Soc.* **2014**, *136*, 5981-5992.

8. Dössel, L. F. et. al. *J. Am. Chem. Soc.* **2012**, *134*, 5876-5886.

9. Lee, K. J. et. al. *Phys. Chem. Chem. Phys.* **2016**, *18*, 7875-7887.

10. a) Becker, K. et. al. *Angew. Chem. Int. Ed*. **2007**, *46*, 3450-3455, b) Sakida, T. et. al. *Angew. Chem. Int. Ed*. **2011**, *50*, 2280-2283, c) Schlosser, F. et. al. *Chem. Sci.,* **2012**, *3*, 2778-2785.

11. Zhang, F. et. al. *Angew. Chem. Int. Ed*. **2009**, *48*, 6632-6635

12. Iwamoto, T. S. et. al. *J. Am. Chem. Soc*. **2011**, *133*, 8354-8361.

13. Bold, K. et. al. *Angew. Chem. Int. Ed.* **2022**, *61*, e202113598.

14. Ball, M. L. et. al. *J. Am. Chem. Soc.* **2018**, *140*, 10135-10139.

15. Ball, M. et. al. *J. Am. Chem. Soc.* **2015**, *137*, 9982-9987.

16. a) X. Zhao, X. Zhan, *Chem. Soc. Rev*. **2011**, *40*, 3728, b) A. C. Arias, J. D. MacKenzie, I. McCulloch, J. Rivnay, A. Salleo, *Chem. Rev*. **2010**, *110*, 3-24.

17. a) A. J. Heeger, *Chem. Soc. Rev*. **2010**, *39*, 2354, b) A. Facchetti, *Chem. Mater*. **2011**, *23*, 733-758.

18. C. Wang, H. Dong, W. Hu, Y. Liu, D. Zhu, *Chem. Rev*. **2012**, *112*, 2208-2267.

19. A. Pron, P. Gawrys, M. Zagorska, D. Djurado, R. Demadrille, Chem. *Soc. Rev*. **2010**, *39*, 2577.

# Chapter 1: Section 1

# Nature Insights: Photoexcited State Progresses in Molecular Assemblies

## 1.1.1. Introduction

In biological molecules, the transport of electrons has spurred innovative and enthusiastic ideas for developing chemical systems with similar performance. In photosynthesis, two thermodynamically challenging processes - 1) water oxidation and 2) carbon dioxide reduction - are carried out by combining light harvesting, separation of photoinduced charges, and catalysis.[1,2] Moreover, photo-driven electron transfer (ET) in natural and synthetic donor-acceptor (D-A) motifs has garnered much attention because of its importance in complex biological processes such as photosynthesis,[2] as well as solar light harvesting,[3] and its implications in the development of novel molecular machines for efficient light-to-energy conversion. However, numerous researchers are exploring new approaches to the fundamentals of electron-transfer reactions in streamlined model systems due to the significance and complexity of these activities in nature. This research has mainly focused on exploring photoinduced charge separation processes as a method of absorbing and storing solar energy.[4] The long-term objective of this study is to achieve sufficiently sophisticated knowledge of photoinitiated electron transfer processes to develop laboratory systems for transforming solar energy into chemical potential.[4,5] A key source of inspiration for the invention of artificial photosynthetic systems is the molecular mimicry of natural photosynthesis, in which successive energy and electron transfer cascades promote long-lasting charge separation (CS) with 100% efficiency.[5-7]

Hence to study in detail and to investigate how the distance and orientation of donor-acceptor units, electronic coupling, and free energy of the reaction affect the electron-transfer rate constants, synthetic D-A units have been designed.[8] The components required for bio-inspired units involving photochemical solar energy conversion are high electronic absorptions that cover the solar spectrum, ease of synthesis, and stability. As in photosynthetic reaction center proteins, multicomponent D-A units that work in multistep charge-separation reactions are well suited for the production of long-running charge-separated states.[6,7] Modern molecular scale applications in optoelectronics, photonics, and semiconducting might be affected by progress in research aimed at removing barriers in this area.

## 1.1.2. Natural Light Harvesting

In most photosynthetic organisms, light harvesting is a very effective process. Particularly well-tuned mechanisms are the first stages of photosynthesis's light phase, the capture of light quanta, and the fundamental charge separation process.[5-7] The quantum efficiency of these fundamental processes occurring within the photosystems in plants is remarkable, achieving 80% and 100% in photosystems II and I, respectively.[9] One of the best examples of the effective use of solar energy in nature is the light-collecting process used by photosynthetic bacteria, algae, and plants.[10]  Globally, the photosynthetic mechanism converts energy from sunlight into a proton descent over the cellular membrane that drives a variety of chemical activities necessary for the efficient conversion of light into biomass at a rate of $1.2 \times 10^{11}$ terawatts (TW) per year (about 50 times the energy consumed by humans).[10-12]
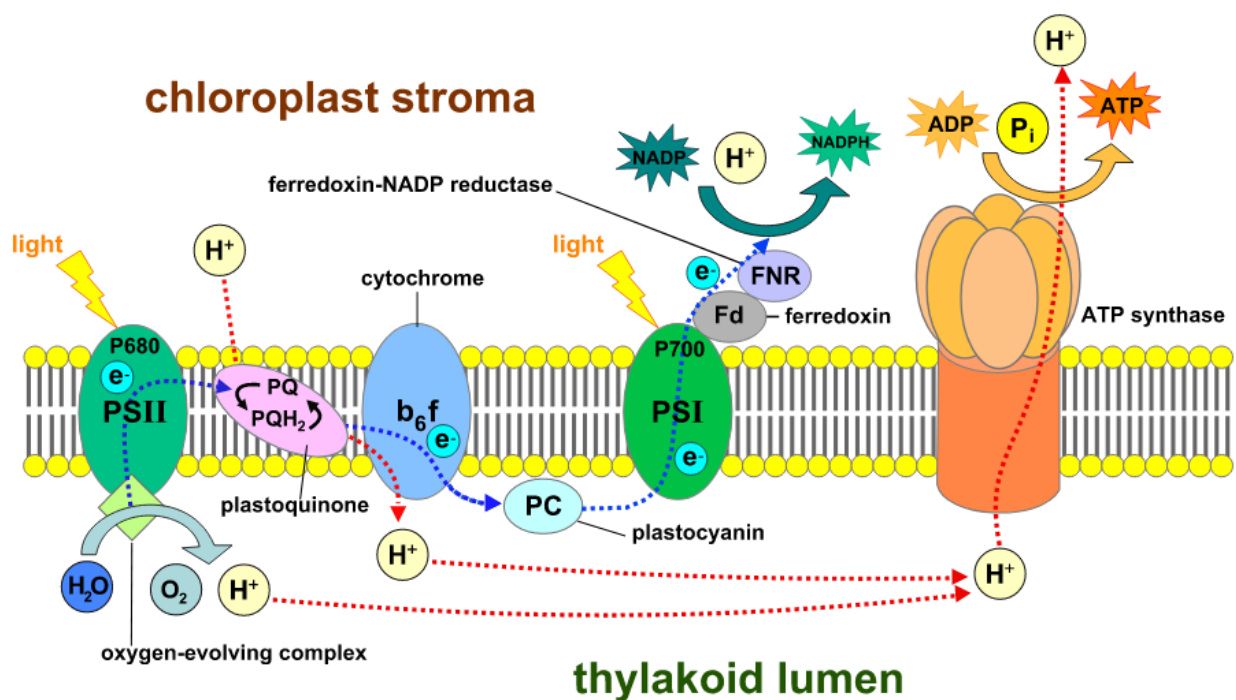


**Figure 1.1.1.** Light-dependent reactions of photosynthesis at the thylakoid membrane

The process of turning sunlight into chemical energy takes place in and around the thylakoid membranes of all organisms that engage in oxygenic photosynthesis and is referred to as the "light reactions" (Figure.1.1.1). During the water oxidation into oxygen, oxygen evolving complexes (OEC) present in photosystem II (PSII) combine with the holes. Ferredoxin NADP+ reductase in photosystem I (PSI) absorbs the protons and electrons produced by water oxidation

to make NADPH. Nature has created intricate biological material that will transform carbon dioxide gas into carbohydrates for $CO_2$ fixation (Figure 1.1.1).[10,11]

## 1.1.3. Artificial Photosynthetic Systems

From a future point of view, the development of reusable energy sources has become crucial for our planet. Traditional energy sources, including nonrenewable energy sources, were utilized in various industries. Fossil fuels would eventually run out since they are a limited resource. Solar energy is a renewable, non-depletable resource that meets about 10000 times the daily world energy consumption. Therefore, if solar energy can be captured and used effectively, it can supply all of our energy needs.[10] Solar energy harvesting, charge separation, and redox reactions The three main solar energy conversion processes such as solar energy harvesting, separation of charges, and oxidation-reduction reactions are mainly used in solar energy conversion processes, and they are all extremely effective.[10-12] Thus, "artificial photosynthesis" has emerged as an interesting field of research in the upcoming years. It focuses to understand these processes in plants and other organisms involved in photosynthesis and to imitate their mechanism of solar-energy conversion in similar man-made models and systems, without compromising on efficiency level for scale-up application. [3,13]

## 1.1.3.1. Designing Artificial Photosynthetic Systems

The fundamentals of photosynthesis are utilized to develop artificial photosynthesis for the production of solar fuels, including a) effective solar harvesting; b) the generation of CS states; and c) water splitting, hydrogen and oxygen gas as well as carbon dioxide fixing into high value-added products like $CH_4$, $CH_3OH$, HCOOH, etc. (Figure 1.1.2).[10-13] These are three basic pathways of photo electrolysis (PE),[14] which uses electrodes with extra electrical energy called photocatalysts, photovoltaic electrolysis (PV),[15] which uses solar energy cells to power an electrolyzer, and photocatalysis (PC), which alters the rate of a photoreaction.[16] This concept presents some fundamental understandings for developing artificial photosynthesis. For constructing a promising artificial photosynthesis system, we need to pay particular attention to five essential aspects, as shown in Figure 1.1.2) Catalyst development is essential for using stable, affordable, and abundant materials on Earth as photocatalysts across the entire solar spectrum. 2) Manufacturing devices, taking scale-up applications into account, especially from a system engineering perspective. 3) Designing device architecture; which is essential for

improving photocatalytic activity.[10] 4) Exploration of mechanisms; the novel, recently discovered mechanisms that are significant and helpful will be represented in addition to previously established ones. Photoreduction of $CO_2$ is challenging.[17] 5) Theoretical investigations; Computational research is a useful tool for understanding the oxidation-reduction properties of photocatalysts, including band gap, group-edge orientations, optical absorbance, and so on. Thus, when combined with experimental techniques, high-throughput computational calculations may quickly be able to anticipate both favorable and unfavorable candidates, which can speed up the discovery of potential photocatalytic applications.[18]
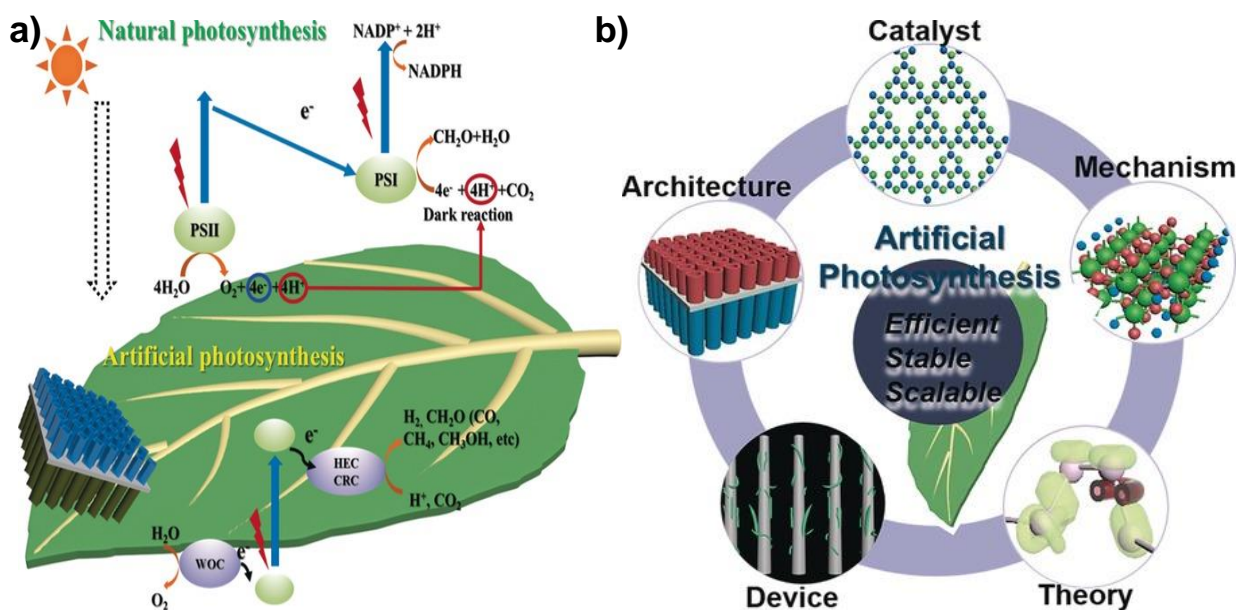


**Figure 1.1.2.** a) From natural to artificial photosynthetic systems, generalized schematic illustration of AP. WOC = water-oxidation catalyst, HEC = $H_2$ - evolution catalyst, CRC = $CO_2$ - reduction catalyst. b) Schematic illustration of the five important aspects for artificial photosynthetic systems.

## 1.1.3.2. Comparison of Natural and Artificial Photosynthesis

In biological systems, energy is captured during photosynthesis in the form of excited molecular states. When these excited states reach reaction sites, the excitons is divided into a hole and an electron *via* electron transfer to a specific molecular electron acceptor. The excited states then travel through molecules until they reach their destination. This splitting of the exciton process results in a maximum energy loss of ~ 200 mV, which is far less than what it costs to split the exciton in solid-state silicon-based devices (Figure 1.1.3).[10] In these systems, specific chemical

species transport electrons, like the Quinone and Cytochrome, shuttles functioning in the electron transport chain of photosynthetic and mitochondrial membranes.[10-12] Precise molecular identification is utilized in photosynthesis and oxidative phosphorylation to prevent undesirable side reactions and "short circuits" and direct electrons to the precise locations required for the intended biochemical reaction. Molecular recognition serves as the biological equivalent of the wires in human-engineered systems and is a vital aspect of their operation. Furthermore, biological systems normally function at ambient pressures and temperatures, with a pH close to neutral, while utilizing only abundant earth resources. Future developments in the transmission of energy in technology will be motivated by these unique biological characteristics.[11] In contrast to biological systems, technological systems use electromotive force (emf) to move electrons down a wire.[14,15] The direction of electron flow is determined by the electrical circuit rather than molecular recognition. As demonstrated by the electronics industry, modern technologies are capable of building very complicated circuits that deliver electrons to precise locations.[13] However, advanced semiconductors are still unable to match the atomic-scale accuracy found in biological 'circuits.' Similarly, technological systems can still not benefit from some of the most remarkable features of biology, such as proton motive force (pmf) driven reactions, precise control of proton activity, and three-dimensional catalyst structures. [14c,16b,19] Considering these aspects, there is much to learn and be inspired by nature. Humans can now manipulate matter on a scale comparable to that of the biological mechanism of life because of recent developments in nanotechnology.[19] As this science develops, it can be possible for technology to create intricate, self-assembling, self-repairing materials that have traditionally been the domain of biological systems.[3,13] The creation of artificial systems will be guided by the fundamental design principles derived from in-depth knowledge of natural systems.[1,3] The study of artificial systems, on the other hand, will increase our knowledge or understanding of complicated biological machinery and ultimately our ability to regulate it.
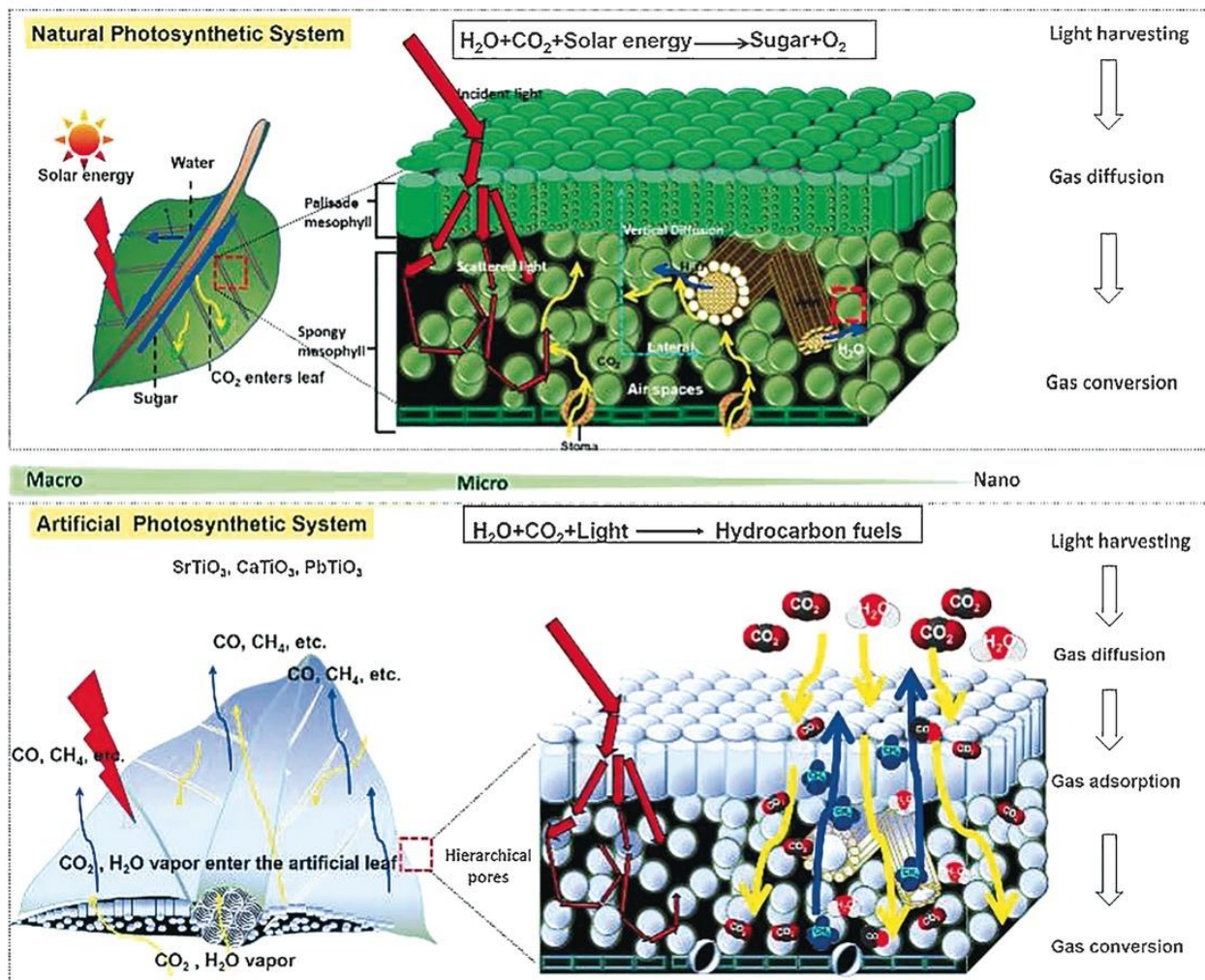
**Figure 1.1.3.** Schematic illustration of the key steps in natural and artificial photosynthetic systems.

## 1.1.4. References

1.  M. R. Wasielewski, *J. Org. Chem*. **2006**, *71*, 5051-5066.

2.  H. B. Gray, J. R. Winkler, *Chem. Phys. Lett*. **2009**, *483*, 1-9.

3.  D. Gust, T. A. Moore, A. L. Moore, *Acc. Chem. Res*. **2001**, *34*, 40-48.

4.  M. R. Wasielewski, *Acc. Chem. Res*. **2009**, *42*, 1910-1921.

5.  M. R. Wasielewski, *Chem. Rev*. **1992**, *92*, 435-461.

6.  T. Mirkovic, E. E. Ostroumov, J. M. Anna, R. van Grondelle, Govindjee, G. D. Scholes, *Chem. Rev*. **2017**, *117*, 249-293.

7.  G. Kodis, Y. Terazono, P. A. Liddell, J. Andréasson, V. Garg, M. Hambourger, T. A. Moore, A. L. Moore, D. Gust, *J. Am. Chem. Soc*. **2006**, *128*, 1818-1827.

8.  S. Fukuzumi, K. Ohkubo, T. Suenobu, *Acc. Chem. Res*. **2014**, *47*, 1455-1464.

9.  Y. Wang, B. Tang, S. Zhang, *RSC Adv*. **2012**, *2*, 5964.

10. a) M. Hambourger, G. F. Moore, D. M. Kramer, D. Gust, A. L. Moore, T. A. Moore, *Chem. Soc. Rev*. **2009**, *38*, 25-35; b) Y. Tachibana, L. Vayssieres, J. R. Durrant, *Nat. Photonics* **2012**, *6*, 511-518; c) H. Zhou, R. Yan, D. Zhang, T. Fan, Chem. *Eur. J*. **2016**, *22*, 9870-9885; d) M. Antonietti, *Angew. Chem. Int. Ed*. **2013**, *52*, 1086-1087.

11. J. Strümpfer, M. Şener, K. Schulten, *J. Phys. Chem. Lett*. **2012**, *3*, 536-542.

12. Mirkovic, T.; Scholes, G. D., Photosynthetic Light Harvesting. in Photobiology: The Science of Light and Life, Björn, L. O., Ed. Springer New York: New York, NY, 2015; 231-241.

13. a)T. Faunce, S. Styring, M. R. Wasielewski, G. W. Brudvig, A. W. Rutherford, J. Messinger, A. F. Lee, C. L. Hill, H. deGroot, M. Fontecave, D. R. MacFarlane, B. Hankamer, D. G. Nocera, D. M. Tiede, H. Dau, W. Hillier, L. Wang, R. Amal, *Energy Environ. Sci.* **2013**, *6*, 1074; b) S. S. Mao, S. Shen, Nature Photon 2013, 7, 944–946. c) T. R. Anderson, T. A. Slotkin, *Biochem Pharmacol* **1975**, *24*, 1469-1474; d) M. D. Kärkäs, O. Verho, E. V. Johnston, B. Åkermark, *Chem. Rev.* **2014**, *114*, 11863-12001; e) D. Kim, K. K. Sakimoto, D. Hong, P. Yang, *Angew. Chem. Int. Ed*. **2015**, *54*, 3259-3266.

14. a) K. Sivula, F. Le Formal, M. Grätzel, *ChemSusChem* **2011**, *4*, 432-449; b) A. Paracchino, V. Laporte, K. Sivula, M. Grätzel, E. Thimsen, *Nature Mater* **2011**, *10*, 456-461; c) M. Woodhouse, B. A. Parkinson, *Chem. Soc. Rev*. **2009**, *38*, 197-210.

15. a) M. Graetzel, R. A. J. Janssen, D. B. Mitzi, E. H. Sargent, *Nature* **2012**, *488*, 304-312; b) O. Khaselev, J. A. Turner, *Science* **1998**, *280*, 425-427.

16. a) K. Maeda, K. Domen, *J. Phys. Chem. Lett*. **2010**, *1*, 2655-2661; b) T. Hisatomi, J. Kubota, K. Domen, *Chem. Soc. Rev*. **2014**, *43*, 7520-7535; c) S. J. A. Moniz, S. A. Shevlin, D. J. Martin, Z.-X. Guo, J. Tang, *Energy Environ. Sci*. **2015**, *8*, 731-759; d) K. Maeda, K. Teramura, D. Lu, T. Takata, N. Saito, Y. Inoue, K. Domen, *Nature* **2006**, *440*, 295-295.

17. a) S. J. Hamrock, M. A. Yandrasits, Journal of Macromolecular Science, Part C: *Polymer Reviews* **2006**, *46*, 219-244; b) B. C. H. Steele, A. Heinzel, *Nature* **2001**, *414*, 345-352.

18. W. J. Jo, H. J. Kang, K.-J. Kong, Y. S. Lee, H. Park, Y. Lee, T. Buonassisi, K. K. Gleason, J. S. Lee, *Proc. Natl. Acad. Sci. U.S.A*. **2015**, *112*, 13774-13778.

19. BESAC Subcommittee on Grand Challenges for Basic Energy Sciences, Directing Matter and Energy: Five Challenges for Science and the Imagination, US Department of Energy, **2007**.

# Chapter 1: Section 2

# Progress in the Synthesis of Perylene Bisimide dyes

## 1.2.1. Introduction

The development of scientific and industrial dyes and pigments has given much attention to dyestuffs based on perylene tetracarboxylic acid bisimide or perylene bisimide.[1,2] PBIs are among the most well-known members of the polyaromatic hydrocarbon family, much as porphyrins, cobalamins, and phthalocyanines, which are significant representatives of the tetrapyrrole color class.[2] Moreover, PBIs are a preferred chromophore due to their excellent chemical and thermal stability, wide spectrum of visible light absorption, and distinctive electrochemical properties. This remarkable function of PBIs has evolved not only due to their characteristics but also as an outcome of the phenomenal advancement in synthetic chemistry for these classes of dyes, particularly in the recent decade. PBIs are currently the focus of intensive research in the field of functional organic optoelectronics materials, initially being utilized only as red pigments and commercial pigments. In light of this, while the first 70 years of PBI research were devoted to changed imide substituents[3] (regulate their solubility), which is essential to achieve the desired color, functionalizations of the electron-withdrawing aromatic core (*bay* as well as *ortho* sides) were only addressed relatively to modify the fluorescence and redox properties. [3,4] It has taken another 20 years to develop synthetic methods to functionalize a specific area of the PBI aromatic ring. This study was driven by the use of PBIs in electronic devices, solar energy systems, photonics, and as substrates for supramolecular photosystems.

## 1.2.2. Core-substituted Perylene Bisimide

As can be seen in Figure 1.2.1, which describes the structure of perylene-3,4,9,10-tetracarboxylic dianhydride (PTCDA), It is regarded as the parent molecule of this class of basic PBI dyes, with the different location indicated with numbers. Modification of substituents in the imide N,N'-region and the 1, 6, 7, and 12 regions of the hydrocarbon core ("bay" region) and 2, 5, 8, and 11 regions of the hydrocarbon core ("ortho" region) has resulted in PBIs with various chemical and physical properties.[3-6] According to the distributions of the HOMO, LUMO, and theoretical studies, clearly shows that there is no electronic connection between the PBI core and any of the substituents linked to the imide nitrogen. [6-8] As a result, the imide substituent has a very small impact on the LUMO energy level, which is unaffected by the corresponding alkyl or aryl functional group, and this impact is observed in the absorption spectrum of dichloromethane is placed at  524, and 527 nm.[9] The perylene "ortho" positions 2, 5, 8, and 11 are now

functionalized using a wide range of methods, including arylation and alkylation,[10] borylation,[11] hydroxylation, [11] halogenation,[12] cyanation,[12] and amination.[13] It is interesting to note that while some of these substituents significantly reduce the fluorescence quantum yields, others have little effect on the region of the absorption max. (505 nm for tetra-chlorinated derivatives, 512 nm for tetraminated derivatives, and 520 nm for tetracyanated derivatives), somewhat dissimilar from those for the corresponding bay-functionalized regioisomers.
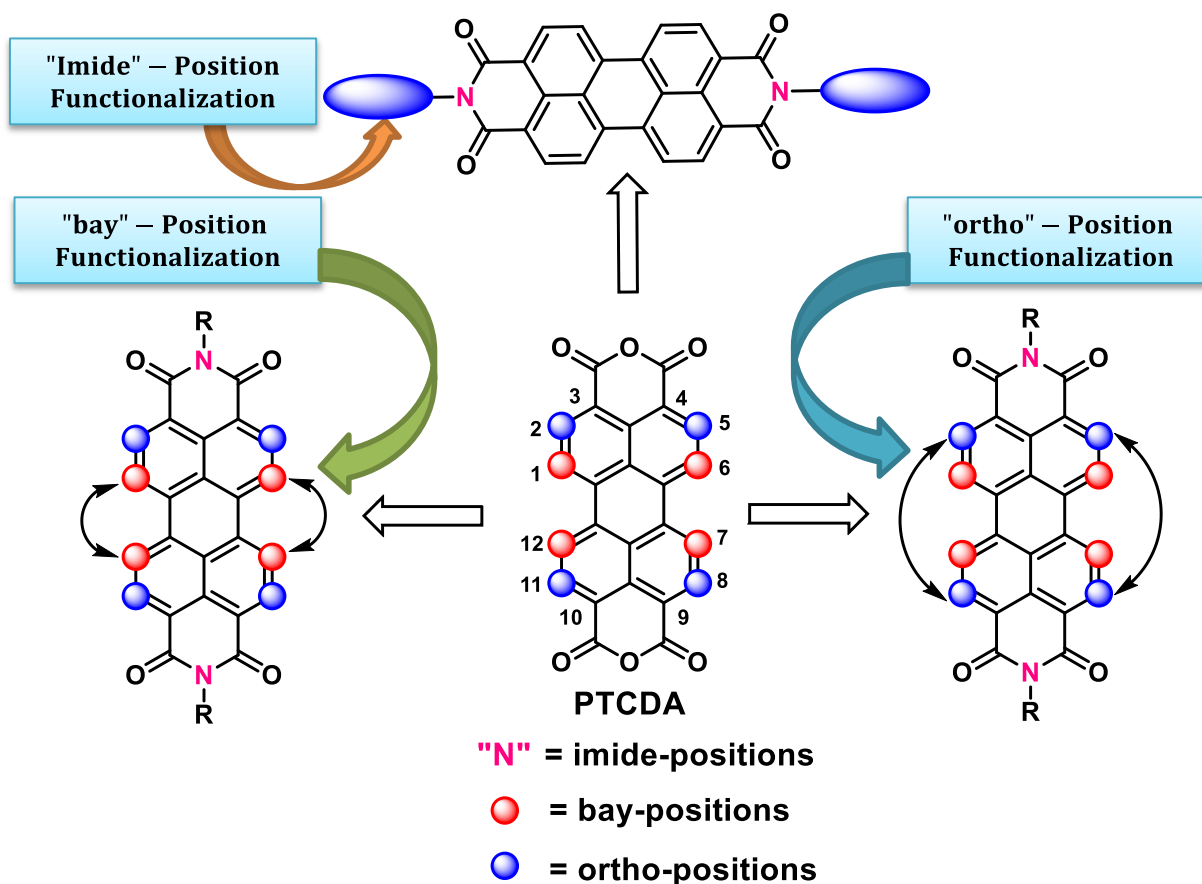


**Figure 1.2.1**. Chemical modification of PBIs

## 1.2.3. Perylene Bisimide

Perylene, a stiff polycyclic aromatic structure, is functionalized at the 3,4- and 9,10-peri-region containing two biscarboxylic acid imide groups is what gives PBI their adaptability for such a wide and varied range of applications (Figure 1.2.1 and 1.2.2). The strong conjugation occurs between the electron-donor perylene core and the effective electron-acceptor imide group (A-D-A scaffold) increases the PBI absorption spectrum band from 435 to 525 nm (Figure 1.2.2).[6,8] Still, the aromatic scaffold's characteristic vibronic progressions are virtually intact. The mirror

image fluorescence of PBI chromophore, with a luminescent quantum yield of (nearly), is one of its most prominent features.[3] High luminescent quantum yields for PBIs have been reported in all widely known solvents, namely alkyl, heterocyclic, chlorinated, and polarisation solvents.[5] This chromophore is remarkable for a variety of applications, the most significant of which are red shade color pigments[4] and light emitters, including for single molecule spectroscopy.[14] It exhibits strong temperature, chemical, and photochemical persistence. Due to the electron-deficient nature of the π-conjugated framework, which makes it highly resistant to the oxidation process and other decomposition mechanisms, this dye has an incredibly high degree of stability. The properties of the electron-deficient material are confirmed by experiments involving cyclic voltammetry. According to CV results, all PBIs-based materials have two reversible reduction peaks around -1.0 V and -1.2 V in dichloromethane solvent v/s the ferrocene/ferrocenium redox potential (Figure 1.2.2).[7] The electronic properties of PBIs, such as energy levels and redox potentials, are typically not significantly affected by functionalized at the two imide region. As a result, molecule absorption and emission characteristics are not significantly altered. This is because, as shown in figure 1.2.2.[6-8] The HOMO and LUMO orbital nodes are located in the imide region. Unlike fullerenes, air-stable organic semiconductor devices with significant electron mobility can be created by modifying the packing arrangement and the placement of the LUMO level. The latter was accomplished by simply substituted at the ortho- or bay-region of the PBI aromatic core with the different functional chromophores.[8]

## 1.2.4. History

The PTCDA was initially discovered in the early 1910s (Figure 1.2.1).[7,15] PTCDA is the starting material for synthesizing PBI derivatives in research and industry. As per Scheme 1.2.1, PTCDA is commercially produced by oxidizing acenaphthene to obtain naphthalene monoanhydride (NMO), which is subsequently subjected to ammonium hydroxide to obtain naphthalene monoimide (NMI). At 200 °C, the naphthalene imide molecules were reacted with potassium hydroxide to produce perylene-3,4,9,10-tetracarboxylicdiimide (PTCDI). Finally, PTCDA is obtained when concentrated sulfuric acid is used to hydrolyze PTCDI at a temperature of about 220 °C. PTCDA can react with different alkyl amines or aromatic amines can yield soluble symmetrical organic PBI with high melting temperatures and high yields, which is useful in the color and dyestuff industries.[2] colorant red 179, also known as dimethyl substituted PBI,

was initially reported in 1913 and is primarily utilized as an industrial pigment.[2] Chemical, thermal, optical, and weather stability are all outstanding attributes of these pigments.[2,7] Furthermore, after painting on plastics and glass, PBI-based paints have great migration stability and can be quickly overcoated onto other painted surfaces.
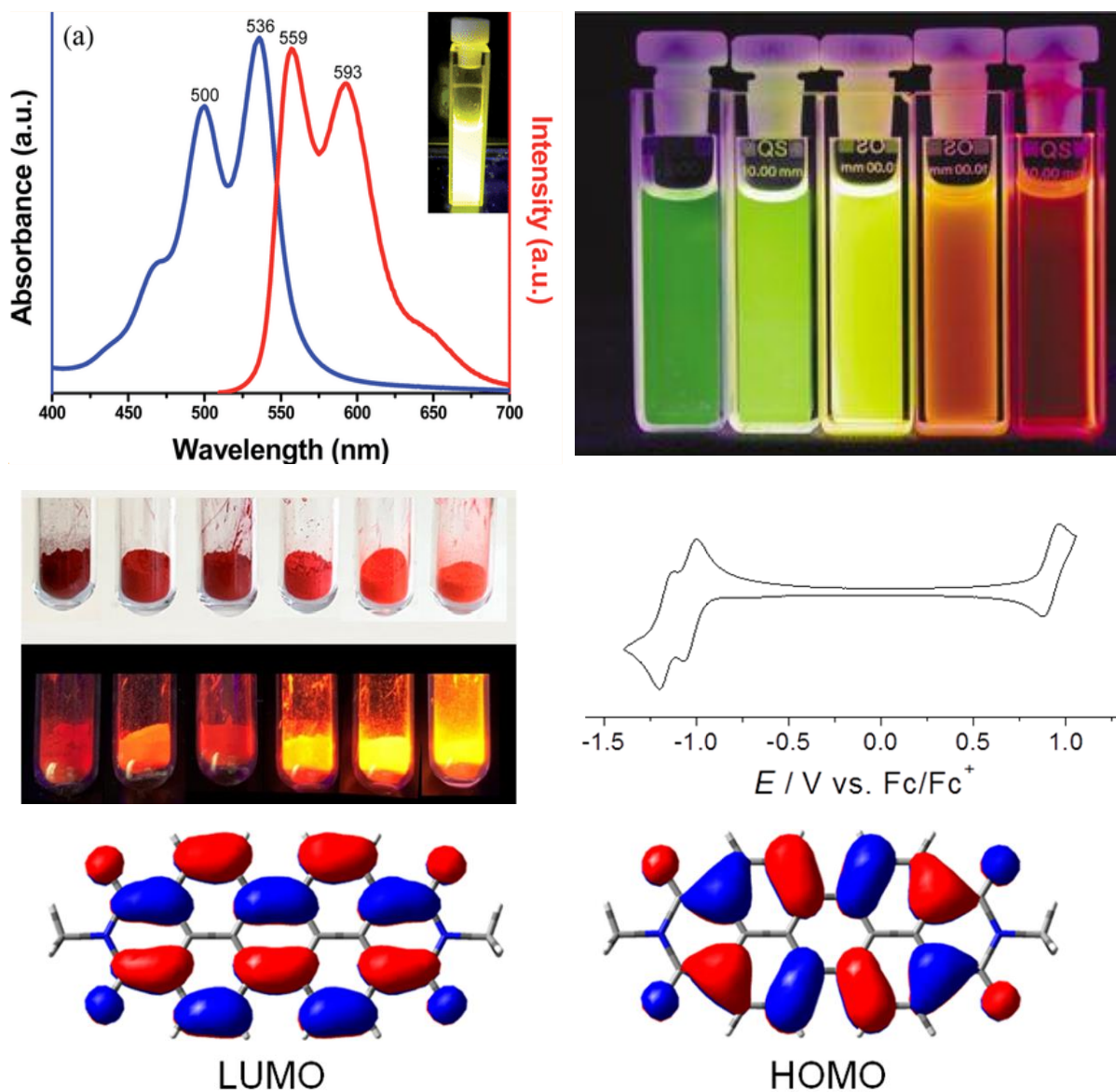


**Figure 1.2.2.** Typical functional properties of PBIs, UV/vis, fluorescence spectrum (solution and solid state), cyclic voltammogram, and HOMO and LUMO orbitals.[8]

As a result, various PBI analogs have been produced and used commercially since the early 1950s, including colorant red 179, colorant red 178, and colorant red 149 (Figure 1.2.3). colorant

red 149 is yellow-shaded, while colorant red 178 and colorant red 179 are blue-shaded red dyes.[2,7] PBI-based colorants are now primarily utilized in textile applications and high-quality industrial paints, especially for such automobile and carpet industries. The color's excellent quality and stability compensate for their comparatively expensive cost.
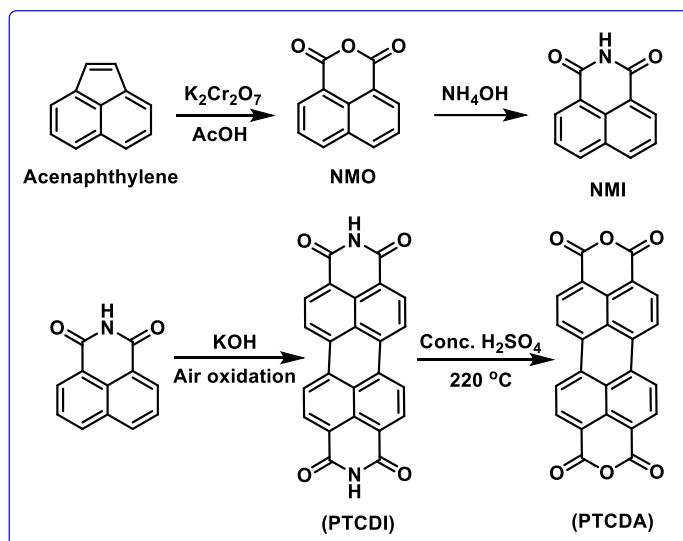


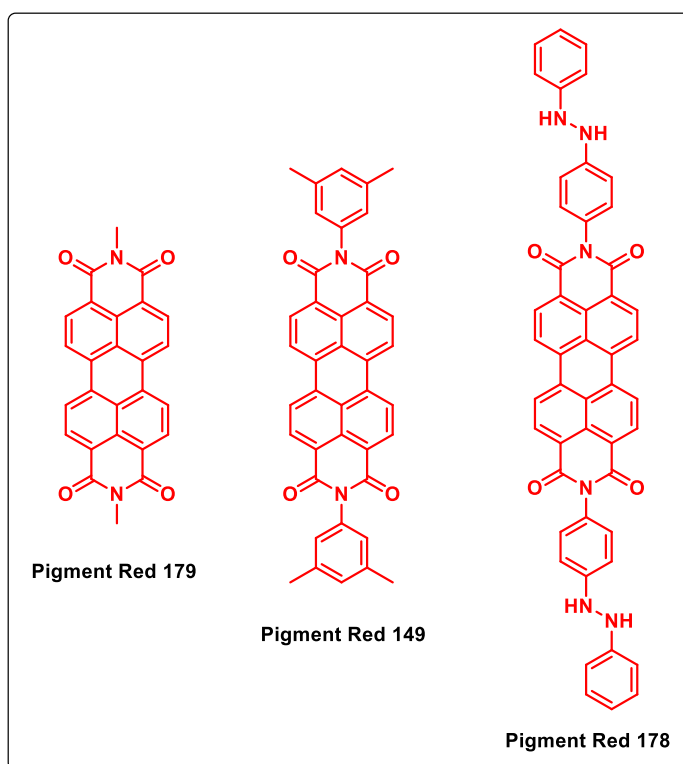**Scheme 1.2.1.** Synthesis of perylene-3,4,9,10-tetracarboxylic dianhydride (PTCDA)



**Figure 1.2.3**. The chemical structure of three PBIs primarily used in industrial pigments.

## 1.2.5. Molecular Synthesis of PBIs

## 1.2.5.1. Imidization

The corresponding PBIs derivative is obtained in a condensation reaction between perylene anhydride with an alkyl-amine and aromatic aniline, which is generally a high yield.[7] Although recent work on PBIs for optoelectronics, photocatalytic processes, and supramolecular structure demands soluble PBIs materials in common organic solvents, the colorant industry still needs poorly soluble and high melting PBI-based materials. As a result, synthetic approaches for highly soluble PBIs based on functionalized at the imide region have been developed. Solubilizing groups such as aliphatic and aromatic amines inserted at the PBI imide region were a widely used method for organic soluble symmetrical PBIs, reported by Langhals and coworkers in the 1990s as shown in Scheme 1.2.2.[3]
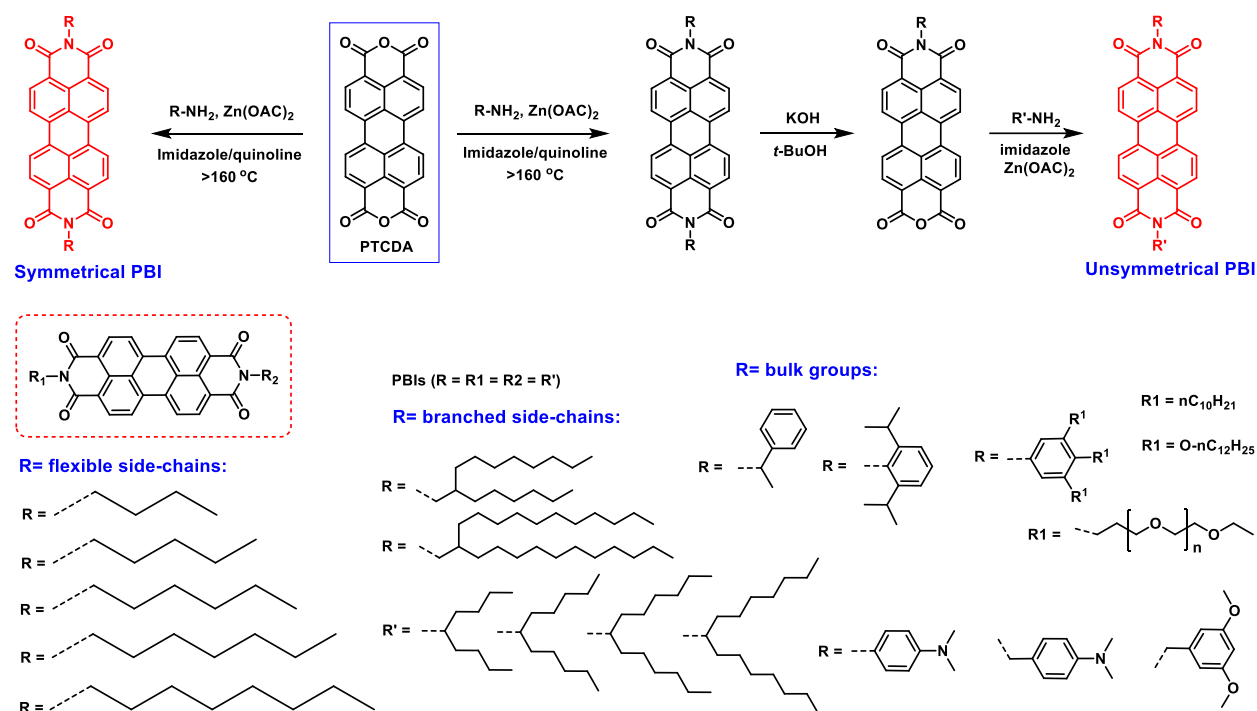


**Scheme 1.2.2.** Synthesis of symmetrical and unsymmetrical PBIs with different parent groups on each imide position.

Long alkyl chains with central positions connected to the perylene imide nitrogen which are remarkably efficient solubilizing groups because the bulky substituents are pushed away from the plane of the PBI dye molecule, restricting the stacking of the PBI moiety. The imide

substituted aliphatic and aromatic PBI compounds show excellent solubility in halogenated solvents. It is the conventional route to produce soluble symmetrically N,N'-substituted PBIs by the condensation reaction of perylene dianhydride with alkyl or aromatic amines, in presence of imidazole or quinoline as a solvent, zinc acetate as a catalyst, heated at above 150 °C. The isolated yields often exceed 90%, and The products are simple to purify. (Scheme 2).[7,15]

There have also been reports on asymmetric PBIs with different functional groups on each imide region. Because of divergence in amine reactivity with perylene anhydride, attempts to produce compounds of this form by adding two different amines simultaneously or sequentially to PTCDA are typically unsuccessful. Only lower yields of the desired products are usually obtained, with the two symmetrical PBIs being the dominant species. One approach (Scheme 1.2.2) works on the partial hydrolysis of symmetrical PBIs to perylenemonoimide monoanhydride molecules, which yields around 50%. The required asymmetrical PBI is obtained by imidization of the mixed imide-anhydride with a second amine or aniline.[16] Later, studies on the alkaline hydrolysis of symmetrical PBIs molecules to gave perylenemonoimide monoanhydride molecules, which yields about 50%. The required asymmetrical PBI is obtained by condensation of the mixed perylene imide-anhydride molecules with a different alkyl or aromatic amine or aniline.[16]

## 1.2.5.2. Halogenation at the "*bay*" and "*ortho*" Positions

Effective halogenation methods achieved for the perylene core provide high-value building blocks for subsequent functionalization. Electrophilic substitution predominantly takes place at the bay region of the PBI and PTCDA molecules due to the intrinsic reactivity of the carboxylic acid group present in the perylene molecules.

## 1.2.5.2.1. Bromination at "bay" Position

Compared to the "ortho" position, the "bay" position is highly active for electrophilic substitution reactions. Initially, on a bay position dibromo-PBIs are usually synthesized according to BASF developed method, which involves harsh condition; this methodology involves PTCDA with bromine in conc. $H_2SO_4$ at high temperature and then imidizing the brominated on PTCDA (Scheme 1.2.3).[17] According to Würthner et al.[18], the reaction produces mixture of of constitutional isomers 1,6- and 1,7-brominated PBIs **1,7-2a** and **1,6-2a**, as well as the higher-brominated compound like **3**, in a ratio of approximately 76:20:4, as shown in a

Scheme 1.2.3. Further, imidization on regioisomeric mixture got the **1,6-4a,** and **1,7-4a** mixture of regioisomers isolated with repeated recrystallization in a mixture of solvent (CH$_2$Cl$_2$/ACN) to give milligram of 1,7-brominated PBI, which is isomerically pure.
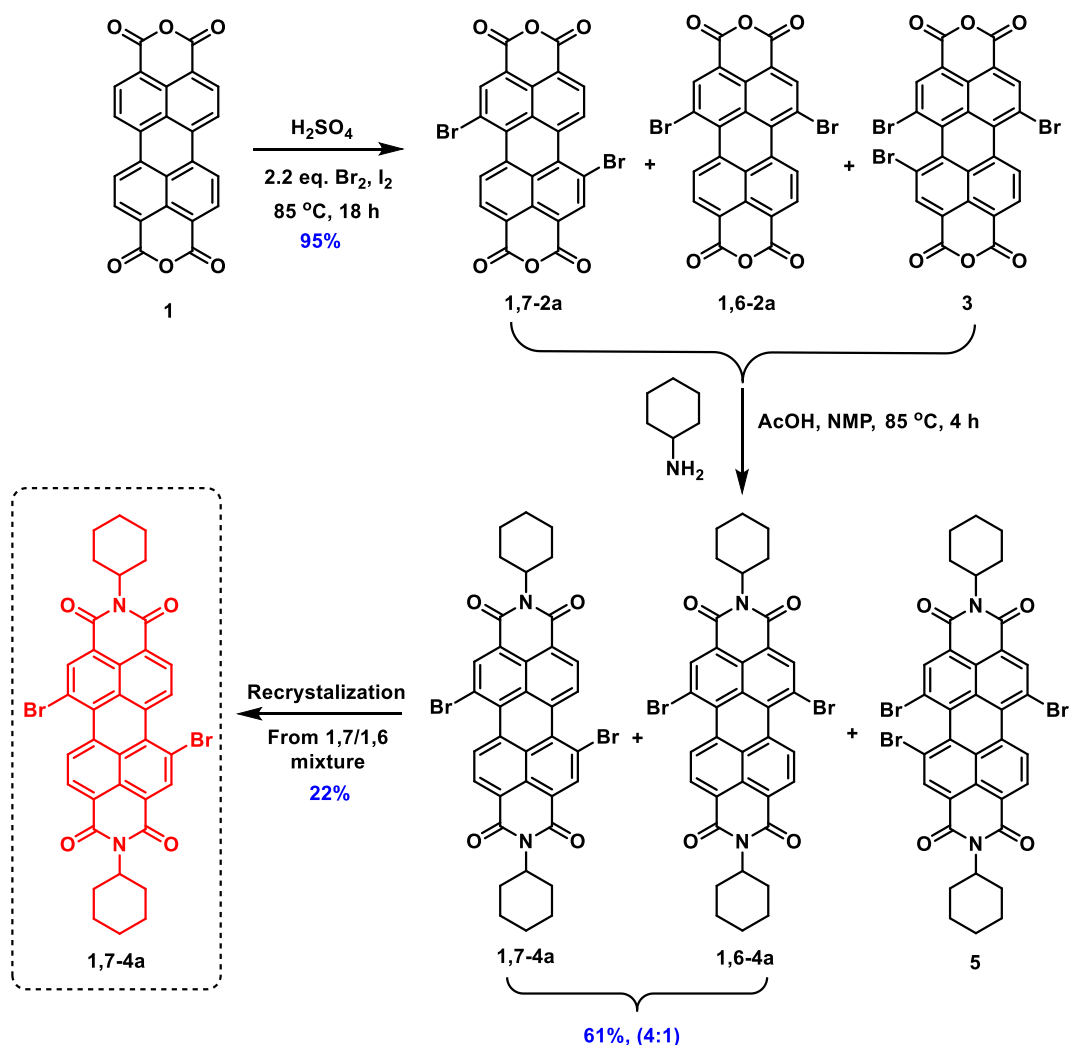


**Scheme 1.2.3.** Synthesis of isomerically pure 1,7-dibromo-PBIs (**1,7-4a**) by bromination of PTCDA and subsequent imidization PBI.

To synthesize the gram scale of 1,7-brominated PBIs**,** Rybtchinski, and coworkers developed a better methodology with milder bromination condition.[19] After Imidization, core-unsubstituted PBI molecules were treated with an excess amount of bromine in presence of dichloromethane to give **1,6-4a** and **1,7-4a** brominated PBI compound in a 3:1 ratio around 90 % yield. Repetitive crystallization was used to isolate the **1,7-4a** isomers (Scheme 1.2.4).
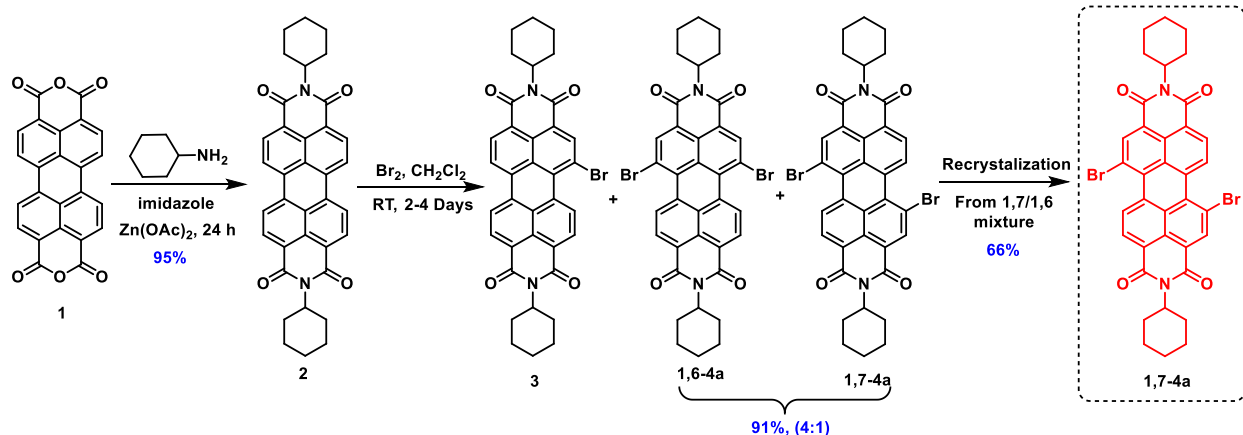
**Scheme 1.2.4.** Synthesis of isomerically pure 1,7-dibromo-PBIs (**1,7-4a**) by bromination of PBI.

## 1.2.5.2.2. "Ortho" Borylation and "Ortho" Halogenation

Shinokubo[11] and Müllen[12,13] firstly, separately published the synthesis of tetraborate PBI at the 2,5,8,11-positions (ortho) in 2011.[11-13] Shinokubo and coworkers used an iridium catalyst. PBIs **6c**, **6j**, and **6i** undergo regioselective borylation (B$_2$pin$_2$) at the controlling imide carbonyl functional groups at the proximal ortho-region (method A, Scheme 1.2.5).
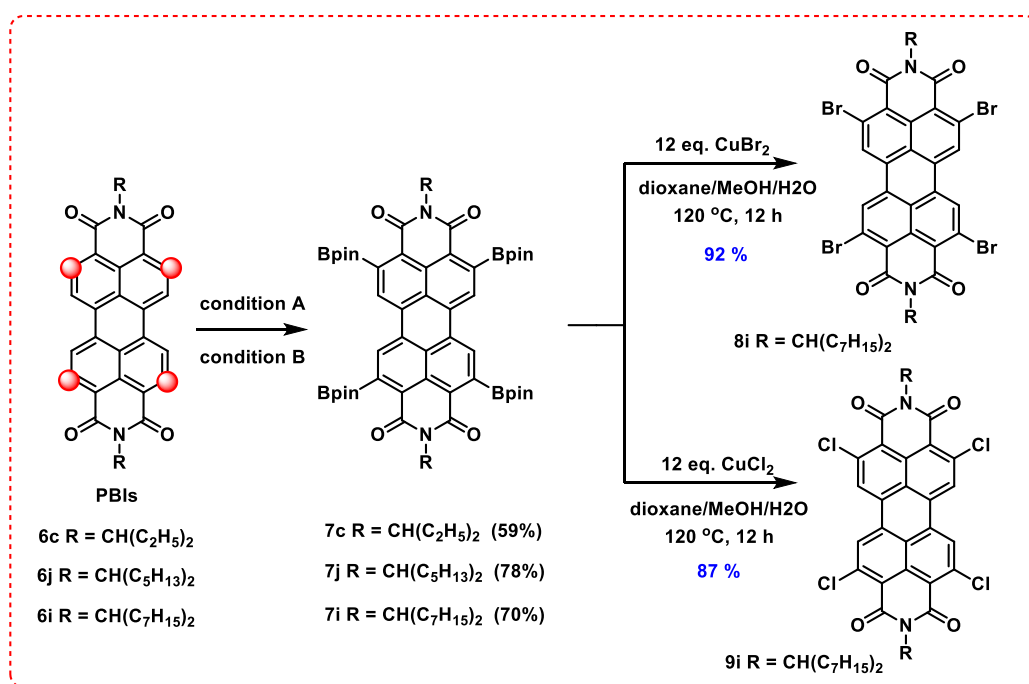


**Scheme 1.2.5.** Ortho-borylation and ortho-halogenation of PBIs. Conditions A: 8 eq. B$_2$pin$_2$, 3-4 mol% [Ir(OMe)cod]$_2$, P(C$_6$F$_5$)$_3$, dioxane, reflux, 2-4 d. Conditions B: 7.9-8.3 eq. B$_2$pin$_2$, 50 mol% [RuH$_2$(CO)(PPh$_3$)$_3$], mesitylene/pinacolone, 140 °C, 24-30 h.

The yields varied from an estimated range of 60% to 80%. At the same time, as Ir catalyst was used in the presence of 4,4′-ditert-tris (3,5-bis (trifluoromethyl)aryl) instead of tris(pentafluorophenyl)phosphine ligand was used (method A, Scheme 1.2.5).[11] G. Battagliarin et al. obtained **7c**, **7j** and **7i** in excellent yields by treating **6c**, **6j**, and **6i** with $B_2pin_2$ under presence of Ru catalysis by using $RuH_2(CO)(PPh_3)_3$ (methode B, Scheme 1.2.5).[13]

In view of Ru catalyzed activity, shows high regioselectivity can be due to the catalysts pre-coordination to the PBI functional groups, Lewis base directing group, which promotes cyclometallation via substitution into the ortho C-H bond to yield ruthenacycle intermediates.[13] Further, tetraborylated PBIs are also used to synthesize halogenated and cynated PBIs, PBIs core substituted at ortho-region containing four heteroatoms. It is easy to synthesize ortho-tetrachloro and ortho-tetrabromo-PBIs **9i** and **8i** *via* halogenation of PBI boronate ester **7i** through copper(II)halide (Scheme 1.2.5).[12]

## 1.2.5.3. Substitution Reactions at Bay Positions

Changing the imide substituents has little effect on these PBI chromophores' optical and electrical properties because the nodes are present in the HOMO and LUMO orbitals at the PBI nitrogen atoms (Figure 1.2.2).[6-9] Seybold and his BASF coworkers reported a more elaborate synthesis method involving substituents to the so-called "bay" area of PTCDA and PBI scaffold.[17] "The substitution at the bay position is the most successful approach for tuning the absorption, emission, and redox properties of PBIs (Scheme 1.2.6).[17] However, substituting four times in bay regions is also generally challenging. As a result, only a small number of nucleophiles can efficiently react with four-fold bay halogenated PBIs (Scheme 1.2.6).[7] Traditional nucleophilic substitution reactions, and several metal-catalyzed coupling reactions, make two-fold bromine exchanges easier (Scheme 1.2.6). An enhanced solubility can be obtained by the insertion of aromatic or aryloxy chromophore groups into the bay region of PBIs, the steric interactions drive the substituents away from the PBI plane.[7,20]

Furthermore, these groups and minor substituents such as bromine might cause the twisting of the dual naphthalene half parts in PBIs. Both effects improve PBI solubility by disrupting face-to-face stacking. Besides, incorporating bulky alkylated or chromophore groups into the bay region may increase solubility[20] in numerous orders of magnitude, for example, bay region

substituted compound such as brominated *N,N'*-dioctyl PBI is soluble in most of the organic solvents, but its non-brominated PBIs are partially soluble.
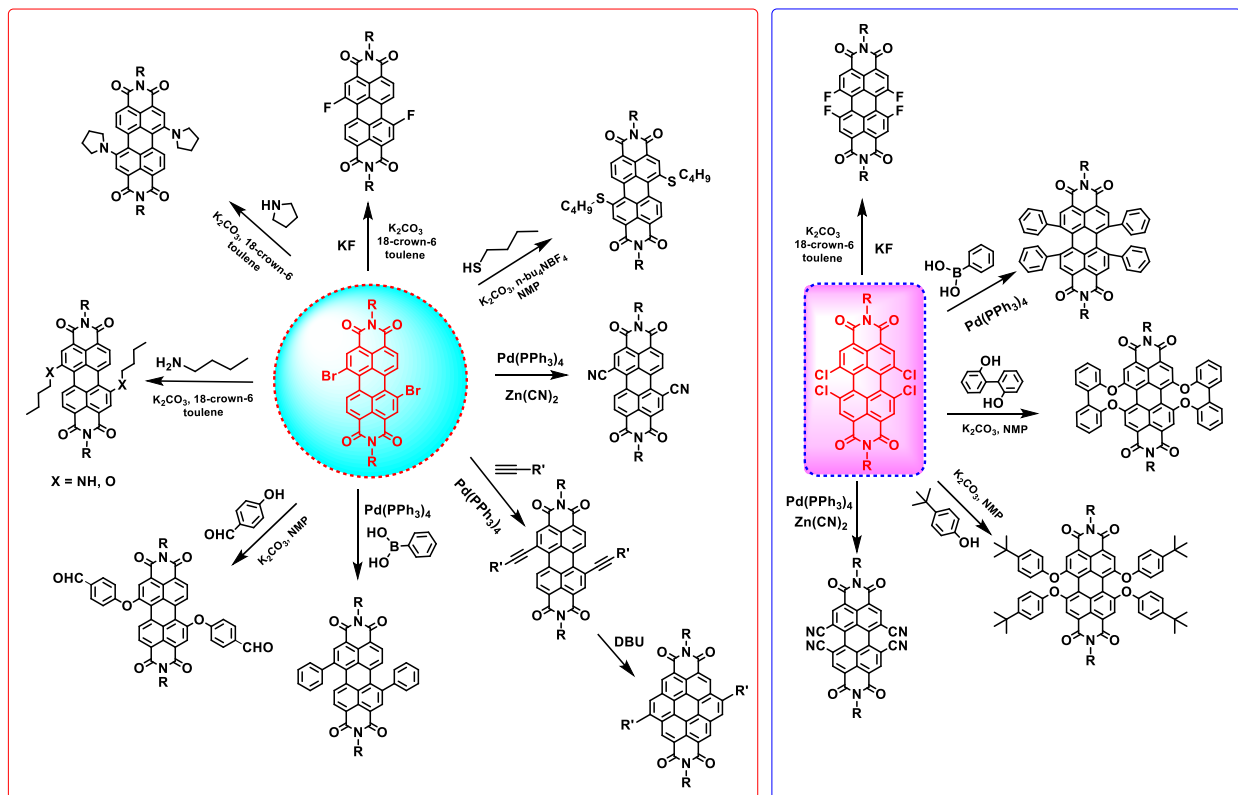


**Scheme 1.2.6.** Synthesis of PBIs with various substituents in the bay positions.

## 1.2.6. Non-conjugated Macrocycles for Host-Guest Interaction

Non-covalent interactions are best studied in well-ordered and well-attributed porous cavities that may enclose specific guest molecules. Recent investigations have been concentrated on the integration of more notable functionalized compounds like fullerenes, [21a] and other polycyclic aromatic hydrocarbons,[21b] whereas most initial studies on host-guest phenomena concentrated on the metal complexes of relatively tiny molecules and ions. Normally in PBI-based systems, host-guest interactions are hampered due to aggregation by the stacking of molecules. Generally, there exist three main strategies for avoiding PBI dye aggregation. The first strategy involves substitution on the imide region with large substituent groups that cover the faces of PBI to prevent intermolecular interaction without compromising the planarity of the perylene core.[12c] Second strategy makes use of steric bulk included on the perylene core at the bay region via nucleophilic aromatic substitution reaction of halogenated PBI cores and can be used to insert sterically bulky compounds. Although adding a steric barrier at the bay region minimizes

stacking, the basic structure of a PBIs core is a planar aromatic form to typically gives a twist.[7,20]

## 1.2.6.1. Diastereomeric Perylene Bisimide Atropisomers

Most of the chiral molecules are commonly used in various fields, including molecular switches,[22] enantioselective catalysis,[23] chiral recognition,[24] and nonlinear optics,[25] in addition to academic research on chirality as a key subject of chemistry and biology.
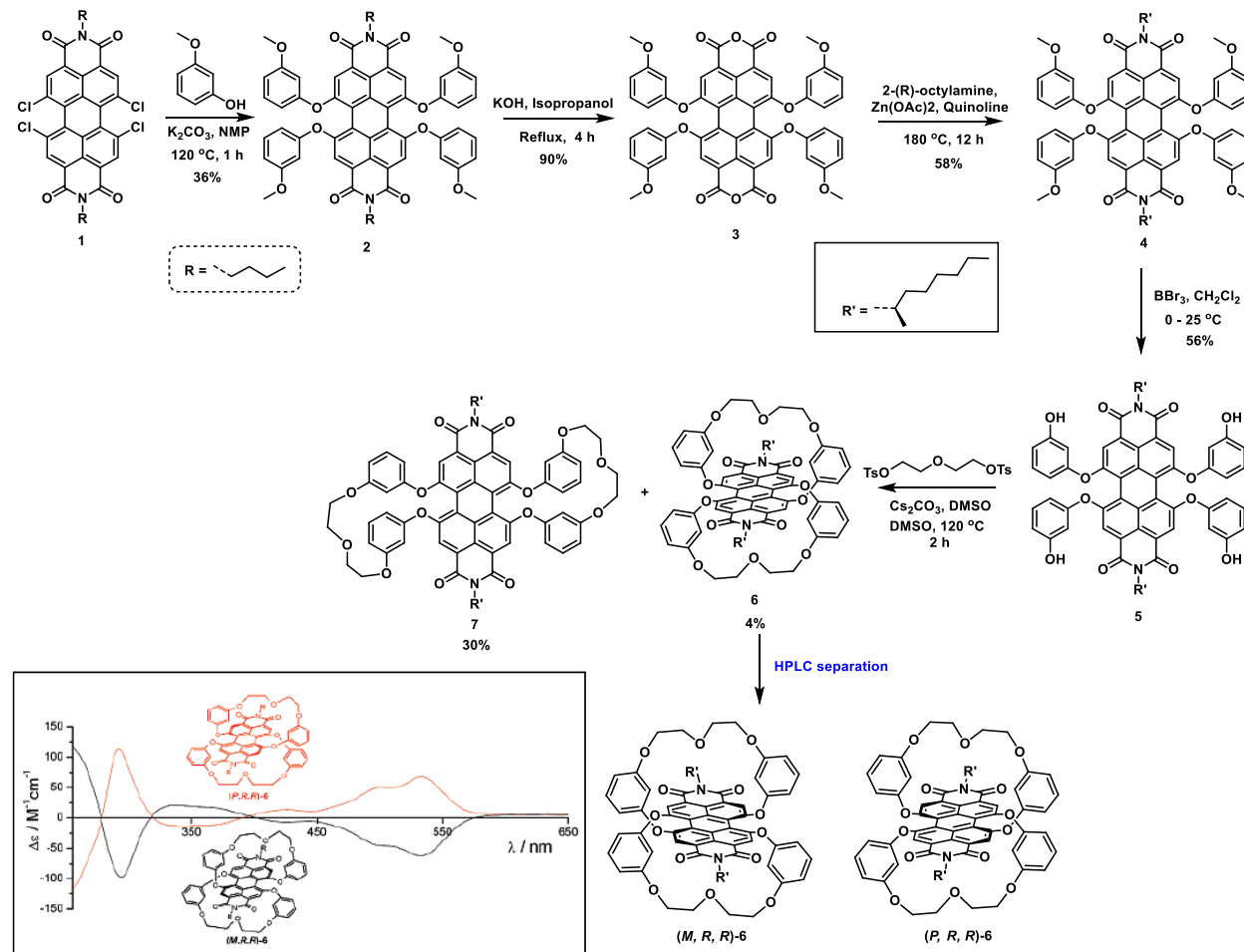


**Scheme 1.2.7.** Synthesis of regioisomeric macrocyclic PBIs **6** and **7** and resolution of the atropo-diastereomers of **6**.

Moreover, because of their circularly polarised emission, chiral dopants or polymeric emitters nematic crystals promise to be used in photo and electroluminescence devices, which should enable stereo imaging.[26] In 2007, According to Würthner and coworkers, etherification with diethylene glycol ditosylate yielded the regioisomers **6** and **7** that are diagonally bridged (1,7 and 6,12 linkage) and laterally bridged (1,12 and 6,7 linkage) as shown in a Scheme 1.2.7.[27] Chiral

column-based semipreparative HPLC was used to differentiate the atropisomers of the crosswise bridged macrocycle **6**. Using a combination of circular dichroism spectroscopy and quantum chemical estimations, their exact configurations were established. These are the first two examples of PBI diastereomeric atropisomers (**P,R,R**)-**6** and (**M,R,R**)-**6**, respectively. As shown in Scheme 1.2.7 of **PBI 6**, If the interconversion mechanism (*P↔M*) is inhibited by effectively bridging alkylene substituents at the bay region, stereoisomers of PBI with a pure (*P*) or (*M*) helically twisted perylene possible to separate.[27]

### 1.2.6.2. Perylene Bisimide Atropo-Enantiomers

A similar approach was used by the same group to synthesize chiral 1,7-aryloxy-substitute PBIs (**2**) and effectively isolated their atropo-enantiomers using a similar process (*M* and *P*).
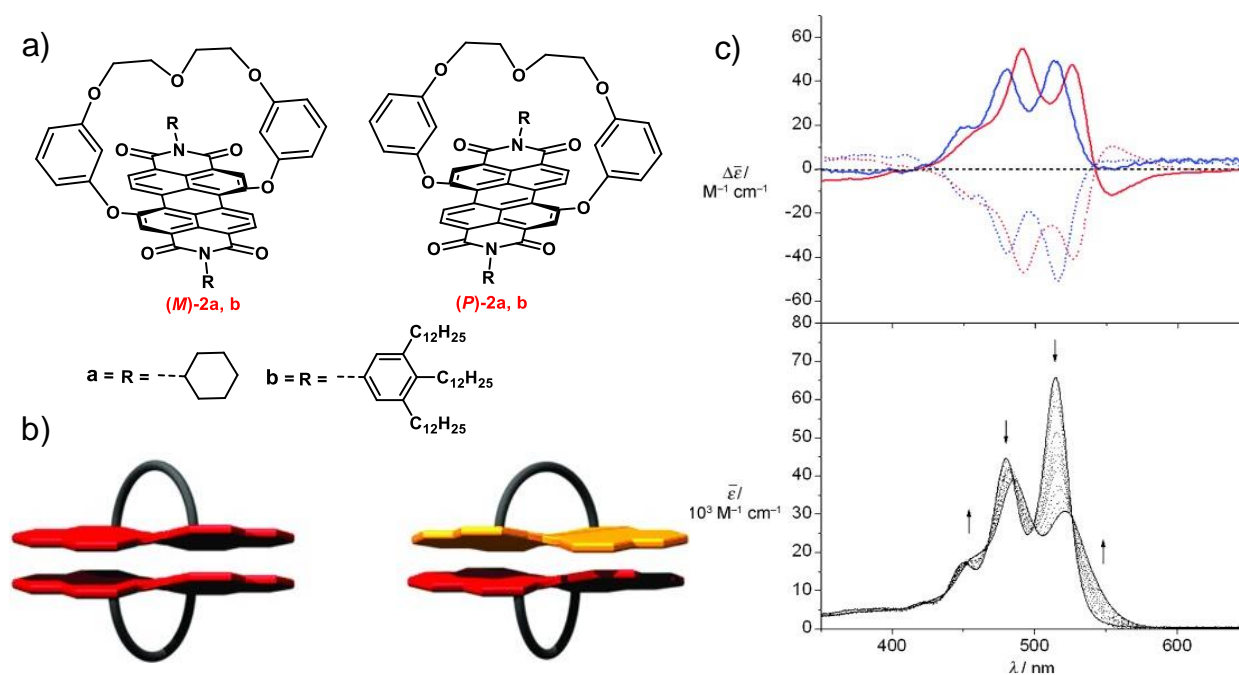


**Figure 1.2.4.** a) Chemical structures of atropo-enantiomeric (**P**)-**2a,b** and (**M**)-**2a,b**; b) schematic representation of homo- and heterochiral dimer aggregates derived thereof; c) CD spectra of (**P**)-**2b** (solid lines) and (**M**)-**2b** (dashed lines) in $CH_2Cl_2$ (blue lines) and *n*-hexane (red lines) at 298 K. Bottom: concentration-dependent UV/Vis absorption spectra of (*rac*)-**2b** in *n*-heptane at 331 K.

They were able to demonstrate for the first time through their spectroscopic analyses of racemic and enantiopure PBI dyes that self-recognition wins over self-identity during the dimerization of PBIs.(Figure 1.2.4a,b).[28] Chiral recognition of PBIs **2b** self-assembly was studied by CD,

UV/Vis- absorption spectroscopy. Due to the inherent molecular chirality, the (*P*)-**2b** and (*M*)-**2b** enantiomers of monomeric in $CH_2Cl_2$ exhibit nondesignated spectra in the wavelength range (400-600 nm) in a mirror-image relationship in their CD spectra (Figure 1.2.4c, top panel, blue lines).[28] It is possible to see a bisignate cotton effect (542 nm) for both enantiomers in the nonpolar *n*-hexane due to the chiral excited state coupling of the transition dipole moments of the chromophores (Figure 1.2.4c, upper panel, red lines). This causes dimer aggregates with a spiral π-π stacking framework to form. According to the exciton chirality hypothesis, the (*P*)-**2b** exciton coupling shows a negative sign (555 nm) for the corresponding dimer aggregation denotes a left-handed helicity (*M*)-**2b**.[29]

## 1.2.6.3. Doubly Encapsulated Perylene Bisimide

Thirdly, Bronstein and coworkers proposed a method where the PBI core is encircled using alkylene straps which are enclosed, as demonstrated by other conjugated substances.[27-31] With this approach, 1,3-dimethoxybenzene groups are inserted using a recently established methodology on the ortho-region of PBIs. The PBI core is then wholly encapsulated by them after being further functionalized with two rings (Scheme 1.2.8).[32]

The final, doubly entrapped **PBI-Encap**, the 4% yield of the isolable product following column chromatography, was obtained through the following encapsulation with dibromooctane under basic, high-dilution conditions, as shown in Scheme 1.2.8. An analysis of **PBI-Encap** using a single crystal X-ray diffraction revealed that the alkylene groups of the peripheral aryl units engage in horizontal entrapped rather than vertical looping or cross entrapped (Figures 1.2.5).[32]
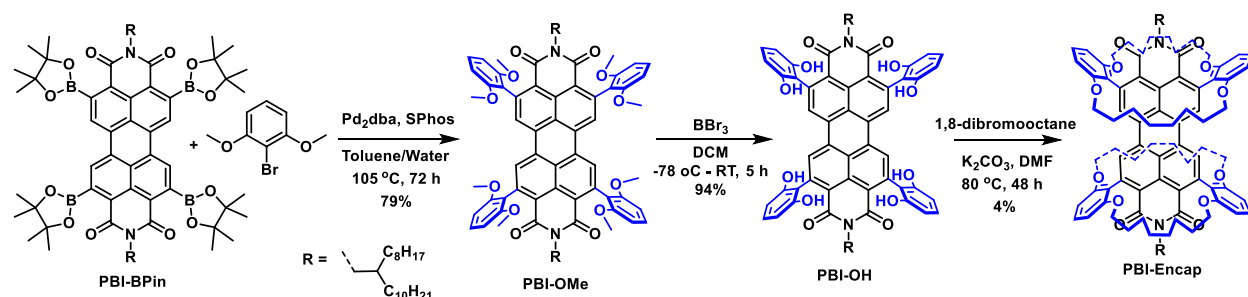


**Scheme 1.2.8**. Synthesis of the Doubly-Encapsulated PBI.
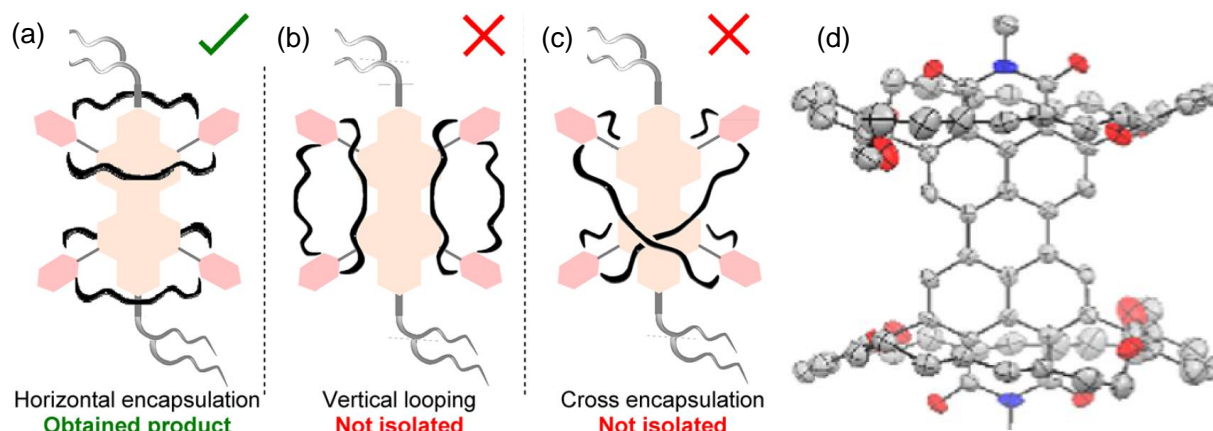
**Figure 1.2.5**. Graphical representation of the potential encapsulation products; a) observed horizontal encapsulation, b) vertical looping, c) crosses encapsulation, and d) single crystal X-ray of **PBI-Encap**.

## 1.2.6.4. Photoresponsive Luminescent Macrocycles

A particular environment for the study of non-covalent interactions is provided by well-defined and well organized pores with the capacity to enclose particular guest molecules.[32] With this in mind, in 2015, Spenst et al. synthesized *p*-xylylene bridged PBI cyclophane,[33] by condensation of a bay-substituted perylene anhydride core with *p*-xylene diamine which produced a rigid, covalently bonded PBI cyclophane (Scheme 1.2.9). For the complexation of wide aromatic compounds exhibiting binding affinities up to $4.6 \times 10^4$ m$^{-1}$, such as perylene and anthracene, the interchromophoric distance of around 6.5 $A^o$ creates the perfect rigid cavity.
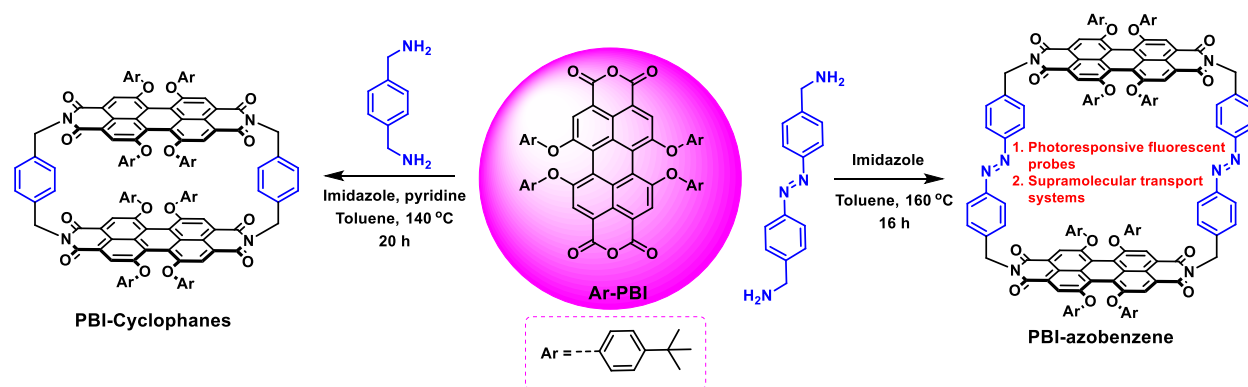


**Scheme 1.2.9**. Synthesis of the *p*-xylylene bridged PBI cyclophane (rigid microcycle) and PBI-azobenzene (flexible microcycle).

The complexation process increases the fluorescence of electron-poor guest molecules, whereas the fluorescence emission of electron-rich guests is drastically reduced by the creation of D-A charge-transfer complexes, as shown in Figure 1.2.6a.[33]
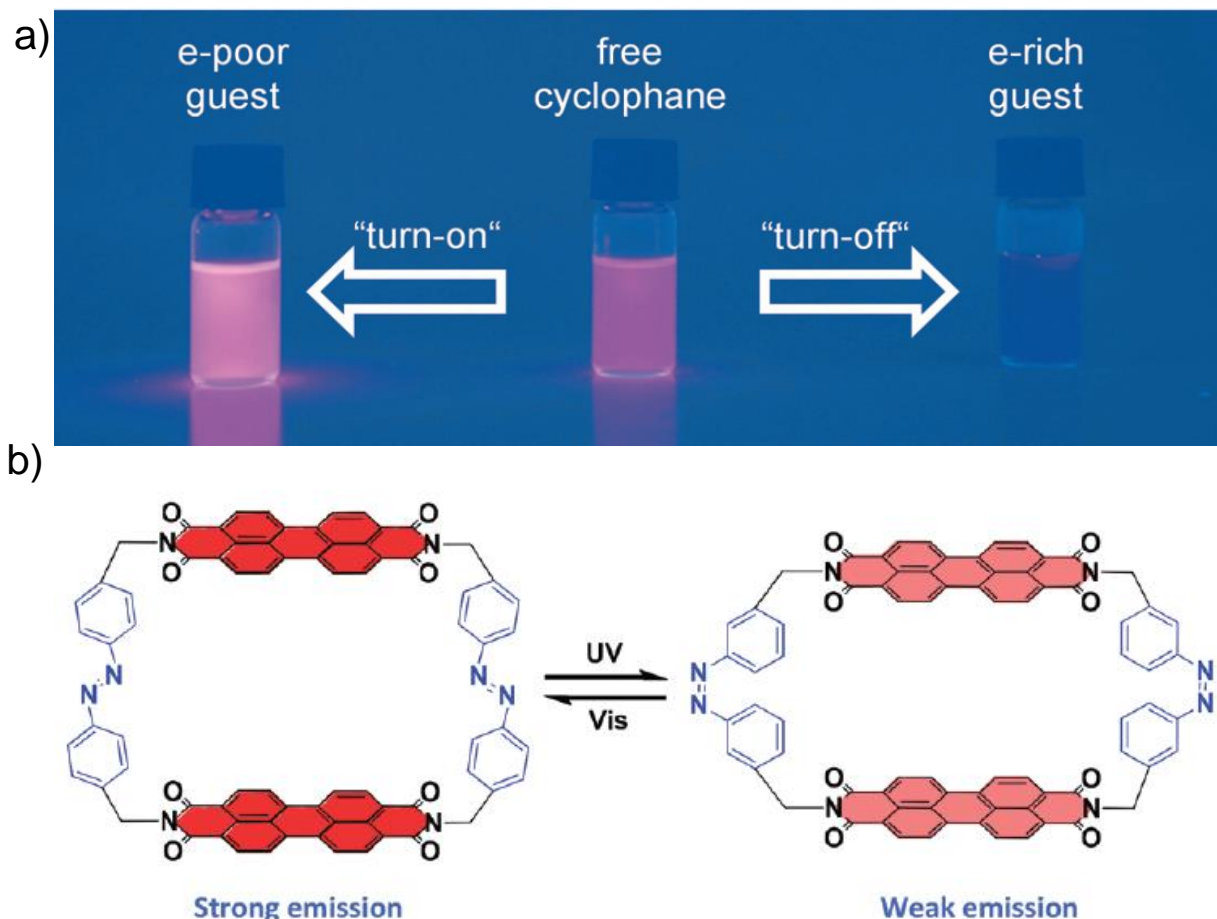


**Figure 1.2.6**. a) Representative photograph for the "turn-on" (phenylnaphthalene@1) and "turn-off" (carbazole@1) fluorescence sensing of electron-poor and electron-rich aromatic hydrocarbons; b) Photoresponsive PBI cyclophane supramolecular elements.

Furthermore, in 2021, Ouyang et al. reported a specific class of PBI cyclophane macrocycles, in which two bay-substituted perylene anhydride chromophores were connected through an azobenzene bridge (Scheme 1.2.9).[34] The researchers discovered that by combining electron-rich azobenzene and electron-acceptor PBI in a well-defined rigid cyclophane,  as evidenced by the PBI units considerable emission quenching, there is electrical contact between the PBI chromophores and azobenzene. When azobenzene is exposed to ultraviolet light, it undergoes photo-isomerization (Figure 1.2.6b). Under UV-visible light exposure, reversible photoswitching

of the azobenzene chromophore is coupled by substantial electronic and structural changes in the PBI-azobenzene unit. It drastically affects the pore size of the PBI-azobenzene and the emission behavior of the PBI chromophore as shown in Figure 1.2.6b.[34]

## 1.2.6.5. Perylene Bisimides- A Cyclic Host for Recognition of Fullerenes

Due to their high electron-accepting capabilities, fullerenes are prominent substances in biomimetic D-A systems that simulate the mechanisms of natural photosynthetic centers' intermolecular transfer of electrons.[35] According to the previous report, PBIs based macrocycles have never been used as material in host systems for guest fullerenes molecules, because dyad formation is electrically unfavorable due to the electron-poor nature of archetypal PBIs. To recognize this, Beer and coworkers described a new design strategy and synthesized of a giant macrocyclic host composed of two electron-donor bis-pyrrolidine PBI compounds that are covalently connected; this structure is known as the "Green Box" because of its appearance (Figure 1.2.7a).[36]
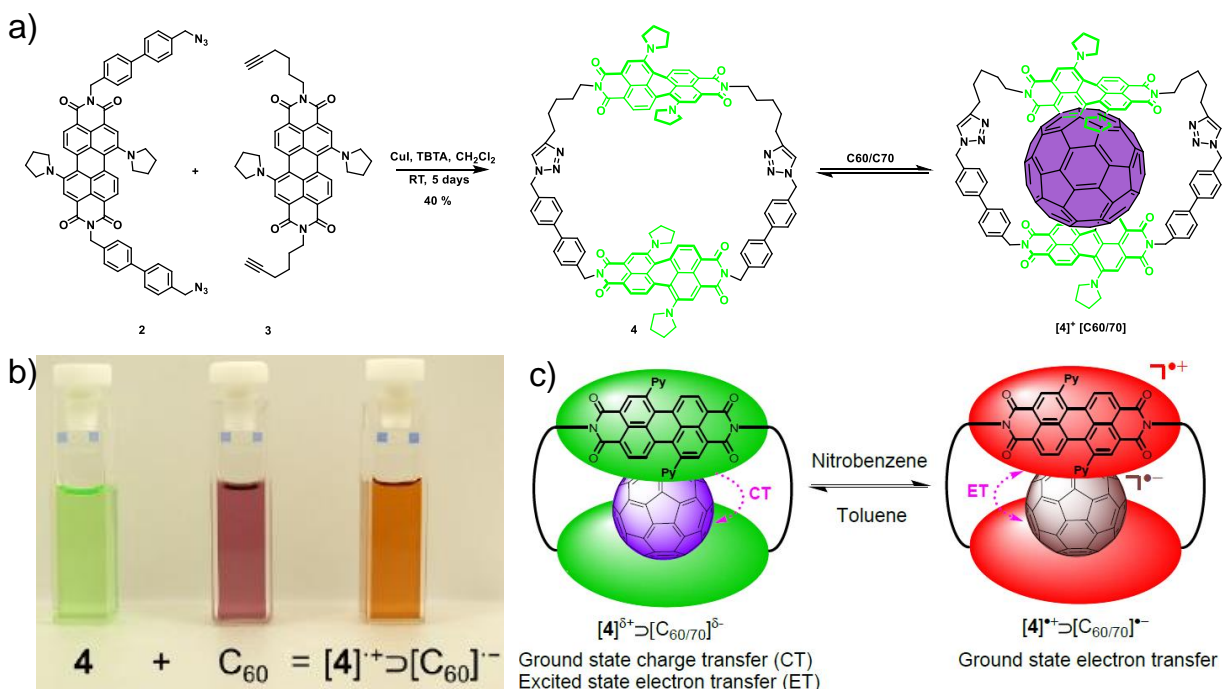


**Figure 1.2.7**. a) Synthesis of bis-PBI macrocycle Green Box 4 and 4$^{\cdot+}$ [C$_{60}$/C$_{70}$]$^{\cdot-}$; b) Photograph showing naked eye color change upon mixing of equimolar solutions of Green Box and C$_{60}$ in nitrobenzene; c) Schematic showing the solvent tuneable ground and excited state electronic

interactions of the Green Box host [4] donor-fullerene guest acceptor supramolecular complex ensemble.

The Green Box recognizes pure fullerenes ($C_{60/70}$) *via* interactions between the excited state and non-covalent ground state during fullerene guest encapsulation (Figure 1.2.7b). A rare, thermally permitted complete electron transfer from the non-conjugated Green Box macrocycle to $C_{60}$ is made possible by raising the polarity of the suitable solvent, which is possible in low-polarity solvents but not in high-polarity ones (Figure 1.2.7c).[36]

## 1.2.7. Conjugated Macrocycles for Organic Electronics

In recent years, conjugated macrocycles have shown various potential applications in optoelectronic materials. We must first comprehend what makes fullerenes valuable to build optoelectronic materials which highlight fullerenes as n-type electron-transporting materials and then seek to incorporate these qualities into other materials *via* synthetic chemistry. Four structural and electrical characteristics of fullerenes make them useful: (1) fully delocalized and conjugated $\pi$-space a three-dimensional geometry; (2) geometry in three dimensions; (3) the surface's interior and exterior; and (4) a low-energy, vacant molecular orbital (s) that allow receiving electrons.[37,38]

## 1.2.7.1. Organic n-Type Electronic Materials

Nuckolls and coworkers synthesized the conjugated macrocycles in 2016 and in 2018 to imitate fullerenes' three-dimensional (3D) shape.[39-41] The design provides numerous advantages, including synthetic adaptability, broad but not "whole-molecule" conjugation, and intramolecular porosities that make it easier to incorporate guests and add sensing capabilities. Mainly three primary macrocycles explored are represented in Figure 1.2.8.[41] These three structures differ in the number of bithiophene or phenyl units attached to PBI units before being wrapped into macrocycles. These "pseudo-fullerenes" are electronic and optoelectronic materials.[39-41]

Prof. Bäuerle[42] and Prof. Yamago[43] developed the stannylated aromatics method used to make multinuclear platinum macrocycles, giving conjugated macrocycles. Nuckolls and coworkers were inspired by this method and developed platinated and stannylated PBI moieties as crucial intermediates. The multinuclear platinum macrocycle is used as an intermediate in each synthesis; **(PBIBBr₄)₃** is obtained *via* an intermediate of trimeric platinum complex,[40] while

**(PBI-BP)₄** as well as **(PBI-Ph-B-Ph)₂** are obtained from an intermediate of tetraplatinum complex.[39a]
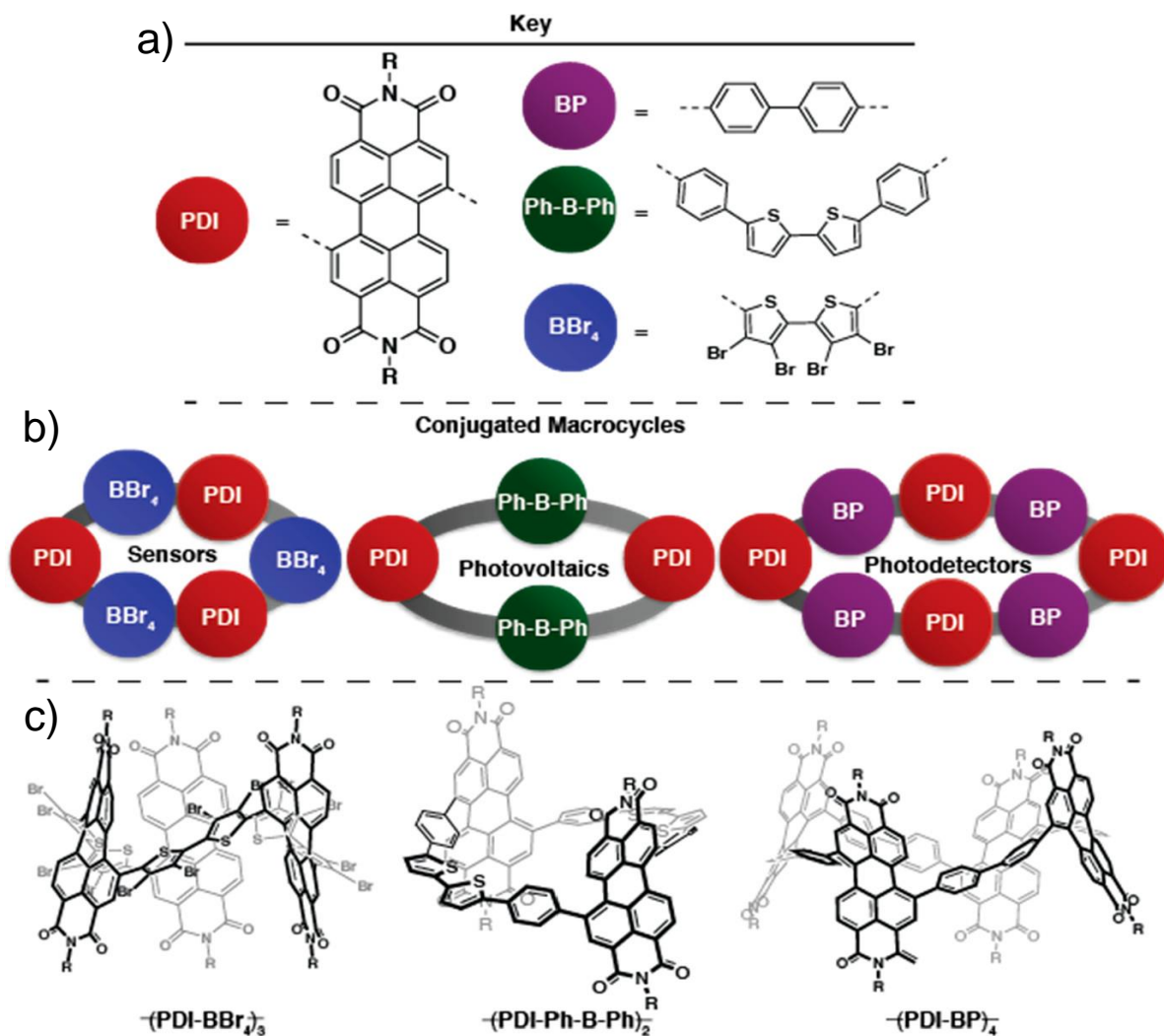


**Figure 1.2.8**. (a, b) Schematic showing the substituents for the conjugated macrocycles; (c) structures of the three macrocycles: −(PDI-BBr₄)₃−, −(PDIPh-B-Ph)₂−, and −(PDI-BP)₄−.

The color of isolated **(PBI-BBr₄)₃**, **(PBI-BP)₄**, and **(PBI-Ph-B-Ph)₂**, are deep red, purple, and black solids, respectively. The size of the macrocycles intramolecular cavities is one of the most noticeable differences. The pore size is lowest observed in **(PBI-BBr₄)₃** (1.1 nm),[40] highest in **(PBI-BP)₄** (2.0 nm), and in-between pore size observed for **(PBI-Ph-B-Ph)₂** (1.6 nm).[39a] The synthetic flexibility of the approach allows subunits with desired electrical characteristics to be included in the macrocycles. Due to PBIs excellent electron-accepting capacity, DFT studies, and electrochemistry estimations show that all molecule has a low-energy LUMO capable of

taking at least two electrons. The LUMO energy levels for the three macrocycles are approximated to be around 3.9 eV, based on the cyclic voltammogram which was used to measure the first reduction potential.[41]    For **(PDI-Ph-B-Ph)₂**, the electron-rich phenyl-bithiophenephenyl essentially affects the HOMO.[39a] Because the HOMO energy of **(PDI-Ph-B-Ph)₂** is higher than that of the other remaining macrocycles (Figure 1.2.9a,b). Since their LUMO energies are the same, the HOMO/LUMO gap is reduced, resulting in a red shift observed in the UV−vis absorption spectrum (Figure 1.2.9c). The three macrocyclic devices' transfer curves are shown in Figure 1.2.9d. The electron mobility of **(PDI-BBr₄)₃** films is ∼$1.5 \times 10^{-2}$ $cm^2/(V.s)$, whereas for **(PDI-BP)₄** and **(PDI-Ph-B-Ph)₂** films is $1.5 \times 10^{-3}$ $cm^2/(V.s)$.[41]
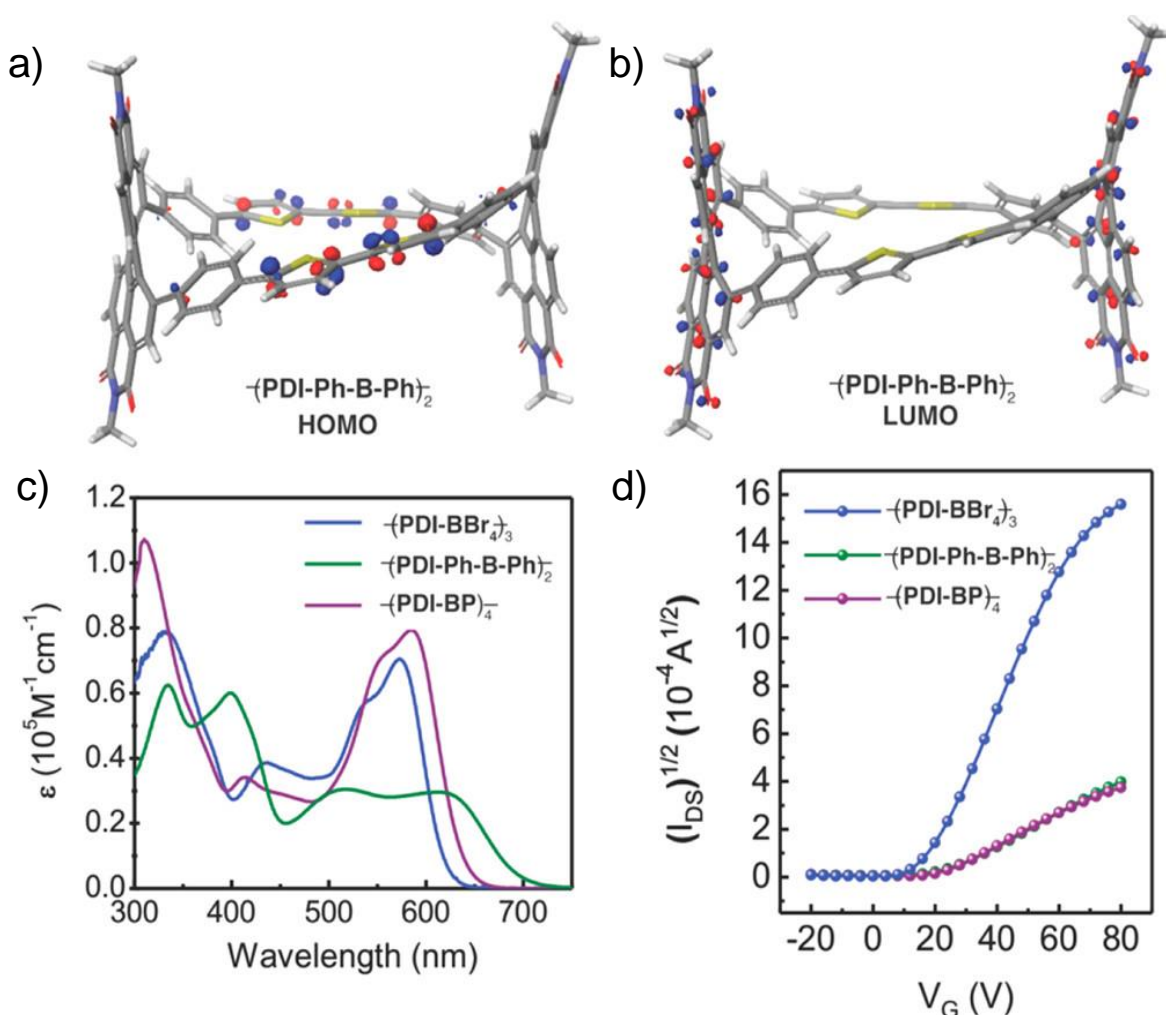


**Figure 1.2.9**. (a) HOMO and (b) LUMO of **(PDI-Ph-B-Ph)₂** showing charge transfer between the bithiophenes and the PBIs. (c) UV−vis absorption spectra for the three macrocycles. (d) Transfer curves for the three macrocycles. The source drain bias is 80 V. The curves for **(PDI-Ph-B-Ph)₂−** and **(PDI-BP)₄** overlap.

Cyclic PBI-based devices generate significantly more photocurrent than acyclic-based devices.[39a]   This study suggests that cyclic acceptors have improved charge transfer and photocarrier formation. According to the observed pattern, short acyclic molecules in particular exhibit high LUMO levels, lead to more recombination and lower *Jsc*. The cyclic molecules have a larger *Jsc* value than the acyclic molecules because they absorb more visible light. Electron transports *via* the film morphology and acceptor phase are two essential aspects of OPV efficiency. AFM pictures revealed clear perfect phase segregation for both -**(PDI-BP)₄** and **(PDI-Ph-B-Ph)₂**; in the acyclic controls, either over aggregation or extremely large domain sizes occurred, with the former leading in carrier combination and low device performance.[39a,41]

## 1.2.7.2. Transport of Electrons in Giant, Conjugated Macrocycles

In 2018, Ball et al. successfully synthesized two conjugated distinct PBI-based macrocycles,[39b] each of which, in 6% yield for **trans-PBIs** and 12% yield for **cis-PBIs**, represents two hPBI2 in dimer form as well as two phenyl-bithiophene-phenyl (**Ph-B-Ph**) molecules enclosed in a cyclic, -a-b-a-b-, and isolated **cDBDB** as shown in Figure 1.2.10a,b.
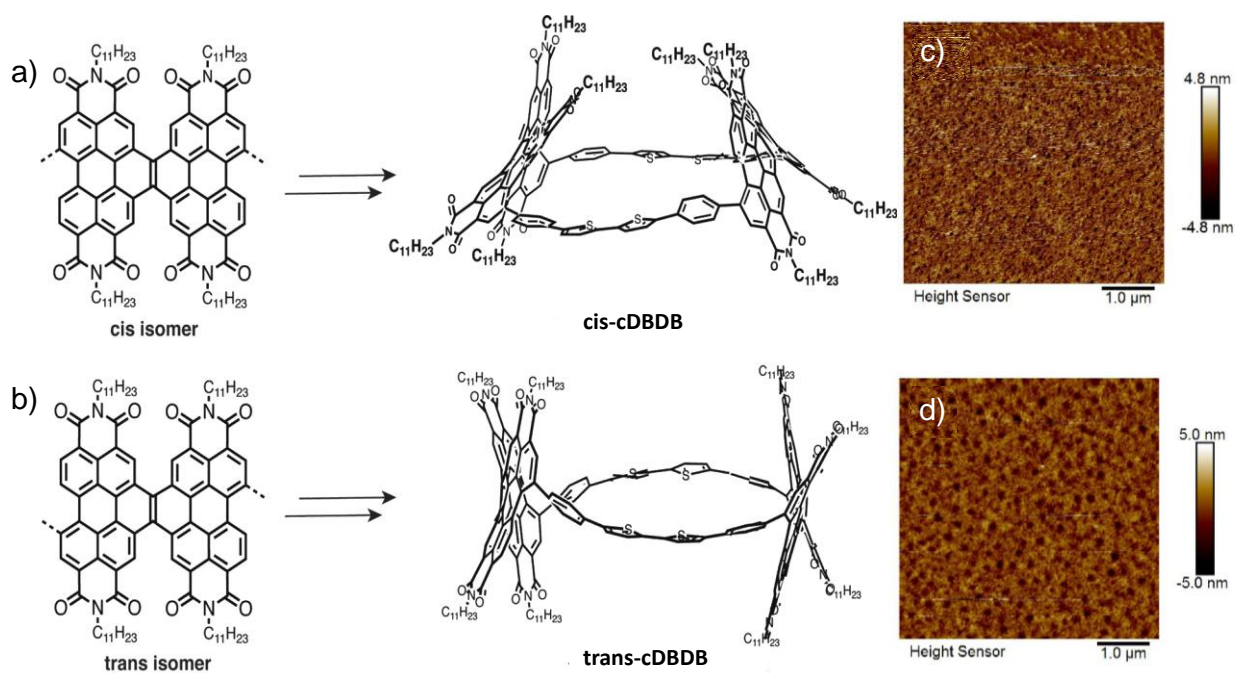


**Figure 1.2.10**. a) Structure of a *cis*-substituted hPBI dimer forming ***cis*-cDBDB**, (b) Structure of a *trans*-substituted hPBI dimer forming ***trans*-cDBDB**, AFM of height images for c) ***cis*-cDBDB** and d) ***trans*-cDBDB** films from OFETs.

Both *cis*-**cDBDB** and *trans*-**cDBDB** are metallic in nature and show dark purple solids. The considering regiochemistry of the hPBI₂ attachments differs between the two macrocycles: the orientation of **Ph-B-Ph** belts connected to the hPBI in dimer form show cis configuration, while the other has them in a trans orientation (Figure 1.2.10 a,b). Next, the authors explored how the interconnectivity of the macrocycles influences charge transfer in a thin film state. They observed that both macrocycles produce thin layers in OFET devices that behave like n-type semiconductors. According to OFET electron mobility, **cis-cDBDB** is significantly larger than **trans-cDBDB**, *trans*-**cDBDB** transistors have a mobility of ~$9.9{\times}10^{-4}$ cm²/(V·s) compared to transistors ~$4.1{\times}10^{-3}$ cm²/(V·s) for *cis*-**cDBDB**, due to the regiochemistry modification.[39b] To comprehend why *trans*-**cDBDB** has substantially lower mobility than *cis*-**cDBDB**, they recognize two points that significantly and generally affect the thin film state for charge transport: (1) morphology of the film and (2) electronic and molecular framework (Figure 1.2.10 c,d).

### 1.2.7.3. Oligothiophene Strapped Perylene Bisimide

Nature inspires researchers to improve the chemical properties of D-A conjugated macrocycles, which are composed of a series of construction materials that are similar like thiophene,[42] phenylenes,[43] porphyrins,[44] carbazoles,[45] BODIPY,[46] and PBIs.[39,40]
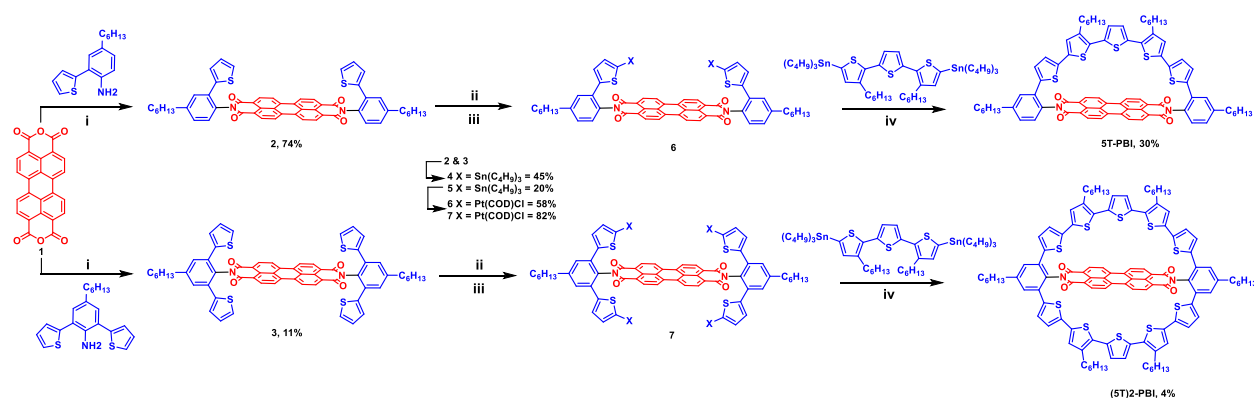


**Scheme 1.2.10**. i) Zn(OAc)₂, imidazole, microwave irradiation. ii) Sn(C₄H₉)₃Cl, *n*-BuLi, THF, RT, overnight. iii) Pt(COD)Cl₂, toluene, 95 °C. iv) Toluene, 75 °C, overnight, then dppf, CH₂Cl₂, RT, 6 h, then *m*-xylene, 120 °C, overnight. Dppf = 1,1′-Ferrocenediyl-bis(diphenylphosphine); COD = 1,5-cyclooctadiene.

Moreover, connecting cyclo[n]oligothiophenes with electron-deficient PBIs generates oligothiophene-strapped PBI. In light of this, Bold et al. successfully synthesized **5T-PBI** and

**(5T)₂-PBI** of two conjugated macrocycles via a cross-coupling reaction by platinum-mediated,[48] including oligothiophene rings that interconnect to the imide regions of a PBI, shown in Scheme 1.2.10. All syn-arranged thiophene rings entirely encapsulate the planar PBI units through a 12-membered macrocycle, as shown by the double-bridged PBI crystal structure (Figure 1.2.11a). DFT calculation suggested that there may be little electronic interaction between the PBI acceptor component and the electron donor oligothiophene chain, based on the localization and shapes of the neutral **(5T)₂-PBI** observed in the LUMO and HOMO (Figures 1.2.11b).
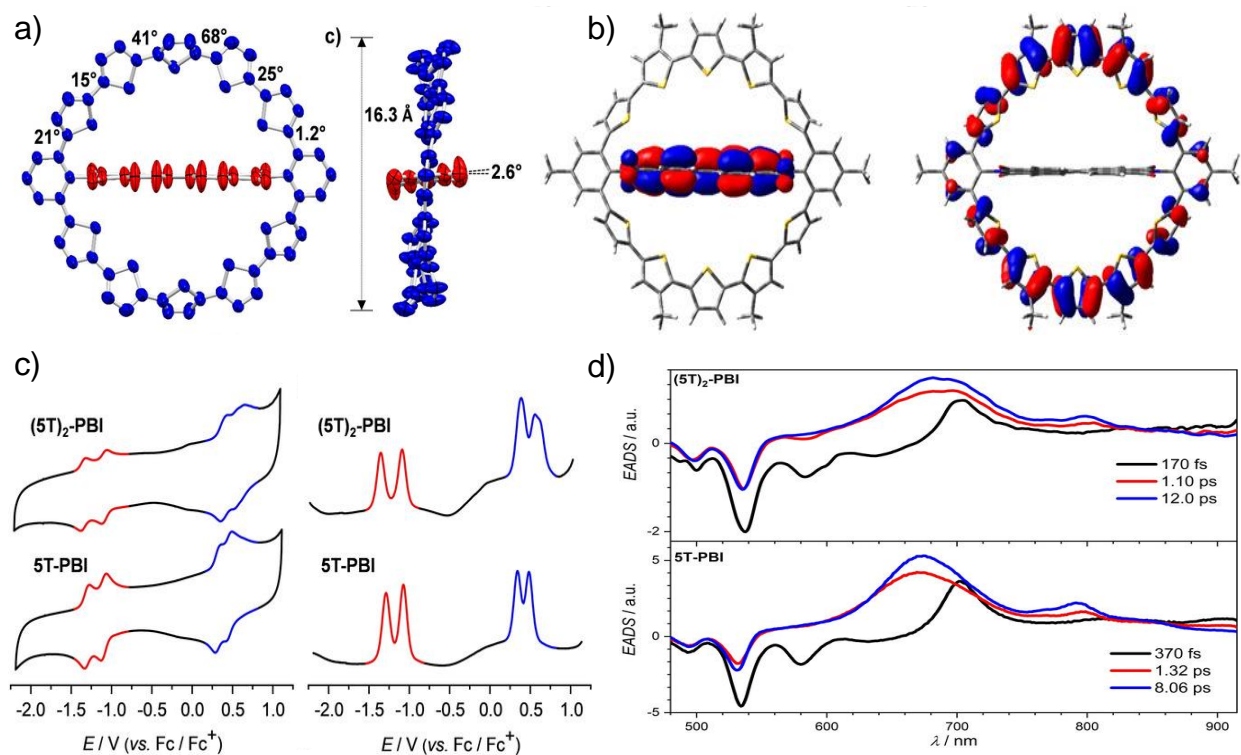


**Figure 1.2.11.** a) LUMO and b) HOMO of **5T2-PBI** based on geometry optimized structures from DFT calculations. b) CV and DPV measurements of **5T-PBI** and **(5T)₂-PBI. c)** Crystal structure of **(5T)₂-PBI**, and d) transient spectra of macrocycles **5T-PBI** and **(5T)₂-PBI** obtained by excitation at 530 nm in CH₂Cl₂ ($c_o = 10^{-4}$ M) at room temperature.

In Figure 1.2.11c, CV and DPV experiments, **5T-PBI**, and **(5T)₂-PBI** both the compounds show two reversible reduction peaks, In the negative potential PBI chromophore formed of an anionic and dianionic radical anion, respectively. Both macrocycles oxidations must be distinguished. The oxidation waves for the half cage of **5T-PBI** show a single electron transfer, however, in a

full cage of **(5T)₂-PBI**, two bridge moieties are oxidized at once. In the two reversible oxidation potentials, each oligothiophene ring contributed to the transfer of one electron.

In a charge-separated (CS) state generated by the extremely fast photoinduced electron transfer from the electron-donor molecule such as the oligothiophene ring to the electron-acceptor PBI subunit, both the radical anionic species created on the PBI unit and the radical cationic species generated on the oligothiophene ring undergo rapid charge recombination within 8 and 12 ps, respectively. The ultrafast photoinduced electron transfer from the oligothiophene ring to the PBI subunit produces a charge-separated state in which both the radical anionic PBI and the radical cationic oligothiophene undergo rapid charge recombination within 8 and 12 ps, respectively, and $k_{CS} = 0.4$ ps$^{-1}$ **5T-PBI** and 0.2 ps$^{-1}$ **(5T)₂-PBI**, respectively (Figure 1.2.11d).[48]

In 2022, the same group reported the synthesis of a sequence number of D-A half-macrocyclic compounds that included an electron-withdrawing PBI unit connected with electron-donor $\alpha$-oligothiophene rings containing 4, 5, 6, and 7 thiophene subunits, through in a cross-coupling reaction of Pt-mediated (Figure 1.2.12).[49] The macrocycles of **4T-PBI** (14%), **5T-PBI** (30%), **6T-PBI** (13%), and **7T-PBI** (3%) are synthesized with relatively low yields.
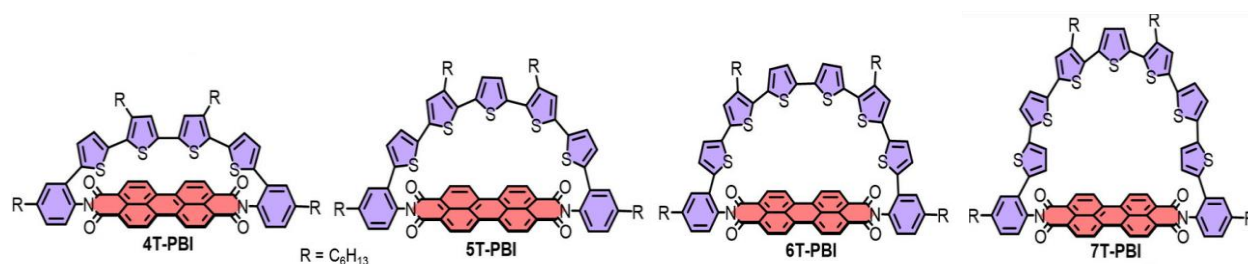


**Figure 1.2.12**. Molecular structures of the macrocyclic architectures **4T-PBI**, **5T-PBI**, **6T-PBI** and **7T-PBI**.

Figure 1.2.13a shows that all macrocyclic compounds exhibit reversible redox waves in the cyclic voltammetry. For all macrocycles, two reversible reduction waves were seen for all macrocycles at around -1.00 V and -1.20 V, which are associated with the monoanionic and dianionic PBI substances, respectively. However, the observed oxidation events within the series show significant variation. Thus, while the first oxidation process for the **4T-PBI** macrocycle, is high, the oxidation of the remaining macrocycles, **5T-PBI** through **7T-PBI**, is occasionally performed at significantly lower oxidation potentials. By comparing the second oxidation potentials of the remaining macrocycles, **5T-PBI** through **7T-PBI** with **4T-PBI** even more variations were observed in the macrocyclic sequence as shown in Figure 1.2.13a. The DPV

spectra with a greater level of wave-by-wave resolution provide the finest visualization of the potential distinction between the dianionic and cationic states. (Figure 1.2.13b).
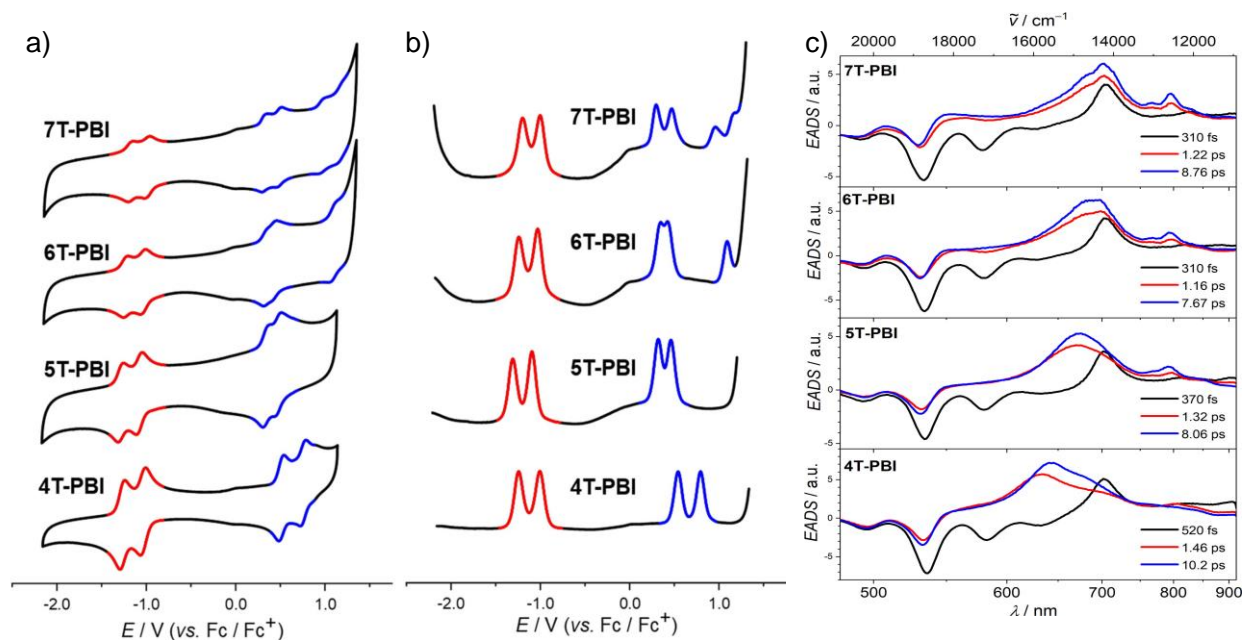


**Figure 1.2.13**. a) CV, b) DPV measure,ements and c) EADS and transient absorption spectra of 4T-PBI, 5T-PBI, 6T-PBI and 7T-PBI (from bottom to top).

Transient absorption spectroscopy has revealed the spectral properties of the excited state, which show the **7T-PBI** oligothiophene macrocycle support complete charge separation into PBI radical anions and oligothiophene radical cations, whereas the dyad with the **4T-PBI** macrocycle, lowest quarter thiophene exhibits a charge transfer state with imperfect charge separation (Figure 1.2.13c).

## 1.2.8. Perylene Bisimide Based Donor-Acceptor Copolymers

Polymeric and organic molecules as semiconductors are advantageous over inorganic molecules in manufacturing large-area, low-cost, and flexible electronic devices *via* solution-casting techniques and high-throughput patterning processes like slot-dye printing or coating.[50] Additionally, flexible substrate integration is made possible by low-temperature manufacturing,[51,52] without affecting the functionality of the substrate, including polymers or textiles.[53]

In the past few years, PBI-based D-A conjugated polymers are gained significant attention in the optoelectronic field and show diverse applications, including organic field-effect transistors,

supercapacitor electrodes, organic solar cells, organic light-emitting diodes, and organic photovoltaics, etc. because of their novel characteristics such as easy processability, thermal stability, low cost, high absorption coefficients, strong electron affinities, and favorable electron transport mobility.[54,55]

## 1.2.8.1. PBI and Electron-Donating Unit Containing Donor-Acceptor Copolymers

As shown in Figure 1.2.14, a variety of copolymers of PBI and several electron donor units containing selenophene, fluorine, tellurophene, thiophene, thienothiophene, dithiophene, cyclopentadithiophene, and benzodithiophene were synthesized. The optoelectronic characteristics of PBI-based polymers can be effectively modified by switching the donor units.[56]

To substantially tune the optoelectronic property, the convenient heteroatom-containing aromatic rings, like selenophene, thiophene, and tellurophene are the basic derivatives and are typically utilized as a conjugated bridge. Zhan et al. synthesized a PBI copolymer **P1** with an alternating pattern of PBI and dithienovinylene,[57] which gave a power conversion efficiency (PCE) of 1.00%. High electron mobilities have been made possible in thin-film transistors (TFTs) of the organic molecule by the use of the weakly electron-donating unit consists of chloronaphthalene.[58] Zhao and coworkers developed PBI-based copolymers **P2**, **P3**, **P4**, and **P5**, which include thiophene, dithiophene, selenophene, and thienothiophene, respectively.[59] The optical band gaps became narrower, and the HOMO energy levels increased due to the electron-rich groups such as thienothiophene or dithiophene. As a result, compared to **P2** and **P3**, the absorption maxima of **P4** and **P5** were nearly 30 nm red-shifted and showed better PCE.

Tellurophene, like the thiophene unit, is a desirable building block for producing optoelectronic devices because of the molecular size and significant spin-orbit interaction, which may lead to a long-lived triplet state and effective interchain π-π layering. Huang and coworkers,[60] synthesized PBI and tellurophene-based copolymer **P6**. It displayed a red-shifted absorption compared to its thiophene analog because tellurophene has a stronger electron-donating ability. Excitingly, a film was found to display a clear bathochromic shift of 12 nm relative to that of the solution, suggesting that the polymer may adopt H aggregation in the solid state. An average efficiency of was 2.61% observed for **P6** based solar cells.
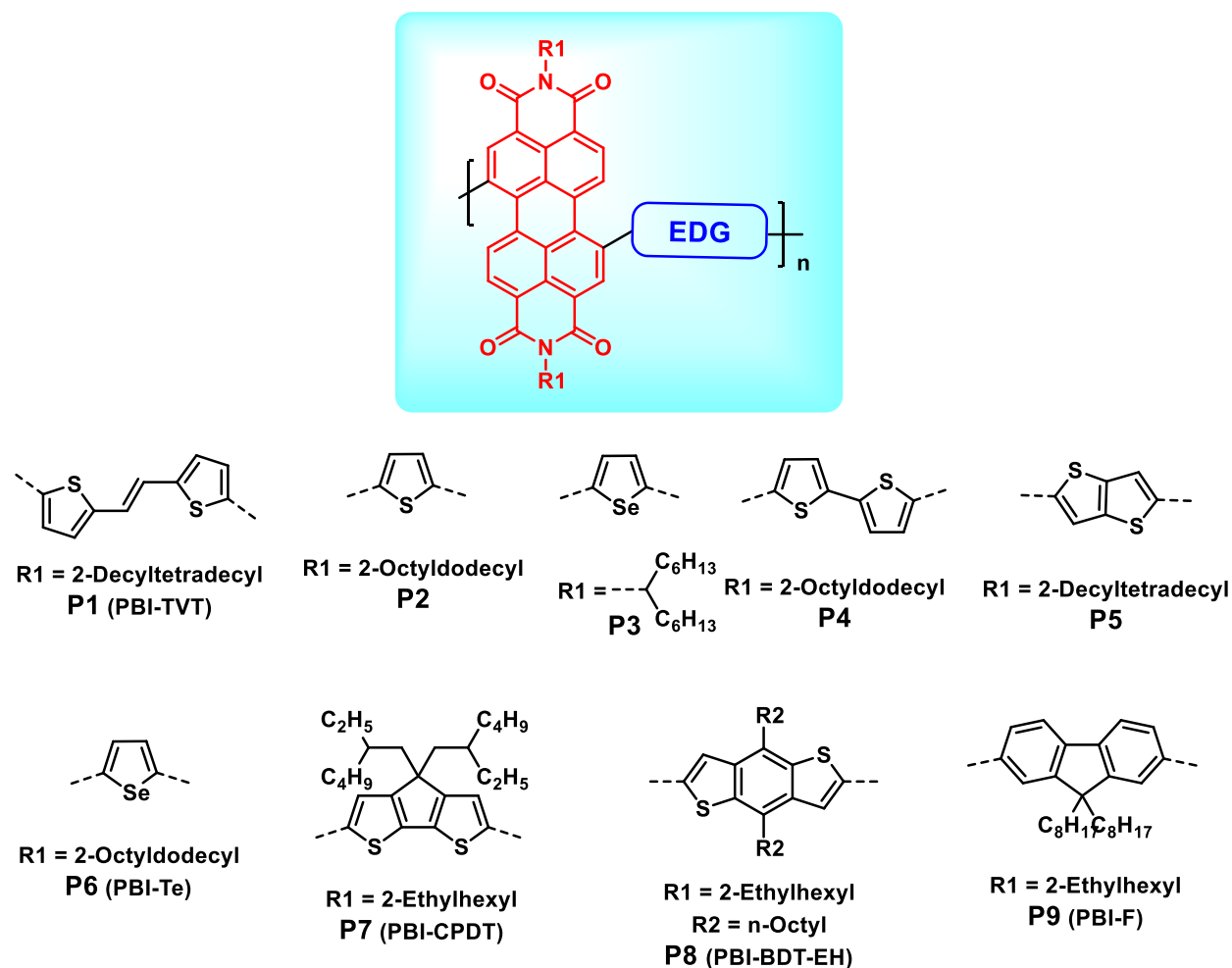
**Figure 1.2.14.** PBI and electron-donating group-based copolymers (EDGs)

Additionally, cyclopentadithiophene as a donor was used in 2015 by Zhou et al. to develop the new PBI acceptor **P7** copolymer,[61] which has broad absorption in thin films from 300 to 850 nm. With the addition of 1.0% chloronaphthalene, **P7** achieved a PCE of 2.13%. Furthermore, using benzodithiophene or fluorene as electron-rich components, Huo and coworkers synthesized PBI-based polymers **P8** and **P9** in 2017.[62] A comparatively weaker lamellar packing and greater steric hindrance was seen in **P9** compared to **P8**. Therefore, **P9** displayed a lower HOMO level and a red-shifted absorption compared to **P8.** The **P9** exhibited a PCE (4.47%), and is around 2-fold higher than **P8** (2.70%).

## 1.2.8.2. PBI and Electron-Withdrawing Unit Containing Copolymers

PBIs has been a low-lying LUMO levels, air-stable n-channel TFTs of organic materials were developed using D-A polymers. Li et al. first synthesized the benzothiadiazole-based copolymers

**P10**, **P11**, **P12 and P13** (Figure 1.2.15).[63]  In order to receive high electron mobilities and extended the absorption spectra, an ethynyl π-linker between **DiTh** and **PBI** was used to afford **P12** and **P13**.[64] Furthermore, the photovoltaic performance of all perovskite solar cell (PSC) devices based on **P10**-**P13** acceptors was incredibly low. Later, Zhao et al. used thiophene as a π spacer to develop **P14** having improved solar system efficiency and enabled a PCE of 4.07%.[65] By combining PBI with weak acceptors, Yu et al. synthesized **P15**, **P16**, and **P17**.[66] However, fluorination of TPTQ used to have a pessimistic impact on a conjugated polymer system and decreased the D-A compounds' dipole moment. As a result, **P17** shows a lower PCE (1.43%) than **P16** (3.52%) and has lower electron-accepting properties.
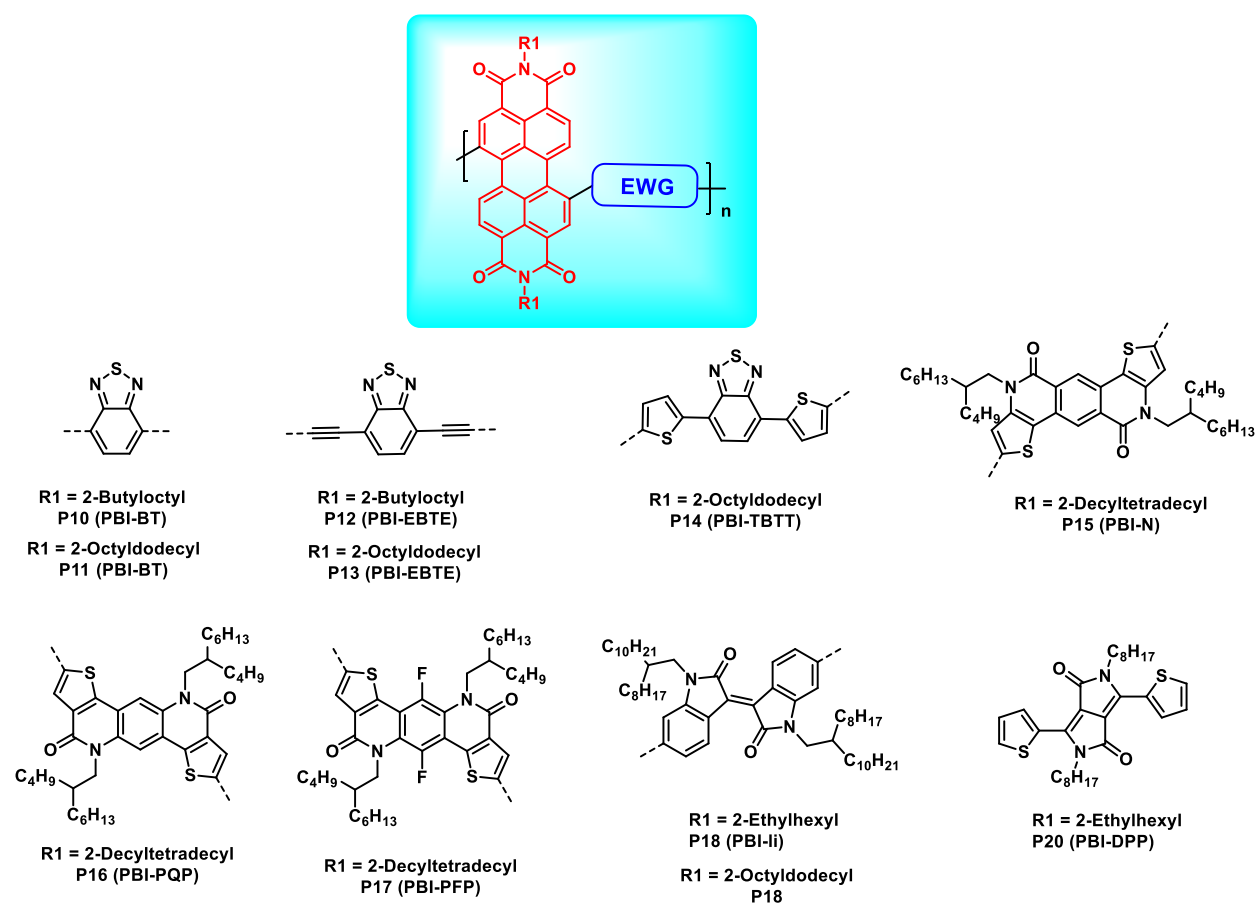


**Figure 1.2.15.** PBI and electron-withdrawing group-based copolymers (EWG)

Huang and coworkers come up with the PBI and indigo-based copolymers **P18** and **P19** in 2016,[67] including 2-octyldodecyl and 2-ethylhexyl alkyl chains, respectively (Figure 1.2.15). **P19**, a compound with a longer alkyl chain, showed a narrower band gap and a somewhat lower LUMO than **P18**. As a result, a PCE of **P19** (2.68 %) was obtained compared to **P18** (2.2%).

Diketopyrrolopyrrole (DPP), a popular building block with high redox properties and broad absorption, is used in many devices. A PBI-DPP copolymer **P20** was synthesized by Zhang et al. and its absorption spectra covered the range from 300-1000 nm with an optical band gap of HOMO-LUMO is 1.28 eV, and its PCE reached 2.01%.[68]

### 1.2.9. Areas of Application

PBIs were recognized as strong candidates for OSCs because of their suitable LUMO levels, exceptional optical and electronic properties as well as high mobility.[59,69] PBIs represent among the most actively researched topics in materials science and chemistry, notably in the area of nanotechnology and nanoscience, where they have been widely exploited as basic components for optoelectronic material.

### 1.2.9.1. Organic Solar Cell (OSCs)

In recent years, OSCs, a key type in photovoltaics, have gained popularity and significant attention for generating electricity from pure solar energy by utilizing their adaptable processing, large-area manufacturing, durability, and low cost.[70] To generate efficient OSCs, It has been established that charge transport must occur after photoinduced energy or electron transfer from the electron-donor group to electron-withdrawing aromatic units.[70,71] In light of this, specified architecture is another important aspect of future OSC device development that is greatly needed, besides the chemical modification of D-A type PBIs, oligomers, or copolymers.[72] Conversely, different from the traditional vacuum-deposition technique, these homogeneous materials can be easily assembled using solution-casting self-assembly, which represents a simple method to make inexpensive and large-area OSCs.

Significant improvements has been made by preassembled 1D nanofibers and solution casting of PBIs with necessary hole mobility in the D/A conjugated polymers in the heterojunction SCs,. As an example shown in Figure 1.2.16a, of **PBI1** xerogels containing amorphous hole transferring conducting polymer and 1D nanowires, **PvDMTPD** has been tested in SCs (Figure 1.2.16b).[73,74] With these **PBI1** and PvDMTPD heterojunction blends, a PCE of 0.041% has been achieved.[73] A system created by combining micrometer-long poly[2-methoxy-5-(3′,7′-dimethyloctyloxy)-1,4-phenylenevinylene] (P3HT) as donor polymer nanoribbons with **PBI2-C8** nanoribbons produced a more encouraging outcome with a PCE of approximately 1%.[74]
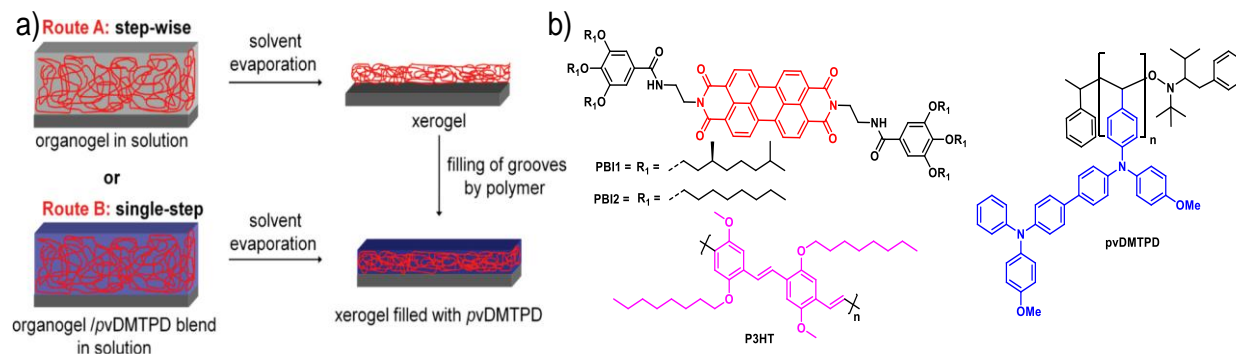
**Figure 1.2.16.** a) Schematic representation of organogel-polymer concept for realization of an interpenetrating organic bulk heterojunction. b) Molecular structures of perylene bisimide organogelator PBI and other polymers tested for SC.

PBIs and polythiophenes (P3HT), are the organic materials most likely to be used as electron D/A in organic photovoltaics, respectively.[70,71] Wasielewski group recently developed several fascinating photoinduced charge-separated devices.[75] The ortho-functionalized PBIs may attract particular attention towards commercial PBI-enrolled OSC devices because of the 1D supramolecular self-assembly approach. Overall, the photovoltaic devices using PBI materials, such as nanofibers, nevertheless have lower reported efficiency than fullerene-based materials. This is mostly because the materials could be better organized and phase separated, which restricts charge transport. The best way to deal with this problem might be to stack electron D/A molecules columnar into various charge-transport channels.

## 1.2.9.2. Linear Optoelectronics

PBI-based 1D self-assembled materials are excellent candidate for orientation-sensitive technologies like optical sensors, polarized OLED displays, flexible displays, nanolasers, optical waveguides, and electrical nanodevices.[76-79] These properties, known as linear optoelectronic characteristics, relate to the conductivity and uniaxial emission along a nanofiber's orientation. In particular, it has been proven that J aggregates are less appropriate for optoelectronic applications than H-type PBI aggregates.[80] Nevertheless, Charge and energy transport along a solid H-type nanofiber can be improved by molecular stacking, PBI compounds typically lose their luminescence because of an aggregation-connected quenching effect that still restricts their linear opticalelectronic characteristics in actual devices.[78,79] According to Zang et al. N,N′-dicyclohexyl-substituted PBI 1D nanobelts exhibit persistent, self-wave directed fluorescence

and strongly polarized, that results from a π-π stacking morphology known as the "flip-flap".[78,80] Further, upon receiving support from the rigid interactions of the stiff aryloxy-substituents at the bay position, observed needle-shaped crystals of **TBPCHPBI** displayed a high mobility of electron (1.8 $cm^2$ $V^1$ $s^1$). Crystals exhibited a luminescence quantum yield of 0.32 and intense red emission (Figure 1.2.17).[81]
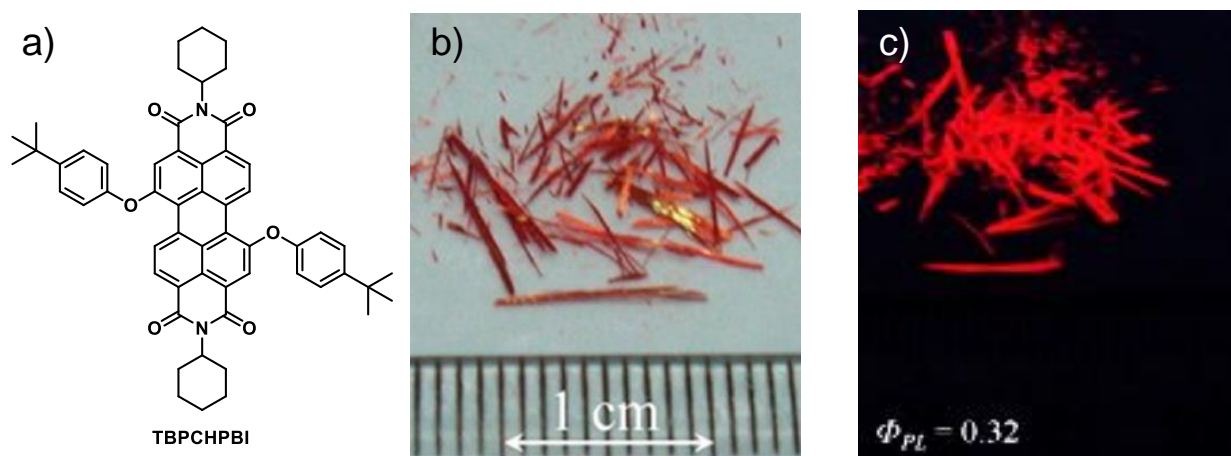


**Figure 1.2.17**. a) Molecular structure and photographs of the crystals under b) visible light, and c) upon excitation with UV light for **TBPCHPBI**.

## 1.2.9.3. Organic Field Effect Transistors (OFETs)

The stronger performance of OFETs, particularly organic materials is widely desired for lightweight, soluble, and flexible organic electronics like complementary inverts, ring oscillators, and integrated circuits. [82,83] Now is the perfect opportunity and period to use PBIs solution-casting 1D nanofibers in this area.[83,84] Due to their strong electron-accepting properties, favorable charge, and electron transport characteristics, to enhance the functionality of n-type OFETs, intermolecular stacking helps generate ordered nanostructures of linear PBI nanofibers.[84] The connections between PBIs' chemical structures and the efficiency of OFET have been the subject of numerous investigations.[84-86]
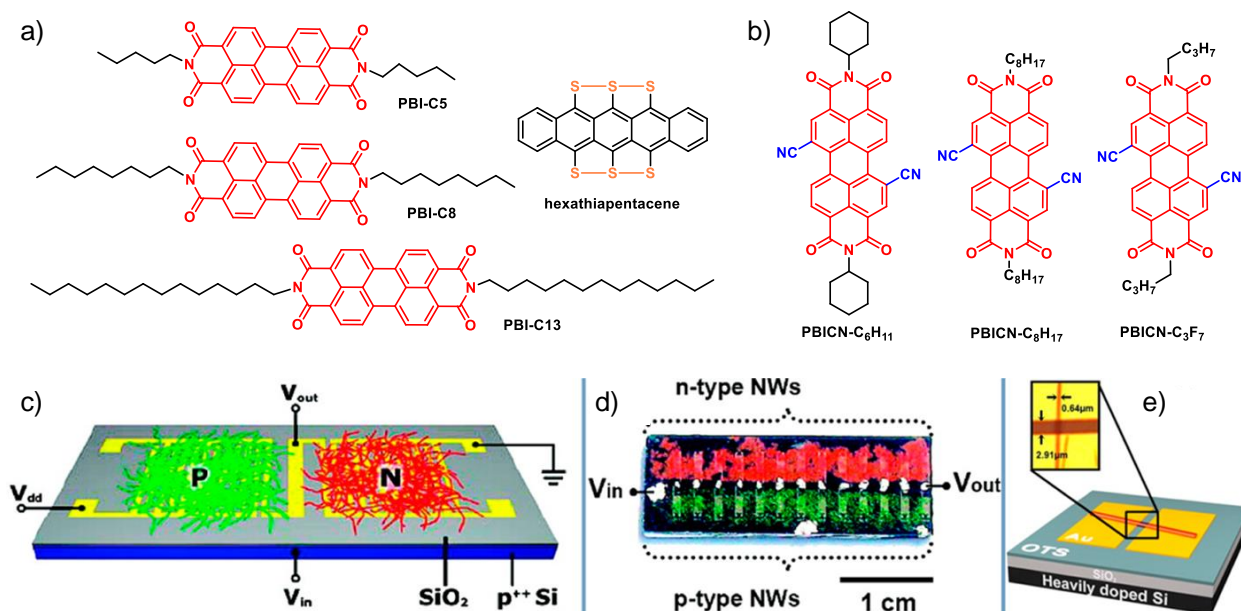
**Figure 1.2.18**. a), b) Chemical structures of the three perylenetetracarboxyldiimide (PBI) derivatives of varying dialkyl chain lengths synthesized as n-type semiconductor. c) Schematic of an inverter with p- and n-type nanowire networks covering interdigitated source drain electrodes, d) a photograph of a substrate containing 13 discrete inverters, and e) a schematic diagram of a single nanowire OFET.

In 2007, Xia and coworkers synthesized the **PBI-C5**, **PBI-C8**, and **PBI-C13** molecules, which attracted a lot of interest in this field (Figure 1.2.18a).[84,85] Inverters with high performance can be built, by mixing these *n-p* type transistors with hexathiapentacene nanowire OFETs as shown in Figure 1.2.18.[84] The imide nodes on the PBIs, there are no obvious variations in LUMO energy levels and shape; nonetheless, the higher alkyl chain leads to higher charge and electron mobility for OFET devices.[84] because they transfer charges in a band-like manner, **PBI-C8** and **PBI-C13** are also found to be significantly better options in the field of OFETs. [84,85,87] PBIs derivatives containing electron-withdrawing groups such as **CN** and **C3F7** (Figure 1.2.18b) helps to modify the LUMO energy levels, leading to developments.[83] The ability to create nanowire arrays of PBIs will probably be attainable by combining templating or etching technologies with solution-form self-assembly, thus boosting the OFETs effectiveness for commercial demands.

## 1.2.9.4. Chemical Vapor Sensing

Considering rapid globalization, digitization, and faster production methods within the industry, it is necessary to monitor our global or geographic environment to maintain safe living and working conditions so that our local areas might prosper. The primary tools for identifying and keeping track of the flammable, dangerous, and explosive analytes that are prevalent in our environment are sensors.[8] There has been a lot of interest in the development of chemical, vapor, and gas sensors, including optical, fluorescent, electrical, and acoustic.[8]
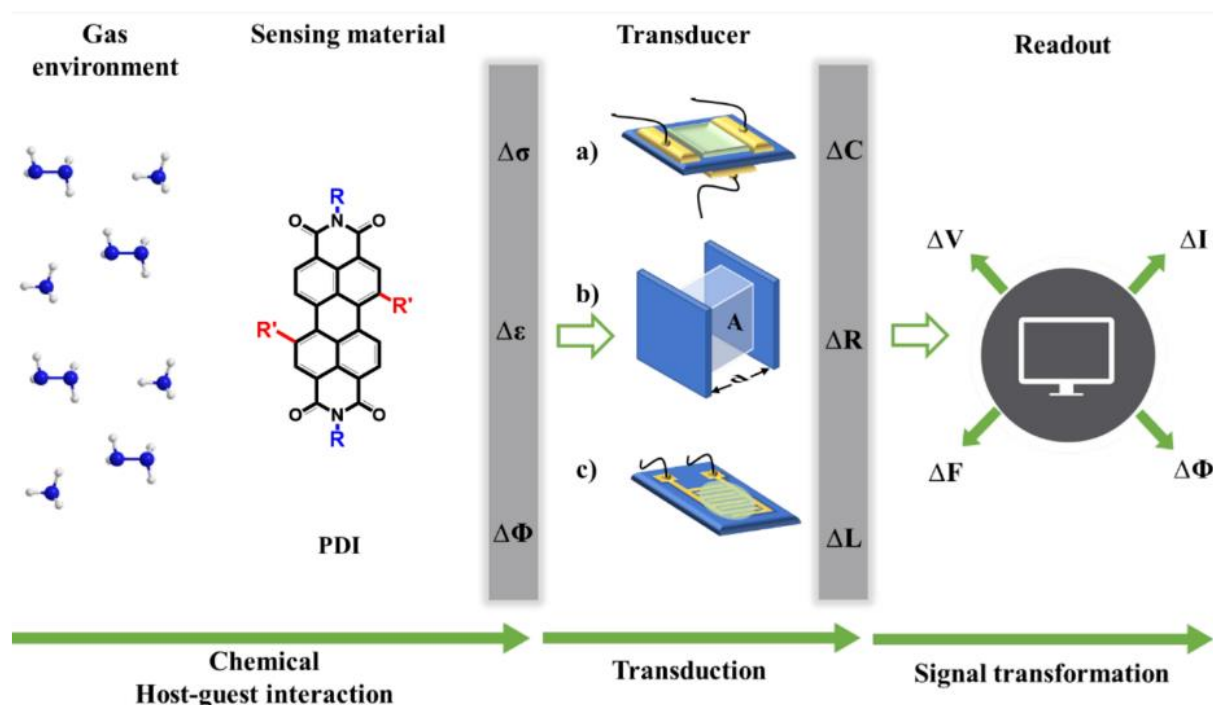


**Figure 1.2.19**. Schematic diagram illustrating the major components required to evaluate an electrical mode gas-sensing mechanism. The transducers are (a) FETs, (b) capacitors, and (c) chemiresistors.

In the early years, PBI-based nanofibers were tested for their potential to detect changes in electrical or fluorescent signals from a variety of reducing gaseous species, including nitric oxide, organic amines, $NH_3$, carbon monoxide, and dioxide, due to their electron-poor characteristics and n-type semiconductor.[76,88,89,90,91]

 In 1975, Lundstrom and coworkers developed the core components of a FET-based gas sensor for the initial time (Figure 19a).[92] Generally, electrical gas sensors typically use the three equipment designs of a capacitor, FET, and chemiresistor to record these gas-solid interactions

(amperometric and resistive).[93] The major application of capacitive-type sensors is the detection of molecules, including big entities like DNA,[94] proteins,[95] humidity,[96] and general gases.[97] A typical capacitive-type sensor consists of two parallel electrodes and an active layer sandwiched between them (Figure 1.2.19b). As shown in Figure 1.2.19c, most PBI-based sensors are chemiresistive. A chemiresistor is typically made up of interdigitated electrodes connected to a detection substance placed on an insulating substrate.[98]
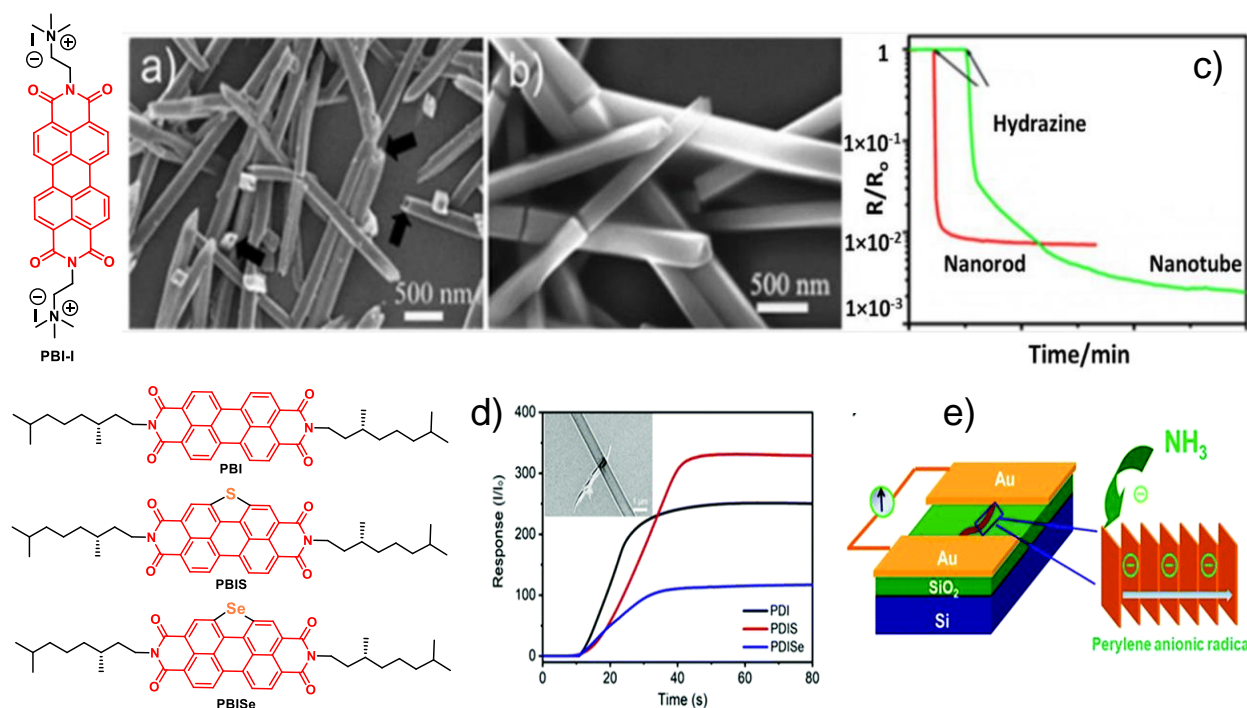


**Figure 1.2.20**. (a), (b) SEM images of nanotubes and nanorods of **PBI-I**. (c) Resistance modulation (R/Ro) vs. time (t) curve measured on a single nanotube and nanorods hydrazine vapor. d) Response (I/I0) of **PBI**, **PBIS**, **PBISe** devices in ammonia (100 ppm) and e) schematics of the sensing mechanism.

In 2009, Huang and coworkers synthesized self-assembled 1D linear nanorods and nanotubes of **PBI-I** (Figure 20) through the vaporization of an aqueous solution of **PBI-I** and they were utilized in resistive sensors.[99] The self-assembled one-dimensional nanotubes (200-300 nm) and nanorods (100-300 nm) (Figure 20a,b) of **PBI-I** showed significant sensitivity (100 and 1000 (R/Ro), respectively) towards hydrazine and phenylhydrazine vapors at 10 ppm (Figure 20c), as well as medium sensitivities (50 and 100, respectively) to vapors of triethylamine at 10 ppm.

A series of **PBI**, **PBIS**, and **PBISe** molecules were used to examine the chalcogenide incorporation effect on the sensing of PBIs (Figure 1.2.20).[100] The **PBI**, **PBIS**, and **PBISe** sense

showed responses to 100 ppm of $NH_4$ gas when used in a two-probe approach (Figure 1.2.20e). Interestingly, the selenide shows a decrease in current magnitude in comparison to carbocyclic **PBI** when treated with 100 ppm of $NH_4$ gas. When compared to the same **PBI**, the **PBIS** derivative increased. The **PBIS** finally demonstrated the best sensor performance, with response magnitudes 1.5 and 3 times larger than **PBI** and **PBISe**, respectively (Figure 1.2.20d).

## 1.2.10. Conclusion

The journey of the PTCDA molecule started in 1917 as insoluble material. After a century, PTCDA has replicated into a large family of synthetic dyes, pigments, and optoelectronic materials, because of the excellent thermal-photo stability, significant absorption coefficient, redox, and higher electron-accepting properties. Moreover, the substitutions at the imide, ortho, and bay positions have yielded an enormous number of PBI derivatives with unique chemical and electrochemical properties. To generate a huge family of PBIs, new functional demands and the availability of unique synthetic procedures, such as simple synthetic pathways and effective reactions under mild conditions with a wide range of substrates and effective functional group tolerance, encouraged a structural modification that made it possible to access structures that were elusive twenty years ago. These synthetic procedures help to control the optical, electrochemical, and conformational properties of PBIs, molecular synthesis of PBIs is achieved by different synthetic strategies like Imidization, ortho borylation, ortho halogenation, and substitution reactions at bay positions. As a result, effective synthetic procedures were available for the making of value-added PBI-based molecules such as small, star-shaped, oligomers, dendrimers, non-conjugated macrocycles, conjugated macrocycles, and Polymers.

## 1.2.11. Future Perspective

The above-described section summarizes the recent synthesis development that happened in the past twenty years of PBIs and the optical and electronic properties of their derivatives. Since the field of PBIs is rapidly expanding, but still, the development of novel synthetic protocols is essential for the ortho and bay position. As a result, the need to find more effective synthetic methods to give solutions where its limits to use. These initiatives will be geared towards minimizing the number of synthetic stages and by-product formation. Still, some problems exist in the synthesis of donor-accepter conjugated macrocycles with two- and four-fold functionalization of bay position.

Hence, clever designing strategies and a facile synthesis approach toward D/A conjugated macrocycle in a specific orientation with high yield will give a new future to the value-added product of perylene derivatives. The number of functional groups that can be substituted into bay areas is currently relatively small, despite some promising reports from recent years. Furthermore, these reactions are often low yielding and, as a result, typically contribute as a bottleneck for the synthesis.

To make PBIs marketable in the field of functional dyes, it will be necessary to address key issues like the synthesis of materials with customized properties, including the scalability of the approach, and the development of novel methodologies that would be more appealing to the industrial sector and would enable large-scale production. One potential future direction in the synthesis of PBI dyes could be the development of new synthetic routes that allow for the controlled assembly of PBI molecules into well-defined nanostructures, such as nanorods, nanotubes, or nanosheets. These PBI nanostructures have the potential to be used in various applications, including sensors, catalysis, and drug delivery. Currently, the research on PBI dye synthesis focuses on developing new synthetic routes that allow for the facile modification of the PBI core structure and the attachment of various substituents to fine-tune their properties. Additionally, efforts are being made to develop sustainable and environmentally friendly synthesis methods.

PBI dyes have demonstrated potential in various optoelectronic applications. Integrating PBI dyes into functional materials, such as metal-organic frameworks (MOFs), covalent organic frameworks (COFs), and supramolecular assemblies, could further expand their applications and enhance their performance. With the growing interest in emerging technologies such as organic bioelectronics, artificial intelligence, and quantum computing, exploring the potential of PBI dyes in these fields could lead to new and exciting applications. For example, PBI dyes have shown promise in biological imaging and sensing applications due to their strong fluorescence and high photostability.

## 1.2.12. References

1.  H. Zollinger, VCH. Weinheim, **2003**.

2.  W. Herbst, K. Hunger, WILEY-VCH. Weinheim, **1997**.

3.  H. Langhals, *Heterocycles*. **1995**, *40*, 477-500.

4.  W. Herbst, K. Hunger, Wiley-VCH, Weinheim, **2004**.

5.  G. Seybold, *Dyes and Pigments* **1989**, *11*, 303-317.

6.  C. Huang, S. Barlow, S. R. Marder, *J. Org. Chem*. **2011**, *76*, 2386-2407.

7.  F. Würthner, *Chem. Commun*. **2004**, *35*, 1564-1579

8.  a) F. Würthner, C. R. Saha-Möller, B. Fimmel, S. Ogi, P. Leowanawat, D. Schmidt, *Chem. Rev*. **2016**, *116*, 962-1052; b) S. Chen, P. Slattum, C. Wang, L. Zang, *Chem. Rev*. **2015**, *115*, 11967-11998; c) N. Liang, D. Meng, Z. Wang, *Acc. Chem. Res*. **2021**, *54*, 961-975.

9.  Z. Chen, B. Fimmel, F. Würthner, *Org. Biomol. Chem*. **2012**, *10*, 5845-5855.

10. a) J. E. Bullock, M. T. Vagnini, C. Ramanan, D. T. Co, T. M. Wilson, J. W. Dicke, T. J. Marks, M. R. Wasielewski, *J. Phys. Chem. B* **2010**, *114*, 1794-1802; b) S. Nakazono, S. Easwaramoorthi, D. Kim, H. Shinokubo, A. Osuka, *Org. Lett*. **2009**, *11*, 5426-5429; c) S. Nakazono, Y. Imazaki, H. Yoo, J. Yang, T. Sasamori, N. Tokitoh, T. Cédric, H. Kageyama, D. Kim, H. Shinokubo, A. Osuka, *Chem. Eur. J*. **2009**, *15*, 7530-7533.

11. T. Teraoka, S. Hiroto, H. Shinokubo, *Org. Lett*. **2011**, *13*, 2532-2535.

12. G. Battagliarin, Y. Zhao, C. Li, K. Müllen, *Org. Lett*. **2011**, *13*, 3399-3401.

13. G. Battagliarin, C. Li, V. Enkelmann, K. Müllen, *Org. Lett*. **2011**, *13*, 3012-3015.

14. T. Weil, T. Vosch, J. Hofkens, K. Peneva, K. Müllen, *Angew. Chem., Int. Ed*. **2010**, *49*, 9068-9093.

15. Y. Nagao, *Prog. Org. Chem*. **1997**, *31*, 43-49.

16. A. Wicklein, P. Kohn, L. Ghazaryan, T. Thurn-Albrecht, M. Thelakkat, *Chem. Commun*. **2010**, *46*, 2328.

17. A. Böhm, H. Arms, G. Henning, P. Blaschka, (BASF AG), *Ger. Pat. Appl,* DE19547209A1, **1997**.

18. F. Würthner, V. Stepanenko, Z. Chen, C. R. Saha-Möller, N. Kocher, D. Stalke, *J. Org. Chem.* **2004**, *69*, 7933-7939.

19. P. Rajasingh, R. Cohen, E. Shirman, L. J. W. Shimon, B. Rybtchinski, *J. Org. Chem.* **2007**, *72*, 5973-5979.

20. F. Würthner, A. Sautter, J. Schilling, *J. Org. Chem.* **2002**, *67*, 3037-3044.

21. a) T. Kawase, K. Tanaka, Y. Seirai, N. Shiono, M. Oda, *Angew. Chem. Int. Ed.* **2003**, *42*, 5597-5600; b) D. Canevet, M. Gallego, H. Isla, A. de Juan, E. M. P¦rez, N. Mart†n, *J. Am. Chem. Soc.* **2011**, *133*, 3184-3190; c) T. Iwamoto, Y. Watanabe, T. Sadahiro, T. Haino, S. Yamago, *Angew. Chem. Int. Ed.* **2011**, *50*, 8342-8344; b) K. A. Colby, J. J. Burdett, R. F. Frisbee, L. Zhu, R. J. Dillon, C. J. Bardeen, *J. Phys. Chem. A* **2010**, *114*, 3471-3482.

22. a) T. W. Bell, N. M. Hext, *Chem. Soc. Rev.* **2004**, *10*.1039.b207182g; b) L. Pu, *Chem. Rev.* **2004**, *104*, 1687-1716.

23. a) P. Wessig, *Angew. Chem. Int. Ed.* **2006**, *45*, 2168-2171; b) J. Ding, D. W. Armstrong, *Chirality* **2005**, *17*, 281-292.

24. E. W. Meijer, B. L. Feringab, *Mol. Cryst. Liq. Cryst.* **1993**, *235*, 169-180.

25. B. L. Feringa, R. A. van Delden, N. Koumura, E. M. Geertsema, *Chem. Rev.* **2000**, *100*, 1789-1816.

26. E. Peeters, M. P. T. Christiaans, R. A. J. Janssen, H. F. M. Schoo, H. P. J. M. Dekkers, E. W. Meijer, *J. Am. Chem. Soc.* **1997**, *119*, 9909-9910.

27. P. Osswald, M. Reichert, G. Bringmann, F. Würthner, *J. Org. Chem.* **2007**, *72*, 3403-3411.

28. M. M. Safont-Sempere, P. Osswald, K. Radacki, F. Würthner, *Chem. Eur. J.* **2010**, *16*, 7380-7384.

29. a) H. Bouas-Laurent, J.-P. Desvergne, A. Castellan, R. Lapouyade, *Chem. Soc. Rev.* **2001**, *30*, 248-263; b) V. Buß, C. Reichardt, *J. Chem. Soc., Chem. Commun.* **1992**, 1636-1638.

30. a) A. Leventis, J. Royakkers, A. G. Rapidis, N. Goodeal, M. K. Corpinot, J. M. Frost, D.-K. Bučar, M. O. Blunt, F. Cacialli, H. Bronstein, *J. Am. Chem. Soc.* **2018**, *140*, 1622-1626; b) C. Sun, M. M. Mróz, J. R. Castro Smirnov, L. Lüer, D. Hermida-Merino, C. Zhao, M. Takeuchi, K. Sugiyasu, J. Cabanillas-González, *J. Mater. Chem. C* **2018**, *6*, 6591-6596.

31. J. Royakkers, A. Minotto, D. G. Congrave, W. Zeng, A. Patel, A. D. Bond, D.-K. Bučar, F. Cacialli, H. Bronstein, *J. Org. Chem.* **2020**, *85*, 207-214.

32. a) J.-M. Lehn, *Science* **1985**, *227*, 849-856; b) M. Yoshizawa, J. K. Klosterman, M. Fujita, *Angew. Chem. Int. Ed.* **2009**, *48*, 3418-3438; c) J. Rebek, *Acc. Chem. Res.* **2009**, *42*, 1660-1668.

33. P. Spenst, F. Würthner, *Angew. Chem. Int. Ed.* **2015**, *54*, 10165-10168.

34. G. Ouyang, D. Bialas, F. Würthner, *Org. Chem. Front.* **2021**, *8*, 1424-1430.

35. V. Nikolaou, A. Charisiadis, C. Stangel, G. Charalambidis, A. G. Coutsolelos, *C* **2019**, *5*, 57.

36. T. A. Barendt, W. K. Myers, S. P. Cornes, M. A. Lebedeva, K. Porfyrakis, I. Marques, V. Félix, P. D. Beer, *J. Am. Chem. Soc*. **2020**, *142*, 349-364.

37. L. Dou, J. You, Z. Hong, Z. Xu, G. Li, R. A. Street, Y. Yang, *Adv. Mater*. **2013**, *25*, 6642-6671.

38. B. M. Savoie, A. Rao, A. A. Bakulin, S. Gelinas, B. Movaghar, R. H. Friend, T. J. Marks, M. A. Ratner, *J. Am. Chem. Soc*. **2014**, *136*, 2876-2884.

39. a) M. Ball, Y. Zhong, B. Fowler, B. Zhang, P. Li, G. Etkin, D. W. Paley, J. Decatur, A. K. Dalsania, H. Li, S. Xiao, F. Ng, M. L. Steigerwald, C. Nuckolls, *J. Am. Chem. Soc*. **2016**, *138*, 12861-12867; b) M. L. Ball, B. Zhang, Q. Xu, D. W. Paley, V. C. Ritter, F. Ng, M. L. Steigerwald, C. Nuckolls, *J. Am. Chem. Soc*. **2018**, *140*, 10135-10139.

40. B. Zhang, R. Hernández Sánchez, Y. Zhong, M. Ball, M. W. Terban, D. Paley, S. J. L. Billinge, F. Ng, M. L. Steigerwald, C. Nuckolls, *Nat Commun* **2018**, *9*, 1957.

41. M. Ball, B. Zhang, Y. Zhong, B. Fowler, S. Xiao, F. Ng, M. Steigerwald, C. Nuckolls, *Acc. Chem. Res*. **2019**, *52*, 1068-1078.

42. a) J. Krömer, I. Rios-Carreras, G. Fuhrmann, C. Musch, M. Wunderlin, T. Debaerdemaeker, E. Mena-Osteritz, P. Bäuerle, *Angew. Chem. Int. Ed*. **2000**, *39*, 3481-3486; b) K. Nakao, M. Nishimura, T. Tamachi, Y. Kuwatani, H. Miyasaka, T. Nishinaga, M. Iyoda, *J. Am. Chem. Soc*. **2006**, *128*, 16740-16747; c) A. Bhaskar, G. Ramakrishna, K. Hagedorn, O. Varnavski, E. Mena-Osteritz, P. Bäuerle, T. Goodson, *J. Phys. Chem. B* **2007**, *111*, 946-954; d) S. K. Maier, S.-S. Jester, U. Müller, W. M. Müller, S. Höger, *Chem. Commun*. **2011**, *47*, 11023; e) J. E. Donehue, O. P. Varnavski, R. Cemborski, M. Iyoda, T. Goodson, *J. Am. Chem. Soc*. **2011**, *133*, 4819-4828.

43. a) T. Iwamoto, Y. Watanabe, Y. Sakamoto, T. Suzuki, S. Yamago, *J. Am. Chem. Soc*. **2011**, *133*, 8354-8361; b) K. Matsui, Y. Segawa, K. Itami, *Org. Lett*. **2012**, *14*, 1888-1891.

44. a) M. J. Langton, J. D. Matichak, A. L. Thompson, H. L. Anderson, *Chem. Sci*. **2011**, *2*, 1897; b) M. C. O'Sullivan, J. K. Sprafke, D. V. Kondratuk, C. Rinfray, T. D. W. Claridge, A. Saywell, M. O. Blunt, J. N. O'Shea, P. H. Beton, M. Malfois, H. L. Anderson, *Nature* **2011**, *469*, 72-75; c) P. Liu, Y. Hisamune, M. D. Peeks, B. Odell, J. Q. Gong, L. M. Herz, H. L. Anderson, *Angew. Chem. Int. Ed*. **2016**, *55*, 8358-8362; d) A. Cnossen, C. Roche, H.

L. Anderson, *Chem. Commun*. **2017**, *53*, 10410-10413; e) P. S. Bols, H. L. Anderson, *Acc. Chem. Res*. **2018**, *51*, 2083-2092.

45.  a) W. Zhang, J. S. Moore, *J. Am. Chem. Soc*. **2004**, *126*, 12796-12796; b) B. Schmaltz, A. Rouhanipour, H. J. Räder, W. Pisula, K. Müllen, *Angew. Chem. Int. Ed*. **2009**, *48*, 720-724; c) T. Zhao, Z. Liu, Y. Song, W. Xu, D. Zhang, D. Zhu, *J. Org. Chem*. **2006**, *71*, 7422-7432; d) Y. Song, C. Di, Z. Wei, T. Zhao, W. Xu, Y. Liu, D. Zhang, D. Zhu, *Chem. Eur. J*. **2008**, *14*, 4731-4740.

46.  a) T. Sakida, S. Yamaguchi, H. Shinokubo, *Angew. Chem. Int. Ed*. **2011**, *50*, 2280-2283; b) X.-S. Ke, T. Kim, V. M. Lynch, D. Kim, J. L. Sessler, *J. Am. Chem. Soc*. **2017**, *139*, 13950-13956; c) Y. Qin, X. Liu, P.-P. Jia, L. Xu, H.-B. Yang, *Chem. Soc. Rev*. **2020**, *49*, 5678-5703.

47.  a) F. Schlosser, V. Stepanenko, F. Würthner, *Chem. Commun*. **2010**, *46*, 8350; b) F. Schlosser, J. Sung, P. Kim, D. Kim, F. Würthner, *Chem. Sci*. **2012**, *3*, 2778.

48.  K. Bold, M. Stolte, K. Shoyama, M. Holzapfel, A. Schmiedel, C. Lambert, F. Würthner, *Angew. Chem. Int. Ed*. **2022**, *61*, e202113598.

49.  K. Bold, M. Stolte, K. Shoyama, A. Krause, A. Schmiedel, M. Holzapfel, C. Lambert, F. Würthner, *Chem. Eur. J*. **2022**, *28*, e202200355.

50.  a) S. R. Forrest, *Nature* **2004**, *428*, 911-918; b) A. C. Arias, J. D. MacKenzie, I. McCulloch, J. Rivnay, A. Salleo, *Chem. Rev*. **2010**, *110*, 3-24.

51.  C. W. Tang, *Appl. Phys. Lett*. **1986**, *48*, 183-185.

52.  F. C. Krebs, *Energy Mater. Sol. Cells* **2009**, *93*, 394-412.

53.  M. S. White, M. Kaltenbrunner, E. D. Głowacki, K. Gutnichenko, G. Kettlgruber, I. Graz, S. Aazou, C. Ulbricht, D. A. M. Egbe, M. C. Miron, Z. Major, M. C. Scharber, T. Sekitani, T. Someya, S. Bauer, N. S. Sariciftci, *Nature Photon* **2013**, *7*, 811-816.

54.  a) C. W. Tang, *Appl. Phys. Lett*. **1986**, *48*, 183-185; b) S. Yu, Y. Chen, J. Wu, D. Xia, S. Hong, X. Wu, J. Yu, S. Zhang, A. Peng, H. Huang, *ACS Appl. Mater. Interfaces* **2018**, *10*, 28812-28818; c) L. Yang, W. Gu, L. Lv, Y. Chen, Y. Yang, P. Ye, J. Wu, L. Hong, A. Peng, H. Huang, *Angew. Chem. Int. Ed*. **2018**, *130*, 1108-1114.

55.  X. Guo, A. Facchetti, T. J. Marks, *Chem. Rev*. **2014**, *114*, 8943-9021.

56.  Q. Shi, J. Wu, X. Wu, A. Peng, H. Huang, *Chem. Eur. J*. **2020**, *26*, 12510-12522

57. S. Dai, Y. Lin, P. Cheng, Y. Wang, X. Zhao, Q. Ling, X. Zhan, *Dyes and Pigments* **2015**, *114*, 283-289.

58. H.-J. Yun, S.-J. Kang, Y. Xu, S. O. Kim, Y.-H. Kim, Y.-Y. Noh, S.-K. Kwon, *Adv. Mater.* **2014**, *26*, 7300-7307.

59. Y. Guo, Y. Li, H. Han, H. Yan, D. Zhao, *Chin J Polym Sci* **2017**, *35*, 293-301.

60. L. Lv, X. Wang, X. Wang, L. Yang, T. Dong, Z. Yang, H. Huang, *ACS Appl. Mater. Interfaces* **2016**, *8*, 34620-34629.

61. B. Xiao, G. Ding, Z. Tan, E. Zhou, *Polym. Chem.* **2015**, *6*, 7594-7602.

62. W. Xiong, X. Meng, T. Liu, Y. Cai, X. Xue, Z. Li, X. Sun, L. Huo, W. Ma, Y. Sun, *Organic Electronics* **2017**, *50*, 376-383.

63. X. Zhao, Y. Wen, L. Ren, L. Ma, Y. Liu, X. Zhan, *J. Polym. Sci. A Polym. Chem.* **2012**, *50*, 4266-4271.

64. C.-W. Ge, C.-Y. Mei, J. Ling, J.-T. Wang, F.-G. Zhao, L. Liang, H.-J. Li, Y.-S. Xie, W.-S. Li, *J. Polym. Sci. Part A: Polym. Chem.* **2014**, *52*, 1200-1215.

65. M. Liu, J. Yang, Y. Yin, Y. Zhang, E. Zhou, F. Guo, L. Zhao, *J. Mater. Chem. A* **2018**, *6*, 414-422.

66. a) I. H. Jung, W.-Y. Lo, J. Jang, W. Chen, D. Zhao, E. S. Landry, L. Lu, D. V. Talapin, L. Yu, *Chem. Mater.* **2014**, *26*, 3450-3459; b) I. H. Jung, D. Zhao, J. Jang, W. Chen, E. S. Landry, L. Lu, D. V. Talapin, L. Yu, *Chem. Mater.* **2015**, *27*, 5941-5948.

67. X. Wang, L. Lv, L. Li, Y. Chen, K. Zhang, H. Chen, H. Dong, J. Huang, G. Shen, Z. Yang, H. Huang, *Adv. Funct. Mater.* **2016**, *26*, 6306-6315.

68. Y. Li, Y. Yang, X. Bao, M. Qiu, Z. Liu, N. Wang, G. Zhang, R. Yang, D. Zhang, *J. Mater. Chem. C* **2016**, *4*, 185-192.

69. a) G. Li, R. Zhu, Y. Yang, *Nat. Photonics* **2012**, *6*, 153-161. b) X. Guo, N. Zhou, S. J. Lou, J. Smith, D. B. Tice, J. W. Hennek, R. P. Ortiz, J. T. L. Navarrete, S. Li, J. Strzalka, L. X. Chen, R. P. H. Chang, A. Facchetti, T. J. Marks, *Nat. Photonics* **2013**, *7*, 825-833. c) Y. Zou, A. Najari, P. Berrouard, S. Beaupré, B. Réda Aïch, Y. Tao, M. Leclerc, *J. Am. Chem. Soc.* **2010**, *132*, 5330-5331.

70. C. Li, H. Wonneberger, *Adv. Mater.* **2012**, *24*, 613-636.

71. E. Kozma, M. Catellani, *Dyes and Pigments* **2013**, *98*, 160-179.

72. Q. Yan, Z. Luo, K. Cai, Y. Ma, D. Zhao, *Chem. Soc. Rev.* **2014**, *43*, 4199-4221.

73.   A. Wicklein, S. Ghosh, M. Sommer, F. Würthner, M. Thelakkat, *ACS Nano* **2009**, *3*, 1107-1114.

74.   S. Karak, S. K. Ray, A. Dhar, *Appl. Phys. Lett*. **2010**, *97*, 043306.

75.   L. E. Shoer, S. W. Eaton, E. A. Margulies, M. R. Wasielewski, *J. Phys. Chem. B* **2015**, *119*, 7635-7643.

76.   L. Zang, Y. Che, J. S. Moore, *Acc. Chem. Res*. **2008**, *41*, 1596-1608.

77.   X.-Q. Li, X. Zhang, S. Ghosh, F. Würthner, *Chem. Eur. J*. **2008**, *14*, 8074-8078.

78.   Y. Che, X. Yang, K. Balakrishnan, J. Zuo, L. Zang, *Chem. Mater*. **2009**, *21*, 2930-2934.

79.   Y. Li, T. Liu, H. Liu, M.-Z. Tian, Y. Li, *Acc. Chem. Res*. **2014**, *47*, 1186-1198.

80.   D. Chaudhuri, D. Li, Y. Che, E. Shafran, J. M. Gerton, L. Zang, J. M. Lupton, *Nano Lett*. **2011**, *11*, 488-492.

81.   M.-M. Shi, V. C. Tung, J.-J. Nie, H.-Z. Chen, Y. Yang, *Organic Electronics* **2014**, *15*, 281-285.

82.   L. Ma, Y. Guo, Y. Wen, Y. Liu, X. Zhan, *Appl. Phys. Lett*. **2013**, *103*, 203303.

83.   Y. Zhao, Y. Guo, Y. Liu, *Adv. Mater*. **2013**, *25*, 5372-5391.

84.   A. L. Briseno, S. C. B. Mannsfeld, C. Reese, J. M. Hancock, Y. Xiong, S. A. Jenekhe, Z. Bao, Y. Xia, *Nano Lett*. **2007**, *7*, 2847-2853.

85.   B. J. Kim, H. Yu, J. H. Oh, M. S. Kang, J. H. Cho, *J. Phys. Chem. C* **2013**, *117*, 10743-10749.

86.   A. Arulkashmir, B. Jain, J. C. John, K. Roy, K. Krishnamoorthy, *Chem. Commun*. **2014**, *50*, 326-328.

87.   A. V. Mumyatov, L. I. Leshanskaya, D. V. Anokhin, N. N. Dremova, P. A. Troshin, *Mendeleev Commun*. **2014**, *24*, 306-307.

88.   a) A. Zandi, A. Gilani, H. Ghafoori fard, J. Koohsorkhi, *Diam. Relat. Mater*. **2019**, *93*, 224-232. b) L. Gao, J. Zhang, L. Zhai, X. Wang, L. Fan, T. Hu, *Polyhedron* **2019**, *165*, 171-176. c) M. Shafiei, P. G. Spizzirri, R. Arsat, J. Yu, J. du Plessis, S. Dubin, R. B. Kaner, K. Kalantar-zadeh, W. Wlodarski, *J. Phys. Chem. C* **2010**, *114*, 13796-13801. d) S. Chen, N. Gao, B. R. Bunes, L. Zang, *J. Mater. Chem. C* **2019**, *7*, 13709-13735. e) S. Ali, A. Gupta, M. Shafiei, S. J. Langford, *Chemosensors* **2021**, *9*, 30.

89.   Y. Huang, L. Fu, W. Zou, F. Zhang, Z. Wei, *J. Phys. Chem. C* **2011**, *115*, 10399-10404.

90.    Y. Che, A. Datar, X. Yang, T. Naddo, J. Zhao, L. Zang, *J. Am. Chem. Soc*. **2007**, *129*, 6354-6355.

91.    Y. Che, X. Yang, S. Loser, L. Zang, *Nano Lett*. **2008**, *8*, 2219-2223.

92.    K. I. Lundström, M. S. Shivaraman, C. M. Svensson, *J. Appl. Phys*. **1975**, *46*, 3876-3881.

93.    a) C. Zhang, P. Chen, W. Hu, *Chem. Soc. Rev*. **2015**, *44*, 2087-2107. b) M.-S. Yao, W.-X. Tang, G.-E. Wang, B. Nath, G. Xu, *Adv. Mater*. **2016**, *28*, 5229-5234.

94.    H. Cui, C. Cheng, X. Lin, J. Wu, J. Chen, S. Eda, Q. Yuan, *Sens. Actuators B* **2016**, *226*, 245-253.

95.    M. Tahir, M. H. Sayyad, J. Clark, F. Wahab, F. Aziz, M. Shahid, M. A. Munawar, J. A. Chaudry, *Sens. Actuators B* **2014**, *192*, 565-571.

96.    O. Yassine, O. Shekhah, A. H. Assen, Y. Belmabkhout, K. N. Salama, M. Eddaoudi, *Angew. Chem*. **2016**, *128*, 16111-16115.

97.    Z. Lou, L. Li, L. Wang, G. Shen, *Small* **2017**, *13*, 1701791.

98.    G. Neri, *Chemosensors* **2015**, *3*, 1-20.

99.    Y. Huang, B. Quan, Z. Wei, G. Liu, L. Sun, *J. Phys. Chem. C* **2009**, *113*, 3929-3933.

100.   Q. Deng, E. Zhou, Y. Huang, W. Qing, H. Zhai, Z. Liu, Z. Wei, *Chem. Commun*. **2019**, *55*, 4379-4382.

# Chapter–2

# Oligothiophene-Ring-Strapped Perylene Bisimides: Functionalizable Coaxial Donor-Acceptor Macrocycles

# Chapter–2

# Oligothiophene-Ring-Strapped Perylene Bisimides: Functionalizable Coaxial Donor-Acceptor Macrocycles
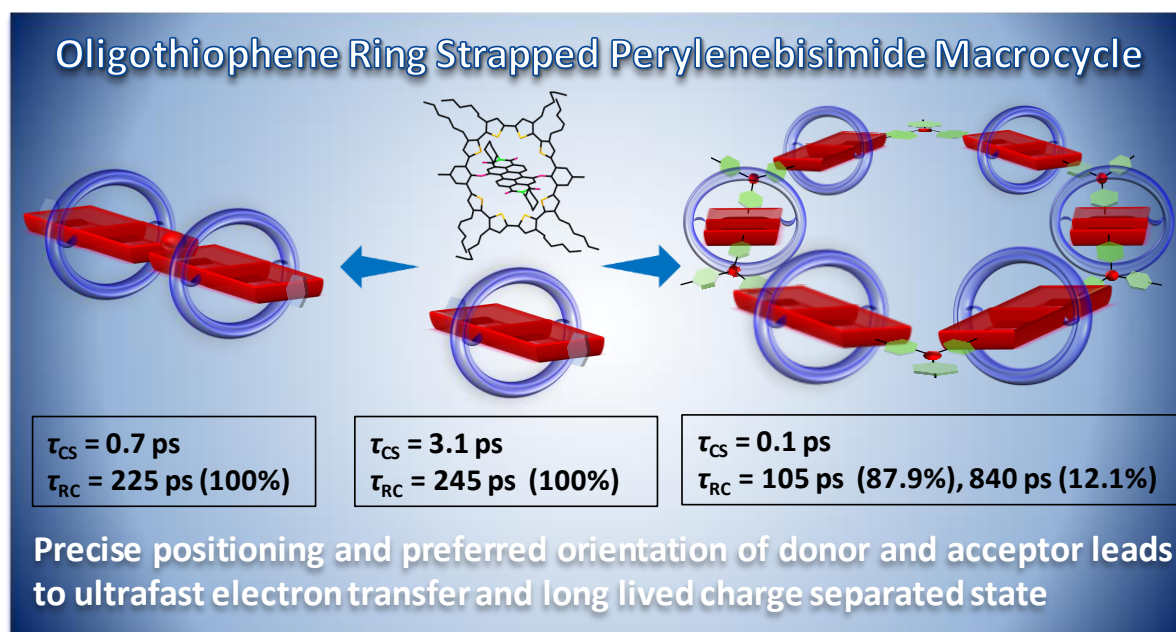


Aesthetic designs from nature enable to gain new knowledge and, at the same time, inspire to materialize the unattempted scientific models. In this context, multicomponent macrocycles embody the advantage of precisely positioning the structural units to achieve efficient communication between them. However, a functionalizable macrocycle to achieve ultrafast charge separation and stabilization has not been attempted. Here, we report the synthesis, crystal structure, and transient absorption of a new functionalizable macrocycle consisting of oligothiophene ring-strapped perylene bisimide. Transient absorption results point to a sequential improvement in charge separation and stabilization from the macrocycle to the corresponding linear dimer and 2D-polymer due to the unique design. Our macrocycle design with a supportive spatial arrangement of the donor and acceptor units will urge more complex synthetic systems with exciting electron transfer and charge separation features.

## 2.1. Introduction

Nature always inspires to draw new molecular and supramolecular designs to solve many fundamental scientific challenges. For instance, the natural photosynthetic system having long-lived charge separation (CS) is still a fascinating concept to mimic and realize in a lab.[1-3] The presence of an ordered molecular unit with optimized energy leads to efficient energy, and electron-transfer (ET) processes urge the design of many synthetic analogs. A detailed understanding of the topic revealed that the preferred orientation of chromophores in donor-acceptor (D-A) assemblies support achieving long-lived CS.[4-6] Hence, many D-A-based coaxial designs have been trialed in this direction to achieve better CS.[7-10] Among those, a combination of perylene bisimides (PBIs) with various donor molecules exhibited faster ET and a long-lived CS state.[11] PBIs are the widely studied dyes for the fascinating optical and redox features, outstanding electron transport, and self-assembly to form diverse nanostructures.[11-23] Hence PBIs found useful in various applications, including organic solar cells, batteries, supercapacitors, sensors, photocatalysis etc.[16,17,24-31] The synthetic manipulation through core functionalization up to four bay positions (1,6,7,12) and four ortho positions (2,5,8,11) resulted in numerous derivatives, and it made PBIs a favorite choice of organic materials chemists.[32-37] Many supramolecular assemblies of PBIs with CNT, carbon nanodots etc. have also been explored for ET studies.[38,39] In addition, many complex molecular architectures, polymers, and macromolecules of PBIs have been reported in combination with other functional molecules.[40-45] The most exploited electron D-A pair of PBIs and thiophenes has led to *p-n*-heterojunctions useful in energy harvesting and storage devices.[46-49] Many research groups were keenly involved in synthesizing PBI-based macrocycles, even using a D-A combination.[50-52] Ball et al. reported giant macrocycles of fused PBI dimer, PBI (acceptor), and bithiophene (donor) strap achieved through multinuclear metal (Pd/Pt) intermediates, and the former exhibits high electron mobility.[50,51] However, a completely donor-strapped PBI remained unexplored until Würthner and co-workers reported macrocyclic D-A dyads through imide functionalization of PBI using cyclic oligothiophene *via* a platinum-mediated cross-coupling reaction.[52,53] In all these oligothiophene-PBI macrocycles, the yield was only moderate.[50-53] Interestingly, the macrocyclic dyad exhibited an ultrafast ET within ca. 1 ps from the donor oligothiophene to the acceptor perylenebisimide. Though the donor-acceptor units are suitably placed in the dyad, fast charge recombination within 8-12 ps was observed. Hence, alternate molecular designs involving high-yield reactions might be considered to fasten the ET process and

achieve a long-lived CS state. Herein, we synthesized half and full oligothiophene ring strapped PBIs substituted at the bay position, resulting in a new D-A macrocycle dyad (Scheme 1). Moreover, the functionalization of the macrocycle delivered the corresponding linear dimer and two-dimensional (2D)-polymer. Our approach focused on bay substituted strapped PBI with D-A units oriented nearly orthogonal to enhance the ET. Though many strapped or encapsulated molecular systems have been reported,[53,54] a combination of electron-donating oligothiophene with electron-accepting PBIs may lead to exciting heterojunction materials.

## 2.2. Experimental section

### 2.2.1. Electrochemical analysis

Cyclic voltammetry (CV) and Differential pulse voltammetry (DPV) measurements were carried out on a CHI voltammetry analyzer at room temperature, employing a three-electrode single compartment cell: glassy carbon electrode (company, d = 2mm) as working electrode, a Pt wire as counter electrode and Ag/AgCl as a reference electrode. The supporting electrolyte, Tetrabutylammonium hexafluorophosphate ($n$-Bu$_4$NPF$_6$), was previously dried under vacuum, dichloromethane was dried and degassed before use, and all measurements were performed under a nitrogen atmosphere. Ferrocene was used as an internal standard for calibrating the potential ($E_{Fc+/Fc}$ = 0.00 V).

The formal redox potentials (half-wave potentials) were calculated using the formula:

$$E_{1/2} = (E_{pa} + E_{pc}) / 2$$

Where $E_{pa}$ is the peak anode potential and

$E_{pc}$ is the peak cathode potential.

HOMO energies were calculated from the first formal redox potentials (half-wave potentials) using the equation:

$$E_{HOMO} = -(4.8 \text{ eV} + E^1_{oxd} \text{ vs. } Fc^+\!/Fc)$$

However, LUMO energies were calculated from the first formal redox potentials (half-wave potentials) using the equation:

$$E_{LUMO} = -(4.8 \text{ eV} + E^1_{red} \text{ vs. } Fc^+\!/Fc)$$

### 2.2.2. Femtosecond transient absorption spectroscopy

The transient experiments were using a Helios Fire pump-probe spectrometer set up (Ultrafast System). Ti:Sapphire amplifier system (Astrella, Coherent, 800 nm, 3mJ/pulse energy, ~ 35 fs pulse width and 1 kHz repetition rate) was used to generate ultrafast pulses.

The output of the laser pulse was then splitted into two parts (95:5) to generate pump and probe beam. The higher energy beam travels to an Optical Parametric Amplifier (OPerA-SOLO) to generate requisite pump wavelengths. The lower energy beam passes through sapphire crystal in order to generate white light. A mechanical delay stage was in place to maintain perfect delay between pump and probe beam. The transient data was recorded keeping the sample in a 2mm quartz cuvette and analyzed using surface xplorer software. All the experimental measurements were carried out at room temperature.

### 2.2.3. Computational Methods

All the DFT calculations were carried out by employing Gaussian09 software using B3LYP/6-31G(d) level of theory. To save computational cost, the long alkyl chains were truncated to methyl group. PCM solvation model was used to take account of long-range interactions as well as the solvation effect of dichloromethane, respectively.

## 2.3. Experimental Procedures: Synthesis

### 2.3.1. Synthesis of oligothiophene ring strapped TSP1 and TSP2 macrocycles
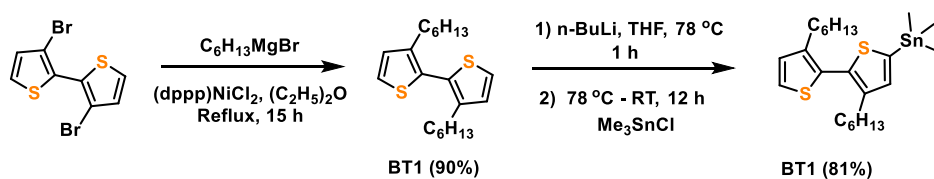


**Scheme 2.1:** Synthesis of **BT1** and **BT2** molecules.
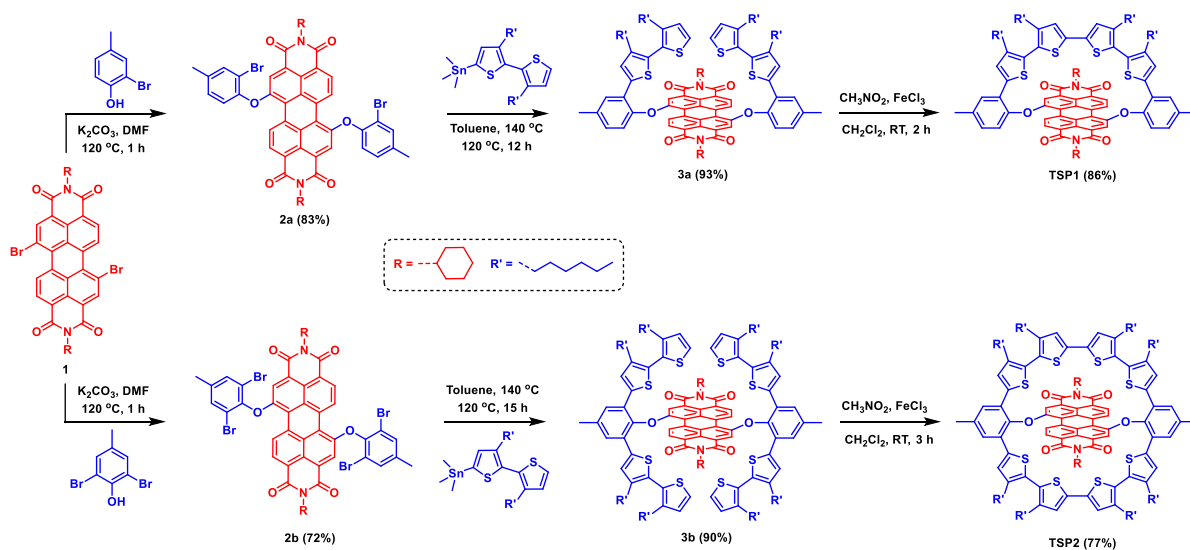


**Scheme 2.2:** Synthesis of oligothiophene ring strapped **TSP1** and **TSP2** macrocycles.

**2.3.1.1. Synthesis of 3,3'-dihexyl-2,2'-bithiophene (BT1)**[55]
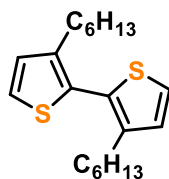


In 250 mL two necked oven-dried round bottom flask hexylmagnesium bromide (65 mL, 2M in diethyl ether) was slowly added to the solution of 3,3'-dibromo-2,2'-bithiophene (10 g, 10 mmol) and dichloro[1,3-bis(diphenylphosphino)propane]nickel (55 mg, 0.10 mmol) in anhydrous diethyl ether (100 mL) at 0 $^o$C. The reaction mixture was refluxed for 15 h under an inert atmosphere. After completion, the reaction mixture was cooled to room temperature and quenched by adding sat. $NH_4Cl$. The mixture was extracted with $CH_2Cl_2$, washed twice with brine, then dried over anhydrous $Na_2SO_4$, concentrated under reduced pressure. The crude product was purified via silica gel column chromatography using petroleum ether as the eluent to yield colorless oil (9.3 g, 90%).

**$^1$H NMR (400 MHz, CDCl$_3$):** $\delta$ **[ppm]** = 7.30 (d, $J$ = 5.2 Hz, 2H), 6.98 (d, $J$ = 5.2 Hz, 2H), 2.51 (t, $J$ = 7.2 Hz, 4H), 1.51-1.58 (m, 4H), 1.22-1.30 (m, 12H), 0.86 (t, $J$ = 6.3 Hz, 6H).

**$^{13}$C NMR (100 MHz, CDCl$_3$):** $\delta$ **[ppm]** = 142.3, 128.7, 128.5, 125.2, 31.6, 30.7, 29.1, 28.8, 22.6, 14.1.

**HRMS (ESI):** *m/z* calculated for $C_{20}H_{31}S_2$ [M+H]$^+$: 335.1862, found: 335.1857.

**2.3.1.2. Synthesis of (3,3'-dihexyl-[2,2'-bithiophen]-5-yl)trimethylstannane (BT2)**[55]
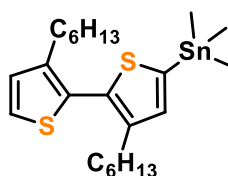


In 100 mL two necked oven-dried round bottom flask added solution of 3,3'-dihexyl-2,2'-bithiophene (5 g, 14.94 mmol) in 40 mL of anhydrous THF, 1.6 M *n*-butyl lithium (9.4 mL, 14.94 mmol) was added dropwise over a 10 min at -78 $^o$C under inert atmosphere. The mixture was stirred at -78 $^o$C for the next one hour, and then trimethyltin chloride (3.9 g, 19.58 mmol) in THF was added dropwise. The reaction mixture was warmed to room temperature and stirred for 12 h. The obtained clear solution was diluted with diethyl ether and washed with water. The organic layer was dried over anhydrous $Na_2SO_4$, and the solvents were concentrated under reduced pressure. The crude product light brownish oil (1.97 g, 81%) was used without further purification for the next step.

**$^1$H NMR (500 MHz, CDCl$_3$):** $\delta$ **[ppm]** = 7.28 (d, *J* = 5.2 Hz, 1H), 7.04 (s, 1H), 6.97 (d, *J* = 5.2 Hz, 1H), 2.49-2.54 (m, 4H), 1.52-1.57 (m, 4H), 1.22-1.28 (m, 12H), 0.86 (t, *J* = 6.3 Hz, 6H), 0.39 (s, 9H).

**HRMS (ESI):** *m/z* calculated for C$_{23}$H$_{39}$S$_2$Sn [M+H]$^+$: 499.1510, found: 499.1502.

### 2.3.1.3. *N,N′*-Dicyclohexyl-1,7-dibromoperylene-3,4:9,10-bisdicarboximide (1)[56]
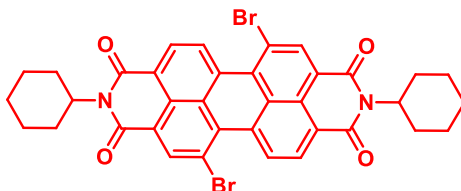


A 100 mL pressure tube is charged with1,7-dibromo-perylene tetracarboxylic acid anhydride (600 mg, 1.09 mmol), cyclohexylamine (325 mg, 3.27 mmol), ethanol (30 mL), DMF (30 mL). The reaction mixture was stirred at 120 °C under an inert atmosphere for 3 h. After the reaction, the tube cooled down to room temperature, and 250 mL CH$_2$Cl$_2$was added to the reaction mixture. The organic layer was washed with (6×50 mL) of water; the combined organic phases dried over anhydrous Na$_2$SO$_4$, and the solvents were removed under reduced pressure. The crude product was purified by silica gel column chromatography using CH$_2$Cl$_2$-petroleum ether (9:1 v/v) to give **1** as a red solid (628 mg, 81 %).

**$^1$H NMR (500 MHz, CDCl$_3$):** $\delta$ **[ppm]** = 9.46 (d, *J* = 8.2 Hz, 2H), 8.86 (s, 2 H), 8.67 (d, *J* = 8.2 Hz, 2H), 5.02 (tt, *J* = 3.7, 12.1 Hz, 2H), 2.55 (qd, *J* = 3.3, 12.5 Hz, 4H), 1.93 (d, *J* = 13.2 Hz, 4H), 1.76 (dd, *J* = 3.5, 8.2 Hz, 6H), 1.44-1.52 (m, 4H), 1.31-1.39 (m, 2H).

**$^{13}$C NMR (125 MHz, CDCl$_3$):** $\delta$ **[ppm]** = 163.3, 162.7, 137.9, 132.7, 132.6, 129.9, 129.2, 128.4, 127.0, 123.7, 123.3, 120.7, 54.2, 29.1, 26.5, 25.4.

**FT-IR** (cm$^{-1}$): 2953-2845, 1738, 1700, 1654, 1461, 1265, 1078, 1013, 790.

**MALDI-TOF:** *m/z* calculated for C$_{36}$H$_{29}$Br$_2$N$_2$O$_4$ [M+H]$^+$: 711.0494, found: 711.0835.

### 2.3.1.4. *N,N'*-Dicyclohexyl-1,7-bis(4-methylphenoxy)perylene-3,4:9,10-bisdicarboximide (rPBI)
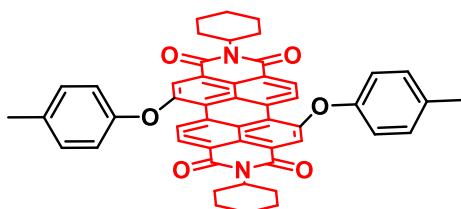


To a degassed solution of **1** (70 mg, 98.25 µmol) in dry DMF (10 mL), potassium carbonate (41 mg, 294.27 µmol) and 4-methylphenol (27 mg, 245.64 µmol) was added. The reaction mixture was stirred at 120 °C for 1 h. After being cooled to room temperature, the solvent is

removed by rotary evaporation. The crude reaction mixture was extracted with $CH_2Cl_2$, and the organic layer was washed with (3×30 mL) of water. The combined organic phase was dried over anhydrous $Na_2SO_4$, and the solvent was removed under reduced pressure. The compound was purified by silica gel column chromatography using $CH_2Cl_2$-petroleum ether (7:3 v/v) as eluent to yield **rPBI** as a red solid (60 mg, 80 %).

**$^1$H NMR (500 MHz, CDCl$_3$):** $\delta$ **[ppm]** = 9.56 (d, $J$ = 8.5 Hz, 2 H), 8.55 (d, $J$ = 8.5 Hz, 2 H), 8.25 (s, 2 H), 7.26 (d, $J$ = 8.2 Hz, 4 H), 7.06 (d, $J$ = 8.2 Hz, 4 H), 4.99 (t, $J$ = 12.1 Hz, 2 H), 2.46 - 2.57 (m, 4 H), 2.41 (s, 6 H), 1.89 (d, $J$ = 12.5 Hz, 4 H), 1.69 - 1.79 (m, 6 H), 1.44 (q, $J$ = 12.8 Hz, 4 H), 1.26 - 1.35 (m, 2 H).

**$^{13}$C NMR (100 MHz, CDCl$_3$):** $\delta$ **[ppm]** = 163.8, 163.4, 155.6, 152.7, 134.9, 133.3, 131.0, 130, 129.1, 128.7, 124.9, 124.2, 123.4, 123.3, 122.6, 119.6, 53.9, 29.1, 26.5, 25.4, 20.8.

**MALDI-TOF:** $m/z$ calculated for $C_{50}H_{42}N_2O_6$ [M]$^+$ 766.3043, found: 766.653.

### 2.3.1.5. *N,N'*-Dicyclohexyl-1,7-bis(2-bromo-4-methylphenoxy)perylene-3,4:9,10-bisdicarboximide (2a)
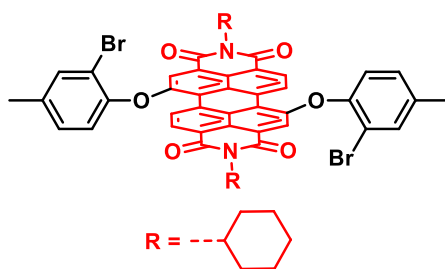


A 250 mL two necked flask is charge with **1** (1g, 1.40 mmol), potassium carbonate (582 mg, 4.21 mmol), 2-bromo-4-methylphenol (656 mg, 3.51 mmol) and into that added anhydrous, degassed DMF (100 mL) under argon, then the reaction mixture was stirred at 120 °C for 1 h. After being cooled to room temperature, the solvent is removed by rotary evaporation. The crude reaction mixture was extracted with $CH_2Cl_2$, and the organic layer was washed with (6×100 mL) of water. The combined organic phases dried over anhydrous $Na_2SO_4$, and the solvents were removed under reduced pressure. The compound was purified by silica gel column chromatography using $CH_2Cl_2$-petroleum ether (8:2 v/v) to give **2a** as an orange solid (1.08 mg, 83%).

**$^1$H NMR (400 MHz, CDCl$_3$):** $\delta$ **[ppm]** = 9.67 (d, $J$ = 8.4 Hz, 2H), 8.62 (d, $J$ = 8.4 Hz, 2H), 8.09 (s, 2H), 7.58 (d, $J$ = 1.2 Hz, 2H), 7.20 (dd, $J$ = 1.2, 8.3 Hz, 2H), 7.04 (d, $J$ = 8.3 Hz, 2H), 4.94-5.04 (tt, $J$ = 3.5, 12.2 Hz, 2H), 2.45-2.57 (m, 4H), 2.42 (s, 6H), 1.89 (d, $J$ = 12.6 Hz, 4H), 1.74 (d, $J$ = 9.9 Hz, 6H), 1.43 (q, $J$ = 12.8 Hz, 4H), 1.25-1.35 (m, 2H).

**$^{13}$C NMR (100 MHz, CDCl$_3$):** $\delta$ **[ppm]** = 163.8, 163.4, 155.0, 149.0, 137.3, 134.8, 133.1, 130.1, 129.4, 129.2, 124.9, 124.2, 122.6, 122.6, 121.8, 121.2, 115.3, 54.0, 29.1, 26.5, 25.4, 20.6.

**FT-IR** (cm$^{-1}$): 2953-2850, 1742, 1705, 1658, 1462, 1378, 1257, 1189, 1080, 801.

**MALDI-TOF:** *m/z* calculated for C$_{50}$H$_{41}$Br$_2$N$_2$O$_6$ [M+H]$^+$: 923.1331, found: 923.644.

### 2.3.1.6. *N,N'*-Dicyclohexyl-1,7-bis(2,6-dibromo-4-methylphenoxy)perylene-3,4:9,10-bisdicarboximide (2b)
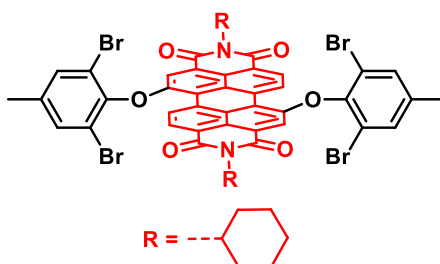


To a degassed solution of **1** (1g, 1.40 mmol) in dry DMF (100 mL), potassium carbonate (582 mg, 4.21mmol) and 2,6-dibromo-4-methylphenol (933 mg, 3.51 mmol) was added. The reaction mixture was stirred at 120 °C for 1 h. After being cooled to room temperature, the solvent is removed by rotary evaporation. The crude reaction mixture was extracted with CH$_2$Cl$_2$, and the organic layer was washed with (6×100 mL) of water. The combined organic phase was dried over anhydrous Na$_2$SO$_4$, and the solvent was removed under reduced pressure. The compound was purified by silica gel column chromatography using CH$_2$Cl$_2$-petroleum ether (6:4 v/v) as eluent to yield **2b** as an orange solid (1.1 g, 72 %).

**$^1$H NMR (400 MHz, CDCl$_3$):** $\delta$ **[ppm]** = 9.75 (d, *J* = 8.4 Hz, 2H), 8.68 (d, *J* = 8.4 Hz, 2H), 7.91 (s, 2H), 7.55 (s, 4H), 5.01 (tt, *J* = 3.1, 12.0 Hz, 2H), 2.48-2.59 (m, 4H), 2.45 (s, 6H), 1.89 (d, *J* = 12.1 Hz, 4H), 1.73-1.76 (m, 6H), 1.43 (q, *J* = 12.6 Hz, 4H), 1.25-1.35 (m, 2H).

**$^{13}$C NMR (100 MHz, CDCl$_3$):** $\delta$ **[ppm]** = 163.8, 163.6, 154.2, 145.7, 139.4, 134.0, 133.3, 130.0, 129.9, 129.6, 124.9, 124.2, 122.5, 121.7, 118.3, 117.8, 54.0, 29.1, 26.5, 25.4, 20.6.

**FT-IR** (cm$^{-1}$): 2957-2873, 1735, 1697, 1651, 1455 1380, 1259, 1193, 1081.

**MALDI-TOF:** *m/z* calculated for C$_{50}$H$_{39}$Br$_4$N$_2$O$_6$ [M+H]$^+$: 1083.4780, found: 1083.635.

### 2.3.1.7.   *N,N'*-Dicyclohexyl-1,7-bis(2-(3,3'-dihexyl-[2,2'-bithiophen]-5-yl)-4-ethylphenoxy) perylene-3,4:9,10-bisdicarboximide (3a)
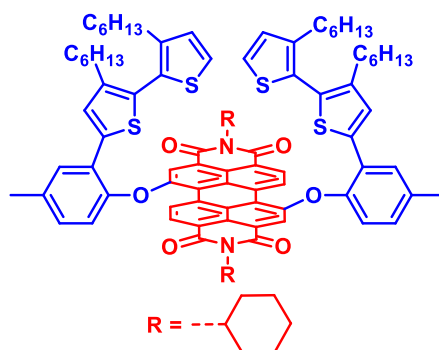
A pressure tube (30 mL) was charged with **2a** (500 mg, 540.72µmol), (3,3'-dihexyl-[2,2'-bithiophen]-5-yl)trimethylstannane (1.08 g, 2.16 mmol) and 10 mL freshly distilled dry toluene. Pd(PPh$_3$)$_2$Cl$_2$ (19 mg, 27.04 µmol) was added to the reaction mixture. The mixture was subsequently heated to 140 °C for 12h. After cooling to RT, CH$_2$Cl$_2$ was added to the reaction mixture to stop the reaction. The later reaction mixture was passed through celite, and the solvent was removed by evaporation under reduced pressure. The compound was purified by silica gel column chromatography using CH$_2$Cl$_2$-petroleum ether (5:5 v/v) as eluent to yield **3a** as a red solid (720 mg, 93 %).

**$^1$H NMR (400 MHz, CDCl$_3$):** $\delta$ **[ppm]** = 9.75 (d, $J$ = 8.4 Hz, 2H), 8.58 (d, $J$ = 8.4 Hz, 2H), 8.19 (s, 2H), 7.67 (d, $J$ = 1.5 Hz, 2H), 7.32 (s, 2H), 7.16 (d, $J$ = 5.3 Hz, 2H), 7.13 (dd, $J$ = 8.2, 1.5 Hz, 2H), 6.96 (d, $J$ = 8.2 Hz, 2H), 6.82 (d, $J$ = 5.3 Hz, 2H), 4.98 (tt, $J$ = 3.1, 12.1 Hz, 2H), 2.48-2.56 (m, 4H), 2.47 (s, 6H), 2.27-2.38 (m, 8H), 1.87 (d, $J$ = 12.9 Hz, 4H), 1.7(d, $J$ = 9.5 Hz, 6H), 1.28-1.48 (m, 14H), 0.97-1.15 (m, 24H), 0.71 (t, $J$ = 7.1 Hz, 6H), 0.76 (t, $J$ = 7.1 Hz, 6H).

**$^{13}$C NMR (125 MHz, CDCl$_3$):** $\delta$ **[ppm]** = 163.7, 163.4, 155.6, 148.4, 142.3, 142.1, 137.2, 135.7, 133.3, 130.0, 129.9, 129.2, 128.9, 128.5, 128.2, 127.5, 127.0, 125.2, 124.9, 124.2, 123.0, 122.5, 122.2, 121.3, 53.9, 31.5, 31.4, 30.5, 29.0, 29.0, 28.8, 28.7, 28.6, 26.5, 25.4, 22.4, 20.9, 14.0.

**FT-IR** (cm$^{-1}$): 2954-2852, 1738, 1694, 1657, 1592, 1405, 1327, 1262, 1196, 811.

**MALDI-TOF:** *m/z* calculated for C$_{90}$H$_{99}$N$_2$O$_6$S$_4$ [M+H]$^+$: 1431.6386, found: 1431.351.

### 2.3.1.8. *N,N'*-Dicyclohexyl-1,7-bis(2,6-bis(3,3'-dihexyl-[2,2'-bithiophen]-5-yl)-4-methyl-phenoxy)perylene-3,4:9,10-bisdicarboximide (3b)
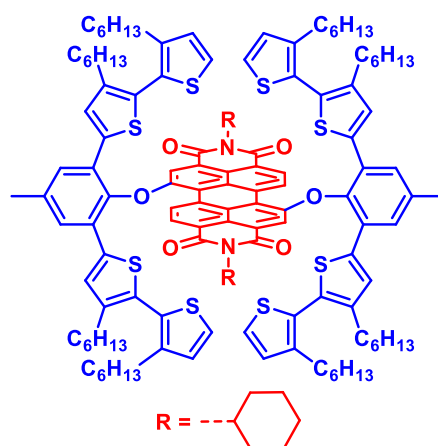
In a pressure tube (30 mL), **2b** (500 mg, 461.90 µmol), (3,3'-dihexyl-[2,2'-bithiophen]-5-yl)trimethylstannane (1.84 g, 3.70 mmol) in 10 mL dry toluene was added, and $Pd(PPh_3)_2Cl_2$ (17 mg, 23.10 µmol) was used as catalyst. The mixture was subsequently heated to 140 ℃ for 12 h. After cooling to RT, $CH_2Cl_2$ was added to the reaction mixture to stop the reaction. The later reaction mixture was passed through celite and the solvent was removed by evaporation under reduced pressure. The compound was purified by silica gel column chromatography using $CH_2Cl_2$-petroleum ether (3:7 v/v) as eluent to yield **3b** as a red solid (870 mg, 90%).

**$^1$H NMR (400 MHz, CDCl$_3$):** $\delta$ **[ppm]** = 9.95 (d, $J$ = 8.5 Hz, 2H), 8.62 (d, $J$ = 8.5 Hz, 2H), 8.0 (s, 2H), 7.55 (s, 4H), 7.19 (s, 4H), 6.93 (d, $J$ = 5.2 Hz, 4H), 6.69 (d, $J$ = 5.2 Hz, 4H), 4.95 (tt, $J$ = 3.1, 12.1 Hz, 2H), 2.54 (s, 6H), 2.42-2.53 (m, 4H), 2.14-2.24 (m, 8H), 2.06 (dq, $J$ = 13.7, 6.9 Hz, 8H), 1.87 (d, $J$ =12.3 Hz, 4H), 1.67 (d, $J$ = 9.6 Hz, 6H), 1.29-1.47 (m, 6H), 1.20-1.28 (m, 8H), 1.11 (dt, $J$ = 13.9, 6.7 Hz, 8H), 0.96-1.05 (m, 30H), 0.79-0.96 (m, 18H), 0.76 (t, $J$ = 7.2 Hz, 12H), 0.69 (t, $J$ = 7.3 Hz, 12H).

**$^{13}$C NMR (100 MHz, CDCl$_3$):** $\delta$ **[ppm]** = 163.7, 163.4, 155.0, 143.3, 142.1, 141.8, 137.0, 136.7, 133.8, 130.0, 129.9, 129.6, 129.5, 129.2, 129.1, 128.2, 128.0, 127.9, 125.2, 124.6, 123.7, 122.1, 121.8, 118.8, 53.8, 31.5, 31.2, 30.3, 30.1, 29.0, 29.0, 28.8, 28.6, 28.5, 26.5, 25.4, 22.6, 22.5, 21.1, 14.0, 13.9.

**FT-IR** (cm$^{-1}$)**:** 2957-2855, 1739, 1702, 1657, 1588, 1411, 1332, 1257, 1190, 733.

**MALDI-TOF:** *m/z* calculated for $C_{130}H_{155}N_2O_6S_8$ [M+H]$^+$: 2095.9650, found: 2095.95.

### 2.3.1.9. Synthesis of TSP1

A solution of bithiophene precursor of **3a** (200 mg, 139.66 µmol) was dissolved in dry $CH_2Cl_2$ (500 mL) and degassed for 30 min. The reaction mixture cooled down to 0 ℃, and iron (III) chloride (134 mg, 837.98 $\mu$mol) was added portion-wise. The reaction was warmed to room temperature and stirred for 2-3 hours.

The progress of the reaction was monitored by TLC, and once the starting material was consumed, the reaction was quenched with methanol. The organic contents were extracted with $CH_2Cl_2$ and were washed with water (3x100 mL). The combined organic phase was dried over anhydrous $Na_2SO_4$, and the solvent was removed under reduced pressure. The crude compound was purified by silica gel column chromatography using $CH_2Cl_2$-petroleum ether (5:5 v/v) as the eluent to afford the cyclized compound, **TSP1** as a red solid (172 mg, 86%).

**$^1$H NMR (500 MHz, $CD_2Cl_2$):** $\delta$ [ppm] = 9.86 (d, $J$ = 8.5 Hz, 2H), 8.52 (d, $J$ = 8.5 Hz, 2H), 7.92 (s, 2H), 7.79 (d, $J$ = 1.3 Hz, 2H), 7.33 (s, 2H), 7.30-7.33 (m, 2H), 7.23 (d, $J$ = 8.2 Hz, 2H), 6.77 (s, 2H), 4.89 (tt, $J$ = 3.5, 12.0 Hz, 2H), 2.55 (s, 6H), 2.45-2.51 (m, 4H), 2.38-2.45 (m, 8H), 1.83 (d, $J$ = 12.6 Hz, 4H), 1.59-1.70 (m, 10H), 1.45-1.51 (m, 4H), 1.27-1.45 (m, 6H), 1.17-1.25 (m, 24H), 0.80-0.84 (m, 12H).

**$^{13}$C NMR (125 MHz, $CD_2Cl_2$):** $\delta$ [ppm] = 164.2, 163.9, 156.8, 147.1, 141.1, 140.3, 137.8, 137.8, 137.7, 134.4, 132.0, 131.0, 130.2, 130.0, 129.8, 129.6, 129.6, 128.7, 128.6, 125.1, 124.6, 123.9, 123.6, 123.0, 122.0, 119.0, 32.2, 32.0, 30.7, 30.7, 30.0, 29.8, 29.7, 29.7, 29.5, 27.1, 26.1, 23.2, 23.1, 21.4, 14.4.

**FT-IR** (cm$^{-1}$)**:** 2951-2858, 1695, 1658, 1589, 1328, 1259, 1109, 815.

**MALDI-TOF:** $m/z$ calculated for $C_{90}H_{97}N_2O_6S_4$ [M+H]$^+$: 1429.6229, found: 1429.56

**2.3.1.10. Synthesis of TSP2**
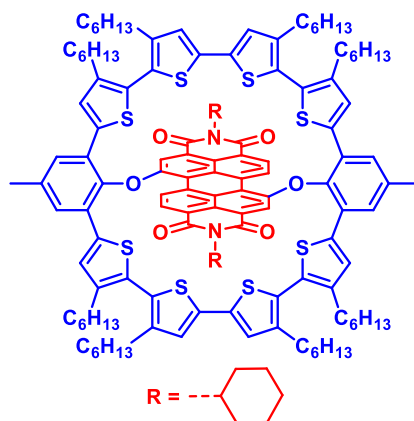
A solution of bithiophene precursor of **3b** (150 mg, 71.53 μmol) was dissolved in dry $CH_2Cl_2$ (500 mL) and degassed for 30 min. The reaction mixture cooled down to 0 °C, and iron (III) chloride (128 mg, 786.78 $\mu$mol) was added portion-wise. The reaction was warmed to room temperature and stirred for 2-3 hours. The progress of the reaction was monitored by TLC, and once the starting material was consumed, the reaction was quenched with methanol. The organic contents were extracted with $CH_2Cl_2$ and were washed with water (3x100 mL). The combined organic phase was dried over anhydrous $Na_2SO_4$, and the solvent was removed under reduced pressure. The crude compound was purified by silica gel column chromatography using $CH_2Cl_2$-petroleum ether (3:7 v/v) as the eluent to afford the cyclized compound, **TSP2** as a red solid (115 mg, 77%).

**¹H NMR (500MHz, CDCl₃):** $\delta$ **[ppm]** = 9.77 (d, $J$ = 8.5 Hz, 2H), 8.47 (d, $J$ = 8.5 Hz, 2H), 8.24 (s, 2H), 7.53 (s, 4H), 7.22 (s, 4H), 6.69 (s, 4H), 4.91-4.98 (m, 2H), 2.52 (s, 6H), 2.44-2.51 (m, 12H), 2.39-2.43 (m, 8H), 1.83 (d, $J$ = 12.9 Hz, 4H), 1.65-1.72 (m, 6H), 1.58-1.62 (m, 8H), 1.46-1.52 (m, 8H), 1.30-1.42 (m, 6H), 1.20-1.26 (m, 48H), 0.81-0.86 (m, 24 H).

**¹³C NMR (125 MHz, CDCl₃):** $\delta$ **[ppm]** = 164.0, 163.7, 156.8, 143.7, 140.7, 139.7, 138.8, 137.5, 136.4, 135.0, 132.8, 132.1, 130.2, 129.9, 129.3, 128.7, 128.7, 125.2, 123.5, 122.3, 122.2, 122.0, 119.2, 77.3, 76.7, 53.7, 31.9, 31.6, 31.5, 30.2, 30.1, 29.7, 29.4, 29.2, 29.0, 29.0, 26.5, 25.4, 22.6, 22.5, 20.6, 14.0, 14.0.

**FT-IR** (cm⁻¹)**:** 2951-2853, 1696, 1658, 1584, 1397, 1248, 1192, 814.

**MALDI-TOF:** *m/z* calculated for $C_{130}H_{151}N_2O_6S_8$ [M+H]⁺: 2091.9337, found: 2091.93.

### 2.3.2. Synthesis of TSP-Dimer (TSP1D and TSP2D) Macrocycles
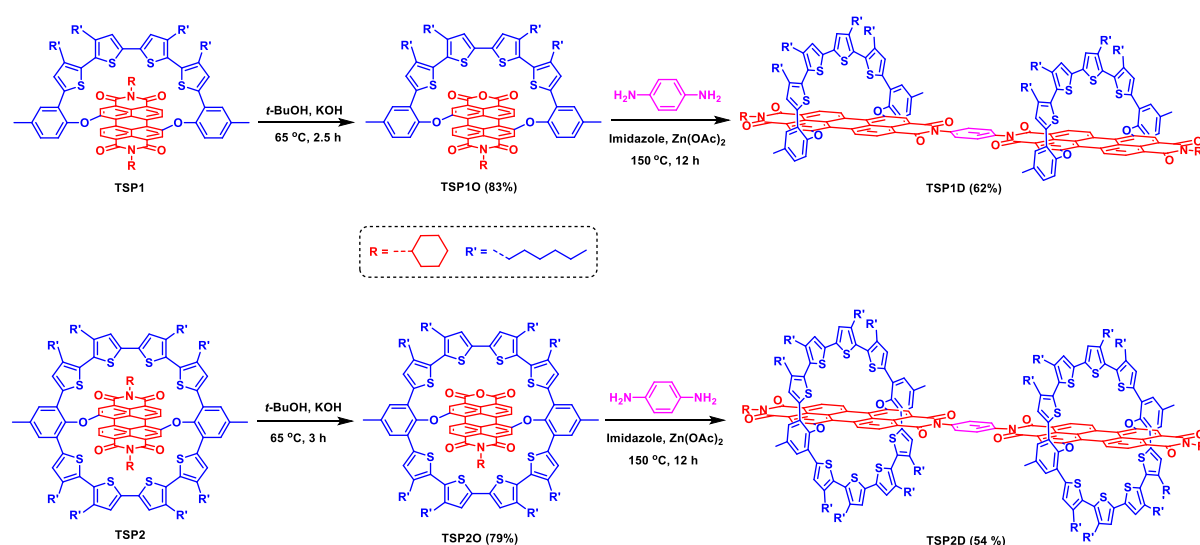


**Scheme 2.3.** Synthesis of oligothiophene ring strapped **TSP1D** and **TSP2D** dimer macrocycles.

### 2.3.2.1. Synthesis of TSP1O
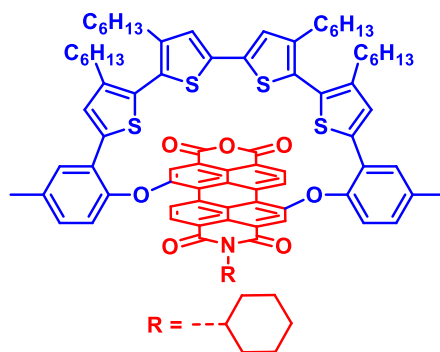


A two necked round bottom flask (100 mL) was charged with **TSP1** (200 mg, 139.86 μmol) and KOH (392 mg, 6.99 mmol) was suspended in 60 mL *t*-BuOH, and heated to 60 °C for 2.5 to 3.5 h. The reaction progress was monitored by TLC to stop the reaction after a good amount of cleaved product was observed. The reaction mixture was then brought to room temperature and dissolved in $CH_2Cl_2$, washed with aq. HCl until washings were neutral, dried over anhydrous $Na_2SO_4$, filtered, and evaporated under reduced pressure. The crude compound obtained was purified by silica gel column chromatography using $CH_2Cl_2$-petroleum ether (7:3 v/v) as the eluent to afford the monoimide-anhydride **TSP1O** as a deep red solid (153 mg, 81%).

**$^1$H NMR (400 MHz, CD$_2$Cl$_2$):** $\delta$ [ppm] = 9.89 (dd, *J* = 6.6, 8.4 Hz, 2H), 8.50-8.56 (m, 2H), 7.95 (s, 1H), 7.89 (d, *J* = 1.63 Hz, 1H), 7.78 (dd, *J* = 1.6, 5.6 Hz, 2H), 7.32 (br. s, 2H), 7.31 (br. s, 2H), 7.22-7.26 (m, 2 H), 6.76 (s, 2 H), 4.88 (tt, *J* = 3.3, 12.0, Hz, 1 H), 2.56 (s, 3H), 2.55 (s, 3H), 2.37-2.52 (m, 10H), 1.83 (d, *J* = 12.5 Hz, 2H), 1.58-1.72 (m, 7H), 1.43-1.52 (m, 4H), 1.28-1.42 (m, 3H), 1.13-1.25 (m, 24H), 0.78-0.85 (m, 12H).

**$^{13}$C NMR (100 MHz, CD$_2$Cl$_2$):** $\delta$ [ppm] = 164.1, 163.7, 160.6, 160.5, 157.5, 156.3, 146.9, 146.7, 141.2, 141.2, 140.7, 140.5, 138.0, 137.9, 137.8, 137.8, 137.7, 137.6, 136.3, 133.6, 132.2, 132.0, 132.0, 131.2, 131.1, 130.6, 130.5, 130.3, 130.0, 129.9, 129.6, 129.4, 129.4, 129.0, 128.8, 128.6, 128.6, 127.3, 125.4, 124.9, 123.9, 123.9, 123.8, 123.7, 123.6, 123.5, 121.1, 120.6, 119.2, 119.0, 117.8, 32.1, 32.0, 30.7, 30.3, 30.0, 30.0, 29.8, 29.7, 29.7, 29.6, 29.5, 27.1, 27.0, 26.1, 23.2, 23.1, 21.4, 21.4, 14.4.

**FT-IR** (cm$^{-1}$): 2954-2852, 1766, 1735, 1697, 1658, 1591, 1493, 1317, 1258, 1189, 1011, 803.

**MALDI-TOF:** *m/z* calculated for $C_{84}H_{86}NO_7S_4$ [M+H]$^+$: 1348.5287, found: 1348.607.

### 2.3.2.2. Synthesis of TSP2O

R = ---cyclohexyl
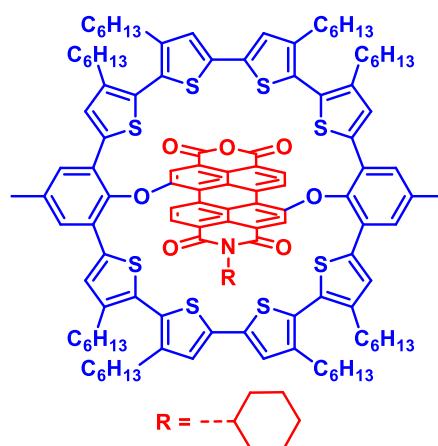
**TSP2** (200 mg, 95.55 $\mu$mol) and KOH (322 mg, 5.73 mmol) was suspended in 60 mL *t*-BuOH and heated to 60 °C for 3 to 5 h. The crude compound obtained was purified by silica gel column chromatography using $CH_2Cl_2$-petroleum ether (6:4 v/v) as the eluent to afford the **TSP2O** as a deep red solid (152 mg, 79%).

**$^1$H NMR (400MHz, $CDCl_3$): $\delta$ [ppm]** = 9.79-9.84 (m, 2H), 8.45-8.51 (m, 2H), 8.26 (s, 1H), 8.24 (s, 1H), 7.52-7.56 (m, 4H), 7.20-7.24 (m, 4H), 6.70 (s, 4H), 4.93 (tt, *J* = 4.4, 12.7 Hz, 1H), 2.54 (s, 3H), 2.53 (s, 3H), 2.45-2.51 (m, 9H), 2.38-2.44 (m, 9H), 1.84 (d, *J* = 12.8 Hz, 2H), 1.69 (d, *J* = 9.3 Hz, 3H), 1.60 (br. s., 8H), 1.45-1.53 (m, 8H), 1.32-1.42 (m, 3H), 1.22 (br. s., 48H), 0.80-0.86 (m, 24H).

**$^{13}$C NMR (100 MHz, $CDCl_3$): $\delta$ [ppm]** = 163.8, 163.5, 160.3, 160.1, 157.3, 156.4, 143.5, 143.3, 140.9, 140.8, 139.9, 139.8, 138.5, 138.5, 137.5, 137.5, 136.8, 136.7, 134.2, 133.0, 132.9, 132.2, 132.2, 132.0, 130.5, 130.3, 130.1, 130.0, 129.8, 129.1, 128.8, 128.5, 128.4, 128.1, 127.4, 125.5, 125.0, 124.3, 124.1, 123.1, 122.1, 121.4, 121.0, 119.3, 118.4, 117.4, 53.8, 31.9, 31.6, 31.5, 31.4, 30.3, 30.2, 30.1, 29.7, 29.6, 29.4, 29.3, 29.2, 29.2, 29.1, 29.0, 28.9, 26.5, 25.4, 22.7, 22.6, 22.5, 20.6, 18.7, 14.1, 14.0, 14.0, 14.0, 11.3.

**FT-IR (cm$^{-1}$):** 2957-2850, 1773, 1741, 1700, 1662, 1599, 1462, 1317, 1249, 1185, 1012, 807.

**MALDI-TOF:** *m/z* calculated for $C_{124}H_{140}NO_7S_8$ [M+H]$^+$: 2010.8395, found: 2010.976

### 2.3.2.3. Synthesis of TSP1D
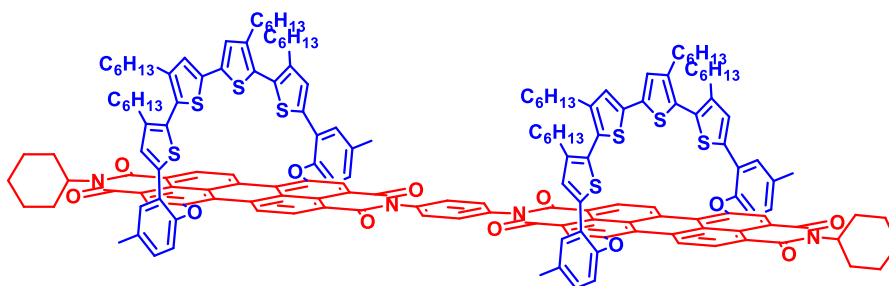
A sealed tube (5 mL) was charged with **TSP1O** (100 mg, 74.14 µmol), *p*-phenylenediamine (6.5 mg, 59.31µmol), $Zn(OAc)_2$ (27 mg, 148.28 µmol), and imidazole (500 mg), and heated to 150 °C for 7 h. After completion of the reaction, the reaction mixture was allowed to cool to RT, and it was quenched by the addition of hydrochloric acid (2N, 15 mL). The reaction mixture was extracted with $CH_2Cl_2$ (3x20 mL). The organic layer was dried over anhydrous $Na_2SO_4$, and the solvent was removed under reduced pressure. The crude product was purified by silica gel column chromatography using $CH_2Cl_2$-petroleum ether (7:3 v/v) as an eluent to yield **TSP1D** as a deep red solid (64 mg, 62 %).

**$^1$H NMR (500MHz, CDCl$_3$): $\delta$ [ppm]** = 9.91 (t, *J* = 7.9 Hz, 4H), 8.62 (d, *J* = 8.5 Hz, 2H), 8.54 (d, *J* = 8.5 Hz, 2H), 8.03 (s, 2H), 7.96 (s, 2H), 7.79-7.81 (m, 2H), 7.78 (s, 2H), 7.37 (s, 4H), 7.34 (s, 4H), 7.33 (s, 4H), 7.26 (dd, *J* = 5.4, 7.9Hz, 4H), 6.78 (s, 4H), 4.86-4.95 (m, 2H), 2.56 (s, 6H), 2.54 (s, 6H), 2.47-2.52 (m, 8H), 2.40-2.46 (m, 12H), 1.84 (d, *J* = 12.3 Hz, 4H), 1.59-1.71 (m, 14H), 1.46-1.52 (m, 8H), 1.31-1.44 (m, 6H), 1.20 (br. s., 48H), 0.78-0.84 (m, 24H).

**$^{13}$C NMR (125 MHz, CDCl$_3$): $\delta$ [ppm] =** 164.2, 164.0, 163.8, 163.6, 157.1, 156.7, 147.1, 147.0, 141.1, 140.3, 137.8, 136.0, 135.3, 134.2, 132.0, 132.0, 131.1, 130.6, 130.2, 130.1, 130.0, 129.9, 129.6, 128.7, 128.6, 125.5, 125.1, 124.9, 123.9, 123.8, 123.6, 123.3, 122.9, 122.3, 121.8, 119.5, 119.0, 32.1, 32.0, 30.7, 30.3, 30.0, 29.8, 29.7, 29.5, 27.1, 26.1, 23.2, 23.1, 21.4, 14.4.

**FT-IR** (cm$^{-1}$)**:** 2950-2856, 1738, 1700, 1654, 1588, 1458, 1330, 1256, 1081, 801.

**MALDI-TOF:** *m/z* calculated for $C_{174}H_{175}N_4O_{12}S_8$ [M+H]$^+$: 2768.0972, found: 2768.322

### 2.3.2.4. Synthesis of TSP2D

**TSP2O** (100 mg, 49.70 µmol), *p*-phenylenediamine (4.3 mg, 39.76 µmol), $Zn(OAc)_2$ (18 mg, 99.41 µmol), and imidazole (500 mg) was heated at 150 °C for 10 h under an argon atmosphere. The crude product obtained was purified by silica gel column chromatography using $CH_2Cl_2$-petroleum ether (4:6 v/v) as the eluent to yield **TSP2D** as a red solid (56 mg, 55%).
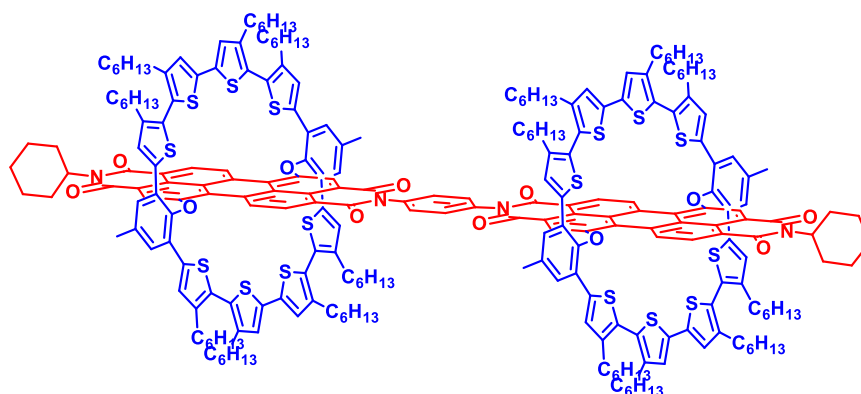
**$^1$H NMR (500MHz, CDCl$_3$):** $\delta$ **[ppm]** = 9.81 (dd, $J$ = 5.0, 8.5 Hz, 4H), 8.53 (d, $J$ = 8.5 Hz, 2H), 8.48 (d, $J$ = 8.5 Hz, 2H), 8.29 (s, 2H), 8.26 (s, 2H), 7.53 (s, 4H), 7.51 (s, 4H), 7.39 (s, 4H), 7.22 (s, 4H), 7.19 (s, 4H), 6.70 (s, 8H), 4.94 (t, $J$ = 11.8 Hz, 2H), 2.53 (s, 6H), 2.50 (br. s., 6H), 2.44-2.49 (m, 20H), 2.39-2.43 (m, 16H), 1.84 (d, $J$ = 10.7 Hz, 4H), 1.67-1.72 (m, 6H), 1.58-1.63 (m, 16H), 1.49 (br. s., 16H), 1.34-1.41 (m, 6H), 1.22 (br. s., 96H), 0.79-0.85 (m, 48H).

**$^{13}$C NMR (125 MHz, CDCl$_3$):** $\delta$ **[ppm]** = 164.0, 163.7, 163.4, 163.2, 156.9, 143.7, 143.6, 140.7, 139.8, 138.8, 138.7, 137.6, 137.5, 136.5, 136.4, 135.6, 135.1, 134.9, 132.9, 132.8, 132.1, 132.0, 130.5, 130.3, 130.2, 129.9, 129.5, 129.3, 129.2, 128.8, 128.7, 128.7, 125.6, 125.1, 123.6, 123.0, 122.8, 122.5, 122.1, 119.6, 119.2, 53.7, 31.9, 31.6, 31.4, 30.2, 30.1, 29.7, 29.4, 29.2, 29.0, 26.5, 25.4, 22.6, 22.5, 20.6, 14.

**FT-IR** (cm$^{-1}$)**:** 2954-2852, 1713, 1697, 1657, 1597, 1461, 1328, 1257, 1092, 801.

**MALDI-TOF:** *m/z* calculated for C$_{254}$H$_{283}$N$_4$O$_{12}$S$_{16}$ [M+H]$^+$: 4092.7189, found: 4092.9024

## 2.3.3. Synthesis of TSP-2DP Polymer
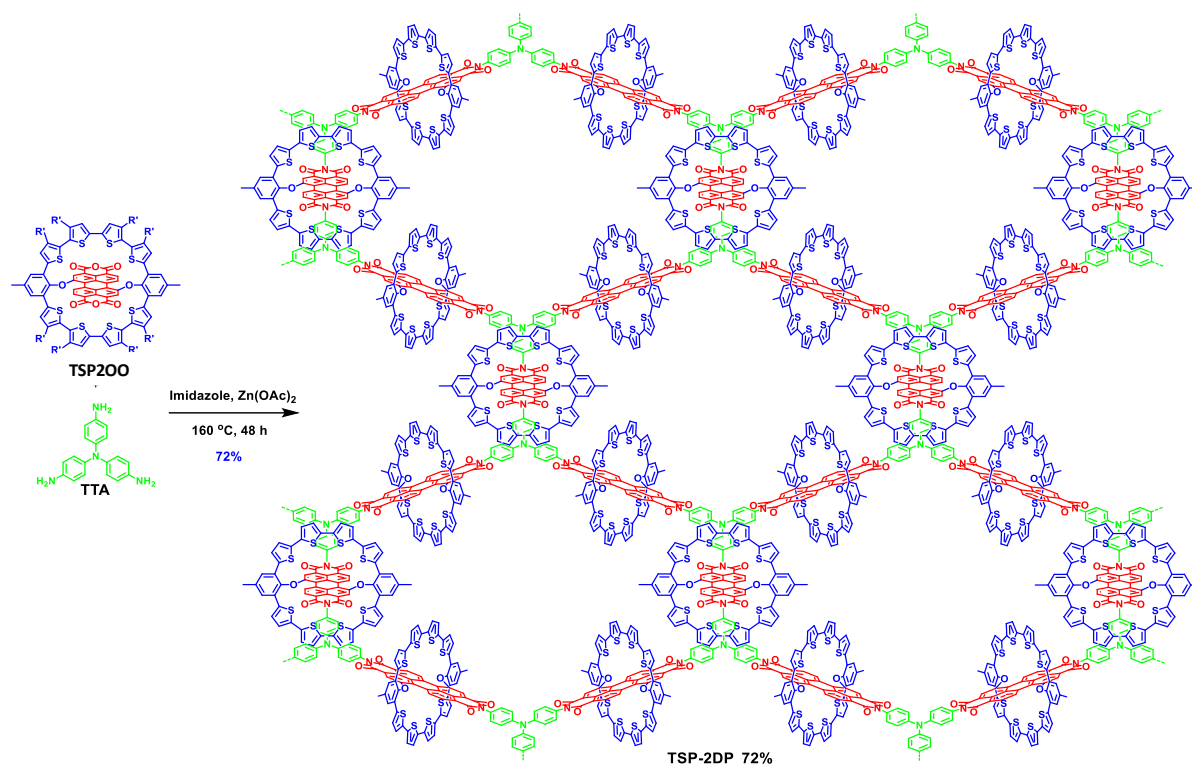


*In TSP-2DP; alkyl chains and hydrogen atoms are removed for clarity*

**Scheme 2.4.** Synthesis of **TSP-2DP** polymer.

## 2.3.3.1. Synthesis of TSP2OO
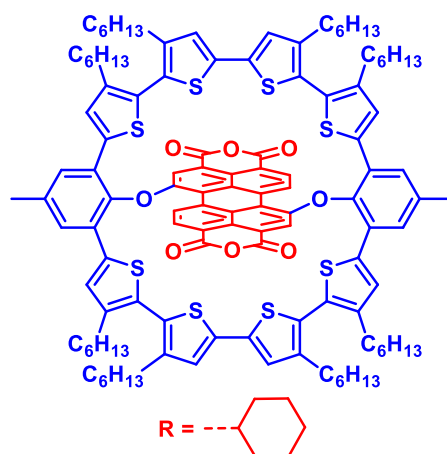


**TSP2** (200 mg, 95.55 µmol) and solid KOH (536 mg, 9.56 mmol) was suspended in 60 mL *t*-BuOH and heated to 100 °C for 4 to 5 h. The crude compound obtained was purified by silica gel column chromatography using $CH_2Cl_2$-petroleum ether (6:4 v/v) as the eluent to afford the **TSP2OO** as a deep red solid (136 mg, 74%).

**$^1$H NMR (400MHz, CDCl₃):** $\delta$ **[ppm]** = 9.87 (d, *J* = 8.5 Hz, 2H), 8.51 (d, *J* = 8.5 Hz, 2H), 8.28 (s, 2H), 7.55 (s, 4H), 7.22 (s, 4H), 6.71 (s, 4H), 2.55 (s, 6H), 2.50 (t, *J* = 8.11Hz, 8H),

2.42 (t, $J$ = 8.01Hz, 8H), 1.58-1.65 (m, 8H), 1.46-1.53 (m, 8H), 1.22 (br. s., 48H), 0.82-0.86 (m, 24H).

**$^{13}$C NMR (100 MHz, CDCl$_3$): $\delta$ [ppm]** = 160.0, 159.8, 157.0, 143.2, 141.1, 140.1, 138.3, 137.5, 137.1, 135.9, 133.0, 132.3, 131.9, 130.7, 129.9, 129.0, 128.3, 127.2, 123.2, 122.2, 121.2, 119.3, 118.2, 31.6, 31.5, 30.2, 29.4, 29.2, 29.1, 29.0, 22.6, 22.5, 20.6, 14.0, 14.0.

**FT-IR** (cm$^{-1}$): 2957-2855, 1775, 1767, 1735, 1599, 1462, 1286, 1243, 1180, 1005, 808.

**MALDI-TOF:** *m/z* calculated for $C_{118}H_{129}O_8S_8$ [M+H]$^{+}$: 1929.7453, found: 1929.854.

### 2.3.3.2. Synthesis of TSP-2DP

An oven-dried pressure tube (10 mL) charged with **TSP2OO** (20 mg, 10.36 $\mu$mol), triaminopheynilamine (2 mg, 6.91$\mu$mol), Zn(OAc)$_2$ (7 mg, 37.98 $\mu$mol), and imidazole (1 g, 14.85 mmol). The pressure tube was heated at 160 °C for 48 h. The reaction mixture was then cooled down at room temperature, and 20 mL of 2N HCl were added to the reaction mixture and filtered. Polymer was washed with different solvents such as H$_2$O, EtOH, CHCl$_3$, CH$_2$Cl$_2$ and THF, dried in vacuum oven at 90 °C and **TSP-2DP** was obtained as a dark red solid (13.6 mg, 72 %).

**$^{13}$C CP-MAS NMR:** 162.83, 155.24, 147.82, 139.38, 129.93, 122.74, 30.35, 23.08, 14.16

**FT-IR** (cm$^{-1}$)**:** 3340, 3186, 2953-2850, 1707, 1673, 1597, 1506, 1395, 1342, 1278, 1250, 1175, 1145, 756.

## 2.4. Results and Discussion

Synthesis of half and full oligothiophene ring strapped PBI molecules **TSP1**, and **TSP2** were accomplished through aromatic nucleophilic substitution, Grignard recation, Sonogashira coupling Stille coupling, and oxidative coupling reactions in good yields (Scheme 2.1,2.2). The synthesis started with commercially available 1,7-dibromo-perylene-3,4,9,10-tetracarboxylic dianhydride, which on treatment with cyclohexylamine in a mixture of DMF and ethanol (1:1), gave molecule **1** with 81% yield. Upon heating with 2-bromo-4-methylphenol and 2,6-dibromo-4-methylphenol at 120 °C in the presence of K$_2$CO$_3$ in dimethylformamide, molecule **1** yielded **2a** (83%) and **2b** (72%), respectively. Stille coupling reaction of **2a** and **2b** with (3,3'-dihexyl-[2,2'-bithiophen]-5-yl)trimethylstannane delivered **3a** (93%) and **3b** (90%). Further, we optimized the oligothiophene ring closure using FeCl$_3$ mediated oxidative coupling reaction to yield half and full oligothiophene ring strapped PBI molecules **TSP1** (86%) and **TSP2** (77%) in high isolated yields with 100 % conversion. It has to be noted that compared to other reported macrocycles, the yields of the present systems

are significantly high.[50-53] All the synthesized molecules were characterized by ^{1}H, ^{13}C nuclear magnetic resonance (NMR), and matrix-assisted laser desorption ionization time-of-flight mass spectrometry (MALDI-TOF MS).

A detailed 2D-NMR study sheds light on the possible cross-coupling between the various proton and nullifies any interaction between the protons of the thiophene ring and the PBI units The structures of **TSP1** and **TSP2** were confirmed by extensive 2D NMR analysis. The HMBC spectra of **TSP1** helped to fix the position of protons **a** and **b** as these two protons show strong cross-peaks with imide carbon (Figure 2.1). The ^{1}H-^{1}H COSY spectra of **TSP1** provide a clear idea about protons that are chemically bonded and near to each other (Figure 2.2). The strong cross-peaks were observed for PBI proton **b**, and **c** confirm that these two protons are from the unsubstituted side of PBI. Moreover, the substituted phenyl ring protons **d** and **e** also show a strong cross-peak, helping to assign the respective protons in the aromatic region. The [1]H-^{1}H NOESY of **TSP1** shows the cross-peaks for the **d** proton (phenyl) with the center PBI (**a**, **b**, **c** proton), indicating these protons are close to each other in space. The cross peak for the phenyl ring proton **f** and thiophene ring proton **g** shows the thiophene ring, i.e., sulfur atom from the thiophene ring is pointing inside (Figure 2.3). The ^{1}H-^{13}C HSQC spectra show the protons attached to the respective carbon atoms (Figure 2.4).
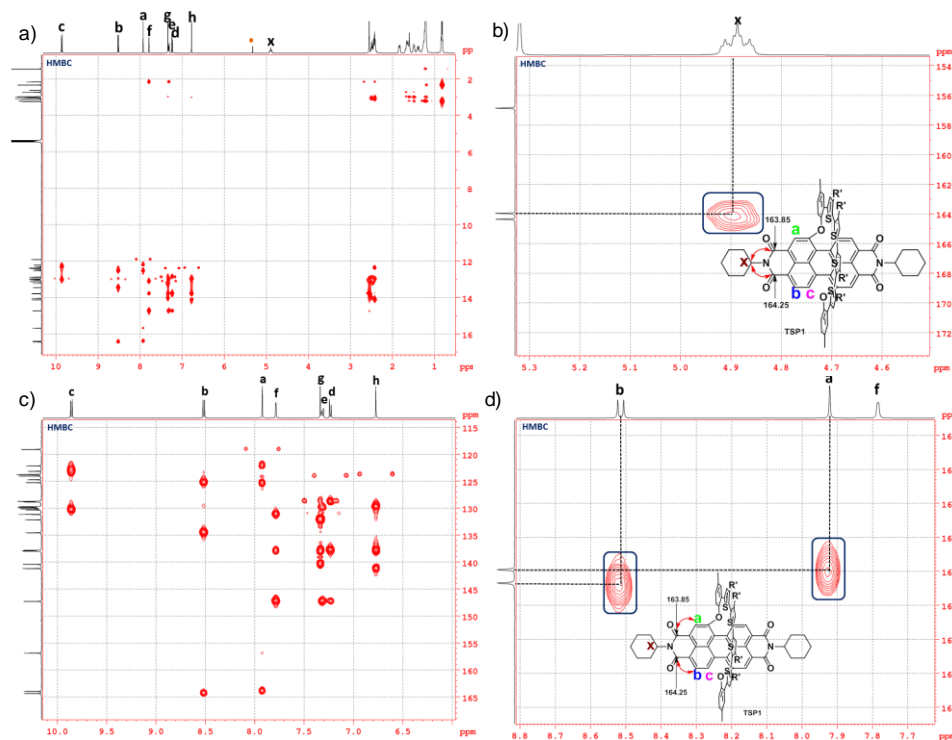


**Figure 2.1.** HMBC spectrum of **TSP1** at 500 MHz, recorded in CDCl$_3$ at 298 K. Intermolecular cross-peaks are indicated by circles.
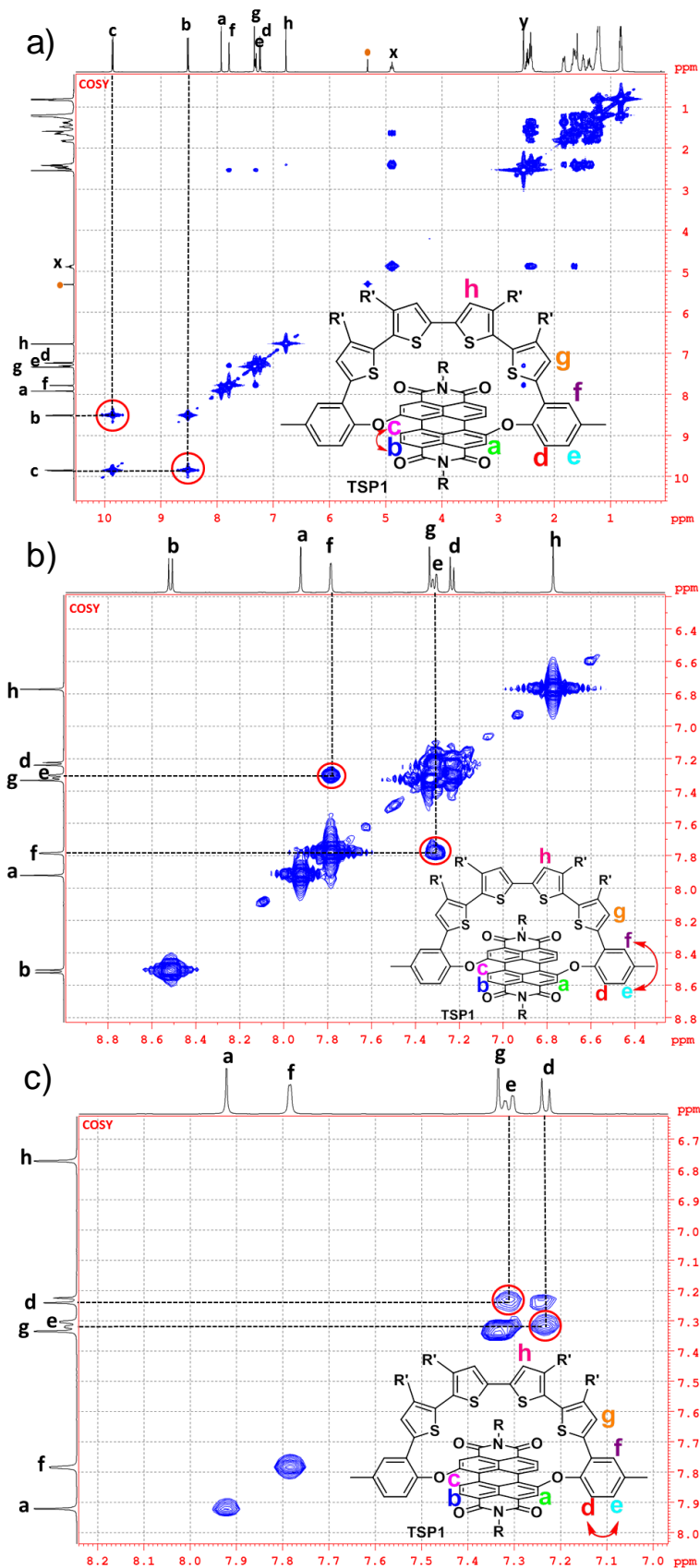
**Figure 2.2.** COSY spectrum of **TSP1** at 500 MHz, recorded in CDCl$_3$ at 298 K. Intermolecular cross-peaks are indicated by circles.
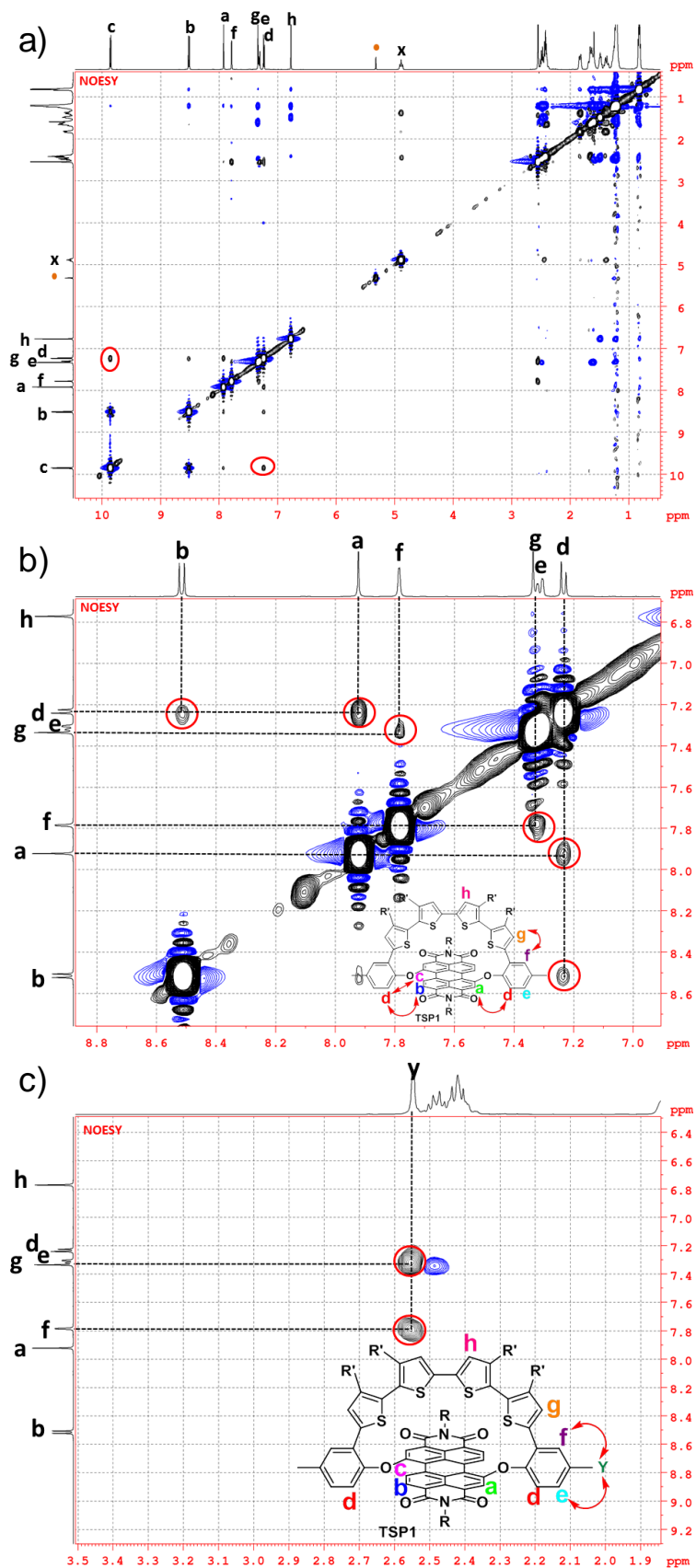
**Figure 2.3.** NOESY spectrum of **TSP1** at 500 MHz, recorded in CDCl$_3$ at 298 K. Intermolecular cross-peaks are indicated by circles.
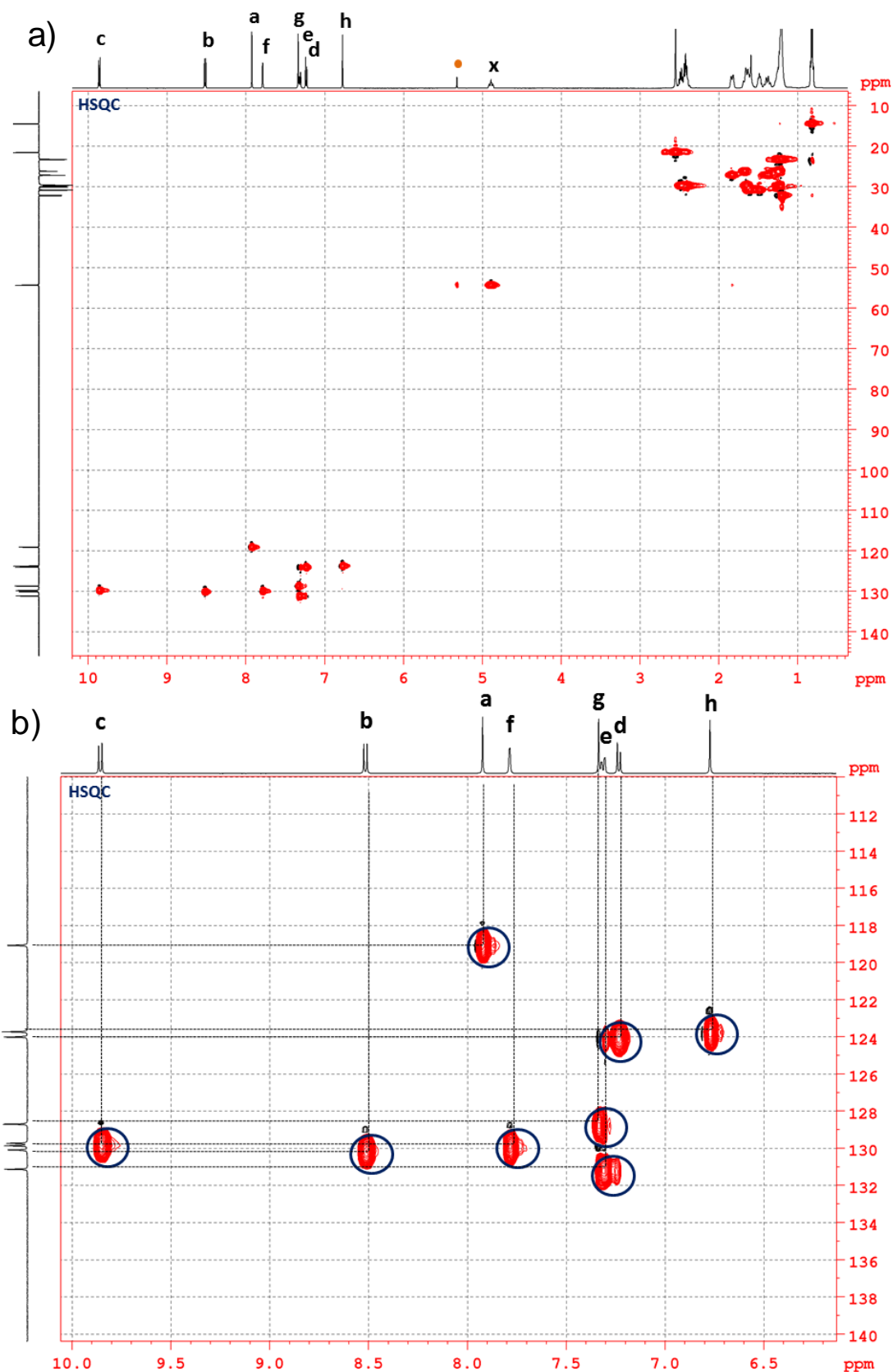
**Figure 2.4.** HSQC spectrum of **TSP1** at 500 MHz, recorded in CDCl$_3$ at 298 K. Intermolecular cross-peaks are indicated by circles.

In the case of full cage macrocycle **TSP2**, the HMBC spectrum shows strong cross-peaks of **a** and **b** with imide carbon, which helped to fix the position of PBI protons (Figure 2.5). As seen in Figure 2.6, the $^1$H-$^1$H COSY shows the strong cross-peaks for the PBI proton **b** and **c**, which are the only adjacent protons present in the **TSP2** in the aromatic region. However, the NOESY spectra show the cross-peak signals for phenyl proton **d** with thiophene proton **e** and methyl proton **y**. Moreover, the thiophene proton **f** shows cross-peak with alkyl **z** proton indicating these two protons are closer in space (Figure 2.7). The PBI proton **a** shows cross-peaks with thiophene proton **e** and phenyl proton **d**, indicating the position of PBI is orthogonal and in-between these two rings (Figure 2.7). The $^1$H-$^{13}$C HSQC spectra help us determine the protons attached to the carbon atoms (Figure 2.8).
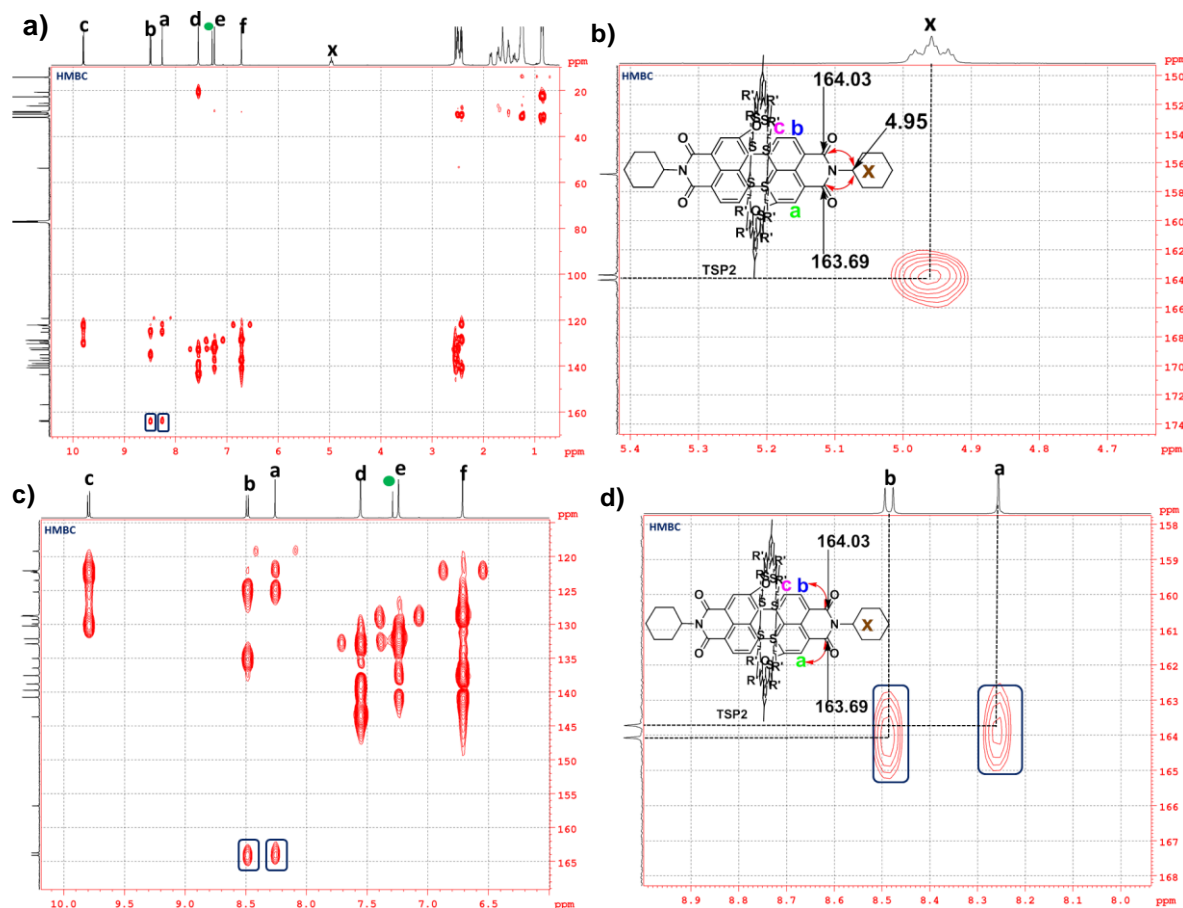


**Figure 2.5.** HMBC spectrum of **TSP2** at 500 MHz, recorded in CDCl$_3$ at 298 K. Intermolecular cross-peaks are indicated by circles.
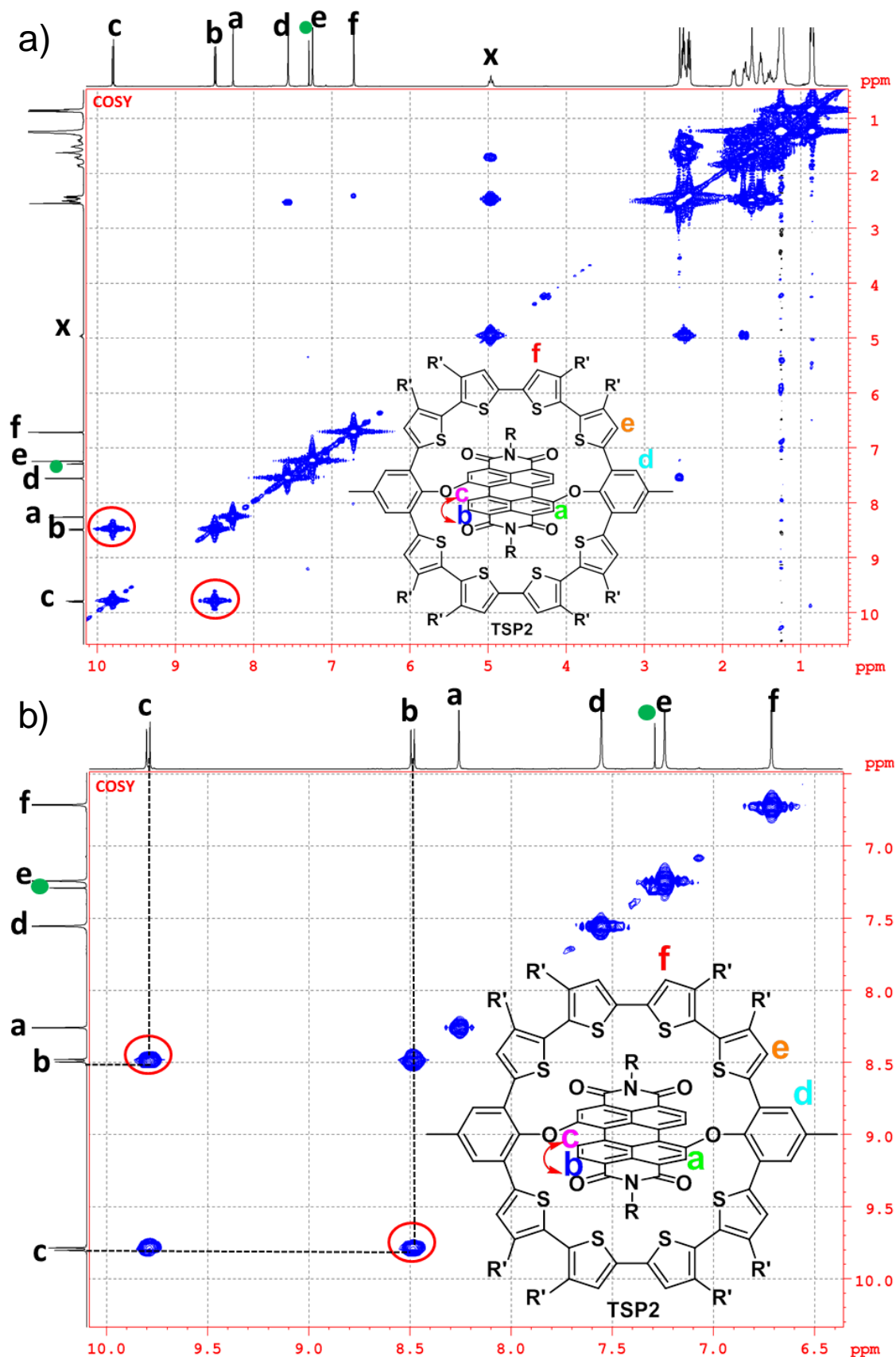
**Figure 2.6.** COSY spectrum of **TSP2** at 500 MHz, recorded in CDCl₃ at 298 K. Intermolecular cross-peaks are indicated by circles.
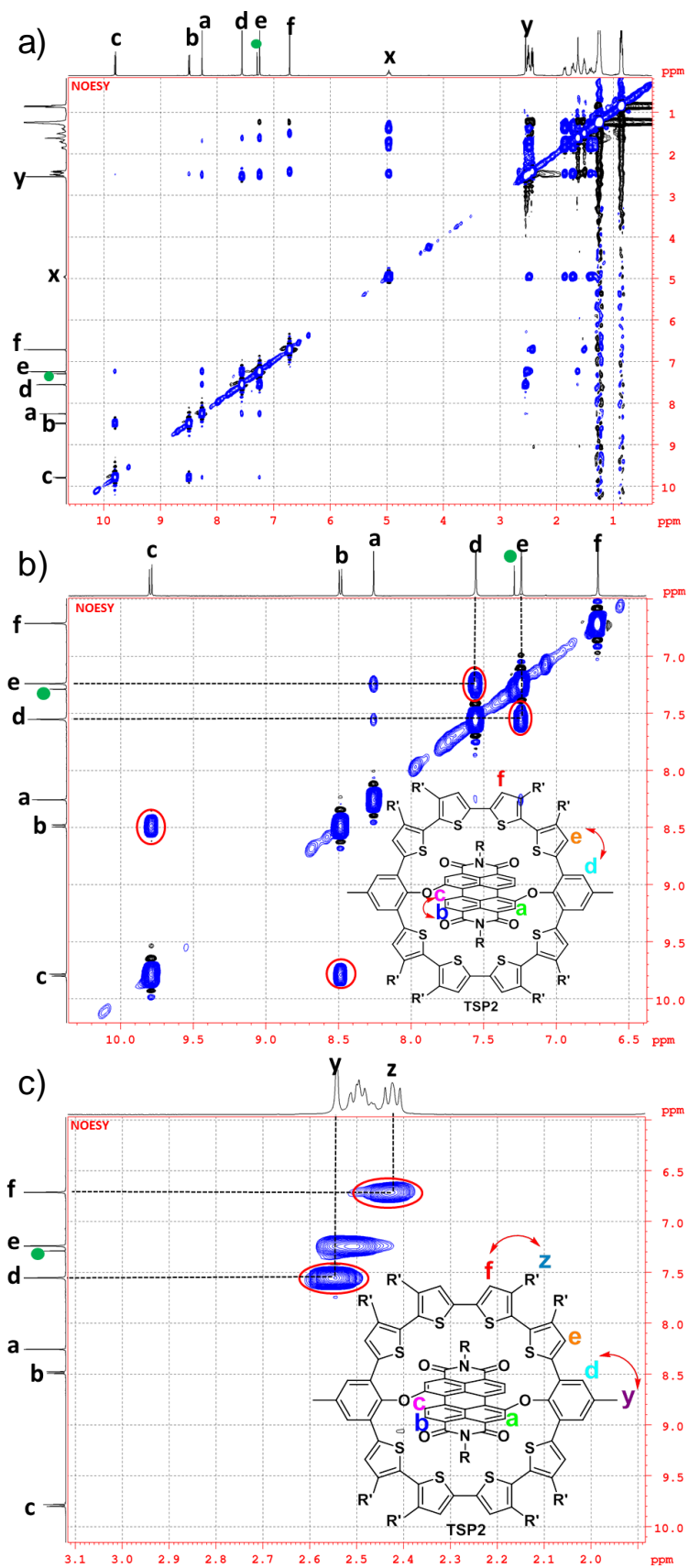
**Figure 2.7.** NOESY spectra of **TSP2** at 500 MHz, recorded in CDCl₃ at 298 K. Intermolecular cross-peaks are indicated by circles.
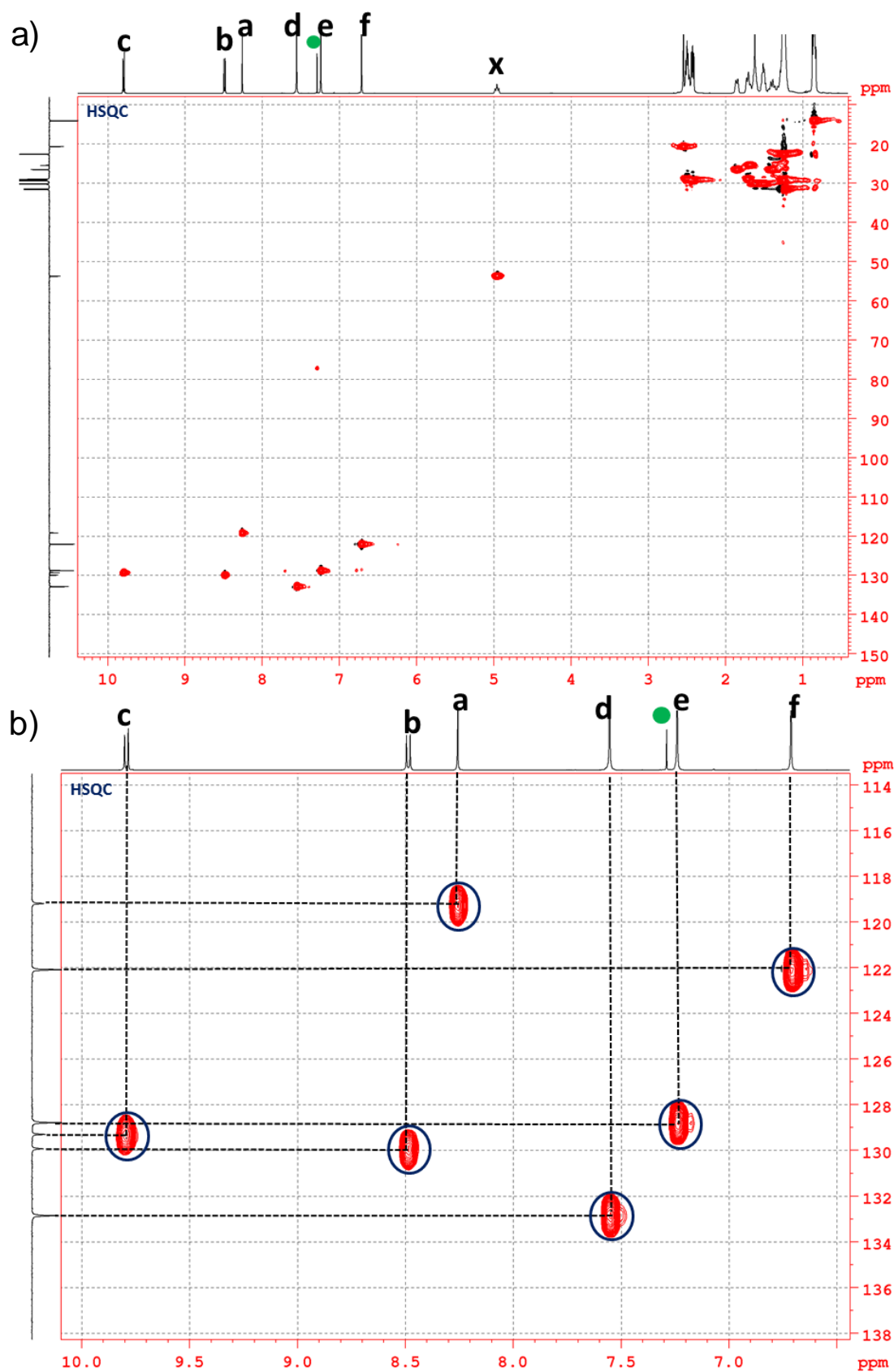
**Figure 2.8.** HSQC spectra of **TSP2** at 500 MHz, recorded in CDCl₃ at 298 K. Intermolecular cross-peaks are indicated by circles.

To study the effect of core isolation of PBI using oligothiophene rings, absorption and steady-state emission of reference molecule **rPBI**, and **TSP1, 2** were recorded in $CH_2Cl_2$ (Figure 2.9 a,b). Normalized absorption spectra showed a clear red-shift of around 18 nm in the absorption maximum from **rPBI** to **TSP1** and **TSP2** (Figure 2.9c). The emission intensity of **TSP1** and **TSP2** in the solution is negligibly low in $CH_2Cl_2$ (Figure 2.9b,d). A comparison indicated no change in absorption or emission features upon oligothiophene ring closure (Figure 2.9c,d). The variation observed in the visible and fluorescence color is displayed in figure 2.9e.
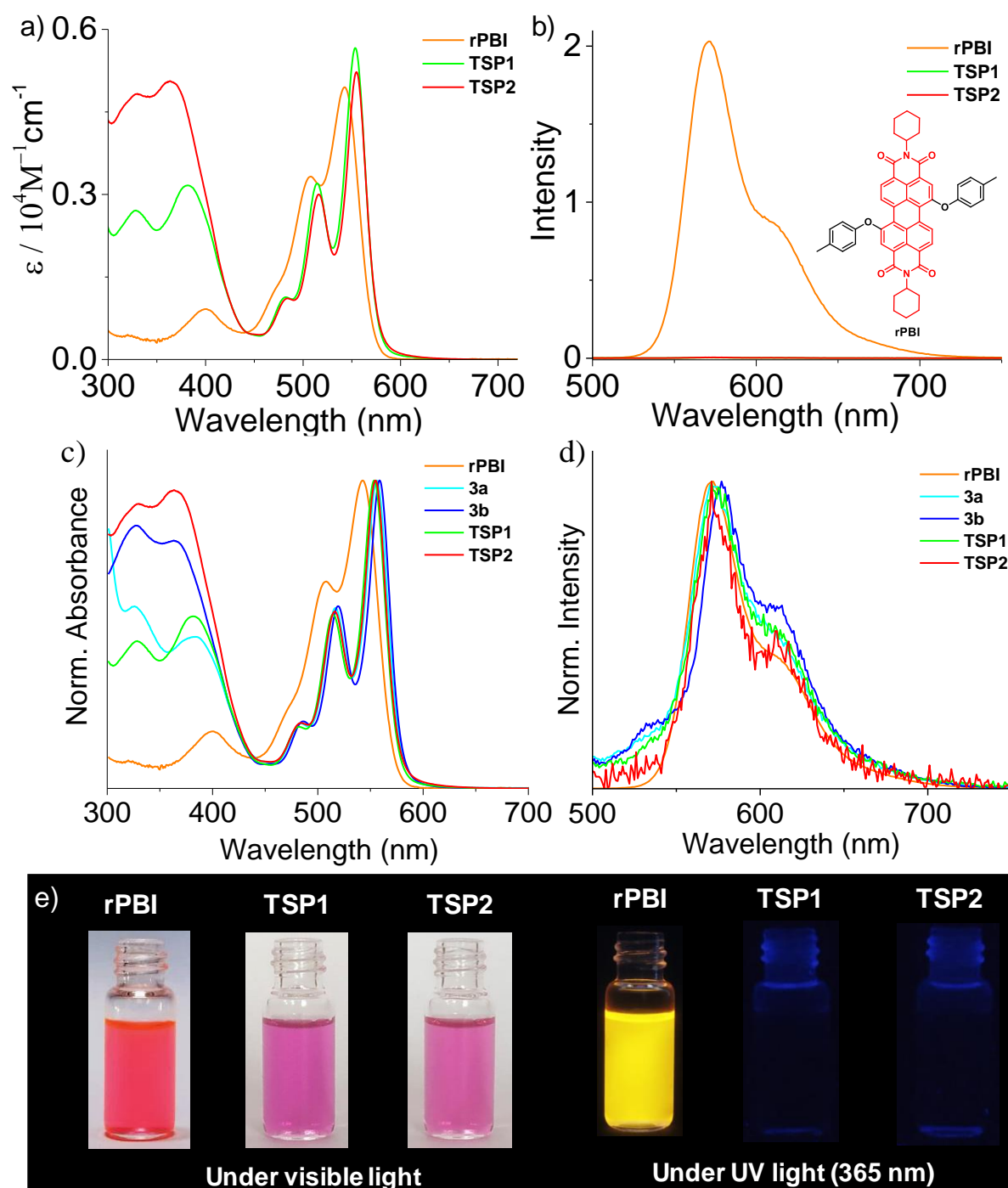
**Figure 2.9.** a) UV-Vis absorption and b) steady-state fluorescence spectra of **rPBI**, **TSP1**, and **TSP2** in $CH_2Cl_2$; inset shows the chemical structure of **rPBI**. Normalized c) UV-Vis absorption and d) steady-state fluorescence spectra of **rPBI**, **TSP1**, and **TSP2** in $CH_2Cl_2$ ($\lambda_{ex}$ = 460 nm for **rPBI**, 475 nm for **3a**, 480 nm for **3b**, 480 nm for **TSP1** and 485 nm for **TSP2**). e) Photograph of **rPBI**, **TSP1**, and **TSP2** in $CH_2Cl_2$ under visible and UV (365 nm) lights.

To see the redox behaviour of **TSP1** and **TSP2**, cyclic voltammetry (CV) and differential pulse voltammetry (DPV) were recorded. These experiments were carried out in $CH_2Cl_2$ ($C$ = 1 mM) using $Bu_4NPF_6$ as the supporting electrolyte. Two reversible reduction waves at potentials of -1.22, -1.39 V for **TSP1** and -1.24, -1.47 V for **TSP2** (Figure 2.10, 2.11, Table 2.5.1) were observed. Two reversible reduction waves point to the first and the second one-electron stepwise reductive process leading to anion and dianion formation of PBI core. The observed reduction potentials are slightly shifted to the negative potential than **rPBI** (Figure 2.12, Table 2.5.1). There are two reversible oxidation peaks at 0.54, 0.79 V for **TSP1**, and 0.57, 0.87 V for **TSP2** in the positive potential sweep due to the oxidation of oligothiophene rings (Figure 2.10, 2.11, Table 2.5.1). Though the donor and acceptor units are linked together in the macrocycles, the redox features indicate that the electronic states are only slightly affected.
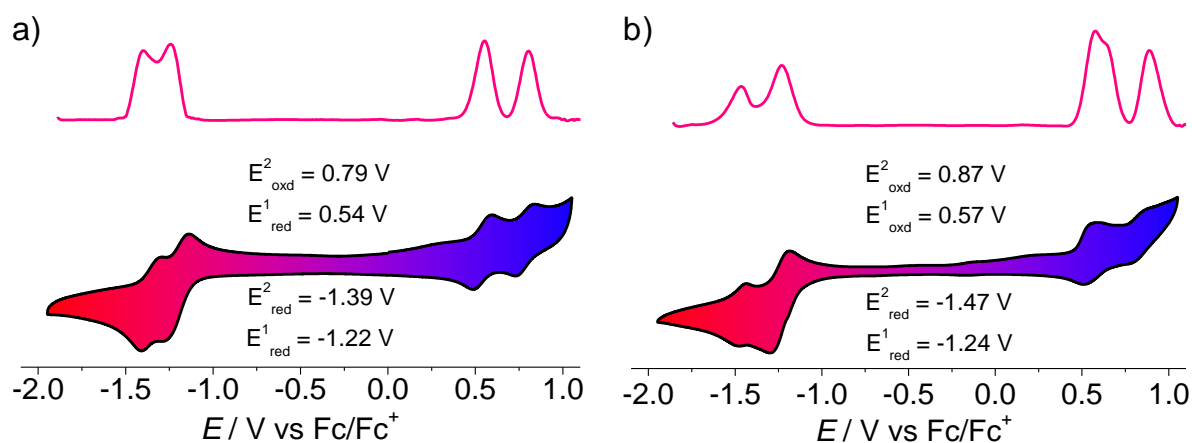


**Figure 2.10.** CV and DPV measurements of a) **TSP1** and b) **TSP2** in $CH_2Cl_2$ ($C$ = 1 mM) with $Bu_4NPF_6$ at 100 mV/s scan rate.
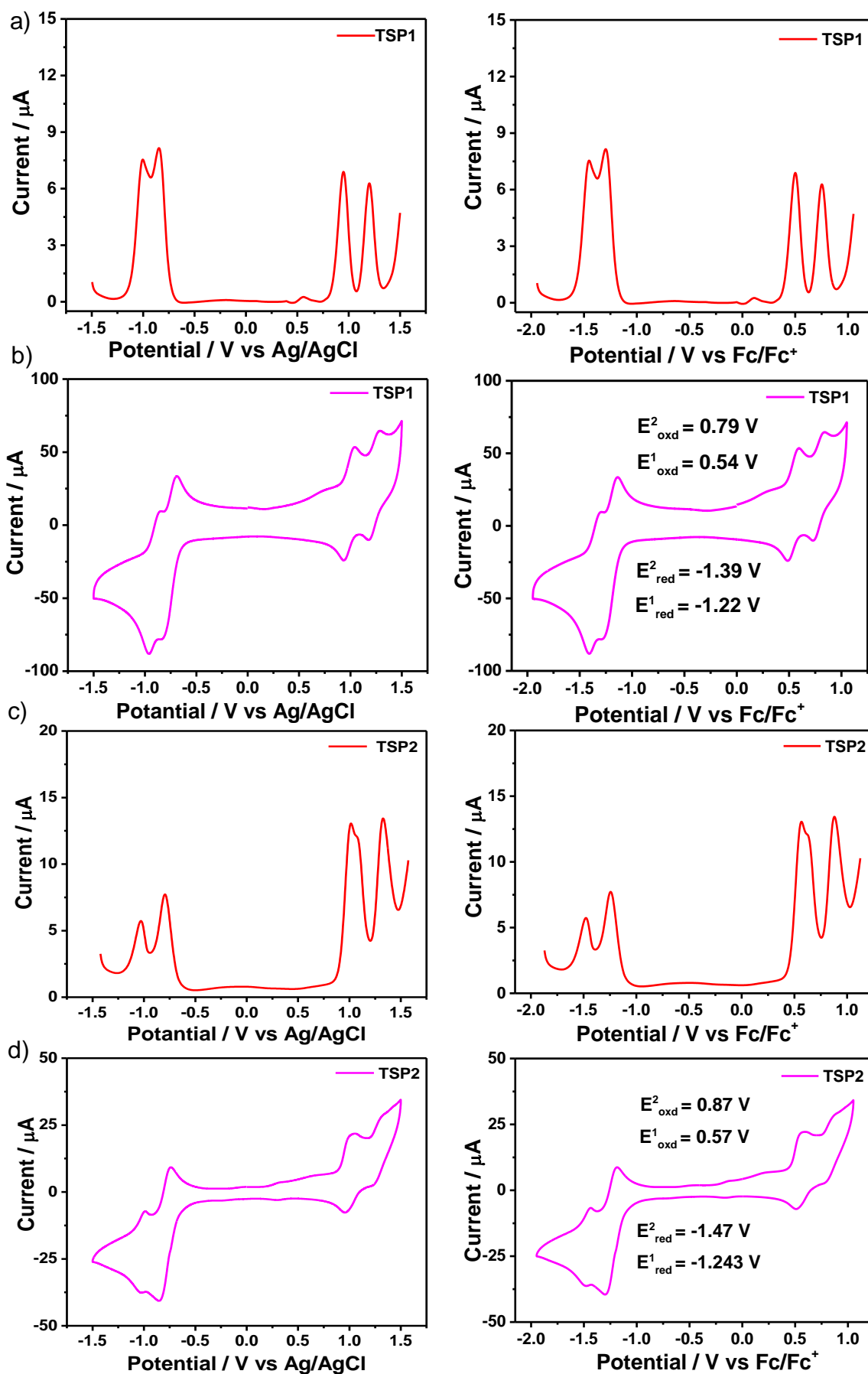
**Figure 2.11.** a) and c) DPV measurements at 100 mV/s scan rate (left) and calculated as Ferrocene as internal reference standard ($E_{Fc+/Fc}$ = 0.00 V) (right) of **TSP1** and **TSP2** (1 mM). b) and d) CV at 100 mV/s scan rate (left) and CV calculated as Ferrocene as internal reference standard ($E_{Fc+/Fc}$ = 0.00 V) (right) of **TSP1** and **TSP2** (1 mM).
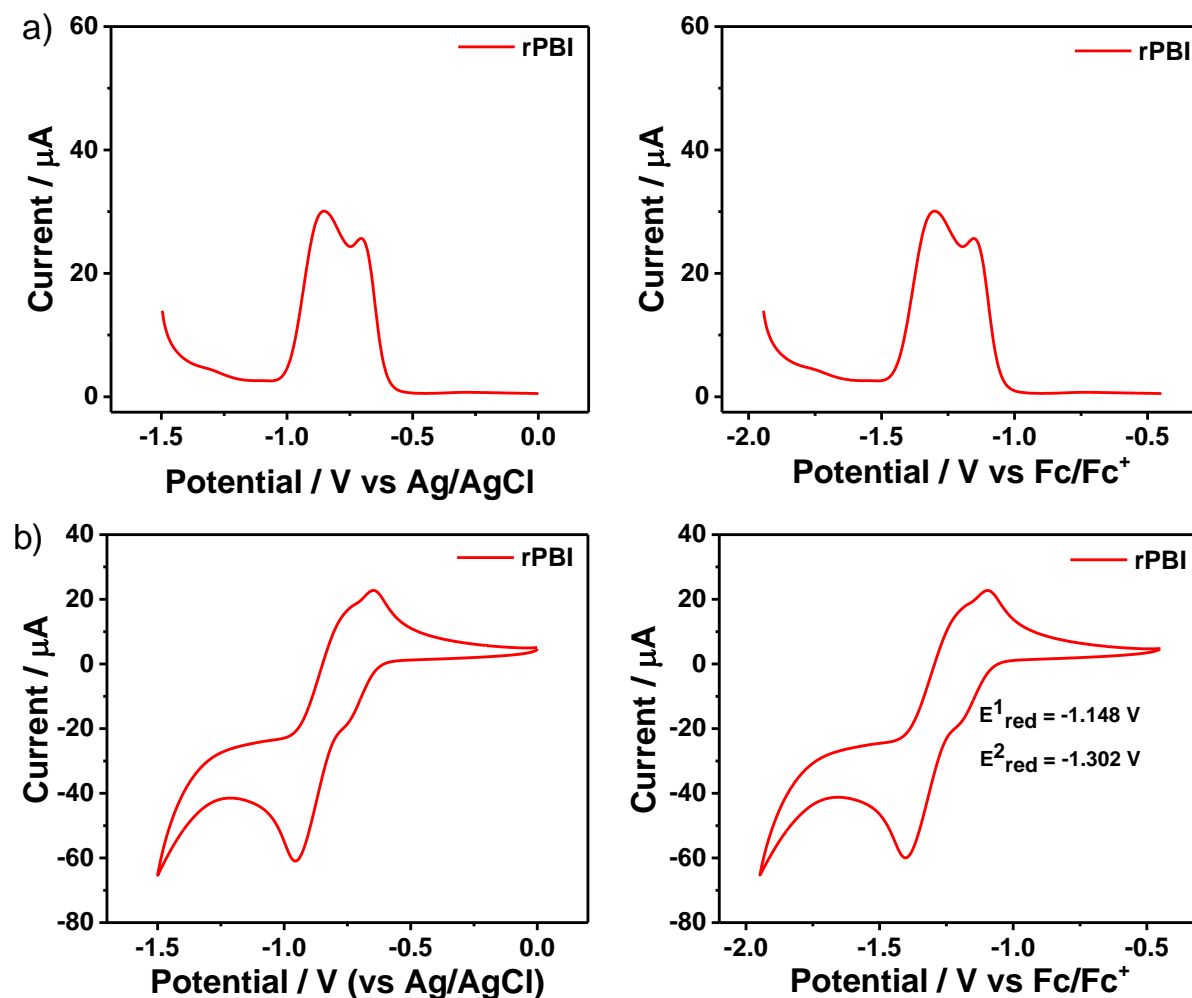


**Figure 2.12.** a) DPV measurements at 100 mV/s scan rate (left) and calculated as Ferrocene as internal reference standard ($E_{Fc+/Fc}$ = 0.00 V) (right) of **rPBI** (1mM). b) CV at 100 mV/s scan rate (left) and CV calculated as Ferrocene as internal reference standard ($E_{Fc+/Fc}$ = 0.00 V) (right) of **rPBI** (1mM).

The energies and electronic wave function distributions for the frontier molecular orbitals (MOs) demonstrate predominant contributions of the oligothiophene unit in the highest occupied molecular orbital (HOMO) and those of the PBI blocks in the lowest unoccupied molecular orbital (LUMO) (Figure 2.13a,b), validating the preferred photoinduced ET direction from oligothiophene to PBI blocks mediated through the lowest energy excited states. The connection of the oligothiophene ring through oxygen to the PBI unit prevents

electronic communication between the D-A units. Besides, the presence of two phenyl rings through ortho connection fails to delocalize the lobes all over the ring. The lack of CT bands in the absorption spectra and photographs of **TSP2** under visible light (Figure 2.9a, 2.14) and the redox behavior of the macrocycles (Figure 2.10,2.11) ascertain the above observations.
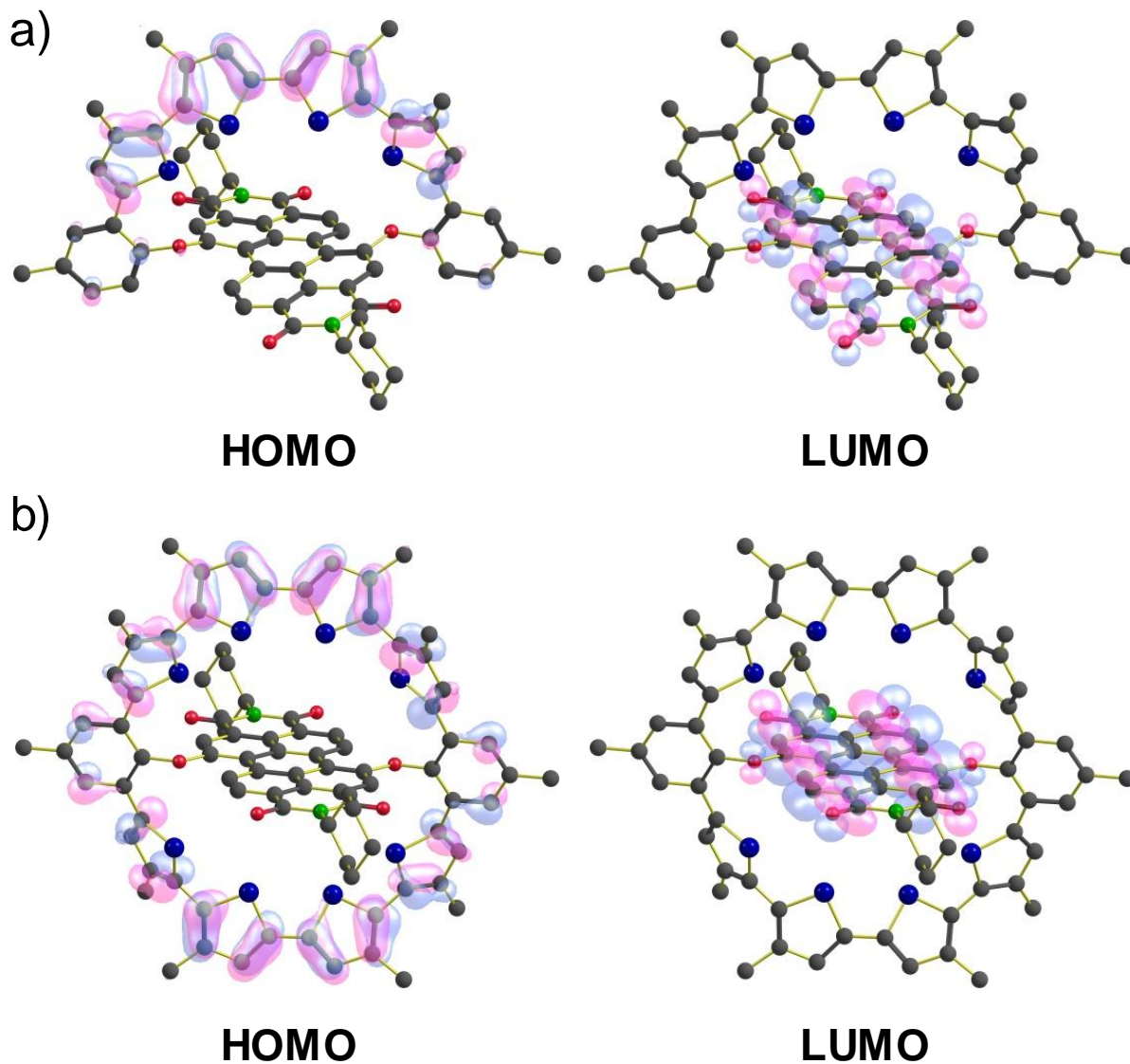


**Figure 2.13.** HOMO and LUMO of a) **TSP1** and b) **TSP2** based on geometry optimized structures from DFT calculations, alkyl chains are replaced with methyl groups.
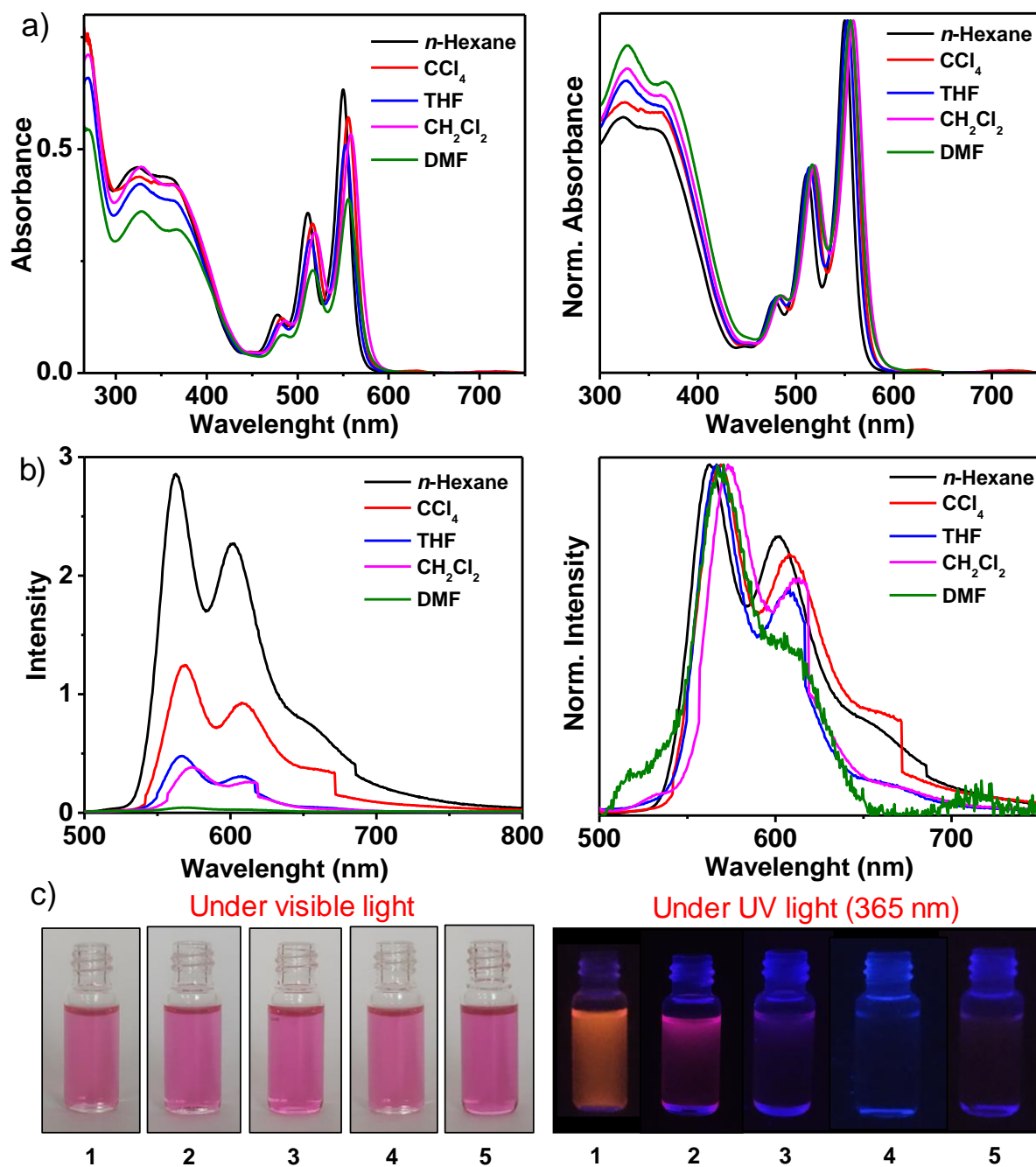
**Figure 2.14.** a) Absorption and corresponding normalized spectra of **TSP2** in 1. *n*-hexane, 2. $CCl_4$, 3. THF, 4. $CH_2Cl_2$, 5. DMF solution ($C$ = 1 x $10^{-5}$ M, $l$ = 1 cm) at 25 ˚C, b) Steady state emission and corresponding normalized spectra of **TSP2** in ($C$ = 1 x $10^{-5}$ M, $l$ = 1 cm) at 25 ˚C ($\lambda_{ex}$ = 485 nm) and Corresponding photographs of **TSP2** under c) visible and UV (365 nm) light.

To understand the orientation of the oligothiophene ring around the PBI, a single crystal of **TSP2** was grown from $CH_2Cl_2$:$CH_3OH$ mixture. The final structure of **TSP2** was confirmed by single-crystal X-ray analysis of the needle-like crystals (Figure 2.15-2.18). The crystal structure of **TSP2** belongs to triclinic *P*-1 space group containing one and a half molecules in the asymmetric unit (CCDC: 2166196). Out of two molecules, one of them occupies a special position (inversion center) (Figure 2.16). Most of the *n*-hexane moieties display thermal disorder due to conformational flexibility. The crystal structure shows that PBI is nearly perpendicular (~80°) to the strapped oligothiophene ring (Figure 2.17). The thiophene core unit of the **TSP2** molecules, which occupies an inversion center, is more planar compared to the thiophene core unit of the other **TSP2** molecule, which is more twisted from the planarity. The crystal structure is stabilized by several hydrogen-bonding interactions involving the carbonyl group of the PBI unit and H-atom of the thiophene unit (C-H•••O, 2.474 Å, 144.5°; 2.573 Å, 167.9°). The crystal structure is also supported by several C-H•••π contacts engaging alkyl chain C-H and π-cloud of thiophene moiety. Hence the presence of such multiple noncovalent interactions was found to be the major driving force for extended molecular packing.
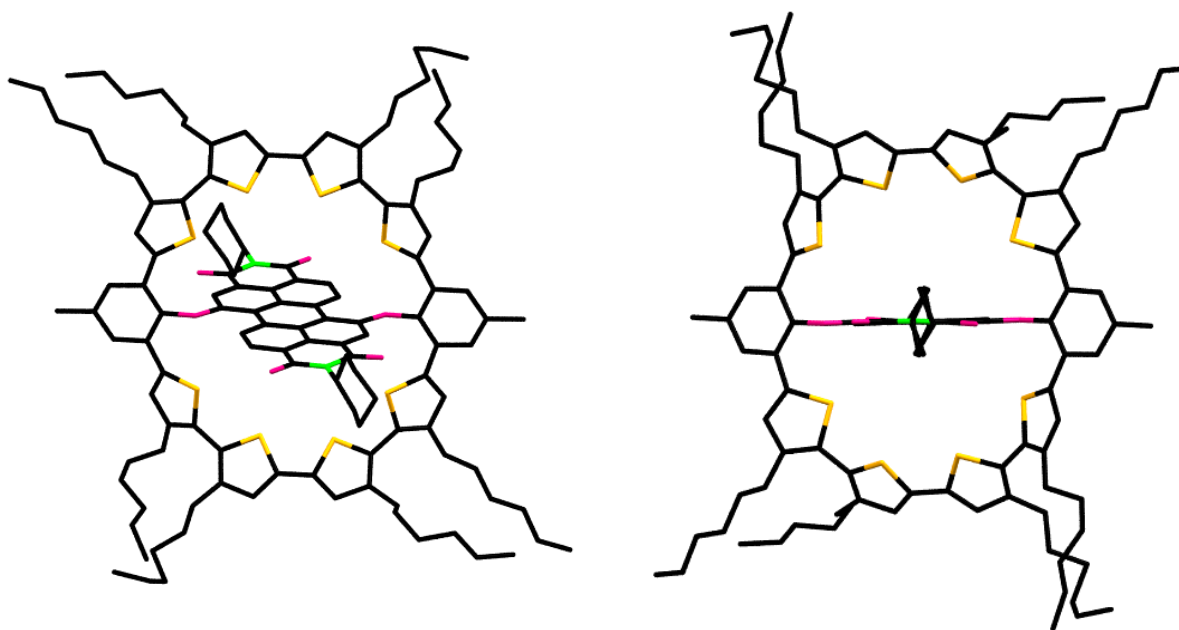


**Figure 2.15.** Crystal structure of **TSP2** showing the individual molecule; hydrogen atoms are removed for clarity.
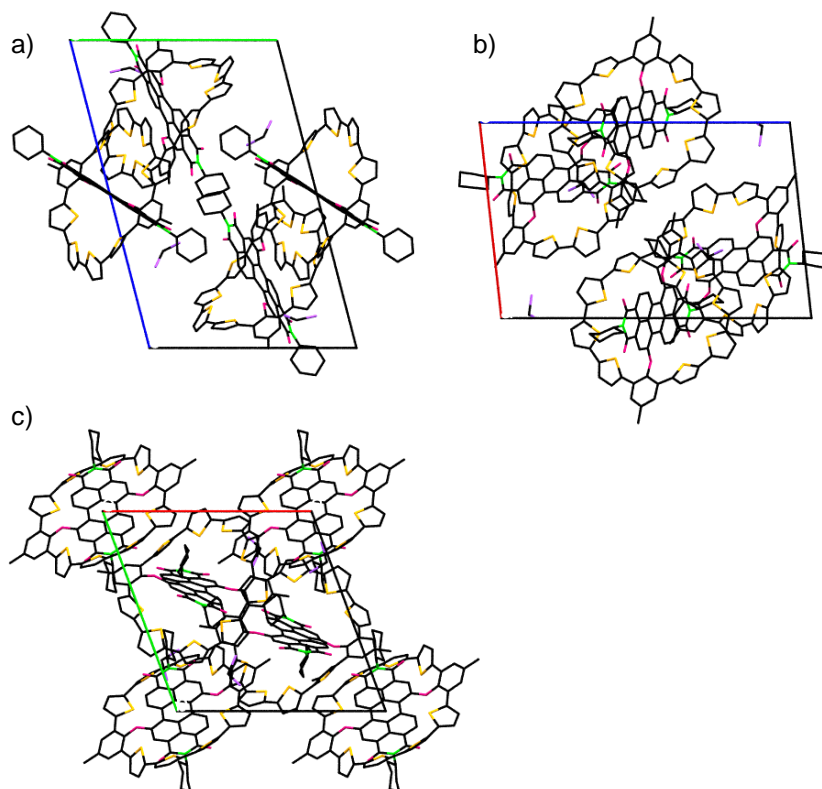
**Figure 2.16.** The unit cell of **TSP2** viewed along a) a, b) b, and c) c axes.
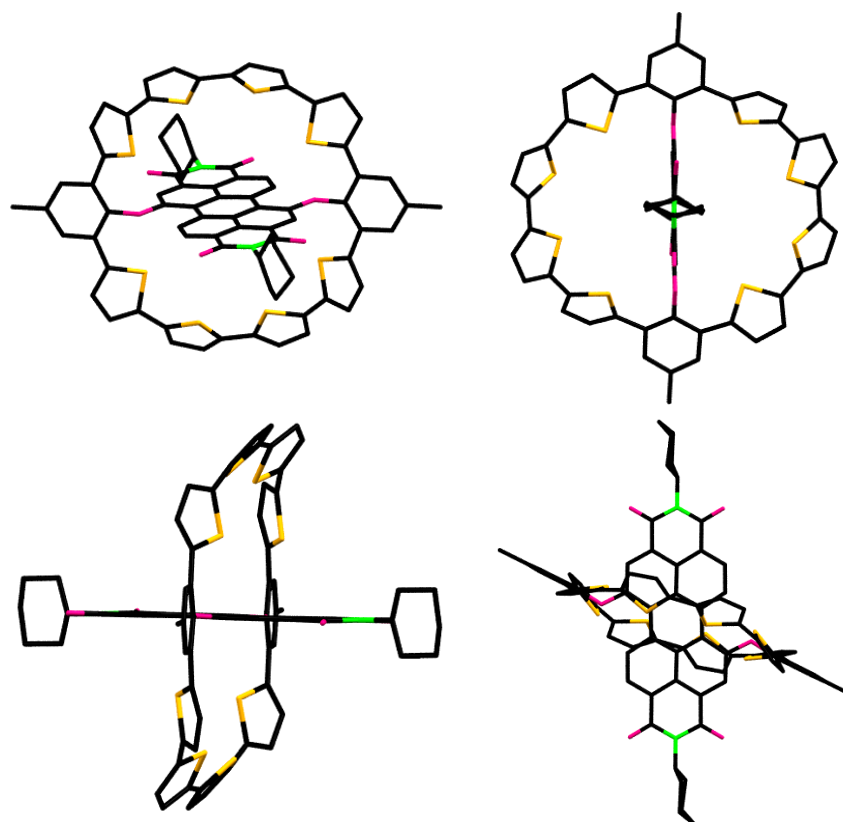


**Figure 2.17.** Crystal structure of **TSP2**. The hydrogen atoms and alkyl chains are removed for clarity.
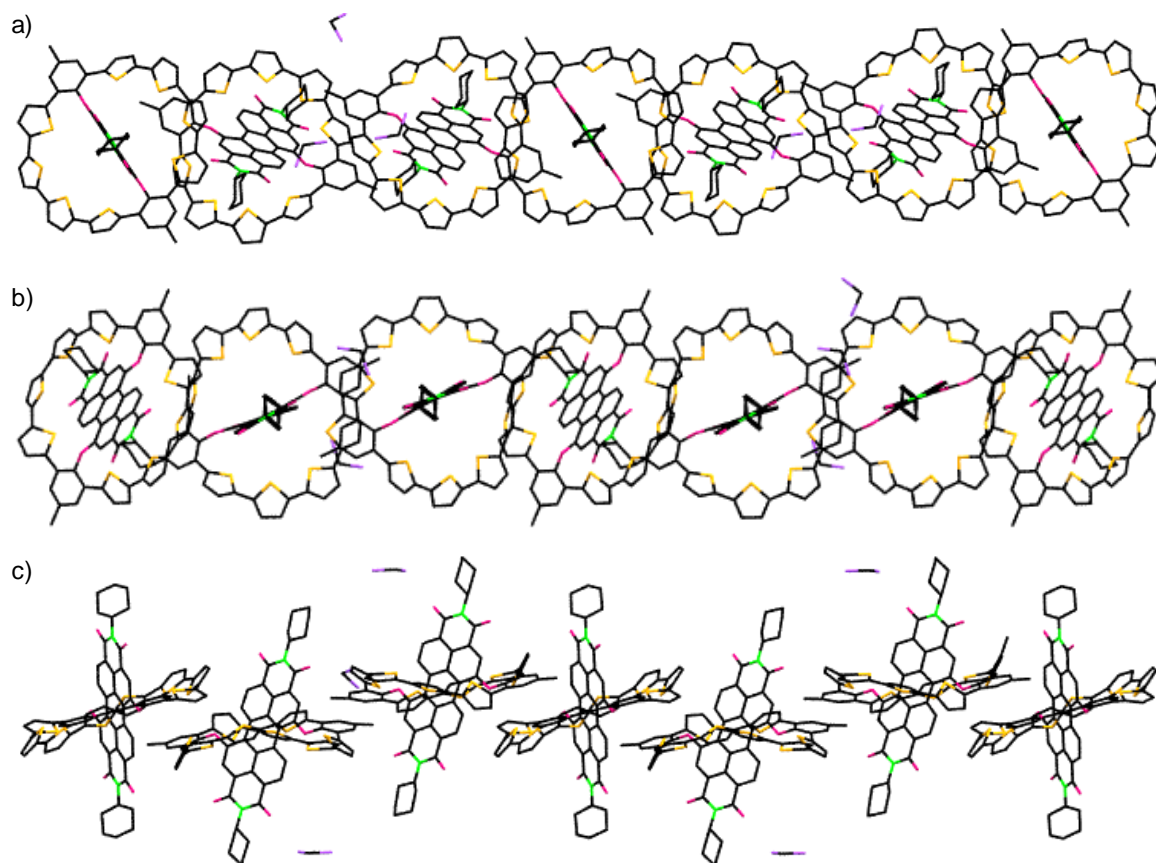
**Figure 2.18.** The extended molecular packing of **TSP2** shows the presence of both planar and twisted PBI cores.
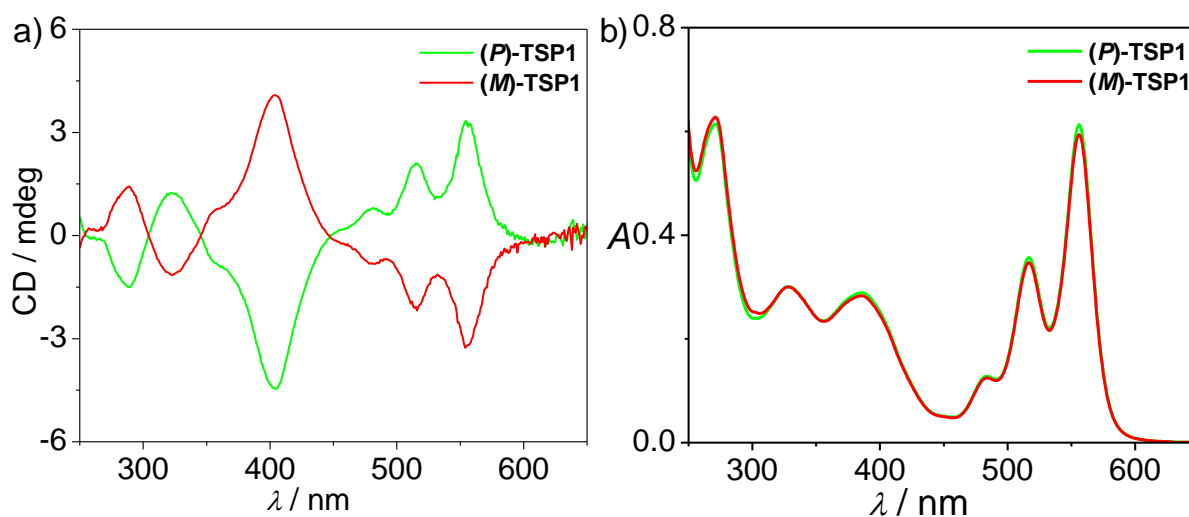


**Figure 2.19** a) Circular dichroism and b) UV-Vis absorption spectra of (*P*)-**TSP1** and (*M*)-**TSP1** in $CH_2Cl_2$ ($C = 10^{-5}$ M).

As reported, strapped PBIs obtained through bay functionalization will result in *M*- and *P*-isomers,[36] and it is confirmed by the crystal structure of **TSP2**. Hence chiral separation was

attempted for both **TSP1** and **TSP2,** and only the racemic mixture of *M*-**TSP1** and *P*-**TSP1** isomers were successfully separated by semi-preparative high-performance liquid chromatography (HPLC) on a chiral column using a mixture of *n*-hexane:isopropanol (95:5) as eluent. The isomerically pure *M*-**TSP1** and *P*-**TSP1** were characterized by circular dichroism (CD) spectroscopy. The mirror image CD signals confirm the formation of atropisomers by **TSP1** (Figure 2.19a,b).

Transient absorption (TA) spectroscopy was employed to elucidate the excited-state dynamics in these systems. Figure 2.20a,b represents TA spectra of **TSP1** and **TSP2,** respectively, following the photoexcitation of 460 nm pump pulses probing in the visible region of the spectrum for a variety of pump-probe delay times ranging between 2.5-200 ps time scale.
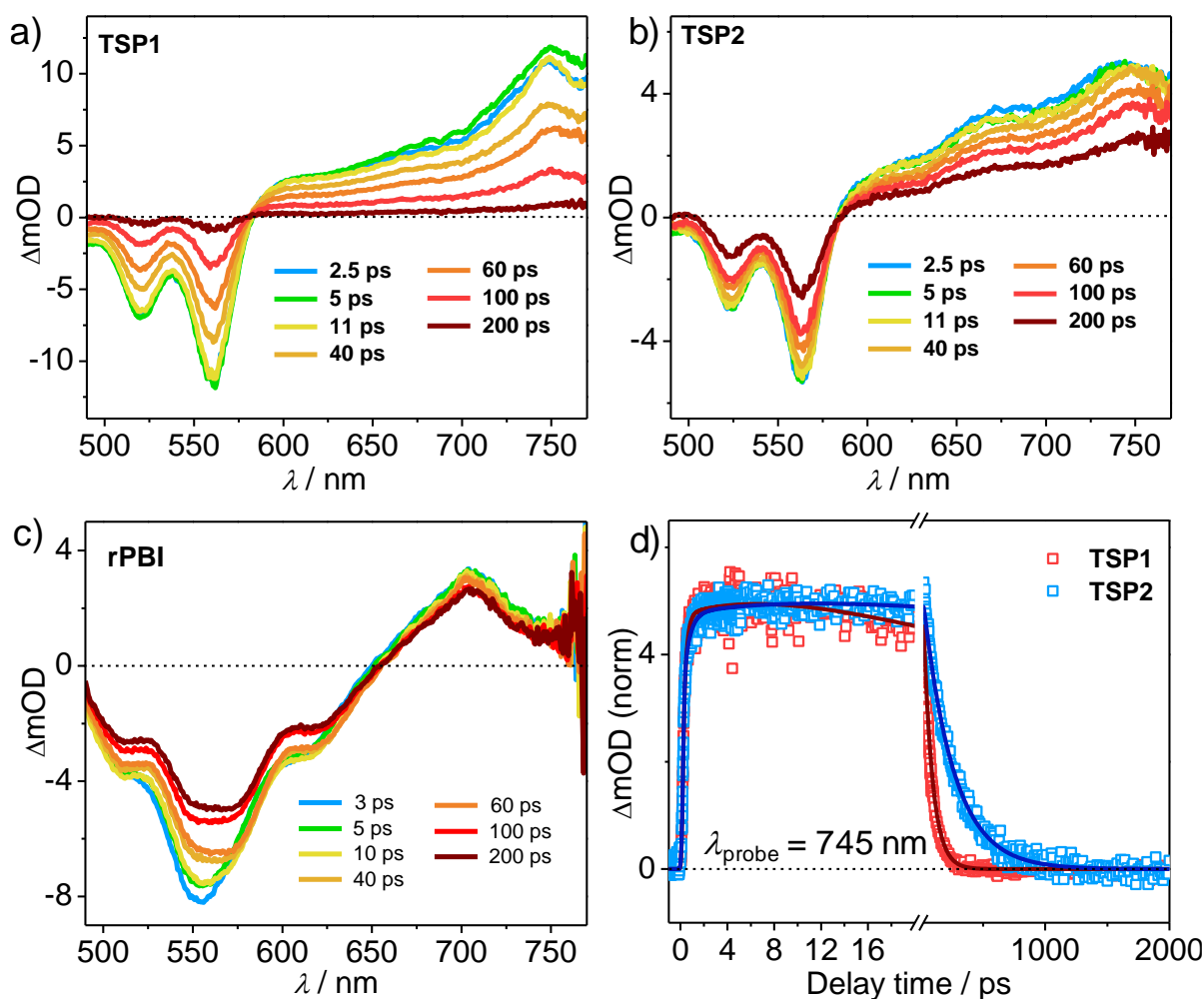


**Figure 2.20.** a) Femtosecond transient absorption spectra of a) **TSP1**, b) **TSP2**, and c) **rPBI** in $CH_2Cl_2$ after the laser excitation at 460 nm. d) Comparative dynamic profiles of **TSP1** and **TSP2** monitoring at 745 nm.

Both spectra possess two closely placed photoinduced bleach features around 520 and 563 nm (Figure 2.20a-c), resembling their peak positions in steady-state spectra. The 460 nm pump does not possess enough energy to excite the thiophene ring. Hence, these negative signatures must originate from the ground state bleaching (GSB) of $S_0$-$S_n$ transitions in the PBI moiety of the macrocycle (**PBI\***). Along with the presence of these GSB signatures, the spectra were dominated by the presence of a broad photoinduced absorption signal throughout the red regime peaking at around 750 nm. This spectrum is quite unique in nature and different from that of **rPBI** (Figure 2.20c). The TA spectra of **rPBI** are composed of a photoinduced bleach signal at 554 nm and a stimulated emission (SE) signature at 617 nm, along with a sharp positive feature at 705 nm. This positive signal necessarily arises from the photoinduced absorption of $S_1$ states. However, the positive features in **TSP1** and **TSP2** are quite broad and very different from the **rPBI** positive signature. This must originate due to the formation of **PBI** radical anion in the macrocycle system (Figure 2.21).[57-60] Interestingly, we did not observe any SE feature in the TA spectra of **TSP1** and **TSP2**, unlike **rPBI**.
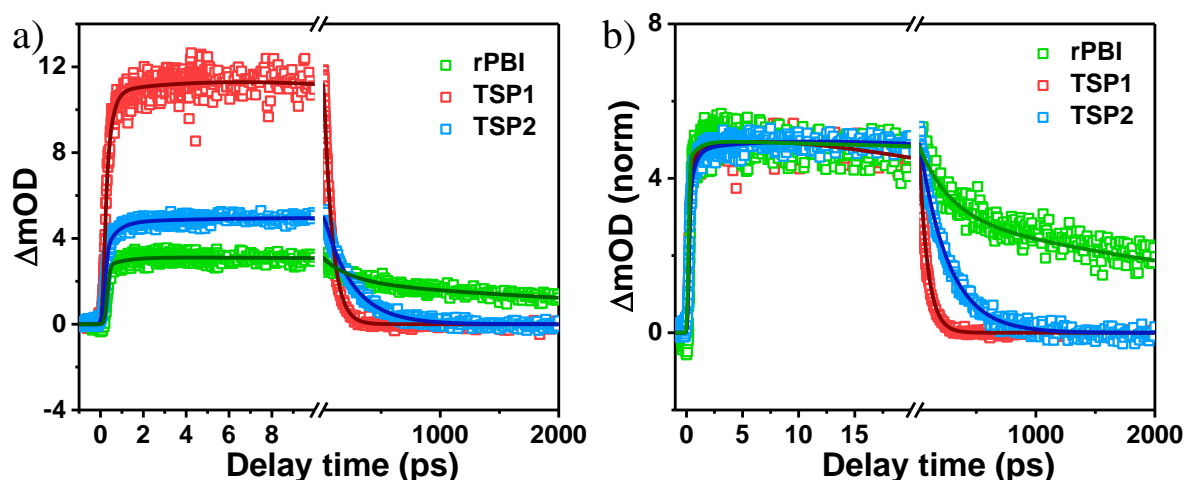


**Figure 2.21.** a) Un-normalized dynamic profiles of **rPBI**, **TSP1** and **TSP2** monitoring the positive signature at the red wing of the spectra, at 705, 745 and 745 nm, respectively. b) Normalized dynamic profiles of **rPBI**, **TSP1** and **TSP2** monitoring the positive signature at the red wing of the spectra, at 705, 745 and 745 nm, respectively.

Further, we monitored the dynamic profiles of these various features found in our systems to examine different plausible phenomena occurring in the macrocycle, such as photoinduced ET, separation of charge carriers, formation of cationic/anionic species, etc. These dynamic profiles were fitted with multi exponential time components and listed in Table 2.5.2. In Figure 2.20d, we have plotted the kinetic profiles of **TSP1** and **TSP2** monitoring at 745 nm

(PBI radical anion position). The positive signal in the red region of the spectra may well be composed of excited state absorption of PBI*, but the signal would be primarily dominated by the PBI anion as the CS process is supposed to occur at a very fast time scale. The absence of any SE signature in the macrocycle system substantiates this assumption. On applying global fitting analysis, a short-lived SE signature appeared in the case of **TSP1** (Figure 2.22a). It was associated with very fast decay (200 fs), and because of that, this feature was not noticed in the normal spectra plot. For **TSP2**, we could not locate any SE signature (Figure 2.22b). These observations point to a very fast charge separation process in these macrocycles. In this case, the rise times were found to be enhanced from **TSP1** to **TSP2**, as well as their recovery dynamics. Here, these growth time scales necessarily signify the charge separation process ($\tau_{CS}$).[52,57-60] From the multi-exponential fitting, charge separation processes were found to be occurring in 1.8 ps ($k_{CS} \sim 0.5 \times 10^{12}$ S$^{-1}$) and 3.1 ps ($k_{CS} \sim 0.3 \times 10^{12}$ S$^{-1}$) time scale for **TSP1** and **TSP2**, respectively. The recovery of the radical anion in **TSP2** system takes place at a much slower rate than that occurs in **TSP1**, indicating superior separation of charge in the closed cycle (Table 2.5.2). This data very well corroborates the dynamical change found in the case of GSB and confirms the separation of charge from **PBI\*** (S1) to **PBI** anionic state. The macrocycle molecule, **TSP2**, allows extensive CS and would be a great contender for organic photovoltaic material.
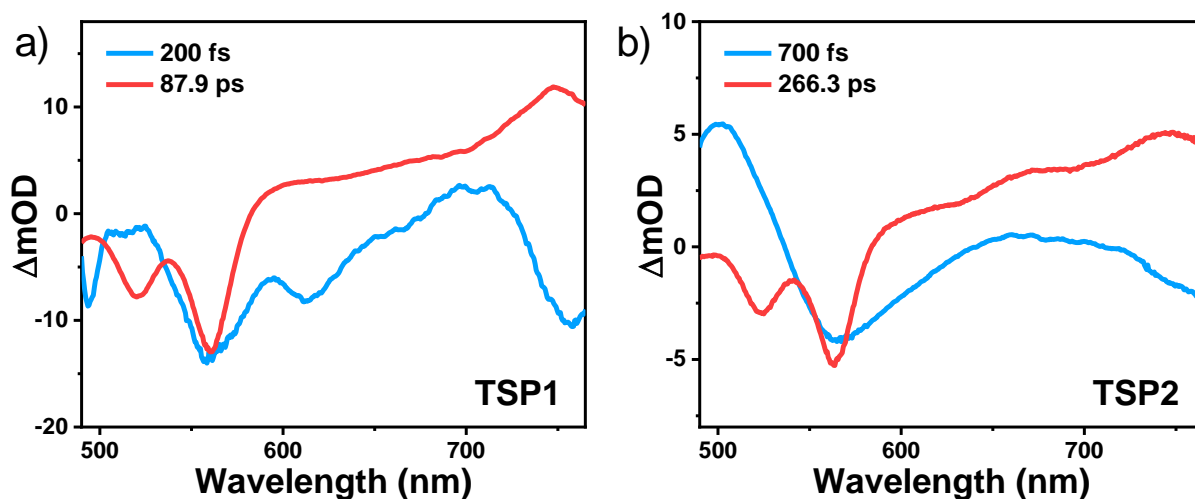


**Figure 2.22**. Spectral distributions of the pre-exponential coefficients from the global fitting for each of the calculated lifetimes, in case of a) **TSP1** and b) **TSP2**.

One of the attractions of the current design is the opportunity to functionalize the macrocycles further. The present oligothiophene strapped perylene bisimide macrocycles (**TSP1,2**) can be used for the synthesis of monoimide-monoanhydride (**TSP1O** and **TSP2O**)

(Scheme 2.3) and dianhydride (**TSP2OO**) macrocycles (Scheme 2.4). Monoimide-mono anhydride macrocycles can be used to prepare linear dimer analogs, and dianhydride macrocycles can make various types of 1D and 2D polymers (Scheme 2.3,2.4). In order to widen the scope of strapped PBIs, corresponding monoimide-monoanhydrides were synthesized from **TSP1** and **TSP2** (Scheme 2.3). The formation of the anhydrides was characterized by ^{1}H, ^{13}C NMR, Fourier-transform infrared (FT-IR), and MALDI-TOF MS and proceeded towards further synthesis (Figure 2.23).
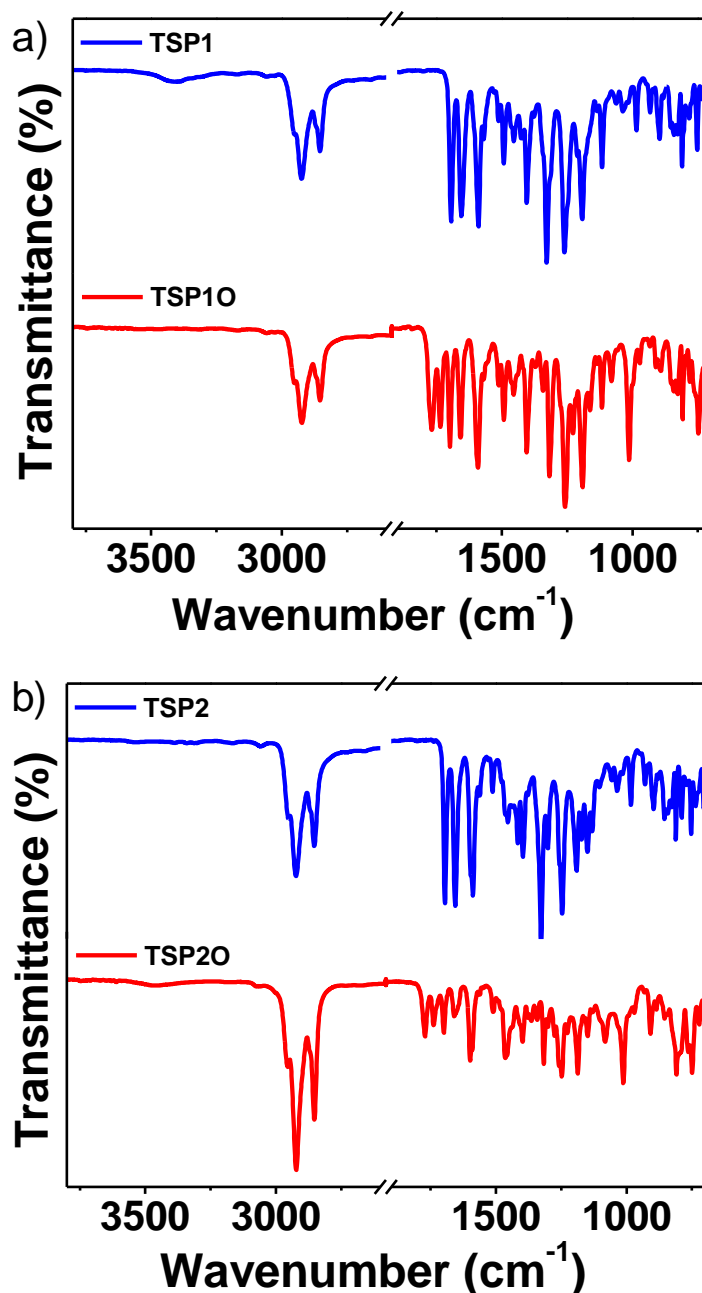


**Figure 2.23.** Comparison of the FT-IR spectra of a) **TSP1** and **TSP1O**, and b) **TSP2** and **TSP2O**.

The reaction of the monoimide-monoanhydride derivative with benzene-1,4-diamine resulted in the corresponding dimers **TSP1D** and **TSP2D** (Scheme 2.3). The formation of dimers is confirmed by comparing the FT-IR spectrum of the starting materials and corresponding dimers (Figure 2.24).
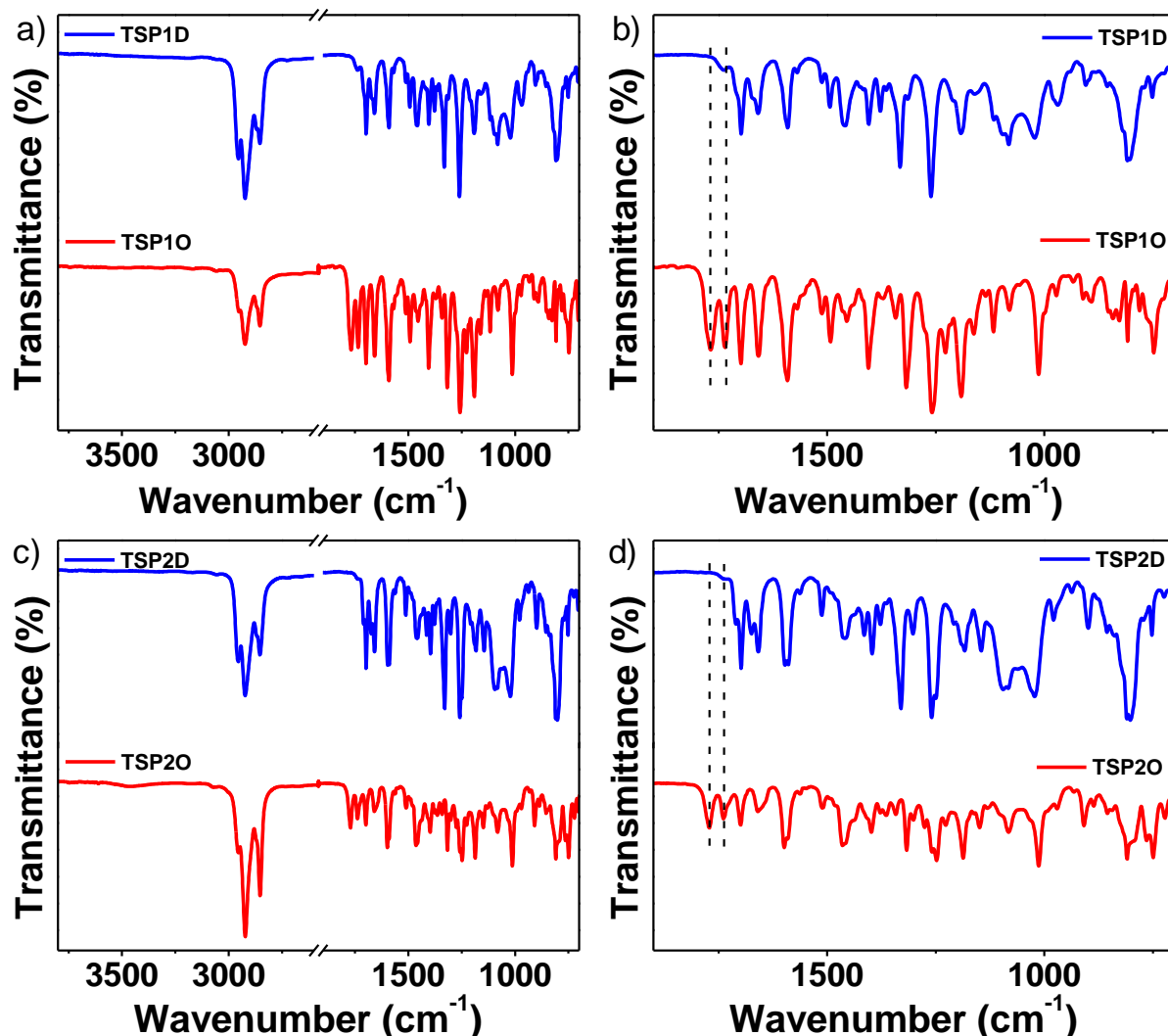


**Figure 2.24.** Comparison of the FT-IR spectra of a) and b) **TSP1O** and **TSP1D**, and c) and d) **TSP2O** and **TSP2D**.

^{1}H NMR spectra of **TSP1,2** and the corresponding dimers showed marked differences and hence confirmed the formation of the latter (Figure 2.25,2.26). A singlet at 7.37 and 7.39 ppm corresponding to the middle phenyl ring connecting the two macrocycles points to the formation of **TSP1D** and **TSP2D** (Figure 2.25,2.26). The structure of **TSP1D** and **TSP2D** was finally confirmed by extensive 2D NMR analyses (Figure 2.27-2.34).
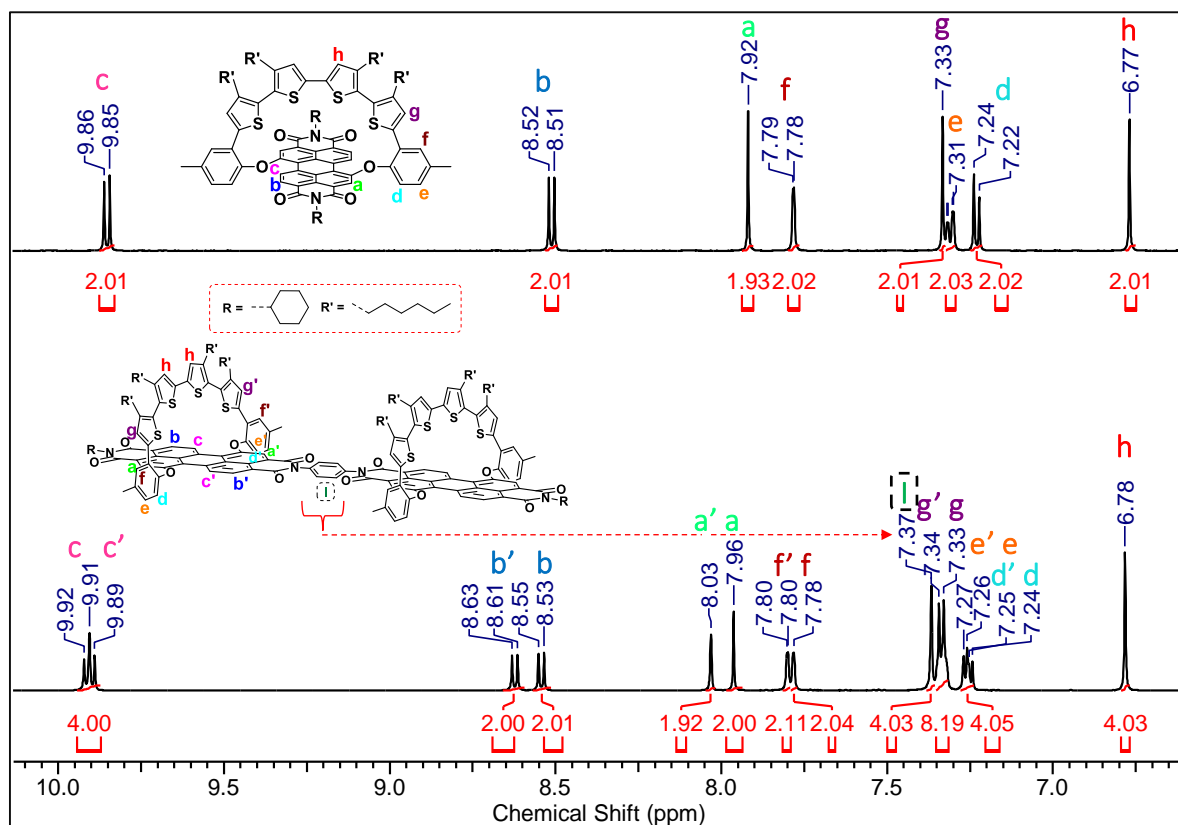
**Figure 2.25.** Comparison of the $^1$H NMR spectra of **TSP1** and **TSP1D** in CDCl$_3$.
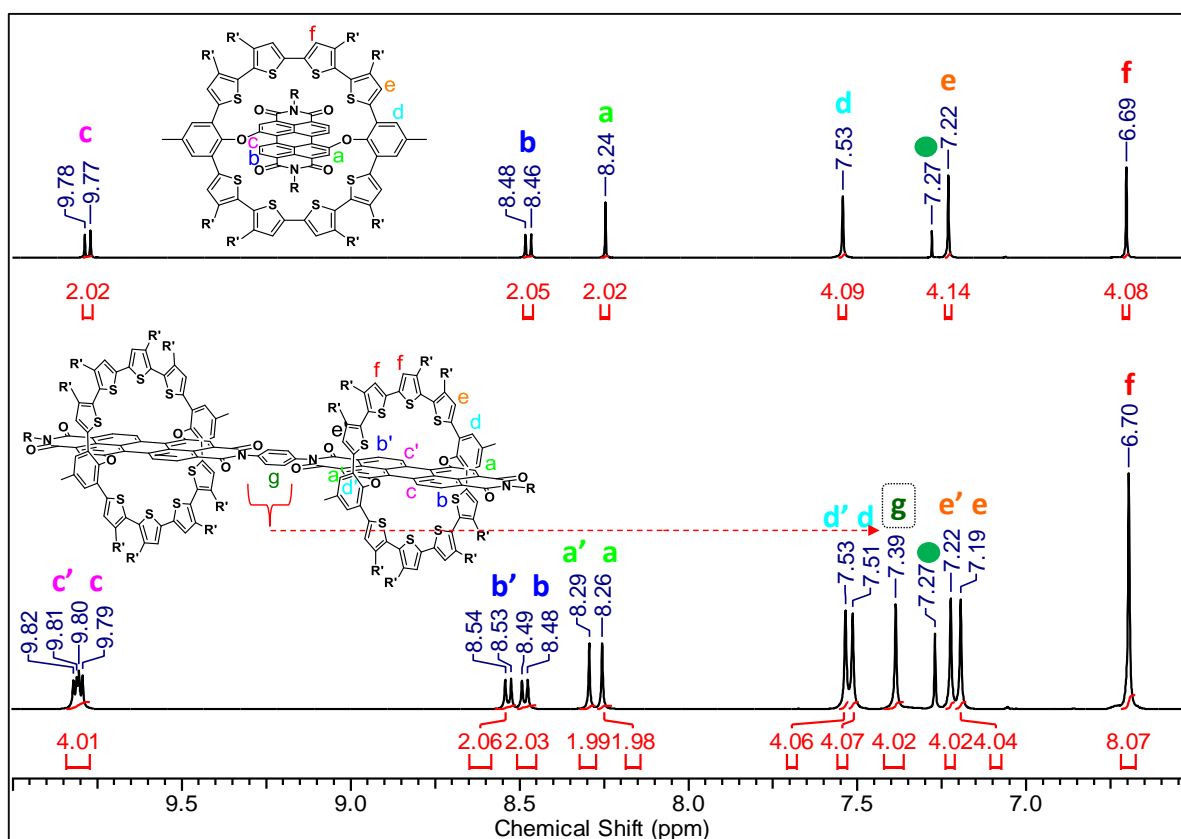


**Figure 2.26.** Comparison of the $^1$H NMR spectra of **TSP2** and **TSP2D** in CDCl$_3$.

As in the **TSP1D** molecule, the HMBC spectrum shows strong cross-peaks of **a, a′** and **b, b′** with imide four carbon, which helped to fix the position of PBI protons (Figure 2.27). [1]H-[1]H Correlation Spectroscopy (COSY) of **TSP1D** showed strong cross-peaks for the PBI protons b, b′ and c, c′ and confirmed that these two protons are from the unsubstituted side of PBI (Figure 2.28). The phenyl ring protons f, f′ show strong cross-peaks with methyl protons y, y′ on it and adjacent thiophene ring protons g, g′ (Figure 2.28). The protons y, y′ show cross-peaks with protons e, e′ in the ortho position of the phenyl ring (Figure 2.28). Strong intermolecular cross-peaks were observed between the protons of phenyl rings and PBI in the Nuclear Overhauser Effect Spectroscopy (NOESY) spectrum, indicating their close proximity (Figure 2.29). Phenyl proton d shows cross-peaks with protons a, a′ of PBI. We observed cross-peaks of the thiophene protons f and g / h and z, which support their adjacent positions in space. As shown in Figure 2.30, Heteronuclear Single Quantum Coherence (HSQC) spectra helped assign the proton position with respect to the attached carbon. The HMBC spectra of **TSP2D** indicate protons b, a, b′, and a′ belong to PBI (Figure 2.31). However, the strong cross-peaks in ^{1}H-^{1}H COSY confirm protons b, c, and b′, c′ are on the same side of PBI (Figure 2.32). The cross-peaks between PBI protons c, c′ with e, e′ (thiophene) and d, d′ (phenyl) in NOESY spectra show their close proximity (Figure 2.33). At the same time, the cross-peaks with PBI protons a, a′ and b, b′ are also visible. Moreover, PBI protons a, a′ show strong cross-peaks with e, e′, and d, d′ of thiophene and phenyl ring, respectively. As shown in figure S34, the HMBC spectrum shows strong cross-peaks of **a, a′**, **b, b′** and **c, c′** with perylenebisimide carbon, which helped to fix the position of PBI protons. From 2D NMR results, it can be concluded that the position of the PBI ring is orthogonal and in between the thiophene and phenyl ring.
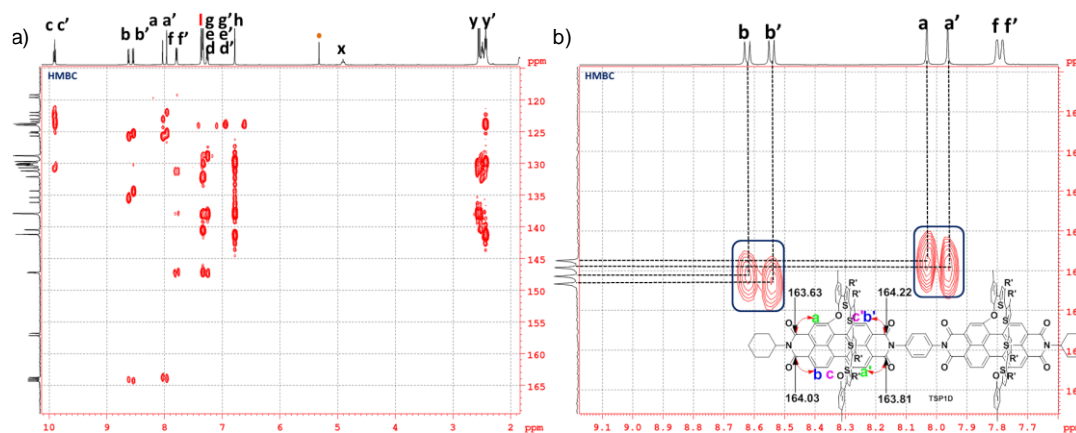


**Figure 2.27.** HMBC spectra of **TSP1D** at 500 MHz, recorded at 318 K. Intermolecular cross-peaks are indicated by circles.
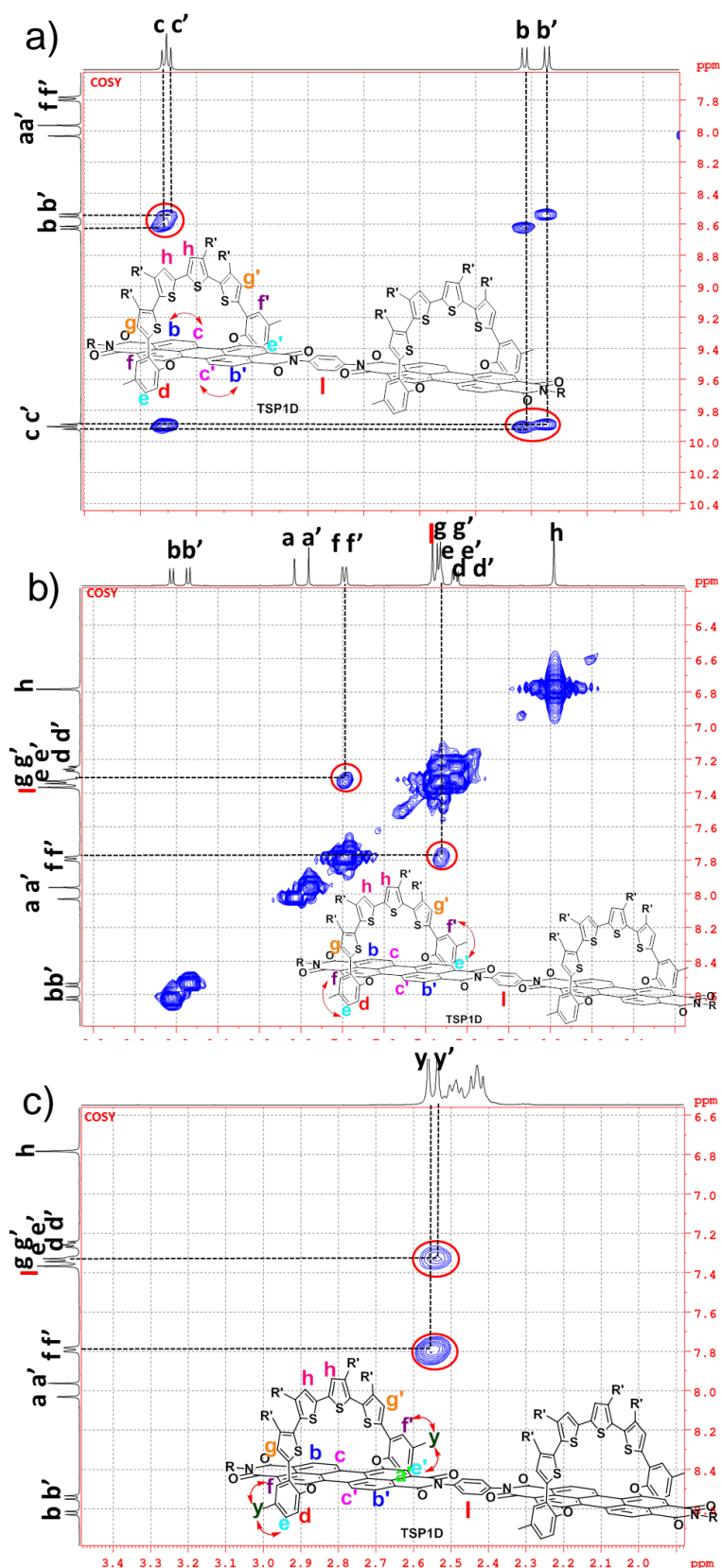
**Figure 2.28.** COSY spectra of **TSP1D** at 500 MHz, recorded at 318 K. Intermolecular cross-peaks are indicated by circles.
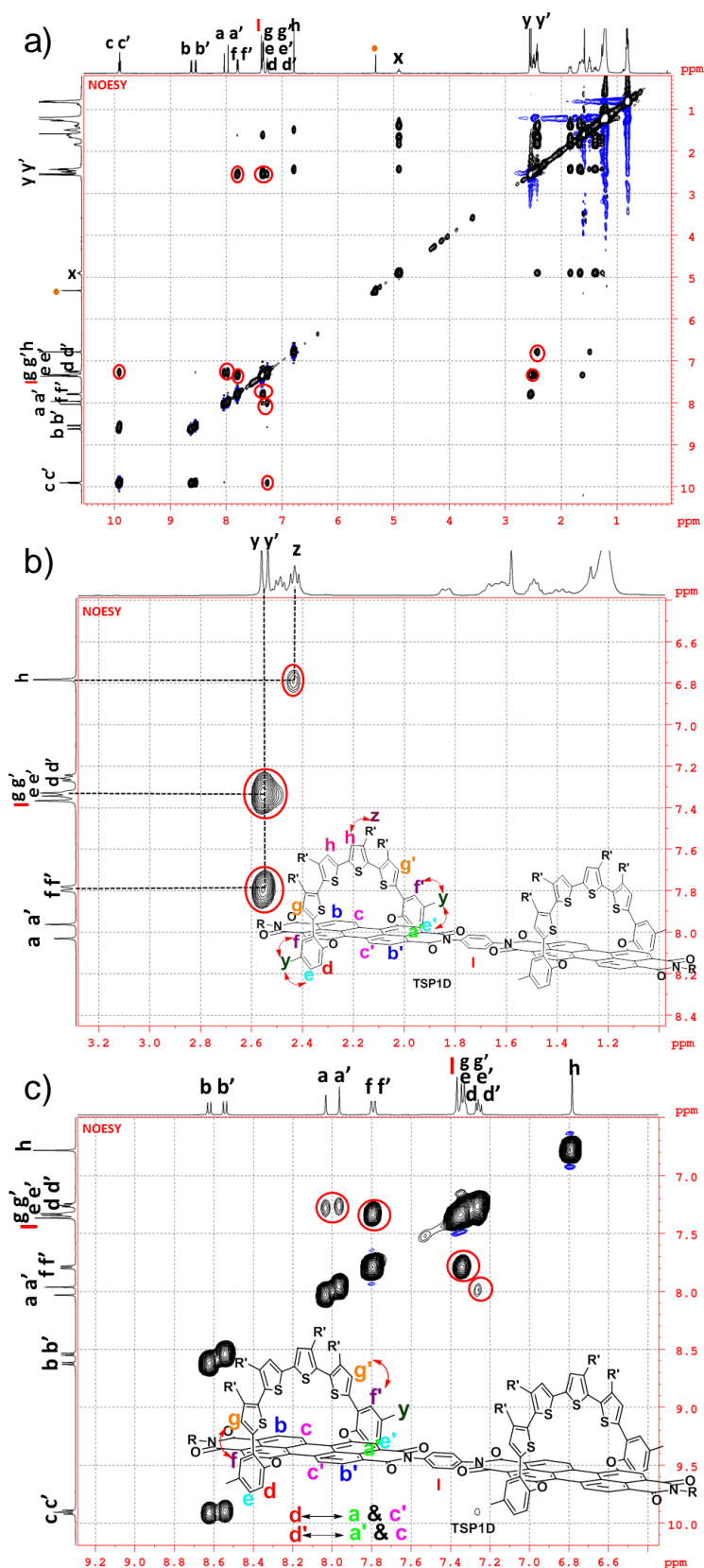
**Figure 2.29.** NOESY spectra of **TSP1D** at 500 MHz, recorded at 318 K. Intermolecular cross-peaks are indicated by circles.
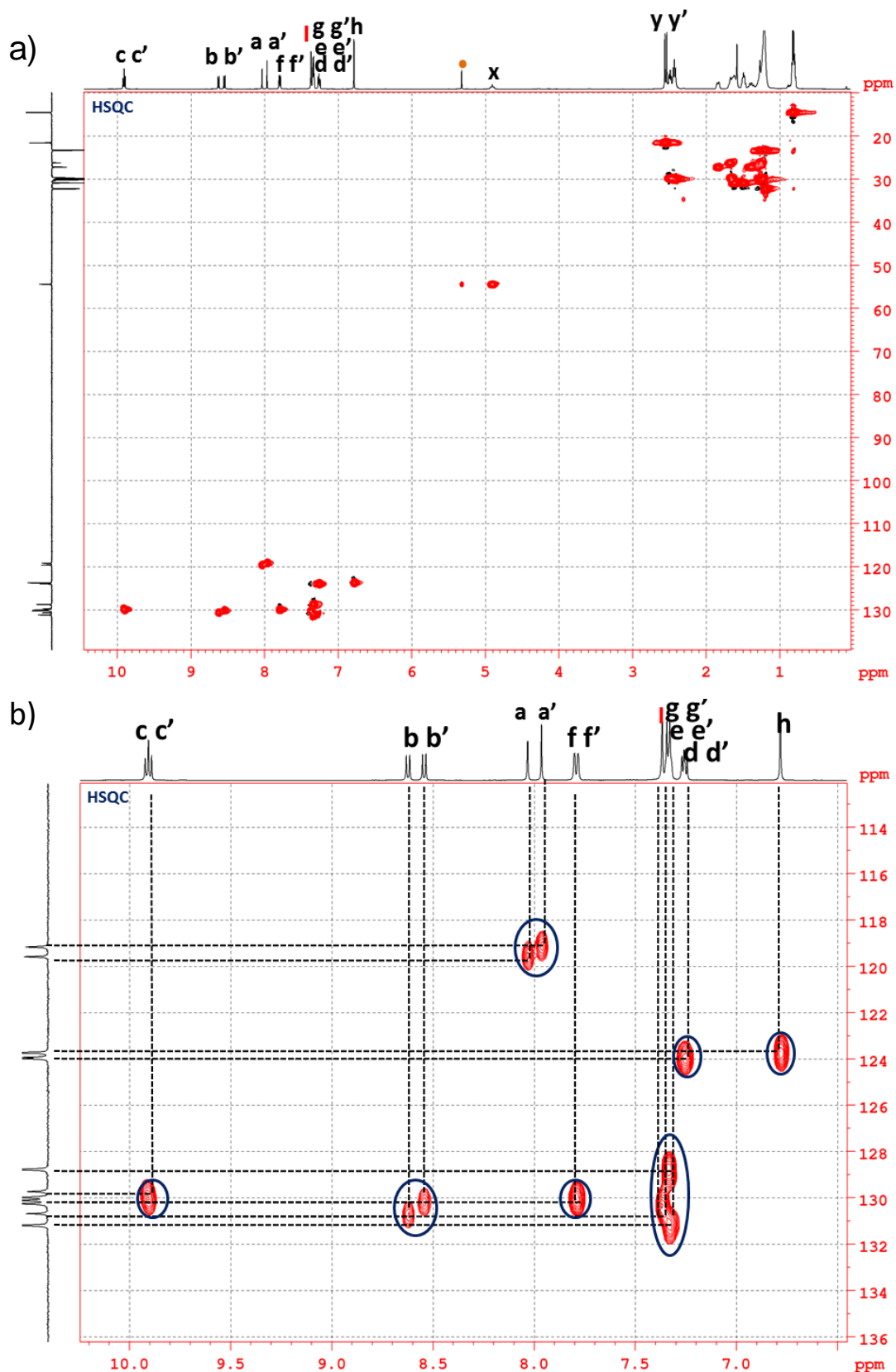
**Figure 2.30.** HSQC spectra of **TSP1D** at 500 MHz, recorded at 318 K. Intermolecular cross-peaks are indicated by circles.
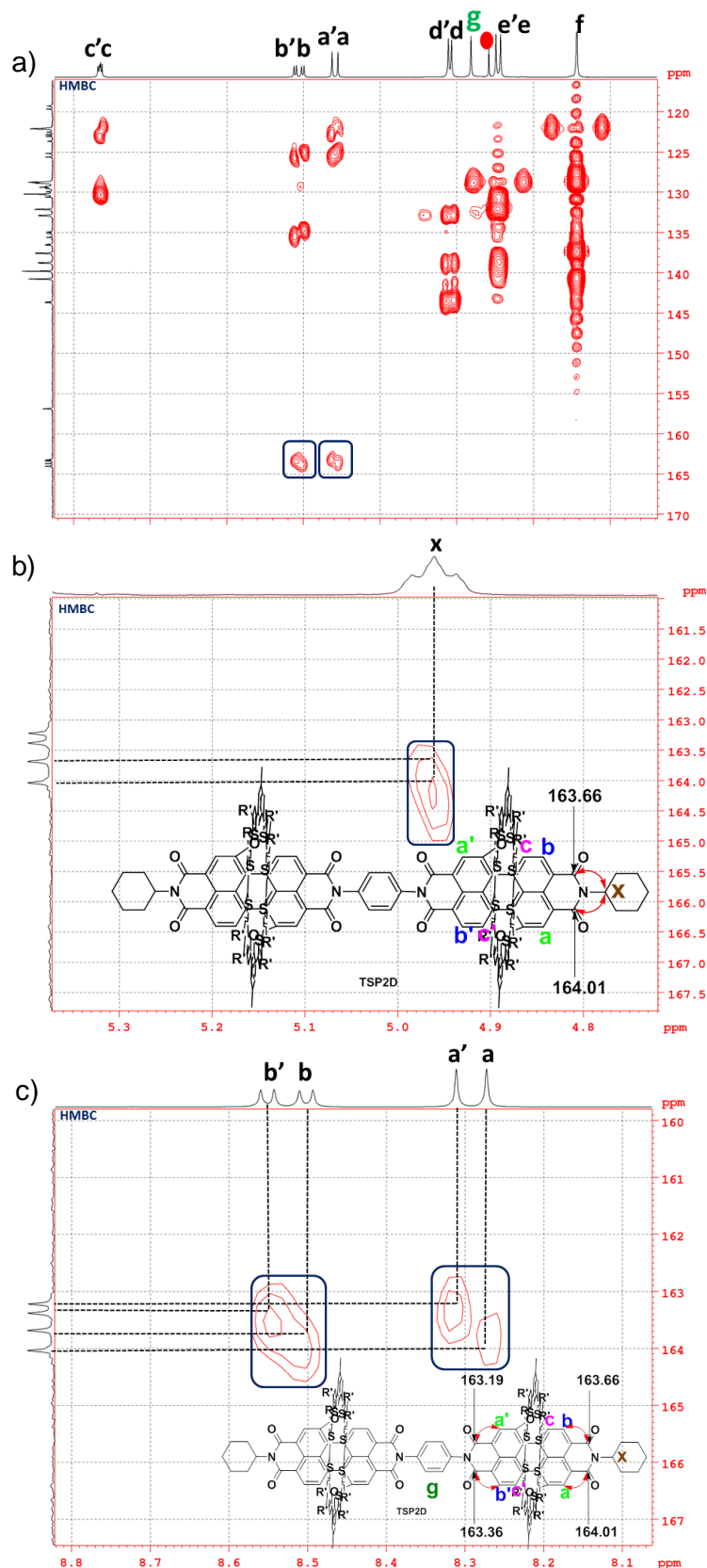
**Figure 2.31.** HMBC spectra of **TSP2D** at 500 MHz, recorded at 318 K. Intermolecular cross-peaks are indicated by circles.
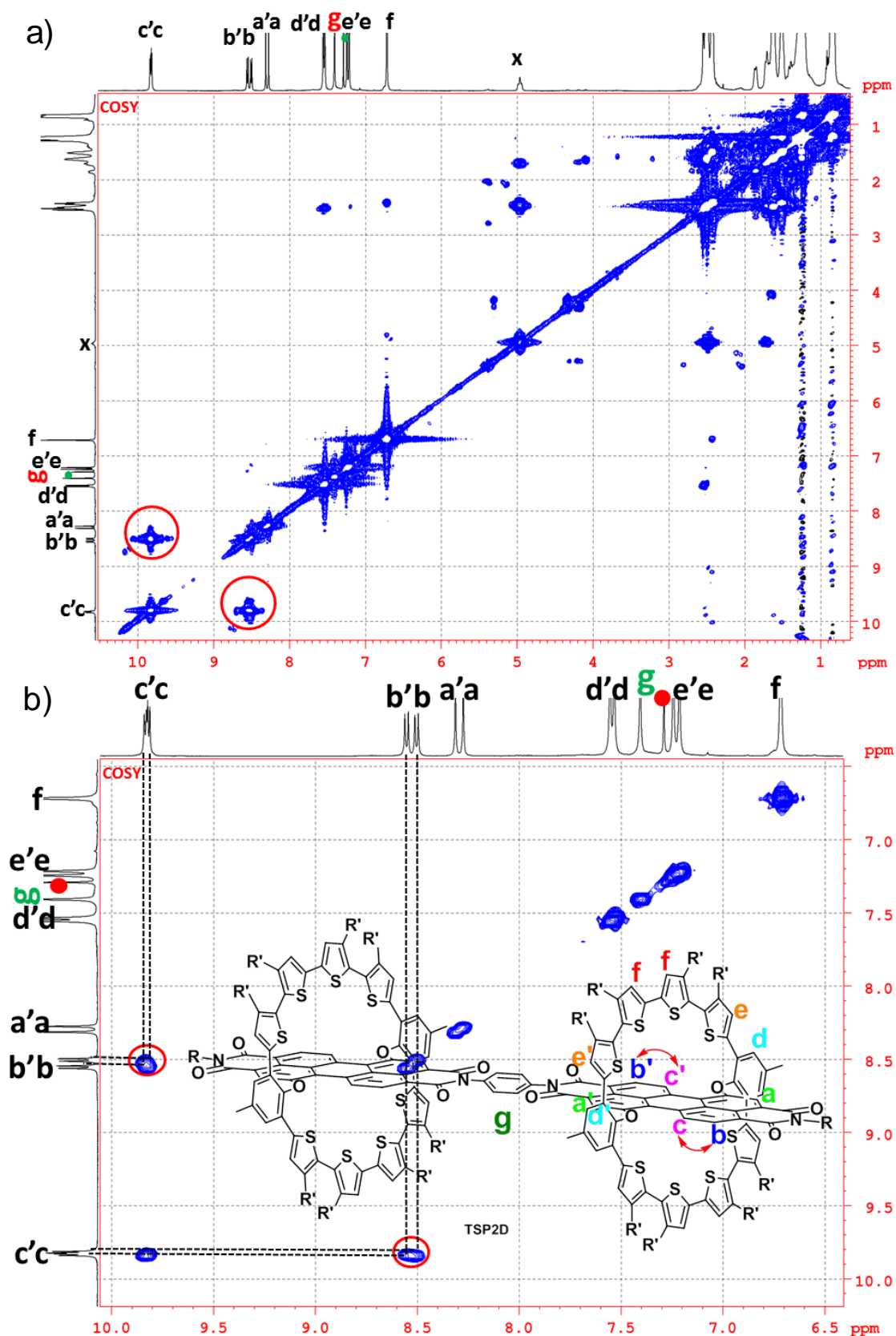
**Figure 2.32.** COSY spectra of **TSP2D** at 500 MHz, recorded at 318 K. Intermolecular cross-peaks are indicated by circles.
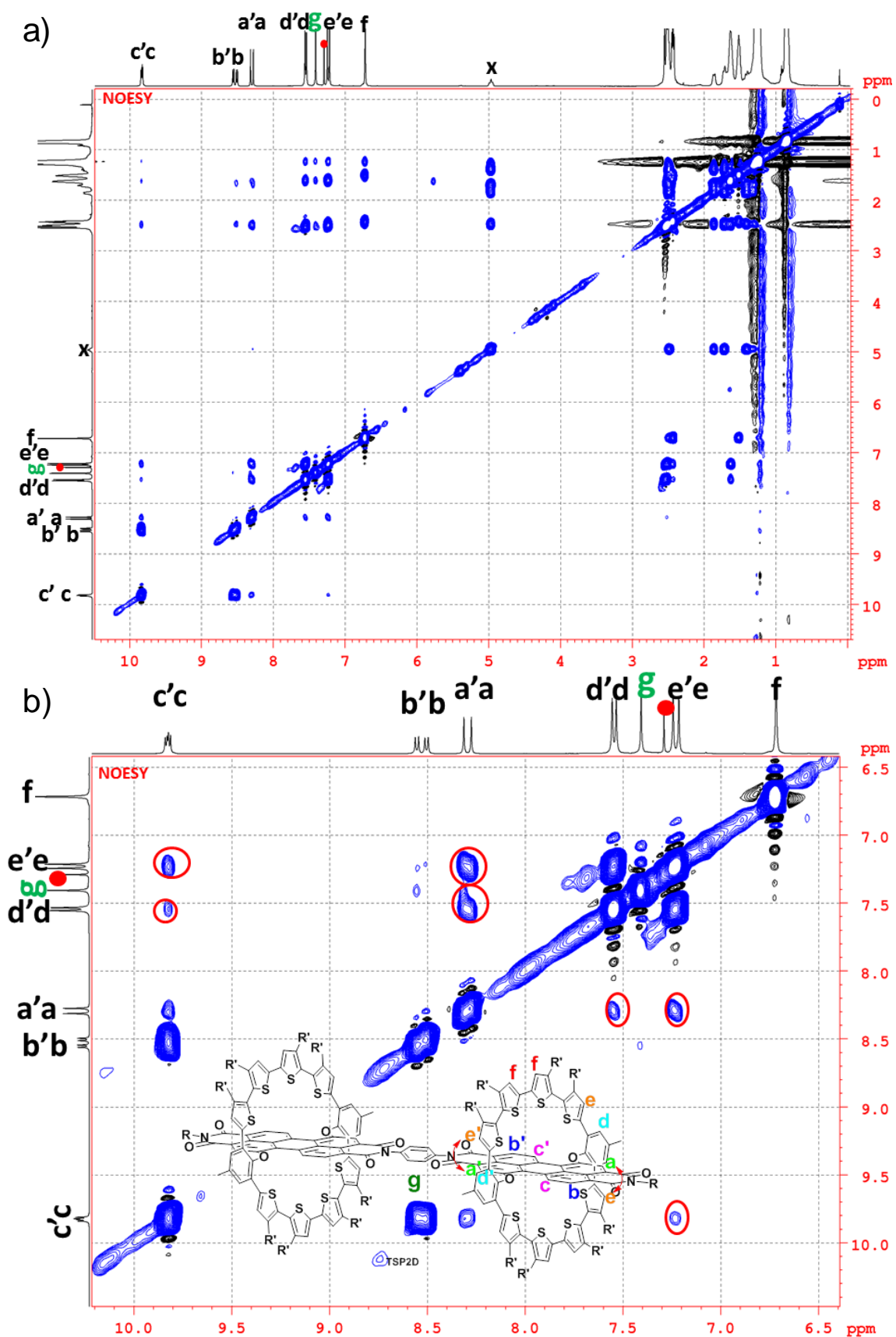
**Figure 2.33.** NOESY spectra of **TSP2D** at 500 MHz, recorded at 318 K.
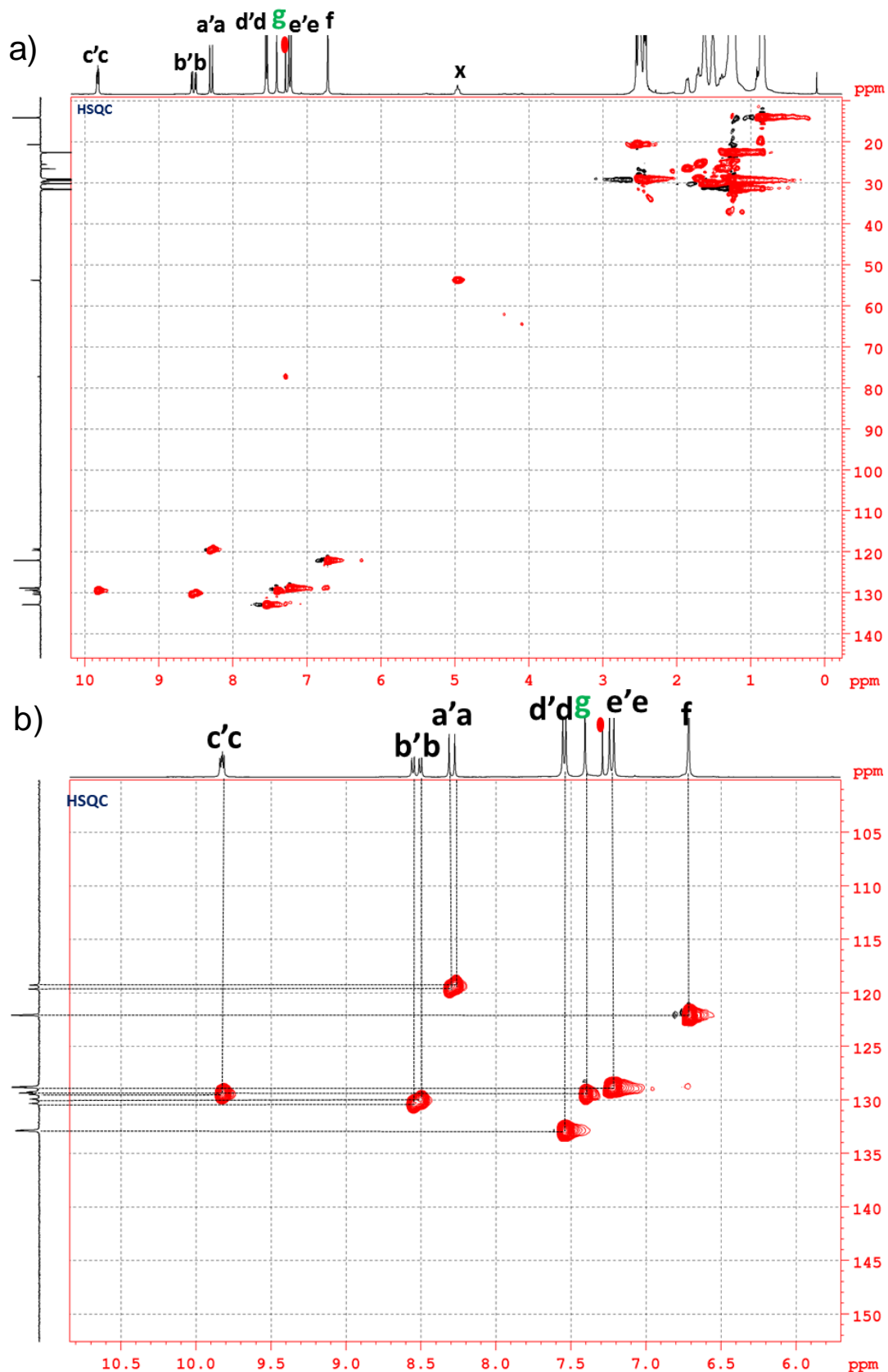
**Figure 2.34.** HSQC spectra of **TSP2D** at 500 MHz, recorded at 318 K. Intermolecular cross-peaks are indicated by circles.

Similar to **TSP1** and **TSP2**, the corresponding dimers also exhibit two reversible oxidation and reduction peaks in CV and DPV (Figure 2.35-2.37). Oxidation peaks at 0.52, 0.76 eV and 0.63, 0.96 eV and reduction peaks at -1.19, -1.40 eV and -1.22, -1.49 eV, were observed, respectively, for **TSP1D** and **TSP2D**.
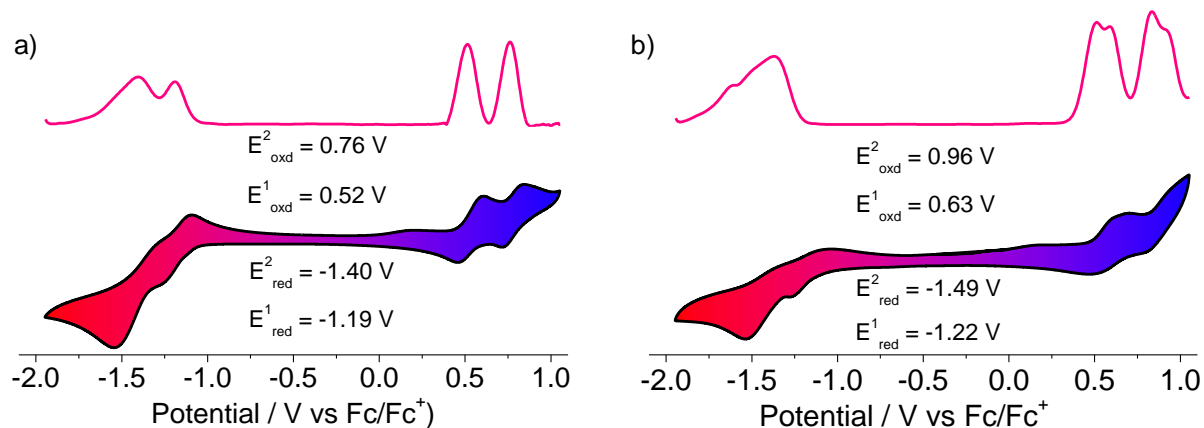


**Figure 2.35.** CV and DPV measurements of a) **TSP1D** and b) **TSP2D** in $CH_2Cl_2$ ($C$ = 1 mM) with $Bu_4NPF_6$ at 100 mV/s scan rate.
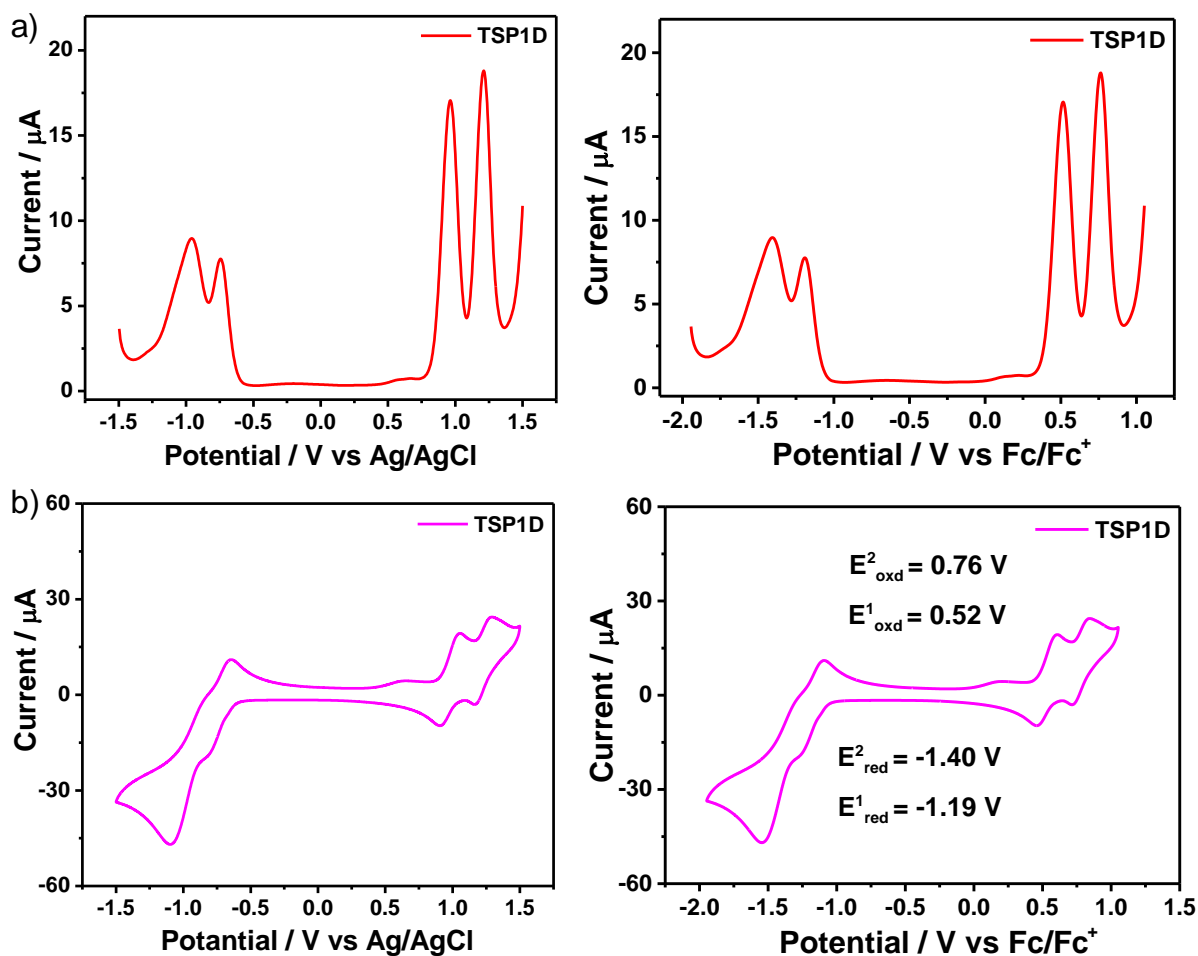
**Figure 2.36.** a) DPV measurements at 100 mV/s scan rate (left) and calculated as Ferrocene as internal reference standard ($E_{Fc+/Fc}$ = 0.00 V) (right) of **TSP1D** (1 mM). b) CV at 100 mV/s scan rate (left) and CV calculated as Ferrocene as internal reference standard ($E_{Fc+/Fc}$ = 0.00 V) (right) of **TSP1D** (1 mM).
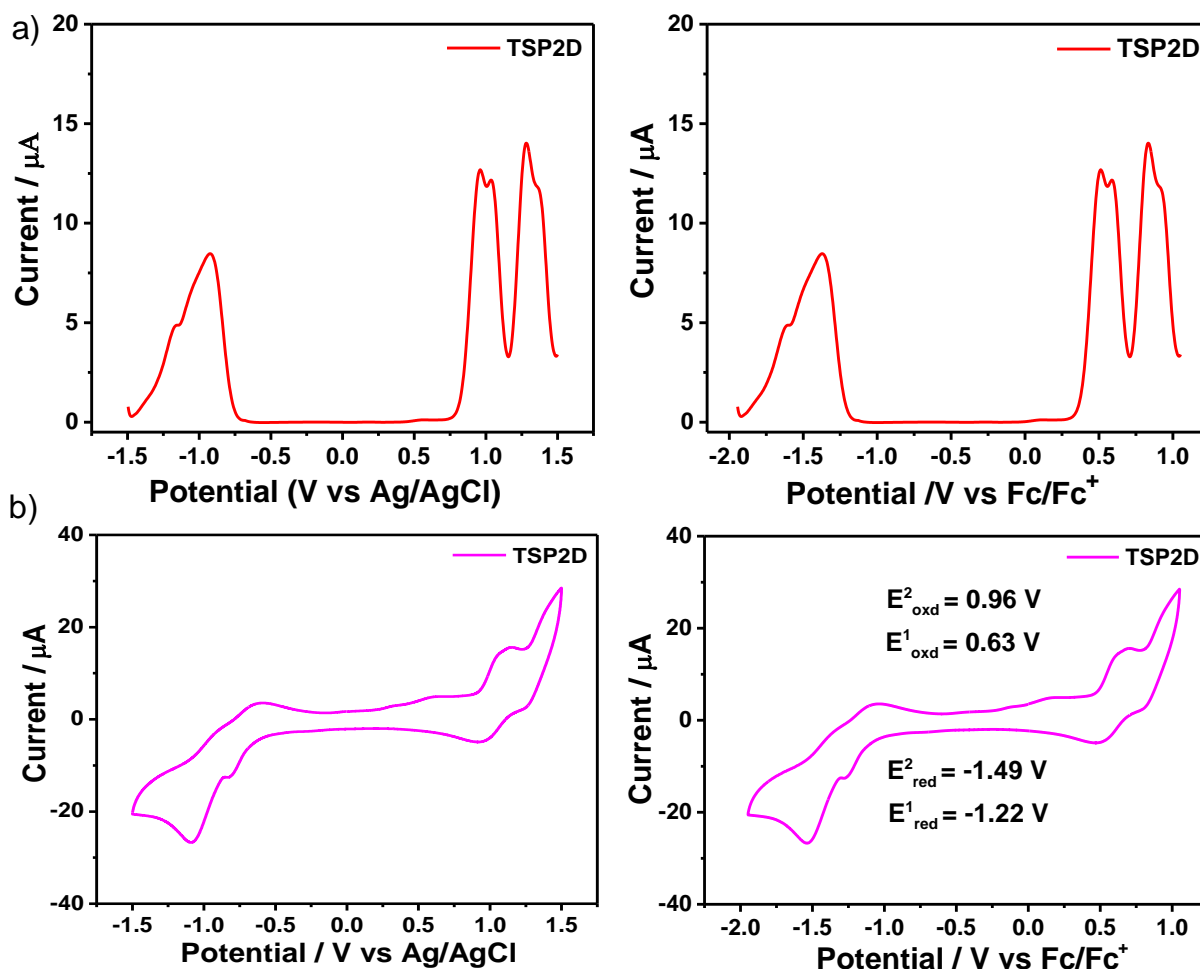


**Figure 2.37.** a) DPV measurements at 100 mV/s scan rate (left) and calculated as Ferrocene as internal reference standard ($E_{Fc+/Fc}$ = 0.00 V) (right) of **TSP2D** (1 mM). b) CV at 100 mV/s scan rate (left) and CV calculated as Ferrocene as internal reference standard ($E_{Fc+/Fc}$ = 0.00 V) (right) of **TSP2D** (1mM).
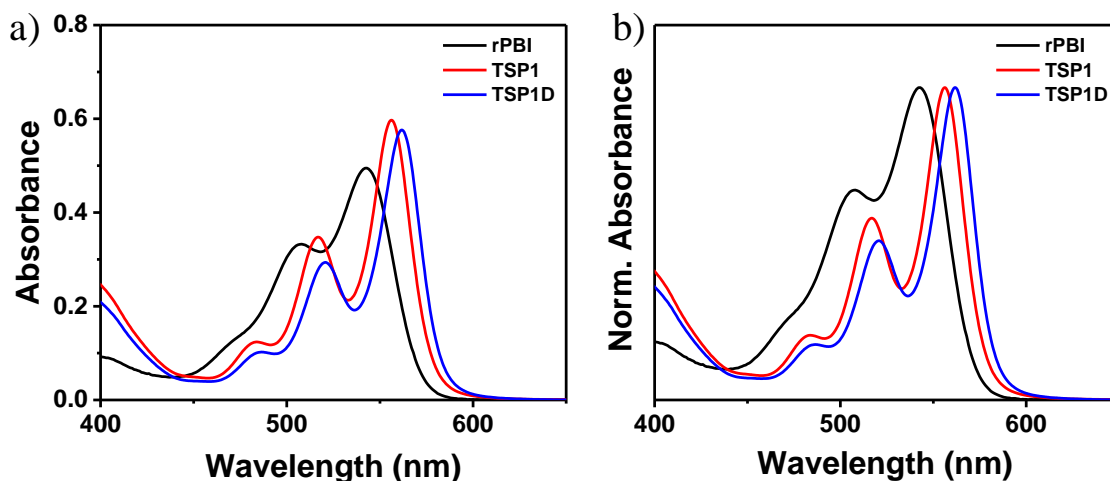
**Figure 2.38.** a) Absorption and corresponding b) normalized spectra of **rPBI**, **TSP1** and **TSP1D** in CH$_2$Cl$_2$ solution ($C = 1$ x $10^{-5}$ M, $l = 1$ cm) at 25 ˚C.
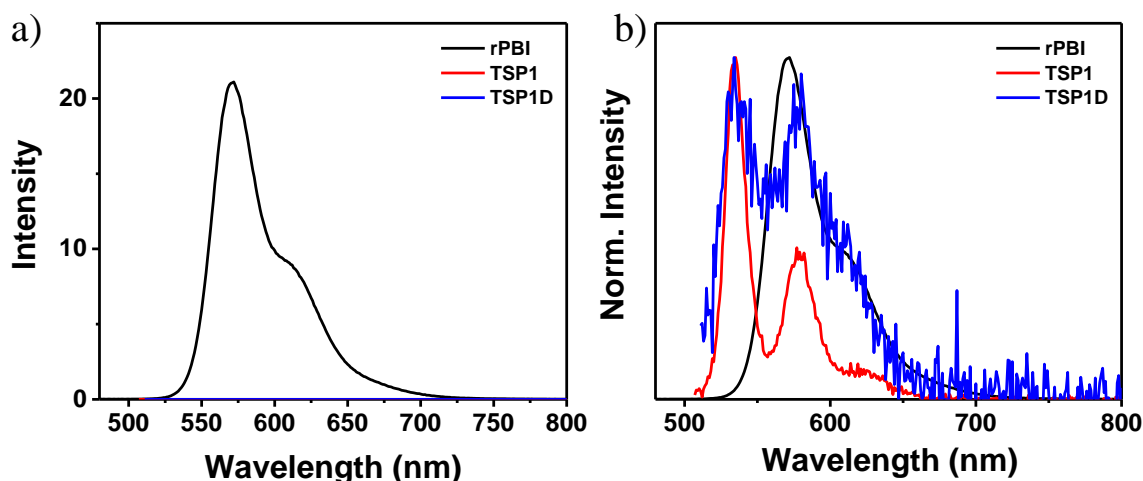


**Figure 2.39.** a) Steady state emission and corresponding b) normalized spectra of **rPBI**, **TSP1** and **TSP1D** in CH$_2$Cl$_2$ solution ($C = 1$ x $10^{-5}$ M, $l = 1$ cm) at 25 ˚C ($\lambda_{ex} = 460$ nm for **rPBI**, 480 nm for **TSP1**, and 485 nm for **TSP1D**).
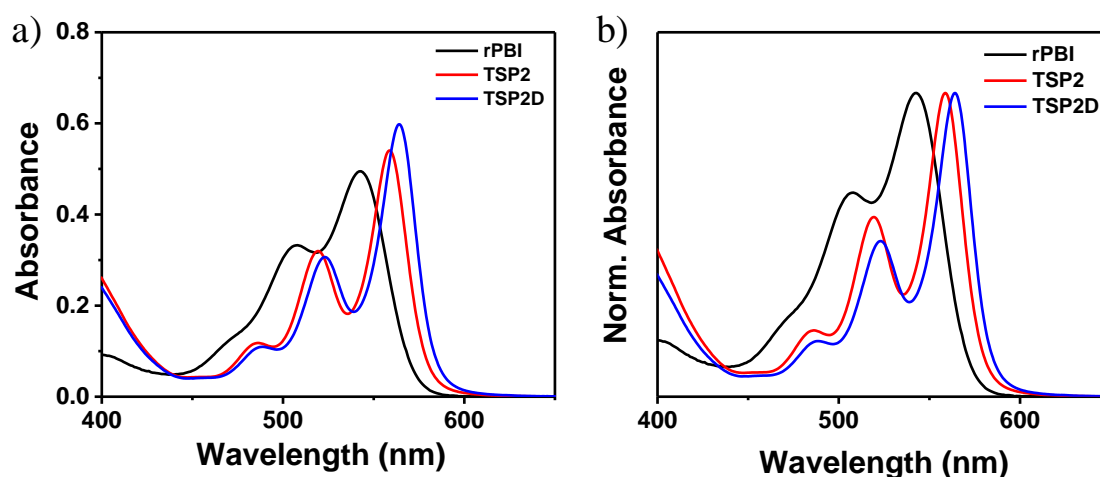
**Figure 2.40.** a) Absorption and corresponding b) normalized spectra of **rPBI**, **TSP2** and **TSP2D** in $CH_2Cl_2$ solution ($C$ = 1 x $10^{-5}$ M, $l$ = 1 cm) at 25 ˚C.
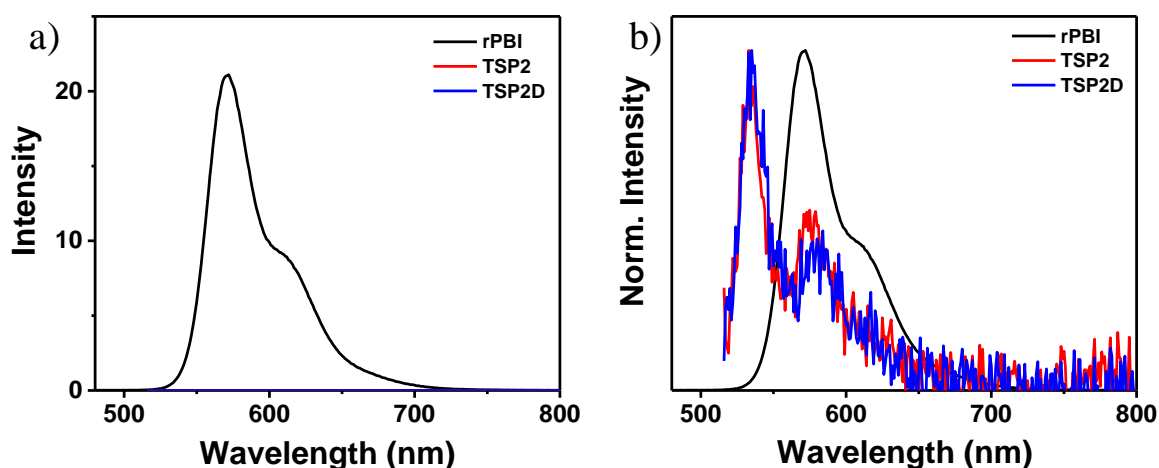


**Figure 2.41.** a) Steady state emission corresponding b) normalized spectra of **rPBI**, **TSP2** and **TSP2D** in $CH_2Cl_2$ solution ($C$ = 1 x $10^{-5}$ M, $l$ = 1 cm) at 25 ˚C ($\lambda_{ex}$ = 460 nm for **rPBI**, 485 nm for **TSP2**, and 485 nm for **TSP2D**).

Dimers exhibited only a slight red shift in the absorption compared to **TSP1**, **2**, and the emission remained quenched (Figure 2.38-2.42). Such a coaxial D-A macrocycle dimer offers the possibility of one-dimensional polymers for efficient electron and hole transport.[7-10]
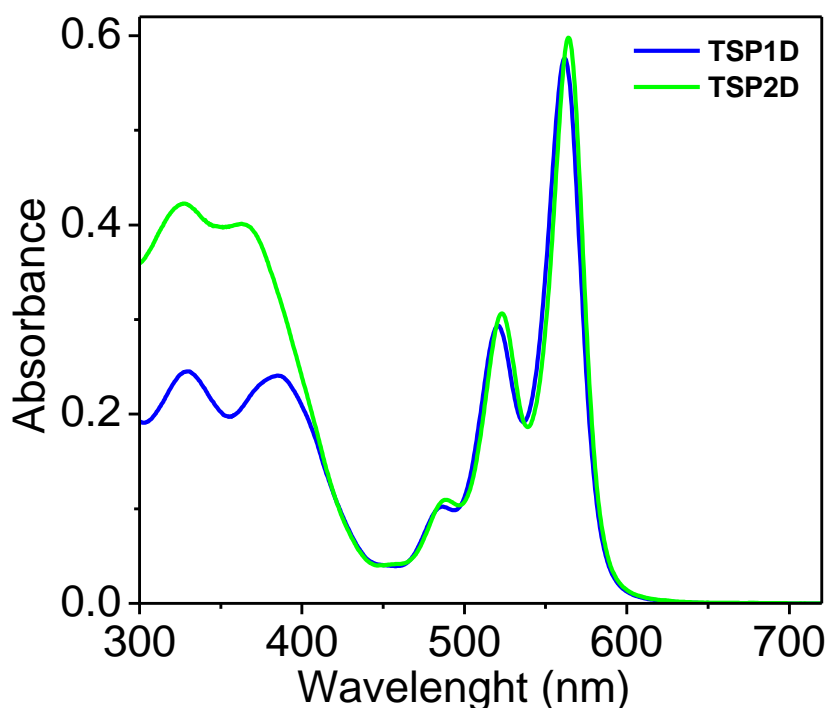


**Figure 2.42.** Comparison of the absorption spectra of **TSP1D** and **TSP2D** in $CH_2Cl_2$ solution ($C$ = 1 x $10^{-5}$ M, $l$ = 1 cm) at 25 ˚C.

After noticing the importance of the full oligothiophene ring around the PBI unit to support ultrafast ET and stabilization of the CS state, a three-component 2D-polymer **TSP-2DP** was synthesized using the dianhydride of **TSP2** (Scheme 2.4) and $N^1,N^1$-bis(4-aminophenyl)benzene-1,4-diamine (Scheme 2.4). Polymerization in the presence of $Zn(OAc)_2$ in imidazole started to precipitate **TSP-2DP** after 24 h, and the reaction was completed after 48 h. The formation of 2D-polymer was characterized by solid-state $^{13}C$ cross-polarization magic angle spinning nuclear magnetic resonance ($^{13}C$ CP-MAS NMR), The formation of **TSP-2DP** analyzed by $^{13}C$ CP-MAS NMR spectrum showed signals at 162.8 (C=O), 155.2 (C-O, carbon of PBI, and oxygen of phenyl ring), and 147.8 (C-O/N, two different carbons; one from (C-O) of the phenyl ring and another from (C-N) of triphenylamine) ppm due to carbon atoms of PBI and triphenylamine (Figure 2.43). There are signals at 139.3, 129.9, 122.7 ppm from remaining aromatic rings and at 30.3, 23.1, 14.1 ppm from the alkyl chains also substantiate the incorporation of both monomers in the 2D-polymer.
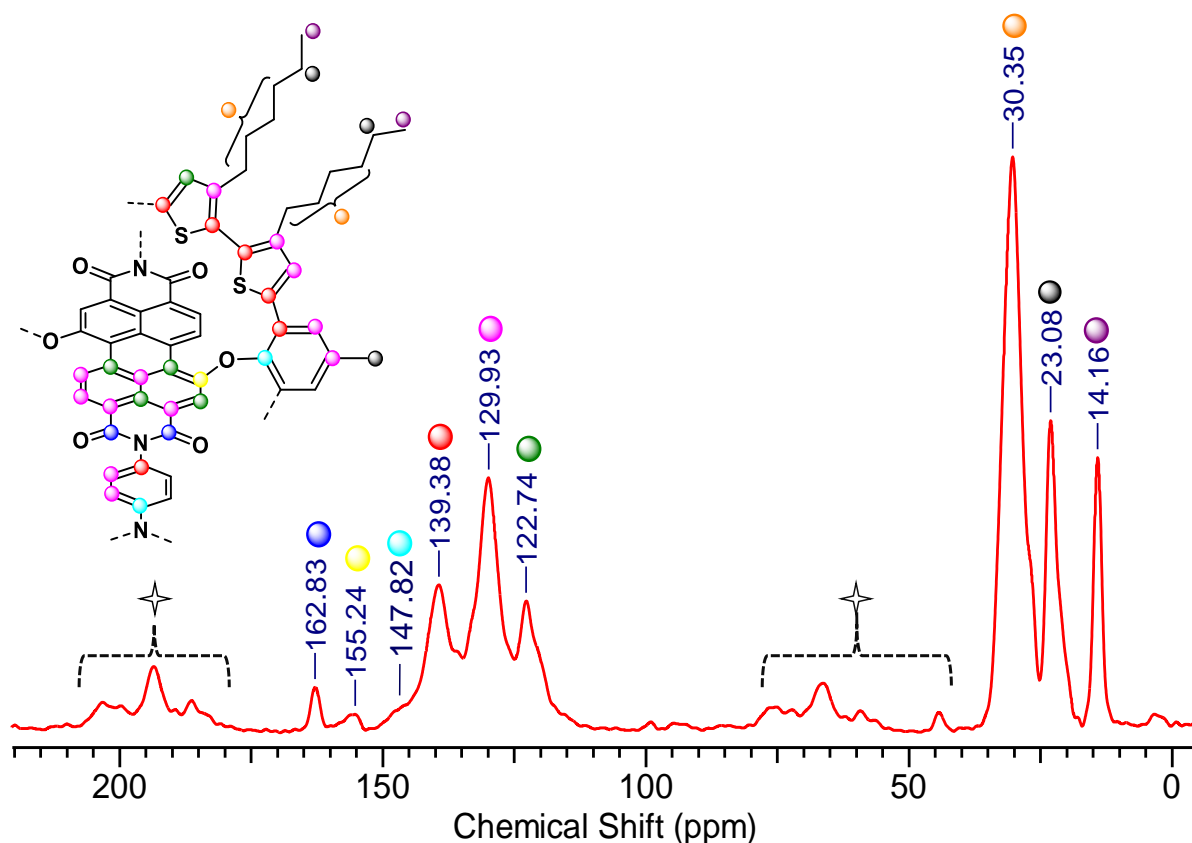


**Figure 2.43.** $^{13}C$ CP-MAS NMR spectrum of **TSP-2DP**, asterisks denote spinning sidebands.

Furthermore, **TSP**-**2DP** polymer conformed by FT-IR, X-ray photoelectron spectroscopy (XPS), powder X-ray diffraction (PXRD), thermogravimetric analysis (TGA), CV, DPV diffuse reflectance UV-Vis-NIR spectrum and morphological analyses (Figure 2.44-2.51).[61]A comparison of FT-IR spectra of **TSP-2DP** with the starting materials showed that the characteristic N-H stretching bands at 3410 and 3340 cm$^{-1}$ and N-H bending band at 3205 cm$^{-1}$ of $N^I,N^I$-bis(4-aminophenyl)benzene-1,4-diamine and C=O stretching bands at 1825, 1767, 1738 cm$^{-1}$ of the anhydride were disappeared, while intense new bands appeared at 1706 and 1671 cm$^{-1}$ (C=O), which can be assigned to vibrations of the imide carbonyl group (Figure 2.44,2.45). The disappearance of the characteristic peaks (marked in the box) suggested the complete consumption of monomers during 2D-polymerization (Figure 2.44). Transmission electron microscope (TEM) images of **TSP-2DP** suspended in CH$_3$OH revealed the presence of multilayer stacks of the 2D-polymer structure (Figure 2.46b). It hints at the extended 2D-polymerization during the reaction and further stacking between the 2D-polymer layers.
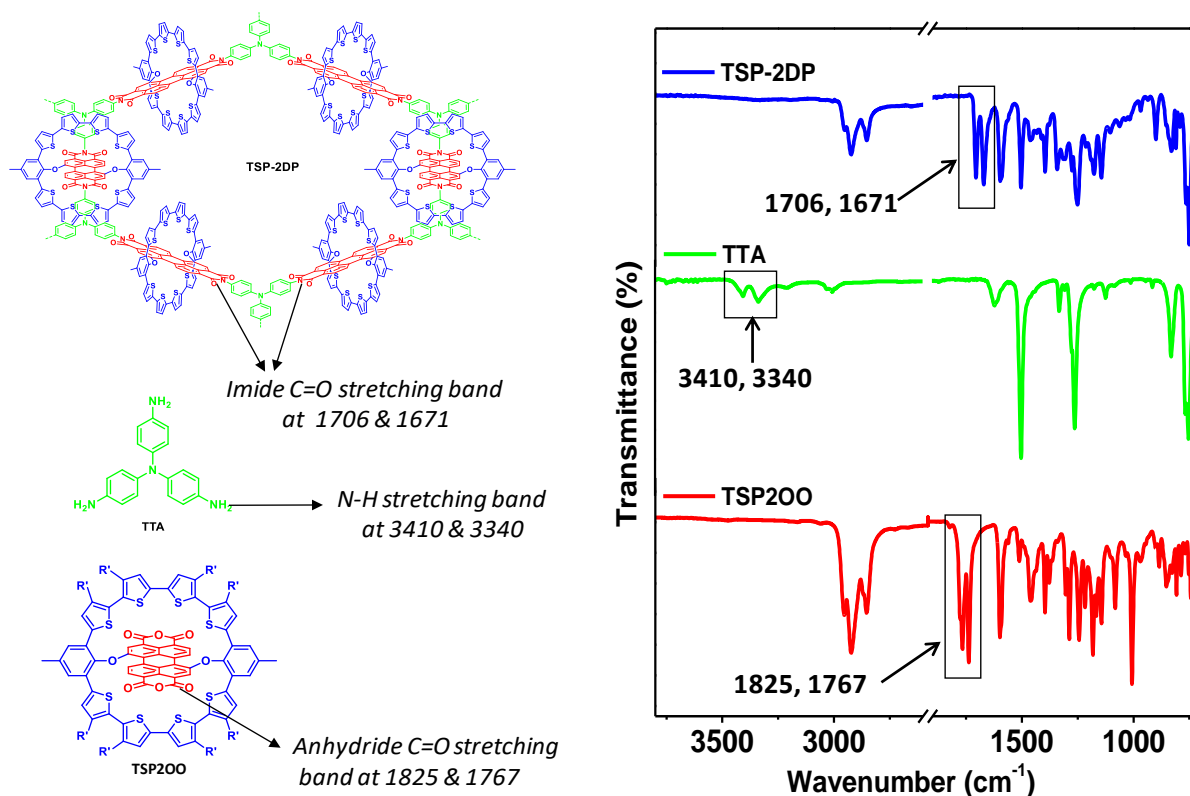


**Figure 2.44.** Comparison of the FT-IR spectra of **TSP-2DP**, **TTA**, and **TSP2OO**.
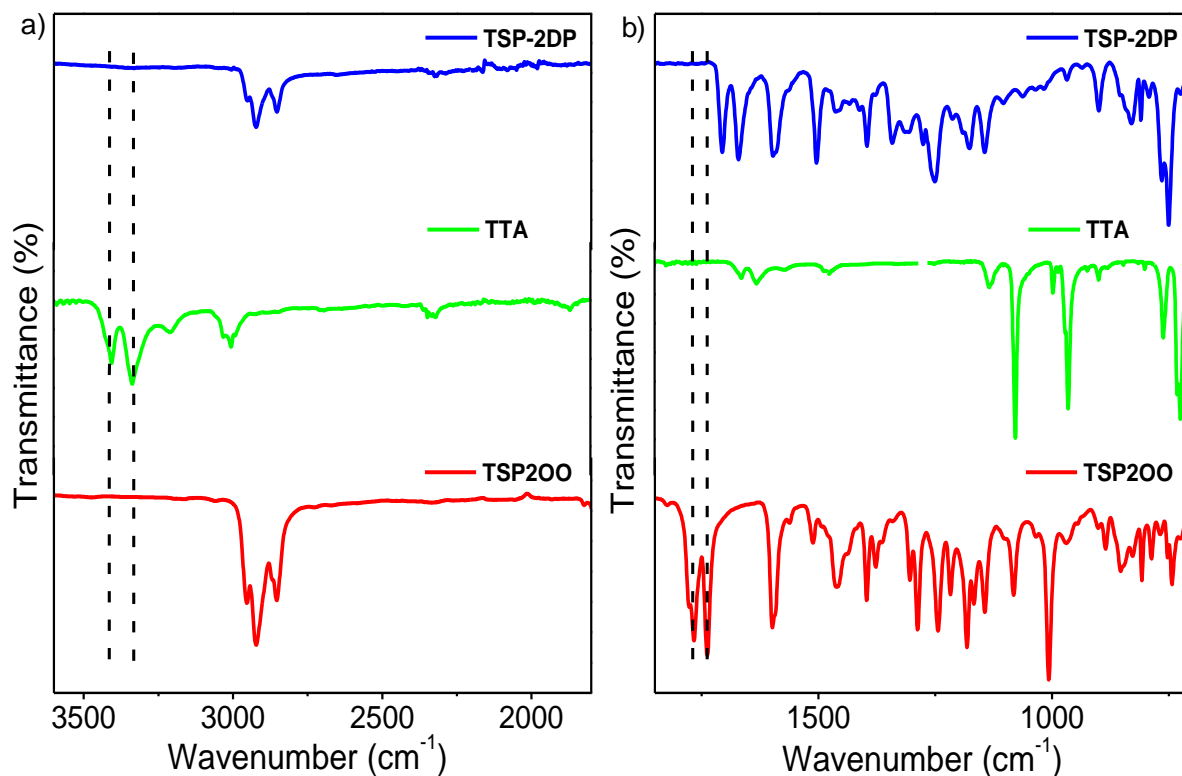
**Figure 2.45.** Comparison of the FT-IR spectra of **TSP-2DP**, **TTA**, and **TSP2OO** from a) 3600-1800 cm$^{-1}$ and b) 1800-700 cm$^{-1}$.
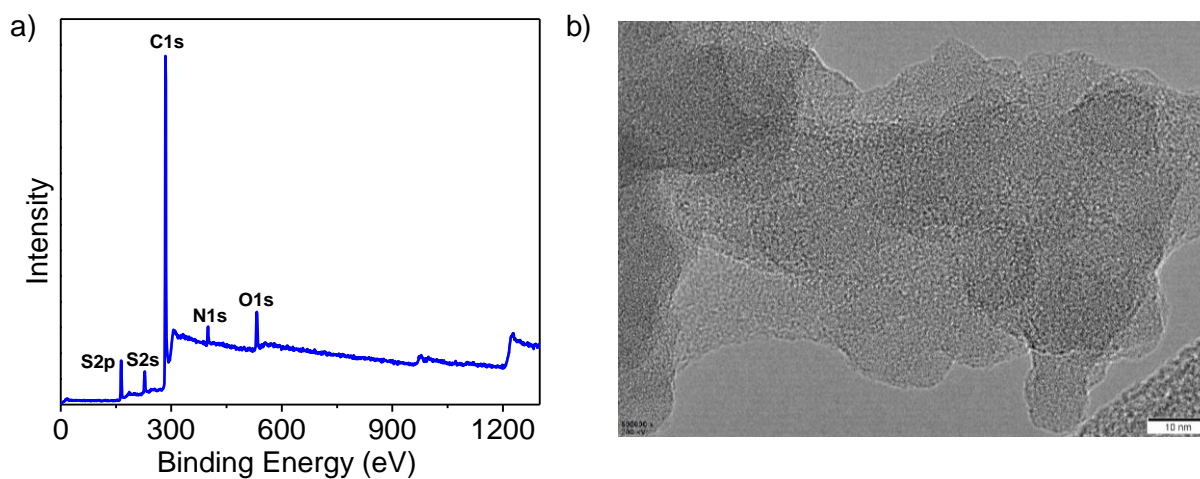


**Figure 2.46.** a) XPS survey and, b) HR-TEM image of **TSP-2DP** suspended in CH$_3$OH.
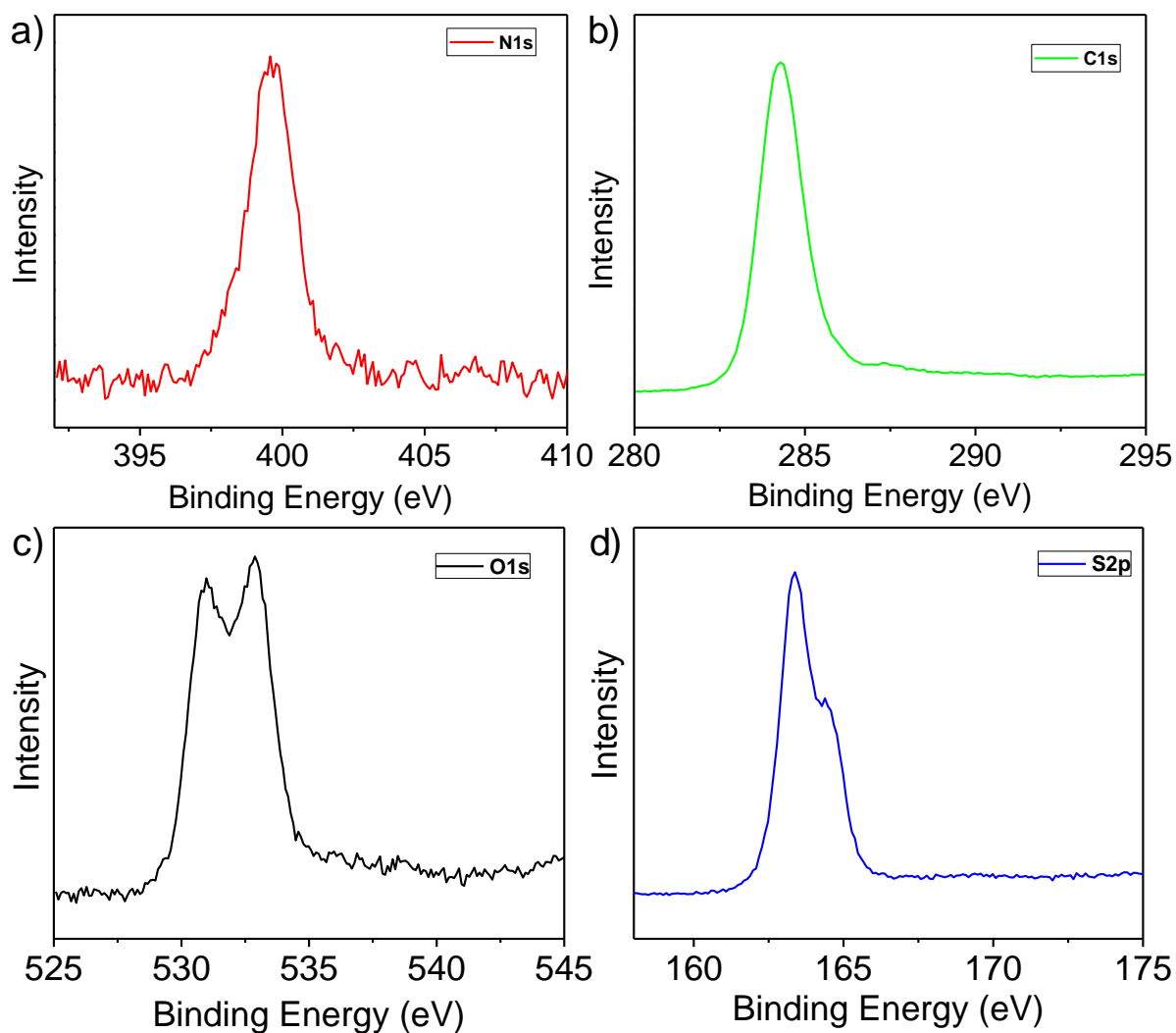
**Figure 2.47.** XPS analysis showing profiles of a) $N_{1s}$, b) $C_{1s}$, c) $O_{1s}$, d) $S_{2p}$ of **TSP-2DP**.

The stability of **TSP-2DP** was checked by thermogravimetric analysis (TGA), and found that 5% weight loss occurred at 322 °C. It shows reasonably good stability of **TSP-2DP** compared with the other reported 2DPs (Figure 2.48a). The PXRD pattern of **TSP-2DP** exhibited an intense peak at 5.5 °. However, the complex structure of the monomer macrocycle and the presence of long alkyl chains leads to a broad peak centred on $2\theta = 20°$ (Figure 2.48b).
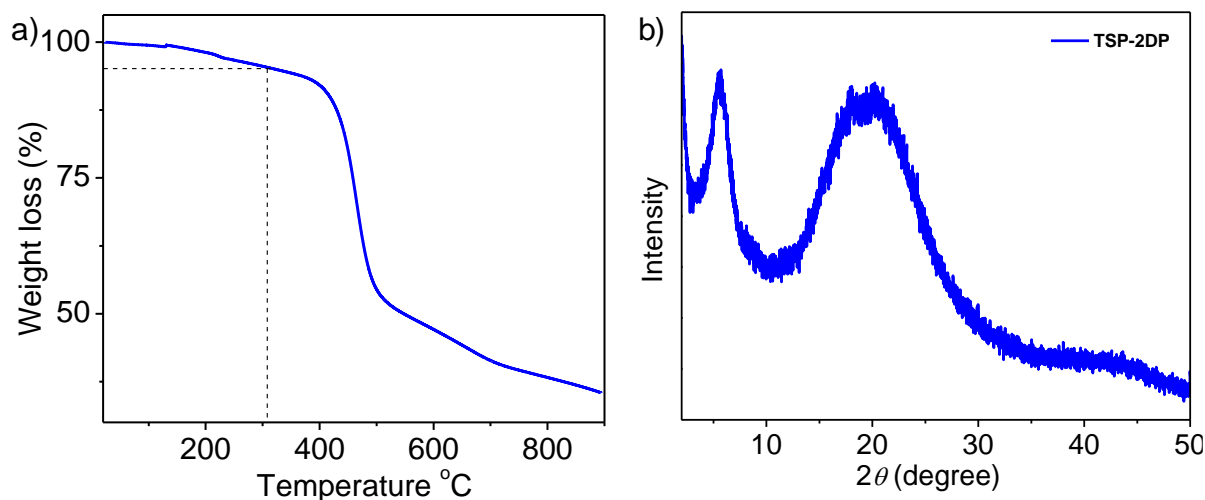
**Figure 2.48.** a) TGA and, b) PXRD pattern of **TSP-2DP**.

A comparatively broad solid-state diffuse reflectance UV-Vis-NIR spectrum of **TSP-2DP** is in line with **TSP2** and **TSP2D**, and points to the lack of ground-state charge-transfer interaction between the D-A units (Figure 2.49a). Two reversible oxidation and reduction peaks at 0.04, 0.63 eV, and reduction peaks at -1.28, -1.98 eV were observed in CV and DPV, respectively, of the thin films of **TSP-2DP** measured in acetonitrile (Figure 2.49b).
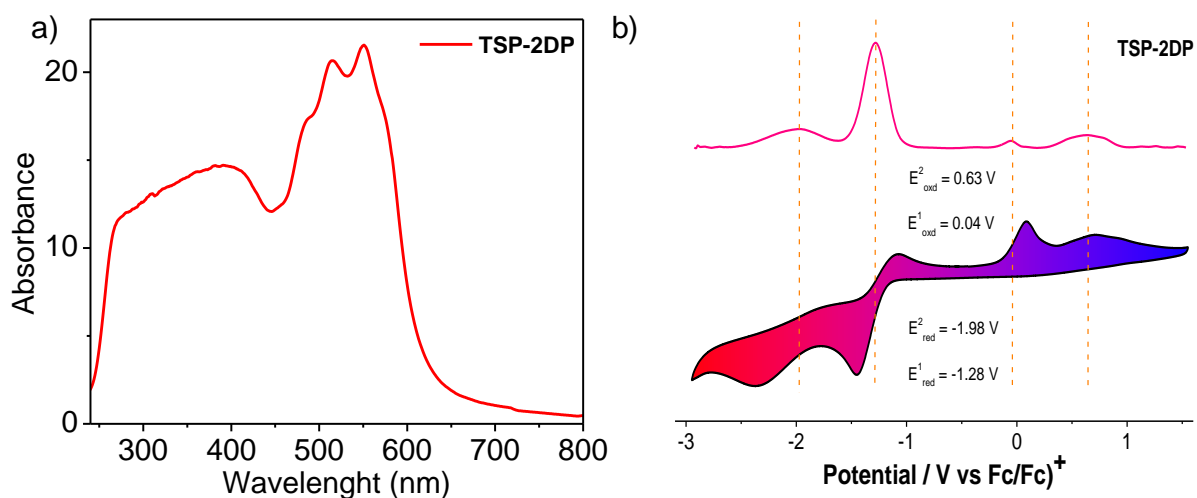


**Figure 2.49.** a) Solid-state diffuse reflectance UV-Vis-NIR spectra and, b) DPV and CV measurements of **TSP-2DP** thin film in acetonitrile at 100 mV/s scan rate calculated as Ferrocene as the internal reference standard ($E_{Fc+/Fc} = 0.00$ V).
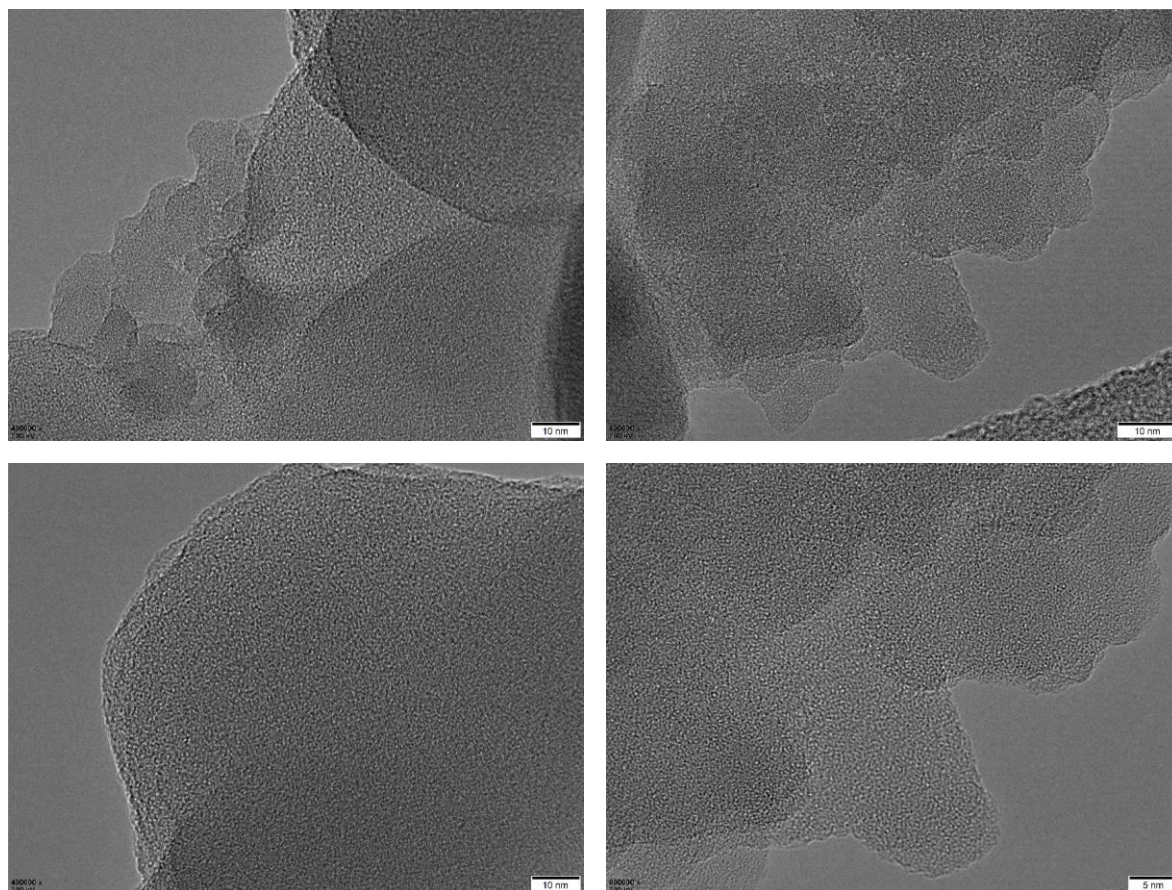
**Figure 2.50.** HR-TEM image of **TSP-2DP**.
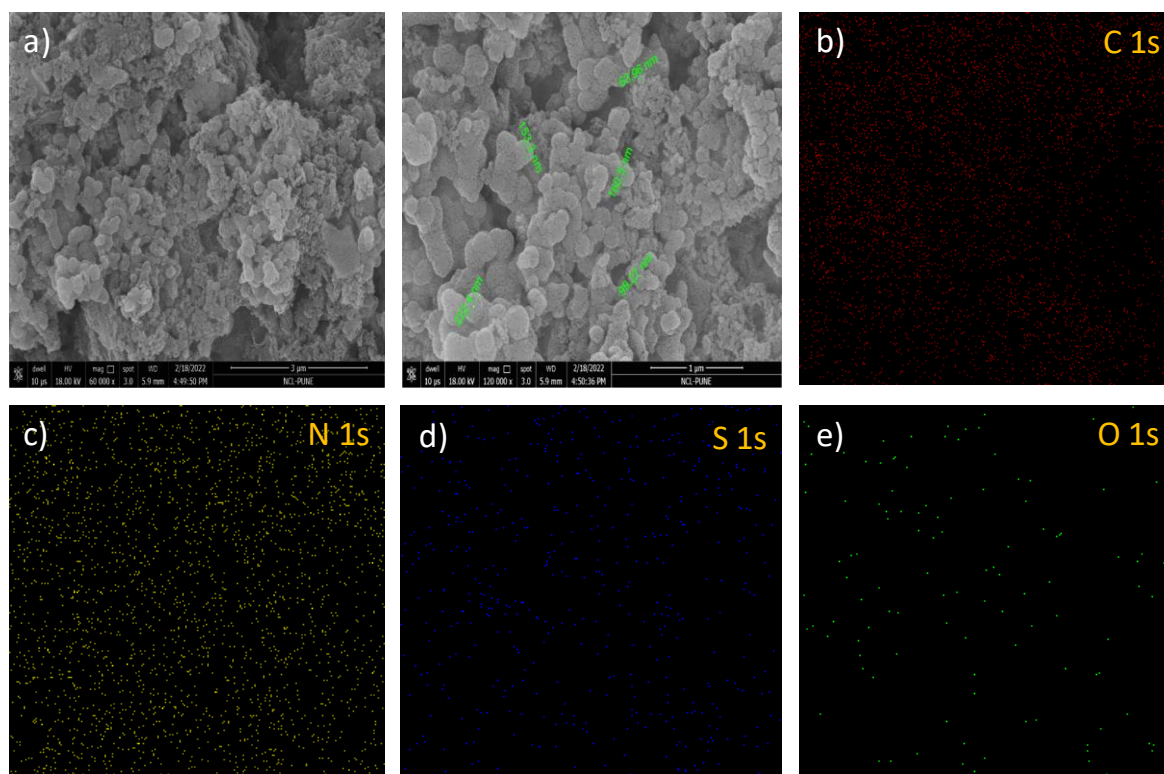


**Figure 2.51** a) SEM image and elemental analysis of b) C, c) N, d) S, e) O of **TSP-2DP**.

In figure 2.52a presents the TA spectra of the polymeric **TSP-2DP** system, obtained following the photoexcitation by 460 nm pump pulses. The spectra resemble the signature of **TSP1** and **TSP2**. However, the GSB signals are now red-shifted, and the radical anion feature was also observed in the red wing of the spectra. We have compared the dynamic profile of this feature in three different macrocyclic systems, **TSP2**, **TSP2D**, and **TSP-2DP**, as shown in figure 2.52b. Interestingly, **TSP2** and **TSP2D** possess almost the same dynamics, and the only difference was the decreased growth time scale (Figure 2.53, 2.54, Table 2.5.2).
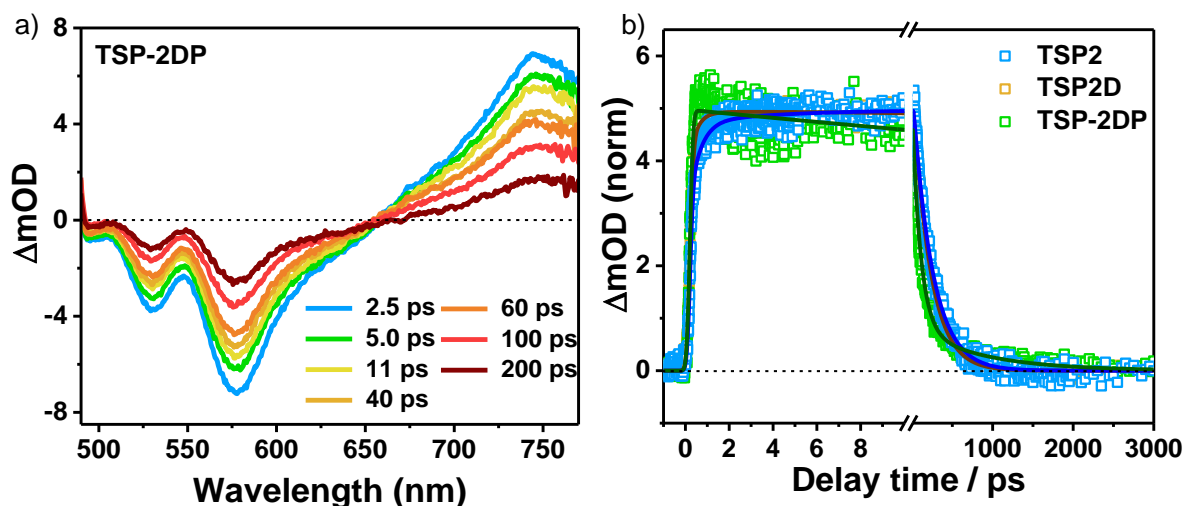


**Figure 2.52.** a) Femtosecond transient absorption spectra of **TSP-2DP** in $CH_3OH$ after the laser excitation at 460 nm. b) The comparative dynamic profiles of **TSP2**, **TSP2D**, and **TSP-2DP** monitoring the PBI anionic signature at the red wing of the spectra.
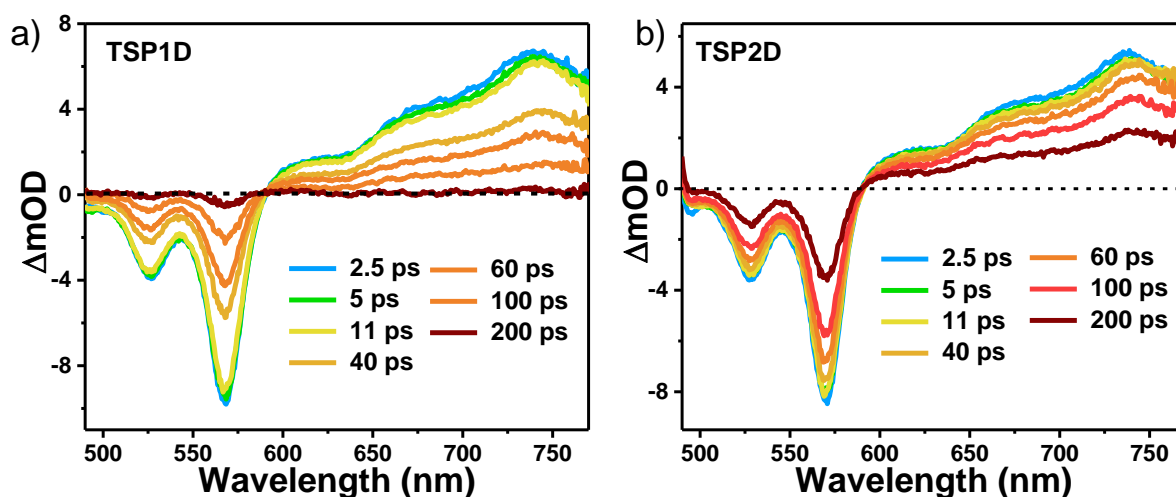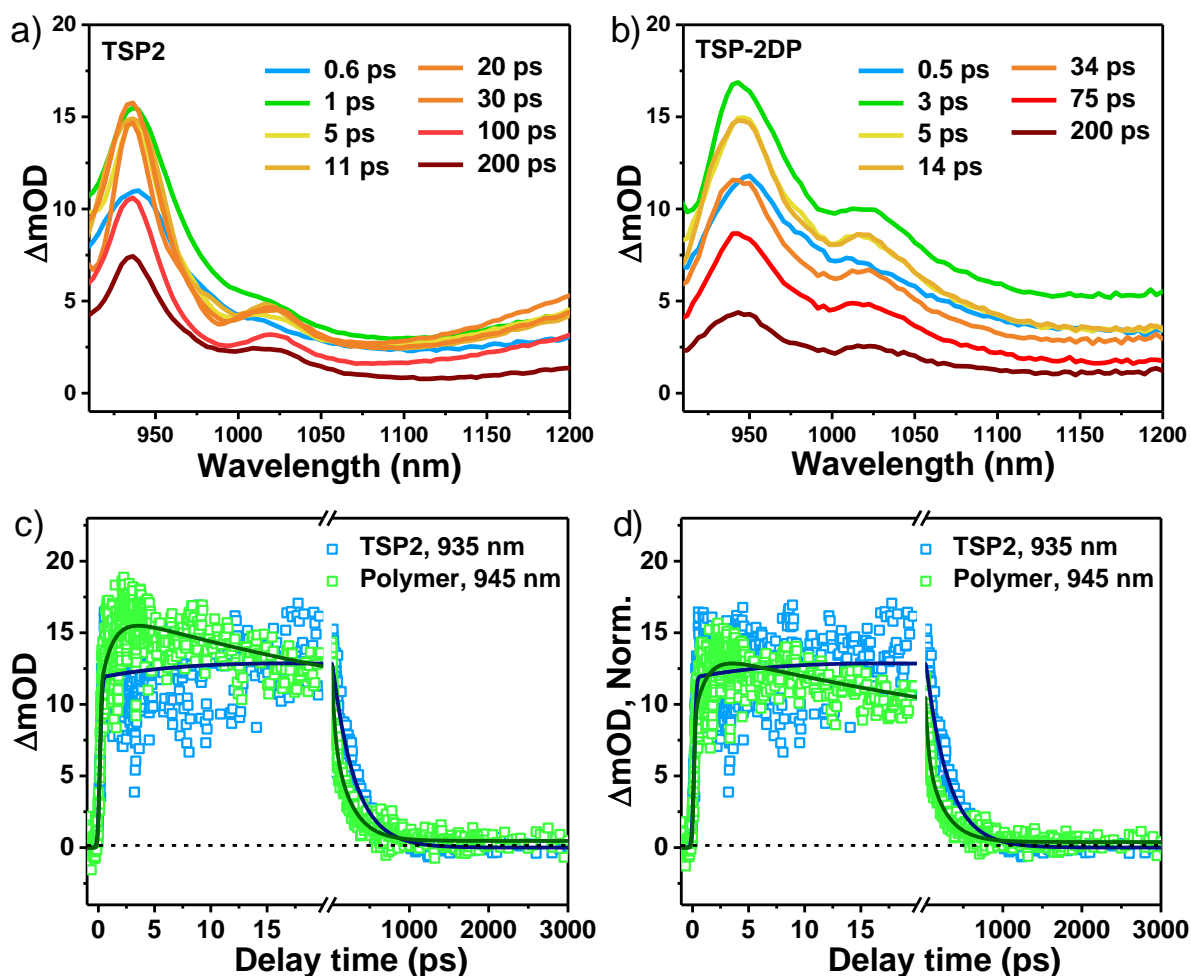


**Figure 2.53.** Femtosecond transient absorption spectra of a) **TSP1D** and b) **TSP2D** in $CH_2Cl_2$ after the laser excitation at 460 nm.
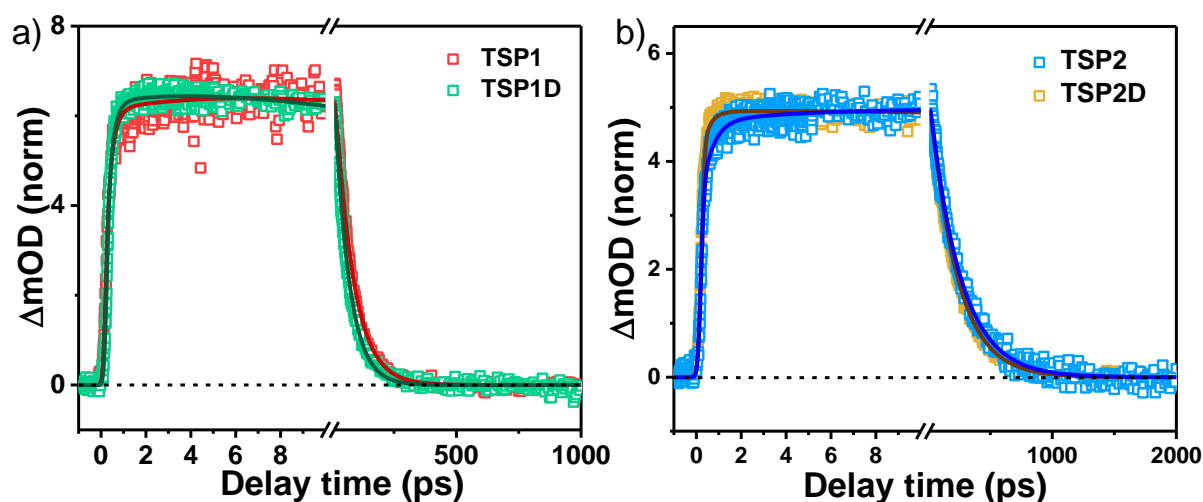
**Figure 2.54.** The comparative dynamic profiles of a) **TSP1**, **TSP1D** and b) **TSP2**, **TSP2D** monitoring the PBI radical anionic signature at the red wing of the spectra.

Hence, in the dimer system, the CS rate is getting increased. From multi-exponential fitting data, the CS time scales were calculated, $\tau_{CS}$ ~ 1.0 ps ($k_{CS}$ ~ 1.0 x $10^{12}$ S$^{-1}$) and 0.7 ps ($k_{CS}$ ~ 1.4 x $10^{12}$ S$^{-1}$), respectively, for **TSP1D** and **TSP2D**. In the case of **TSP-2DP**, the CS rate was found to be maximum ($\tau_{CS}$ ~ 0.1 ps and $k_{CS}$ ~ 10 x $10^{12}$ S$^{-1}$) (Table 2.5.2). This is attributed to the precise positioning of the D-A units and extreme interaction between donor and acceptor due to close proximity. Interestingly, the recovery rate was found to be the slowest in this polymeric system. This **TSP-2DP** radical anion decays biexponentially with $\tau_{CR}$ ~ 105 ps (87.9 %) and 840 ps (12.1 %) time components. Hence, **TSP-2DP** possesses not only the fastest CS but also the slowest recovery time among all. As we moved from **TSP2** to **TSP2D** and to **TSP-2DP**, the CS time scale was changed from 3.1 to 0.7 and further to 0.1 ps, respectively, and recovery of the radical anion was significantly slowed down. It can be attributed to the following reasons, 1. The covalently linked donor-acceptor macrocycle in the dimer and 2D-polymer converts the CS into an efficient intramolecular process in the individual macrocycle itself and thereby delays the charge recombination process. 2. The presence of spatially and electronically separated donor-acceptor units connected in series is most supportive in this process. 3. In the dimer and 2D-polymer, the macrocycle connected by phenyl and triphenylamine units, respectively, imparts more rigidification than that of **TSP2**. The global fitting analysis revealed the presence of a short-lived SE signature for **TSP1D**, **TSP2D,** and **TSP-2DP** (Figure 2.55).
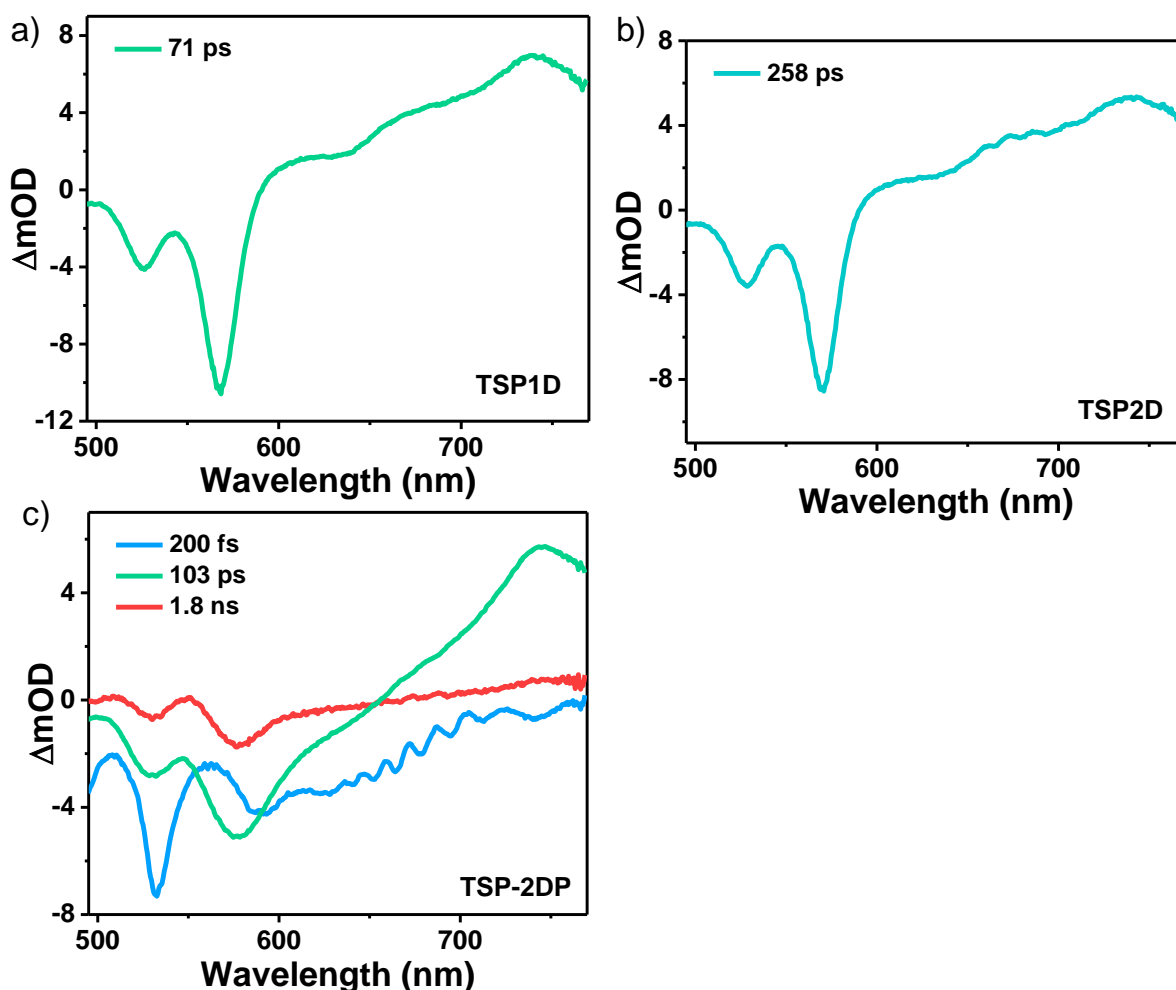
**Figure 2.55.** Spectral distributions of the pre-exponential coefficients from the global fitting for each of the calculated lifetimes, in the case of a) **TSP1D**, b) **TSP2D** and c) **TSP-2DP**.

NIR part of the TA spectra supports the radical cation formation (Figure 2.56, Table 2.5.2) and hence unambiguously confirms the reason for long-lived charge-separated states in TSP macrocycles.[52,53,60] The trends in TA study indicate the strong supportive role of molecular design[63] in fastening the CS process and its stabilization compared to the similar macrocyclic D-A dyads of PBI and oligothiophene reported by Würthner and co-workers.[52,53] A distinctly different photoinduced ET process is exhibited by the present D-A macrocycle developed by the bay functionalization of PBI using an oligothiophene ring connected through an electron-donating phenoxy group. D-A macrocycle synthesized through bay functionalization of PBI supersedes the similar one obtained through imide functionalization[52,53] in terms of fast electron transfer and stabilization of the CS state.

**Figure 2.56.** Femtosecond transient absorption spectra of a) **TSP2** and b) **TSP-2DP** in $CH_2Cl_2$ after the laser excitation at 460 nm. c) The comparative dynamic profile and d) normalized profile of **TSP2**, and **TSP-2DP** monitoring the oligothiophene radical cation signature at the red wing of the spectra.

## 2.5. Tables

**Table 2.5.1.** Optical and redox properties of **rPBI**, **TSP1**, **TSP2**, **TSP1D**, **TSP2D** and **TSP-2DP**.

| Sample | $\lambda_{max, ab}$ (nm) | $\varepsilon_{max}$ ($M^{-1}cm^{-1}$) | $\lambda_{max, em}$ (nm) | $E_{ox}, 1$ (eV) | $E_{ox}, 2$ (eV) | $E_{red}, 1$ (eV) | $E_{red}, 2$ (eV) | $E_{HOMO}$ (eV) | $E_{LUMO}$ (eV) | $E_g$ (eV) |
|---|---|---|---|---|---|---|---|---|---|---|
| **rPBI** | 542 | 49575 | 570 | - | - | -1.14 | -1.30 | - | -3.66 | - |
| **TSP1** | 555 | 59858 | 534 | 0.54 | 0.79 | -1.22 | -1.39 | -5.34 | -3.58 | 1.76 |
| **TSP2** | 558 | 60600 | 534 | 0.57 | 0.87 | -1.24 | -1.47 | -5.37 | -3.56 | 1.81 |
| **TSP1D** | 562 | 58241 | 534 | 0.52 | 0.76 | -1.19 | -1.40 | -5.32 | -3.61 | 1.71 |
| **TSP2D** | 564 | 59945 | 535 | 0.63 | 0.96 | -1.22 | -1.49 | -5.43 | -3.58 | 1.85 |

**Table 2.5.2** Fitting parameters of transient dynamic profiles of PBI radical anion in **TSP1**, **TSP2**, **TSP1D**, **TSP2D**, and **TSP-2DP**, along with **rPBI**, and oligothiophene radical cation of **TSP2**, and **TSP-2DP**.

| System | Wavelength (nm) | $\tau_g$ (ps) | $\tau_1$ (ps) | $\tau_2$ (ps/ns) | $\tau_3$ (ps/ns) |
|---|---|---|---|---|---|
| **TSP1** | 745 | 1.8 | 71.4 (100 %) | - | - |
| **TSP1D** | 741 | 1.0 | 57.3 (100 %) | - | - |
| **TSP2** | 745 | 3.1 | 245.3 (100 %) | - | - |
| **TSP2D** | 737 | 0.7 | 225 (100 %) | - | - |
| **TSP-2DP** | 745 | 0.1 | 105 (87.9 %) | 840 ps (12.1%) | - |
| **rPBI** | 705 | 1.1 | 240 (48.5 %) | 705 (51.5 %) | - |
| **TSP2** | 935 | 4.8 | 346 (100 %) | - | - |
| **TSP-2DP** | 945 | 0.9 | 37.8 (68.9 %) | 234 ps (27.8 %) | > 1 ns (3.3 %) |

## 2.6. Conclusion

In conclusion, a new macrocycle with a perylenebisimide acceptor unit perpendicular to the strapped oligothiophene ring is synthesized and studied for its ET properties by TA. A nearly orthogonal orientation of the D-A units in the macrocycle, confirmed by single-crystal X-ray analysis, results in an ultrafast ET and stabilization of the CS state for a longer duration. The macrocycle design achieved by bay functionalization of PBI enabled the development of the corresponding linear dimer and 2D-polymer. Precise positioning of the D-A units in the macrocycle prevents strong direct intermolecular interactions through $\pi$-$\pi$ stacking and slows down the charge recombination process. Hence, the presence of coaxial thiophene-PBI macrocycle along with a second triphenylamine donor in the three-component 2D-polymer facilitates efficient CS and its stabilization. In short, a molecular design-assisted control over the excited-state CS and its stabilization is demonstrated. Such a nature-inspired synthetic route toward complex structures could lead to new materials for artificial photosynthesis and organic electronics.

## 2.7. References

1.  R. J. Cogdell, A. Gall, J. Q. Köhler, *Rev. Biophys.* **2006**, *39*, 227−324.

2.  K. N.Ferreira, T. M.Iverson, K. Maghlaoui, J. Barber, S. Iwata, *Science* **2004**, *303*, 1831−1838.

3.  D. M.Guldi, *J. Phys. Chem. B* **2005**, *109*, 11432−11441.

4.  A. A. Bakulin, A. Rao, V. G. Pavelyev, P. H. M. van Loosdrecht, M. S. Pshenichnikov, D. Niedzialek, J. Cornil, D. Beljonne, R. H. Friend, *Science* **2012**, *335*, 1340−1344.

5.  L. Giribabu, A. A. Kumar, V. Neeraja, B. G. Maiya, Orientation *Angew. Chem. Int. Ed.* **2001**, *40*, 3621−3624.

6.  C. Wiebeler, F. Plasser, G. J. Hedley, A. Ruseckas, I. D. W. Samuel, S.Schumacher, *J. Phys. Chem. Lett.* **2017**, 8, 1086−1092.

7.  S. Prasanthkumar, S. Ghosh, V. C. Nair, A. Saeki, S. Seki, A. Ajayaghosh, *Angew. Chem. Int. Ed.* **2015**, *54*, 946-950.

8.  J. López-Andarias, M. J. Rodriguez, C. Atienza, J. L. López, T. Mikie, S. Casado, S. Seki, J. L. Carrascosa, N. Martín, *J. Am. Chem. Soc.* **2015**, *137*, 893−897.

9.  D. Ley, C. X. Guzman, K. H. Adolfsson, A. M. Scott, A. B. Braunschweig, *J. Am. Chem. Soc.* **2014**, *136*, 7809−7812.

10. Y.-L. Wu, K. E. Brown, M. R. Wasielewski, *J. Am. Chem. Soc.* **2013**, *135*, 13322−13325.

11. M. R. Wasielewski, *Acc. Chem. Res.* **2009**, *42*, 1910−1921.

12. E. Krieg, A. Niazov-Elkan, E. Cohen, Y. Tsarfati, B. Rybtchinski, *Acc. Chem. Res.* **2019**, *52*, 2634−2646.

13. F. Würthner, C. R. Saha-Möller, B. Fimmel, S. Ogi, P. Leowanawat, D. Schmidt, *Chem. Rev.* **2016**, *116*, 962−1052.

14. S. Chen, P.Slattum, C. Wang, L.Zang, *Chem. Rev.* **2015**, *115*, 11967−11998.

15. T. Seki, X. Lin, S. Yagai, *Asian J. Org. Chem.* **2013**, *2*, 708−724.

16. T. Weil, T. Vosch, J. Hofkens, K. Peneva, K. Müllen, *Angew. Chem. Int. Ed.* **2010**, *49*, 9068−9093.

17. C. Li, K. Müllen, (**2013**) Perylenes in Organic Photovoltaics. In: Zhou Y. (eds) Eco- and Renewable Energy Materials. Springer, Berlin, Heidelberg.

18. M. Ogasawara, X. Lin, H. Kurata, H. Ouchi, M. Yamauchi, T. Ohba, T. Kajitani, T. Fukushima, M. Numata, R. Nogami, B. Adhikari, S. Yagai, *Mater. Chem. Front.* **2018**, *2*, 171−179.

19. R. Sethy, J. Kumar, R. Métivier, M. Louis, K. Nakatani, N. M. T. Mecheri, A. Subhakumari, K. G.Thomas, T. Kawai, T. Nakashima, *Angew. Chem. Int. Ed.* **2017**, *56*, 15053−15057.

20. W. Wagner, M. Wehner, V. Stepanenko, S. Ogi, F. Würthner, *Angew. Chem. Int. Ed.* **2017**, *56*, 16008−16012.

21. C. Roche, H.-J. Sun, P. Leowanawat, F. Araoka, B. E. Partridge, M. Peterca, D. A. Wilson, M. E.Prendergast, P. A. Heiney, R. Graf, H. W. Spiess, X. Zeng, G.Ungar, V. A. Percec, *Nat. Chem.* **2016**, *8*, 80−89.

22. X. Zhang, S. Rehm, M. M. Safont-Sempere, F. Würthner, *Nat. Chem.* **2009**, *1*, 623−629.

23. S. Yagai, T. Seki, T. Karatsu, A. Kitamura, F. Würthner, *Angew. Chem. Int. Ed.* **2008**, *47*, 3367−3371.

24. P. Cheng, G. Li, X. Zhan, Y. Yang, *Nat. Photon.* **2018**, *12*, 131−142.

25. C. Wang, F. N. Miros, J. Mareda, N.Sakai, S. Matile, *Angew. Chem. Int. Ed.* **2016**, *55*, 14422−14426.

26. D. Liu, J. Wang, X. Bai, R. Zong, Y. Zhu, *Adv. Mater.* **2016**, *28*, 7284−7290.

27. S. Kaloyanova, Y. Zagranyarski, S. Ritz, M. Hanulová, K. Koynov, A. Vonderheit, K. Müllen, K. Peneva, *J. Am. Chem. Soc.* **2016**, *138*, 2881−2884.

28. P. D. Frischmann, Y. Hwa, E. J. Cairns, B. A. Helms, *Chem. Mater.* **2016**, *28*, 7414−7421.

29. J. M. Mativetsky, E. Orgiu, I. Lieberwirth, W. Pisula, P. Samorì, *Adv. Mater.* **2014**, *26*, 430−435.

30. X. Zhan, A. Facchetti, S. Barlow, T. J. Marks, M. A. Ratner, M. R. Wasielewski, S. R. Marder, *Adv. Mater.* **2011**, *23*, 268−284.

31. M. Bonchio, Z. Syrgiannis, M.Burian, N. Marino, E. Pizzolato, K. Dirian, F. Rigodanza, G. A. Volpato, G. L. Ganga, N. Demitri, S.Berardi, H. Amenitsch, D. M. Guldi, S. Caramori, C. A.Bignozzi, A. Sartorel, M. Prato, *Nat. Chem.* **2019**, *11*, 146−153.

32. C. E. Ramirez, S. Chen, N. E. Powers-Riggs, I. Schlesinger, R. M. Young, M. R. Wasielewski, *J. Am. Chem. Soc.* **2020**, *142*, 18243−18250.

33. D. Schmidt, M.Stolte, J. Süß, A. Liess, V. Stepanenko, F. Würthner, *Angew. Chem. Int. Ed.* **2019**, *58*, 13385−13389.

34. B. Zhang, H. Soleimaninejad, D. J. Jones, J. M. White, K. P. Ghiggino, T. A. Smith, W. W. H. Wong, *Chem. Mater.* **2017**, *29*, 8395−8403.

35. Á. J. Jiménez, M.-J. Lin, C. Burschka, J. Becker, V. Settels, B. Engels, F. Würthner, *Chem. Sci.* **2014**, *5*, 608−619.

36. P. Osswald, F. Würthner, *Chem. Eur. J.* **2007**, *13*, 7395−7409.

37. E. Sebastian, M. Hariharan, *J. Am. Chem. Soc.* **2021**, *143*, 13769−13781.

38. V. Strauss, J. T. Margraf, K. Dirian, Z. Syrgiannis, M. Prato, C. Wessendorf, A. Hirsch, T. Clark, D. M. Guldi, *Angew. Chem. Int. Ed.* **2015**, *54*, 8292−8297.

39. C. Schmidt, F. Hauke, M. Prato, A. Hirsch, D. M. Guldi, *J. Am. Chem. Soc.* **2011**, *133*, 4580−4586.

40. M. Ball, B. Zhang, Y. Zhong, B. Fowler, S. Xiao, F. Ng, M. Steigerwald, C. Nuckolls, *Acc. Chem. Res.* **2019**, *52*, 1068−1078.

41. M. Sapotta, A. Hofmann, D. Bialas, F. Würthner, *Angew. Chem. Int. Ed*, **2019**, *58*, 3516−3520.

42. P. Spenst, R. M. Young, B. T. Phelan, M. Keller, J. Dostál, T. Brixner, M. R. Wasielewski, F. Würthner, *J. Am. Chem. Soc.* **2017**, *139*, 2014−2021.

43. P. Spenst, F. Würthner, *Angew. Chem. Int. Ed*, **2015**, *54*, 10165−10168.

44. Y. Wu, R. M. Young, M. Frasconi, S. T. Schneebeli, P. Spenst, D. M. Gardner, K. E. Brown, F. Würthner, J. F. Stoddart, M. R. Wasielewski, *J. Am. Chem. Soc.* **2015**, *41*, 13236−13239.

45. F. Schlosser, J. Sung, P. Kim, D. Kim, F. Würthner, *Chem. Sci.* **2012**, *3*, 2778−2785.

46. M. Hecht, T. Schlossarek, M. Stolte, M. Lehmann, F. Würthner, *Angew. Chem. Int. Ed.* **2019**, *58*, 12979−12983.

47. J. L. Segura, H. Herrera, P. Bäuerle, *J. Mater. Chem.* **2012**, *22*, 8717−8733.

48. H. Wonneberger, C.-Q. Ma, M. A. Gatys, C. Li, P. Bäuerle, K. Müllen, *J. Phys. Chem. B*, **2010**, *114*, 14343−14347.

49. C.-C. You, P. Espindola, C. Hippius, J. Heinze, F. Würthner, *Adv. Funct. Mater.* **2007**, *17*, 3764−3772.

50. M. L. Ball, B. Zhang, Q. Xu, D. W. Paley, V. C. Ritter, F. Ng, M. L. Steigerwald, C. Nuckolls, *J. Am. Chem. Soc.* **2018**, *140*, 10135−10139.

51. M. Ball, B. Fowler, P. Li, L. A. Joyce, F. Li, T. Liu, D. Paley, Y. Zhong, H. Li, S. Xiao, F. Ng, M. L. Steigerwald, C. Nuckolls, *J. Am. Chem. Soc.* **2015**, *137*, 9982−9987.

52. K. Bold, M. Stolte, K. Shoyama, M. Holzapfel, A. Schmiedel, C. Lambert, F. Würthner, *Angew. Chem. Int. Ed.* **2022**, *61*, e202113598.

53. K. Bold, M. Stolte, K. Shoyama, A.-M. Krause, A. Schmiedel, M. Holzapfel, C. Lambert, F. Würthner, *Chem. Eur. J.* 2022, 28, e202200355.

54. T. M. Swager, *Acc. Chem. Res.* **2008**, *41*, 1181−1189.

55. Z. Q. Chen, T. Chen, J. -X. Liu, G. -F. Li, C. Zhang, W. -L. Gong, Z. -J. Xiong, N. -H. Xie, Tang, Z. B. M. –Q. Zhu, *Macromolecules*, **2015**, *48*, 7823−7835.

56. J. E. A. Webb, K. Chen, S. K. K. Prasad, J. P. Wojciechowski, A. Falber, P. Thordarson, J. M. Hodgkiss, *Phys. Chem. Chem. Phys*. **2016**, *18*, 1712−1719.

57. N. Pearce, K. E. A. Reynolds, S. Kayal, X. Z. Sun, E. S. Davies, F.  Malagreca, C. J. Schürmann, S. Ito, A. Yamano, S. P. Argent, M. W. George, N. R. Champness, *Nat. Commun.* **2022**, 13:415.

58. T. W. Kim, S. Jun, Y. Ha, R. K.Yadav, A. Kumar, C.-Y. Yoo, I. Oh, H.-K. Lim, J. W. Shin, R. Ryoo, H. Kim, J. Kim, J.-O. Baeg, H. Ihee, *Nat. Commun.* **2019**, 10:1873.

59. R. F. Kelley, W. S. Shin, B. Rybtchinski, L. E. Sinks, M. R.Wasielewski, *J. Am. Chem. Soc.* **2007**, *129*, 3173−3181.

60. M. Fujitsuka, K.Harada, A. Sugimoto, T. Majima, *J. Phys. Chem. A* **2008**, *112*, 10193−10199.

61. V. C. Wakchaure, A. Kottaichamy, A. Nidhankar, K. C. Ranjeesh, M. Nazrulla, M. Thotiyl, S. S.Babu, A*CS Appl. Energy Mater.* **2020**, *3*, 6352−6359.

62. R. Renner, M. Stolte, J. Heitmüller, T. Brixner, C. Lambert, F. Würthner, *Mater. Horiz.* **2022**, 9, 350−359.

63. J. Sukegawa, C. Schubert, X. Zhu, H. Tsuji, D. M. Guldi, E. Nakamura, *Nat. Chem.* **2014**, *6*, 899−905.

# Chapter–3

# Donor Strapped Perylene Bisimide Macrocycle and Lemniscate Dimer with Extended Charge Separation

# Chapter–3

# Donor Strapped Perylene Bisimide Macrocycle and Lemniscate Dimer with Extended Charge Separation



Macrocyclic structures are fascinating due to their unique design and capability to place chromophores in specific orientations, resulting in exciting optoelectronic properties. However, the synthetic challenges limit the broad exploration of such systems. Herein, we report a thiophene-diacetylene-based ring strapped perylene bisimide macrocycle and its notably different electron transfer features. Single-crystal analysis of the macrocycle points to the nearly orthogonal placement of donor-acceptor units, facilitating better electronic communication between them. Interestingly, introducing an alkyl substituent on the peripheral thiophene ring opened the possibility of forming a higher oligomer macrocycle consisting of multiple strapped perylene bisimide units. Diffusion and two-dimensional NMR experiments provided insight into the structure of the figure-eight-shaped lemniscate dimer. Transient absorption measurements showed faster electron transfer and extended stabilization of the charge-separated state. The thiophene-diacetylene-based ring is a better donor unit to facilitate rapid electron transfer and long-lived charge separation in the macrocycle and its lemniscate dimer. The new macrocycle design enables the formation of higher analogs equally capable of stabilizing the charge-separated state.

## 3.1. Introduction

The photosynthetic system is a perfect example, where chlorophyll molecules are organized in an orderly pattern to ensure effective light harvesting and redox reactions.[1-2] Inspired by this ideal concept, researchers have attempted to create various multicomponent π-conjugated systems. Such macrocyclic arrays have attracted significant interest due to their promising capability to efficiently collect solar energy and transform it into chemical, electric, or other forms of energy.[3-7] Although there have been many synthetic structural resemblances of light-harvesting assemblies, it has only rarely been thought of to use the focused and channeled excitation energy.[8-10] In this direction, there has been a lot of interest in chromophores that can harvest light and create long-lived charge-separated states using molecular assemblies, particularly macrocycles comprised of suitably placed donor and acceptor units.[11] A variety of macro-cyclic arrays based on porphyrins,[12] oligothiophenes,[13] BODIPY,[14] carbazoles,[15] and perylene bisimides (PBIs)[5,16] have been used as light-absorbing components in macrocycles.

PBI is one of the most distinctly studied fluorescent dyes among organic materials.[17] Moreover, PBIs are indeed a preferred chromophore due to their excellent chemical and thermal stability, wide spectrum of visible light absorption, and distinctive electrochemical properties.[6,18,19] The chemical functionalization of PBIs is possible at many positions, including the imide-, ortho-, and bay positions.[19] However, since the imide nitrogen atoms of PBI act as the nodes of frontier orbitals, linking PBI units through these nitrogen atoms would not disrupt the PBI frontier orbitals.[18,19] On the other hand, introducing new substituents at the bay positions of PBI has shown to be successful in changing the frontier orbital levels. Besides, specific substituents in the bay position facilitate easy tuning of the optoelectronic characteristics, making them ideal for light harvesting and luminescent applications.[20] Nuckolls and coworkers previously reported that PBIs-based cyclic conjugated macrocycles generate substantially higher photocurrent than acyclic-analogs.[21] In 2021, the research group of Würthner reported a completely strapped donor-acceptor PBI through imide position exhibiting ultrafast electron transfer.[22] Moreover, a considerable number of α-conjugated macrocyclic oligothiophenes containing various cyclo(n)thiophenes have been reported through the thiophene-acetylene linkage by Bäuerle and coworkers.[13] Recently, our group also reported another oligothiophene strapped PBI, functionalized on the bay position via oxidative coupling reaction, along with corresponding linear dimer and 2D polymer.[23] Our aim was to develop macrocyclic donor-acceptor systems with extended

charge separation (CS) and stabilization. In this work, we demonstrate another straightforward approach with acetylene chemistry,[24] which allows easily achievable covalently bonded, rigid macrocyclic scaffolds. The unique design consists of rigid donor-acceptor units oriented nearly orthogonal to each other for improved CS. Most importantly, the Hay-Glasear coupling reaction yields diacetylene-thiophene-strapped PBIs (**SP1** and **2**) in good yield and opens up the possibility of generating a dimer (**SP2D**) and higher analogs (Scheme 3.3). The present study describes the rational design, synthesis, and electron transfer properties of new donor-acceptor macrocycles.

## 3.2. Experimental section

### 3.2.1. Electrochemical analysis

Cyclic voltammetry (CV) and Differential pulse voltammetry (DPV) measurements were carried out on a CHI voltammetry analyzer at room temperature, employing a three-electrode single compartment cell: glassy carbon electrode (company, d = 2mm) as working electrode, a Pt wire as counter electrode and Ag/AgCl as a reference electrode. The supporting electrolyte, Tetrabutylammonium hexafluorophosphate ($n$-Bu$_4$NPF$_6$), was previously dried under vacuum, dichloromethane was dried and degassed before use, and all measurements were performed under a nitrogen atmosphere. Ferrocene was used as an internal standard for calibrating the potential ($E_{Fc+/Fc}$ = 0.00 V).

The formal redox potentials (half-wave potentials) were calculated using the formula:

$$E_{1/2} = (E_{pa} + E_{pc}) / 2$$

Where $E_{pa}$ is the peak anode potential and

$E_{pc}$ is the peak cathode potential.

HOMO energies were calculated from the first formal redox potentials (half-wave potentials) using the equation:

$$E_{HOMO} = -(4.8 \text{ eV} + E^1_{oxd} \text{ vs. } Fc^+\!/Fc)$$

However, LUMO energies were calculated from the first formal redox potentials (half-wave potentials) using the equation:

$$E_{LUMO} = -(4.8 \text{ eV} + E^1_{red} \text{ vs. } Fc^+\!/Fc)$$

### 3.2.2. Femtosecond transient absorption spectroscopy

The transient experiments were using a Helios Fire pump-probe spectrometer setup (Ultrafast System). Ti: Sapphire amplifier system (Astrella, Coherent, 800 nm, 3mJ/pulse energy, ~ 35 fs pulse width, and 1 kHz repetition rate) was used to generate ultrafast pulses. The output of

the laser pulse was then splitted into two parts (95:5) to generate the pump and probe beam. The higher energy beam travels to an Optical Parametric Amplifier (OPerA-SOLO) to generate requisite pump wavelengths. The lower energy beam passes through sapphire crystal in order to generate white light. A mechanical delay stage was in place to maintain perfect delay between the pump and probe beam. The transient data was recorded while keeping the sample in a 2mm quartz cuvette and analyzed using surface explorer software. All the experimental measurements were carried out at room temperature.

### 3.2.3. Computational Methods

All the DFT calculations were carried out by employing Gaussian09 software using B3LYP/6-31G(d) level of theory. To save computational cost, the long alkyl chains were truncated to a methyl group. PCM solvation model was used to take account of long-range interactions as well as the solvation effect of dichloromethane, respectively.

## 3.3. Experimental Procedures: Synthesis

### 3.3.1. Synthesis of Triisopropyl((5-(trimethylstannyl)thiophen-2-yl)ethynyl)silane (T2)
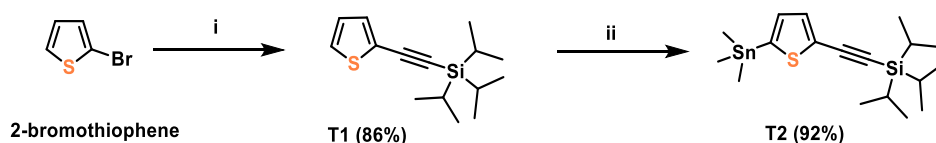


**Scheme 3.1.** Synthesis of **T2**. (i) (Triisopropylsilyl)acetylene, Pd(PPh$_3$)$_2$Cl$_2$, CuI, Et$_3$N, THF, RT, 12 h, (ii) **a**. *n*-BuLi, THF, -78 °C, 1 h; **b**. Me$_3$SnCl, -78 °C to RT, 12 h.

### 3.3.2. Triisopropyl((5-(trimethylstannyl)3-hexylthiophene-2-yl)ethynyl)silane (T6)
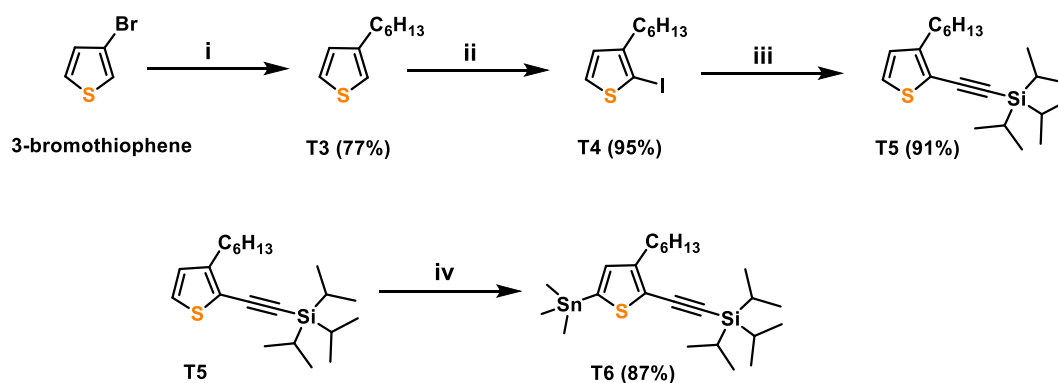


**Scheme 3.2.** Synthesis of **T6**. (i) **a**. Mg, I$_2$, C$_6$H$_{13}$Br, THF, Reflux, 5 h; **b**. Ni(dppp)Cl$_2$, THF, Reflux, 15 h, (ii) NIS, CH$_2$Cl$_2$:AcOH (1:1), RT, 12 h, (iii) (Triisopropylsilyl)acetylene, Pd(PPh$_3$)$_2$Cl$_2$, CuI, DIPA:THF (1:1), 60 °C, 12 h, (iv) **a**. *n*-BuLi, THF, -78 °C, 45 min; **b**. Me$_3$SnCl, -78 °C to RT, 12 h.

### 3.3.3. Synthesis of Diacetylene-Thiophene-Ring-Strapped PBIs Macrocycles of SP1,2 and SP2D
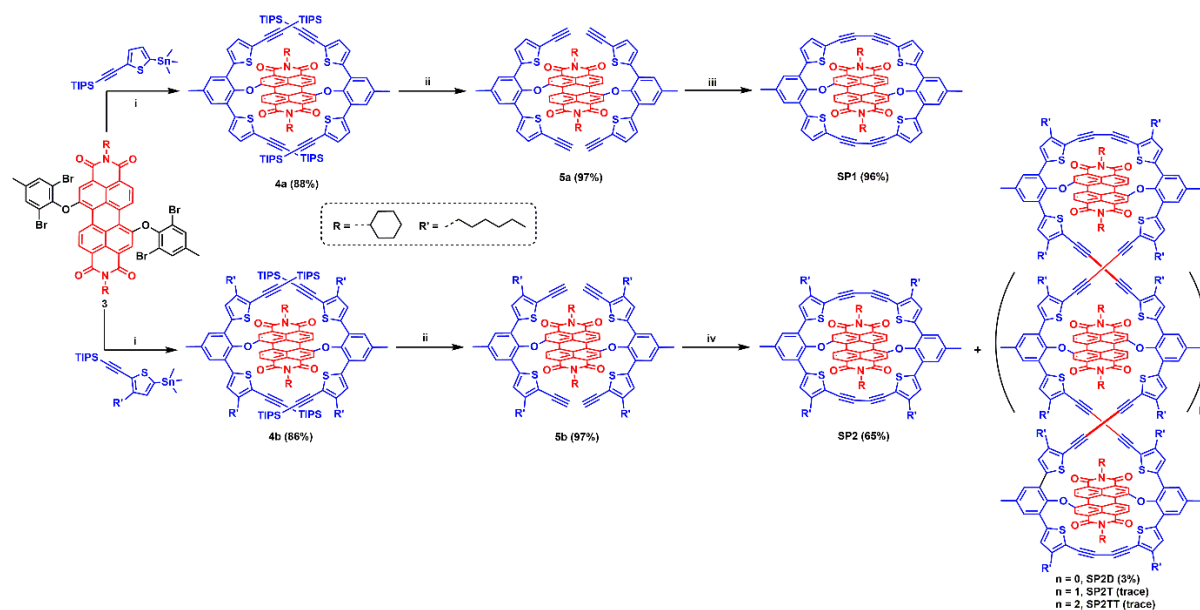


**Scheme 3.3**. Synthesis of diacetylene-thiophene strapped PBIs. (i) Pd(PPh$_3$)$_2$Cl$_2$, toluene, 140 °C, 12 h, (ii) TBAF, THF, RT, 15 min., (iii) TMEDA, CuCl, THF, RT, 6 h, (iv) TMEDA, CuCl, THF, RT, 12 h.

**Scheme 3.1.**

### 3.3.1.1. Synthesis of Compound (T1):[25]
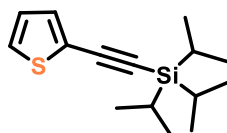


30 mL schlenk tube was charged with 2-bromothiophene (1.5 g, 9.20 mmol), CuI (53 mg, 276.02 μmol), and Pd(PPh$_3$)$_2$Cl$_2$ (194 mg, 276.02 μmol). To that, THF (15 mL) and triethylamine (5 mL) were added, kept in an ice-cold solution, degassed for 30 min., and Triisopropylsilylacetylene (2.27 mL, 10.12 mmol) was added drop by drop. The mixture was stirred at room temperature for 12 h. After completion of the reaction, dichloromethane was added, and the resultant mixture was filtered through celite. The filtrate was extracted with water, and the solvent was removed under reduced pressure and dried over anhydrous Na2SO4. The crude product was purified by silica gel column chromatography using petroleum ether to obtain pure product triisopropyl(thiophen-2-ylethynyl)silane **T1**.

**Nature and Yield**: colorless oil, 2.1 g (86%).

**¹H NMR (500 MHz, CDCl₃):** $\delta$ [ppm] = 7.22-7.25 (m, 2H), 6.96 (dd, *J* = 5.0, 3.7 Hz, 1H), 1.13 (s, 21H).

**$^{13}$C NMR (125 MHz, CDCl$_3$):** $\delta$ **[ppm]** = 132.4, 126.9, 126.8, 123.6, 99.3, 95.3, 18.6, 11.3.

**HRMS (ESI):** *m/z* calculated for C$_{15}$H$_{25}$SSi [M+H]$^+$: 265.1441, found: 265.1440.

### 3.3.1.2. Synthesis of Compound (T2):[25]
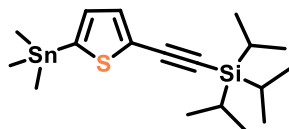


In a 50 mL two-neck round bottom flask, a solution of triisopropyl(thiophen-2-ylethynyl)silane (1.5 g, 5.67 mmol) in 20 mL anhydrous THF was refrigerated to -78 °C under argon. To that, n-butyllithium (1.6 M, 3.9 mL, 6.24 mmol) was added dropwise over 15 minutes and stirred for 1 h at -78 °C. Later, a solution of trimethyltin chloride (1.47 g, 7.37 mmol) in THF was added dropwise, and the reaction mixture was warmed to room temperature and stirred for 12 h. The clear solution was diluted with diethyl ether and rinsed with water. The organic layer was dried over anhydrous Na$_2$SO$_4$, and the solvents were concentrated at reduced pressure. Triisopropyl((5-(trimethylstannyl)thiophen-2-yl)ethynyl)silane (**T2**) was obtained as a light brownish oil without further purification.

**Nature and Yield**: light brownish oil, 2.23 g (92%).

**$^1$H NMR (200 MHz, CDCl$_3$):** $\delta$ **[ppm]** = 7.32 (d, *J* = 3.37 Hz, 1H), 7.05 (d, *J* = 3.37 Hz, 1H) 1.11 (s, 21H), 0.36 (t, 9H).

**HRMS (ESI):** *m/z* calculated for C$_{18}$H$_{33}$SSiSn [M+H]$^+$: 429.1089, found: 429.1098.

**Scheme 3.2.**

### 3.3.2.1 Synthesis of Compound (T3):[26]



A 100 mL two-neck round bottom flask (1.04 g, 42.94 mmol) containing magnesium and I$_2$ was flame-dried under vacuum and filled with argon. To that, 30 mL of anhydrous THF was added and refluxed. 1-bromohexane (5.15 ml, 36.80 mmol) was added dropwise while keeping the THF refluxing. After that, the suspension was stirred for 5 h under argon until all of the magnesium had reacted. The hexylmagnesium bromide product was transferred to a second 100 mL two-neck flask chilled with ice and containing (582 mg, 1.07 mmol) of [Ni(dppp)Cl$_2$] and (5 g, 30.67 mmol) of 3-bromothiophene in 30 mL of anhydrous THF

through a cannula needle. The reaction mixture was refluxed by stirring under argon for 15 h. After that, the reaction was cooled by pouring a solution of diluted HCl and ice. Following phase separation, the aqueous phase was extracted with ethyl acetate, and the content of organic phases was washed with (3×50 mL) of water and, one time, with 25 mL of saturated aq.NaHCO₃. The organic layer was dried over $Na_2SO_4$, and the solvent was removed under vacuum. The crude product was purified by silica gel column chromatography using petroleum ether as the eluent to obtain the product (**T3**).

**Nature and Yield**: colorless oil, 4 g (77%).

**¹H NMR (500 MHz, CDCl₃):** $\delta$ **[ppm]** = 7.25 (dd, *J* = 5.01, 2.8 Hz, 1H), 6.93-6.96 (m, 2H), 2.64 (t, *J* = 7.5 Hz, 2H), 1.59-1.67 (m, 2H), 1.30-1.37 (m, 6H), 0.90 (t, *J* = 6.3 Hz, 3H).

**¹³C NMR (125 MHz, CDCl₃):** $\delta$ **[ppm]** = 143.3, 128.3, 125, 119.7, 31.7, 30.5, 30.3, 29, 22.6, 14.1.

**HRMS (ESI):** *m/z* calculated for $C_{10}H_{17}S[M+H]^+$: 169.1051, found: 169.9772.

**3.3.2.2. Synthesis of Compound (T4):**



In a 50 mL round bottom flask, 3-hexylthiophene (**T3**) (3.1 g, 18.42 mmol) was dissolved in anhydrous dichloromethane and acetic acid (1:1, 30 mL). To that, N-iodosuccinimide (4.14 g, 18.42 mmol) was added portion-wise. The reaction mixture was stirred for 12 h at room temperature. After 12 h, the reaction was quenched with sodium thiosulfate, and the compound was extracted with ethyl acetate. The combined organic layer was washed with water (3×25 mL), dried over anhydrous $Na_2SO_4$, and concentrated to obtain a yellow oil. The crude product was purified by silica gel column chromatography using petroleum ether as the eluent to get the product (**T4**).

**Nature and Yield**: colorless oil, 5.15 g (95%).

**¹H NMR (400 MHz, CDCl₃):** $\delta$ **[ppm]** = 7.39 (d, *J* = 5.5 Hz, 1H), 6.77 (d, *J* = 5.5 Hz, 1H), 2.56 (t, *J* = 6.5 Hz, 2H), 1.58 (m, 2H), 1.30-1.38 (m, 6H), 0.91 (t, *J* = 6.5 Hz, 3H).

**¹³C NMR (125 MHz, CDCl₃):** $\delta$ **[ppm]** = 147.2, 130.3, 127.9, 73.9, 32.1, 31.6, 29.9, 28.9, 22.6, 14.1.

**HRMS (ESI):** *m/z* calculated for $C_{10}H_{15}IS$ [M]$^+$: 293.1939, found: 293.2957 and $C_{10}H_{16}IS$ [M+H]$^+$: 295.0017, found: 295.3023.

### 3.3.2.3. Synthesis of Compound (T5):
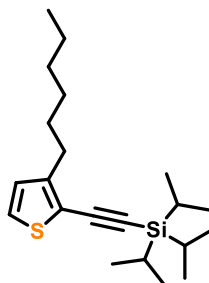


In a 30 mL Schlenk tube, 2-iodo-3-hexylthiophene (**T4**) (1 g, 3.40 mmol), CuI (26 mg, 136 µmol), Pd(PPh$_3$)$_2$Cl$_2$ (95 mg, 136 µmol) in anhydrous THF (8 mL), and diisopropyl amine (8 mL), was added. The schlenk tube was kept in an ice-cold solution, degassed for 30 min. and Triisopropylsilylacetylene (1 mL, 4.59 mmol) was added. The reaction mixture was stirred at 60 °C, for 12 h. Dichloromethane was added, and the resultant mixture was passed through celite before being washed with water. Under reduced pressure, the solvent was removed after drying over anhydrous Na$_2$SO$_4$. The crude product was purified by silica gel column chromatography using petroleum ether as the eluent to obtain the product (**T5**).

**Nature and Yield**: colorless oil, 1.08 g (91%).

**$^1$H NMR (500 MHz, CDCl$_3$):** $\delta$ [ppm] = 7.12 (d, *J* = 5.3 Hz, 1H), 6.84 (d, *J* = 5.3 Hz, 1H), 2.72 (t, *J* = 7.75 Hz, 2H), 1.58-1.65 (m, 2H), 1.28-1.35 (m, 6H), 1.14 (s, 21H), 0.89 (t, *J* = 6.8 Hz, 3H).

**$^{13}$C NMR (100 MHz, CDCl$_3$):** $\delta$ [ppm] = 148.6, 128.1, 125.5, 118.7, 99.1, 97.1, 31.7, 30.3, 29.7, 29.1, 22.6, 18.7, 14.1, 11.3.

**HRMS (ESI):** *m/z* calculated for $C_{21}H_{37}SSi$ [M+H]$^+$: 349.2380, found: 349.2375.

### 3.3.2.4. Synthesis of Compound (T6):
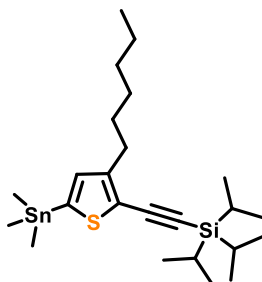


In a 100 mL round bottom flask, a solution of ((3-hexylthiophene-2-yl)ethynyl)triisopropylsilane (1.5 g, 4.30 mmol) in 20 mL of anhydrous THF was cooled to -

78 °C under an argon atmosphere. Then 1.6 M n-butyllithium (3 mL, 4.73 mmol) was added dropwise and stirred for 45 minutes. The solution of trimethyl tinchloride (1.11 g, 5.59 mmol) in THF was added drop-by-drop to the reaction mixture, maintaining -78 °C for 30 minutes. The mixture was then warmed to room temperature and stirred for 12 h. The clear solution was diluted with diethyl ether and rinsed with water. The organic layer was dried over anhydrous $Na_2SO_4$ and the solvent was removed under reduced pressure. Triisopropyl((5-(trimethylstannyl)3-hexylthiophene-2-yl)ethynyl)silane (**T6**) was obtained as the crude product as a light brownish oil and used directly without further purification.

**Nature and Yield**: light brownish oil, 1.92 g (87%).

**$^1$H NMR (500 MHz, CD$_2$Cl$_2$):** $\delta$ **[ppm]** = 6.92 (s, 1H), 2.71 (t, $J$ = 7.75 Hz, 2H), 1.59-1.65 (m, 2H), 1.29-1.36 (m, 6H), 1.13 (s, 21H), 0.88 (t, $J$ = 7.17 Hz, 3H), 0.35 (t, 9H).

**HRMS (ESI):** *m/z* calculated for $C_{24}H_{45}SSiSn$ [M+H]$^+$: 513.2028, found: 513.2017.

**Scheme 3.3.3.**

*N,N'-Dicyclohexyl-1,7-bis(2,6-dibromo-4-methylphenoxy)perylene-3,4:9,10-bisdicarboximide* (**3**) was synthesized in quantitative yield by adapting a previously reported chapter.[23]

**3.3.3.1. Synthesis of 4a:**
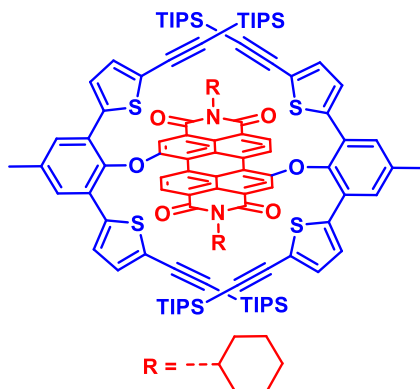


10 mL pressure tube was charged with compound **3** (200 mg, 184.76 µmol), triisopropyl((5-(trimethylstannyl)thiophen-2-yl)ethynyl)silane (513 mg, 1.20 mmol), and Pd(PPh$_3$)$_2$Cl$_2$ (6.5 mg, 9.24 µmol) in 4 mL anhydrous toluene. The reaction mixture was subsequently heated to 140 °C for 12 h. Further, the reaction mixture was allowed to cool down to room temperature, followed by adding dichloromethane, passing through celite before water workup, and the solvent was removed by evaporation under reduced pressure. The crude product was purified by silica gel column chromatography using dichloromethane-petroleum ether (6:4 v/v) to obtain pure product **4a**.

**Nature and Yield**: Red solid, 296 mg (88%).

**$^1$H NMR (500 MHz, CDCl$_3$):** $\delta$ **[ppm]** = 9.96 (d, *J* = 8.4 Hz, 2H), 8.66 (d, *J* = 8.4 Hz, 2H), 7.94 (s, 2H), 7.52 (s, 4H), 7.10 (d, *J* = 3.8 Hz, 4H), 6.83 (d, *J* = 3.8 Hz, 4H), 4.96 (t, *J* = 12.0 Hz, 2 H), 2.52 (s, 6H), 2.43-2.51 (m, 4H), 1.87 (d, *J* = 13.0 Hz, 4H), 1.70 (d, *J* = 12 Hz, 6H), 1.28-1.45 (m, 6H), 0.91-0.97 (m, 84 H).

**$^{13}$C NMR (125 MHz, CDCl$_3$):** $\delta$ **[ppm]** = 163.7, 163.4, 154.7, 143.5, 138.9, 137.1, 133.6, 132.5, 131.1, 129.9, 129.3, 129.2, 128.6, 126.1, 124.9, 124.3, 124, 122.5, 121.4, 118.3, 98.8, 97.2, 53.9, 29.7, 29, 26.5, 25.4, 21.1, 18.4, 11.1.

**FT-IR** (cm$^{-1}$): 2942, 2866, 2142, 1701, 1661, 1594, 1514, 1461, 1407, 1330, 1260, 1199, 882, 761, 679.

**MALDI-TOF:** *m/z* calculated for C$_{110}$H$_{131}$N$_2$O$_6$S$_4$Si$_4$ [M+H]$^+$: 1815.7967, found: 1815.75.

### 3.3.3.2. Synthesis of 4b:
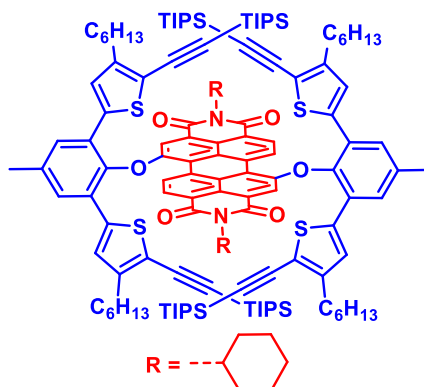


10 mL pressure tube was charged with compound **3** (300 mg, 277.14 μmol), triisopropyl ((5-(trimethylstannyl)3-hexylthiophen-2-yl)silane (950 mg, 1.86 mmol), and Pd(PPh$_3$)$_2$Cl$_2$ (10 mg, 13.86 μmol) in 4 mL anhydrous toluene were added. The reaction mixture was subsequently heated to 140 °C for 12 h. Further, the reaction mixture was cooled down to room temperature, followed by adding dichloromethane and passing through celite before water workup, and the solvent was removed by evaporation under reduced pressure. The crude product was purified by silica gel column chromatography using dichloromethane-petroleum ether (5:5 v/v) to obtain pure product **4b**.

**Nature and Yield**: Red solid, 511 mg (86%).

**$^1$H NMR (400 MHz, CDCl$_3$):** $\delta$ **[ppm]** = 10.06 (d, *J* = 9.2 Hz, 2H), 8.70 (d, *J* = 9.2 Hz, 2H), 7.96 (s, 2H), 7.50 (s, 4H), 7.11 (s, 4H), 4.95 (t, *J* = 12.01 Hz, 2 H),  2.51 (s, 6H), 2.41-2.50 (m, 4H), 2.29 (ddd, *J* = 14.7, 9.0, 6.1 Hz, 4 H), 2.18 (ddd, *J* = 14.7, 8.6, 6.5 Hz, 4 H), 1.87 (d, *J* = 12.2 Hz, 4 H), 1.69 (d, *J* = 9.2 Hz, 6 H), 1.20-1.48 (m, 8H), 0.94-1.00 (m, 84 H), 0.70-0.92 (m, 24 H), 0.55- 0.61 (m, 6 H), 0.53 (t, *J* = 7.61 Hz, 12 H).

**$^{13}$C NMR (100 MHz, CDCl$_3$): $\delta$ [ppm]** = 163.7, 163.2, 154.9, 148.8, 142.9, 137.3, 133.8, 130.6, 129.8, 129.2, 128.9, 127.1, 124.9, 124.2, 122.4, 120.9, 119.3, 118, 99, 98.5, 53.9, 31.2, 29.6, 29.5, 29, 28.8, 26.5, 25.4, 22.3, 21.1, 18.5, 13.9, 11.1.

**FT-IR** (cm$^{-1}$): 2922, 2856, 2136, 1702, 1655, 1599, 1469, 1403, 1329, 1263, 1198, 881, 750, 675.

**MALDI-TOF:** *m/z* calculated for C$_{134}$H$_{179}$N$_2$O$_6$S$_4$Si$_4$ [M+H]$^+$: 2152.1723, found: 2152.13.

**3.3.3.2. Synthesis of 5a:**
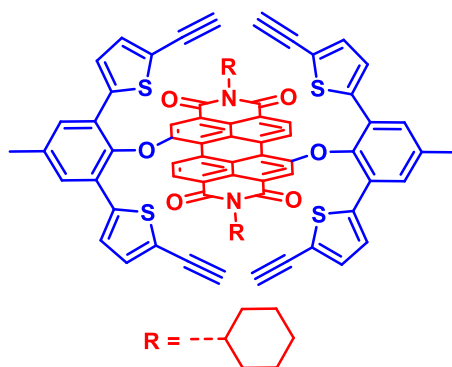


To a 25 mL round bottom flask, compound **4a** (100 mg, 55.04 μmol) was added by dissolving in 10 mL anhydrous THF under an argon atmosphere, then tetrabutylammonium fluoride hydrate (246 mg, 825.61 μmol) was added. The solution was stirred at room temperature for 15 minutes. The reaction was monitored by TLC and confirmed the product. Later, the mixture was quenched with water, and the workup was done with dichloromethane. The organic layer was dried over anhydrous Na$_2$SO$_4$, and the solvents were concentrated under reduced pressure. The crude product was purified by silica gel column chromatography using dichloromethane-petroleum ether (8:2 v/v) as eluent, affording compound **5a**.

**Nature and Yield**: Red solid, 64 mg (97%).

**$^1$H NMR (500 MHz, CDCl$_3$): $\delta$ [ppm]** = 9.82 (d, *J* = 8.4 Hz, 2H), 8.65 (d, *J* = 8.4 Hz, 2H), 7.90 (s, 2H), 7.54 (s, 4H), 7.09 (d, *J* = 3.8 Hz, 4H), 6.91 (d, *J* = 3.8 Hz, 4H), 4.96 (t, *J* = 12.0 Hz, 2H), 3.76 (s, 1H), 3.18 (s, 3H), 2.53 (s, 6H), 2.49-2.44 (m, 4H), 1.85-1.89 (m, 4H), 1.72 (m, 6H), 1.40 (q, *J* = 12.8 Hz, 4H), 1.28-1.33 (m, 2H).

**13C NMR (100 MHz, CDCl3): $\delta$ [ppm]** = 163.8, 163.4, 154.8, 143.9, 139.1, 137.2, 133.4, 133.3, 131.1, 129.9, 129.4, 129.1, 128.5, 126.3, 124.8, 124.1, 122.9, 122.6, 121.7, 118.4, 82.5, 76.4, 54.0, 31.6, 29.1, 26.5, 25.4, 21.1, 14.1

**FT-IR** (cm$^{-1}$): 3309, 3253, 2957, 2929, 2873, 2095, 1767, 1721, 1693, 1655, 1590, 1459, 1329, 1263, 1193, 733.

**MALDI-TOF:** *m/z* calculated for C$_{74}$H$_{51}$N$_2$O$_6$S$_4$ [M+H]$^+$: 1191.2630, found: 1191.430.

### 3.3.3.3. Synthesis of 5b:
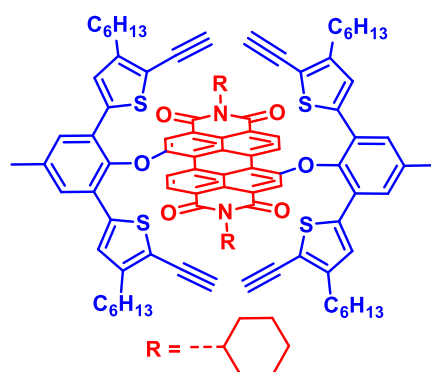


The synthesis of **5b** followed a similar process to that of **5a**. In 15 mL THF, 4b (200 mg, 92.87 μmol) and Tetrabutylammonium fluoride hydrate (260 mg, 928.73 μmol) were added and stirred at room temperature for 15 minutes. The completion of the reaction was monitored by TLC. The crude product was purified by silica gel column chromatography using dichloromethane-petroleum ether (7:3 v/v) as eluent, affording compound **5b**.

**Nature and Yield**: Red solid, 138 mg (97%).

**$^1$H NMR (400 MHz, CDCl$_3$):** $\delta$ **[ppm]** = 10.03 (d, $J$ = 8.5 Hz, 2 H), 8.70 (d, $J$ = 8.5 Hz, 2 H), 7.90 (s, 2 H), 7.54 (s, 4 H), 7.14 (s, 4 H), 4.95 (t, $J$ = 12.1 Hz, 2 H), 3.29 (s, 4 H), 2.53 (s, 6 H), 2.41-2.50 (m, 4 H), 2.29-2.38 (m, 4 H), 2.20-2.28 (m, 4 H), 1.87 (d, $J$ = 12.8 Hz, 4 H), 1.68 (t, $J$ = 10.6 Hz, 6H), 1.31-1.47 (m, 6 H), 0.93-1.05 (m, 16 H), 0.76-0.89 (m, 16 H), 0.66 (t, $J$ = 6.6 Hz, 12 H).

**$^{13}$C NMR (100 MHz, CDCl$_3$):** $\delta$ **[ppm]** = 163.7, 163.3, 154.8, 149.2, 143.1, 137.5, 137.2, 133.7, 130.5, 129.9, 129.3, 129.2, 128.6, 127.2, 124.9, 124.1, 122.5, 121.3, 118.1, 117.9, 84.5, 76.2, 53.9, 31.1, 29.5, 29.2, 29.0, 28.8, 26.5, 25.4, 22.5, 21.1, 13.9

**FT-IR** (cm$^{-1}$): 3306, 3259, 2960, 2923, 2858, 2100, 1699, 1657, 1590, 1405, 1330, 1258, 1094, 1018, 796.

**MALDI-TOF:** $m/z$ calculated for C$_{98}$H$_{99}$N$_2$O$_6$S$_4$ [M+H]$^+$: 1527.6386, found: 1527.620.

### 3.3.3.4. Synthesis of molecule SP1:
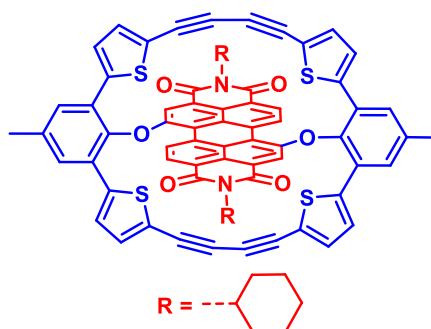
In a 250 mL two-neck round bottom flask, compound **5a** (50 mg, 41.97 µmol) was dissolved in 200 mL anhydrous THF. Then, copper (I) chloride (42 mg, 419.65 µmol) and N,N,N′,N′-tetramethylethylenediamine (98 mg, 839.30 µmol) were added dropwise to the solution of **5a**. The reaction mixture was stirred for 6 hours. The progress of the reaction was monitored by TLC. Once the reaction was completed, the mixture was poured into (3×40 mL) CH₂Cl₂ before being washed with water. The organic layer was dried over anhydrous Na₂SO₄, and then the solvents were concentrated an under reduced pressure. Product **SP1** (48 mg, 96%) was successfully obtained without purification. The compound solubility is very poor, and hence $^{13}$C cannot be recorded.

**Nature and Yield**: Red solid, 48 mg (96%).

**$^{1}$H NMR (400 MHz, CDCl₃): δ [ppm] =** 9.71 (d, $J$ = 8.9 Hz, 2 H), 8.63 (d, $J$ = 8.1 Hz, 2 H), 7.71 (s, 4 H), 7.47 (s, 2 H), 7.24 (d, $J$ = 4.0 Hz, 4 H), 6.82 (d, $J$ = 3.8 Hz, 4 H), 4.90-4.98 (m, 2 H), 2.62 (s, 6 H), 2.45-2.47 (s, 4 H), 1.87 ($J$ = 10.4 Hz, 4 H), 1.7-1.74 (s, 6 H), 1.38-1.39 (m, 6 H).

**FT-IR** (cm$^{-1}$): 2958-2851, 2155, 2108, 1697, 1653, 1593, 1512, 1451, 1325, 1261, 1161, 811.

**MALDI-TOF:** $m/z$ calculated for C₇₄H₄₇N₂O₆S₄ [M+H]$^{+}$: 1187.2317, found: 1187.11.

### 3.3.3.5. Synthesis of molecule SP2:
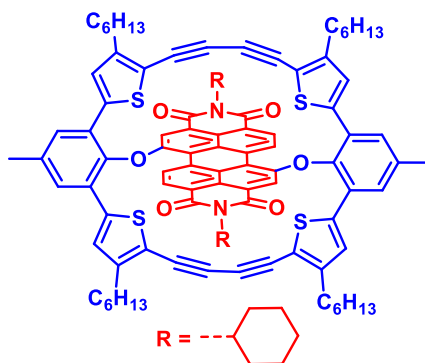


In a 500 mL two-neck round bottom flask, compound **5b** (100 mg, 65.44 µmol) was dissolved in 350 mL anhydrous THF. Then, copper (I) chloride (65 mg, 654.40 µmol) and N,N,N′,N′-tetramethylethylenediamine (152 mg, 1.31 mmol) were added to the solution of **5b**. The reaction mixtures were stirred for 12 hours and progress was monitored by TLC. Once the reaction was completed, the reaction mixture was poured into (5×40 mL) CH₂Cl₂ before being washed with water. The organic layer was dried over anhydrous Na₂SO₄, and then the solvents were concentrated an under reduced pressure. The crude product was purified by silica gel column chromatography using dichloromethane-petroleum ether (6:4 (v/v)) to yield **SP2** and **SP2D**.

**Nature and Yield**: **SP2** = Red solid, 65 mg (65%), **SP2D** = Red solid, 6 mg (3%).

**SP2:**

**$^1$H NMR (500 MHz, CDCl$_3$):** $\delta$ **[ppm]** = 9.78 (d, $J$ = 8.8 Hz, 2H), 8.64 (d, $J$ = 8.8 Hz, 2H), 7.66 (s, 4H), 7.46 (s, 2H), 7.08 (s, 4H), 4.96 (t, $J$ = 12.0 Hz, 2 H), 2.59 (s, 6H), 2.43-2.52 (m, 4 H), 2.36-2.42 (m, 8 H), 1.87 (d, $J$ = 12.6 Hz, 4 H), 1.69-1.71 (m, 6H), 1.40-1.52 (m, 12 H), 1.29-1.32 (m, 2 H), 1.19 (m, 24H), 0.80-0.85 (m, 12 H).

**$^{13}$C NMR (125 MHz, CDCl$_3$):** $\delta$ **[ppm]** = 164, 163.6, 153.3, 146.1, 142.8, 140.8, 137.2, 133.4, 130.4, 129.8, 129.1, 128.7, 128.6, 127.9, 124.7, 123.4, 122.5, 121.5, 120.2, 116.1, 84.1, 82.7, 53.7, 31.3, 30.1, 29.7, 29, 28.7, 26.5, 25.4, 22.6, 21.6, 14.

**FT-IR** (cm$^{-1}$): 2953, 2925, 2850, 2165, 2130, 1693, 1655, 1599, 1403, 1329, 1254, 1016, 801.

**MALDI-TOF:** *m/z* calculated for C$_{98}$H$_{95}$N$_2$O$_6$S$_4$ [M+H]$^+$: 1523.6073, found: 1523.56.

**Dimer (SP2D):**
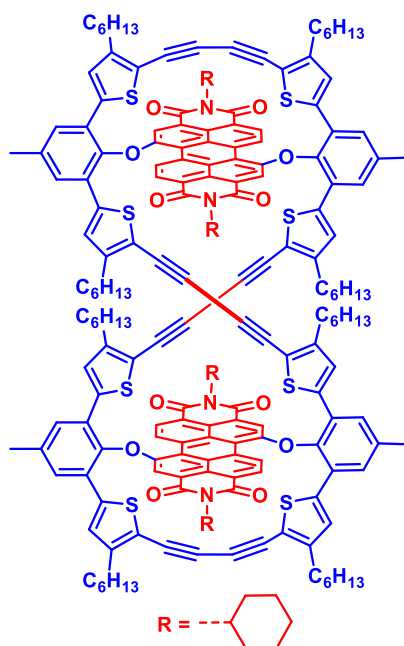


**$^1$H NMR (400 MHz, CDCl$_3$):** $\delta$ **[ppm]** = 9.84 (d, $J$ = 8.5 Hz, 2 H), 9.71 (d, $J$ = 8.5 Hz, 2 H), 8.58 (dd, $J$ = 8.4, 5.8 Hz, 4 H), 7.89 (d, $J$ = 8.4 Hz, 4 H), 7.74 (s, 2 H), 7.72 (s, 2 H), 7.52 (s, 2 H), 7.44 (s, 2 H), 7.21 (d, $J$ = 7.3 Hz, 4 H), 7.06 (s, 2 H), 6.99 (s, 2 H), 4.93 (t, $J$ = 11.4 Hz, 4 H), 2.54 (s, 12 H), 2.41-2.48 (m, 16 H), 2.25-2.35 (m, 8 H), 1.83-1.85 (d, $J$ = 10.4 Hz, 8 H), 1.66 (br. s., 12 H), 1.52 (br. s., 12 H), 1.31-1.42 (m, 12 H), 1.23 (br. s., 24 H), 1.04-1.08 (m, 4 H), 0.78-0.89 (m, 24 H), 0.67-0.76 (m, 12 H), 0.44-0.50 (m, 12 H).

**$^{13}$C NMR (125 MHz, CDCl$_3$) :** $\delta$ **[ppm]** = 163.7, 163.7, 163.5, 163.4, 155.3, 155, 151.6, 151.4, 144.8, 144.7, 142.7, 142.3, 139.6, 139.5, 139.4, 139.1, 137.1, 133.8, 133.7, 131.9,

131.4, 130.9, 130.1, 130.0, 129.9, 129.7, 129.6, 129.4, 129.2, 128.7, 128.5, 128.0, 127.9, 127.8, 127.7, 127, 126.8, 125.3, 125.2, 124.2, 124.1, 122.7, 121.6, 121.3, 119.7, 118.3, 118.2, 117.3, 117.1, 85.3, 85.2, 84.3, 81.1, 53.8 , 53.8, 31.4, 31.2, 30.2, 30.0, 29.9, 29.8, 29.8, 29.7, 29.5, 29.4, 29.4, 28.9, 28.8, 28.7, 28.5, 26.5, 25.4, 22.5, 22.2, 22.2, 21.1, 14, 13.9.

**FT-IR** (cm$^{-1}$): 2954, 2926, 2852, 2150, 2102, 1738, 1702, 1655, 1590, 1403, 1329, 1254, 1198, 750.

**MALDI-TOF:** *m/z* calculated for $C_{196}H_{189}N_4O_{12}S_8$ [M+H]$^+$: 3046.2067, found: 3046.6940 and $C_{196}H_{188}N_4NaO_{12}S_8$ [M+Na]$^+$: 3068.1887, found: 3068.1258.

## 3.4. Results and Discussion

Strapped PBI molecules are synthesized through a series of reactions, including nucleophilic aromatic substitution, Stille, Sonogashira, and Hay-Glaser coupling reactions (Scheme 3.3). Molecule **3** was successfully synthesized in quantitative yield by adapting a previously reported procedure.[23] The next reaction proceeded with triisopropyl((5-(trimethylstannyl)thiophen-2-yl)ethynyl)silane derivative without alkyl chain on the thiophene ring (**T2**, Scheme 3.1) delivered molecule **4a**  in 88% yield. Cleavage of the triisopropylsilyl group of **4a** using tetrabutylammonium fluoride delivered the free acetylene molecule **5a**, which is less stable under ambient conditions. Hence, we proceeded further with the crude for Hay-Glasear coupling reaction in the presence of CuCl and TMEDA in tetrahydrofuran in high dilution at room temperature resulting in the strapped PBI derivative **SP1** (Scheme 3.3). The Hey-Glaser coupling reaction of **5a** exclusively yielded **SP1** in 96% yield. This reaction seems faster in delivering the product within 6 h without purification. However, **SP1** is less soluble in common organic solvents, and the suspension obtained after ultrasound sonication settles down within no time. Hence we coupled 3 with ((3-hexyl-5-(trimethylstannyl)thiophen-2-yl)ethynyl)triisopropylsilane (**T6**, Scheme 3.2) to yield products **4b** and subsequently **5b**. In the case of **5b**, the subsequent reaction was slowed to 12 h for complete conversion to yield **SP2** in 65% (**Scheme 3.3**). Interestingly, we also observed the formation of a dimer **SP2D** in a very low yield (3%), trimer **SP2T**, and tetramer **SP2TT** in trace amounts exclusively when **5b** was used (**Scheme 3.3**). Both trimer **SP2T** and tetramer **SP2TT** were only characterized by MALDI-TOF-MS. Since the dimer to tetramer is formed only by **5b**, the presence of an alkyl chain on the thiophene ring plays a critical role in the formation of higher analogs. We compared the infrared spectra of **SP1**, **2**, and **SP2D** with that of **4a**, **4b**, **5a**, and **5b** to monitor the formation of diacetylene between the thiophene rings (Figure 3.1,3.2). The typical terminal alkyne (-C≡C-H) stretching frequency of **5a** and **5b**,

respectively, at 3103 cm$^{-1}$ and 3306 cm$^{-1}$, disappeared in **SP1**, **2**, and **SP2D**. It indicates the complete consumption of terminal acetylene in **5a** and **5b**. The alkyne (-C≡C-) vibration of **5a** and **5b** was recognised at 2203 cm$^{-1}$ and 2100 cm$^{-1}$, whereas the stretching frequency of the Hay-Glasear coupled symmetric and asymmetric alkynes (-C≡C-) was noticed at 2155 cm$^{-1}$, 2108 cm$^{-1}$ for **SP1**; 2165 cm$^{-1}$, 2130 cm$^{-1}$ for **SP2** and 2150 cm$^{-1}$, 2102 cm$^{-1}$ for **SP2D**, respectively (Figure 3.2).[27] Further, all the pure products were confirmed by 1H, 13C NMR, FT-IR spectroscopies, and MALDI-TOF spectrometry. Since **SP1** exhibits limited solubility in common organic solvents, we proceeded with **SP2** and **SP2D** for further detailed analysis.
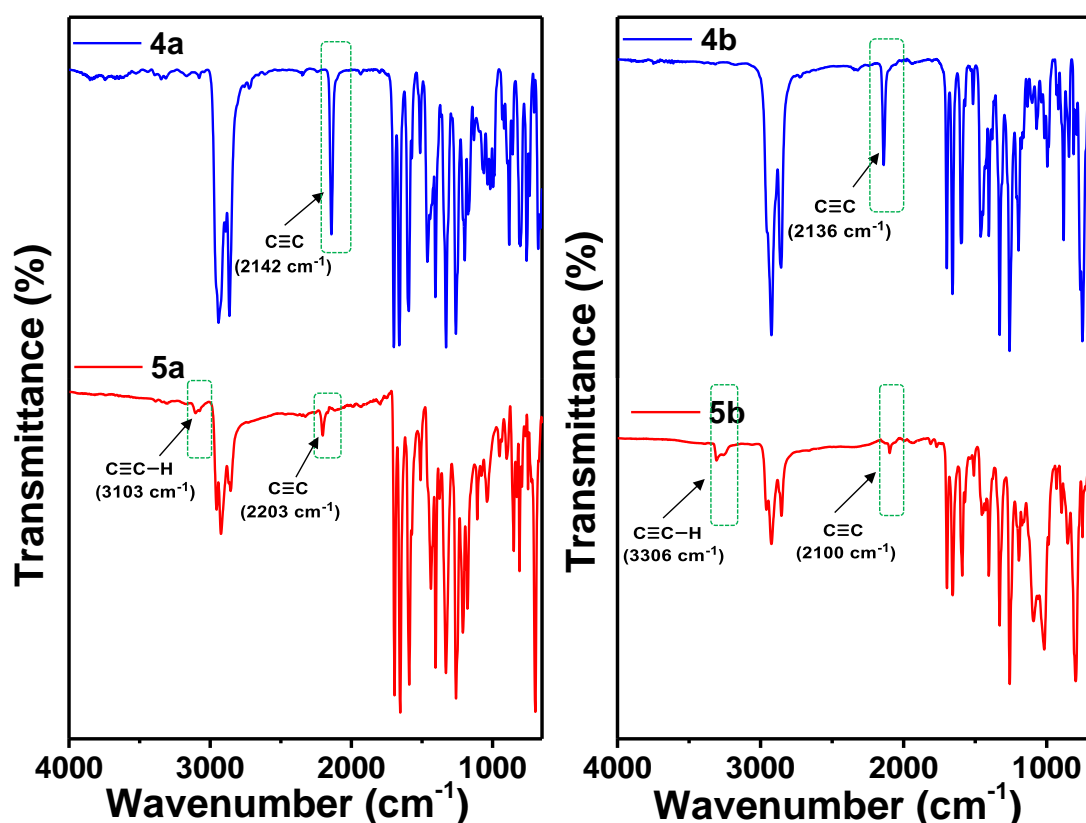


**Figure 3.1.** Comparison of the FT-IR spectra of a) **4a** and **5a**, and b) **4b** and **5b**.
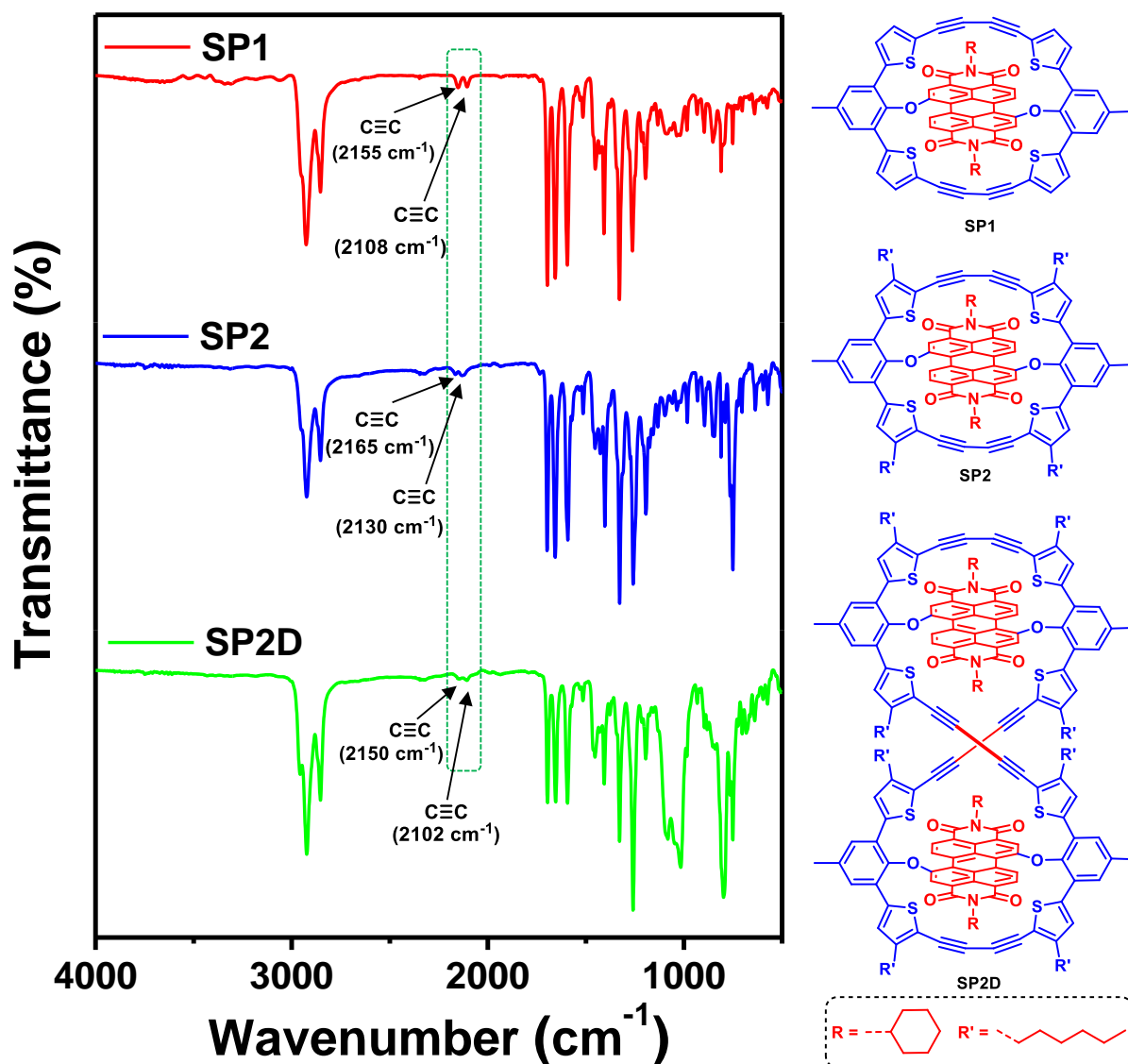
**Figure 3.2.** Comparison of the FT-IR spectra, **SP1**, **SP2**, and **SP2D** molecules.

Absorption and emission of molecules **SP2** and **SP2D** were recorded in $CH_2Cl_2$ (Figure 3.3a,b, and Table 3.5.1). Normalized absorption spectra showed ~19 nm redshift in the absorption maximum from **rPBI**[23] to **SP2** (Figure 3.3a, 3.4). A similar redshift was noticed in the case of **TSP1** as well and is due to the bay functionalization of PBI.[23] The dimer **SP2D** also retained almost the same redshift (~15 nm) in absorption maximum compared to **rPBI**. The emission of **SP2** and **SP2D** is completely quenched in $CH_2Cl_2$, and the intensity varies with solvent polarity (Figure 3.3b,c, 3.4-3.8). **SP2** exhibited slightly higher emission intensity in $CCl_4$ and *p*-Xylene, and emission was negligibly low in the rest of the solvents (Figure 3.7). Figure 3.8 shows the change in SP2's fluorescence intensity and visible color that was detected in various solvents. The normalized spectra of **SP2** and **SP2D** showed no shift in emission maxima, indicating no noticeable spectral change upon dimer formation

(Figure 3.3b). When we monitored the fluorescence lifetime, the long-lived component was increased from **rPBI** (5.1 ns (100%)), to **SP2** (6.7 ns (30%), 3.3 ns (70%) and **SP2D** (8.7 ns (26%), 3.2 ns (74%) **(Figure 3.9, Table 3.5.2)**. The electrochemical property of **SP2** was investigated using CV and DPV. These studies were conducted in $CH_2Cl_2$ ($C$ = 1 mM) using $Bu_4NPF_6$ as the supporting electrolyte. CV and DPV of **SP2** in $CH_2Cl_2$ displayed three reversible oxidation and two reversible reduction processes with half-wave oxidation potentials ($E_{1/2}$ ox) of +0.81/+1.06/+1.18 V and half-wave reduction potentials ($E_{1/2}$ red) of –1.28/–1.57 V (Figure 3.3d, 3.10 and Table 3.5.1). The observed reduction potentials have a slight shift towards the negative potential compared to **rPBI**.[23]
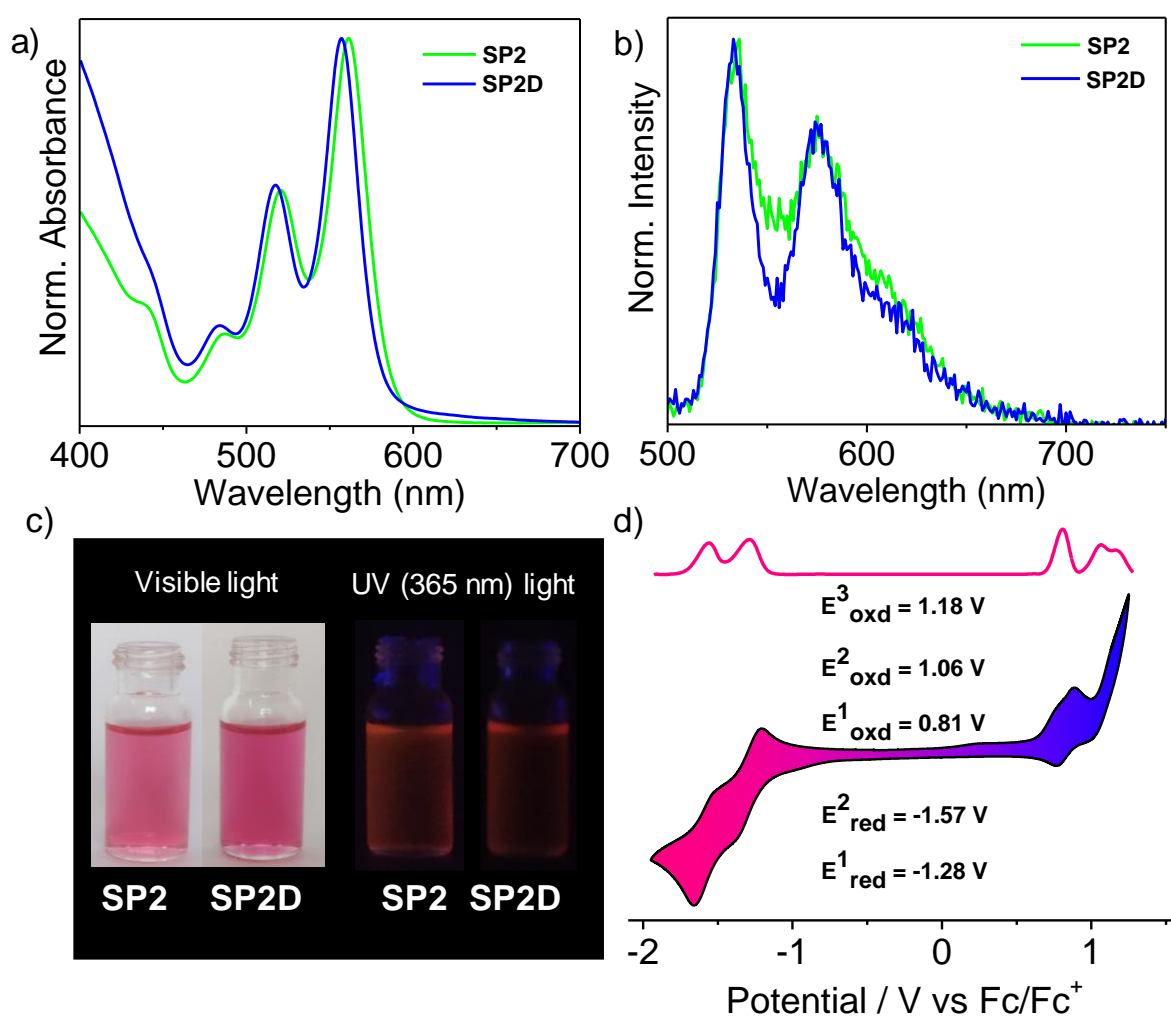


**Figure 3.3.** Normalized a) absorption and b) emission spectra of **SP2** and **SP2D** in $CH_2Cl_2$. c) Photographs of **SP2** and **SP2D** in $CH_2Cl_2$ under visible (left) and UV (365 nm) (right) lights.
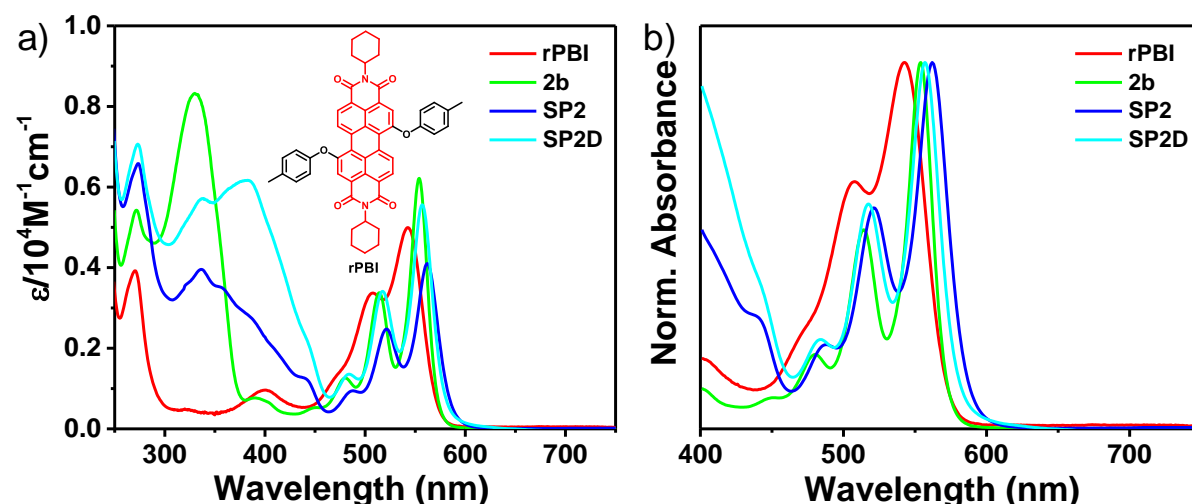
**Figure 3.4.** a) Absorption and corresponding b) normalized spectra of **rPBI**, **4b**, **SP2** and **SP2D** in $CH_2Cl_2$ solution ($C$ = 1 x $10^{-5}$ M, $l$ = 1 cm) at 25 °C. Inset shows the chemical structure of **rPBI**.
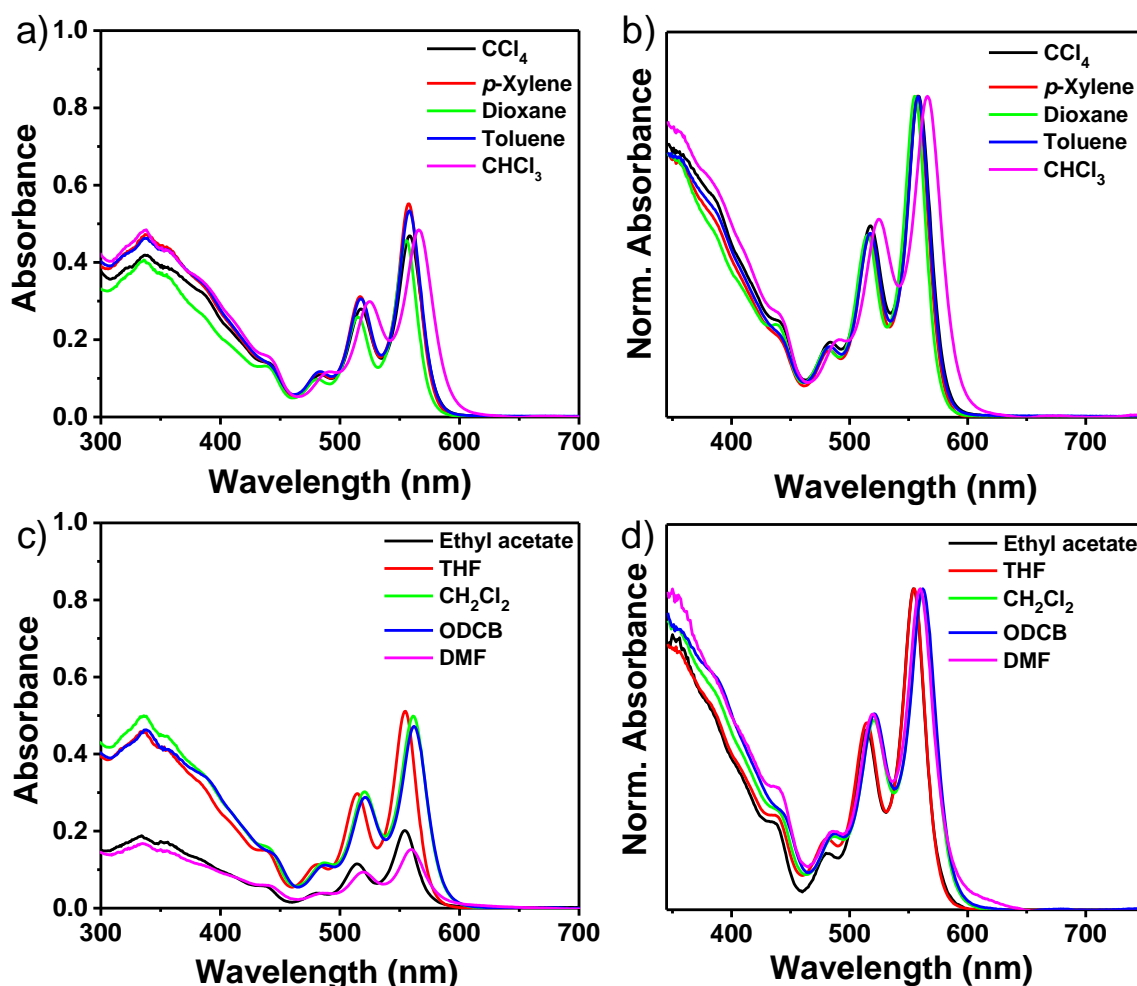


**Figure 3.5.** a) and c) Absorption and corresponding b) and d) normalized spectra of **SP2** in $CCl_4$, *p*-xylene, dioxane, toluene, $CHCl_3$, ethyl acetate, THF, $CH_2Cl_2$, ODCB, DMF solution ($C$ = 1 x $10^{-5}$ M, $l$ = 1 cm) at 25 °C.
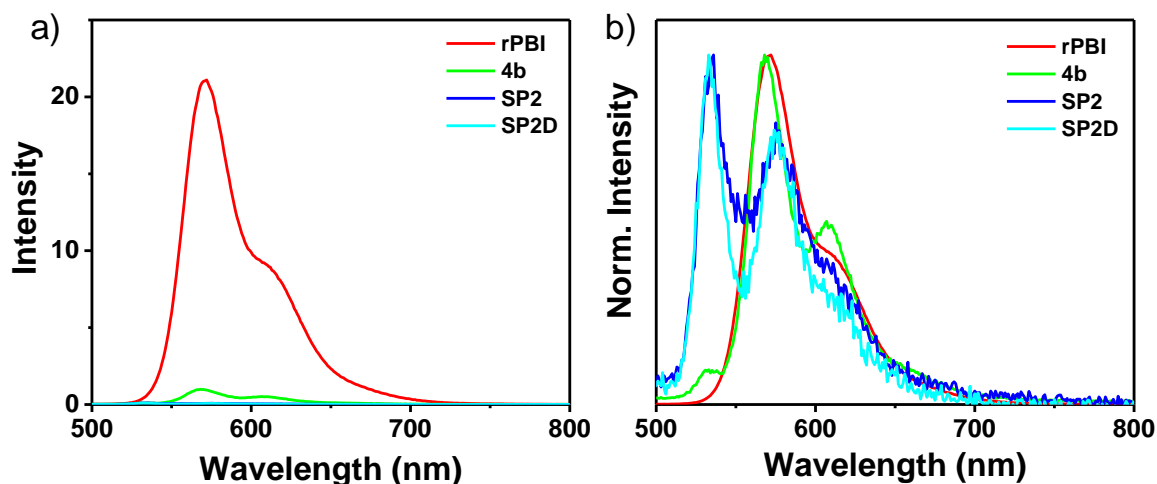
**Figure 3.6.** a) Steady-state emission and corresponding b) normalized spectra of **rPBI**, **4b**, **SP2** and **SP2D** in $CH_2Cl_2$ solution ($C$ = 1 x $10^{-5}$ M, $l$ = 1 cm) at 25 °C ($\lambda_{ex}$ = 460 nm for **rPBI**, 480 nm for **4a**, and 480 nm for **SP2** and **SP2D**).
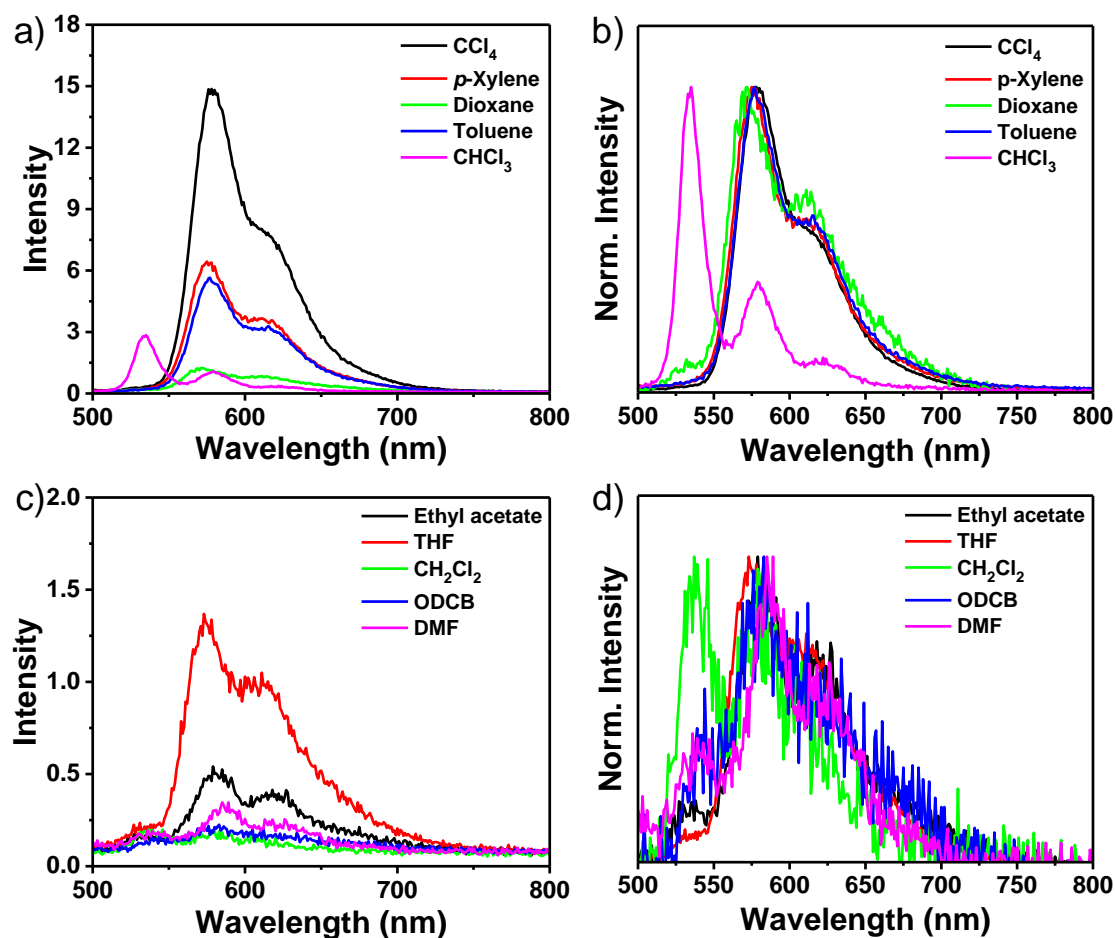


**Figure 3.7.** a) and c) Steady-state emission and corresponding b) and d) normalized spectra of **SP2**, ($C$ = 1 x $10^{-5}$ M, $l$ = 1 cm) at 25 °C ($\lambda_{ex}$ = 480 nm for **SP2** in $CCl_4$, *p*-xylene, dioxane, toluene, ethyl acetate, THF, 485 nm for **SP2** in $CH_2Cl_2$, ODCB, DMF and 490 nm for **SP2** in $CHCl_3$ solvent).
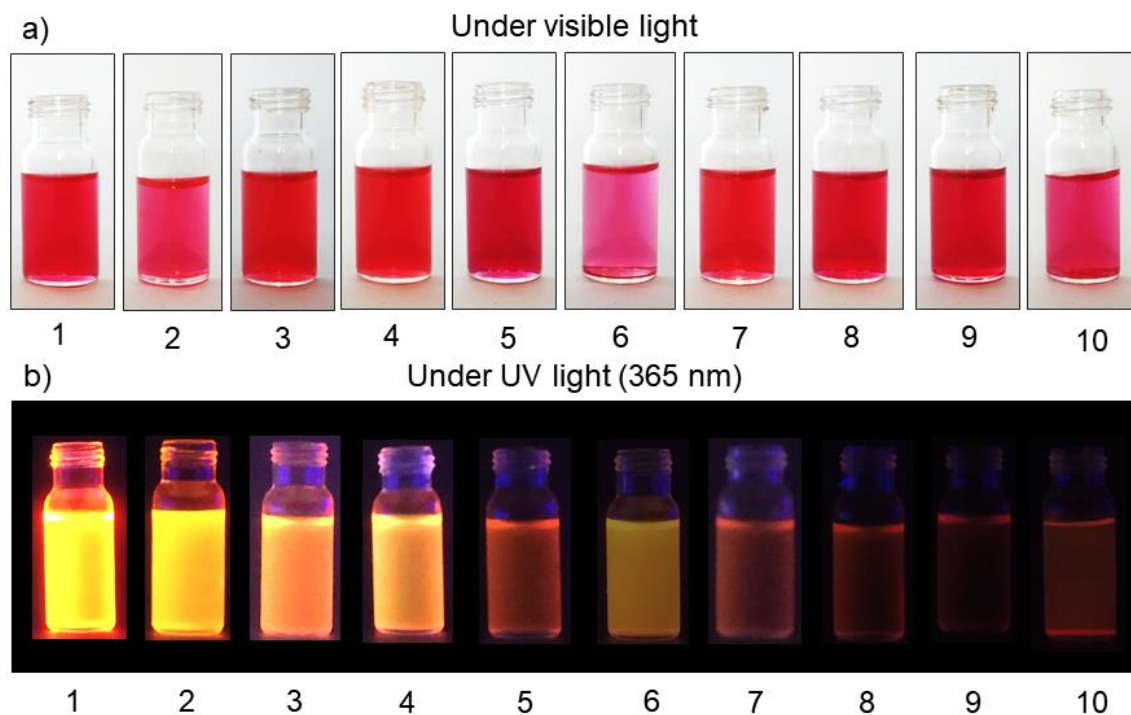
**Figure 3.8.** Photographs of **SP2**, a) visible and b) UV (365 nm) light in 1. CCl₄, 2. *p*-xylene, 3. dioxane, 4. toluene, 5. CHCl₃, 6. ethyl acetate, 7. THF, 8. CH₂Cl₂, 9. ODCB, 10. DMF.
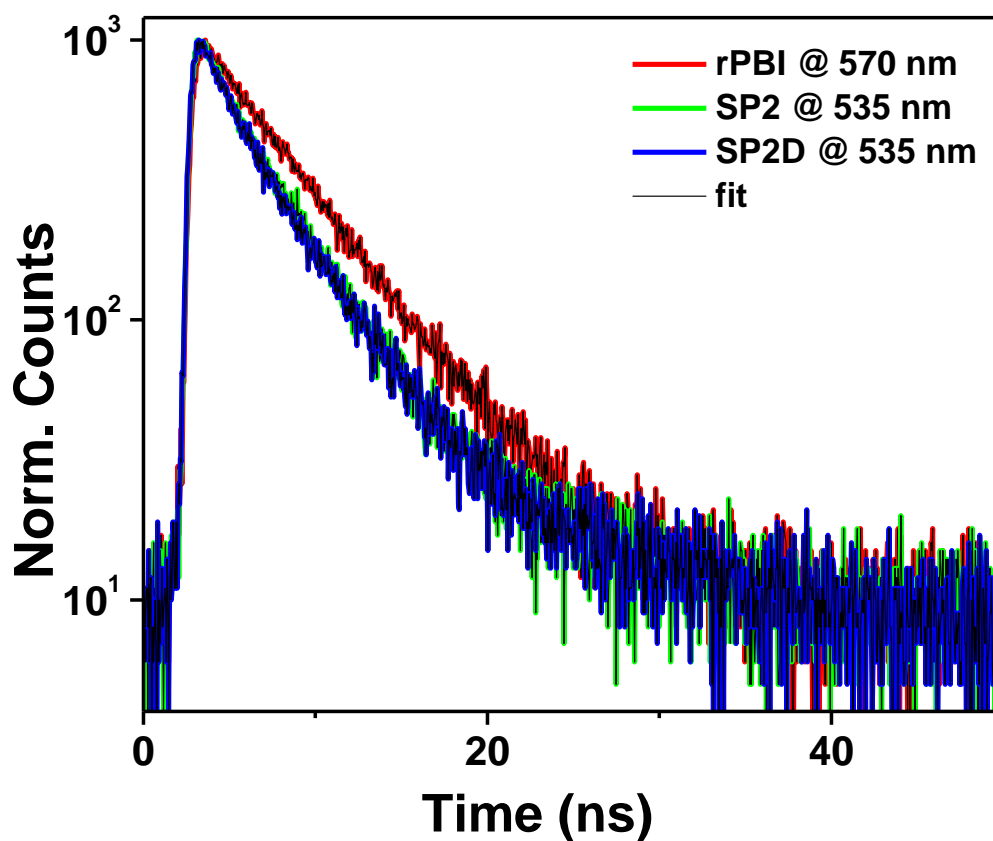


**Figure 3.9.** Fluorescence lifetime decay profile of **SP2** and **SP2D** in CH₂Cl₂ ($C = 1 \times 10^{-5}$ M, $\lambda_{ex}$ = 448 nm).
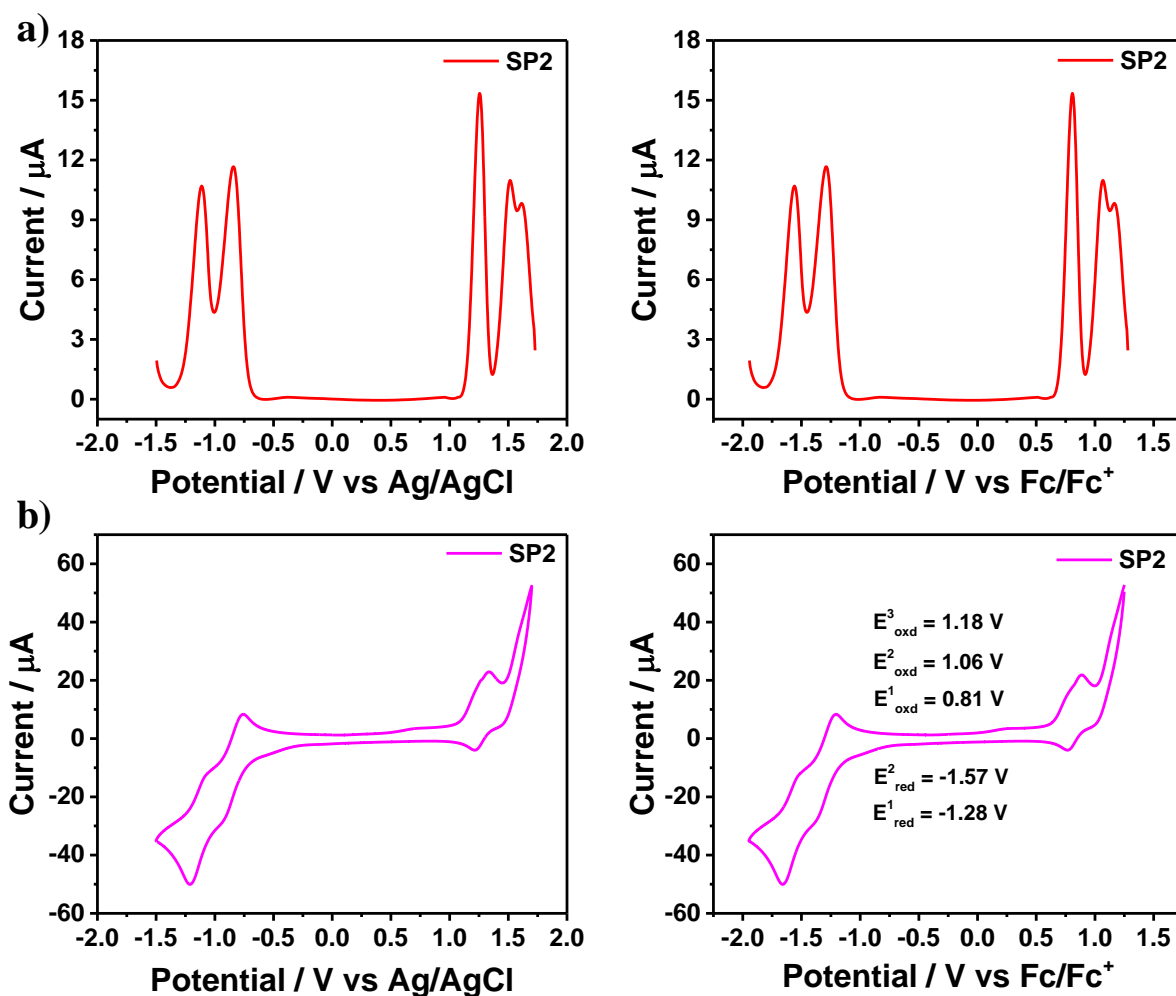
**Figure 3.10.** a) DPV measurements at 100 mV/s scan rate (left) and calculated as Ferrocene as the internal reference standard ($E_{Fc+/Fc}$ = 0.00 V) (right) of **SP2** (1mM). b) CV at 100 mV/s scan rate (left) and CV calculated as Ferrocene as the internal reference standard ($E_{Fc+/Fc}$ = 0.00 V) (right) of **SP2** (1mM).

In order to understand the difference in reactivity of **5a** and **5b**, crystallization of **4a** and **4b** was attempted from the solvent mixtures $CH_2Cl_2$:MeOH (v/v; 50:50) and $CH_2Cl_2$:*n*-hexane (v/v; 50:50), respectively. The single crystal structure of **4a** (CCDC: 2247679) and **4b** (CCDC: 2247688) showed a marked difference in the orientation of the thiophene arm containing TIPS acetylene moieties. In **4a**, the absence of an alkyl chain on the thiophene ring enabled the direction of the arms in a supportive way for ring closure using diacetylene linkage (Figure 3.11a, 3.12). However, in **4b**, the presence of an additional $C_6$-alkyl chain on the thiophene moiety changed the orientation of the thiophene rings. Interestingly, all four thiophene rings protrude outwards (Figure 3.11b, 3.13). It could be due to the hydrophobic interactions between the alkyl chains, which are stacked over each other. The methylene

groups on the alkyl chains also participate in a marginal C-H…π interaction involving the central **PBI** moiety. These supramolecular interactions seem to be stabilizing the crystal structure. Such outward orientation of thiophene moieties could slow the macrocyclization of **SP2**, resulting in the formation of corresponding dimer **SP2D** and higher analogs, trimer **SP2T** and tetramer **SP2TT**. The crystal structure of **SP2** (CCDC: 2247690) is confirmed by single crystal structure analysis. Needles of **SP2** were grown from the mixture of solvents, CHCl$_3$:MeOH (v/v, 50:50) (Figure 3.11c). The intra-molecular geometry of **SP2** revealed that the **PBI** unit is perpendicular (86.38°) to the strapped thiophene ring (Figure 3.11c). The presence of hydrogen bonding, >C=O···H, between adjacent **PBI** units parallel to the a-axis generates a one-dimensional molecular string comprising **SP2** molecules (Figure 3.14). The adjacent 1D strings are linked along the b-axis using >C=O···H hydrogen bonds involving >C=O of PBIs and H atoms of the macrocycle unit to form a compact packing on the ab plane.
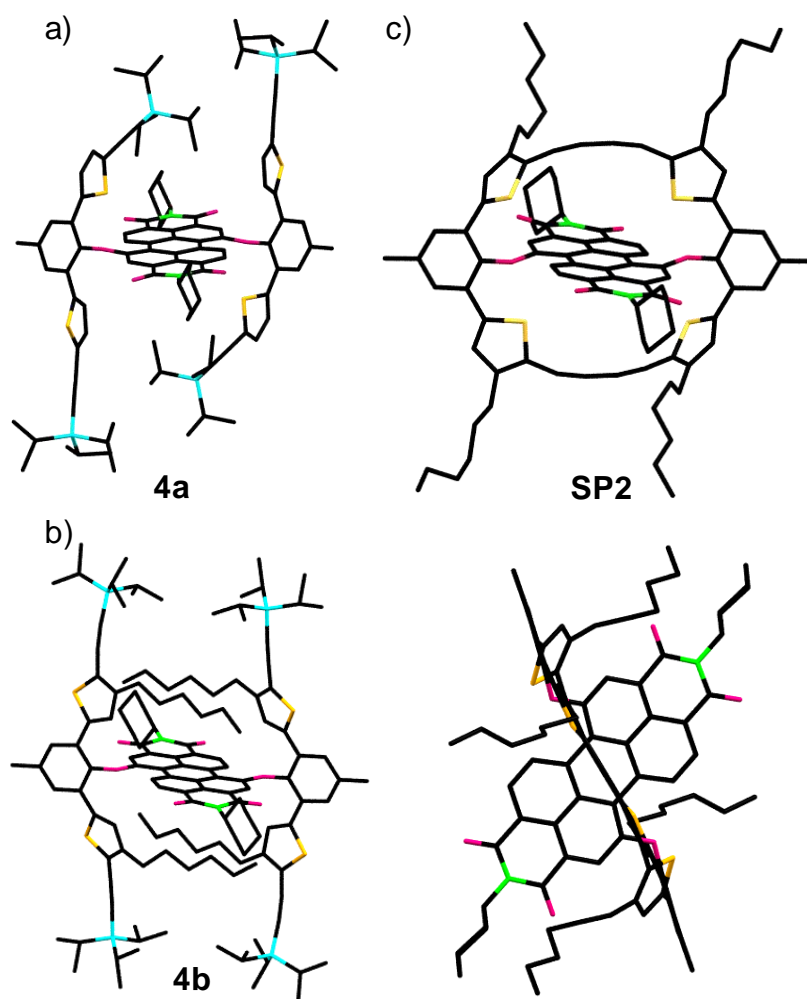


**Figure 3.11.** Crystal structure of a) **4a**, b) **4b**, and c) **SP2**. Hydrogen atoms are removed for clarity.
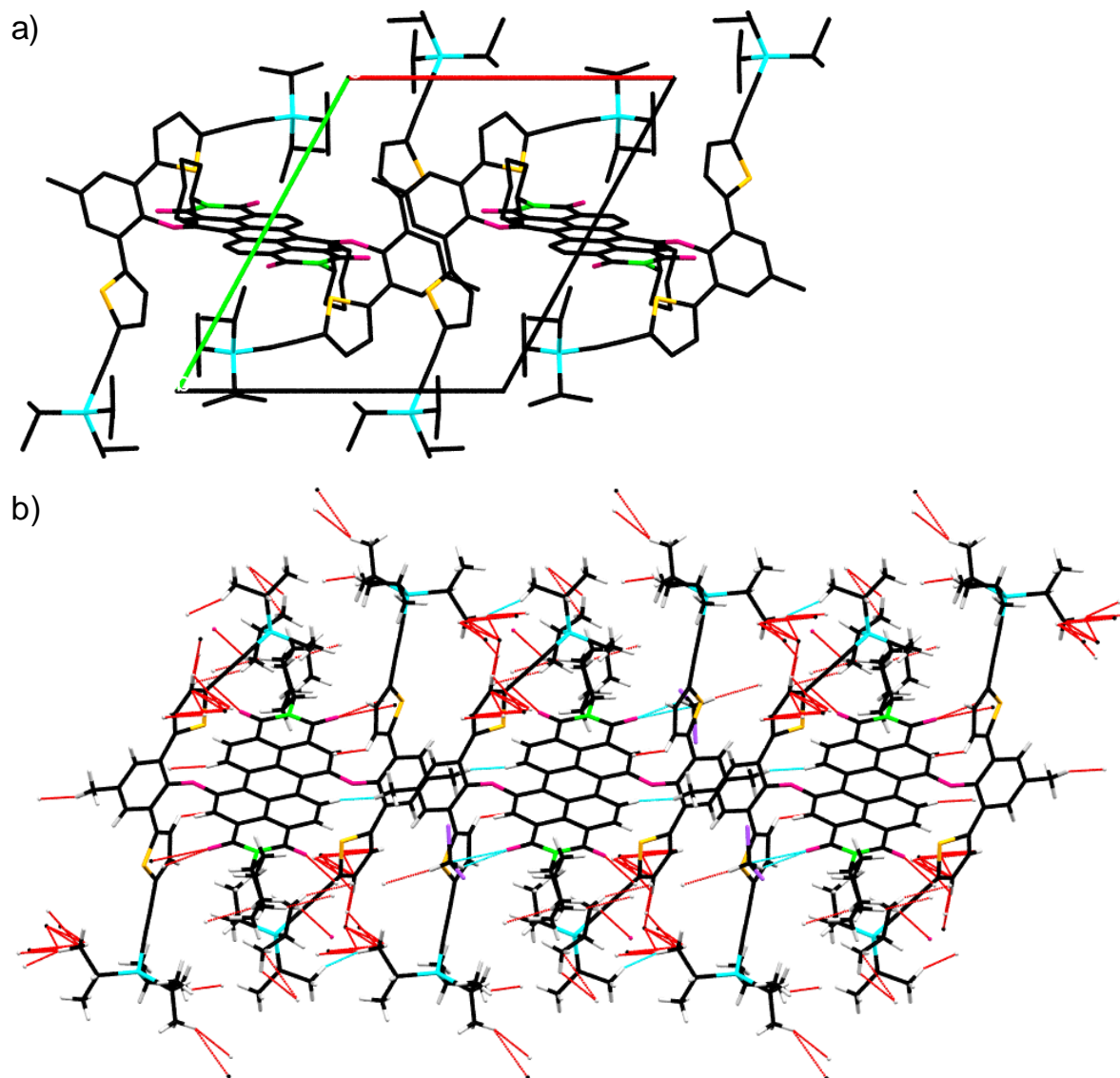
**Figure 3.12.** a) Unit cell of **4a** consists of 2 molecules. b) Extended molecular packing of **4a** using various noncovalent interactions.

a)



b)
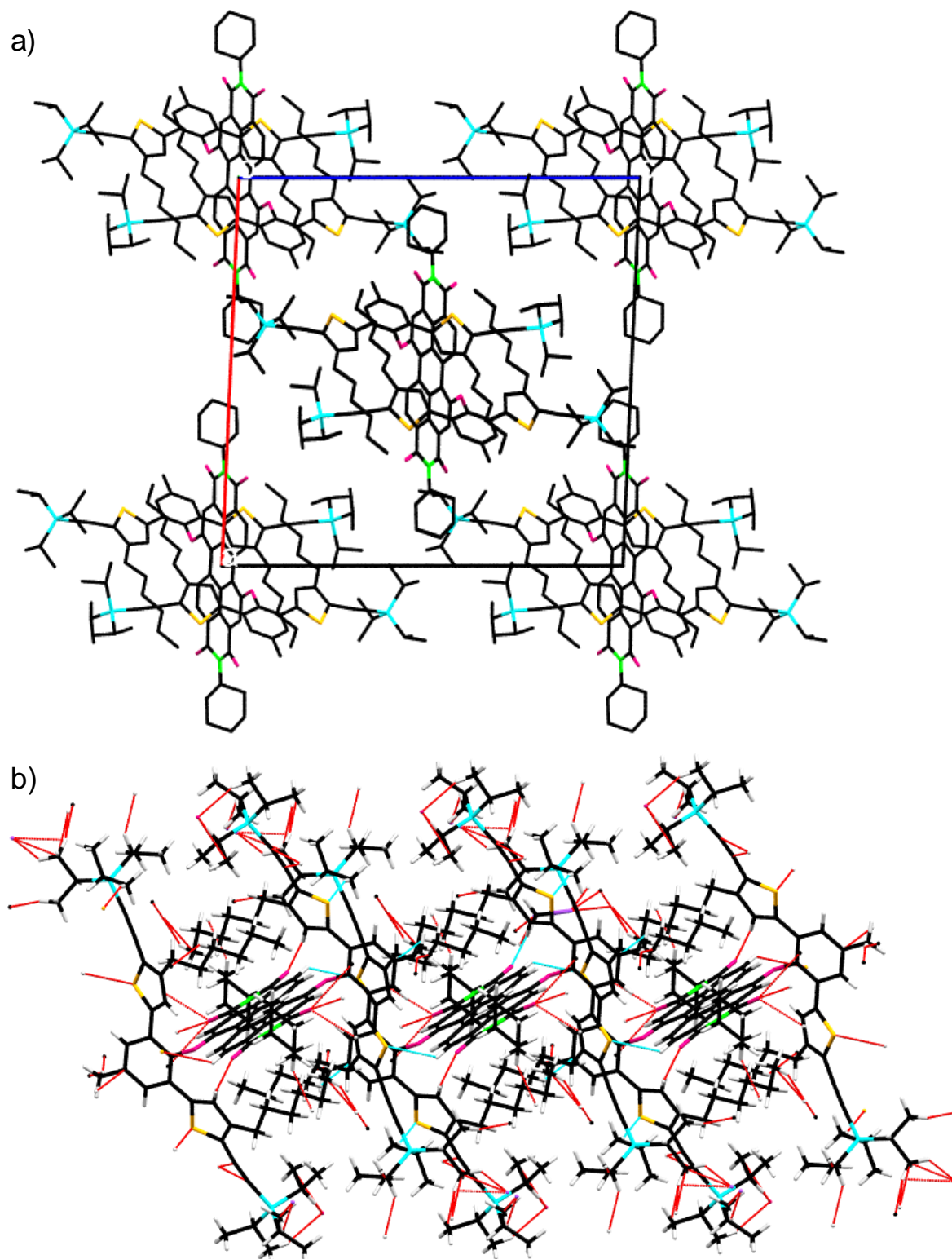


**Figure 3.13.** a) Unit cell of **4b** consists of 6 molecules. b) Extended molecular packing of **4b** using various noncovalent interactions.
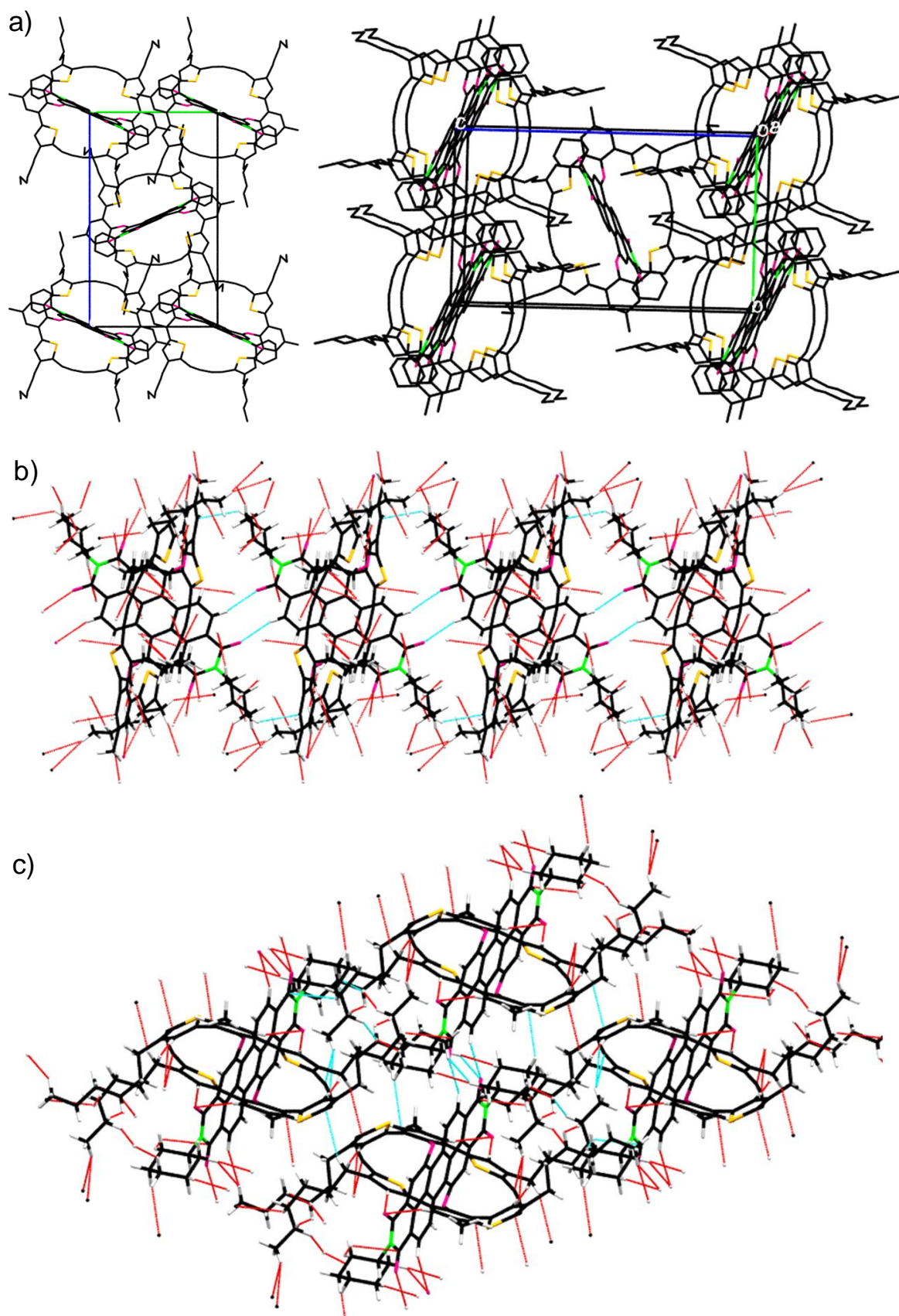
**Figure 3.14.** a) The unit cell of **SP2** consists of 9 molecules. b) and c) Extended molecular packing of **SP2** using various noncovalent interactions.

A comparison of 1H NMR spectra of **SP2** and **SP2D** showed a doubling of signals from the PBI unit in **SP2D** (Figure 3.15, 3.16). The aromatic signals from the thiophene-diacetylene unit show further splitting of signals indicating molecular symmetry breaking during dimer formation. Extra signals resulting from dimerization are also observed in 13C spectra (Figure 3.17-3.19). Dimer formation was confirmed by comparing diffusion-ordered spectra of **SP2** and **SP2D** measured under identical conditions (Figure 3.20a). The diffusion of **SP2D** is almost twice as slow as that of **SP2**, as expected for a dimer (Figure 3.20a). On the other hand, the solvent diffusion coefficient does not change significantly, indicating identical conditions in the two measurements. Dimer formation results in distinct environments for both alkyl and aromatic protons. Correlations observed in the total correlation spectroscopy (TOCSY) clearly show distinct connectivities between protons belonging to different environments observed in the dimer (Figure 3.20b, 3.21,3.22). This was subsequently confirmed by 1H-13C heteronuclear multiple bond correlation (HMBC) and heteronuclear single quantum coherence (HSQC) experiments (Figure 3.23). Signals from different environments show unique correlations in 2D rotating frame overhauser effect spectroscopy (ROESY) and nuclear overhauser spectroscopy (NOESY) spectra (Figure 3.20c, 3.24,3.25). For example, protons d1, d4 correlate strongly with e1, e4 indicating their mutual proximity, while d2, d3 protons are close to e2, e3, thus representing distinct environments. While the loss of symmetry during dimerization results in non-degenerate signals for all protons in **SP2D**, the outer diacetylene-thiophene ring protons "d" and "e" show further chemical shift distinctions.

This implies that the outer ring partially twists into a nearly "8" shape. The two halves of the diacetylene-thiophene ring are aligned at an angle with respect to each other to eliminate steric effects from the long alkyl chains. Dimerization and a tilt in the orientation of the two halves of the outer ring result in four distinct signals for "d" and "e". The structure of **SP2D** inferred on the basis of NMR data (Figures 3.16-3.25) agrees with the optimal geometry determined from DFT calculations, shown in Figure 3.20d. Calculations show that the two halves of the diacetylene-thiophene ring are twisted with respect to each other, and the "dimer-forming" diacetylene links are separated by ~7.3 Å. Variable temperature 1H NMR spectra of **SP2D** revealed that signals corresponding to different environments arising from dimerization do not undergo significant chemical shift or linewidth changes, indicating that the dimer conformation is reasonably stable (Figure S24).
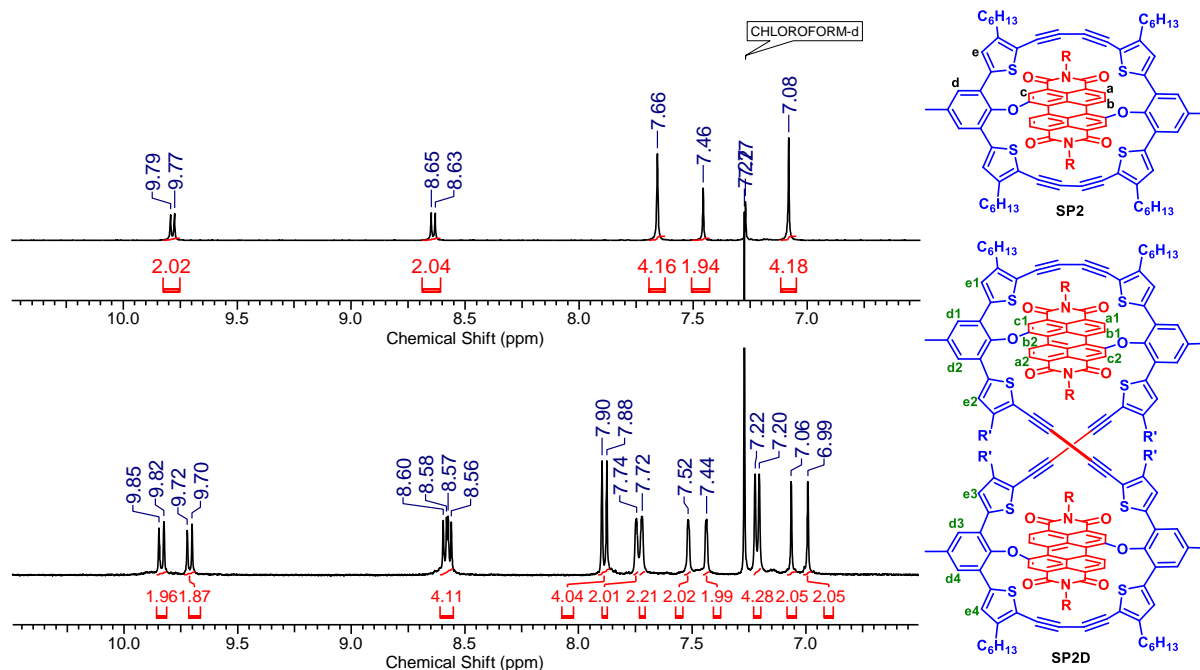
**Figure 3.15.** Comparison of the aromatic region of **SP2** and **SP2D** ^{1}H NMR spectra.
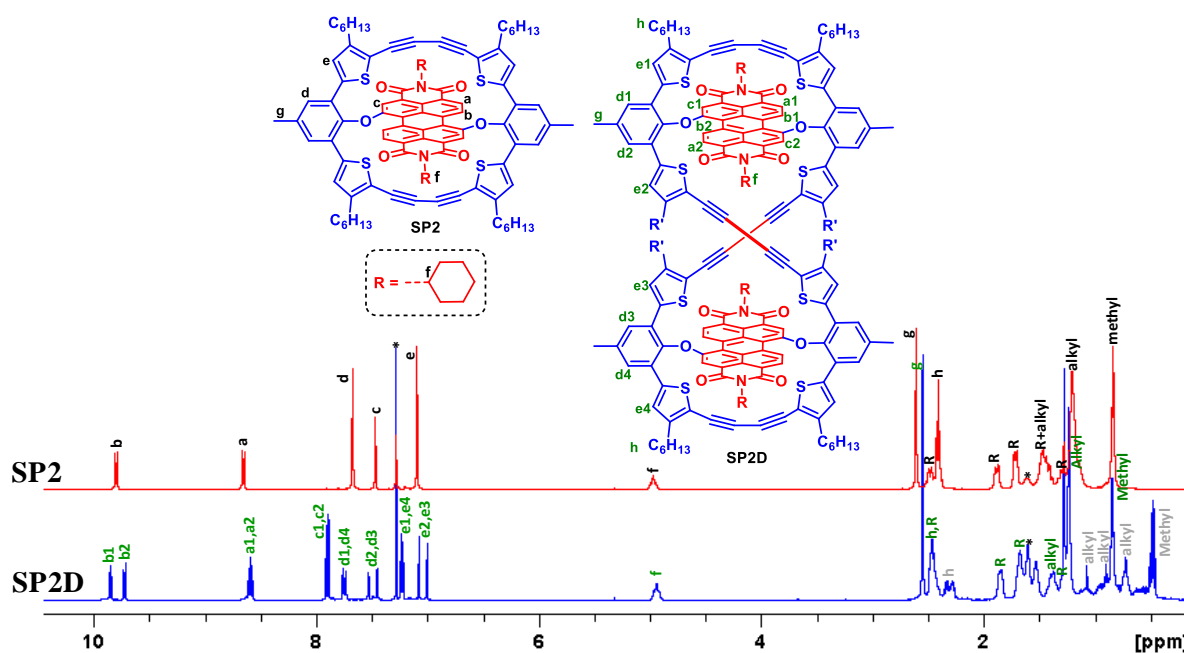


**Figure 3.16.** Comparison of ^{1}H NMR spectra of **SP2** (red) and **SP2D** (blue) recorded at 298K. All signals show doubling in **SP2D,** which implies that different environments are generated due to molecular symmetry breaking due to dimer formation. Grey labels mark additional environments in the alkyl chain of SP2D. Cyclohexyl ring "CH2" protons are labelled R. Solvent (CDCl₃) and asterisks indicate residual water signals.
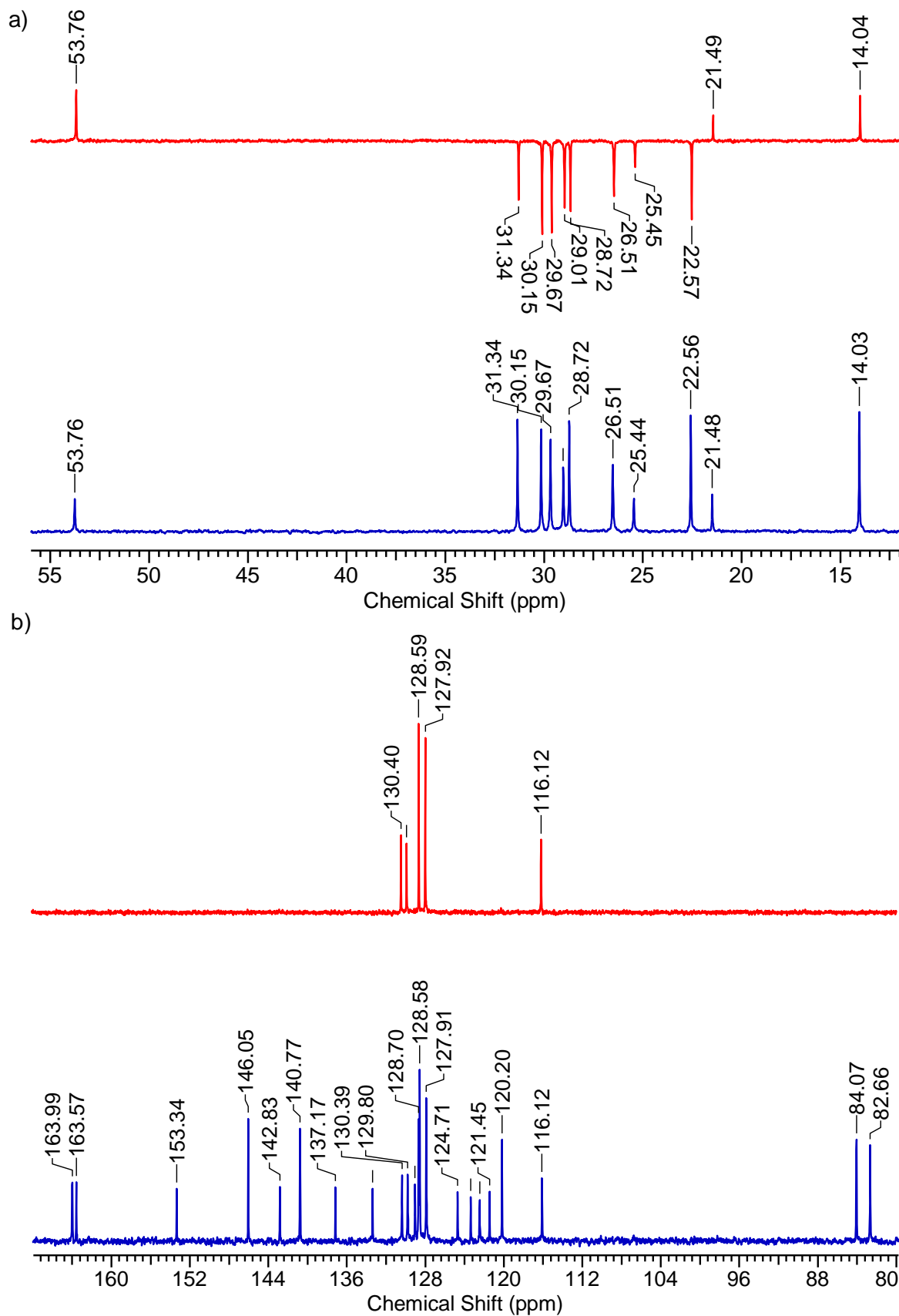
**Figure 3.17.** [13]C (blue) and DEPT (red) spectra of **SP2** recorded at 298 K, a) spectra range from 12 to 56 ppm, and b) spectra range from 80 to 165 ppm.
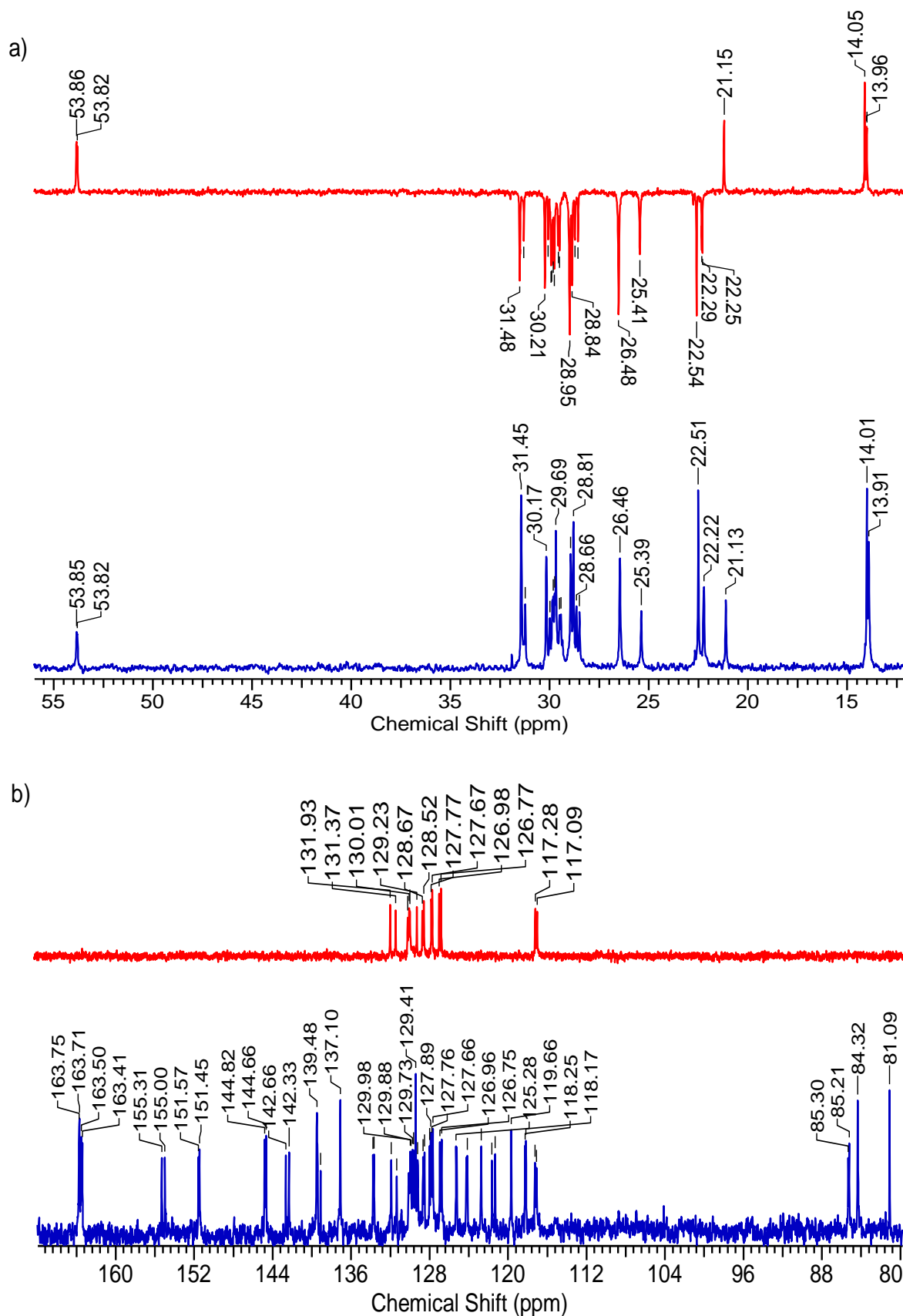
**Figure 3.18.** $^{13}$C (blue) and DEPT (red) spectra of **SP2D** recorded at 298 K, a) spectra range from 12 to 56 ppm, and b) spectra range from 80 to 165 ppm.
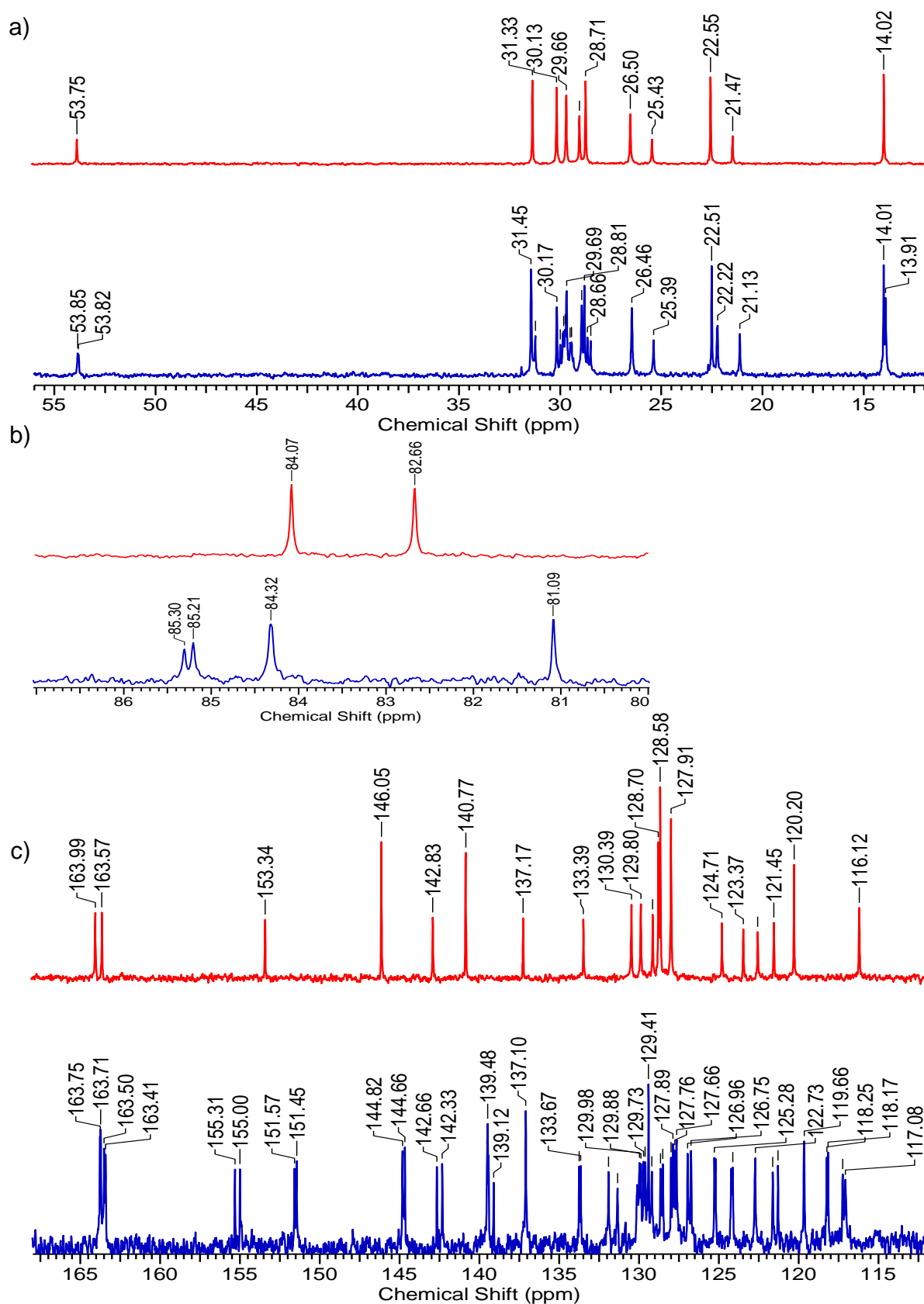
**Figure 3.19.** $^{13}$C spectra of **SP2** (red) and **SP2D** (blue) recorded at 298 K, a) spectra range from 12 to 55 ppm, b) spectra range from 80 to 87 ppm, and c) spectra range from 112 to 168

ppm. Extra signals corresponding to additional environments caused by dimerization are observed in **SP2D**.
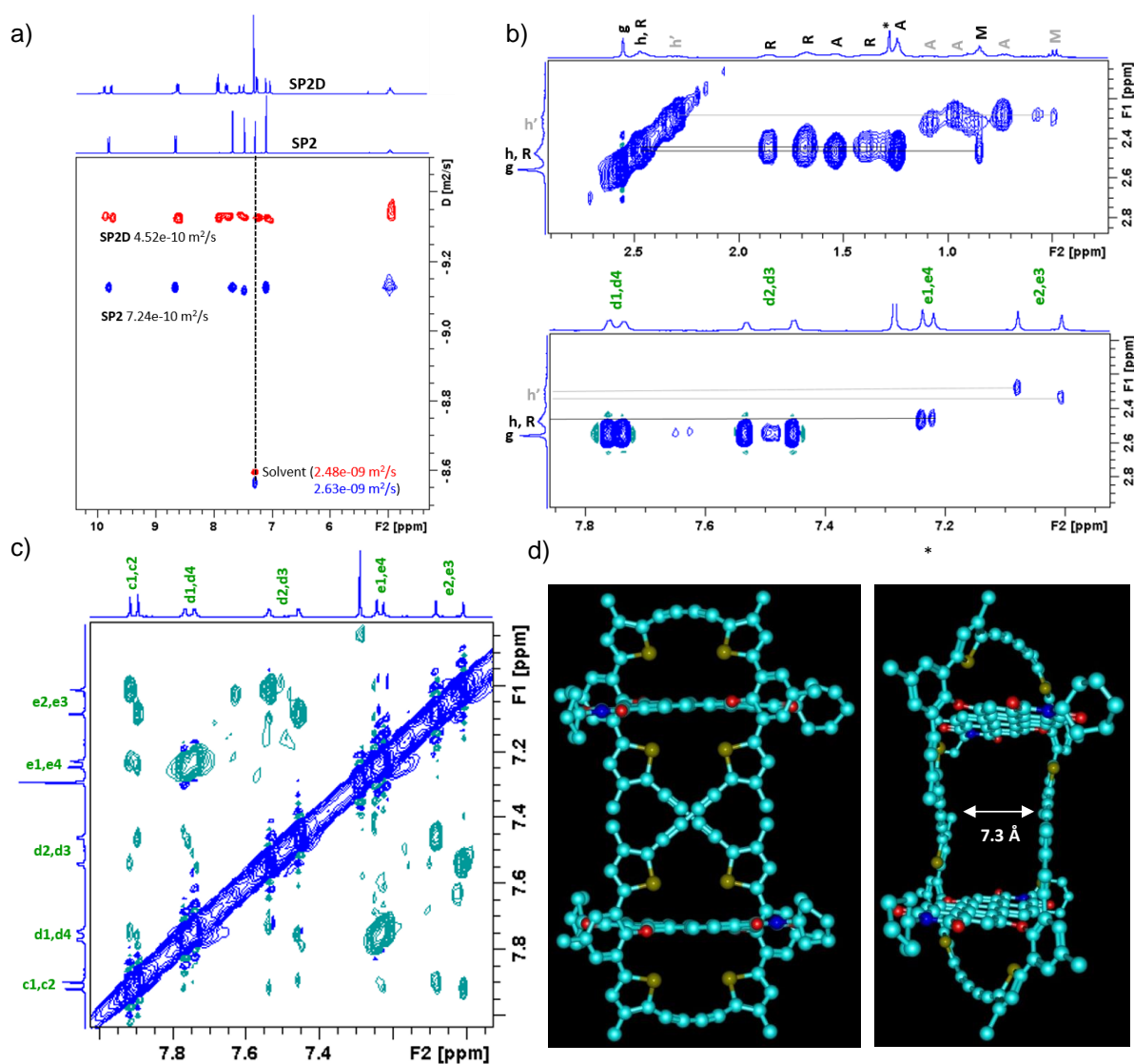


**Figure 3.20.** a) Comparison of the aromatic region of diffusion ordered spectra of **SP2** (blue) and **SP2D** (red) at 298 K with an overlay of 1H NMR spectra on top. b) Regions from TOCSY spectrum of **SP2D** showing distinct correlations between protons belonging to different environments. c) Aromatic proton correlations in ROESY spectrum of **SP2D**. Cyclohexyl ring protons and methyl/methylene protons of the alkyl chain are labeled R and M/A, respectively. Signal labeling is the same as in Figure 3.16. Grey labels refer to additional alkyl proton environments arising from dimer formation, while additional aromatic proton signals are indicated explicitly by numerals. Residual solvent and water signals are marked by asterisks. d) Optimized structure showing the geometry of **SP2D** by DFT calculation, alkyl chain, and hydrogens are avoided for clarity.
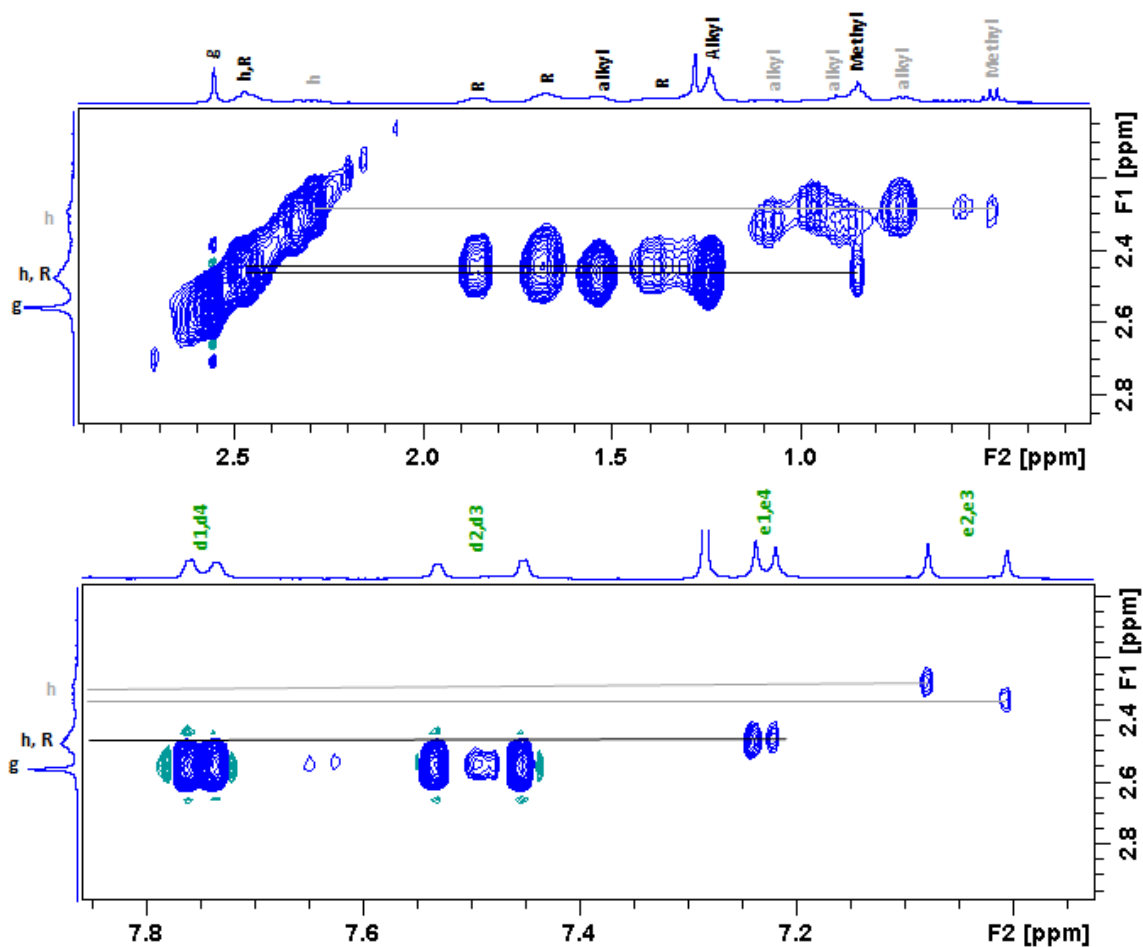
**Figure 3.21.** Regions from the TOCSY spectrum of **SP2D**. The unique correlations for different environments arising from dimerization and twisting of the outer ring are indicated in grey and black.
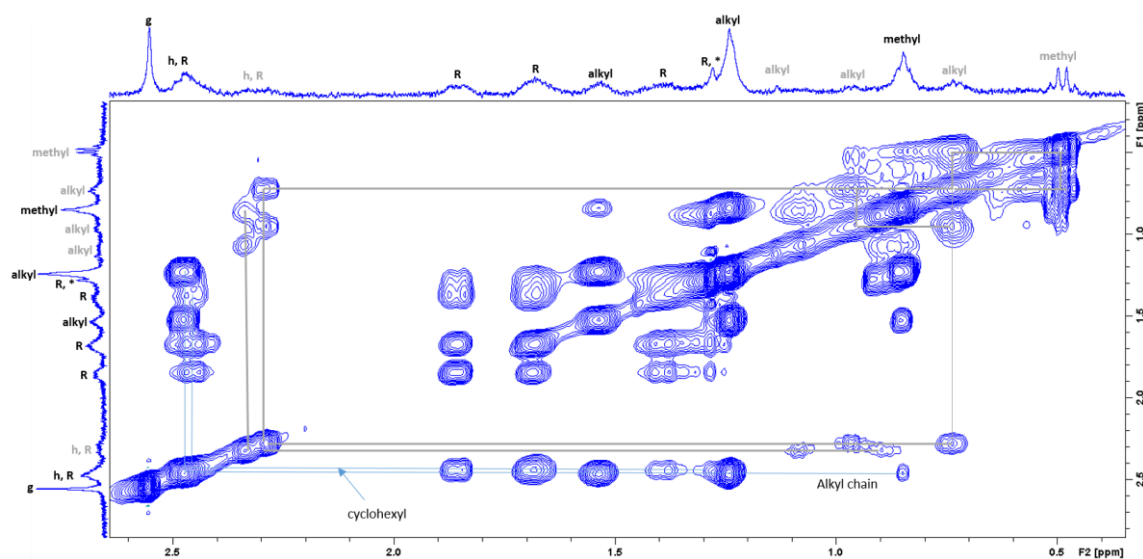


**Figure 3.22.** Alkyl region of TOCSY spectrum of **SP2D** showing aliphatic and cyclohexyl correlations. 1D traces at the top and left are from diffusion experiments where the intensity

of residual water signal from the solvent is attenuated. Cyclohexyl ring protons are labelled R. Grey labels refer to additional alkyl proton environments arising from dimer formation.
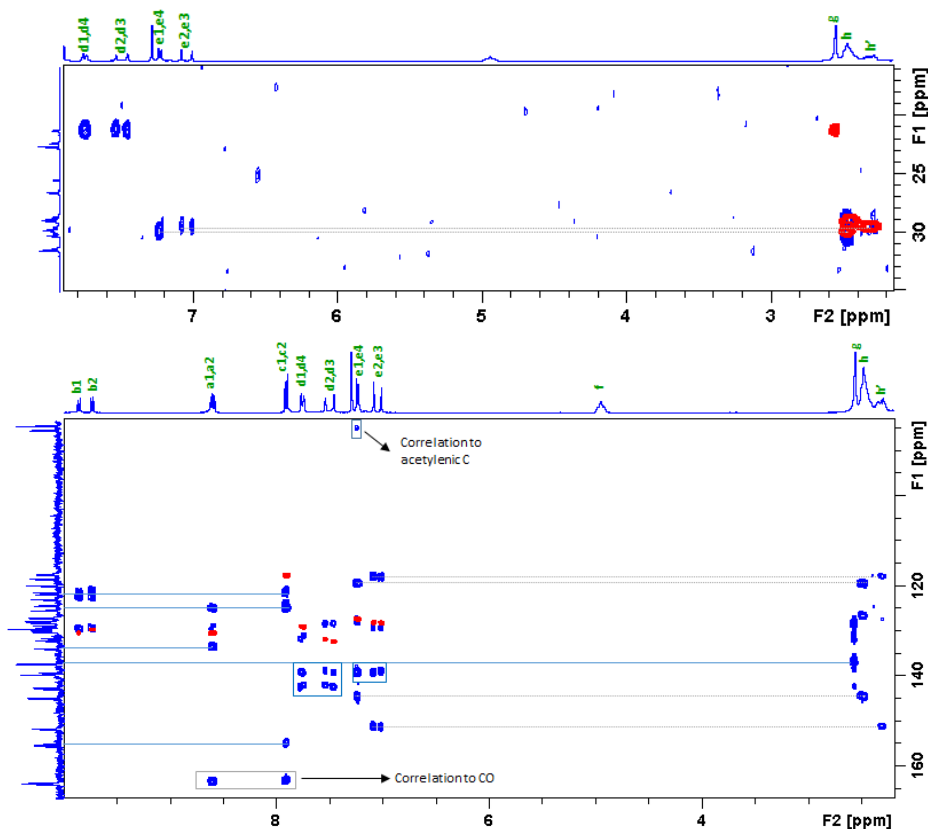


**Figure 3.23.** Overlay of $^1$H-$^{13}$C HSQC (red) and HMBC (blue) spectra of **SP2D**. Non-equivalent alkyl chain protons correlating to different sets of aromatic *e* protons (grey lines) are labelled *h* and *h'*. Blue boxes/lines indicate correlations to quaternary carbons.
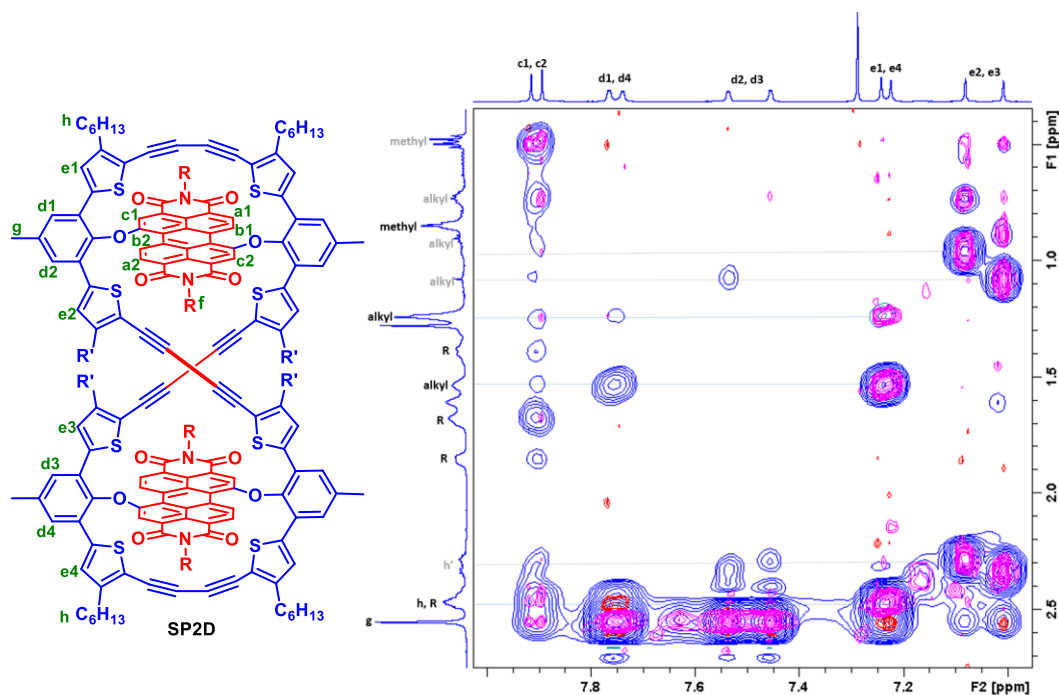
**Figure 3.24.** Overlay of NOESY (blue) and ROESY (magenta) spectral regions of **SP2D** showing aromatic to aliphatic proton correlations. Cross-peaks connect pairs of aromatic and aliphatic protons corresponding to different environments arising as a result of dimerization. Cyclohexyl ring protons are labelled R. Grey labels refer to additional alkyl proton environments arising from dimer formation, while numerals specifically indicate additional aromatic proton signals.
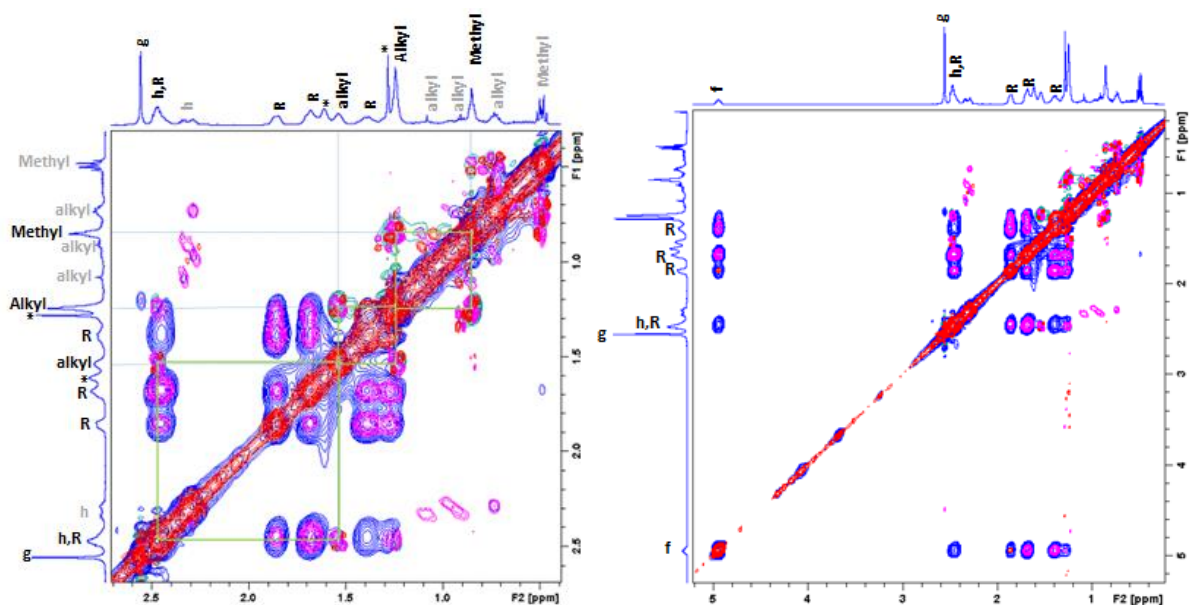


**Figure 3.25.** Overlay of NOESY (blue) and ROESY (magenta) spectral regions of **SP2D** showing aliphatic (left) and cyclohexyl (right) correlations. Grey labels correspond to alkyl proton signals which arise due to the non-degeneracy of chemical shifts induced by dimerization. Weak cross-peaks are observed between these protons, indicating alkyl chains with a different orientation. The data supports the geometry of **SP2D** shown in Figure 3.20d.

These macromolecular systems' excited state electron transport kinetics require further analysis in order to be completely understood, femtosecond transient absorption spectroscopy (FTAS) was utilized in the $CH_2Cl_2$ solutions of **SP2** and **SP2D**. Figure 3.26a,b represents the visible range FTAS spectra of these two systems after 460 nm pump excitation. Both spectra are very similar, having two ground-state bleach features at 525 and 565 nm and a strong signal of photoinduced absorption at the red region peaking around 730 nm. These spectra are very different from the pristine **rPBI** system (Figure 3.27), where a sharp positive signal owing to the S1-Sn transition dominates the spectra. On the contrary, macrocycles possess very different and broad positive signals, which must arise from the formation of the acceptor radical anion and donor radical cation.[28-30] The dynamic profile of **SP2** and **SP2D** were plotted in Figure 3.26c, monitoring at the maximum peak position. Multiexponential time

components were applied to these profiles, which are listed in Table 3.5.3. The rise time of **SP2** was found to be substantially enhanced than the **SP2D** system. As this positive signal signifies the formation of the PBI radical anion, in these donor-acceptor systems, we can designate this rising time as the CS time scale ($\tau$CS).[28] From the fitting data, $\tau_{CS}$ were calculated to be 2.7 and 8.4 ps, corresponding to electron transfer rate constants of $0.4 \times 10^{12}$ $S^{-1}$ and $0.1 \times 10^{12}$ $S^{-1}$ for **SP2** and **SP2D**, respectively. Hence, the CS process is slower in **SP2D** than in **SP2**.
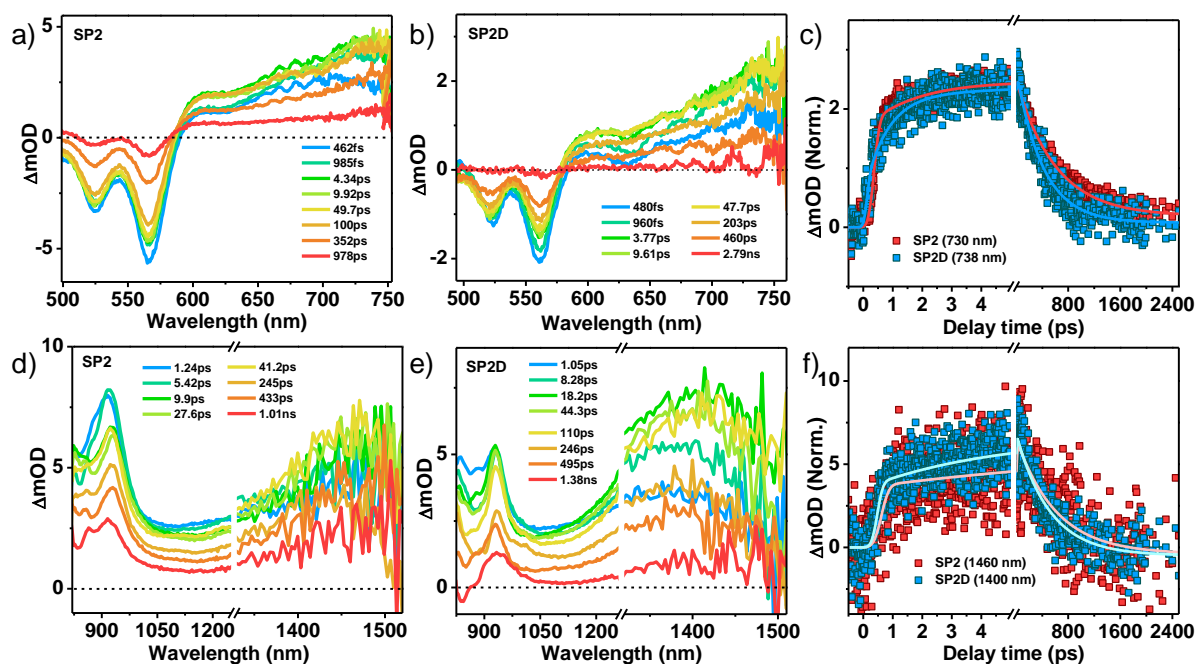


**Figure 3.26.** FTAS spectra of a) **SP2** and b) **SP2D** in the visible region following the photoexcitation at 460 nm (left) and NIR region after the laser excitation at 420 nm (right). c) Normalized kinetic profiles of the radical anions in **SP2** and **SP2D** monitoring at 730 and 738 nm, respectively. d) Normalized kinetic profiles of the oligothiophene radical cation in **SP2** and **SP2D** monitoring at 1460 and 1400 nm, respectively.

Next, we plotted the FTAS spectra of these two systems by monitoring the NIR region (820-1520 nm) after 420 nm photoexcitation (Figure 3.26d,e). These spectra are comprised of two distinct positive features, one around 930 nm and another around 1400 nm. The 930 nm signature closely resembles the sharp positive signal observed in **rPBI** (Figure 3.27). As this signal appears in the **rPBI** molecule, it cannot be any radical or anionic signature, it must originate from the excited state absorption from the S1 state of PBI.[30] On the other hand, the 1400 nm broad positive signal is observed only in the macrocycles.
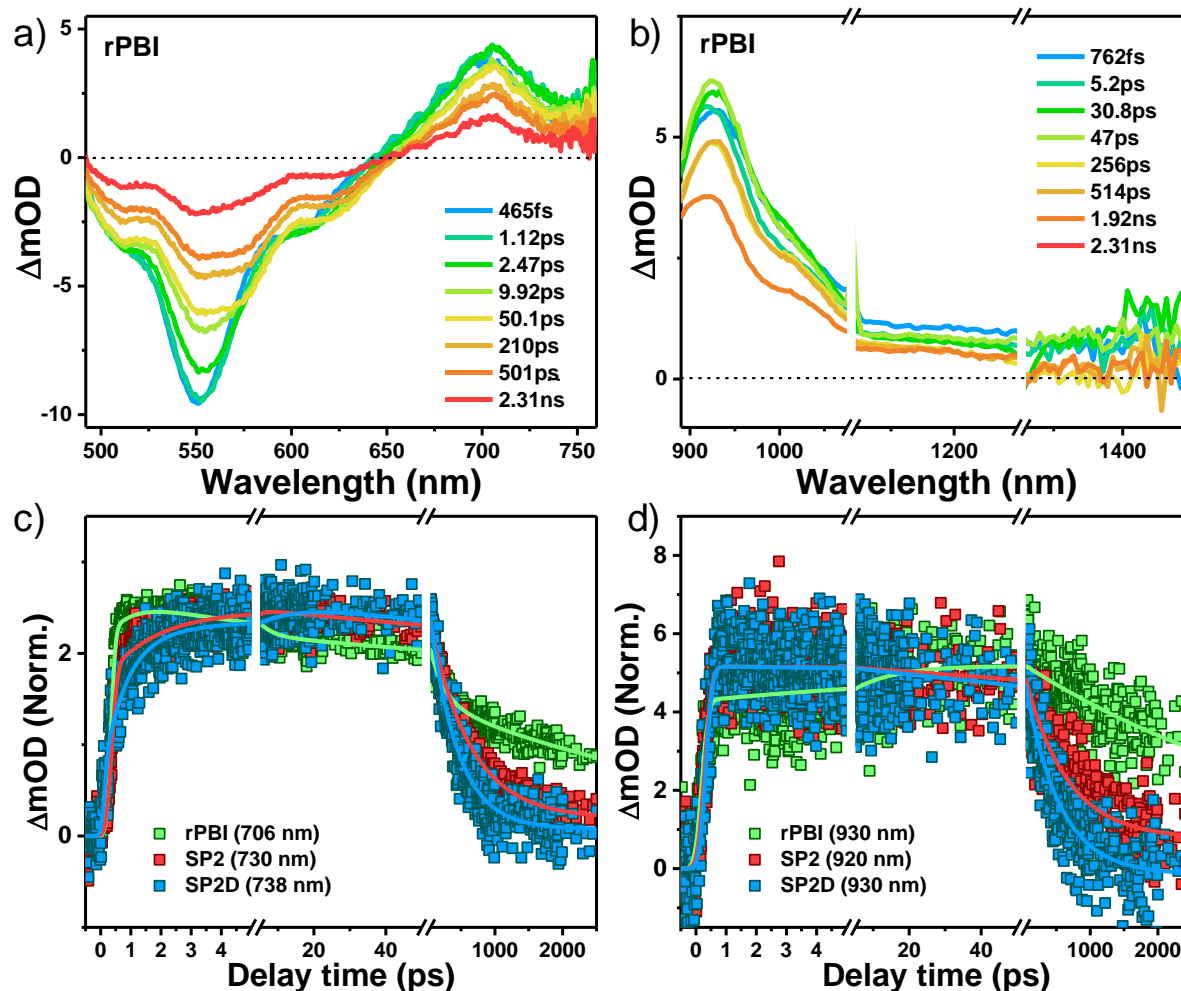
**Figure 3.27**. FTAS spectra of **rPBI** in CH₂Cl₂ a) in the visible region for 460 nm excitation and b) in the NIR region for 420 nm excitation. c) Normalized dynamic profiles of **rPBI**, **SP2,** and **SP2D** monitoring at 706, 730, and 738 nm, respectively. d) Normalized dynamic profiles of **rPBI**, **SP2,** and **SP2D** monitoring at 930, 9200, and 930 nm, respectively.

According to previous reports, oligothiophene radical cations have strong absorption in this region.[30] So, we assign this signature as the formation of oligothiophene radical cation. Observation of both the cationic and anionic species confirmed efficient separation of charge in the macrocycle system. In Figure 3.26f, the dynamic profile plotted of the radical cation originating in **SP2** and **SP2D**. The multiexponential fitting parameters are provided in Table 3.5.3. Both the dynamics are very similar, the only difference being the marginal decrement in the growth time scale in **SP2** (11.8 ps) from that of **SP2D** (7.3 ps). This can be anticipated due to the similarity in the structural components of **SP2** and **SP2D**, leading to nearly identical optical properties. However, the spectral pattern of **SP2D** in the NIR region is more intense and distinguishable than **SP2**.

The role of acetylene bridged thiophene ring is critical in this molecular design. The CS process in the case of previously reported oligothiophene ring strapped **TSP2**[23] and the present acetylene bridged thiophene ring strapped **SP2** was found to be occurring on a time scale of 2.7 ps ($k_{CS} \sim 0.4 \times 10^{12}$ S$^{-1}$) and 3.1 ps ($k_{CS} \sim 0.3 \times 10^{12}$ S$^{-1}$), respectively. However, a significant enhancement is observed in the charge recombination time scale of **SP2**, 545 ps (85.6 %), > 1 ns (14.4 %), compared to that of **TSP2** 245.3 ps (100 %).[23] The charge separation process persists longer than **(5T)₂-PBI**, and **7T-PBI**, $\tau_{CS} = \sim 12$ ps.[22,30] It is attributed to the rigid structure in the donor unit due to the acetylene bridge that prevents the C-C (sp$^3$) bond rotation and eventually enhances the effective conjugation of the donor unit.[31] Even the dimer **SP2D** also exhibits a reasonably high stabilization of the charge-separated state supported by the rigid structure, as indicated by the temperature-dependent NMR experiments (Figure 3.28).
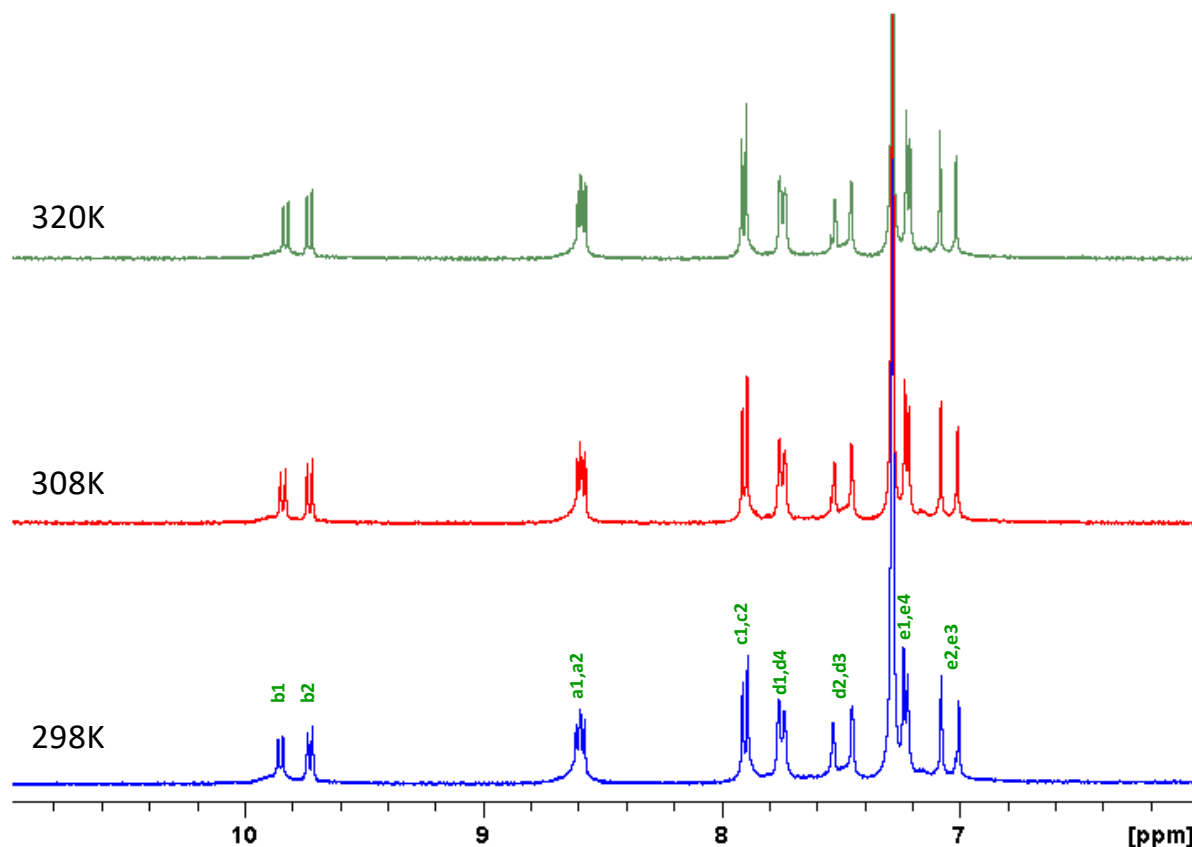


**Figure 3.28.** Aromatic region of $^1$H NMR spectra of **SP2D** at different temperatures. Signals corresponding to different environments arising from dimerization do not undergo significant chemical shifts or linewidth changes, indicating that the dimer conformation is fairly stable.

## 3.5. Tables

**3.5.1. Table** Optical and redox properties of **rPBI**, **SP1**, **SP2**, and **SP2D**.

| Sample | $\lambda_{max, ab}$ (nm) | $\varepsilon_{max}$ (M$^{-1}$cm$^{-1}$) | $\lambda_{max, em}$ (nm) | $E_{ox, 1}$ (eV) | $E_{ox, 2}$ (eV) | $E_{ox, 3}$ (eV) | $E_{red, 1}$ (eV) | $E_{red, 2}$ (eV) |
|---|---|---|---|---|---|---|---|---|
| **rPBI** | 542 | 49,575 | 570 | - | - | - | -1.14 | -1.30 |
| **SP2** | 561 | 48,853 | 535 | 0.81 | 1.06 | 1.18 | -1.28 | -1.57 |
| **SP2D** | 557 | 55,758 | 535 | - | - | - | - | - |

**3.5.2. Table.** Fluorescence lifetime of **rPBI**, **SP2**, and **SP2D** in CH$_2$Cl$_2$ ($C$ = 1x10$^{-5}$ M).

| Sample | Lifetime in ns | Contribution in % |
|---|---|---|
| **rPBI@570 nm** | 5.09 | 100 |
| **SP2@535 nm** | 6.7 | 30 |
|  | 3.3 | 70 |
| **SP2D@535 nm** | 8.7 | 26 |
|  | 3.2 | 74 |

**3.5.3. Table** Fitting parameters of FTAS dynamic profiles of **SP2** and **SP2D** monitoring at both visible and NIR region.

| System | Wavelength (nm) | $\tau_g$ (ps) | $\tau_1$ (ps) | $\tau_2$ (ns) |
|---|---|---|---|---|
| **SP2 VIS** | 730 | 2.7 | 545 (85.6 %) | > 1 ns (14.4 %) |
| **SP2 NIR** | 1460 | 11.8 | 613 (100 %) | - |
| **SP2D VIS** | 738 | 8.4 | 448 (93 %) | > 1 ns (7 %) |
| **SP2D NIR** | 1400 | 7.3 | 517 (100 %) | - |

## 3.6. Conclusion

In conclusion, we describe the synthesis, crystal structure, and transient absorption studies of novel thiophene-diacetylene strapped perylene bisimide macrocycles. Single-crystal X-ray analysis shows the preferred perpendicular orientation of the planar perylene bisimide inside the thiophene diacetylene ring. The presence of an alkyl chain on the thiophene ring enables the formation of higher oligomers such as a dimer, trimer, and tetramer. Transient absorption studies point to the stabilization of the charge-separated states due to the unique macrocycle

design. Though the placement of chromophores in the preferred orientation in macrocycles is challenging, here, it is achieved through a unique molecular design. Hence, it supports the electronic communication between the donor-acceptor units in the molecule and enables fast electron transfer. Besides, it results in the formation of a higher analog, figure-eight-shaped lemniscate dimer with similar electron transfer and stabilization of the charge-separated states. The concept of functionalizable macrocycles offers the inclusion of multiple donor-acceptor units in a single system and, at the same time, delivers exciting electron transfer features due to the unique positioning in the macrocycle. Such larger multicomponent macrocyclic systems are of fundamental importance and pave the way for futuristic applications.

## 3.7. References

1.  a) T. Pullerits, V. Sundström, *Acc. Chem. Res*. **1996**, *29*, 381−389; b) X. Hu, A. Damjanović, T. Ritz, K. Schulten, *Proc. Natl. Acad. Sci. U.S.A.* **1998**, *95*, 5935−5941; c) A. W. Roszak, T. D. Howard, J. Southall, A. T. Gardiner, C. J. Law, N. W. Isaacs, R. J. Cogdell, *Science* **2003**, *302*, 1969−1972; d) S. Scheuring, J. Se-guin, S. Marco, D. Lévy, B. Robert, J.-L. Rigaud, *Proc. Natl. Acad. Sci. U.S.A.* **2003**, *100*, 1690−1693.

2.  a) Y. Zhao, Y. Cotelle, L. Liu, J. López-Andarias, A.-B. Bornhof, M. Akamatsu, N. Sakai, S. Matile, *Acc. Chem. Res*. **2018**, *51*, 2255−2263; b) S. Sengupta, F. Würthner, *Acc. Chem. Res*. **2013**, *46*, 2498−2512; c) R. Bhosale, J. Míšek, N. Sakai, S. Matile, *Chem. Soc. Rev*. **2010**, *39*, 138−149.

3.  a) C. Kaufmann, D. Bialas, M. Stolte, F. Würthner, *J. Am. Chem. Soc.* **2018**, *140*, 9986−9995; b) B. Fimmel, M. Son, Y. M. Sung, M. Grüne, B. Engels, D. Kim, F. Würthner, *Chem. Eur. J*. **2015**, *21*, 615−630; c) V. Dehm, M. Büchner, J. Seibt, V. Engel, F. Würthner, *Chem. Sci.* **2011**, *2*, 2094.

4.  a) J. J. Han, A. D. Shaller, W. Wang, A. D. Q. Li, *J. Am. Chem. Soc*. **2008**, *130*, 6974−6982; b) A. D. Q. Li, W. Wang, L.-Q. Wang, *Chem. Eur. J.* **2003**, *9*, 4594−4601.

5.  F. Schlosser, M. Moos, C. Lambert, F. Würthner, *Adv. Mater.* **2013**, *25*, 410−414.

6.  P. Spenst, F. Würthner, *J. Photochem. Photobiol. C: Photochem. Rev*. **2017**, *31*, 114−138.

7.  a) A.-B. Bornhof, A. Bauzá, A. Aster, M. Pupier, A. Frontera, E. Vauthey, N. Sakai, S. Matile, *J. Am. Chem. Soc*. **2018**, *140*, 4884−4892; b) S. Sao, S. Naskar, N. Mukhopadhyay, M. Das, D. Chaudhuri, *Chem. Commun*. **2018**, *54*, 12186−12189; c) A. Takai, T. Kajitani, T. Fukushima, K. Kishikawa, T. Yasuda, M. Takeuchi, *J. Am. Chem. Soc*. **2016**, *138*, 11245−11253.

8.  a) G. Calzaferri, S. Huber, H. Maas, C. Minkowski, *Angew. Chem. Int. Ed*. **2003**, *42*, 3732−3758; b) V. S.-Y. Lin, S. G. Di-Magno, M. J. Therien, *Science* **1994**, *264*, 1105−1111; c) D. Gust, T. A. Moore, A. L. Moore, *Acc. Chem. Res.* **2001**, *34*, 40−48.

9.  a) A. Adronov, J. M. J. Fréchet, *Chem. Commun*. **2000**, *18*, 1701−1710; b) D.-L. Jiang, T. Aida, *Nature* **1997**, *388*, 454−456; c) C. Deva-doss, P. Bharathi, J. S. Moore, *J. Am. Chem. Soc*. **1996**, *118*, 9635−9644; d) D. Liu, S. De Feyter, M. Cotlet, A. Stefan, U.-M. Wies-ler, A. Herrmann, D. Grebel-Koehler, J. Qu, K. Müllen, F. C. De Schryver, *Macromolecules* **2003**, *36*, 5918−5925; e) T. Weil, E. Reuther, K. Müllen, *Angew. Chem. Int. Ed.* **2002**, *41*, 1900−1904.

10. S. Setayesh, A. C. Grimsdale, T. Weil, V. Enkelmann, K. Müllen, F. Meghdadi, E. J. W. List, G. Leising, *J. Am. Chem. Soc*. **2001**, *123*, 946−953.

11. a) F. J. M. Hoeben, P. Jonkheijm, E. W. Meijer, A. P. H. J. Schenning, *Chem. Rev*. **2005**, *105*, 1491−1546; b) O. Mongin, A. Schuwey, M.-A. Vallot, A. Gossauer, *Tetrahedron Lett*. **1999**, *40*, 8347−8350; c) S. Anderson, H. L. Anderson, A. Bashall, M. McPartlin, J. K. M. Sanders, *Angew. Chem. Int. Ed*. **1995**, *34*, 1096−1099; d) A. Ambroise, J. Li, L. Yu, J. S. Lindsey, *Org. Lett*. **2000**, *2*, 2563−2566.

12. a) M. J. Langton, J. D. Matichak, A. L. Thompson, H. L. Ander-son, *Chem. Sci.* **2011**, *2*, 1897; b) M. C. O'Sullivan, J. K. Sprafke, D. V. Kondratuk, C. Rinfray, T. D. W. Claridge, A. Saywell, M. O. Blunt, J. N. O'Shea, P. H. Beton, M. Malfois, H. L. Anderson, *Nature* **2011**, *469*, 72−75; c) P. Liu, Y. Hisamune, M. D. Peeks, B. Odell, J. Q. Gong, L. M. Herz, H. L. Anderson, *Angew. Chem. Int. Ed.* **2016**, *55*, 8358−8362; d) A. Cnossen, C. Roche, H. L. An-derson, *Chem. Commun*. **2017**, *53*, 10410−10413; e) P. S. Bols, H. L. Anderson, *Acc. Chem. Res*. **2018**, *51*, 2083−2092.

13. a) J. Krömer, I. Rios-Carreras, G. Fuhrmann, C. Musch, M. Wunderlin, T. Debaerdemaeker, E. Mena-Osteritz, P. Bäuerle, *Angew. Chem. Int. Ed.* **2000**, *39*, 3481−3486; b) K. Nakao, M. Nishimura, T. Tamachi, Y. Kuwatani, H. Miyasaka, T. Nishina-ga, M. Iyoda, *J. Am. Chem. Soc*. **2006**, *128*, 16740−16747; c) A. Bhaskar, G. Ramakrishna, K. Hagedorn, O. Varnavski, E. Mena-Osteritz, P. Bäuerle, T. Goodson, *J. Phys. Chem. B* **2007**, *111*, 946−954; d) S. K. Maier, S.-S. Jester, U. Müller, W. M. Müller, S. Höger, *Chem. Commun*. **2011**, *47*, 11023; e) J. E. Donehue, O. P. Varnavski, R. Cemborski, M. Iyoda, T. Goodson, *J. Am. Chem. Soc*. **2011**, *133*, 4819−4828.

14. a) T. Sakida, S. Yamaguchi, H. Shinokubo, *Angew. Chem. Int. Ed*. **2011**, *50*, 2280−2283; b) X.-S. Ke, T. Kim, V. M. Lynch, D. Kim, J. L. Sessler, J. *Am. Chem. Soc*. **2017**, *139*, 13950−13956; c) Y. Qin, X. Liu, P.-P. Jia, L. Xu, H.-B. Yang, *Chem. Soc. Rev*. **2020**, *49*, 5678−5703.

15. a) W. Zhang, J. S. Moore, *J. Am. Chem. Soc*. **2004**, *126*, 12796−12796; b) B. Schmaltz, A. Rouhanipour, H. J. Räder, W. Pisula, K. Müllen, *Angew. Chem. Int. Ed*. **2009**, *48*, 720−724; c) T. Zhao, Z. Liu, Y. Song, W. Xu, D. Zhang, D. Zhu, *J. Org. Chem*. **2006**, *71*, 7422−7432; d) Y. Song, C. Di, Z. Wei, T. Zhao, W. Xu, Y. Liu, D. Zhang, D. Zhu, *Chem. Eur. J*. **2008**, *14*, 4731−4740.

16. a) F. Schlosser, V. Stepanenko, F. Würthner, *Chem. Commun*. **2010**, *46*, 8350; b) F. Schlosser, J. Sung, P. Kim, D. Kim, F. Würthner, *Chem. Sci*. **2012**, *3*, 2778.

17. a) X. Guo, A. Facchetti, T. J. Marks, *Chem. Rev.* **2014**, *114*, 8943−9021; b) X. Zhan, A. Facchetti, S. Barlow, T. J. Marks, M. A. Ratner, M. R. Wasielewski, S. R. Marder, *Adv. Mater.* **2011**, *23*, 268−284; c) J. L. Segura, H. Herrera, P. Bäuerle, *J. Mater. Chem.* **2012**, *22*, 8717; d) Y. Avlasevich, C. Li, K. Müllen, *J. Mater. Chem.* **2010**, *20*, 3814.

18. a) F. Würthner, C. R. Saha-Möller, B. Fimmel, S. Ogi, P. Le-owanawat, D. Schmidt, *Chem. Rev.* **2016**, *116*, 962-1052; b) S. Chen, P. Slattum, C. Wang, L. Zang, *Chem. Rev.* **2015**, *115*, 11967−11998.

19. a) F. Würthner, *Chem. Commun.* **2004**, *35*, 1564-1579; b) C. Huang, S. Barlow, S. R. Marder, *J. Org. Chem.* **2011**, *76*, 2386−2407.

20. a) P. Osswald, F. Würthner, *Chem. Eur. J.* **2007**, *13*, 7395-7409; b) Á. J. Jiménez, M.-J. Lin, C. Burschka, J. Becker, V. Settels, B. Engels, F. Würthner, *Chem. Sci.* **2014**, *5*, 608−619; c) E. Ramirez, S. Chen, N. E. Powers-Riggs, I. Schlesinger, R. M. Young, M. R. Wasielewski, *J. Am. Chem. Soc.* **2020**, *142*, 18243−18250; d) E. Se-bastian, M. Hariharan, *J. Am. Chem. Soc.* **2021**, *143*, 13769−13781.

21. a) M. Ball, Y. Zhong, B. Fowler, B. Zhang, P. Li, G. Etkin, D. W. Paley, J. Decatur, A. K. Dalsania, H. Li, S. Xiao, F. Ng, M. L. Steigerwald, C. Nuckolls, *J. Am. Chem. Soc.* **2016**, *138*, 12861−12867; b) B. Zhang, R. Hernández Sánchez, Y. Zhong, M. Ball, M. W. Terban, D. Paley, S. J. L. Billinge, F. Ng, M. L. Stei-gerwald, C. Nuckolls, *Nat. Commun.* **2018**, *9*, 1957; c) M. L. Ball, B. Zhang, Q. Xu, D. W. Paley, V. C. Ritter, F. Ng, M. L. Stei-gerwald, C. Nuckolls, *J. Am. Chem. Soc.* **2018**, *140*, 10135−10139.

22. K. Bold, M. Stolte, K. Shoyama, M. Holzapfel, A. Schmiedel, C. Lambert, F. Würthner, *Angew. Chem. Int. Ed.* **2022**, *61*, e202113598.

23. S. D. Veer, V. C. Wakchaure, K. Asokan, R. Dixit, T. Goswami, R. Saha, R. Gonnade, H. N. Ghosh, S. S. Babu, *Angew. Chem. Int. Ed.* **2023**, *62*, e202212934.

24. Q. Liu, C. L. Ho, Y. H. Lo, H. Li, W. Y. Wong, *J. Inorg. Organomet. Polym. Mater.* **2015**, *25*, 159−168.

25. A, Schmitt, S, Samal, B, C, Thompson, *Polym. Chem.* **2021**, *12*, 2840-2847.

26. a) P. Siemsen, R. C. Livingston, F. Diederich, *Angew. Chem. Int. Ed.* **2000**, *39*, 2632−2657; b) K. S. Sindhu, G. Anilkumar, *RSC Adv.* **2014**, *4*, 27867−27887.

27. G. Baranović, L. Colombo, K. Furić, J. R. Durig, J. F. Sullivan, J. Mink, *J. Mol. Struct.*, **1986**, *144*, 53−69.

28. R. F. Kelley, W. S. Shin, B. Rybtchinski, L. E. Sinks, M. R. Wasielewski, *J. Am. Chem. Soc.* **2007**, *129*, 3173−3181.

29. M. Fujitsuka, K. Harada, A. Sugimoto, T. Majima, *J. Phys. Chem. A* **2008**, *112*, 10193−10199.

30. K. Bold, M. Stolte, K. Shoyama, A. Krause, A. Schmiedel, M. Holzapfel, C. Lambert, F. Würthner, *Chem. Eur. J.* **2022**, *28*, e202200355.

31. P. Pachfule, A. Acharjya, J. Roeser, T. Langenhahn, M. Schwarze, R. Schomäcker, A. Thomas, J. *J. Am. Chem. Soc.* **2018**, *140*, 1423−1427.

# Chapter–4

# Donor-Strapped Perylene Bisimide Based Donor-Acceptor $\pi$-Conjugated Polymers and Larger Macrocycles

# Chapter–4

# Donor-Strapped Perylene Bisimide Based Donor-Acceptor π-Conjugated Polymers and Larger Macrocycles
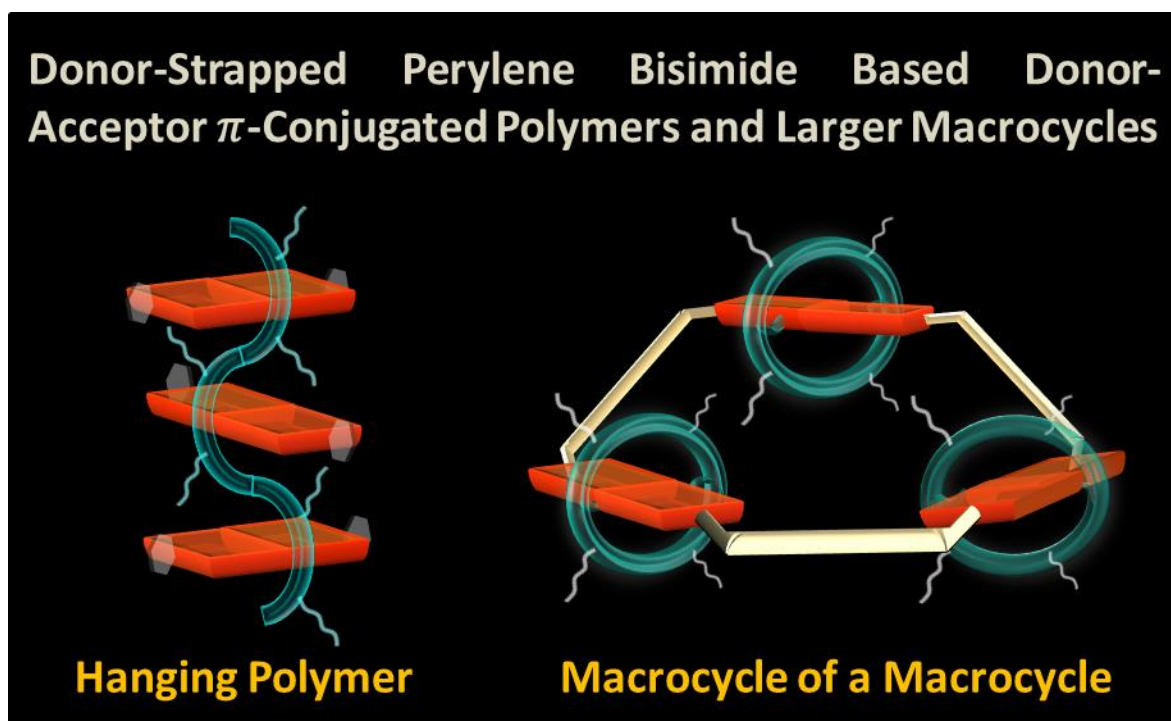


## Chapter 4. Part A: Donor-Strapped Perylene Bisimide Based Donor-Acceptor π-Conjugated Polymers

The development of organic electronic materials depends critically on the electronic structure of π-conjugated polymers. Hence positioning of the donor, acceptor units is a decisive factor in achieving supportive electronic features. In this direction, a strapped donor-acceptor segment is hitherto tested in a conjugated polymer. We aim to study the optical and electronic properties of a new class of donor-strapped acceptor polymer. In this study, four novel π-conjugated copolymers, two hanging and two linear, were designed and synthesized *via* Hay-Glasear and Oxidative coupling polymerization reactions. These copolymers contain bithiophene, thiopheneacetylene core as the "donor," and bay position substituted perylene bisimide (PBI) as

the "acceptor". The polymers were characterized by ^{1}H NMR spectroscopy, FT-IR, gel permeation chromatography (GPC), UV-vis absorption spectroscopy, and cyclic voltammetry. Thus obtained polymers exhibit excellent solubility in common organic solvents points to the importance of design strategy. As an extension of the previous chapters, a new donor-acceptor polymer containing donor-strapped acceptor repeating unit is developed. Besides, a larger macrocyclic structure of the donor-acceptor macrocycle is also designed and synthesized. This chapter covers the synthesis of two new alternate donor-acceptor designs; donor-strapped acceptor polymer and a larger macrocycle of a donor-acceptor macrocycle, exhibiting high solution processability.

## 4.1. Introduction

Over the past decade, significant developments have been achieved in understanding the structure-function correlations determining material performance in organic electronics.[1] π-conjugated polymers and small molecules, which can be solution-processed over large-area substrates, are essential building blocks in developing printed light-harvesting technologies and mechanically conformable circuit logics.[1,2] Consequently, high-throughput processing techniques, including spin coating, inkjet printing, gravure printing, and flexographic printing, can be used to create these devices on flexible substrates.[2] Recently, optoelectronic devices based on conjugated polymers are an effective alternative to microelectronics based on inorganic materials because of their affordability, lightweight, broad absorption of light, high charge carrier advantages, mobilities, and flexibility.[3] Therefore, conjugated polymer-based organic light-emitting diodes (OLEDs), organic photovoltaic cells (OPVs), and organic field-effect transistors (OFETs) are slowly but surely making their way onto the market.[3;4]

Perylene bisimides (PBIs) are potential candidates for use as the active materials of *n*-channel technology due to their inherent characteristics, including excellent thermal and photostability, intense absorption in the visible region, a low LUMO level because of good electron-accepting properties, easily tunable electronic as well as morphological properties by substituents at the ortho and bay positions.[5-7] Hence, it was helpful in many different applications such as active material in organic solar cells (OSC), fluorescent probes for imaging studies, optoelectronic devices, and semiconducting components for organic field effect transistors (OFETs).[8] Numerous types of small molecules,[8] star-shaped molecules[9], and n-type ladder-conjugated

polymers[10] are known as suitable organic semiconductors with sufficient electron and hole mobility with excellent stability because of their giant, rigid, and planar frameworks with extended conjugation.[10,11] Even so, such ladder-conjugated polymers also have incredibly poor solubility in most organic solvents, which limits their use in solution-processed organic electron devices. Large, flexible alkyl side chains have been added to improve solubility to solve this issue.[11,12] However, for most of these technologies, *p-n* doping is required to create effective conducting polymers that can move electrons or holes. Therefore, synthesizing these donor-acceptor novel soluble n-type ladder-conjugated polymers is a current trend.[12] Besides smaller optical band gaps, copolymers made of π-conjugated PBI units (substituted through the aromatic core) exhibit good electron transport properties.[13] As a result, these polymers have been utilized as fullerene replacements in all-polymer organic solar cells with smaller optical band gaps, broader visible spectrum absorption, and deep HOMO and LUMO energy levels.[14] From another perspective, PBI is easily copolymerized with a range of electron-rich (donor) units to tune the optoelectronic properties of the resulting polymers because it consists of an electron-deficient (acceptor) segment.

 In light of the above discussion, we have designed, synthesized, and characterized four novel polymers (**P1-P4)** embedding a perylene bisimides (PBIs) acceptor along with the donor segments by changing the orientation of thiopheneacetylene and bithiophene moieties as a spacer with respective to **PBIs**. Our strategy synthesized a two-hanging and two-linear extended π-conjugated copolymer based on donor and accepter unit *via* Hay-Glaser and oxidative coupling reaction. For improved solubility, we have inserted a long branched alkyl chain into the PBI unit and a $C_6$ alkyl chain into the thiophene and bithiophene groups. The structural architecture allowed for easy tuning of the energy levels of the resultant polymers. All polymers exhibited excellent thermal, electrochemical, and photostabilities and high solubilities in dichlorobenzene, $CHCl_3$, THF, and chlorinated aromatic solvents. Applying these electron acceptor polymers combined with suitable donor polymers to electron mobility was also investigated.

## 4.2. Experimental Section

### 4.2.1. Electrochemical analysis

Cyclic voltammetry (CV) and Differential pulse voltammetry (DPV) measurements were carried out on a CHI voltammetry analyzer at room temperature, employing a three-electrode single

compartment cell: glassy carbon electrode (company, d = 2mm) as working electrode, a Pt wire as counter electrode and Ag/AgCl as a reference electrode. The supporting electrolyte, Tetrabutylammonium hexafluorophosphate ($n$-Bu$_4$NPF$_6$), was previously dried under vacuum, dichloromethane was dried and degassed before use, and all measurements were performed under a nitrogen atmosphere. Ferrocene was used as an internal standard for calibrating the potential ($E_{Fc+/Fc}$ = 0.00 V).

The formal redox potentials (half-wave potentials) were calculated using the formula:

$$E_{1/2} = (E_{pa} + E_{pc}) / 2$$

Where $E_{pa}$ is the peak anode potential and

$E_{pc}$ is the peak cathode potential.

HOMO energies were calculated from the first formal redox potentials (half-wave potentials) using the equation:

$$E_{HOMO} = -(4.8 \text{ eV} + E^1_{oxd} \text{ vs. Fc}^+/\text{Fc})$$

However, LUMO energies were calculated from the first formal redox potentials (half-wave potentials) using the equation:

$$E_{LUMO} = -(4.8 \text{ eV} + E^1_{red} \text{ vs. Fc}^+/\text{Fc})$$

## 4.3. Experimental Procedures: Synthesis

### 4.3.1. Synthesis of D-A PBI-based conjugated hanging polymers.

*Tricosan-12-amine, Synthesis of (3,3'-dihexyl-[2,2'-bithiophen]-5-yl)trimethylstannane (**BT2**) and ((3-hexyl-5-(trimethylstannyl)thiophen-2-yl)ethynyl)triisopropylsilane (**T6**) was synthesized in quantitative yield by adapting a previously reported procedure.[15]*
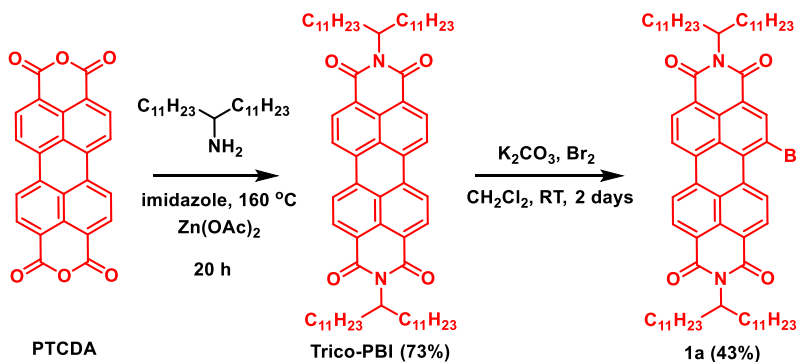


**Scheme 4.1.** Synthesis of molecule **1a**.
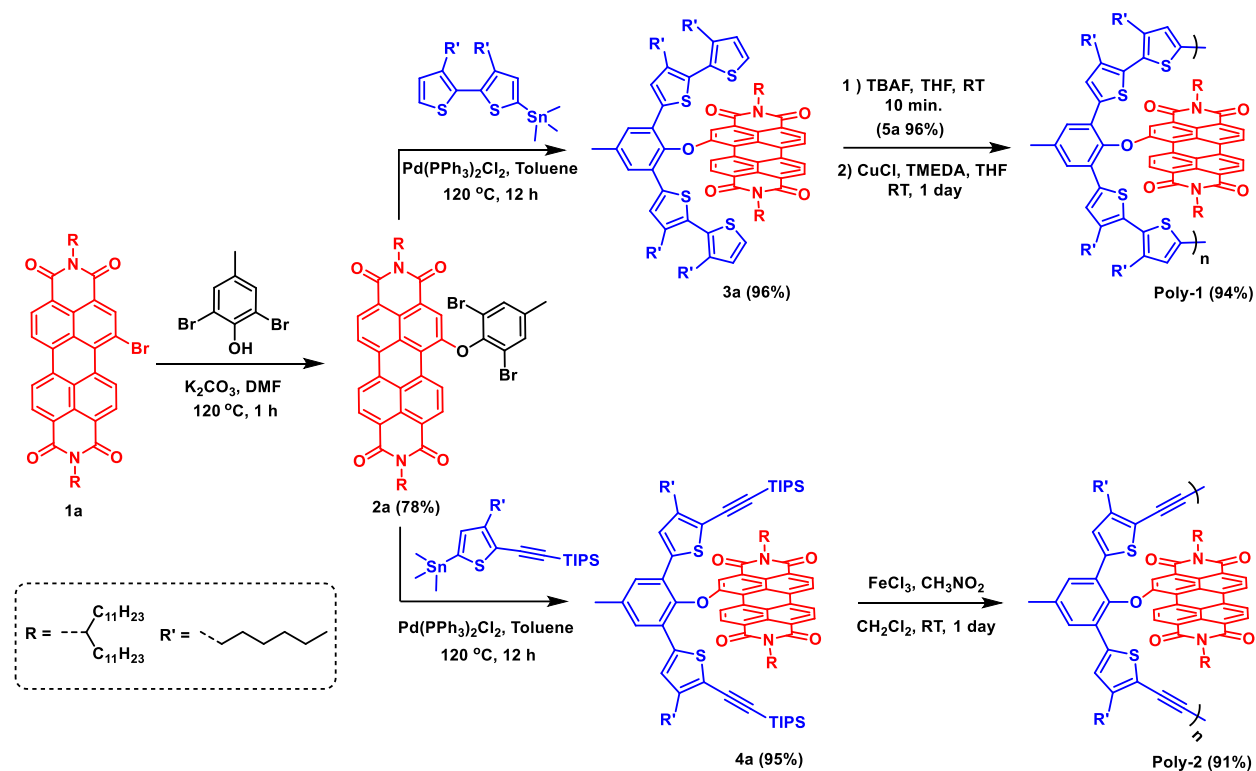
**Scheme 4.2.** Synthesis of hanging polymers.

## 4.3.2. Synthesis of D-A PBI-based conjugated linear polymers.
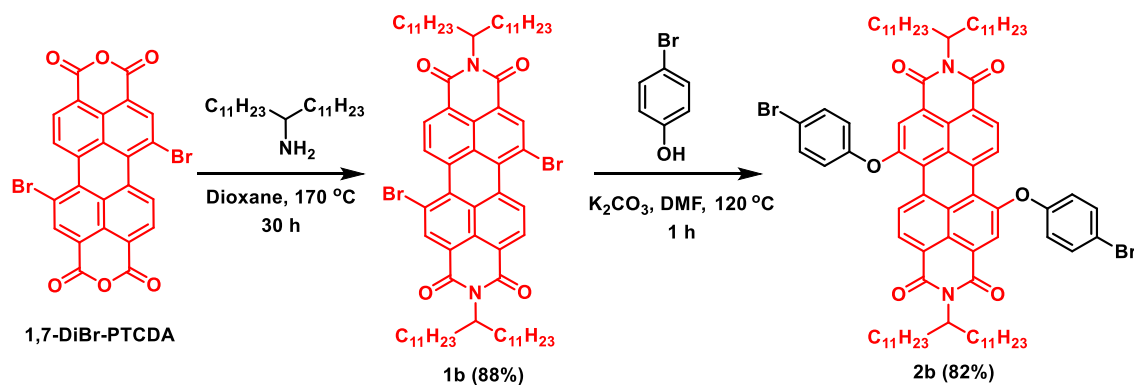


**Scheme 4.3.** Synthesis of molecule **2b**.
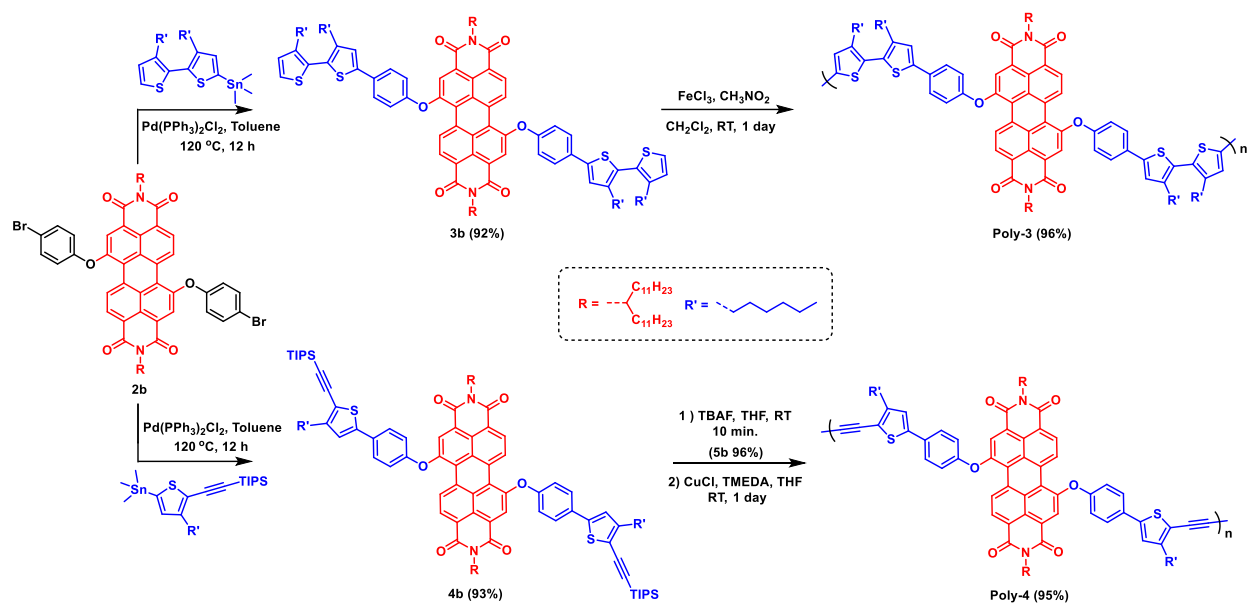
**Scheme 4.4.** Synthesis of linear polymers.

### 4.3.1.1. Synthesis of Synthesis of *N,N′*-bis(12-tricosanyl)perylene bisimides (Trico-PBI).
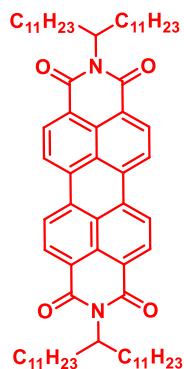


In a 100 mL round-bottom flask, PTCDA (2 g, 5.10 mmol), Zn(OAc)$_2$ (935 mg, 5.10 mmol) and tricosan-12-amine (4.33 g, 12.74 mmol) were added to imidazole (7 g, 101.96 mmol). The mixture was stirred at 160 °C for 4 h and then cooled to room temperature. In to that 2N HCl solution (50 mL) was added and stirred for a further 2 h, filtered. The precipitate was washed with the excess amount of MeOH, and extracted with CH$_2$Cl$_2$, and then the compound was purified by column chromatography (silica gel, dichloromethane).

**Nature and Yield**: Blood red solid, 5 gm (95%).

**$^1$H NMR** (400MHz, CDCl$_3$): $\delta$ [ppm] = 8.68-8.61 (m, 8H), 5.23-5.15 (m, 2H), 2.29-2.21 (m, 4H), 1.90-1.83 (m, 4H), 1.32-1.20 (m, 72H), 0.84 (t, 12H, *J* = 6.67Hz).

**¹³C NMR** (100 MHz, CDCl₃): $\delta$ [ppm] = 164.64, 163.55, 134.49, 131.89, 131.12, 129.59, 126.44, 123.94, 123.20, 123.17, 123, 54.75, 32.34, 31.88, 30.92, 29.58, 29.56, 29.52, 29.30, 26.94, 22.65, 14.08.

**FT-IR** (cm⁻¹): 2971, 2853, 1695, 1650, 1593, 1460, 1404, 1338, 1251, 1114, 810, 747.

**MALDI-TOF:** *m/z* calculated for $C_{70}H_{103}N_2O_4$ [M+H]⁺: 1035.7918, found: 1035.8685.

**4.3.1.2. Synthesis of *N,N′*-bis(12-tricosanyl)-monobromoperylene-3,4:9,10-bisdicarboximide (1a)**
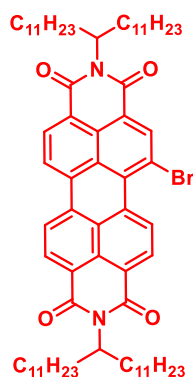


In 250 mL, two neck round-bottom flask, a mixture of compound **Trico-PBI** (4.0 g, 3.86 mmol**),** K₂CO₃ (10.68 g, 77.25 mmol), 150 mL CH₂Cl₂ and Br₂ (10 mL,193.32 mmol) was added and stirred at room temperature for 2 days. The reaction progress was monitored with the help of TLC. The excess bromine was removed by adding aqueous Na₂SO₃. Then, the crude product was purified by silica gel column chromatography (Silica gel, dichloromethane: Pet ether (1:1), v/v)) as eluent.

**Nature and Yield**: Red solid, 1.85 gm (43%).

**¹H NMR** (400MHz, CDCl₃): $\delta$ [ppm] = 8.56 - 8.77 (m, 8 H), 5.14 - 5.24 (m, 2 H), 2.19 - 2.33 (m, 4 H), 1.81 - 1.94 (m, 4 H), 1.18 - 1.35 (m, 73 H), 0.84 (t, *J* = 6.9 Hz, 12 H).

**¹³C NMR** (100 MHz, CDCl₃): $\delta$ [ppm] = 164.6, 163.6, 134.5, 131.9, 131.1, 129.6, 126.4, 123.9, 123.2, 123.2, 123.0, 54.8, 32.3, 31.9, 30.9, 29.6, 29.6, 29.5, 29.3, 26.9, 22.6, 14.1.

**FT-IR** (cm⁻¹): 2921, 2852, 1700, 1657, 1592, 1462, 1462, 1399, 1331, 1244, 852, 810, 746.

**MALDI-TOF:** m/z calculated for $C_{70}H_{101}BrN_2O_4$ [M]+: 1112.6945, found: 1112.7291.

**4.3.1.3.** **Synthesis of** *N,N'*-**bis(12-tricosanyl)-Mono-(2,6-dibromo-4-methylphenoxy) perylene-3,4:9,10-bisdicarboximide (2a):**
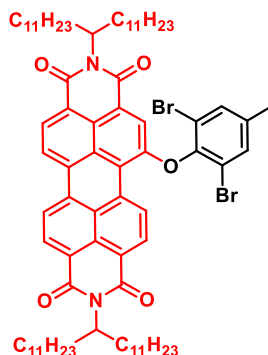


In 100 mL two neck round-bottom flask, a mixture of **1a** (1.2 g, 1.01 mmol) in dry DMF (60 mL), potassium carbonate (277 mg, 2.01 mmol), and 2,6-dibromo-*p*-cresol (401 mg, 1.51 mmol) was added. The reaction mixture was stirred at 120 °C for 1 h. After being cooled to room temperature, the solvent is removed by rotary evaporation. The crude reaction mixture was extracted with $CH_2Cl_2$, and the organic layer was washed with ($6\times100$ mL) of water. The combined organic phase was dried over anhydrous $Na_2SO_4$, and the solvent was removed under reduced pressure. The compound was purified by using silica gel column chromatography using $CH_2Cl_2$-petroleum ether (3:7 v/v) eluent as product **2a**.

**Nature and Yield**: Reddish orange solid, 1.02 g (78%).

**¹H NMR** (400MHz, CDCl$_3$): $\delta$ [ppm] = 9.70 (d, *J* = 8.4 Hz, 1 H), 8.58 - 8.80 (m, 5 H), 7.90 (d, *J* = 12.5 Hz, 1 H), 7.56 (s, 2 H), 5.11 - 5.25 (m, 2 H), 2.46 (s, 3 H), 2.14 - 2.32 (m, 4 H), 1.79 - 1.91 (m, 4 H), 1.18 - 1.34 (m, 72 H), 0.84 (t, *J* = 6.7 Hz, 12 H).

**¹³C NMR** (125 MHz, CDCl$_3$): $\delta$ [ppm] = 165.0, 164.6, 164.1, 163.9, 163.6, 162.9, 155.0, 145.5, 139.5, 134.4, 134.0, 133.7, 132.5, 131.8, 131.3, 130.5, 130.1, 129.7, 129.3, 128.9, 127.1, 125.6, 124.7, 124.0, 123.6, 123.0, 122.9, 122.3, 121.4, 119.8, 119.0, 117.8, 55.1, 54.7, 54.6, 32.4, 31.9, 30.9, 29.6, 29.5, 29.5, 29.3, 26.9, 22.6, 20.6, 14.1.

**FT-IR** (cm⁻¹): 2922, 2852, 1696, 1655, 1593, 1453, 1405, 1332, 1258, 851, 810, 746.

**MALDI-TOF:** *m/z* calculated for $C_{77}H_{107}Br_2N_2O_5$ [M+H]⁺: 1297.6547, found: 1297.6649.

**4.3.1.4. Synthesis of (3a):**
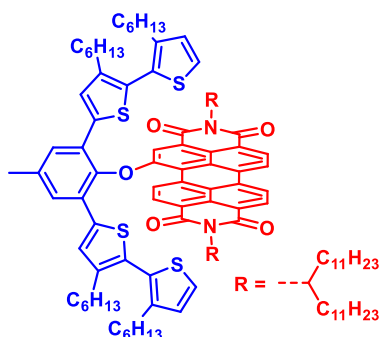


In a 15 mL pressure tube, **2a** (650 mg, 500.19 µmol), (3,3'-dihexyl-[2,2'-bithiophen]-5-yl)trimethylstannane (995 mg, 2.00 mmol) in 8 mL dry toluene was added, and Pd(PPh$_3$)$_2$Cl$_2$ (18 mg, 25.01 µmol) was used as a catalyst. The mixture was subsequently heated to 140 °C for 12 h. After cooling to RT, CH$_2$Cl$_2$ was added to the reaction mixture to stop the reaction. The later reaction mixture was passed through celite, and the solvent was removed by evaporation under reduced pressure. The compound was purified by using silica gel column chromatography using CH$_2$Cl$_2$-petroleum ether (3:7 v/v) as eluent.

**Nature and Yield**: Reddish pink solid, 875 g (96%).

**$^1$H NMR** (400 MHz, CDCl$_3$): $\delta$ [ppm] = 9.93 (d, *J* = 8.5 Hz, 1 H), 8.52 - 8.80 (m, 5 H), 7.98 (d, *J* = 11.3 Hz, 1 H), 7.54 (s, 2 H), 7.13 (s, 2 H), 7.08 (d, *J* = 5.3 Hz, 2 H), 6.73 (d, *J* = 5.1 Hz, 2 H), 5.15 - 5.25 (m, 1 H), 5.10 (br. s., 1 H), 2.54 (s, 3 H), 2.19 - 2.31 (m, 2 H), 2.09 (tq, *J* = 14.5, 7.1 Hz, 10 H), 1.73 - 1.94 (m, 4 H), 1.11 - 1.35 (m, 80 H), 0.96 - 1.06 (m, 12 H), 0.81 - 0.92 (m, 24 H), 0.67 - 0.74 (m, 12 H).

**$^{13}$C NMR** (125 MHz, CDCl$_3$): $\delta$ [ppm] = 164.9, 164.5, 163.9, 163.5, 162.8, 156.2, 143.6, 142.3, 141.9, 137.0, 136.7, 134.6, 134.4, 134.0, 132.7, 131.9, 131.2, 130.5, 130.3, 130.1, 129.6, 129.4, 129.2, 128.7, 128.4, 128.0, 127.9, 127.1, 125.2, 124.3, 123.6, 123.4, 122.8, 122.0, 120.9, 120.2, 55.0, 54.7, 32.4, 32.3, 31.9, 31.5, 31.2, 30.9, 30.2, 29.6, 29.5, 29.3, 28.8, 28.6, 28.5, 28.3, 27.0, 22.7, 22.4, 22.4, 21.1, 14.1, 14.0, 13.9.

**FT-IR** (cm$^{-1}$): 2919, 2852, 1696, 1656, 1591, 1459, 1404, 1330, 1254, 1198, 926, 846, 807, 755, 720.

**4.3.1.5. Synthesis of (4a):**
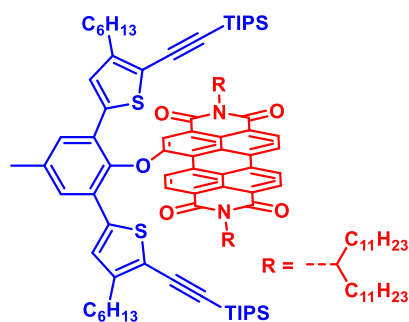


In 15 mL pressure tube, charged with compound **2a** (700 mg, 538.66 μmol), triisopropyl((5-(trimethylstannyl)thiophen-2-yl)ethynyl)silane (1.1 g, 2.15 mmol), and Pd(PPh$_3$)$_2$Cl$_2$ (19 mg, 26.93 μmol) in 8 mL freshly distilled dry toluene were added. The reaction mixture was subsequently heated to 140 °C for 12 h. This was followed by cooling the reaction mixture to room temperature, adding dichloromethane, passing through celite, and removing the solvent by evaporation under reduced pressure. The compound was purified by silica gel column chromatography using CH$_2$Cl$_2$-petroleum ether (3:7 v/v) as eluent.

**Nature and Yield**: Red solid, 945 g (95%).

**$^1$H NMR** (400 MHz, CDCl$_3$): $\delta$ [ppm] = 9.91 (d, $J$ = 8.4 Hz, 1 H), 8.64 - 8.88 (m, 4 H), 8.58 (dd, $J$ = 18.5, 7.6 Hz, 1 H), 7.85 (d, $J$ = 10.8 Hz, 1 H), 7.50 (s, 2 H), 7.07 (s, 2 H), 5.17 - 5.27 (m, 1 H), 5.10 (br. s., 1 H), 4.98 (br. s., 1 H), 2.51 (s, 3 H), 2.23 - 2.36 (m, 6 H), 2.02 - 2.14 (m, 2 H), 1.75 - 1.94 (m, 4 H), 1.19 - 1.35 (m, 76 H), 0.96 - 1.14 (m, 12 H), 0.92 - 0.95 (m, 43 H), 0.86 (t, $J$ = 6.9 Hz, 12 H), 0.70 (t, $J$ = 7.3 Hz, 7 H).

**$^{13}$C NMR** (125 MHz, CDCl$_3$): $\delta$ [ppm] = 164.9, 164.7, 164.5, 163.9, 163.7, 163.5, 162.8, 155.8, 148.5, 143.5, 137.0, 137.0, 134.6, 134.4, 133.9, 132.6, 131.9, 131.3, 130.5, 129.7, 129.3, 129.2, 129.0, 128.6, 128.5, 127.5, 127.0, 125.5, 124.8, 124.0, 123.7, 123.5, 122.9, 122.8, 122.1, 121.2, 120.0, 119.6, 119.3, 98.9, 98.5, 55.0, 54.7, 54.6, 32.4, 32.3, 31.9, 31.2, 29.7, 29.6, 29.5, 29.4, 29.3, 28.7, 27.0, 22.7, 22.4, 21.1, 18.5, 14.1, 13.9, 11.1.

**FT-IR** (cm$^{-1}$): 2922, 2854, 2183, 1693, 1649, 1590, 1461, 1407, 1328, 1255, 1196, 880, 750, 670.

**4.3.1.6. Synthesis of (5a)**
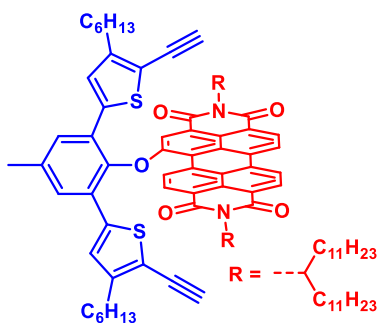


In a 25 mL round bottom flask, the compound **4a** (200 mg, 108.99 μmol) was dissolved in 12 mL anhydrous THF under an argon atmosphere, and then Tetrabutylammonium fluoride hydrate (92 mg, 326.97 μmol) was added. The solution was stirred at room temperature for 10 to 15 minutes, the reaction was monitored by TLC, and once the cleavage of the TIPS group was completed, the mixture was quenched with water and worked up in dichloromethane. After drying the organic layer over anhydrous $Na_2SO_4$, the solvents were concentrated under reduced pressure. The compound was purified by silica gel column chromatography using $CH_2Cl_2$-petroleum ether (1:1 v/v) as eluent.

**Nature and Yield**: Red solid, 160 mg (96%).

**^{1}H NMR** (400 MHz, CDCl3): $\delta$ [ppm] = 9.88 (d, *J* = 8.2 Hz, 1 H), 8.74 - 8.84 (m, 2 H), 8.70 (t, *J* = 7.6 Hz, 2 H), 8.52 - 8.65 (m, 1 H), 7.85 (d, *J* = 15.0 Hz, 1 H), 7.52 (s, 2 H), 7.08 (s, 2 H), 5.19 - 5.27 (m, 1 H), 5.10 (br. s., 1 H), 3.26 (s, 2 H), 2.52 (s, 3 H), 2.21 - 2.36 (m, 6 H), 2.03 - 2.19 (m, 2 H), 1.83 - 1.94 (m, 2 H), 1.80 (br. s., 2 H), 1.15 - 1.39 (m, 76 H), 1.04 (td, *J* = 15.2, 7.2 Hz, 8 H), 0.88 - 0.94 (m, 4 H), 0.84 - 0.87 (m, 12 H), 0.72 (t, *J* = 7.3 Hz, 6 H)

**^{13}C NMR** (125 MHz, CDCl3): $\delta$ [ppm] = 164.9, 164.7, 164.5, 163.8, 163.6, 163.5, 162.7, 155.7, 149.2, 143.4, 137.5, 137.1, 134.6, 134.3, 134.0, 132.7, 131.9, 131.4, 130.7, 129.8, 129.4, 129.0, 128.5, 128.4, 127.3, 127.1, 125.4, 124.7, 123.9, 123.6, 122.9, 122.2, 121.0, 119.8, 119.1, 118.0, 84.4, 76.1, 55.0, 54.7, 54.6, 32.4, 32.3, 31.9, 31.1, 30.9, 29.6, 29.5, 29.3, 29.1, 28.6, 27.0, 22.6, 22.5, 22.4, 21.1, 14.1, 13.9.

**FT-IR** (cm$^{-1}$): 3314, 3260, 2920, 2853, 2097, 1731, 1693, 1650, 1590, 1462, 1330, 1254, 813, 748.

### 4.3.1.7. Synthesis of (Poly-1):



**Poly-1**
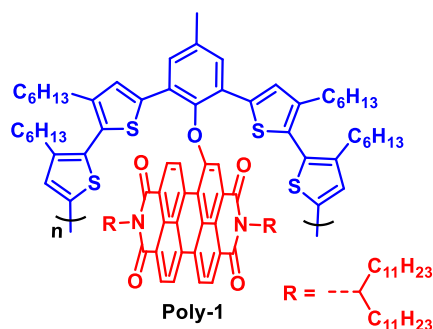
In a 10 mL schlenk tube, bithiophene precursor of **3a** (150 mg, 83.02 μmol) was dissolved in dry CH$_2$Cl$_2$ (3 mL) and degassed for 30 min. The reaction mixture cooled down to 0 °C, and iron (III) chloride (202 mg, 1.25 mmol) was added portion-wise. The reaction was warmed to room temperature and stirred for 1 day. The progress of the reaction was monitored by precipitation; the reaction was quenched with methanol. The crude polymer was then purified using soxhlet extraction with methanol, acetone, and chloroform.

**Nature and Yield**: Black solid, 141 mg (94%).

**$^1$H NMR** (500 MHz, CDCl$_3$): δ [ppm] = 9.89 (br. s., 1 H), 8.62 (br. s., 5 H), 7.96 (br. s., 1 H), 7.49 (br. s., 2 H), 7.10 (br. s., 2 H), 6.64 (br. s., 2 H), 5.16 (br. s., 2 H), 2.51 (br. s., 3 H), 2.03 - 1.20 (m, 12 H), 1.86 (br. s., 6 H), 1.09 - 1.25 (m, 118 H), 0.79 – 0.81 (m, 48 H).

**FT-IR** (cm$^{-1}$): 2919, 2849, 1699, 1654, 1590, 1457, 1406, 1327, 1255, 1195, 1169, 929, 847, 809, 747, 720.

### 4.3.1.8. Synthesis of (Poly-2):



**Poly-2**
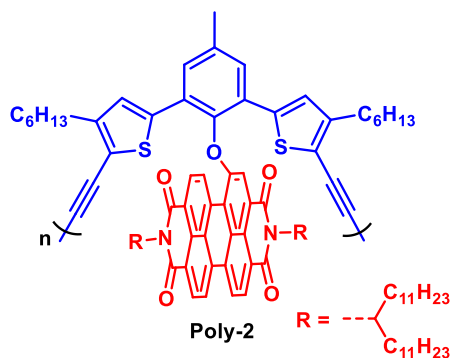
In a 10 mL schlenk tube, compound **5a** (150 mg, 98.53 μmol) was dissolved in 3 mL anhydrous THF. Then, copper (I) chloride (146 mg, 1.48 mmol) and N,N,N′,N′-tetramethylethylenediamine (344 mg, 2.96 mmol) was added to the solution of **5b**. The reaction mixtures were stirred for 1

day. Once the reaction was completed, the reaction mixture was quenched with methanol. The crude polymer was then purified using soxhlet extraction with methanol, acetone, and chloroform.

**Nature and Yield**: reddish-black solid, 137 mg (91%).

**$^1$H NMR** (500 MHz, CDCl$_3$): $\delta$ [ppm] = 9.74 (br. s., 1 H), 8.66 (br. s., 5 H), 7.74 (br. s., 1 H), 7.44 (br. s., 2 H), 7.02 (br. s., 2 H), 5.17 (br. s., 2 H), 2.47 (br. s., 3 H), 2.18 (br. s., 6 H), 1.09 - 1.25 (m, 76 H), 0.72-0.92 (m, 36 H).

**FT-IR** (cm$^{-1}$): 2922, 2850, 1697, 1654, 1591, 1457, 1410, 1333, 1254, 808, 746.

**4.3.2.1. Synthesis of *N,N′*- bis(12-tricosanyl)- 1,7-dibromoperylene -3,4:9,10-bisdicarbox imide (1b):**
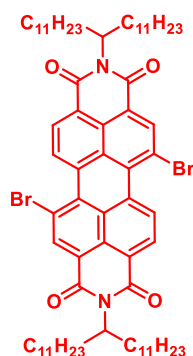


In 100 mL seal tube, a mixture of PTCDA-Br$_2$ (1.5 g, 2.73 mmol), 12-tricosanamine (2.32 g, 6.82 mmol), and 1,4-dioxane (50 mL) was heated at 170 °C for 30 h. The reaction mixture was then allowed to cool to room temperature, and concentrated on a rotary evaporator. Then, the crude product was purified through silica gel column chromatography (Silica gel, dichloromethane: Pet ether (3:7), v/v)) as eluent.

**Nature and Yield**: Red solid, 2.85 gm (88%).

**$^1$H NMR** (400MHz, CDCl$_3$): $\delta$ [ppm] = 9.79 (d, *J* = 8.3 Hz, 1 H), 8.93 (d, *J* = 17.4 Hz, 1 H), 8.60 - 8.75 (m, 5 H), 5.12 - 5.24 (m, 2 H), 2.19 - 2.32 (m, 4 H), 1.79 - 1.91 (m, 4 H), 1.18 - 1.33 (m, 73 H), 0.84 (t, *J* = 6.9 Hz, 12 H).

**$^{13}$C NMR** (125 MHz, CDCl$_3$): $\delta$ [ppm] = 164.7, 164.4, 163.6, 163.3, 162.4, 139.5, 138.8, 133.9, 133.6, 131.5, 131.0, 130.8, 130.3, 129.0, 128.8, 128.1, 127.1, 124.2, 124.0, 123.7, 123.4, 123.0, 122.7, 120.9, 55.0, 54.8, 32.3, 32.3, 31.9, 30.9, 29.6, 29.5, 29.3, 26.9, 26.9, 22.6, 14.1.

**FT-IR** (cm$^{-1}$): 2922, 2851, 1701, 1660, 1589, 1462, 1327, 1238, 860, 810, 747.

**MALDI-TOF:** *m/z* calculated for C$_{70}$H$_{100}$Br$_2$N$_2$O$_4$ [M]$^+$: 1190.6050, found: 1190.6593.

**4.3.2.2. Synthesis of *N,N'*-bis(12-tricosanyl)-1,7-bis(4-bromo-phenoxy)perylene-3,4:9,10-bisdicar-boximide (2b):**
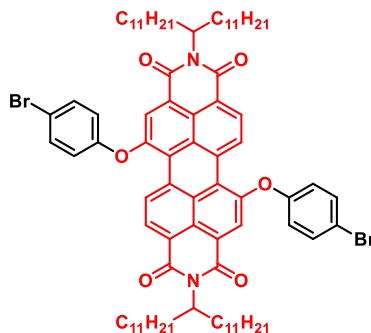


In 100 mL two neck round-bottom flask, a mixture of **1b** (1.2 g, 1.01 mmol) in dry DMF (60 mL), potassium carbonate (560 mg, 4.05 mmol) and 4-bromo-phenol (438 mg, 2.53 mmol) was added. The reaction mixture was stirred at 120 °C for 1 h. After being cooled to room temperature, the solvent is removed by rotary evaporation. The crude reaction mixture was extracted with $CH_2Cl_2$, and the organic layer was washed with (6×100 mL) of water. The combined organic phase was dried over anhydrous $Na_2SO_4$, and the solvent was removed under reduced pressure. The compound was purified by silica gel column chromatography using $CH_2Cl_2$-petroleum ether (4:6 v/v) as eluent.

**Nature and Yield**: Red solid, 1.02 g (78%).

**$^1$H NMR** (400 MHz, CDCl$_3$): $\delta$ [ppm] = 9.50 (d, $J$ = 8.4 Hz, 2 H), 8.61 (d, $J$ = 7.3 Hz, 2 H), 8.28 (s, 1 H), 8.32 (s, 1 H), 7.57 (d, $J$ = 8.9 Hz, 4 H), 7.06 (d, $J$ = 8.8 Hz, 4 H), 5.13 (br. s., 2 H), 2.18 (br. s., 4 H), 1.83 (br. s., 4 H), 1.17 - 1.35 (m, 72 H), 0.85 (t, $J$ = 6.9 Hz, 12 H).

**$^{13}$C NMR** (125 MHz, CDCl$_3$): $\delta$ [ppm] = 154.7, 154.2, 133.6, 133.0, 130.9, 129.3, 128.8, 125.6, 124.7, 124.2, 124.1, 123.8, 122.4, 121.1, 121.0, 117.9, 54.8, 32.3, 31.9, 29.6, 29.6, 29.5, 29.5, 29.3, 26.9, 22.6, 14.1.

**FT-IR** (cm$^{-1}$): 2922, 2853, 1699, 1656, 1595, 1481, 1406, 1328, 1259, 1200, 1068, 1009, 812, 751.

**MALDI-TOF:** *m/z* calculated for $C_{82}H_{109}Br_2N_2O_6$ [M+H]$^+$: 1375.6652, found: 1375.6836.

**4.3.2.3. Synthesis of (3b):**
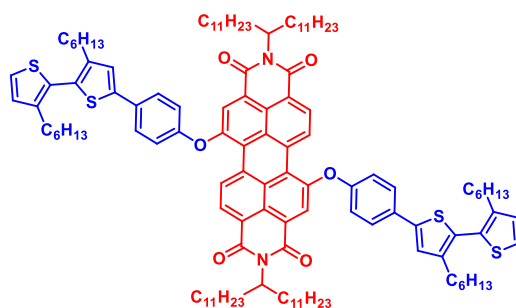


In a pressure tube (15 mL), **2b** (600 mg, 435.55 µmol), (3,3'-dihexyl-[2,2'-bithiophen]-5-yl)trimethylstannane (650 mg, 1.31 mmol) in 8 mL dry toluene was added, and Pd(PPh$_3$)$_2$Cl$_2$ (15 mg, 21.78 µmol) was used as the catalyst. The mixture was subsequently heated to 140 °C for 12 h. After cooling to RT, CH$_2$Cl$_2$ was added to the reaction mixture to stop the reaction. The later reaction mixture was passed through celite, and the solvent was removed by evaporation under reduced pressure. The compound was purified by silica gel column chromatography using CH$_2$Cl$_2$-petroleum ether (3:7 v/v) as eluent.

**Nature and Yield**: Deep pink solid, 755 g (92%).

**$^1$H NMR** (500 MHz, CDCl$_3$): $\delta$ [ppm] = 9.59 (d, $J$ = 8.4 Hz, 2 H), 8.60 (d, $J$ = 7.9 Hz, 1 H), 8.65 (d, $J$ = 8.3 Hz, 1 H), 8.36 (s, 1 H), 8.40 (s, 1 H), 7.68 (d, $J$ = 8.8 Hz, 4 H), 7.32 (d, $J$ = 5.1 Hz, 2 H), 7.17 - 7.22 (m, 6 H), 7.00 (d, $J$ = 5.3 Hz, 2 H), 5.14 (br. s., 2 H), 2.50 - 2.61 (m, 8 H), 2.20 (br. s., 4 H), 1.76 - 1.89 (m, 4 H), 1.60 - 1.65 (m, 4 H), 1.54 - 1.59 (m, 4 H), 1.18 - 1.33 (m, 97 H), 0.82 - 0.90 (m, 24 H).

**$^{13}$C NMR** (125 MHz, CDCl$_3$): $\delta$ [ppm] = 164.5, 164.1, 163.4, 163.0, 155.1, 154.9, 154.3, 143.5, 142.5, 142.3, 133.2, 131.6, 130.8, 130.0, 129.3, 128.8, 128.6, 128.4, 127.7, 125.5, 125.4, 124.9, 124.6, 124.0, 123.8, 123.7, 123.0, 122.3, 120.0, 119.8, 54.9, 54.7, 32.3, 31.9, 31.6, 30.7, 30.7, 29.6, 29.5, 29.3, 29.1, 29.0, 28.9, 26.9, 22.6, 22.6, 14.1.

**FT-IR** (cm$^{-1}$): 2922, 2852, 1696, 1653, 1592, 1505, 1463, 1407, 1327, 1253, 1205, 1164, 906, 812, 722.

**MALDI-TOF:** *m/z* calculated for C$_{122}$H$_{166}$N$_2$O$_6$S$_4$ [M]$^+$: 1883.1629, found: 1883.2980.

**4.3.2.4. Synthesis of (4b):**
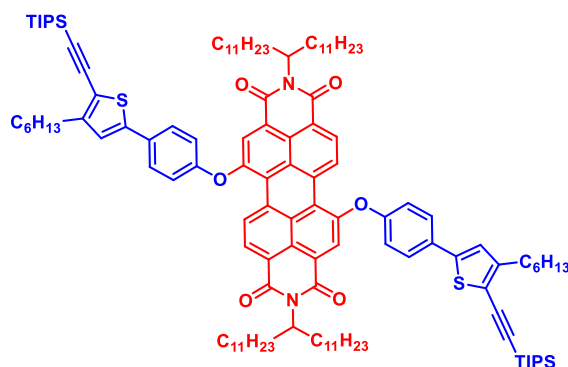


In 15 mL pressure tube, charged with compound **2b** (600 mg, 435.55 µmol), triisopropyl((5-(trimethylstannyl)thiophen-2-yl)ethynyl)silane (891 mg, 1.74 mmol), and Pd(PPh$_3$)$_2$Cl$_2$ (15 mg, 21.78 µmol) in 8 mL freshly distilled dry toluene were added. The reaction mixture was subsequently heated to 140 ºC for 12 h. This was followed by cooling the reaction mixture to room temperature, adding dichloromethane, passing through celite, and removing the solvent by evaporation under reduced pressure. The compound was purified by silica gel column chromatography using CH$_2$Cl$_2$-petroleum ether (3:7 v/v) as eluent.

**Nature and Yield**: Reddish pink solid, 775 g (93%).

**¹H NMR** (400 MHz, CDCl$_3$): $\delta$ [ppm] = 9.54 (d, $J$ = 8.4 Hz, 2 H), 8.52 - 8.69 (m, 2 H), 8.34 (s, 1 H), 8.38 (s, 1 H), 7.64 (d, $J$ = 8.6 Hz, 4 H), 7.17 (d, $J$ = 8.5 Hz, 4 H), 7.06 (s, 2 H), 5.14 (br. s., 2 H), 2.74 (t, $J$ = 7.6 Hz, 4 H), 2.20 (br. s., 4 H), 1.83 (br. s., 4 H), 1.68 (quin, $J$ = 7.3 Hz, 4 H), 1.19 - 1.43 (m, 85 H), 1.16 (s, 42 H), 0.91 (t, $J$ = 6.5 Hz, 6 H), 0.85 (t, $J$ = 6.8 Hz, 12 H).

**¹³C NMR** (125 MHz, CDCl$_3$): $\delta$ [ppm] = 164.4, 164.1, 163.4, 162.9, 154.9, 154.7, 149.8, 142.4, 133.1, 131.1, 130.8, 130.1, 129.2, 128.8, 127.9, 125.5, 124.8, 124.6, 124.4, 124.1, 124.0, 123.9, 123.5, 123.0, 122.3, 119.9, 119.7, 118.2, 115.9, 99.1, 98.4, 54.9, 54.7, 32.3, 31.9, 31.7, 30.3, 30.0, 29.6, 29.5, 29.3, 29.1, 26.9, 22.6, 22.6, 18.7, 14.1, 11.3.

**FT-IR** (cm$^{-1}$): 2920, 2850, 2136, 1698, 1653, 1591, 1503, 1462, 1408, 1327, 1252, 1212, 1171, 904, 810, 765, 677.

**MALDI-TOF:** *m/z* calculated for C$_{124}$H$_{178}$N$_2$O$_6$S$_2$Si$_2$[M]$^+$: 1911.2665 found: 1911.5458.

### 4.3.2.5. Synthesis of (5b):
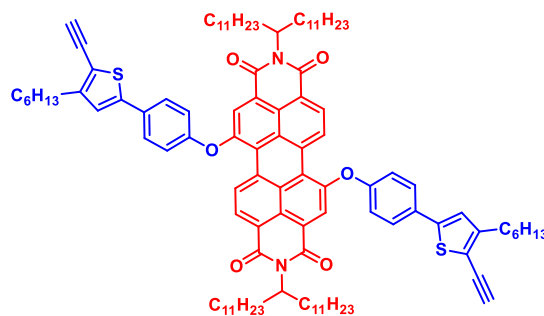


In a 25 mL round bottom flask, the compound **4b** (200 mg, 104.54 μmol) was dissolved in 12 mL anhydrous THF under argon atmosphere, and then Tetrabutylammonium fluoride hydrate (88 mg, 313.63 μmol) was added. The solution was stirred at room temperature for 10 to15 minutes, the reaction was monitored by TLC, and once the cleavage of TIPS group was completed, the mixture was quenched with water and worked up in dichloromethane. After drying the organic layer over anhydrous $Na_2SO_4$, the solvents were concentrated under reduced pressure. The compound was purified by silica gel column chromatography using $CH_2Cl_2$-petroleum ether (4:6 v/v) as eluent.

**Nature and Yield**: Reddish pink solid, 160 g (96%).

**$^1$H NMR** (400 MHz, CDCl$_3$): $\delta$ [ppm] = 9.54 (d, $J$ = 8.4 Hz, 2 H), 8.53 - 8.70 (m, 2 H), 8.34 (s, 1 H), 8.38 (s, 1 H), 7.64 (d, $J$ = 8.5 Hz, 4 H), 7.18 (d, $J$ = 8.5 Hz, 4 H), 7.06 (s, 2 H), 5.13 (br. s., 2 H), 3.52 (s, 2 H), 2.72 (t, $J$ = 7.6 Hz, 4 H), 2.19 (br. s., 4 H), 1.83 (br. s., 4 H), 1.68 (quin, $J$ = 7.3 Hz, 4 H), 1.18 - 1.43 (m, 85 H), 0.91 (t, $J$ = 6.6 Hz, 6 H), 0.85 ppm (t, $J$ = 6.8 Hz, 12 H)

**$^{13}$C NMR** (100 MHz, CDCl$_3$): $\delta$ [ppm] = 164.4, 164.1, 163.4, 162.9, 154.8, 150.3, 143.1, 133.1, 130.9, 130.8, 130.1, 129.3, 128.8, 128.0, 125.5, 124.8, 124.6, 124.2, 123.9, 123.8, 123.1, 122.3, 119.9, 119.8, 116.5, 84.1, 54.9, 54.7, 32.3, 31.9, 31.6, 30.1, 29.7, 29.6, 29.5, 29.5, 29.3, 28.9, 26.9, 22.6, 22.6, 14.1.

**FT-IR** (cm$^{-1}$): 3314, 2922, 2849, 2097, 1699, 1654, 1592, 1501, 1459, 1407, 1327, 1254, 1209, 907, 812.

**MALDI-TOF:** *m/z* calculated for $C_{106}H_{138}N_2O_6S_2[M]^+$: 1598.9996, found: 1599.0618.

**4.3.2.6. Synthesis of (Poly-3):**
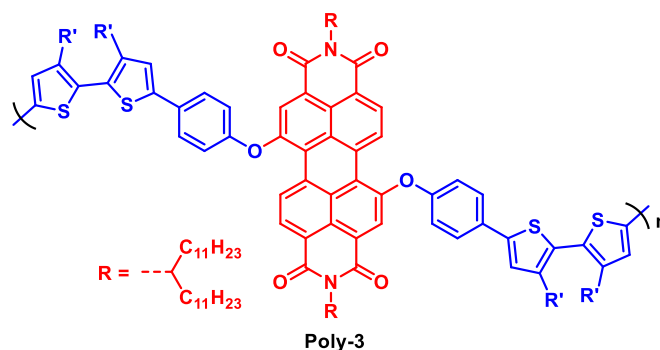


Poly-3

The synthesis of **Poly-3** followed a similar process to that of **Poly-1**. In a 10 mL schlenk tube, bithiophene precursor of **3b** (150 mg, 79.58 μmol) was dissolved in dry $CH_2Cl_2$ (3 mL) and degassed for 30 min. The reaction mixture cooled down to 0 °C, and iron (III) chloride (194 mg, 1.19 mmol) was added portion-wise. The reaction was warmed to room temperature and stirred for 1 day. The progress of the reaction was monitored by precipitation; the reaction was quenched with methanol. The crude polymer was then purified using soxhlet extraction with methanol, acetone, and chloroform.

**Nature and Yield**: Blackish red solid, 145 mg (96%).

**¹H NMR** (500 MHz, CDCl$_3$): $\delta$ [ppm] = 9.59 (br. s., 2 H), 8.63 (br. s., 2 H), 8.36 (br. s., 2 H), 7.69 (br. s., 4 H), 7.20 (br. s., 4 H), 7.08 (br. s., 4 H), 5.13 (br. s., 2 H), 2.58 (br. s., 8 H), 2.26 (br. s., 4 H), 1.83 (br. s., 4 H), 1.35 (br. s., 8 H),1.09 - 1.25 (m, 96 H), 0.72-0.92 (m, 24 H).

**FT-IR** (cm$^{-1}$): 2922, 2850, 1697, 1655, 1595, 1501, 1459, 1407, 1326, 1255, 1213, 1169, 911, 810, 722.

**4.3.2.7. Synthesis of (Poly-4):**
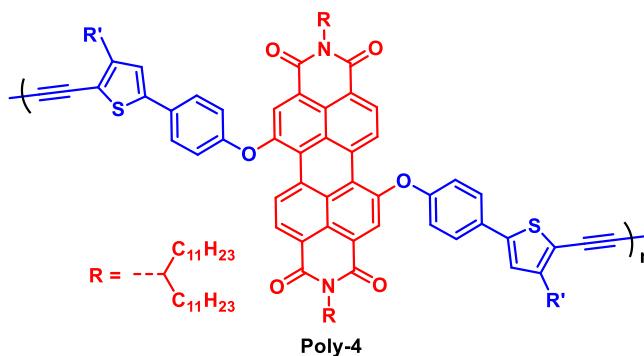


Poly-4

The synthesis of **Poly-3** followed a similar process to that of **Poly-1**. In a 10 mL schlenk tube, compound **5b** (150 mg, 97.13 μmol) was dissolved in 3 mL anhydrous THF. Then, copper (I)

chloride (144 mg, 9.46 mmol) and N,N,N′,N′-tetramethylethylenediamine (339 mg, 2.91 mmol) was added to the solution of **5b**. The reaction mixtures were stirred for 1 day. Once the reaction was completed, the reaction mixture was quenched with methanol. The crude polymer was then purified using soxhlet extraction with methanol, acetone, and chloroform.

**Nature and Yield**: reddish-black solid, 143 mg (95%).

**$^1$H NMR** (400 MHz, CDCl$_3$): $\delta$ [ppm] = 9.48 - 9.56 (m, 2 H), 8.61 (br. s., 2 H), 8.36 (br. s., 2 H), 7.56 – 7.67 (m, 4 H), 7.10 – 7.20 (m, 4 H), 7.06 (br. s., 2 H), 5.12 (br. s., 2 H), 2.55 - 2.79 (m, 4 H), 2.18 (br. s., 4 H), 1.68 (br. s., 4 H), 1.08 - 1.24 (m, 76 H), 0.72-0.92 (m, 24 H).

**FT-IR** (cm$^{-1}$): 2920, 2849, 1697, 1654, 1595, 1501, 1405, 1327, 1257, 1213, 1186, 907, 814, 718.

## 4.4. Results and Discussion

We first synthesized the respective trimethyltin thiophene monomer units, **BT2** and **T6**, to get the polymers using the previously reported method.[15] Synthesis of hanging and linear polymers (**Poly-1,2,3**, and **4**) was accomplished through reactions such as nucleophilic aromatic substitution, Stille coupling, oxidative and Hay-Glaser coupling reactions in good yields (Scheme 4.1-4.4). Firstly, with **PTCDA** and **Br$_2$-PTCDA** as the starting material, molecules **2a** and **2b** were efficiently synthesized in high yields of 78 and 82%, respectively (Scheme 4.1,4.3). Secondly, the thiophene-based PBIs were obtained by Stille coupling reaction of **2a** and **2b** with (3,3'-dihexyl-[2,2'-bithiophen]-5-yl)trimethylstannane and ((3-hexyl-5-(trimethylstannyl)thiophen-2-yl)ethynyl)triisopropylsilane delivered molecule **3a** (93%), **3b** (92%), **4a** (90%), and **4b** (93%), respectively (Scheme 4.2,4.4). To get the free acetylene group, TIPS groups of molecules **4a** and **4b** were deprotected using tetrabutylammonium fluoride at room temperature to yield **5a** and **5b**. Further, to synthesize **Poly-1,3**, we optimized the reaction condition for C-C bond formation of bithiophene to oligothiophene using FeCl$_3$ mediated oxidative coupling reaction at room temperature for one day to obtain hanging and linear PBI-based polymers, **Poly-1** (94%) and **Poly-3** (96%) in high isolated yields (Scheme 4.2,4.4). Polymerization reactions were carried out in an argon-degassed anhydrous CH$_2$Cl$_2$ and CH$_3$NO$_2$ solvent. Moreover, the polymers **Poly-2** and **Poly-4** were synthesized by the cupper-mediated Hay-Glaser coupling reaction. To synthesize acetylene coupled product, we proceeded further with the crude **5a** and **5b** molecules in the presence of CuCl, TMEDA as a catalyst in THF at

room temperature for one day, resulting in hanging and linear polymers, **Poly-2** (91%) and **Poly-4** (95%) in high isolated yields (Scheme 4.2,4.4).The crude polymers were precipitated from methanol, filtered, and dried. The crude polymer was purified in each case using soxhlet extraction with methanol, acetone, and dichloromethane. To remove small monomers and higher oligomers, the dichloromethane fraction was concentrated under reduced pressure and reprecipitated in a mixture of dichloromethane and methanol to obtain blackish red polymer, which was filtered and dried. The resultant polymers are soluble in most of the halogenated solvents, such as $CH_2Cl_2$, chloroform, chlorobenzene, and *o*-dichlorobenzene. All the synthesized monomers and polymers were characterized by ^{1}H NMR spectroscopy, FT-IR, and gel permeation chromatography (GPC) (Figure 4.1-4.4).

## Agilent GPC/SEC Software
## National Chemical Laboratory Pune

**Processing Parameters**

| | |
|---|---|
| Method | Last modified |
| Using Flow Rate Correction | No |
| Mark-Houwink K ((10e-5) dL/g) | 14.100 |
| Mark-Houwink Alpha | 0.700 |
| Concentration Detector Used in Analysis | RI |
| Injection volume (µL) | 100.00 |
| Flow rate (mL/min) | 1.00 |

**MW Ranges Method**

| | |
|---|---|
| Calculate MW Ranges | No |

**Percentage Fractions Method**

| | |
|---|---|
| Calculate Percentage Fractions | No |

## Results

| | |
|---|---|
| Analysed by | Administrator at 8:32:18 AM on Monday, September 26, 2022 |
| Comments | |
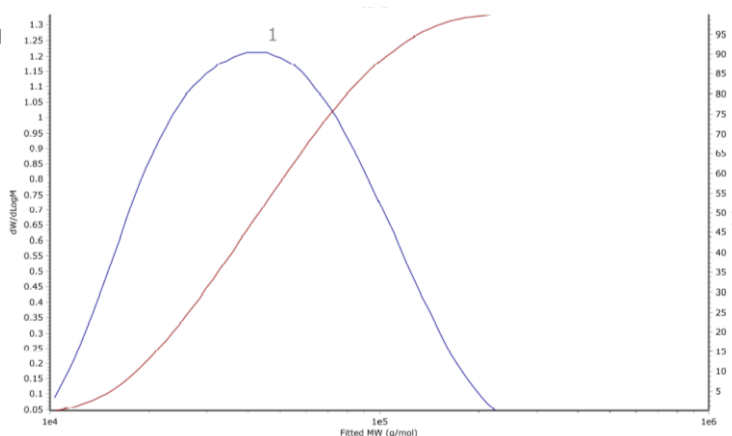
**Molecular Weight Averages**

| Peak | Mp (g/mol) | Mn (g/mol) | Mw (g/mol) | Mz (g/mol) | Mz+1 (g/mol) | Mv (g/mol) | PD |
|---|---|---|---|---|---|---|---|
| Peak 1 | 44686 | 35551 | 54205 | 79906 | 106418 | 76002 | 1.525 |

**Figure 4.1**. Molecular average weight and distribution plot of **poly-1**.

**Agilent GPC/SEC Software**
**National Chemical Laboratory Pune**

**Processing Parameters**
Method                                          Last modified
Using Flow Rate Correction                      No
Mark-Houwink K ((10e-5) dL/g)                   14.100
Mark-Houwink Alpha                              0.700
Concentration Detector Used in                  RI
Analysis
Injection volume (µL)                           100.00
Flow rate (mL/min)                              1.00

**MW Ranges Method**
Calculate MW Ranges                             No

**Percentage Fractions Method**
Calculate Percentage Fractions                  No

**Results**
Analysed by                  Administrator at 2:02:44 PM on Thursday, September 29, 2022
Comments

**Molecular Weight Averages**

| Peak | Mp (g/mol) | Mn (g/mol) | Mw (g/mol) | Mz (g/mol) | Mz+1 (g/mol) | Mv (g/mol) | PD |
|---|---|---|---|---|---|---|---|
| Peak 1 | 24744 | 30165 | 42519 | 59195 | 75461 | 56701 | 1.41 |

**Figure 4.2**. Molecular average weight and distribution plot of **poly-2**.



**Agilent GPC/SEC Software**
**National Chemical Laboratory Pune**

**Processing Parameters**
Method                                          Last modified
Using Flow Rate Correction                      No
Mark-Houwink K ((10e-5) dL/g)                   14.100
Mark-Houwink Alpha                              0.700
Concentration Detector Used in                  RI
Analysis
Injection volume (µL)                           100.00
Flow rate (mL/min)                              1.00

**MW Ranges Method**
Calculate MW Ranges                             No

**Percentage Fractions Method**
Calculate Percentage Fractions                  No

**Results**
Analysed by                  Administrator at 2:22:34 PM on Tuesday, August 30, 2022
Comments

**Molecular Weight Averages**

| Peak | Mp (g/mol) | Mn (g/mol) | Mw (g/mol) | Mz (g/mol) | Mz+1 (g/mol) | Mv (g/mol) | PD |
|---|---|---|---|---|---|---|---|
| Peak 1 | 80398 | 57628 | 99235 | 157354 | 220455 | 148380 | 1.722 |

**Figure 4.3**. Molecular average weight and distribution plot of **poly-3**.

**Agilent GPC/SEC Software**
**National Chemical Laboratory Pune**

**Processing Parameters**
Method                                          Last modified
Using Flow Rate Correction                      No
Mark-Houwink K ((10e-5) dL/g)                   14.100
Mark-Houwink Alpha                              0.700
Concentration Detector Used in                  RI
Analysis
Injection volume (μL)                           100.00
Flow rate (mL/min)                              1.00

**MW Ranges Method**
Calculate MW Ranges                             No

**Percentage Fractions Method**
Calculate Percentage Fractions                  No
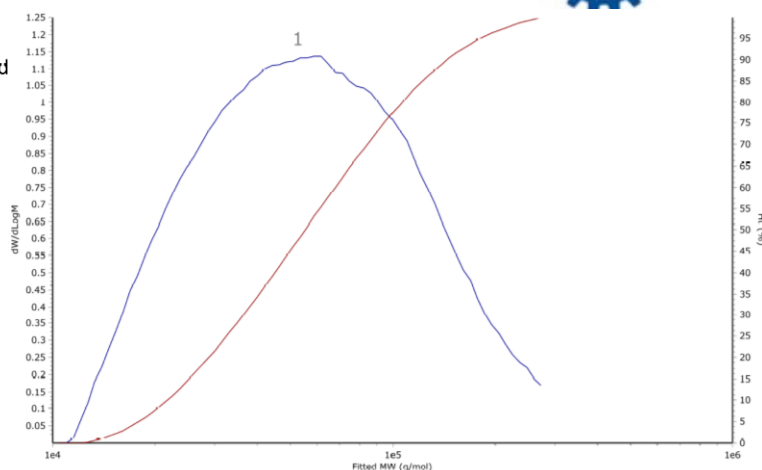
## Results

Analysed by                    Administrator at 1:05:57 PM on Monday, July 4, 2022
Comments

**Molecular Weight Averages**

| Peak | Mp (g/mol) | Mn (g/mol) | Mw (g/mol) | Mz (g/mol) | Mz+1 (g/mol) | Mv (g/mol) | PD |
|------|-----------|-----------|-----------|-----------|-------------|-----------|------|
| Peak 1 | 58863 | 44040 | 71143 | 108756 | 145773 | 103177 | 1.615 |

**Figure 4.4**. Molecular average weight and distribution plot of **poly-4**.

The proton signals in the ^{1}H NMR spectra were broadened and slightly shifted compared to the monomers, indicative of successful polymerization of the monomers. Using 1,2,4 trichlorobenzene as the mobile phase, the molecular weights of the polymers were calculated by GPC and calibrated against polystyrene standards (Table 4.5.1).

The absorption and emission spectra of **rPBI** and **polymers** were recorded in the solution state in dichloromethane ($1\times10^{-5}$ molL$^{-1}$), as shown in Figure 4.5-4.9, and the comparative photophysical parameters are shown in Table 4.5.2 As shown in Figure 4.5.2 the polymers exhibit slightly broad peaks compared to the narrow absorption spectrum from 440 to 560 nm and absorption maximum at 525 nm of reference molecule **rPBI** . The maximum absorption peak of **Poly-1,2** and **Poly-3,4** were varied as 543 nm and 540 nm, respectively, and covered a broad range from 300 to 610 nm. Normalized absorption spectra showed a clear red-shift of around 18 and 15 nm in the absorption maximum from **rPBI** to **Poly-1,2** and **Poly-3,4** (Figure 4.6,4.8). Among the series, **Poly-3,4** showed broader absorption spectra and slight blue shift of around 3 nm in the absorption maximum and absorption edge in the solution state, indicating the sizeable rigid structure could inhibit intermolecular aggregation. Figure 4.5b shows that photograph of **poly-1,2** and **poly-3,4** appearing as flakes and powder forms, respectively.
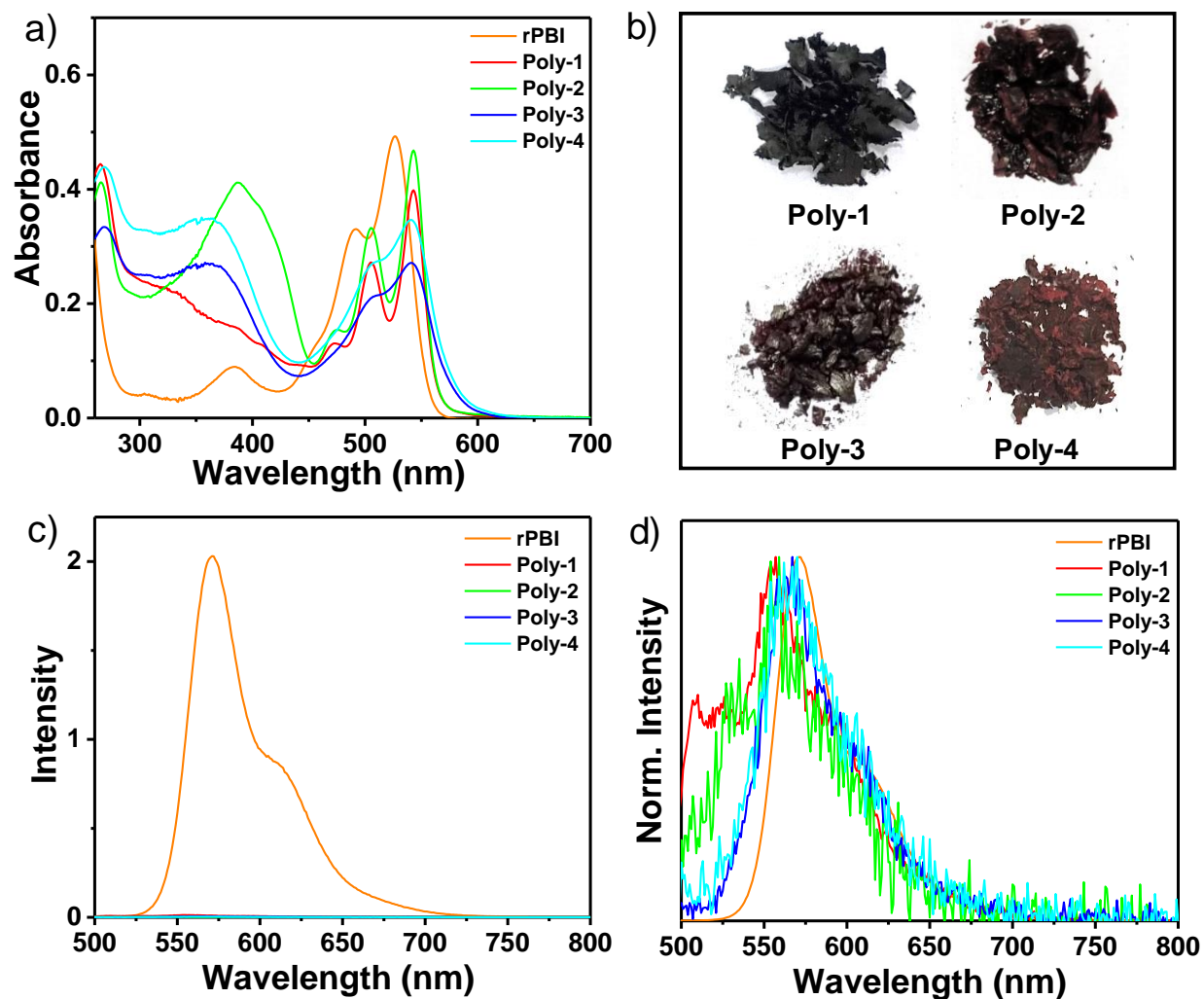
**Figure 4.5.** a) UV-Vis absorption and b) Photograph of **Poly-1,2,3**, and **Poly-4** in solid under visible light. c) Steady-state emission and corresponding d) normalized spectra of **Poly-1,2,3**, and **Poly-4** in CH$_2$Cl$_2$ solution ($C$ = 1 x 10$^{-5}$ M, $l$ = 1 cm) at 25 ˚C ($\lambda_{ex}$ = 460 nm for rPBI, 480 nm for **Poly-1,2,3**, and **Poly-4**).
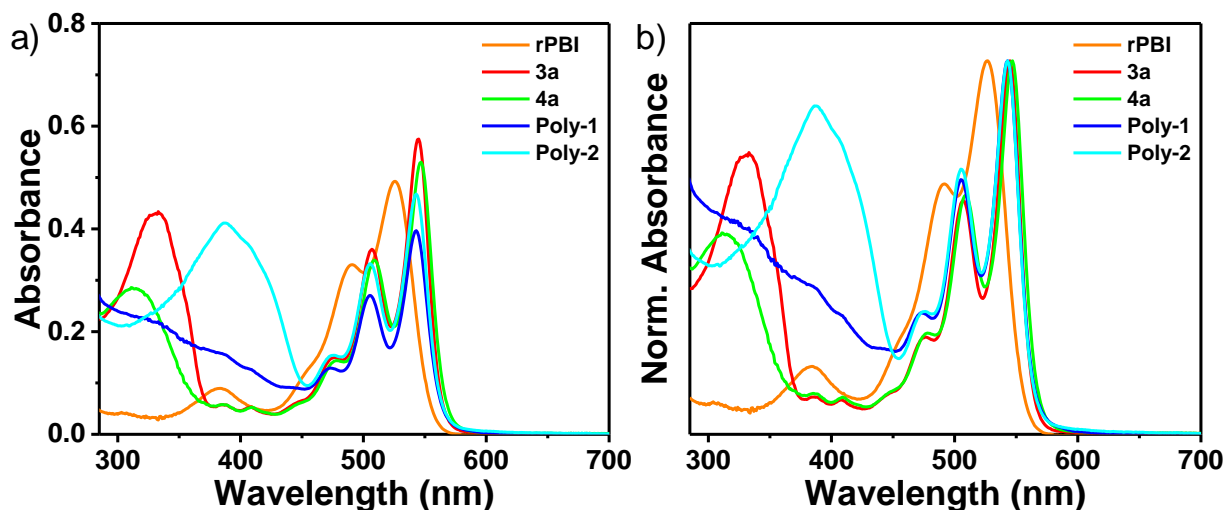
**Figure 4.6.** a) Absorption and corresponding b) normalized spectra of **rPBI**, **3a, 4a, Poly-1,** and **Poly-2** in CH$_2$Cl$_2$ solution ($C$ = 1 x 10$^{-5}$ M, $l$ = 1 cm) at 25 ˚C.
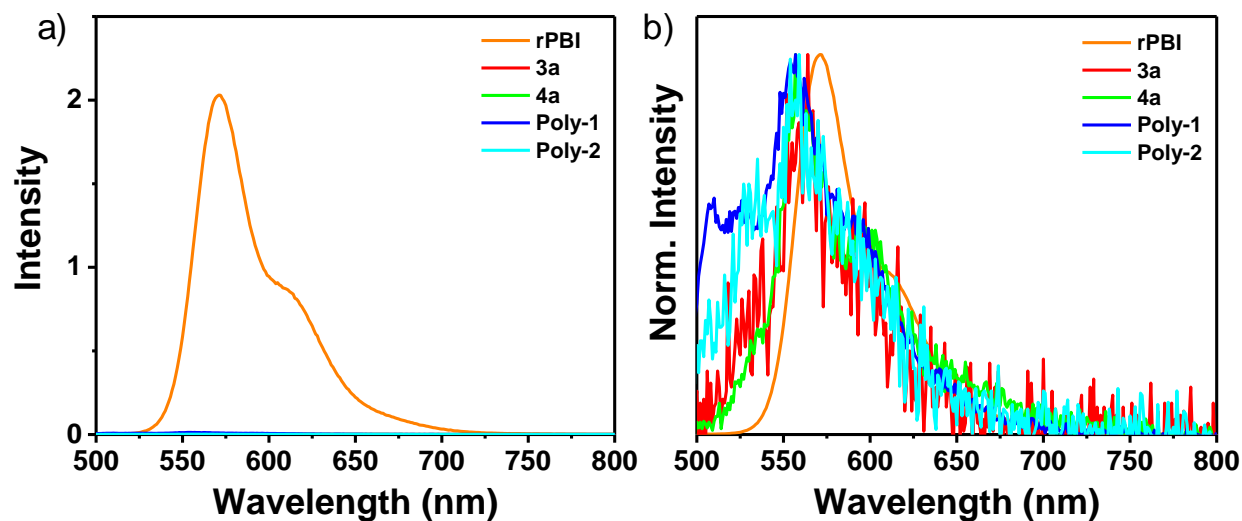


**Figure 4.7.** a) Steady-state emission and corresponding b) normalized spectra of **rPBI**, **3a, 4a, Poly-1,** and **Poly-2** in CH$_2$Cl$_2$ solution ($C$ = 1 x 10$^{-5}$ M, $l$ = 1 cm) at 25 ˚C ($\lambda_{ex}$ = 460 nm for **rPBI**, 480 nm for **3a, 4a, Poly-1,** and **Poly-2**).
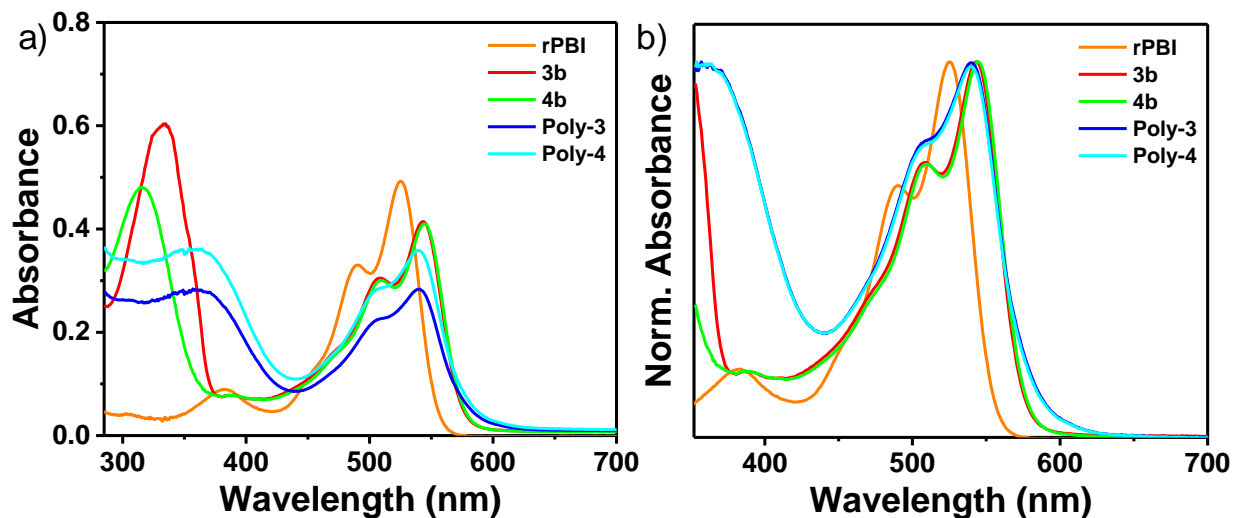
**Figure 4.8.** a) Absorption and corresponding b) normalized spectra of **rPBI**, **3b, 4b, Poly-3,** and **Poly-4** in $CH_2Cl_2$ solution ($C$ = 1 x $10^{-5}$ M, $l$ = 1 cm) at 25 °C.

Figure 4.5c,d from the emission spectra of **rPBI** and **polymers** appear at 560 to 570 nm region, Strong fluorescence intensity was observed for **rPBI** in dichloromethane, however, in the case of polymers, the emission is completely quenched in the solution and solid-state. The weak fluorescence emission of polymers will benefit the charge separation in optoelectronic material. The redox properties of PBI-based polymers were evaluated using CV and DPV, which are used to ascertain the HOMO and LUMO energy levels of the polymers (Figure 4.10-4.14, Table 4.5.2).
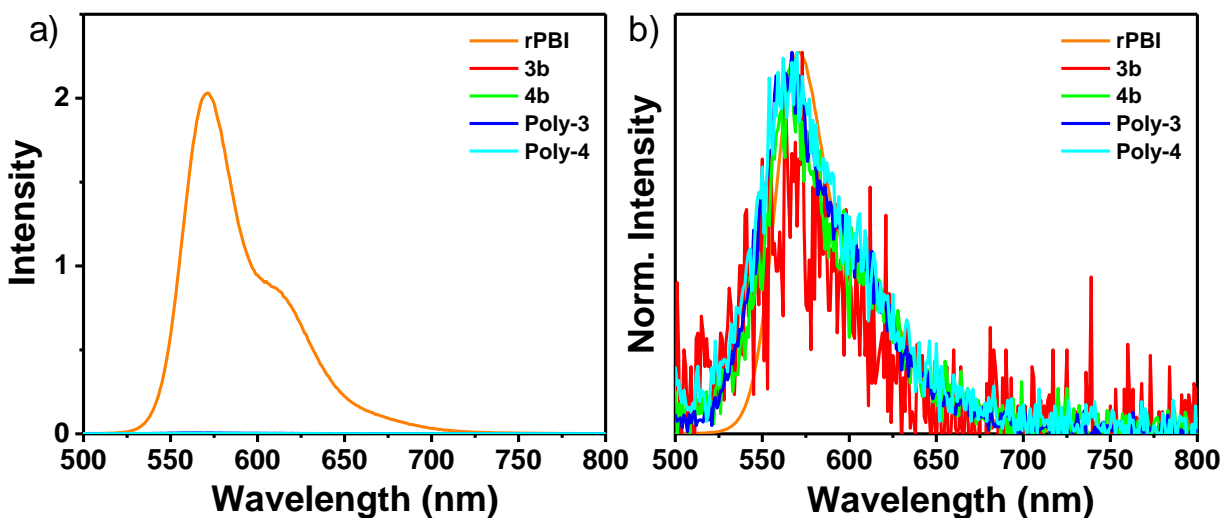
**Figure 4.9.** a) Steady-state emission and corresponding b) normalized spectra of **rPBI**, **3b**, **4b**, **Poly-3,** and **Poly-4** in $CH_2Cl_2$ solution ($C$ = 1 x $10^{-5}$ M, $l$ = 1 cm) at 25 ˚C ($\lambda_{ex}$ = 460 nm for **rPBI**, 480 nm for **3b, 4b, Poly-3,** and **Poly-4**).



a)

$E^3_{oxd}$ = 1.48 V
$E^2_{oxd}$ = 1.24 V
$E^1_{oxd}$ = 0.90 V

$E^1_{red}$ = -1.17 V
$E^2_{red}$ = -1.40 V
$E^3_{red}$ = -1.82 V

b)

$E^3_{oxd}$ = 1.26 V
$E^2_{oxd}$ = 0.89 V
$E^1_{oxd}$ = 0.65 V

$E^1_{red}$ = -1.15 V
$E^2_{red}$ = -1.41 V

c)

$E^3_{oxd}$ = 1.27 V
$E^2_{oxd}$ = 1.10 V
$E^1_{oxd}$ = 0.60 V

$E^1_{red}$ = -1.11 V
$E^2_{red}$ = -1.34 V

d)

$E^3_{oxd}$ = 1.34 V
$E^2_{oxd}$ = 1.08 V
$E^1_{oxd}$ = 0.74 V

$E^1_{red}$ = -1.06 V
$E^2_{red}$ = -1.42 V

Potential / V vs Fc/Fc$^+$
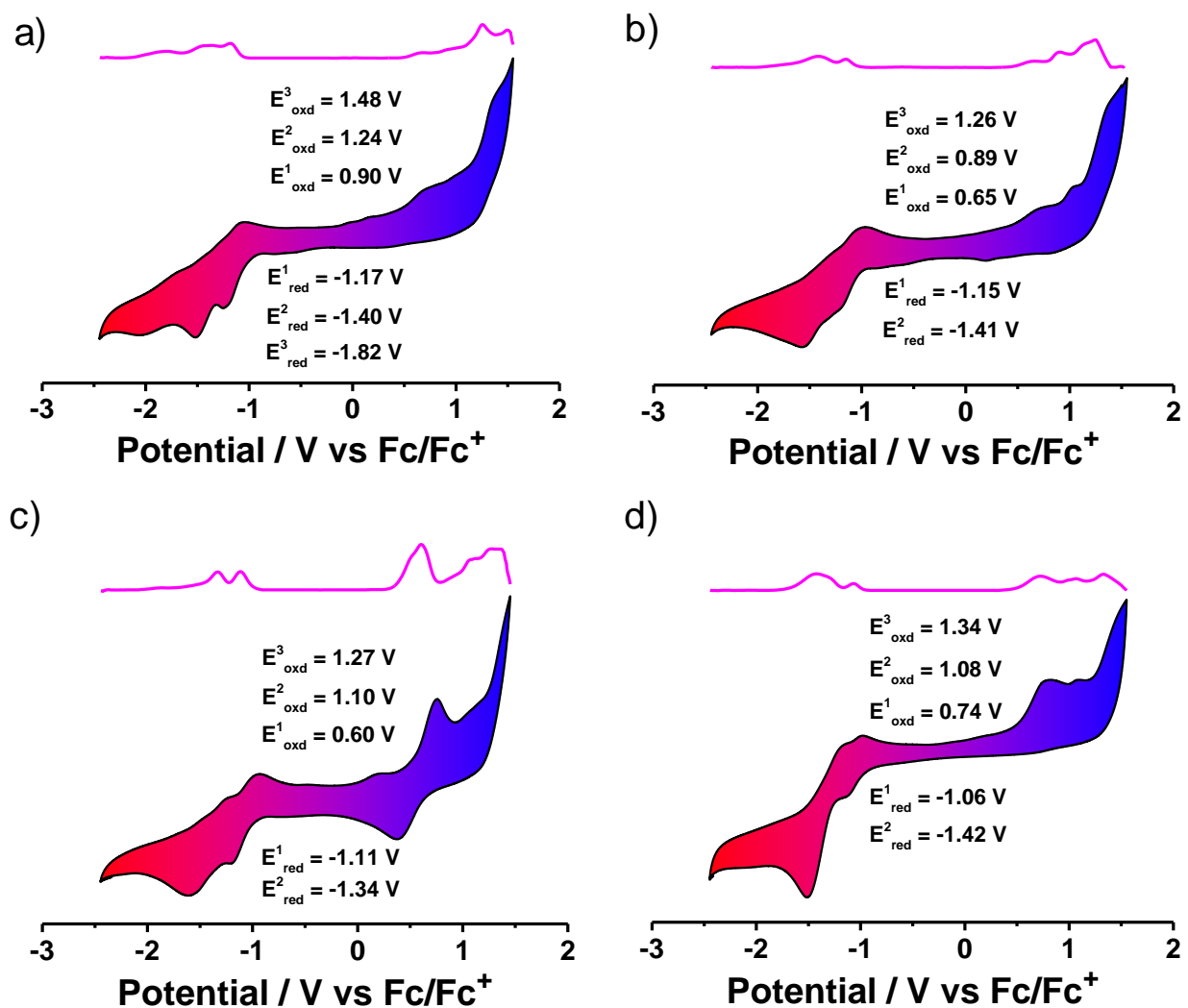
**Figure 4.10.** CV and DPV measurements of a) **Poly-1**, b) **Poly-2**, c) **Poly-3** and d) **Poly-4** in $CH_2Cl_2$ ($C$ = 1 mM) with $Bu_4NPF_6$ at 100 mV/s scan rate.

The electrochemical potentials were calculated from the start of the oxidation and reduction sweeps. The Fc/Fc$^+$ redox pair was used to calibrate each voltammogram. Except for **Poly-1**, all **polymers** and **rPBI** show two reversible reduction peaks, demonstrating their ability to accept two or three electrons, with half-wave reduction potentials ($E_{1/2}$ red) for **Poly-1** (-1.17/-1.40/-1.82), **Poly-2** (-1.15/-1.41), **Poly-3** (-1.11/-1.34), and **Poly-4** (-1.06/-1.42), respectively. In

contrast, three reversible reduction waves are exhibited for **Poly-1**. Most interestingly, **Poly-1,2** and **Poly-3,4** have first half-wave reduction potentials ($E_{1/2}$ red) that are lower than those of **rPBI** by about -1.17 V and -1.15, respectively, and higher by about -1.11 V and -1.06, respectively.
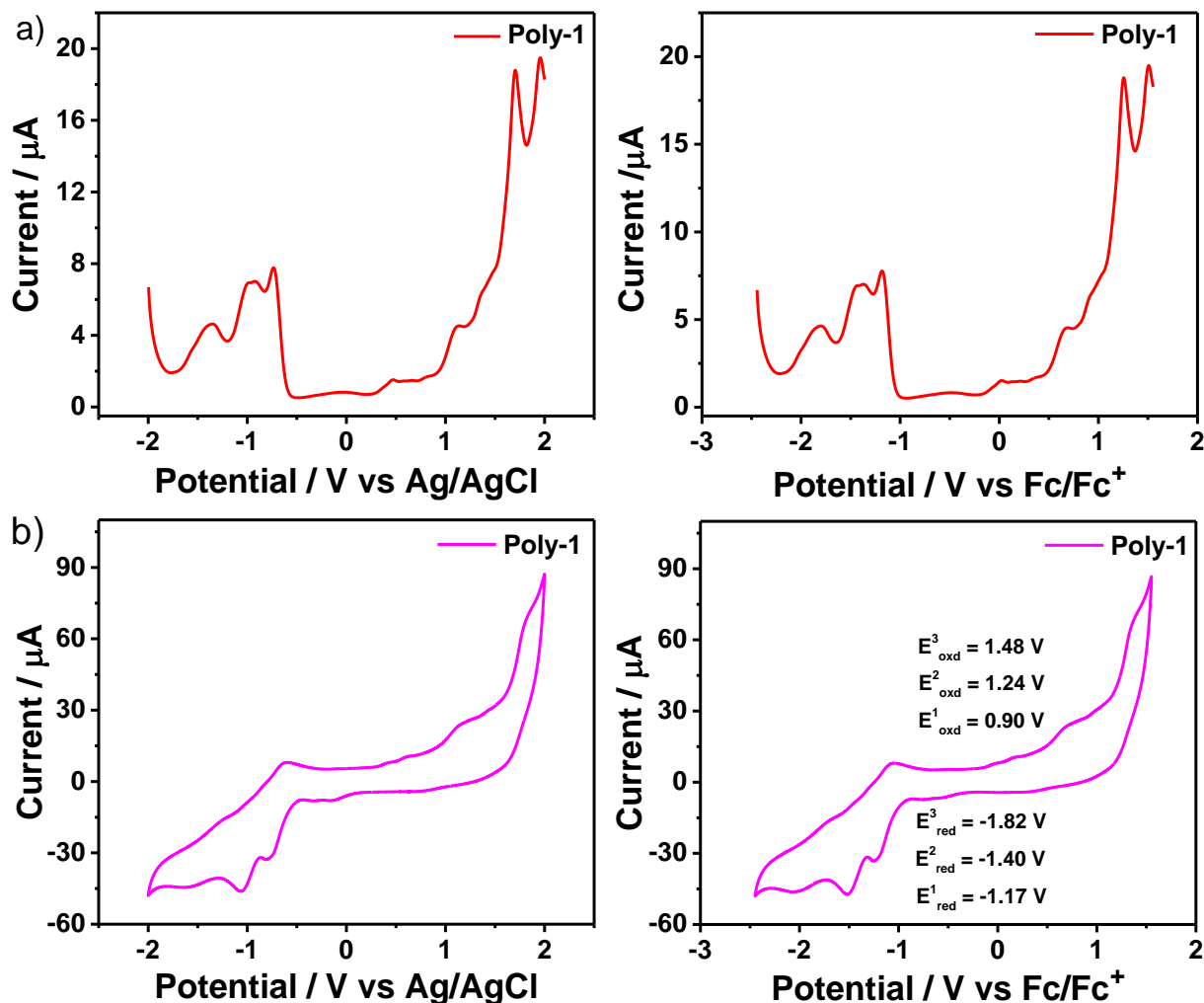


**Figure 4.11.** a) DPV measurements at 100 mV/s scan rate (left) and calculated as ferrocene as an internal reference standard ($E_{Fc+/Fc}$ = 0.00 V) (right) of **poly-1** (1 mM). b) CV at 100 mV/s scan rate (left) and CV calculated as ferrocene as an internal reference standard ($E_{Fc+/Fc}$ = 0.00 V) (right) of **poly-1** (1 mM).

Furthermore, three reversible oxidation peaks are observed for all the polymers, with half-wave oxidation potentials ($E_{1/2}$ ox) for **Poly-1** (+0.90/+1.24/+1.48 V), **Poly-2** (+0.65/+0.89/+0.65 V), **Poly-3** (+0.60/+1.10/+1.27 V), and **Poly-4** (+0.74/+1.08/+1.34 V), respectively (Figure 4.10-4.14, Table 4.5.2).
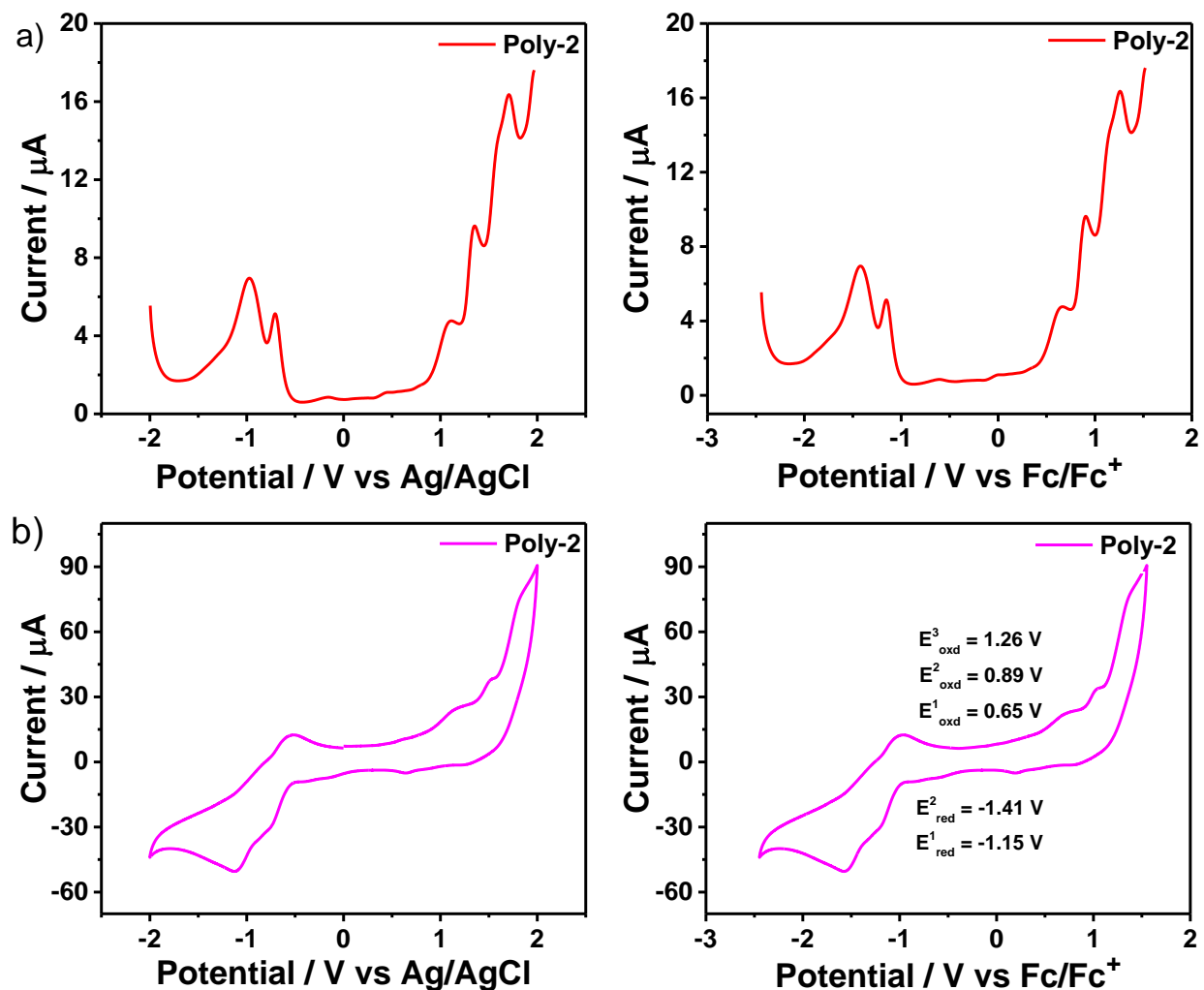
**Figure 4.12.** a) DPV measurements at 100 mV/s scan rate (left) and calculated as ferrocene as an internal reference standard ($E_{Fc+/Fc}$ = 0.00 V) (right) of TSP1 (1 mM). b) CV at 100 mV/s scan rate (left) and CV calculated as ferrocene as an internal reference standard ($E_{Fc+/Fc}$ = 0.00 V) (right) of **poly-2** (1 mM).
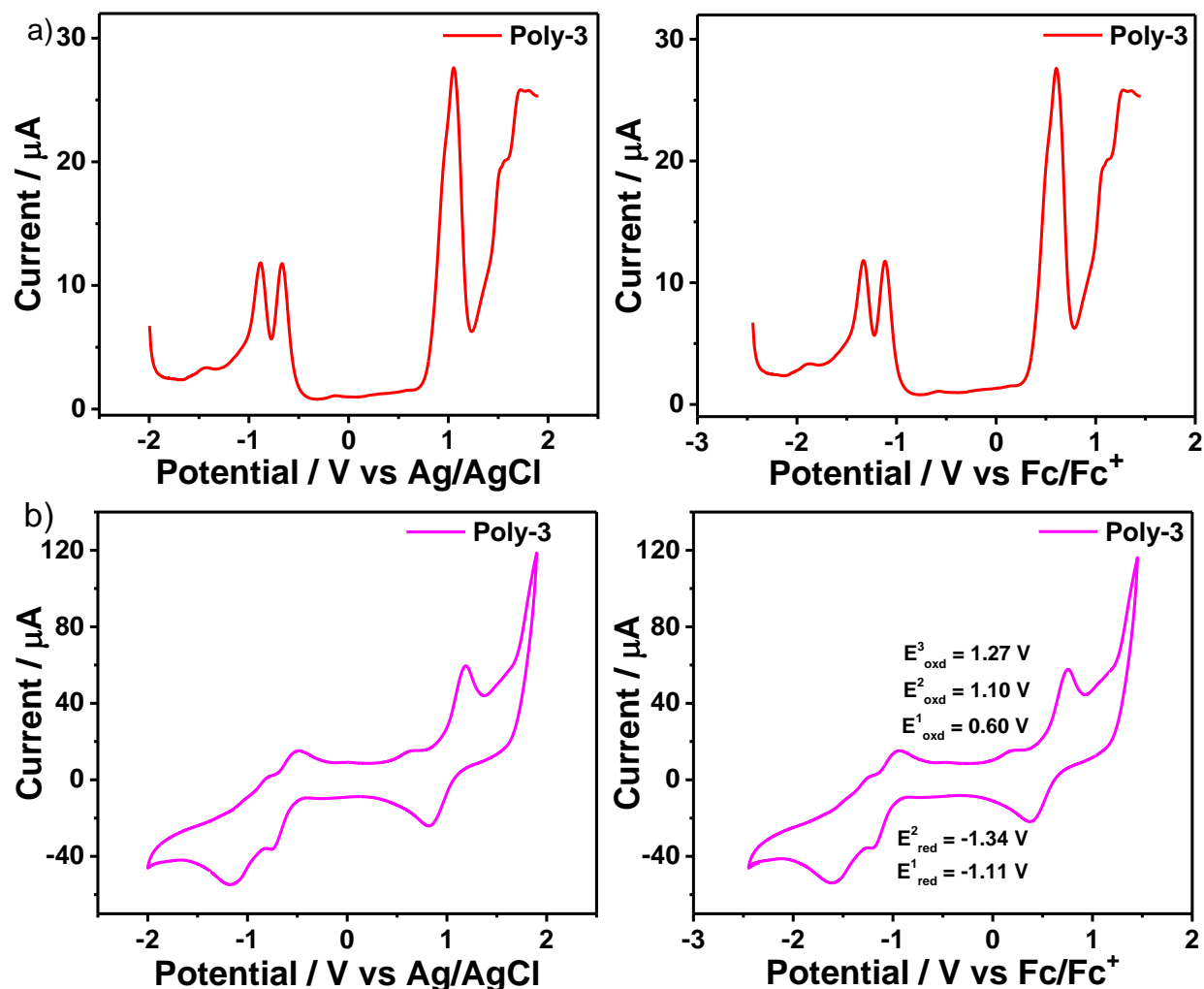
**Figure 4.13.** a) DPV measurements at 100 mV/s scan rate (left) and calculated as ferrocene as an internal reference standard ($E_{Fc+/Fc}$ = 0.00 V) (right) of TSP1 (1 mM). b) CV at 100 mV/s scan rate (left) and CV calculated as ferrocene as an internal reference standard ($E_{Fc+/Fc}$ = 0.00 V) (right) of **poly-3** (1 mM).
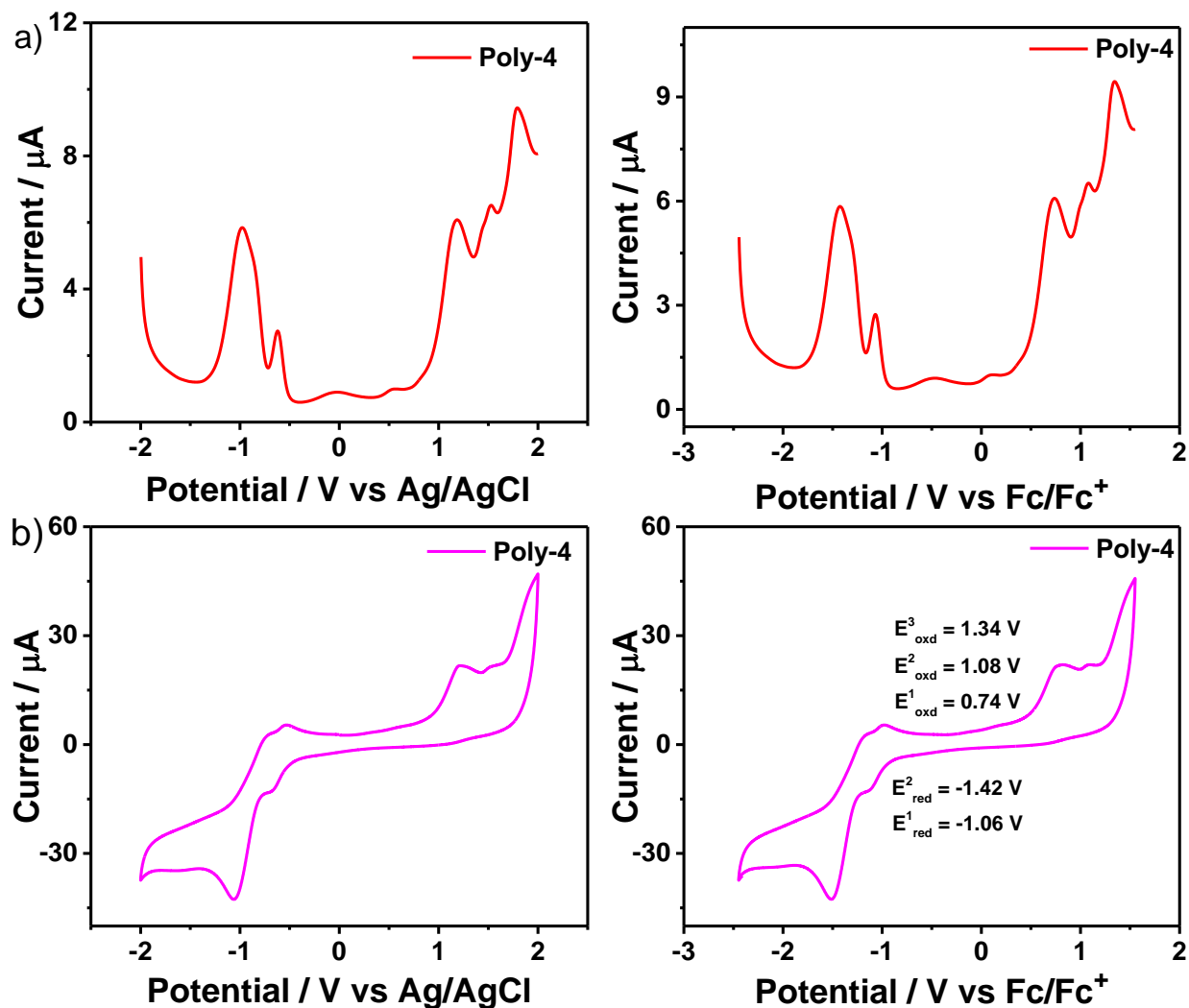
**Figure 4.14.** a) DPV measurements at 100 mV/s scan rate (left) and calculated as ferrocene as an internal reference standard ($E_{Fc+/Fc}$ = 0.00 V) (right) of TSP1 (1 mM). b) CV at 100 mV/s scan rate (left) and CV calculated as ferrocene as an internal reference standard ($E_{Fc+/Fc}$ = 0.00 V) (right) of **poly-4** (1 mM).

## 4.5. Tables

**Table 4.5.1.** Molecular weight of the PBI-based conjugated polymers.

| Polymers | $M_n$ [g/mol] | $M_w$ [g/mol] | PDI |
|:---:|:---:|:---:|:---:|
| **Poly-1** | 35551 | 54205 | 1.52 |
| **Poly-2** | 30165 | 42519 | 1.41 |
| **Poly-3** | 57628 | 99235 | 1.72 |
| **Poly-4** | 44040 | 71143 | 1.61 |

 $M_n$, $M_w$, and PDI of the polymers were determined by GPC using polystyrene standard with 1,2,4 trichlorobenzene as eluent.

**Table 4.5.2.** Optical and redox properties of **rPBI**, **Poly-1**, **Poly-2**, **Poly-3**, and **Poly-4.**

| Sample | $\lambda_{max, ab}$ (nm) | $\varepsilon_{max}$ (M$^{-1}$cm$^{-1}$) | $\lambda_{max, em}$ (nm) | $E_{ox}$, 1 (eV) | $E_{ox}$, 2 (eV) | $E_{ox}$, 3 (eV) | $E_{red}$, 1 (eV) | $E_{red}$, 2 (eV) | $E_{red}$, 3 (eV) | $E_{HOMO}$ (eV) | $E_{LUMO}$ (eV) | $E_g$ (eV) |
|---|---|---|---|---|---|---|---|---|---|---|---|---|
| **rPBI** | 525 | 49281 | 571 | - | - | - | -1.14 | -1.30 | - | - | -3.66 | - |
| **Poly-1** | 543 | 39637 | 556 | 0.90 | 1.24 | 1.48 | -1.17 | -1.40 | -1.82 | -5.70 | -3.63 | 2.07 |
| **Poly-2** | 543 | 46881 | 559 | 0.65 | 0.89 | 1.26 | -1.15 | -1.41 | - | -5.45 | -3.65 | 1.80 |
| **Poly-3** | 540 | 28409 | 566 | 0.60 | 1.10 | 1.27 | -1.11 | -1.34 | - | -5.40 | -3.69 | 1.71 |
| **Poly-4** | 540 | 36219 | 569 | 0.74 | 1.08 | 1.34 | -1.06 | -1.42 | - | -5.54 | -3.74 | 1.80 |

# Chapter 4. Section 2: Macrocycle of a Donor-Strapped Perylene Bisimide Macrocycle.

## 4.2.1. Introduction

Cyclic macrocycles with π-conjugated electroactive properties are being developed as prototype materials to facilitate the efficient transfer of charge and electronic excitation.[16] Building columnar 1D nanotubes, 2D porous surface networks, and 3D inclusion complexes by self-assembly requires fully conjugated cyclic oligomers with well-defined diameters that possess shape-persistent, non-collapsible and fully π-conjugated backbones.[17] Cyclic and conjugated macrocycles, which are organic semiconductors, possess inner voids that offer the potential to modify their electrical and optoelectronic characteristics.[18] Notably, the presence of cyclic arrays of chlorophyll units in many light-harvesting systems is attributed to the enhanced electronic delocalization that results from ring structures.[17] Cyclic compounds such as cyclo-*p*-phenyleneacetylene,[20]   PBI-based macrocycles[15,21]   and porphyrin nanocages[16,18] possess inflexible intramolecular voids that allow for the inclusion and detection of guest molecules. In covalent cyclic oligomers with a rigid π-system, the degree of conformational disorder is typically lower than that of linear chains, owing to the strained electronic properties that arise within these macrocycles.[22] The properties of nanosized conjugated macrocycles, such as luminescence, aromaticity, two-photon absorption, chirality, and redox properties have been studied in relation to aromatic and non-aromatic annulenes and expanded in the polycyclic aromatic hydrocarbone.[23] Recently, large macrocycles have been recognized as ideal for observing single molecules, manipulation, and electronics. However, the novel structures, properties, and functions of nanosized conjugated macrocycles remain fundamentally important. As the synthetic process is flexible, alkyne bridges are mostly employed in making large macrocycles similar to cages out of a cage in oligothiophene ring-strapped perylene bisimide macrocycles.

## 4.2.2 Experimental Procedures: Synthesis

### 4.2.2.1. Synthesis of larger macrocycle of a donor-acceptor macrocycle.
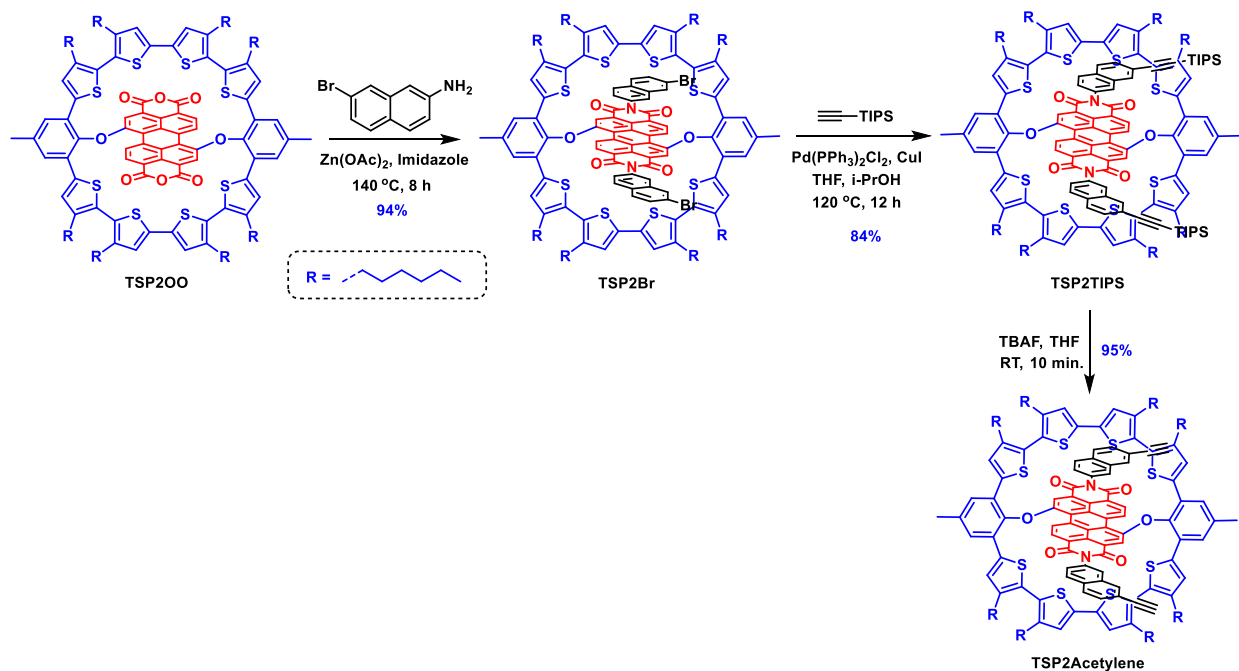


**Scheme 4.2.1:** Synthesis of molecule **TSP2Acetylene**.
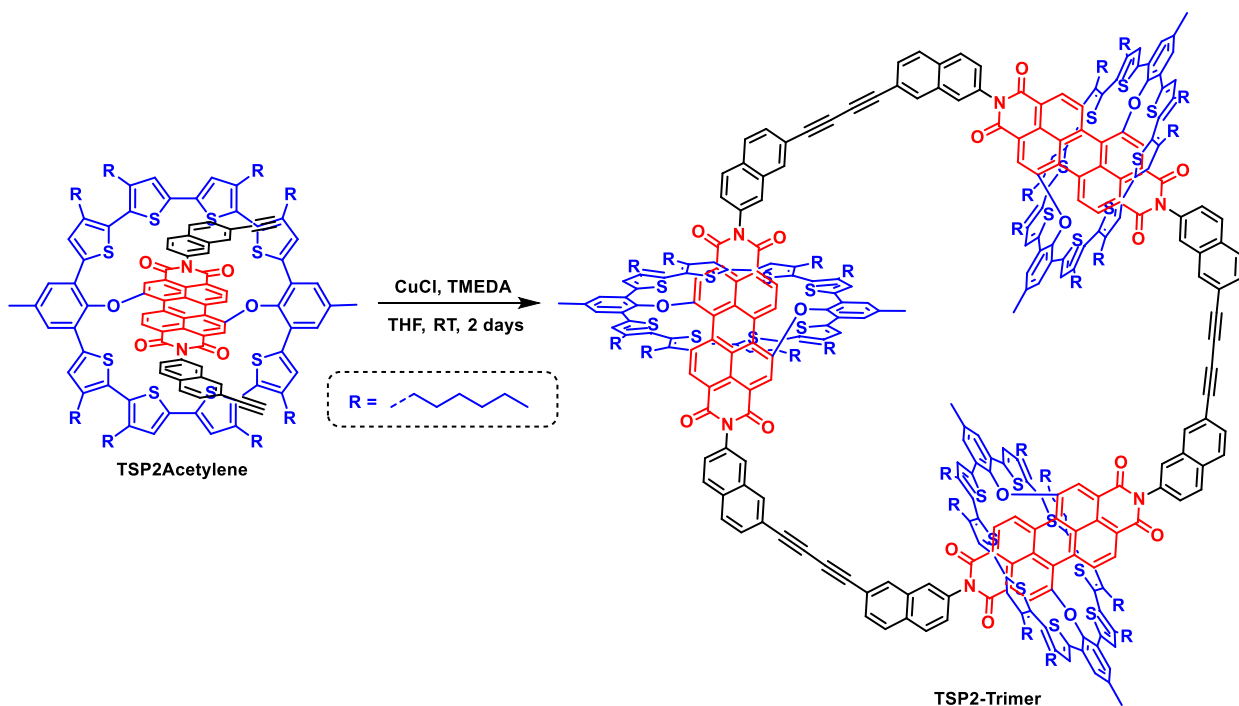


**Scheme 4.2.2.** Synthesis of molecule **TSP2-Trimer**.

**4.2.2.1.1. Synthesis of (TSP2Br).**
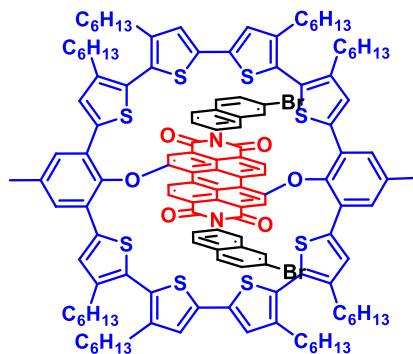


In a 10 mL pressure tube, **TSP2OO** (300 mg, 155.38 μmol), Zn(OAc)$_2$ (28 mg, 155.13 μmol), and 7-bromonaphthalen-2-amine (103 mg, 466.13 μmol) were added to imidazole (500 mg). The mixture was stirred at 150 °C for 8 h and then cooled to room temperature. In to that, 2N HCl solution (50 mL) was added and stirred for further 2 h, filtered. The precipitate was washed with an excess amount of MeOH, and extracted with CH$_2$Cl$_2$, and then the compound was purified by column chromatography (silica gel, dichloromethane).

**Nature and Yield**: Red solid, 340 mg (94%).

**$^1$H NMR** (400MHz, CDCl$_3$): $\delta$ [ppm] = 9.90 (d, $J$ = 8.5 Hz, 2 H), 8.60 (d, $J$ = 8.5 Hz, 2 H), 8.36 (s, 2 H), 7.98 (s, 2 H), 7.92 (d, $J$ = 8.8 Hz, 2 H), 7.77 (d, $J$ = 8.8 Hz, 2 H), 7.73 (s, 2 H), 7.60 (dd, $J$ = 8.8, 1.8 Hz, 2 H), 7.52 (s, 4 H), 7.40 (dd, $J$ = 8.6, 1.8 Hz, 2 H), 7.21 (s, 4 H), 6.76 (s, 4 H), 2.42 - 2.54 (m, 22 H), 1.58 - 1.67 (m, 8 H), 1.48 - 1.56 (m, 8 H), 1.31 (br. s., 4 H), 1.25 (br. s., 44 H), 0.82 (t, $J$ = 6.6 Hz, 12 H), 0.87 (t, $J$ = 6.6 Hz, 12 H).

**$^{13}$C NMR** (100 MHz, CDCl$_3$): $\delta$ [ppm] = 163.7, 163.5, 157.1, 143.6, 140.9, 139.9, 138.6, 137.5, 136.6, 135.6, 134.6, 133.7, 132.8, 132.1, 131.4, 130.6, 130.4, 130.1, 130.1, 130.0, 129.6, 129.4, 128.9, 128.9, 128.6, 126.9, 126.8, 125.6, 123.0, 122.8, 122.2, 122.1, 120.3, 119.8, 31.6, 31.4, 30.2, 30.1, 29.7, 29.4, 29.2, 29.1, 22.6, 22.5, 20.6, 14.1, 14.0.

**MALDI-TOF:** *m/z* calculated for C$_{138}$H$_{140}$Br$_2$N$_2$O$_4$S$_8$ [M]$^+$: 2334.6844, found: 2334.8064.

**4.2.2.1.2. Synthesis of (TSP2TIPS).**
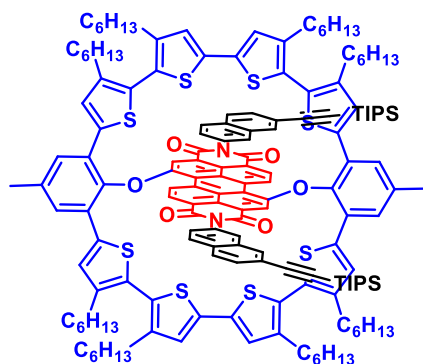


In a 10 mL pressure tube was charged with **TSP2Br** compound (300 mg, 128.26 μmol), CuI (1.2 mg, 6.41 μmol), and Pd(PPh₃)₂Cl₂ (4.5 mg, 6.41 μmol). To that, THF (3 mL) and triethylamine (2 mL) were added, kept in an ice-cold solution, degassed for 30 min., and Triisopropylsilylacetylene (35 mg, 192.40 μmol) was added drop by drop. The mixture was stirred at room temperature for 12 h. After completion of the reaction, dichloromethane was added, and the resultant mixture was filtered through celite. The filtrate was extracted with water, and the solvent was removed under reduced pressure and dried over anhydrous Na₂SO₄. The compound was purified by silica gel column chromatography using CH₂Cl₂-petroleum ether (3:7 v/v) as eluent.

**Nature and Yield**: Red solid, 275 mg (84%).

**¹H NMR** (400MHz, CDCl₃): $\delta$ [ppm] = 9.91 (d, $J$ = 8.5 Hz, 2 H), 8.60 (d, $J$ = 8.2 Hz, 2 H), 8.37 (s, 2 H), 7.97 (s, 2 H), 7.92 (d, $J$ = 8.5 Hz, 2 H), 7.80 - 7.84 (m, $J$ = 8.5 Hz, 2 H), 7.76 (s, 2 H), 7.57 (d, $J$ = 8.2 Hz, 2 H), 7.53 (s, 4 H), 7.37 - 7.42 (m, $J$ = 8.9 Hz, 2 H), 7.22 (s, 4 H), 6.76 (s, 4 H), 2.44 - 2.53 (m, 22 H), 1.60 - 1.66 (m, 8 H), 1.50 - 1.56 (m, 8 H), 1.24 - 1.31 (m, 49 H), 1.17 (s, 42 H), 0.87 (t, $J$ = 6.4 Hz, 12 H), 0.82 (t, $J$ = 6.4 Hz, 12 H)

**¹³C NMR** (125 MHz, CDCl₃): $\delta$ [ppm] = 163.7, 163.5, 157.0, 143.6, 140.9, 139.8, 138.6, 137.5, 136.6, 135.6, 133.3, 133.0, 132.8, 132.4, 132.1, 132.0, 130.6, 130.4, 130.1, 129.6, 128.9, 128.8, 128.6, 127.6, 127.5, 127.0, 125.6, 123.1, 122.8, 122.2, 122.1, 121.3, 119.8, 107.2, 91.4, 31.6, 31.4, 30.2, 30.1, 29.7, 29.4, 29.2, 29.0, 22.6, 22.6, 20.6, 18.7, 14.1, 14.0, 11.3.

**MALDI-TOF:** *m/z* calculated for C₁₆₀H₁₈₂N₂O₆S₈Si₂ [M]⁺: 2539.1302, found: 2539.7166.

**4.2.2.1.3. Synthesis of (TSP2Acetylene)**
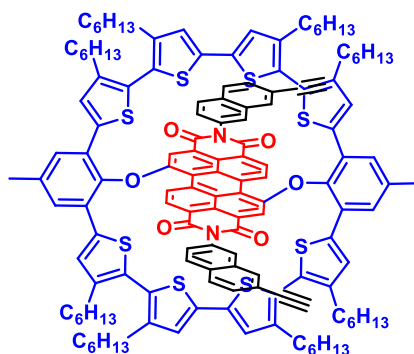


In a 25 mL round bottom flask, the compound **TSP2TIPS** (250 mg, 98.35 μmol) was dissolved in 5 mL anhydrous THF under argon atmosphere, and then Tetrabutylammonium fluoride hydrate (128 mg, 491.76 μmol) was added. The solution was stirred at room temperature for 10 to15 minutes, the reaction was monitored by TLC, and once the cleavage of TIPS group was completed, the mixture was quenched with water and worked up in dichloromethane. After drying the organic layer over anhydrous $Na_2SO_4$, the solvents were concentrated under reduced pressure. The compound was purified by silica gel column chromatography using $CH_2Cl_2$-petroleum ether (4:6 v/v) as eluent.

**Nature and Yield**: Red solid, 208 mg (95%).

**¹H NMR** (500 MHz, CDCl₃): $\delta$ [ppm] = 9.90 (d, $J$ = 8.5 Hz, 2 H), 8.60 (d, $J$ = 8.2 Hz, 2 H), 8.36 (s, 2 H), 8.00 (s, 2 H), 7.94 (d, $J$ = 8.9 Hz, 2 H), 7.83 - 7.87 (m, $J$ = 8.5 Hz, 2 H), 7.78 (s, 2 H), 7.56 - 7.60 (m, $J$ = 8.2 Hz, 2 H), 7.52 (s, 4 H), 7.41 (d, $J$ = 8.5 Hz, 2 H), 7.21 (s, 4 H), 6.76 (s, 4 H), 3.15 (s, 2 H), 2.48 - 2.53 (m, 14 H), 2.45 (t, $J$ = 7.8 Hz, 8 H), 1.59 - 1.66 (m, 8 H), 1.50 - 1.56 (m, 8 H), 1.25 (s, 24 H), 1.27 (s, 24 H), 0.86 (t, $J$ = 6.7 Hz, 12 H), 0.82 (t, $J$ = 6.4 Hz, 12 H).

**¹³C NMR** (100 MHz, CDCl₃): $\delta$ [ppm] = 163.7, 163.5, 157.1, 143.6, 140.9, 139.8, 138.6, 137.5, 136.6, 135.6, 133.5, 132.9, 132.8, 132.6, 132.4, 132.1, 130.6, 130.4, 130.1, 129.6, 129.3, 128.9, 128.8, 128.7, 127.9, 127.6, 127.3, 125.6, 123.1, 122.8, 122.2, 122.1, 119.9, 119.8, 83.8, 77.7, 31.6, 31.4, 30.2, 30.1, 29.7, 29.4, 29.2, 29.1, 22.6, 22.5, 20.6, 14.1, 14.0.

**MALDI-TOF:** *m/z* calculated for $C_{142}H_{143}N_2O_6S_8$ [M+H]⁺: 2227.8712, found: 2228.0234.

**4.2.2.1.4. Synthesis of (TSP2T).**
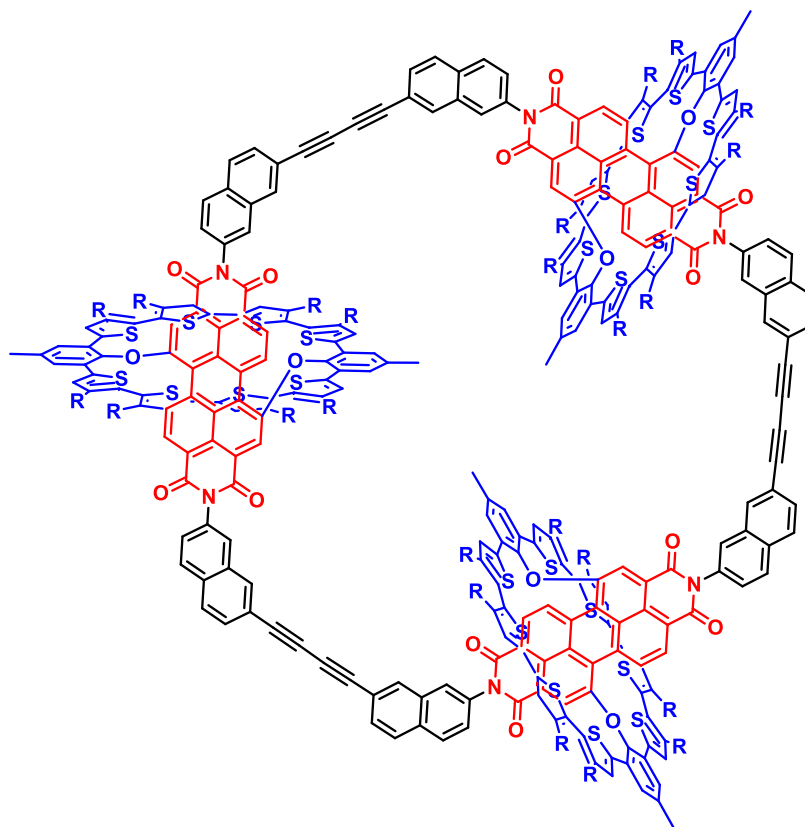


In a 150 mL two neck round bottom flask, compound **TSP2Acetylene** (100 mg, 44.86 μmol) was dissolved in 100 mL anhydrous THF. Then, copper (I) chloride (67 mg, 672.89 μmol) and N,N,N′,N′-tetramethylethylenediamine (160 mg, 1.35 μmol) were added to the solution of **TSP2Acetylne**. The reaction mixtures were stirred for 2 days. Once the reaction was completed, the reaction mixture was quenched with methanol. the crude oligomers and polymer was then purified purified by silica gel column chromatography using $CH_2Cl_2$-petroleum ether (4:6 v/v) as eluent.

**MALDI-TOF:** *m/z* calculated for $C_{426}H_{420}N_6O_{18}S_{24}$ [M]$^+$: 6674.5431, found: 6674.5078.

## 4.2.3. Results and Discussion

Chapters 2 and 3 discussed the design and synthesis of two new functionalizable donor-acceptor macrocycles. Those chapters highlighted the importance of "functionalizable" macrocycles. In this section of chapter 4, part B. we used one of the dianhydride derivatives **TSP2OO**, to develop another larger macrocycle. The synthesis of **TSP2trimer** is as follows (Scheme 4.2.1-4.2.2). At first, **TSP2OO** is reacted with 7-bromonaphthalen-2-amine in the presence of

Zn(OAc)$_2$ and imidazole to get the corresponding imide **TSP2Br** in 94% yield. Next, the Sonogashira coupling reaction of **TSP2Br** with TIPS acetylene yielded **TSP2TIPS** (84%). The cleavage of the TIPS group using TABF in THF at RT resulted in the corresponding free-acetylene compound **TSP2Acetyle** in 95% yield. The final trimer molecule **TSP2Trimer** is obtained by the Hay-Glaser coupling reaction of **TSP2Acetyle** using CuCl and TMEDA in THF at RT as shown in Scheme 4.2.2. A slow addition of CuCl in high dilution conditions slowed down the reaction to yield **TSP2Trimer**. **TSP2-Trimer** is characterized by MALDI-TOF MS. Three donor-acceptor macrocycles can be incorporated in this larger macrocycle. It provides multiple pathways for electron transfer and stabilization of the charge-separated state that has to be explored further.

## 4.2.4. Conclusion

In summary, we successfully synthesized and characterized four alternating D-A π-conjugated polymers using PBI as the "acceptor" unit and thiophene as the "donor" unit. The synthetic difficulties in developing these highly electron-deficient PBI-based polymers were successfully overcome *via* Hay-Glasear and Oxidative coupling reaction at room temperature, greatly enlarging the library of bay functionalized π-conjugated materials. All synthesized polymers are readily soluble in chloroform, THF, CH$_2$Cl$_2$, and chlorobenzene solvents and can readily be processed by solution-casting. These studies set molecular design guidelines for the subsequent generation of D-A conjugated polymers by illustrating clearly the connection between the polymer's backbone structure and the length of the polaron delocalization.

As another attractive strategy to include more electronically active molecular units as a part of the system, a larger macrocycle of the donor-strapped PBI has been synthesized and characterized by MALDI-TOF-MS. The presence of donor and acceptor units at a precise position is expected to impart strong electronic communication between them to facilitate faster electron transfer and extend the charge-separated state lifetimes. Hence the extension of the concept of donor-strapped acceptor macrocycle will be a unique macrocycle design in organic electronics. The idea of functionalizable macrocycles is the new concept introduced in this thesis, which may achieve newer heights in the coming days, and this thesis will inspire to design such new macrocycles.

## 4.2.5. Reference:

1. a) A. Facchetti, *Materials Today* **2007**, *10*, 28-37; b) X. Zhao, X. Zhan, *Chem. Soc. Rev.* **2011**, *40*, 3728; c) A. C. Arias, J. D. MacKenzie, I. McCulloch, J. Rivnay, A. Salleo, *Chem. Rev.* **2010**, *110*, 3-24; d) S. S. Lee, M. A. Loth, J. E. Anthony, Y.-L. Loo, *J. Am. Chem. Soc.* **2012**, *134*, 5436-5439; e) K. Liu, T. T. Larsen-Olsen, Y. Lin, M. Beliatis, E. Bundgaard, M. Jørgensen, F. C. Krebs, X. Zhan, *J. Mater. Chem. A* **2016**, *4*, 1044-1051; f) Y. Sui, Y. Deng, T. Du, Y. Shi, Y. Geng, *Mater. Chem. Front.* **2019**, *3*, 1932-1951; g) M. Liao, J. Duan, P. Peng, J. Zhang, M. Zhou, *RSC Adv.* **2020**, *10*, 41764-41779.

2. a) A. J. Heeger, *Chem. Soc. Rev.* **2010**, *39*, 2354; b) A. Facchetti, *Chem. Mater.* **2011**, *23*, 733-758; c) Y. Li, P. Sonar, S. P. Singh, M. S. Soh, M. van Meurs, J. Tan, *J. Am. Chem. Soc.* **2011**, *133*, 2198-2204; d) Y. Zheng, S. Zhang, J. B.-H. Tok, Z. Bao, J. *Am. Chem. Soc.* **2022**, *144*, 4699-4715; e) V. V. Brus, J. Lee, B. R. Luginbuhl, S. Ko, G. C. Bazan, T. Nguyen, *Adv. Mater.* **2019**, *31*, 1900904.

3. a) A. Tsumura, H. Koezuka, T. Ando, *Appl. Phys. Lett.* **1986**, *49*, 1210-1212; b) C. Wang, H. Dong, W. Hu, Y. Liu, D. Zhu, *Chem. Rev.* **2012**, *112*, 2208-2267; c) M. Melucci, M. Zambianchi, L. Favaretto, M. Gazzano, A. Zanelli, M. Monari, R. Capelli, S. Troisi, S. Toffanin, M. Muccini, *Chem. Commun.* **2011**, *47*, 11840.

4. A. Pron, P. Gawrys, M. Zagorska, D. Djurado, R. Demadrille, *Chem. Soc. Rev.* **2010**, *39*, 2577; a) C. Wang, H. Dong, W. Hu, Y. Liu, D. Zhu, Chem. Rev. 2012, 112, 2208–2267.

5. X. Zhan, A. Facchetti, S. Barlow, T. J. Marks, M. A. Ratner, M. R. Wasielewski, S. R. Marder, *Adv. Mater.* **2011**, *23*, 268-284.

6. C. Huang, S. Barlow, S. R. Marder, *J. Org. Chem.* **2011**, *76*, 2386-2407.

7. F. Würthner, M. Stolte, *Chem. Commun.* **2011**, *47*, 5109.

8. a) J. Li, F. Dierschke, J. Wu, A. C. Grimsdale, K. Müllen, *J. Mater. Chem.* **2006**, *16*, 96-100; b) A. Armin, W. Li, O. J. Sandberg, Z. Xiao, L. Ding, J. Nelson, D. Neher, K. Vandewal, S. Shoaee, T. Wang, H. Ade, T. Heumüller, C. Brabec, P. Meredith, *Adv. Energy Mater.* **2021**, *11*, 2003570. c) W. S. Shin, H.-H. Jeong, M.-K. Kim, S.-H. Jin, M.-R. Kim, J.-K. Lee, J. W. Lee, Y.-S. Gal, *J. Mater. Chem.* **2006**, *16*, 384-390; d) S. M. McAfee, J. M. Topple, I. G. Hill, G. C. Welch, *J. Mater. Chem. A* **2015**, *3*, 16393-16408; e) A. D. Hendsbee, J.-P. Sun, W. K. Law, H. Yan, I. G. Hill, D. M. Spasyuk, G. C. Welch, *Chem. Mater.* **2016**, *28*, 7098-7109.

9.  a) J. Cremer, P. Bäuerle, *J. Mater. Chem.* **2006**, *16*, 874-884; b) J.-L. Wang, J. Yan, Z.-M. Tang, Q. Xiao, Y. Ma, J. Pei, *J. Am. Chem. Soc.* **2008**, *130*, 9952-9962; c) A. L. Kanibolotsky, I. F. Perepichka, P. J. Skabara, *Chem. Soc. Rev.* **2010**, *39*, 2695.; c) Y. Lin, P. Cheng, Y. Li, X. Zhan, *Chem. Commun.* **2012**, *48*, 4773.; d) Y. N. Luponosov, A. N. Solodukhin, A. L. Mannanov, P. S. Savchenko, B. A. L. Raul, S. M. Peregudova, N. M. Surin, A. V. Bakirov, M. A. Shcherbina, S. N. Chvalun, M. S. Pshenichnikov, D. Y. Paraschuk, S. A. Ponomarenko, *Materials Today Energy* **2021**, *22*, 100863.

10. a) R. Schmidt, J. H. Oh, Y.-S. Sun, M. Deppisch, A.-M. Krause, K. Radacki, H. Braunschweig, M. Könemann, P. Erk, Z. Bao, F. Würthner, *J. Am. Chem. Soc.* **2009**, *131*, 6215-6228; b) D. Sun, D. Meng, Y. Cai, B. Fan, Y. Li, W. Jiang, L. Huo, Y. Sun, Z. Wang, *J. Am. Chem. Soc.* **2015**, *137*, 11156-11162; c) P. Gawrys, D. Boudinet, M. Zagorska, D. Djurado, J.-M. Verilhac, G. Horowitz, J. Pécaud, S. Pouget, A. Pron, *Synth. Met.* **2009**, *159*, 1478-1485

11. a) A. Babel, S. A. Jenekhe, *J. Am. Chem. Soc.* **2003**, *125*, 13656-13657.; b) S. Wang, H. Sun, U. Ail, M. Vagin, P. O. Å. Persson, J. W. Andreasen, W. Thiel, M. Berggren, X. Crispin, D. Fazzi, S. Fabiano, *Adv. Mater.* **2016**, *28*, 10764-10771; c) S. Griggs, A. Marks, H. Bristow, I. McCulloch, *J. Mater. Chem. C* **2021**, *9*, 8099-8128; d) K. Feng, H. Guo, J. Wang, Y. Shi, Z. Wu, M. Su, X. Zhang, J. H. Son, H. Y. Woo, X. Guo, *J. Am. Chem. Soc.* **2021**, *143*, 1539-1552; e) J. Surgailis, A. Savva, V. Druet, B. D. Paulsen, R. Wu, A. Hamidi-Sakr, D. Ohayon, G. Nikiforidis, X. Chen, I. McCulloch, J. Rivnay, S. Inal, *Adv. Funct. Mater.* **2021**, *31*, 2010165.1807275; d) W. Jiang, Y. Li, Z. Wang, *Acc. Chem. Res.* **2014**, *47*, 3135-3147.

12. a) W. Yue, A. Lv, J. Gao, W. Jiang, L. Hao, C. Li, Y. Li, L. E. Polander, S. Barlow, W. Hu, S. Di Motta, F. Negri, S. R. Marder, Z. Wang, *J. Am. Chem. Soc.* **2012**, *134*, 5770-5773; b) Y. Zhang, L. Chen, K. Zhang, H. Wang, Y. Xiao, *Chem. Eur. J.* **2014**, *20*, 10170-10178; c) Z. Genene, W. Mammo, E. Wang, M. R. Andersson, *Adv. Mater.* **2019**, *31*,

13. a) H. Yan, Z. Chen, Y. Zheng, C. Newman, J. R. Quinn, F. Dötz, M. Kastler, A. Facchetti, *Nature* **2009**, *457*, 679-686; b) F. S. Kim, X. Guo, M. D. Watson, S. A. Jenekhe, *Adv. Mater.* **2010**, *22*, 478-482; c) Z. Chen, Y. Zheng, H. Yan, A. Facchetti, *J. Am. Chem. Soc.* **2009**, *131*, 8-9; d) S. Wang, D. Fazzi, Y. Puttisong, M. J. Jafari, Z. Chen, T. Ederth, J. W. Andreasen, W. M. Chen, A. Facchetti, S. Fabiano, *Chem. Mater.* **2019**, *31*, 3395-3406; e) S.

Pecorario, J. Royakkers, A. D. Scaccabarozzi, F. Pallini, L. Beverina, H. Bronstein, M. Caironi, *Chem. Mater*. **2022**, *34*, 8324-8335.

14. a) X. Zhan, Z. Tan, E. Zhou, Y. Li, R. Misra, A. Grant, B. Domercq, X.-H. Zhang, Z. An, X. Zhang, S. Barlow, B. Kippelen, S. R. Marder, *J. Mater. Chem*. **2009**, *19*, 5794; b) X. Zhan, Z. Tan, B. Domercq, Z. An, X. Zhang, S. Barlow, Y. Li, D. Zhu, B. Kippelen, S. R. Marder, *J. Am. Chem. Soc*. **2007**, *129*, 7246-7247.

15. a) V. C. Wakcahure, S. D. Veer, A. D. Nidhankar, Goudappagouda, R. Nayak, K. Asokan, S. Ravindranathan, S. S. Babu, *Chem. Commun.*, **2022**, *58*, 1998-2001; b) S. D. Veer, V. C. Wakchaure, K. Asokan, R. Dixit, T. Goswami, R. Saha, R. Gonnade, H. N. Ghosh, S. S. Babu, *Angew. Chem. Int. Ed*. **2023**, *62*, e202212934.

16. M. C. O'Sullivan, J. K. Sprafke, D. V. Kondratuk, C. Rinfray, T. D. W. Claridge, A. Saywell, M. O. Blunt, J. N. O'Shea, P. H. Beton, M. Malfois, H. L. Anderson, *Nature* **2011**, *469*, 72-75.

17. a) G. Calzaferri, S. Huber, H. Maas, C. Minkowski, *Angew. Chem. Int. Ed*. **2003**, *42*, 3732-3758; b) V. S.-Y. Lin, S. G. Di-Magno, M. J. Therien, *Science* **1994**, *264*, 1105-1111; c) D. Gust, T. A. Moore, A. L. Moore, *Acc. Chem. Res*. **2001**, *34*, 40-48.

18. P. Liu, Y. Hisamune, M. D. Peeks, B. Odell, J. Q. Gong, L. M. Herz, H. L. Anderson, *Angew. Chem. Int. Ed*. **2016**, *55*, 8358-8362; d) A. Cnossen, C. Roche, H. L. Anderson, *Chem. Commun*. **2017**, *53*, 10410-10413; e) P. S. Bols, H. L. Anderson, *Acc. Chem. Res*. **2018**, *51*, 2083-2092.

19. a) Y. Zhao, Y. Cotelle, L. Liu, J. López-Andarias, A.-B. Bornhof, M. Akamatsu, N. Sakai, S. Matile, *Acc. Chem. Res*. **2018**, *51*, 2255-2263; b) S. Sengupta, F. Würthner, *Acc. Chem. Res.* **2013**, *46*, 2498-2512; c) R. Bhosale, J. Míšek, N. Sakai, S. Matile, *Chem. Soc. Rev*. **2010**, *39*, 138-149.

20. a) J. Krömer, I. Rios-Carreras, G. Fuhrmann, C. Musch, M. Wunderlin, T. Debaerdemaeker, E. Mena-Osteritz, P. Bäuerle, *Angew. Chem. Int. Ed*. **2000**, *39*, 3481-3486; b) K. Nakao, M. Nishimura, T. Tamachi, Y. Kuwatani, H. Miyasaka, T. Nishina-ga, M. Iyoda, *J. Am. Chem. Soc*. **2006**, *128*, 16740-16747; c) A. Bhaskar, G. Ramakrishna, K. Hagedorn, O. Varnavski, E. Mena-Osteritz, P. Bäuerle, T. Goodson, *J. Phys. Chem. B* **2007**, *111*, 946-954.

21. a) F. Schlosser, V. Stepanenko, F. Würthner, *Chem. Commun*. **2010**, *46*, 8350; b) F. Schlosser, J. Sung, P. Kim, D. Kim, F. Würthner, *Chem. Sci*. **2012**, *3*, 2778.

22. a) M. Ball, Y. Zhong, B. Fowler, B. Zhang, P. Li, G. Etkin, D. W. Paley, J. Decatur, A. K. Dalsania, H. Li, S. Xiao, F. Ng, M. L. Steigerwald, C. Nuckolls, *J. Am. Chem. Soc*. **2016**, *138*, 12861-12867; b) B. Zhang, R. Hernández Sánchez, Y. Zhong, M. Ball, M. W. Terban, D. Paley, S. J. L. Billinge, F. Ng, M. L. Stei-gerwald, C. Nuckolls, *Nat. Commun*. **2018**, *9*, 1957; c)  M. L. Ball, B. Zhang, Q. Xu, D. W. Paley, V. C. Ritter, F. Ng, M. L. Stei-gerwald, C. Nuckolls, *J. Am. Chem. Soc*. **2018**, *140*, 10135-10139.

23. M. J. Langton, J. D. Matichak, A. L. Thompson, H. L. Anderson, *Chem. Sci*. **2011**, *2*, 1897.
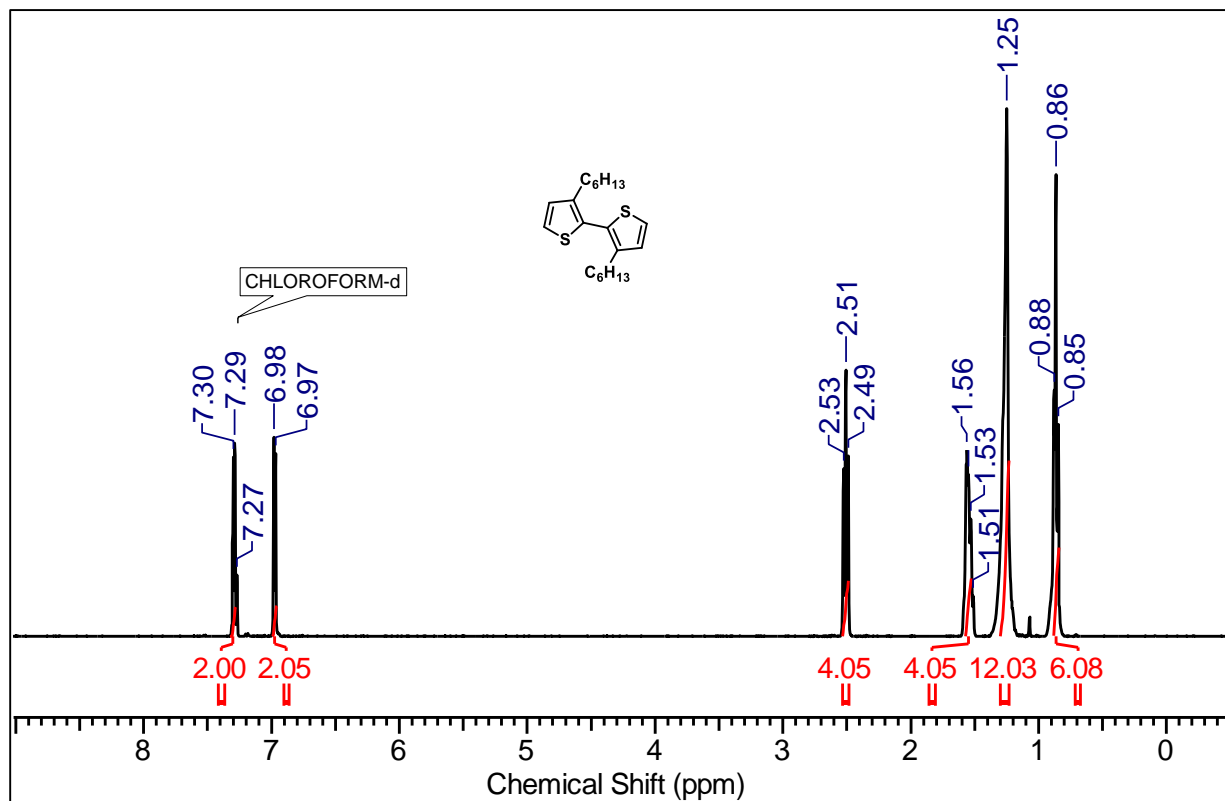
$^1$**H NMR** (500 MHz) spectrum of **BT1** in CDCl$_3$ at 298 K.
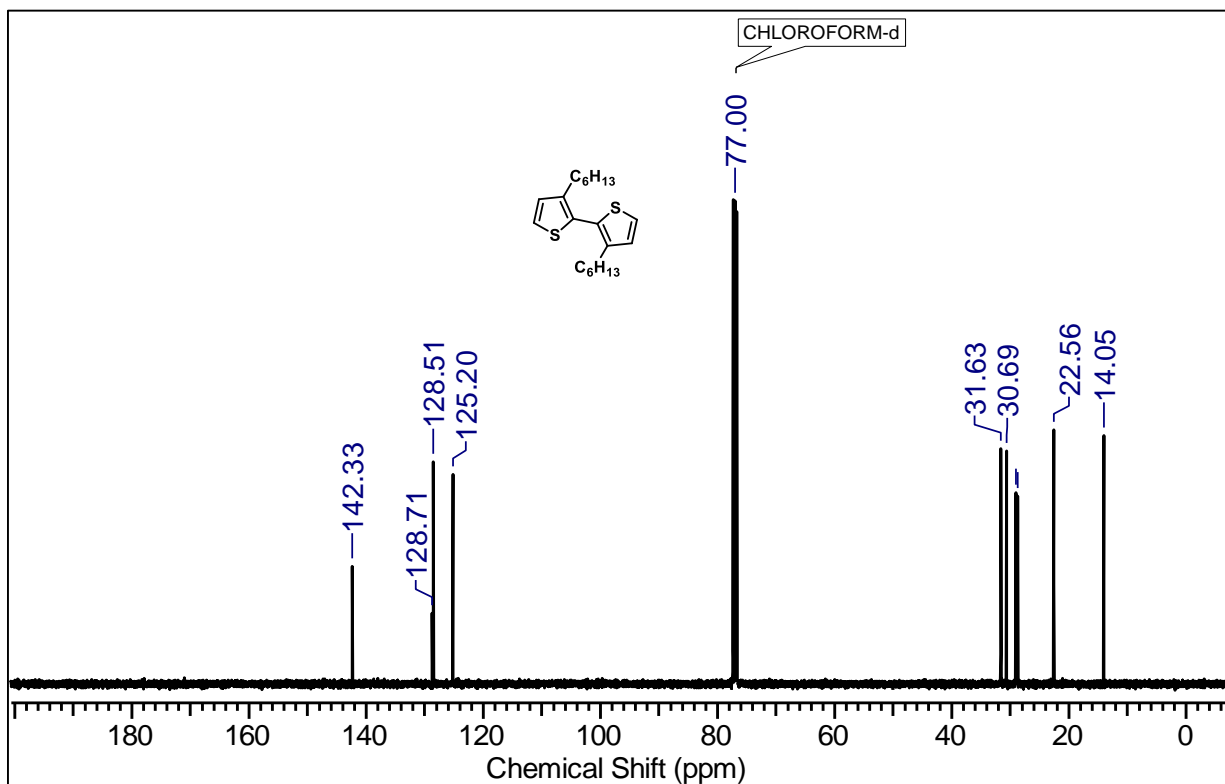


$^{13}$**C NMR** (125 MHz) spectrum of **BT1** in CDCl$_3$ at 298 K.
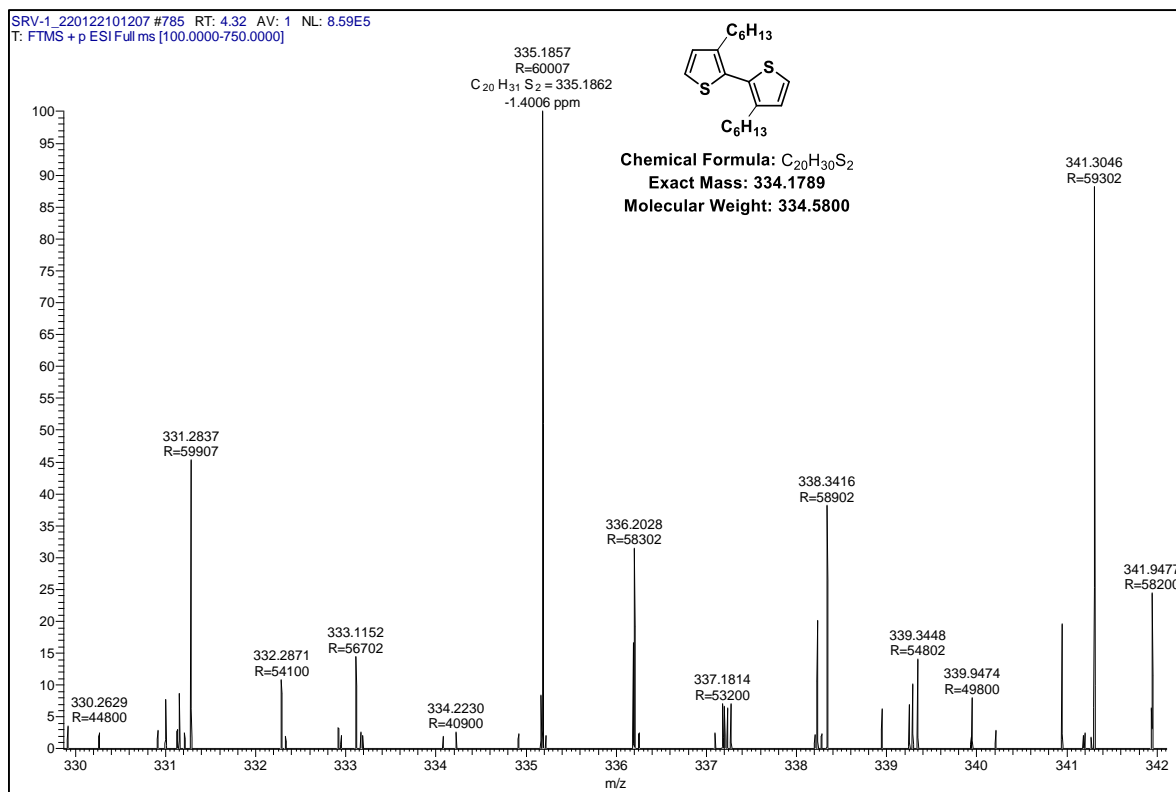
**HRMS** spectrum of 3,3'-dihexyl-2,2'-bithiophene (**BT1**).
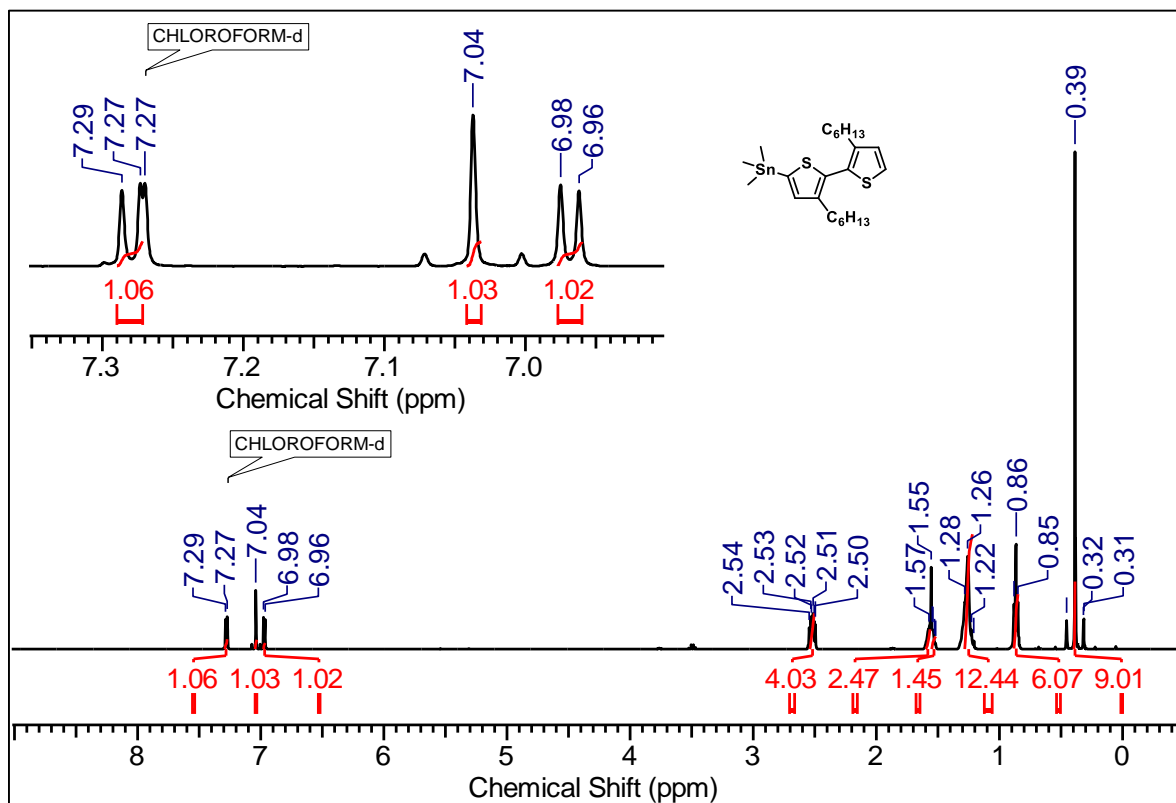


$^1$**H NMR** (500 MHz) spectrum of **BT2** in CDCl$_3$ at 298 K.
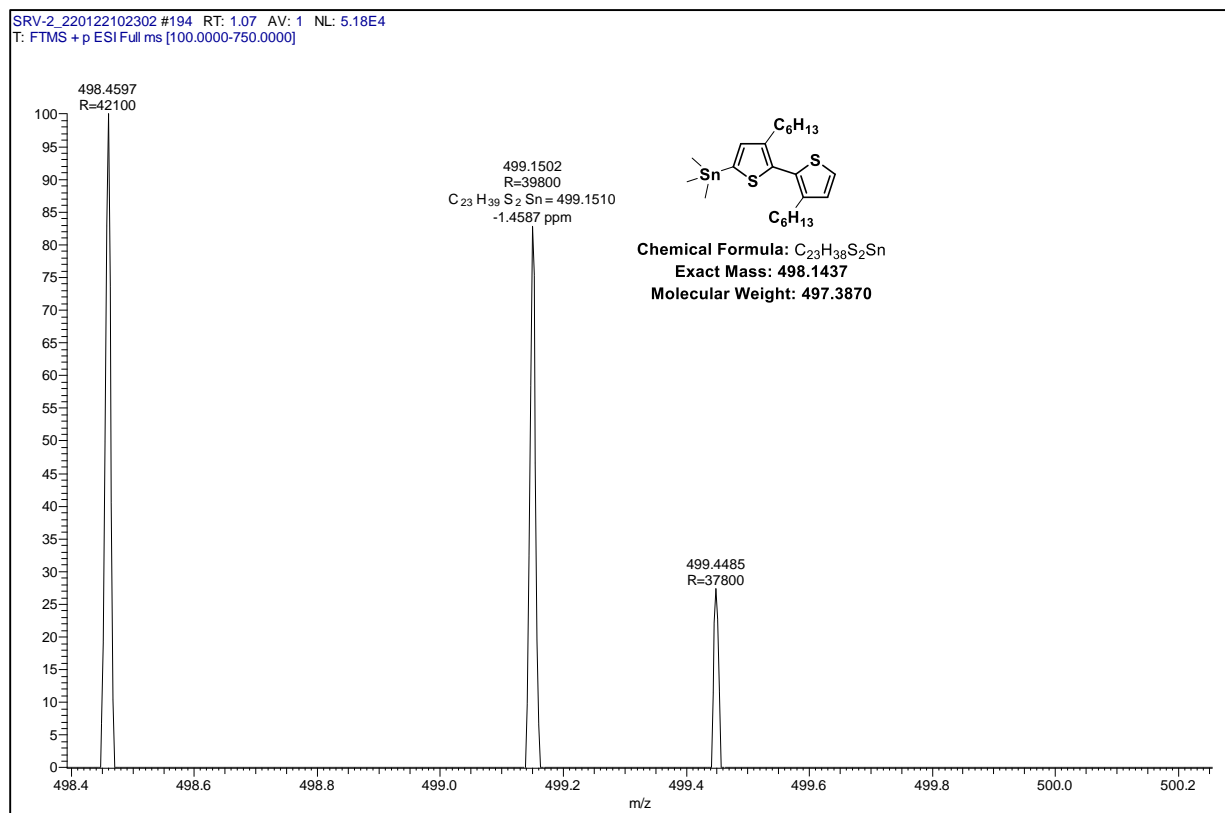
**HRMS** spectrum of 3,3'-dihexyl-2,2'-bithiophene (**BT2**).
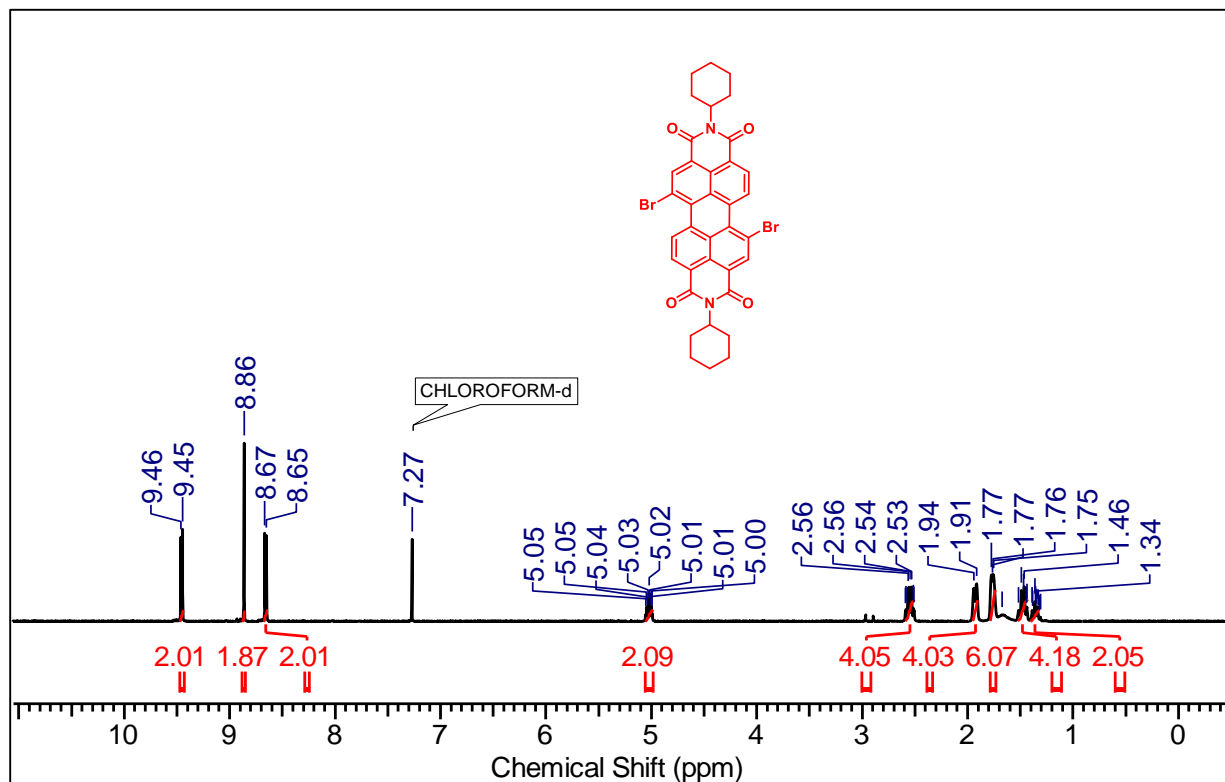


**¹H NMR** (500 MHz) spectrum of **1** in CDCl$_3$ at 298 K.
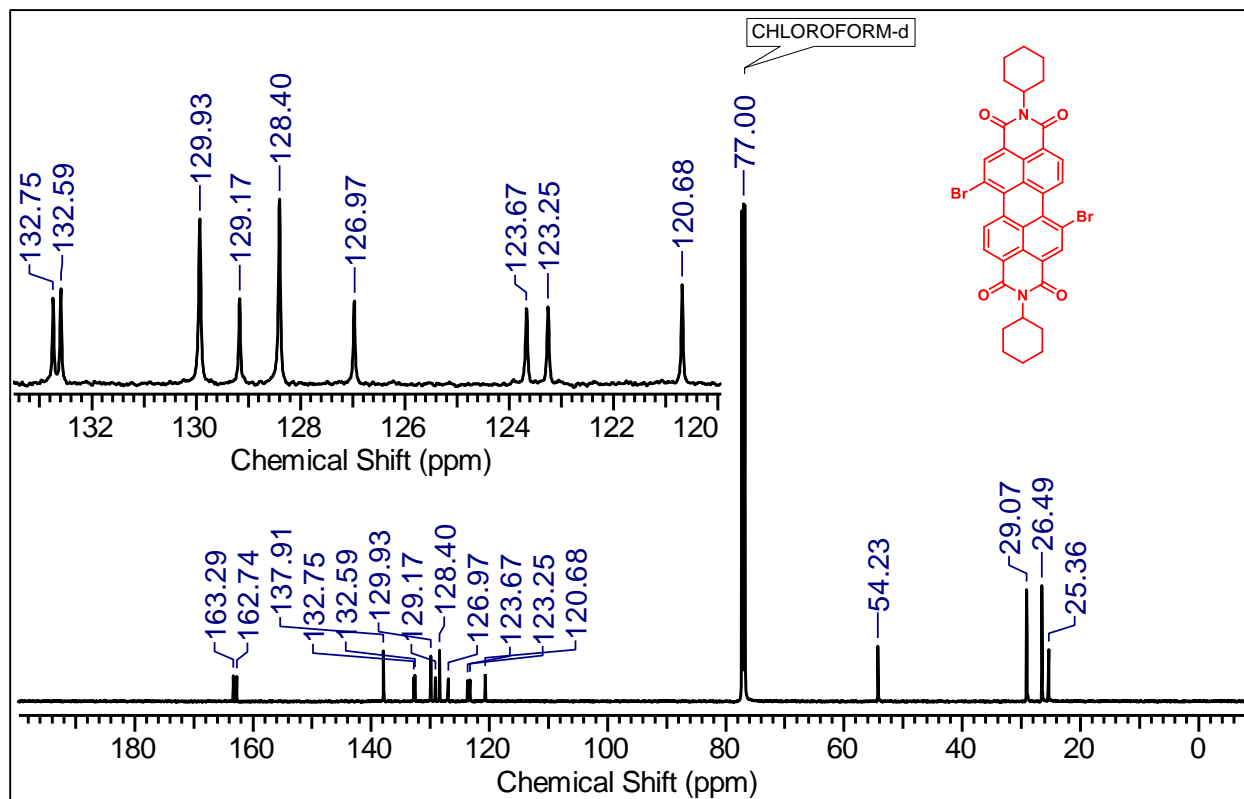
**¹³C NMR** (125 MHz) spectrum of **1** in CDCl₃ at 298 K.
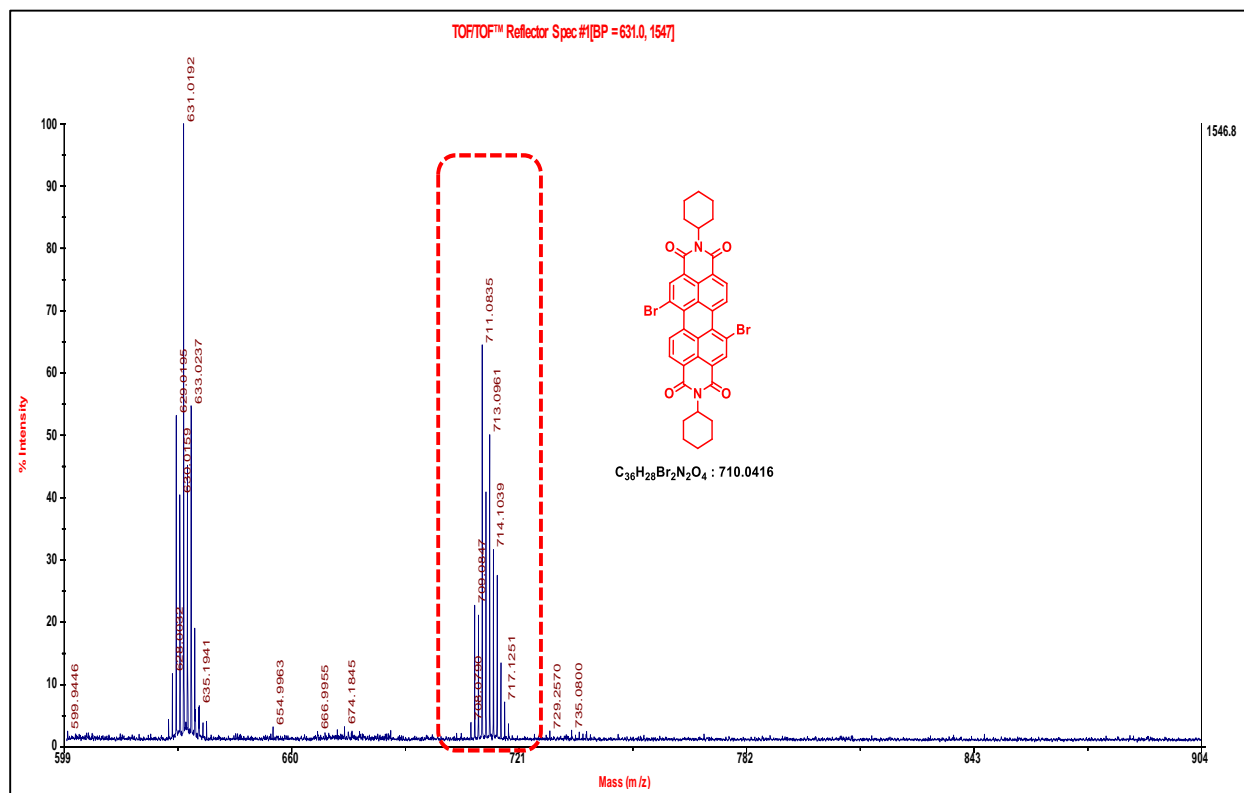


**MALDI-TOF** MS spectra of **1**.
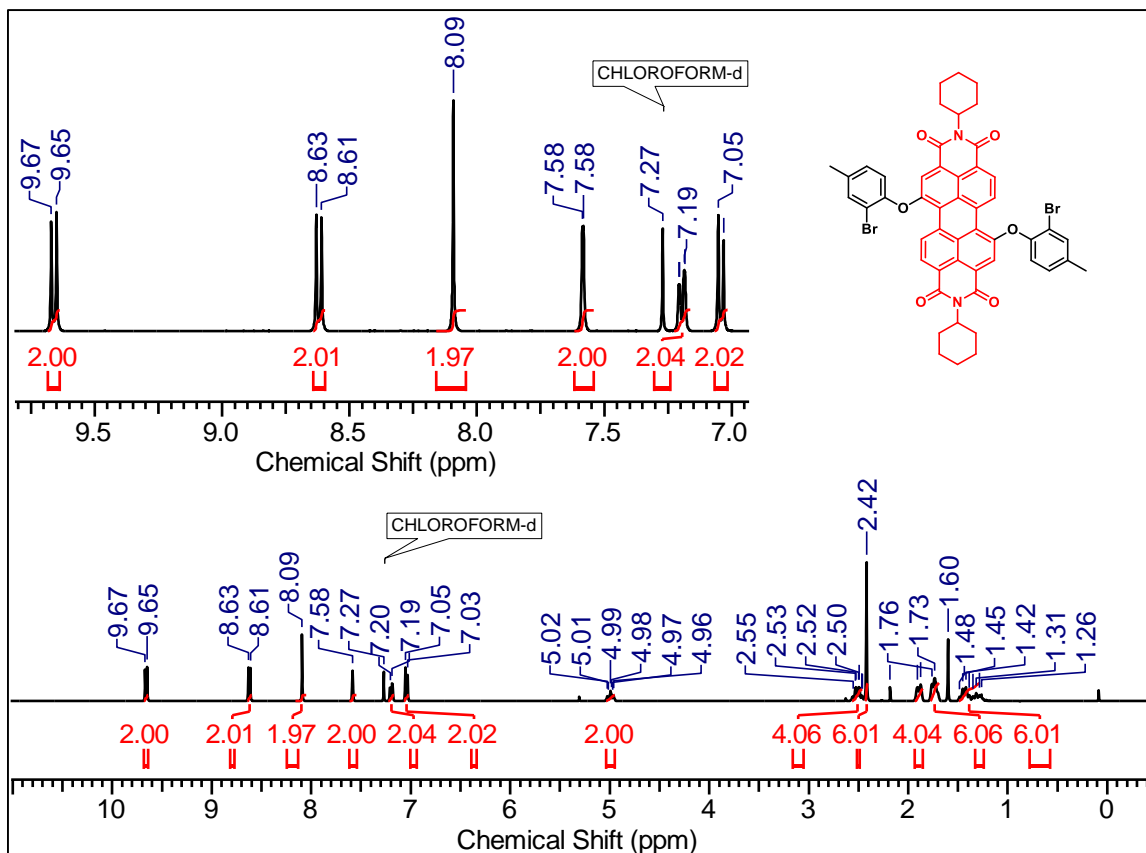
**¹H NMR** (400 MHz) spectrum of **2a** in CDCl₃ at 298 K.
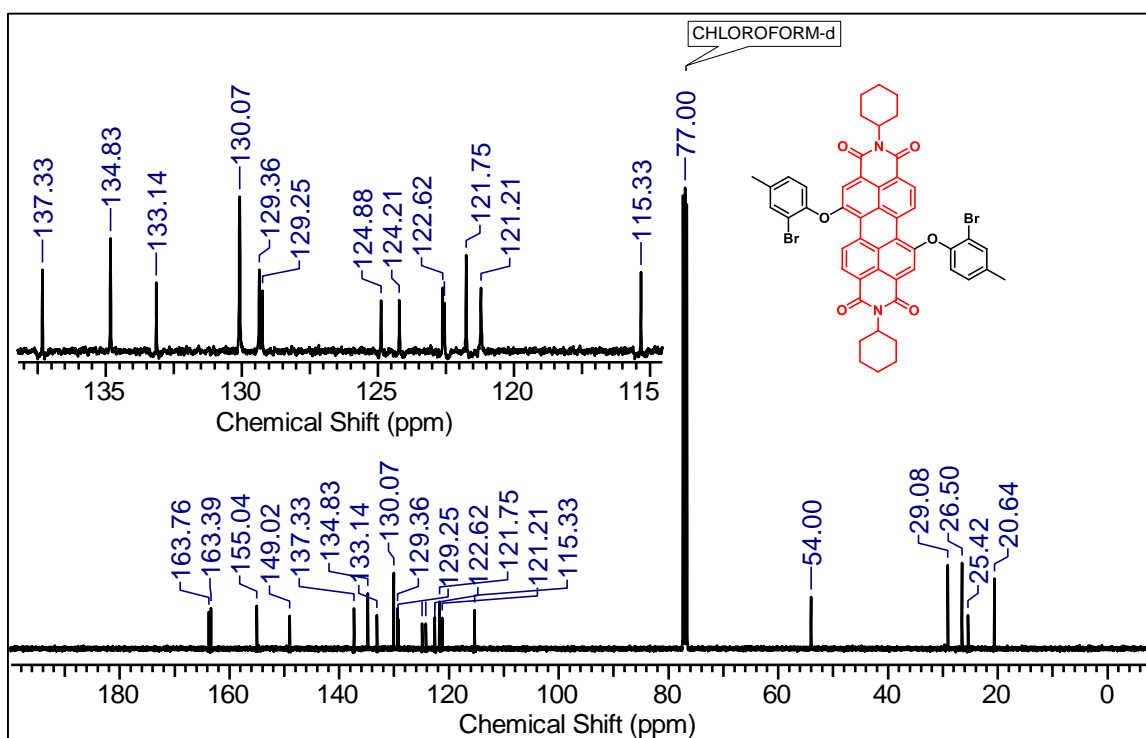


**¹³C NMR** (100 MHz) spectrum of **2a** in CDCl₃ at 298 K.
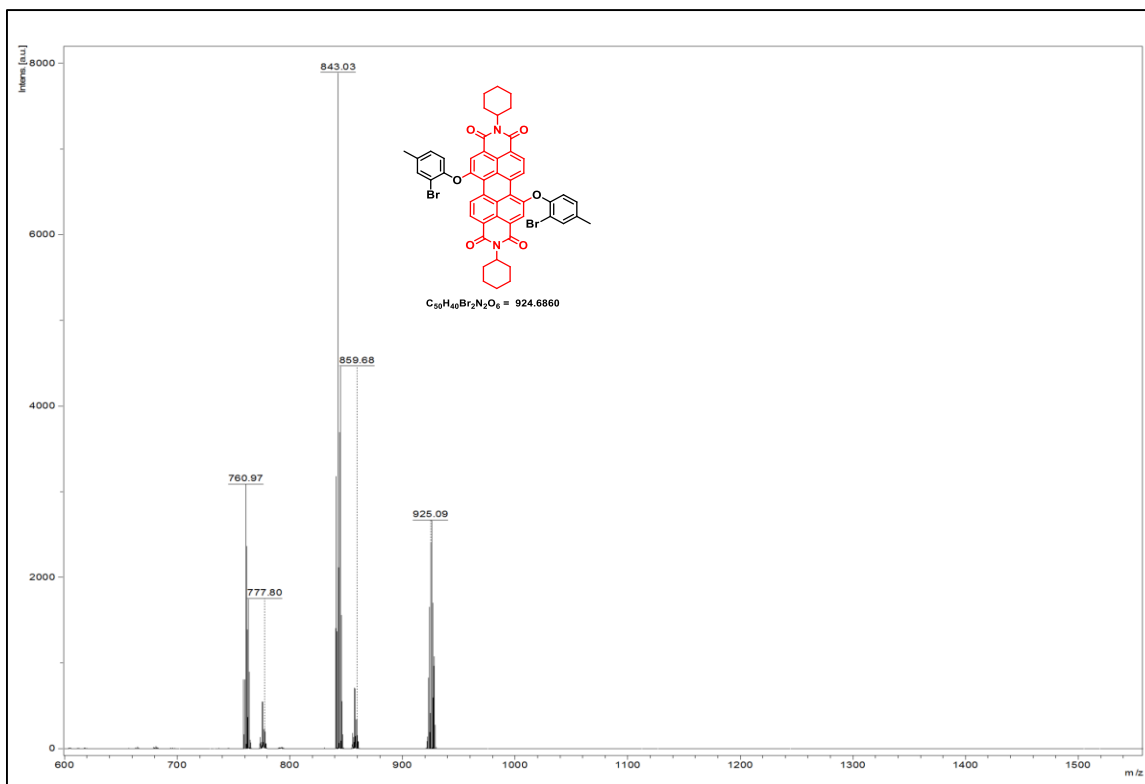
**MALDI-TOF** MS spectra of **2a**.
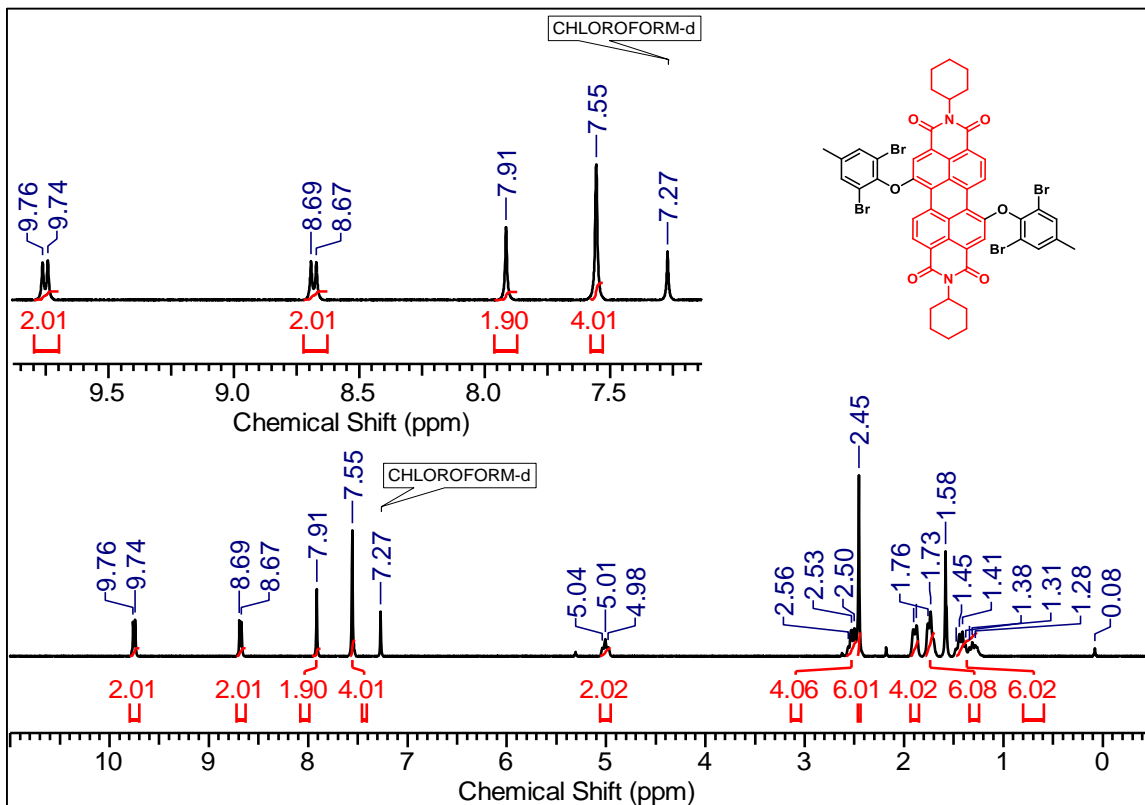


**$^1$H NMR** (400 MHz) spectrum of **2b** in $CDCl_3$ at 298 K.
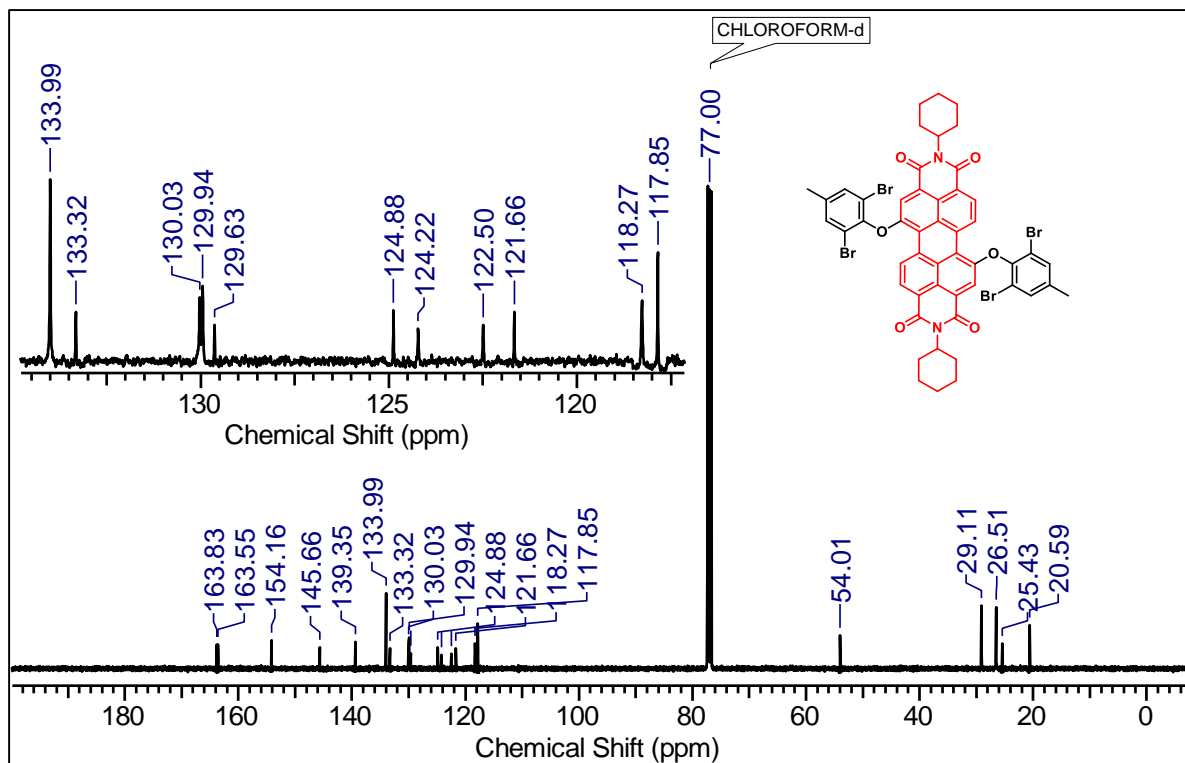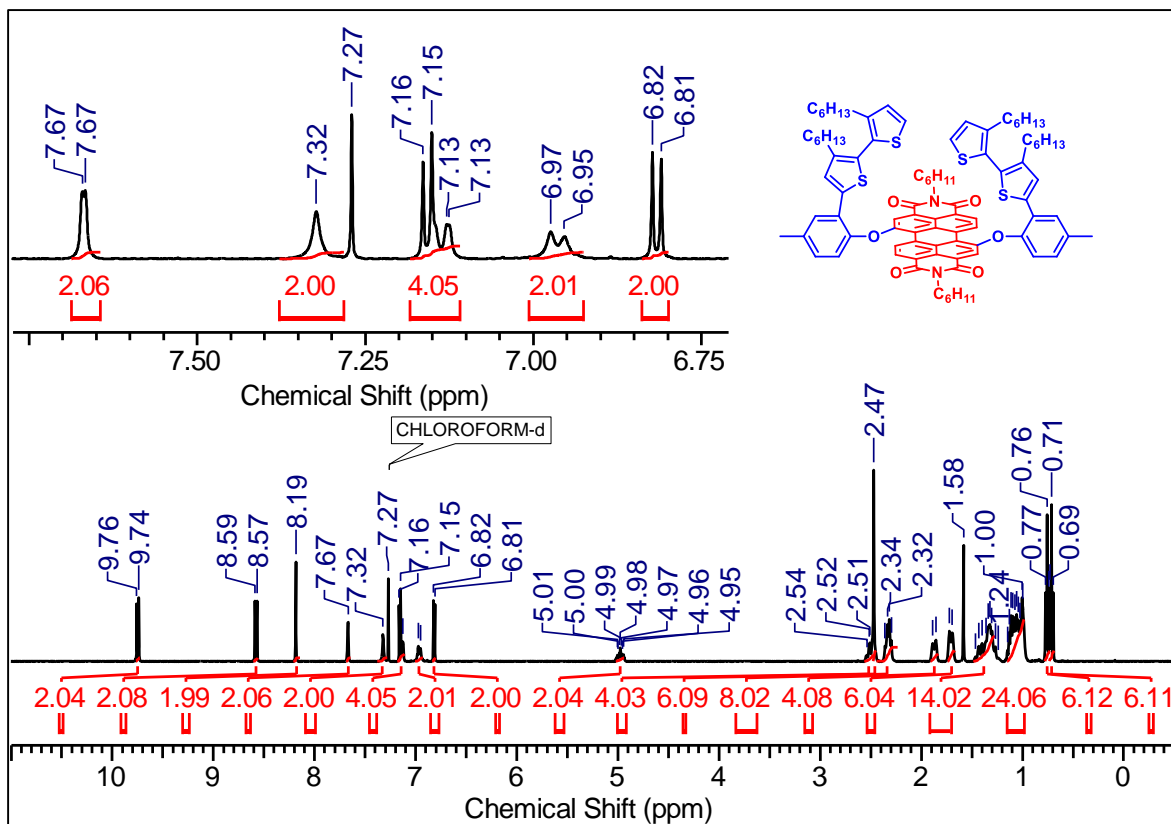
**¹³C NMR** (100 MHz) spectrum of **2b** in CDCl₃ at 298 K.



**MALDI-TOF** MS spectra of molecule **2b**.

**1H NMR** (400 MHz) spectrum of **3a** in CDCl₃ at 298 K.
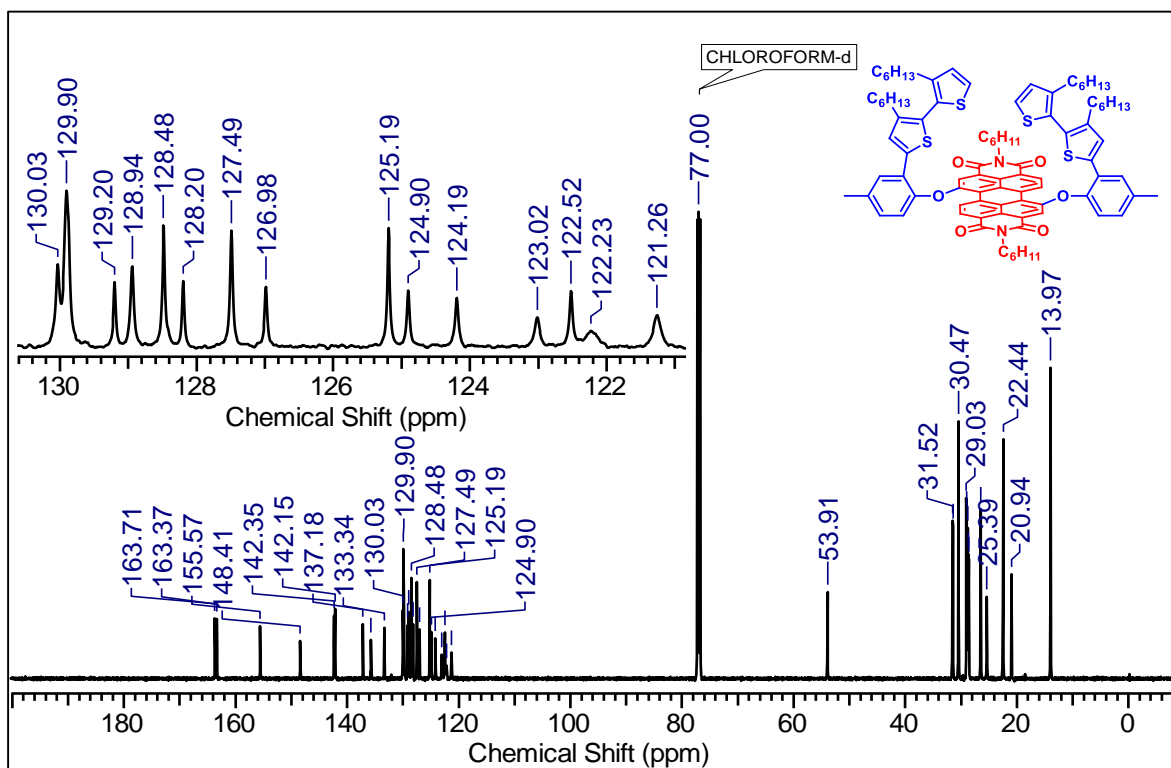


**13C NMR** (125 MHz) spectrum of **3a** in CDCl₃ at 298 K.

**MALDI-TOF** MS spectra of molecule **3a**.



$^1$**H NMR** (400 MHz) spectrum of **3b** in CDCl$_3$ at 298 K.
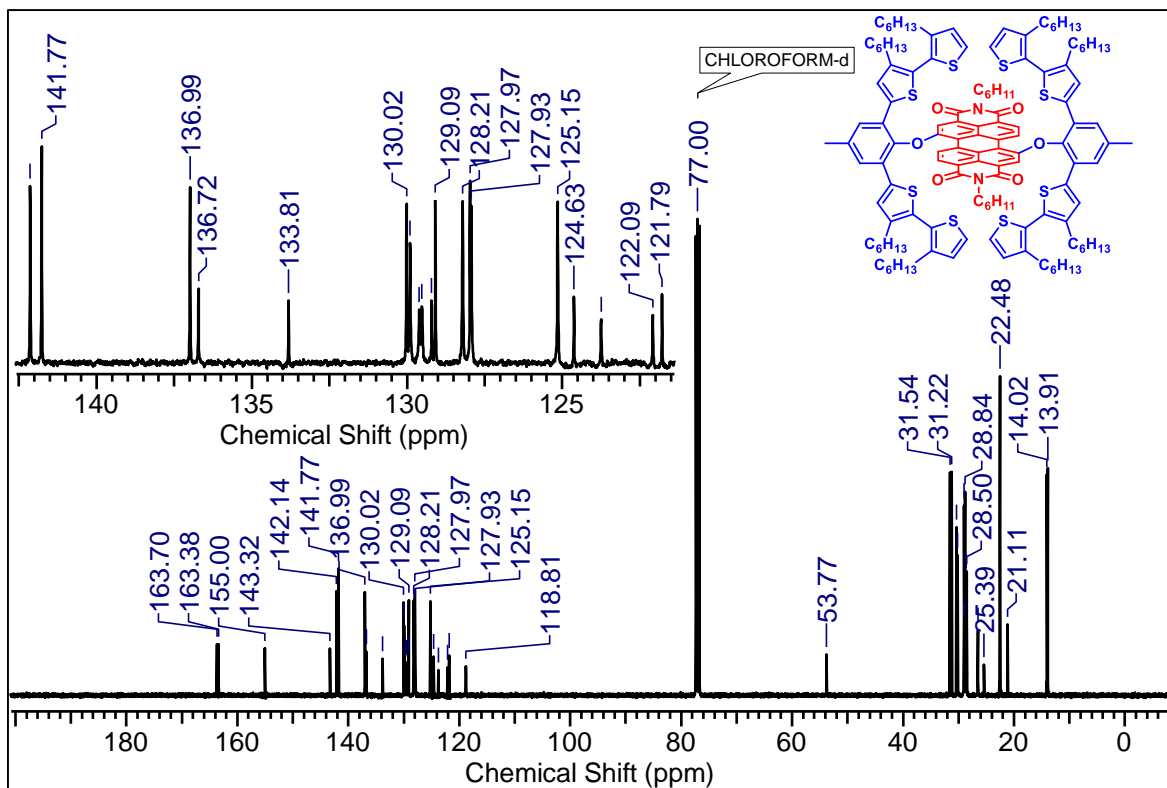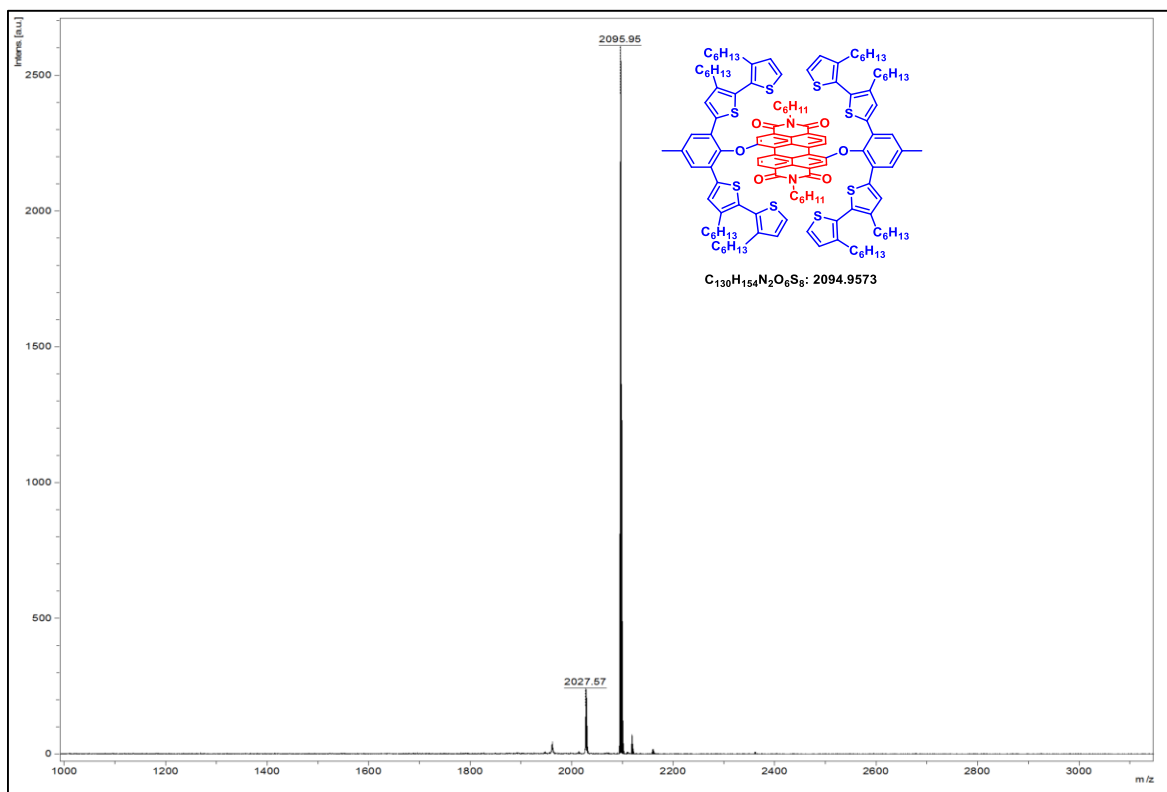
**¹³C NMR** (100 MHz) spectrum of **3b** in CDCl₃ at 298 K



**MALDI-TOF** MS spectra of molecule **3b**.
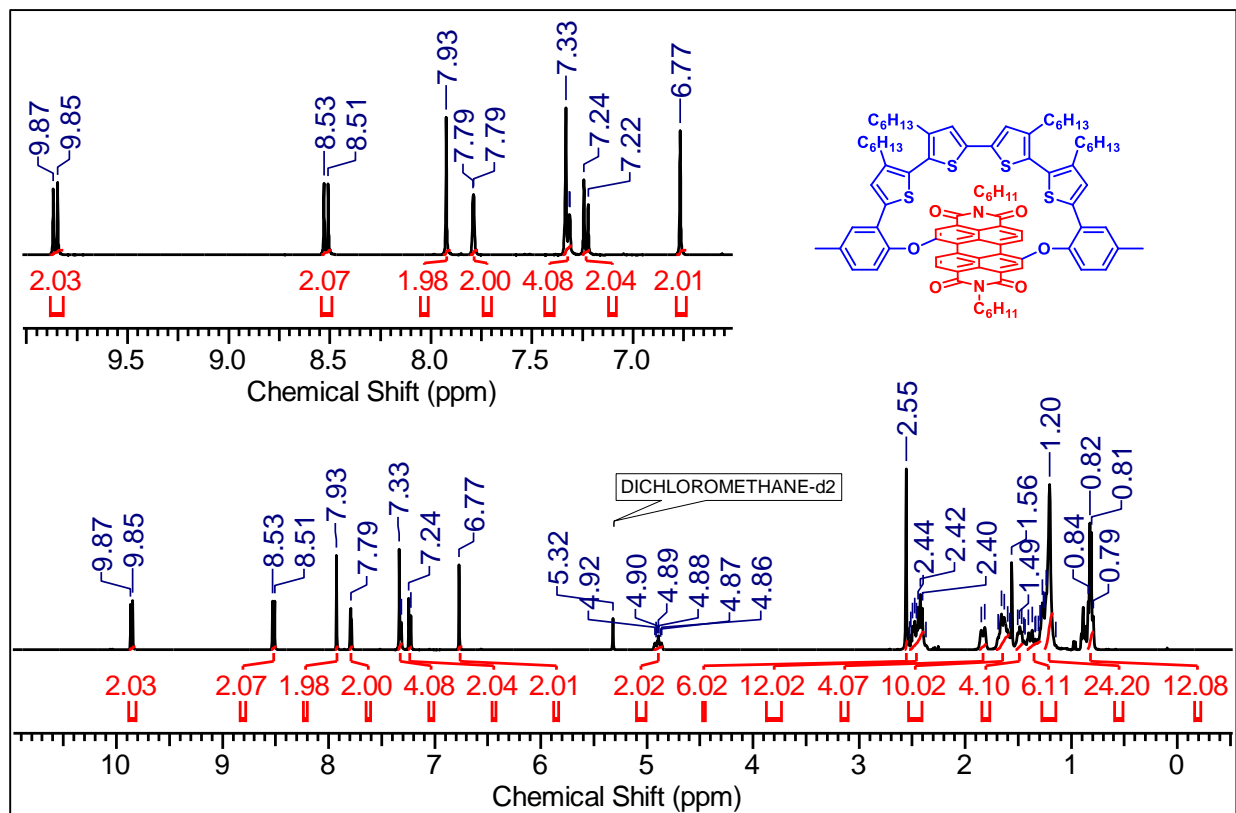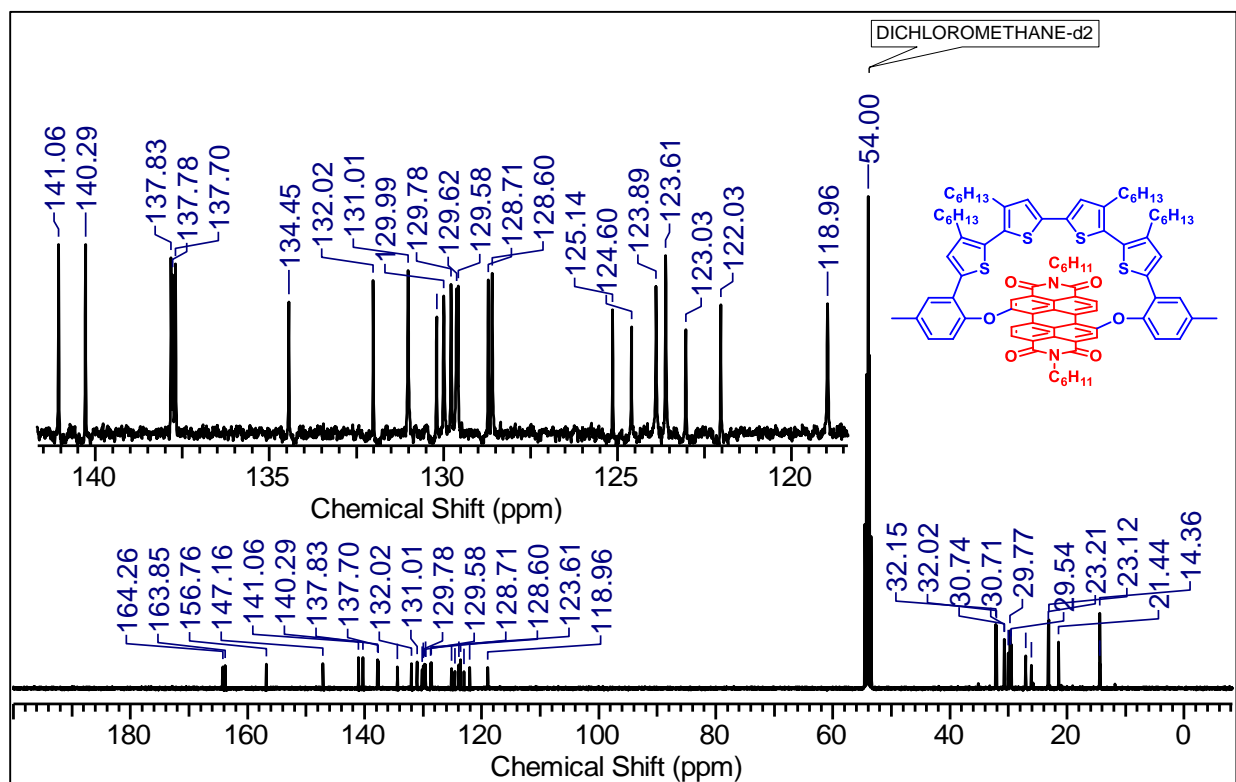
$^1$**H NMR** (500 MHz) spectrum of **TSP1** in CD$_2$Cl$_2$ at 298 K.



$^{13}$**C NMR** (125 MHz) spectrum of **TSP1** in CD$_2$Cl$_2$ at 298 K.
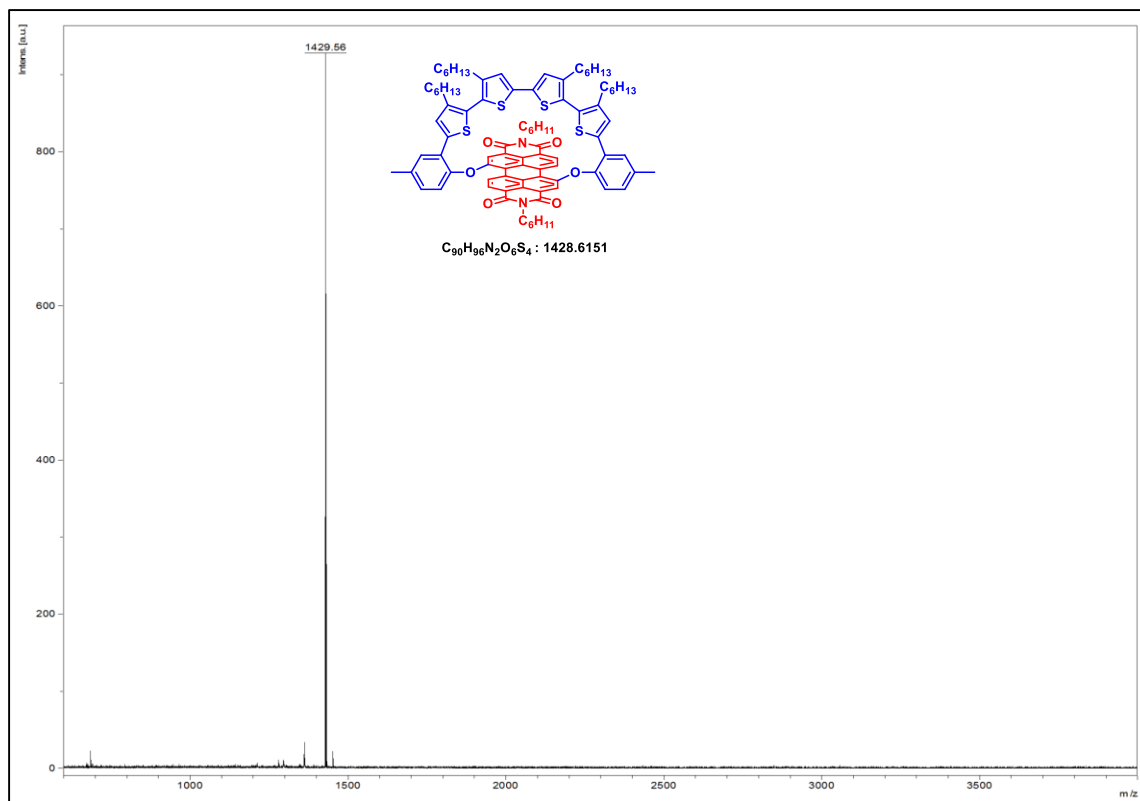
**MALDI-TOF** MS spectra of molecule **TSP1**.
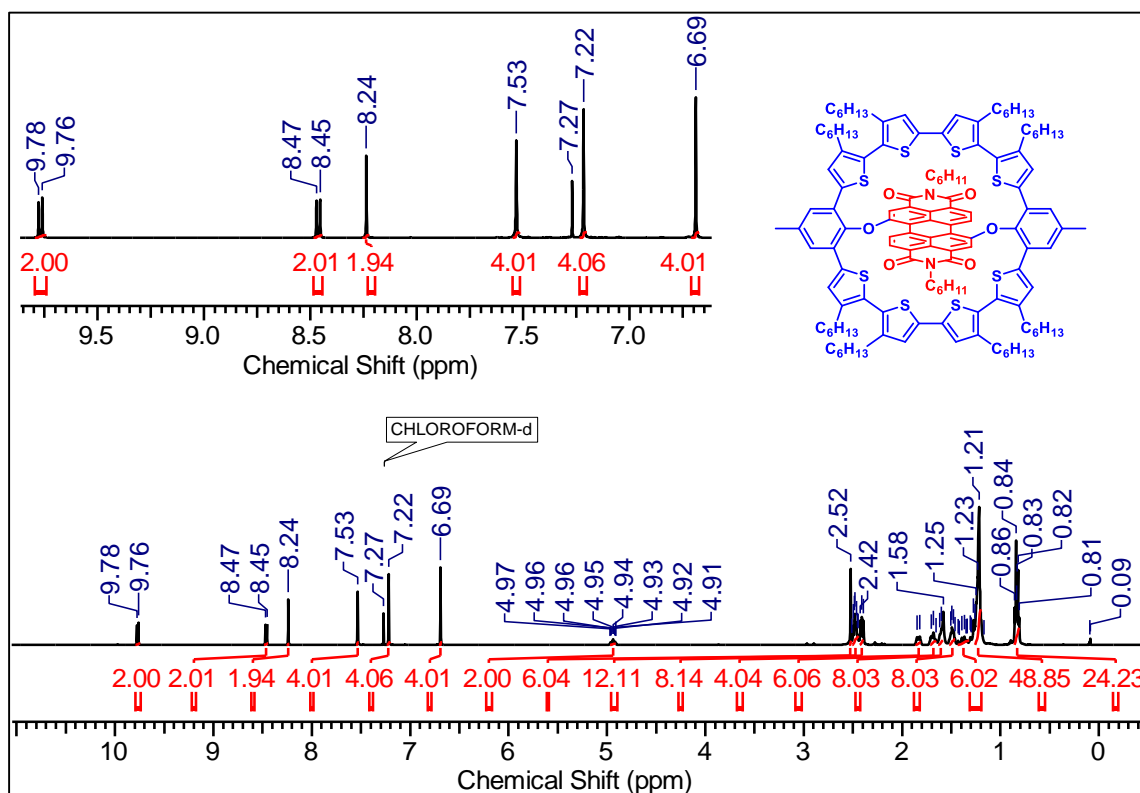


**$^1$H NMR** (500 MHz) spectrum of **TSP2** in CDCl$_3$ at 298 K.
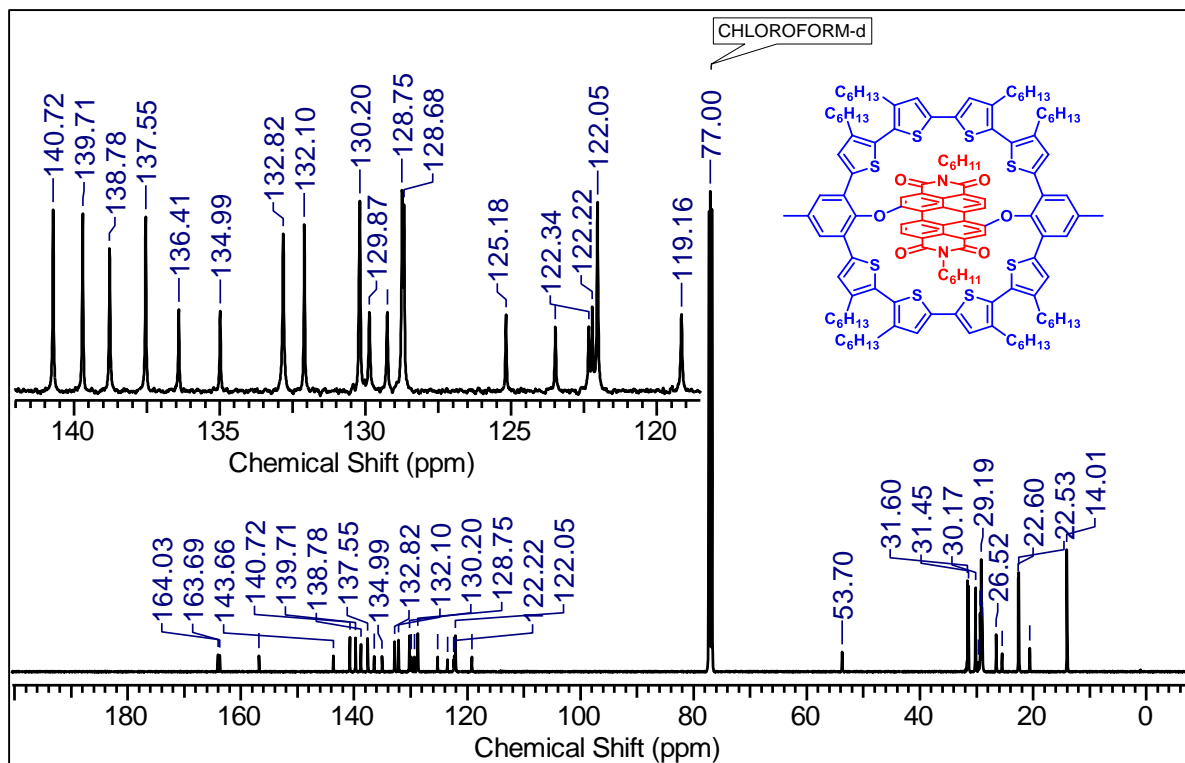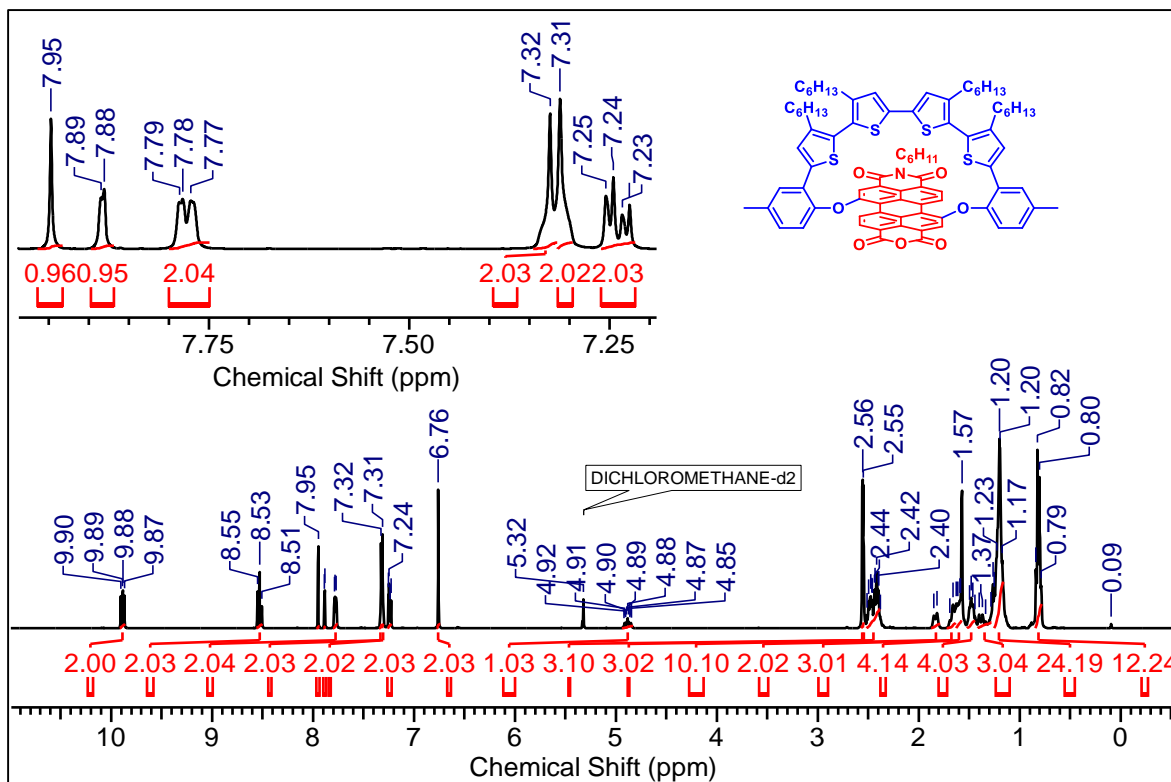
**¹³C NMR** (125 MHz) spectrum of **TSP2** in CDCl₃ at 298 K.



**MALDI-TOF** MS spectra of molecule **TSP2**.

**¹H NMR** (400 MHz) spectrum of **TSP1O** in CD$_2$Cl$_2$ at 298 K.
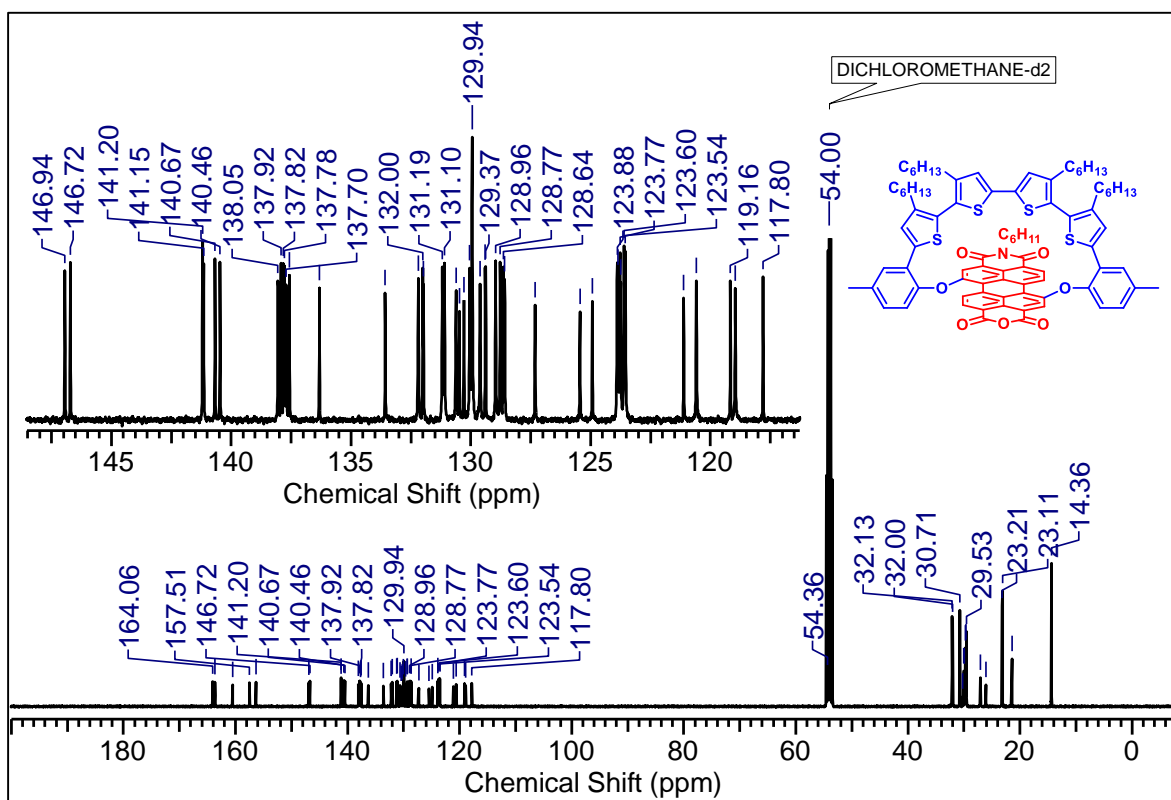


**¹³C NMR** (100 MHz) spectrum of **TSP1O** in CD$_2$Cl$_2$ at 298 K.
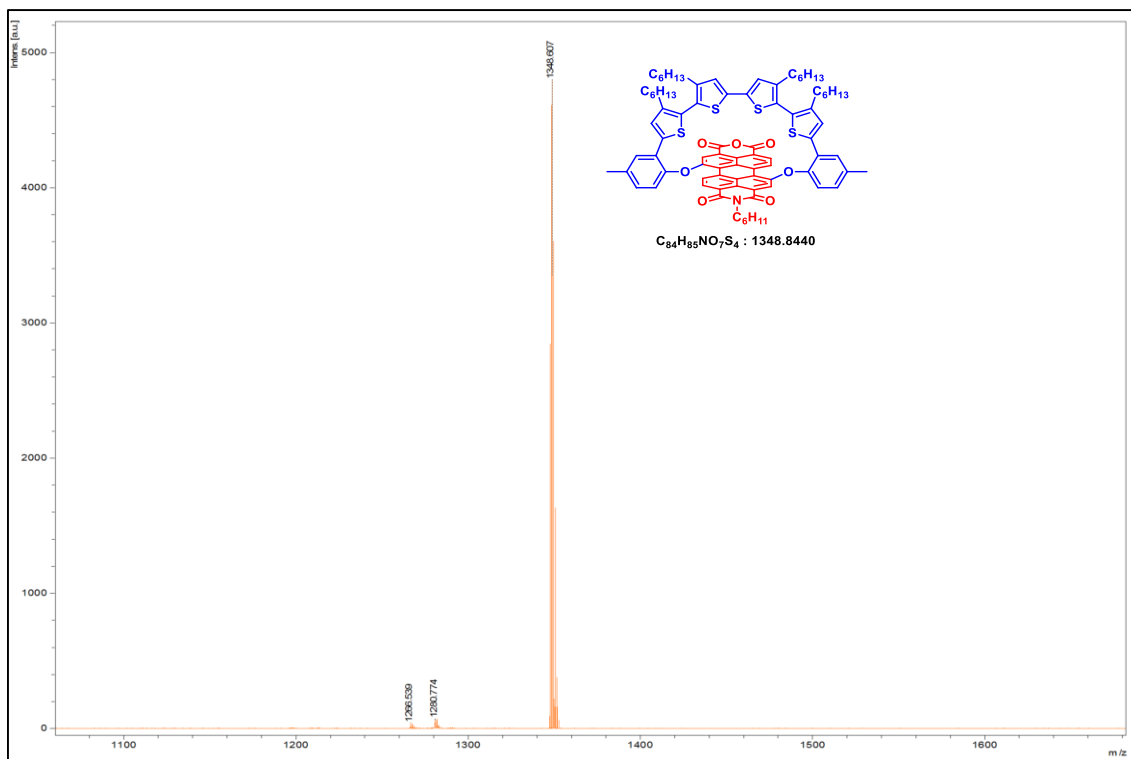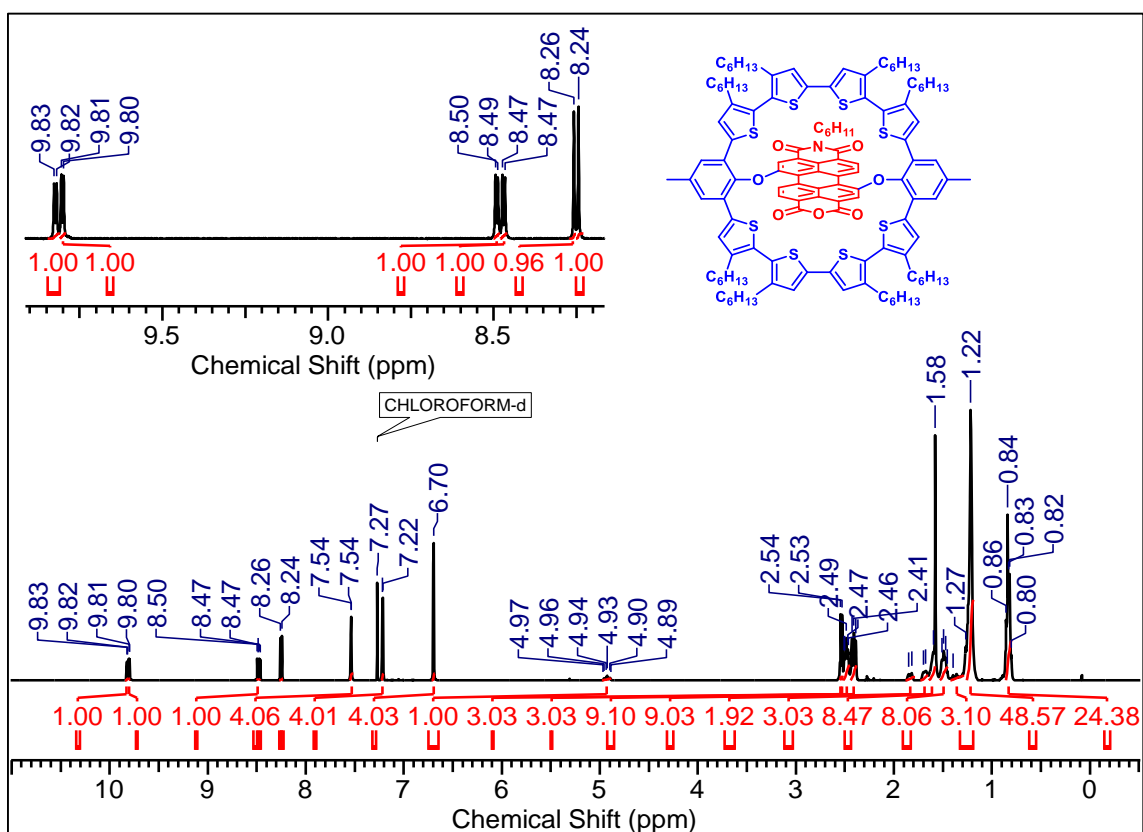
**MALDI-TOF** MS spectra of molecule **TSP1O**.



**¹H NMR** (400 MHz) spectrum of **TSP2O** in CDCl₃ at 298 K.
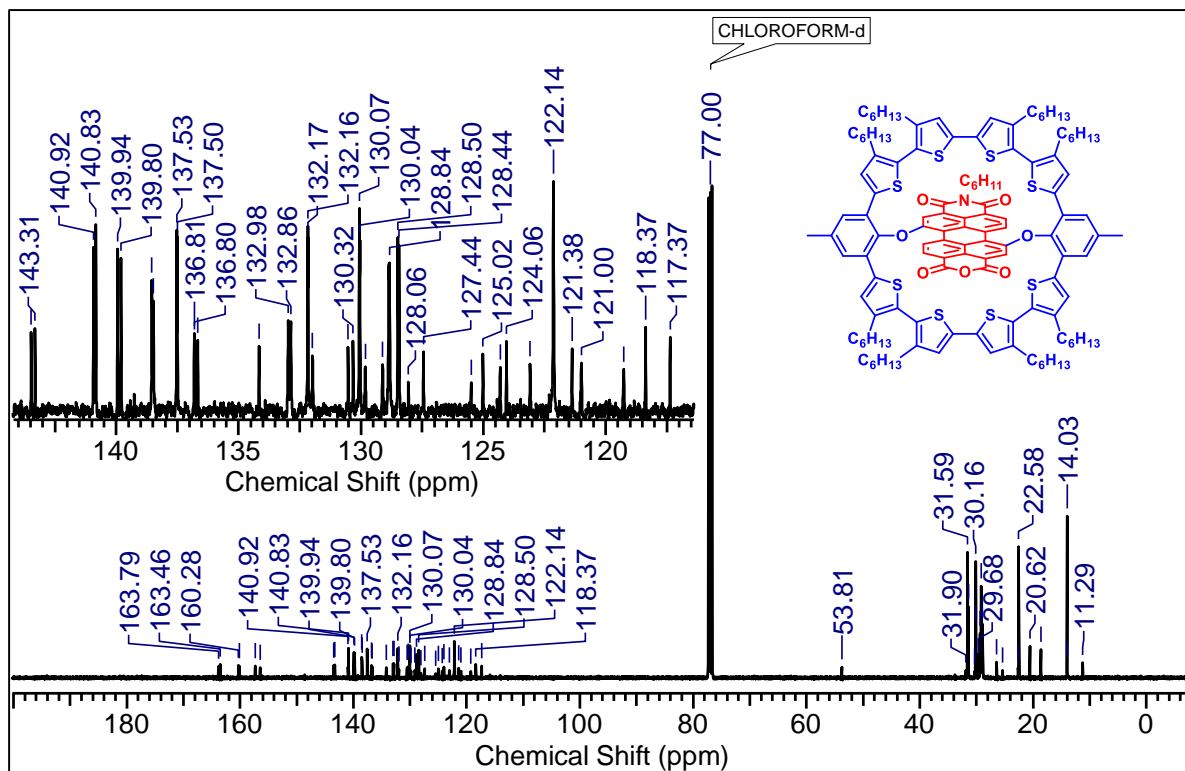
**¹³C NMR** (100 MHz) spectrum of **TSP2O** in CDCl₃ at 298 K.
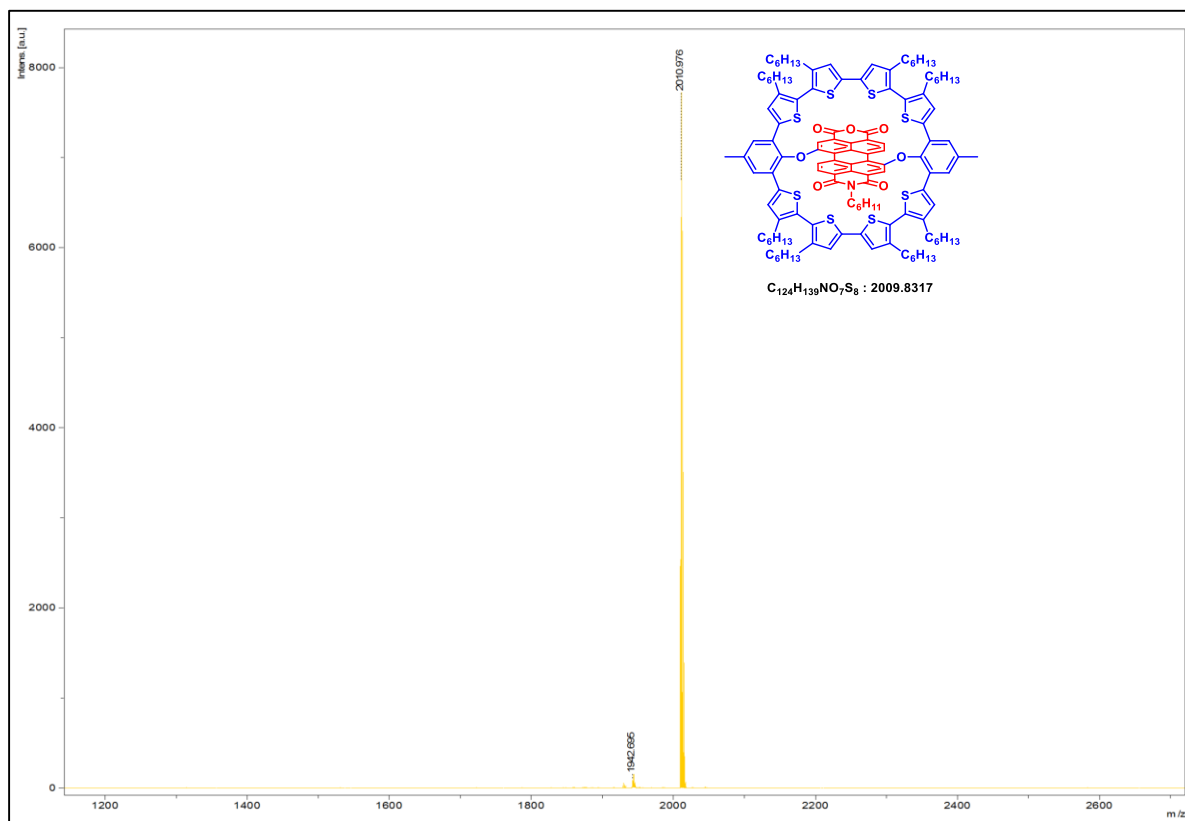


**MALDI-TOF** MS spectra of molecule **TSP2O**.

$^1$**H NMR** (400 MHz) spectrum of **TSP2OO** in CDCl$_3$ at 298 K.
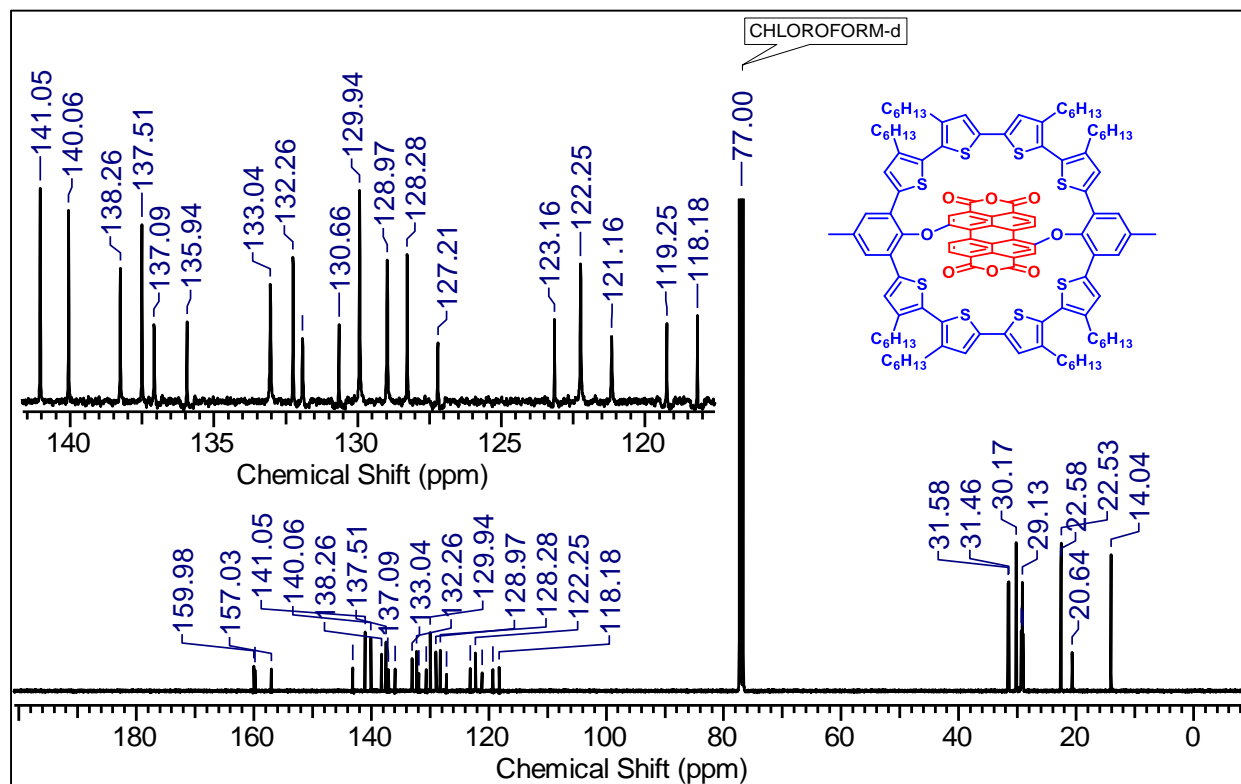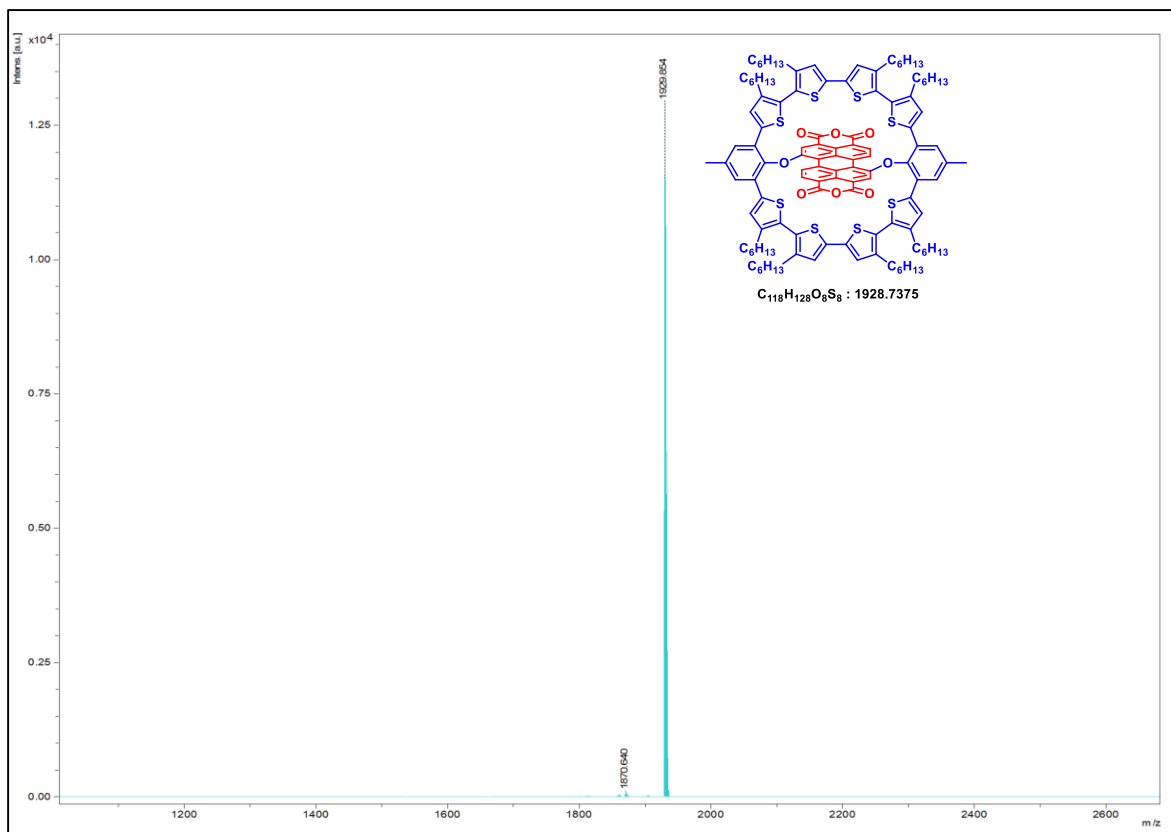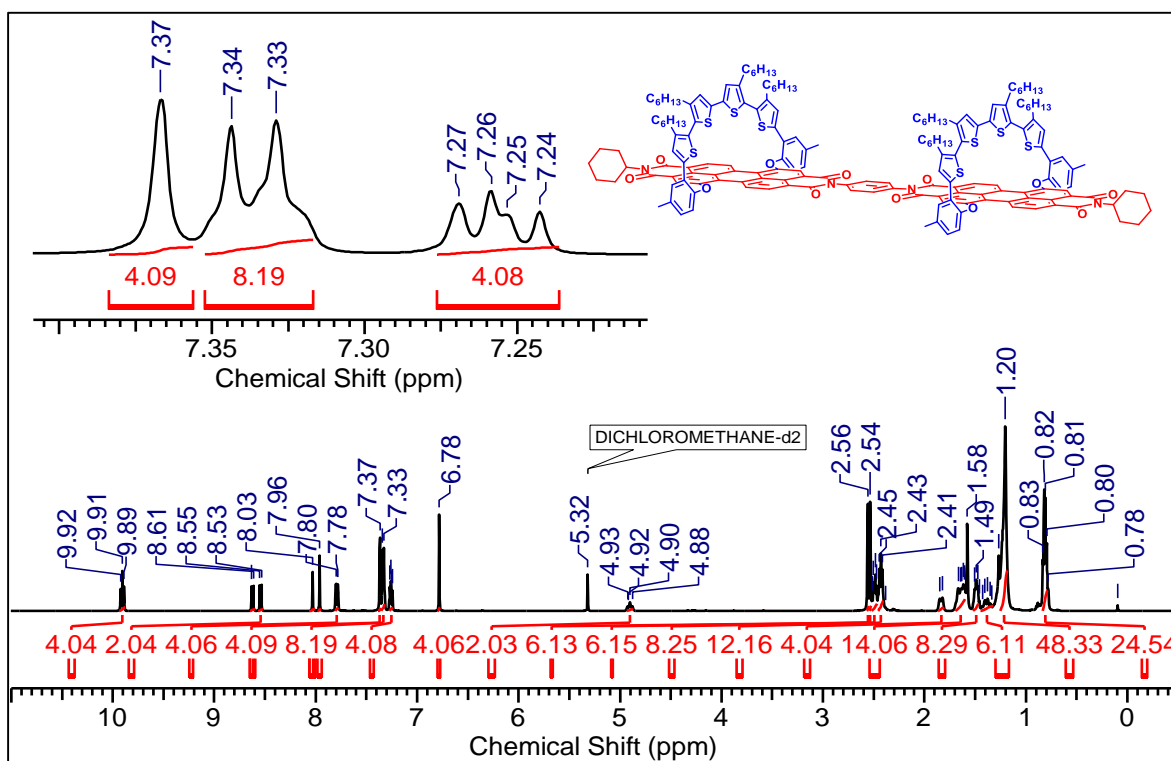


$^{13}$**C NMR** (100 MHz) spectrum of **TSP2OO** in CDCl$_3$ at 298 K.

**MALDI-TOF** MS spectra of molecule **TSP2OO**.



**¹H NMR** (500 MHz) spectrum of **TSP1D** in CD₂Cl₂ at 298 K.
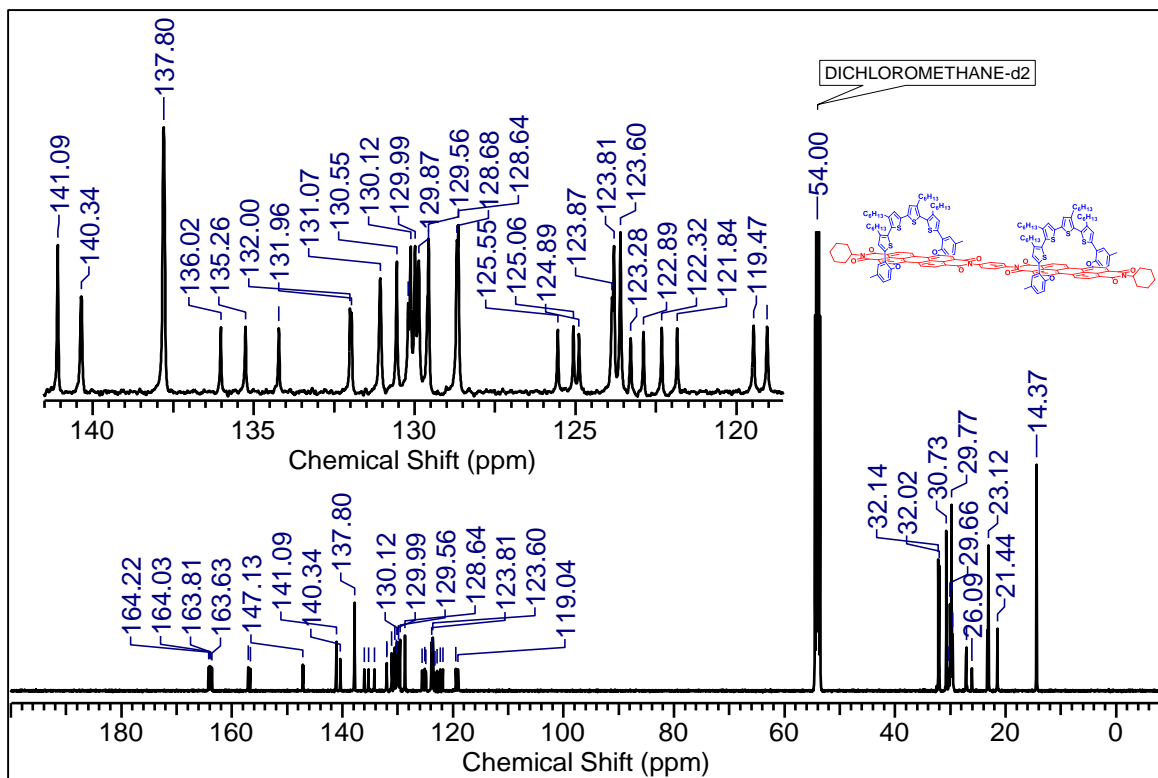
**¹³C NMR** (125 MHz) spectrum of **TSP1D** in CD₂Cl₂ at 298 K.



**MALDI-TOF** MS spectra of molecule **TSP1D**.

**¹H NMR** (500 MHz) spectrum of **TSP2D** in CDCl₃ at 298 K.
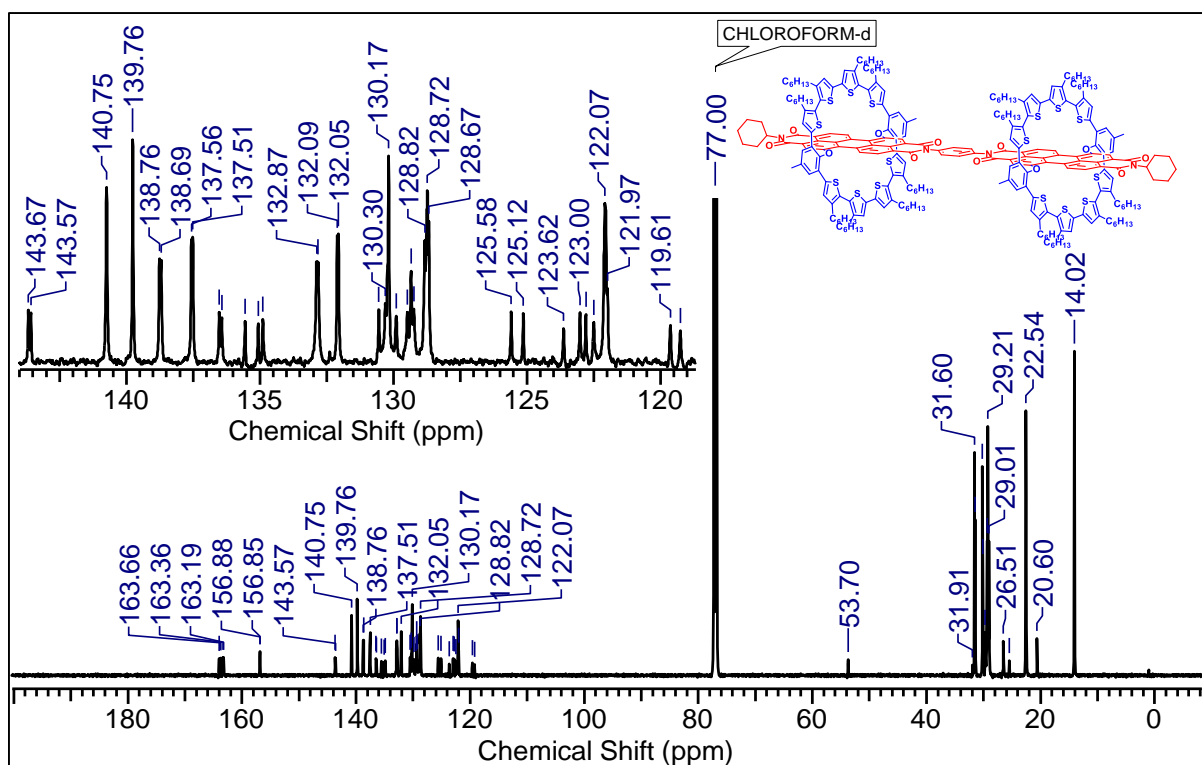


**¹³C NMR** (125 MHz) spectrum of **TSP2D** in CDCl₃ at 298 K.
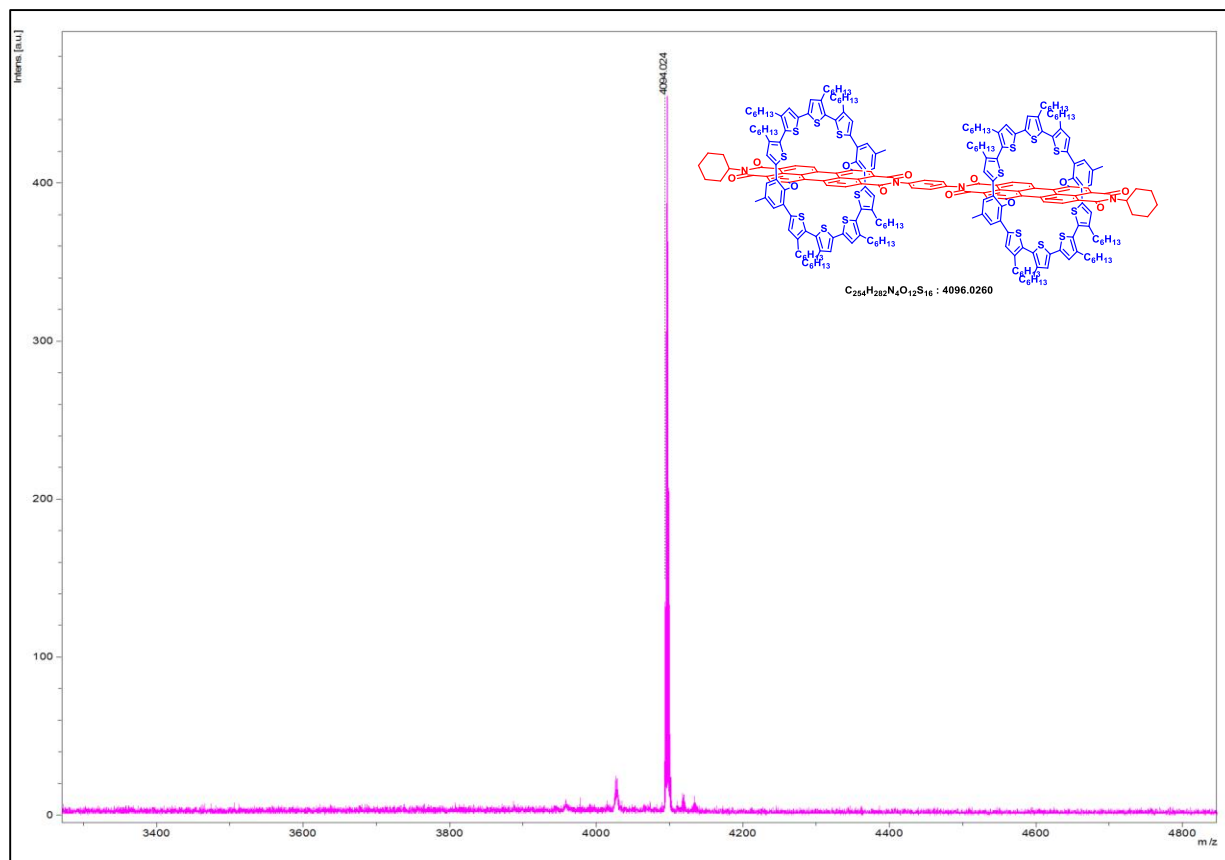
MALDI-TOF MS spectra of molecule **TSP2D**.
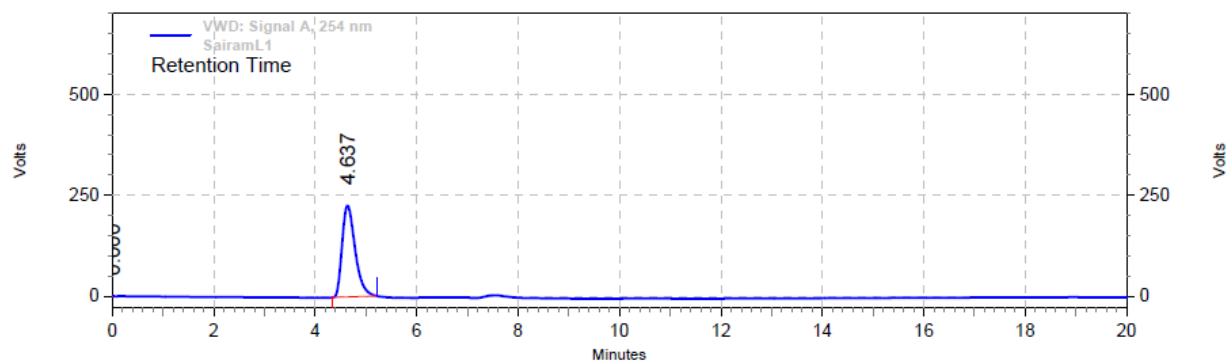


| VWD: Signal A, 254 nm Results | | | | |
|---|---|---|---|---|
| Retention Time | Area | Area % | Height | Height % |
| 0.000 | 0 | 0.00 | 0 | 0.00 |
| 4.637 | 67934995 | 100.00 | 3795852 | 100.00 |

| | | | | |
|---|---|---|---|---|
| Totals | | | | |
| | 67934995 | 100.00 | 3795852 | 100.00 |

HPLC profile of (*P*)-**TSP1** (RT = 4.637) in *n*-hexane:isopropanol (95:05) by monitoring at 254 nm.
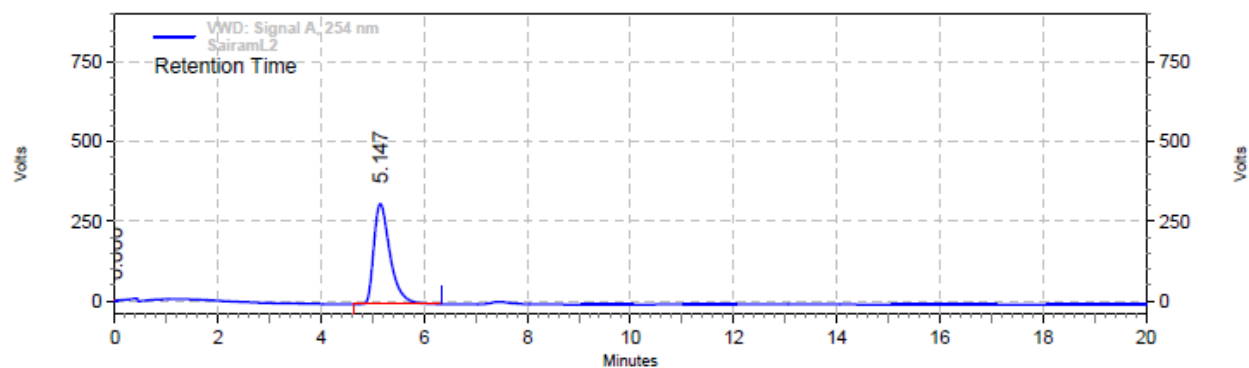
**VWD: Signal A,**
**254 nm Results**

| Retention Time | Area | Area % | Height | Height % |
|---|---|---|---|---|
| 0.000 | 0 | 0.00 | 0 | 0.00 |
| 5.147 | 115871994 | 100.00 | 5274591 | 100.00 |

| | | | | |
|---|---|---|---|---|
| Totals | | | | |
| | 115871994 | 100.00 | 5274591 | 100.00 |

HPLC profile of (*M*)-**TSP1** (RT = 5.147) in *n*-hexane:isopropanol (95:05) by monitoring at 254 nm.
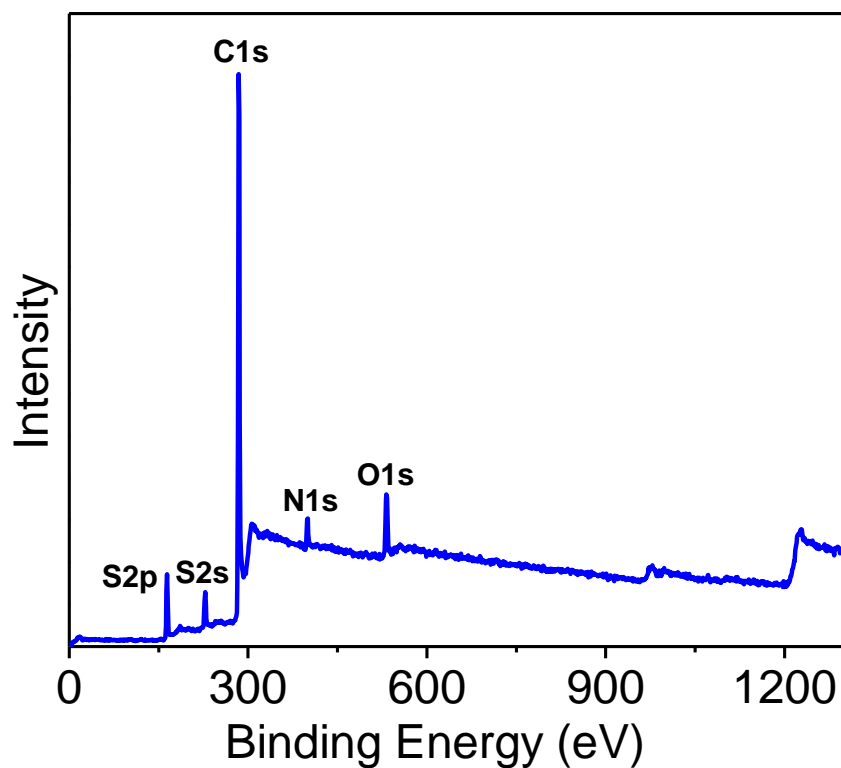


XPS survey scan of **TSP-2DP**.
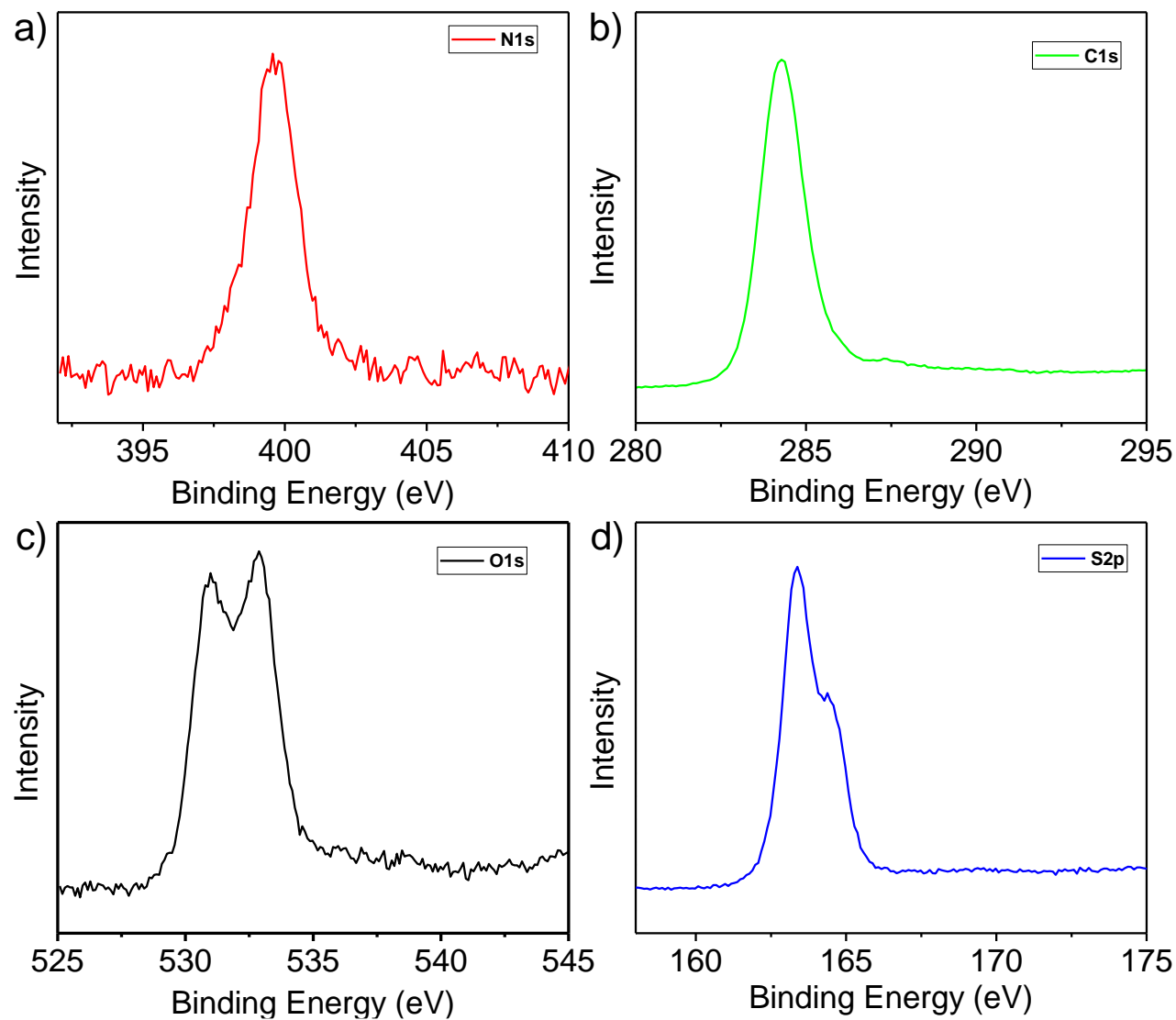
XPS analysis showing profiles of a) $N_{1s}$, b) $C_{1s}$, c) $O_{1s}$, d) $S_{2p}$ of **TSP-2DP**.
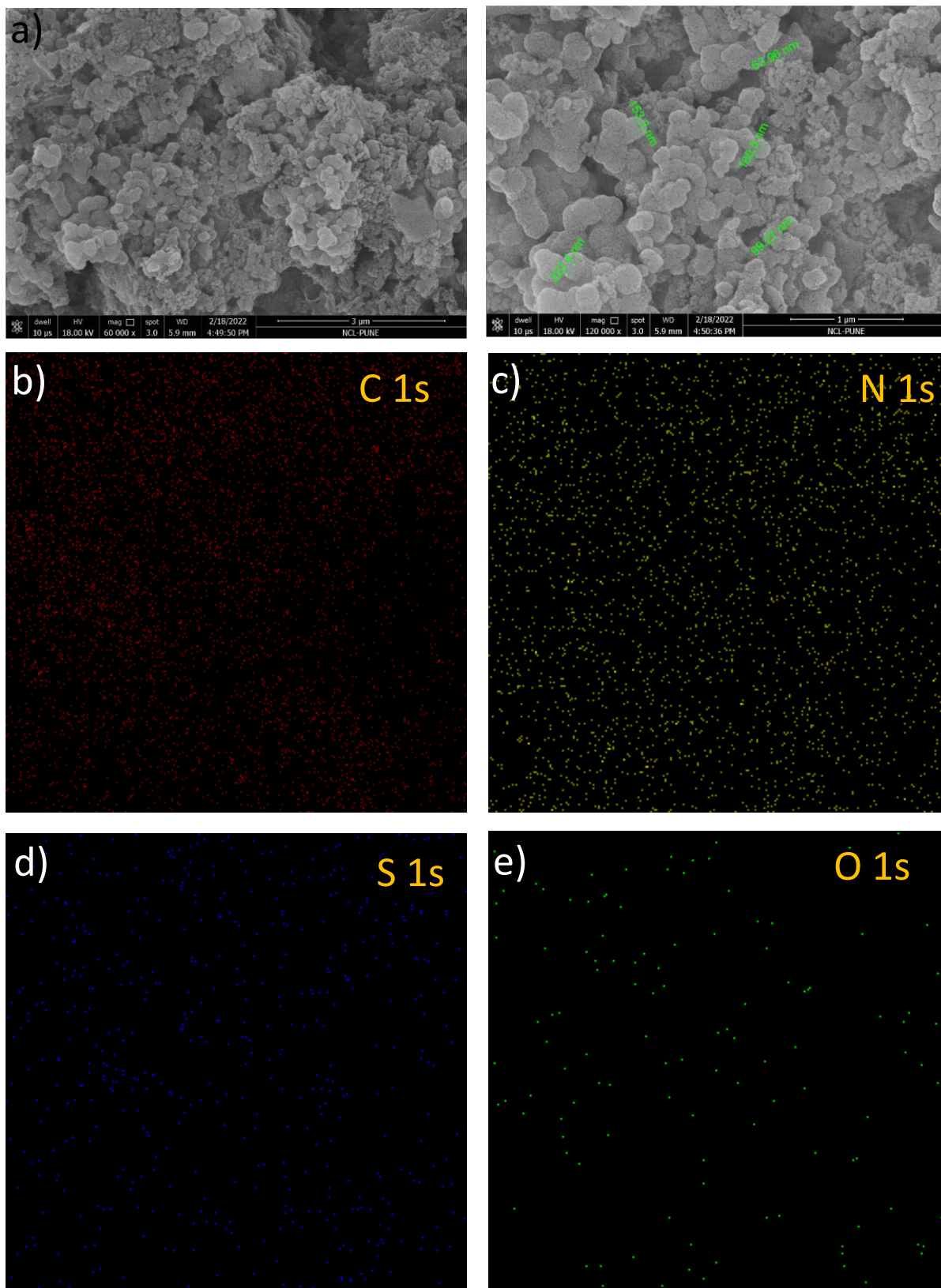
a) SEM image and elemental analysis of b) C, c) N, d) S, e) O of **TSP-2DP**.
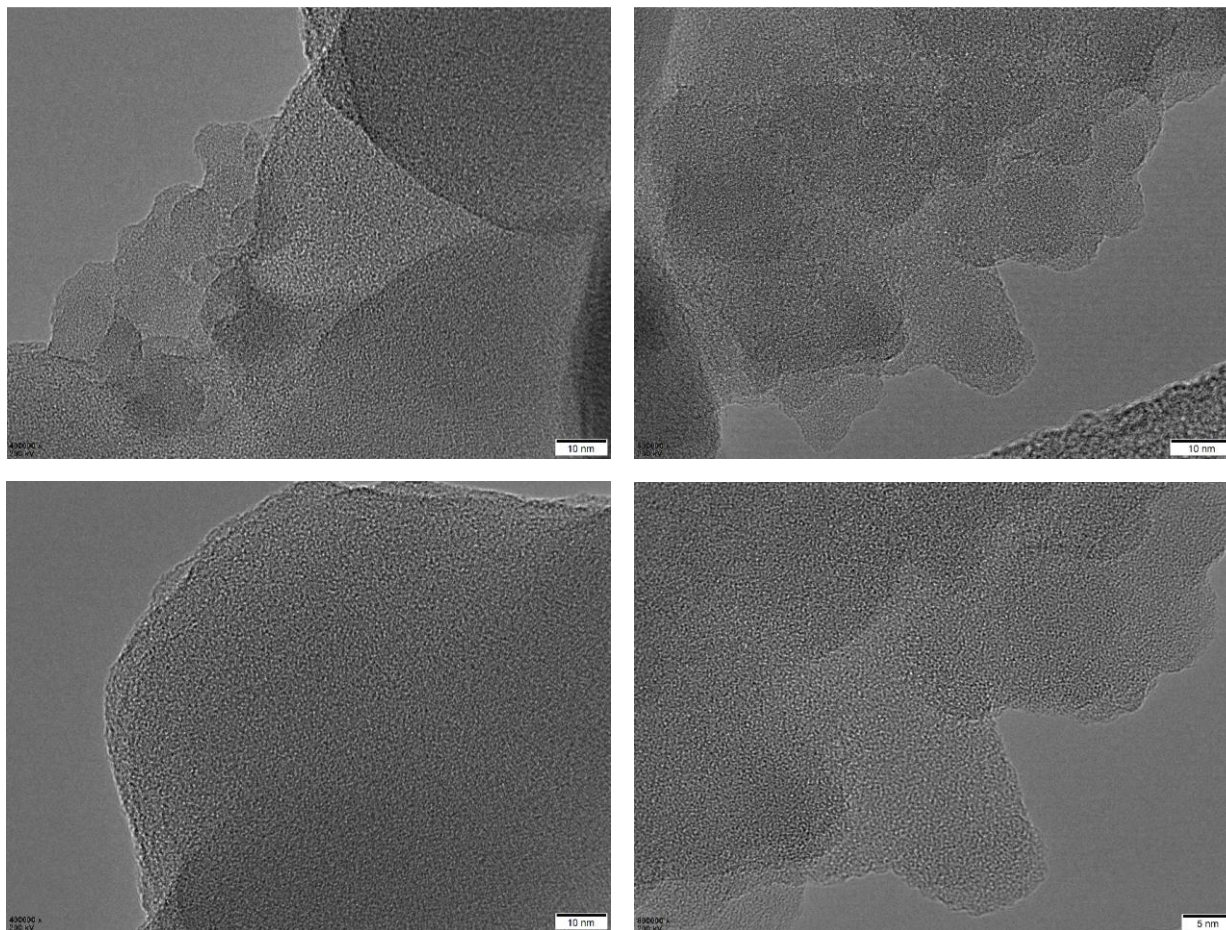
HR-**T**EM image of **TSP-2DP**.
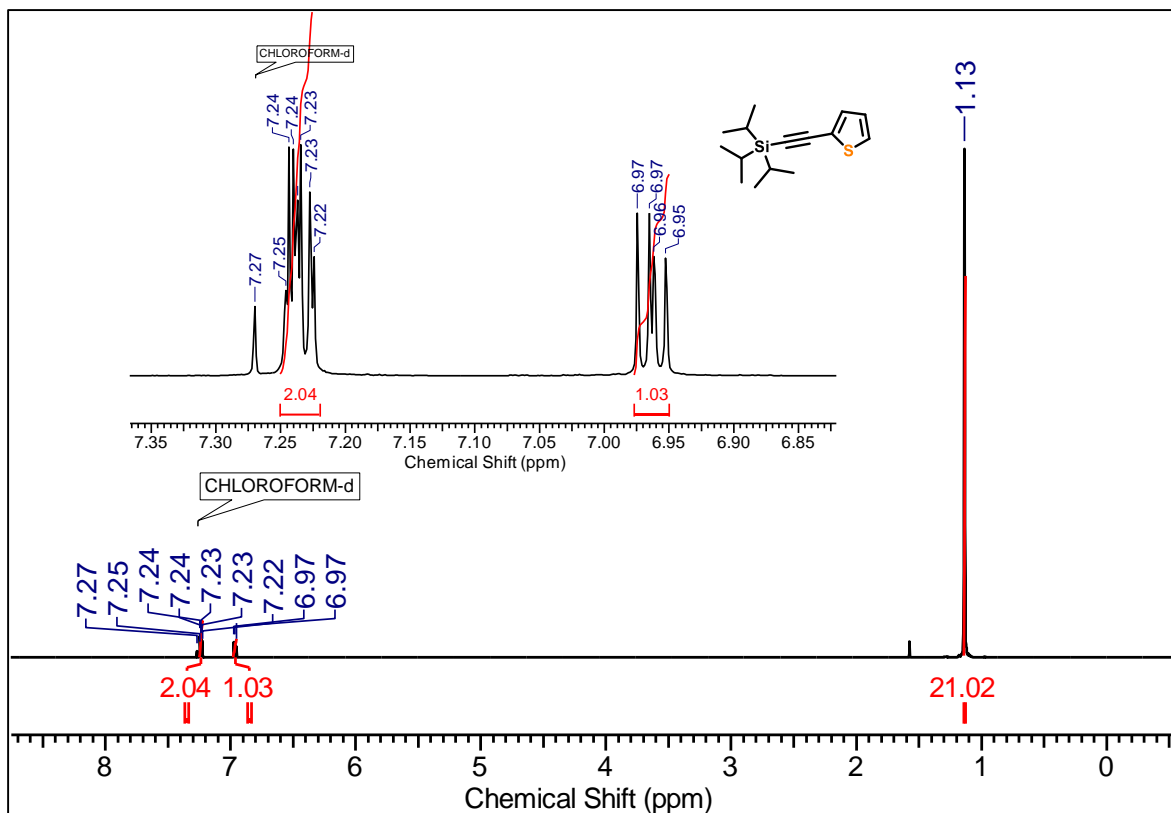
**¹H NMR** (500 MHz) spectrum of **T1** in CDCl₃ at 298 K.
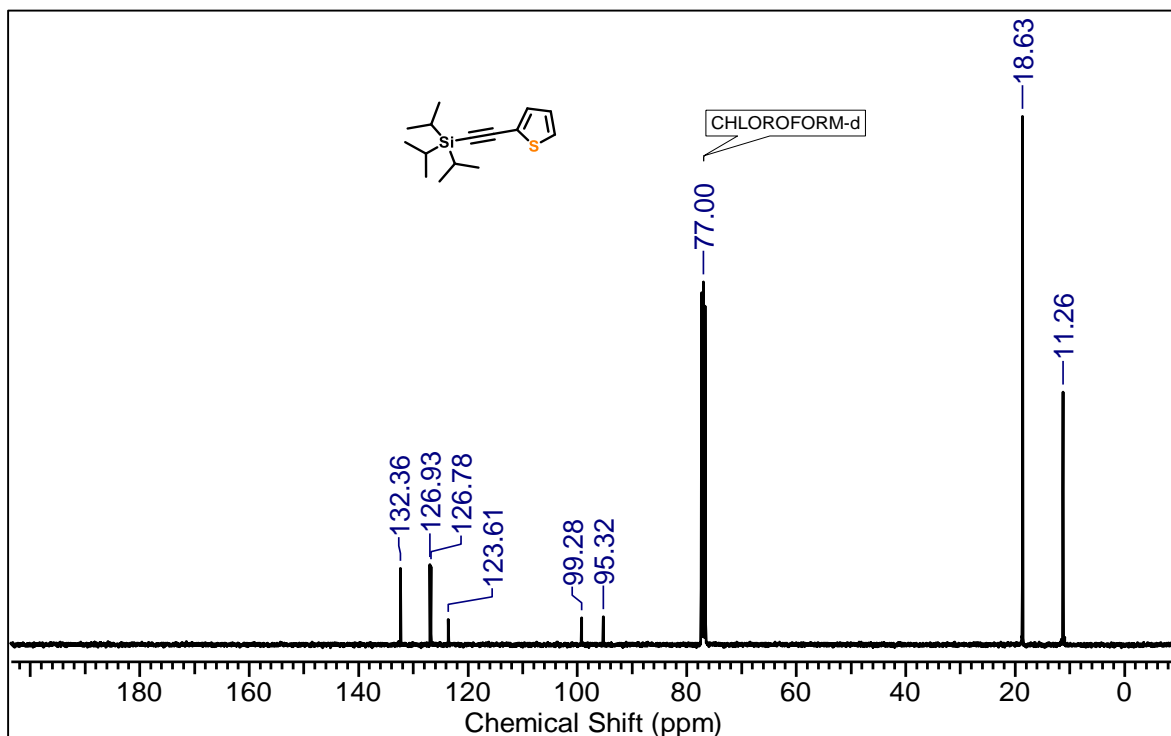


**¹³C NMR** (125 MHz) spectrum of **T1** in CDCl₃ at 298 K.
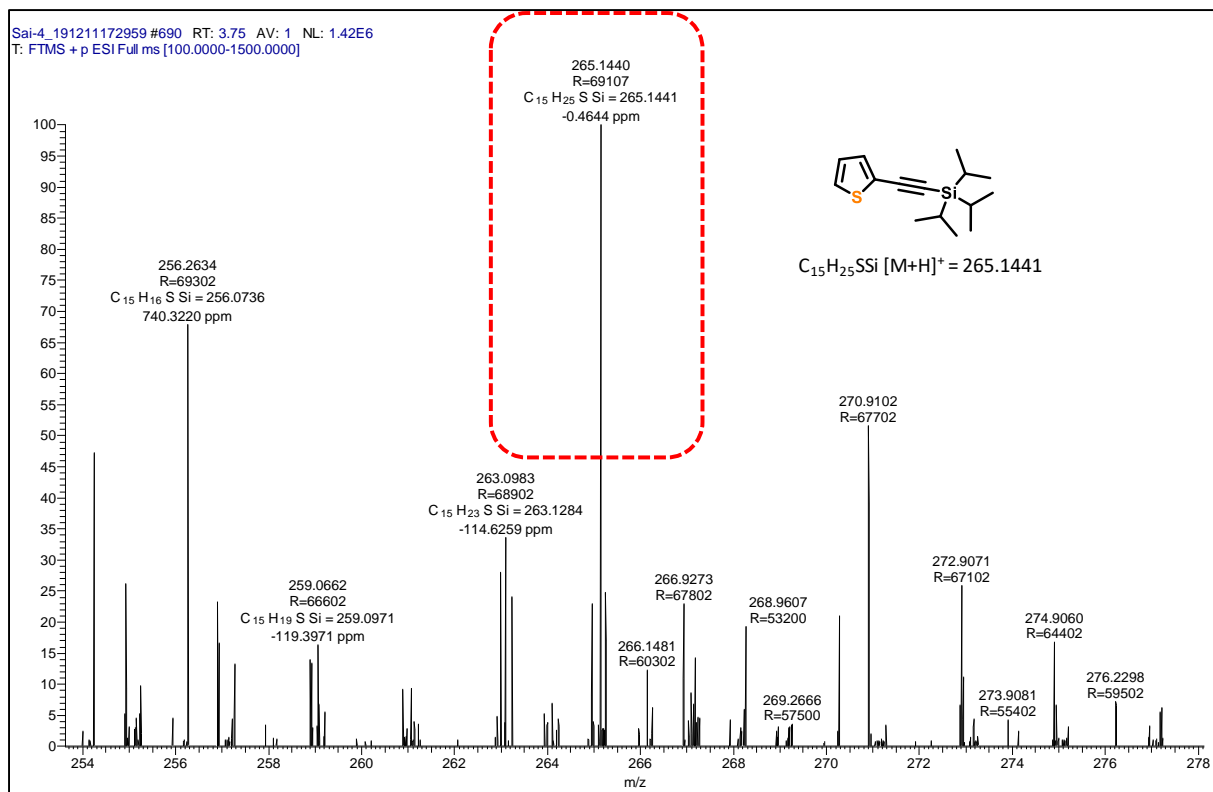
**HRMS** spectrum of triisopropyl(thiophen-2-ylethynyl)silane (**T1**).
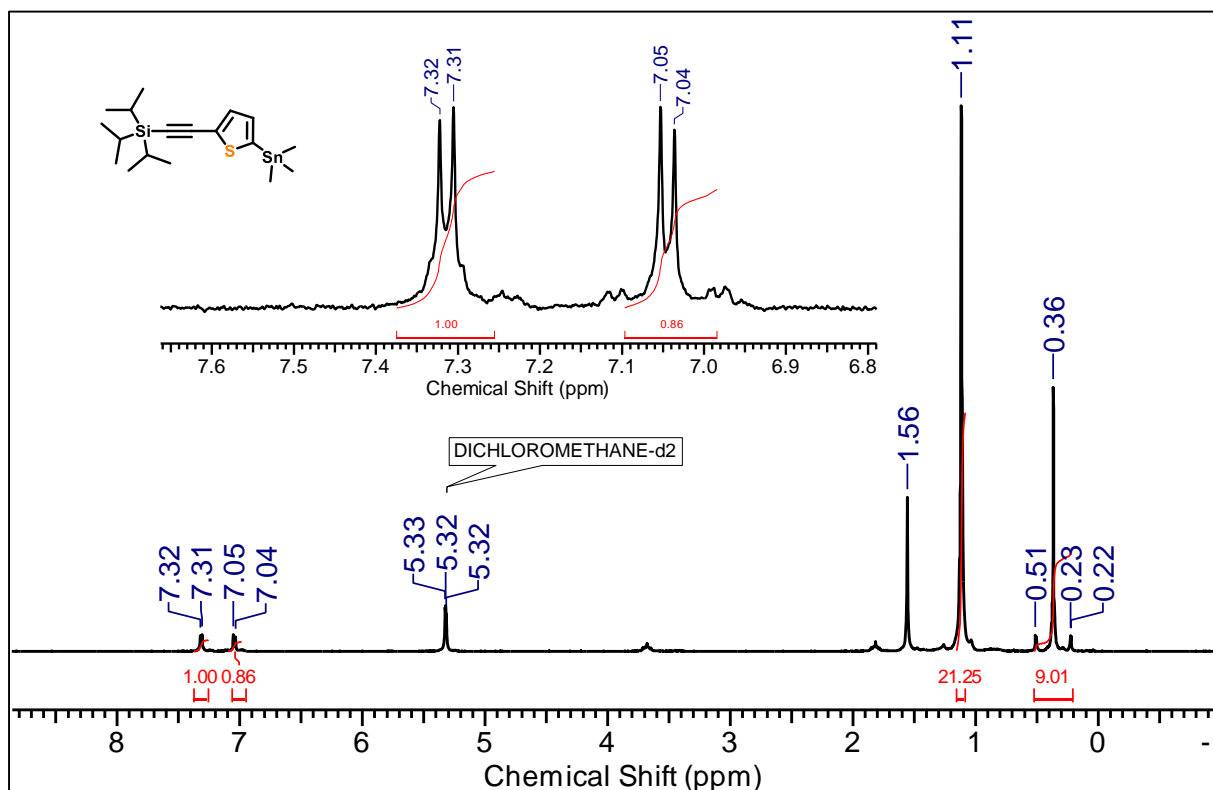


**¹H NMR** (200 MHz) spectrum of **T2** in $CD_2Cl_2$ at 298 K.
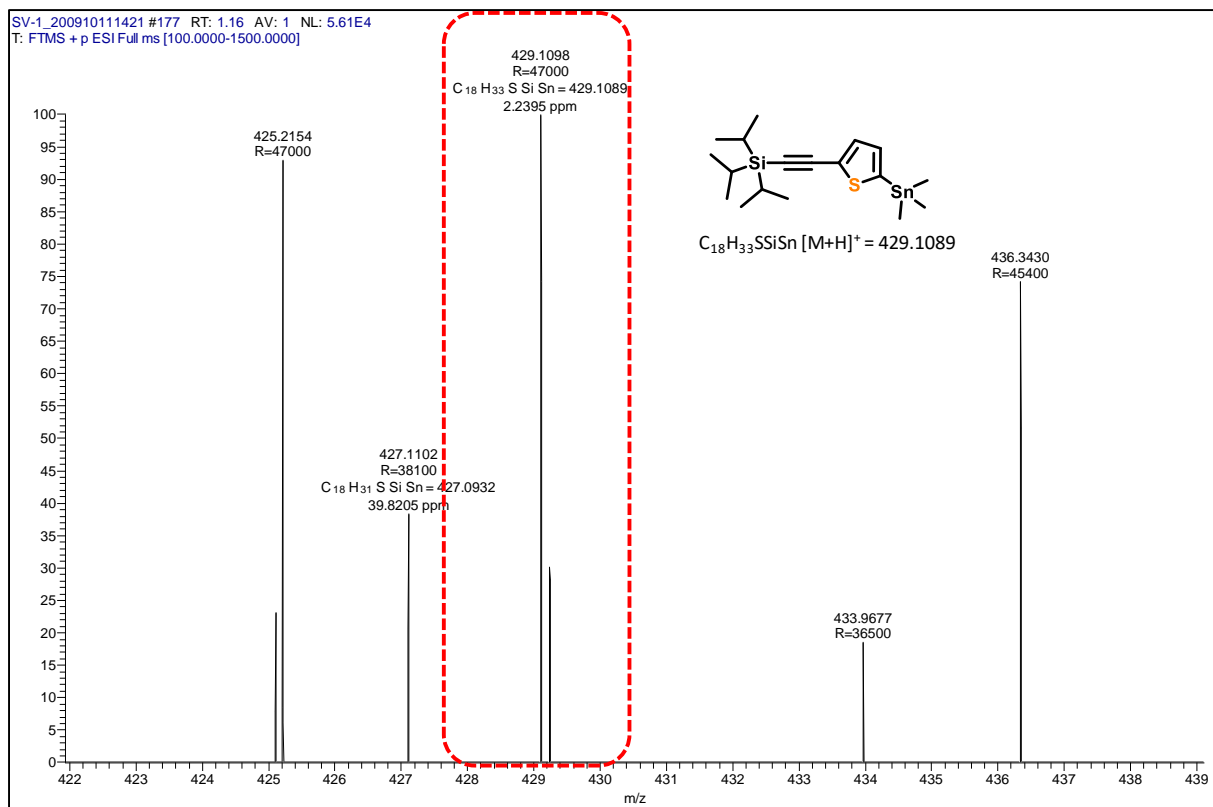
**HRMS** spectrum of triisopropyl((5-(trimethylstannyl)thiophen-2-yl)ethynyl)silane (**T2**).
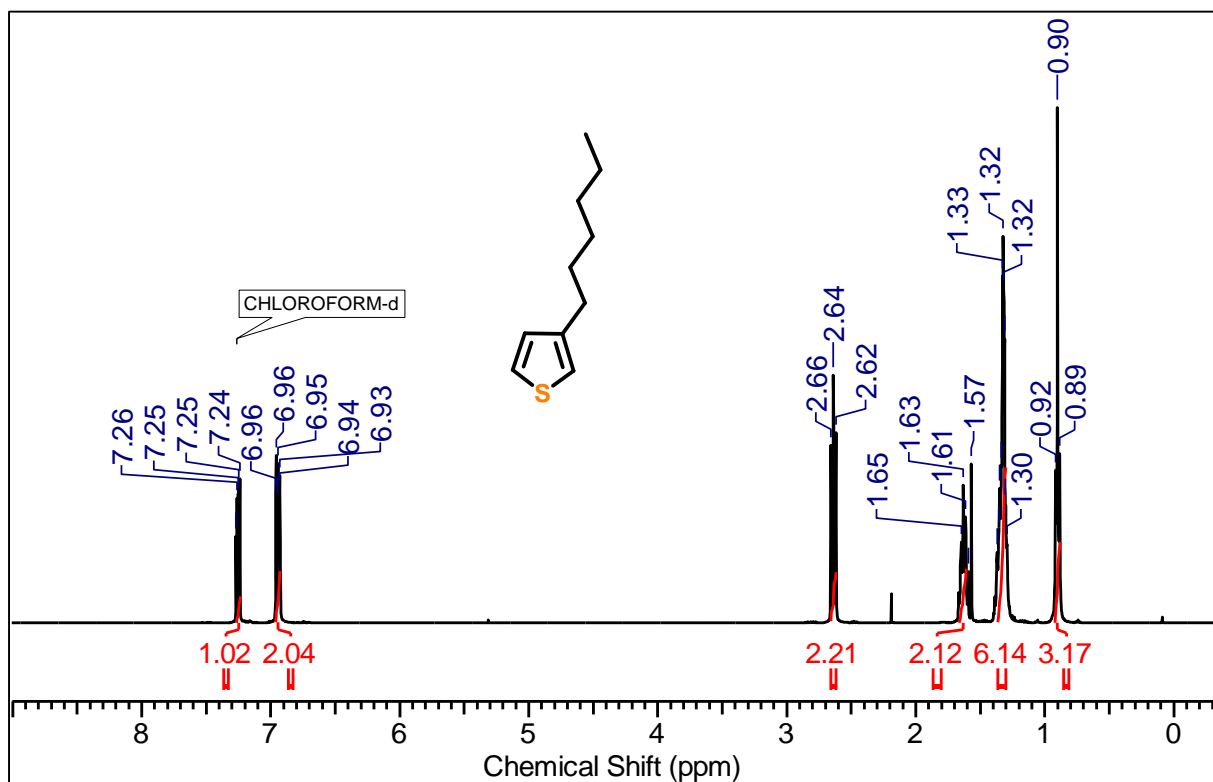


$^1$**H NMR** (500 MHz) spectrum of **T3** in CDCl$_3$ at 298 K.
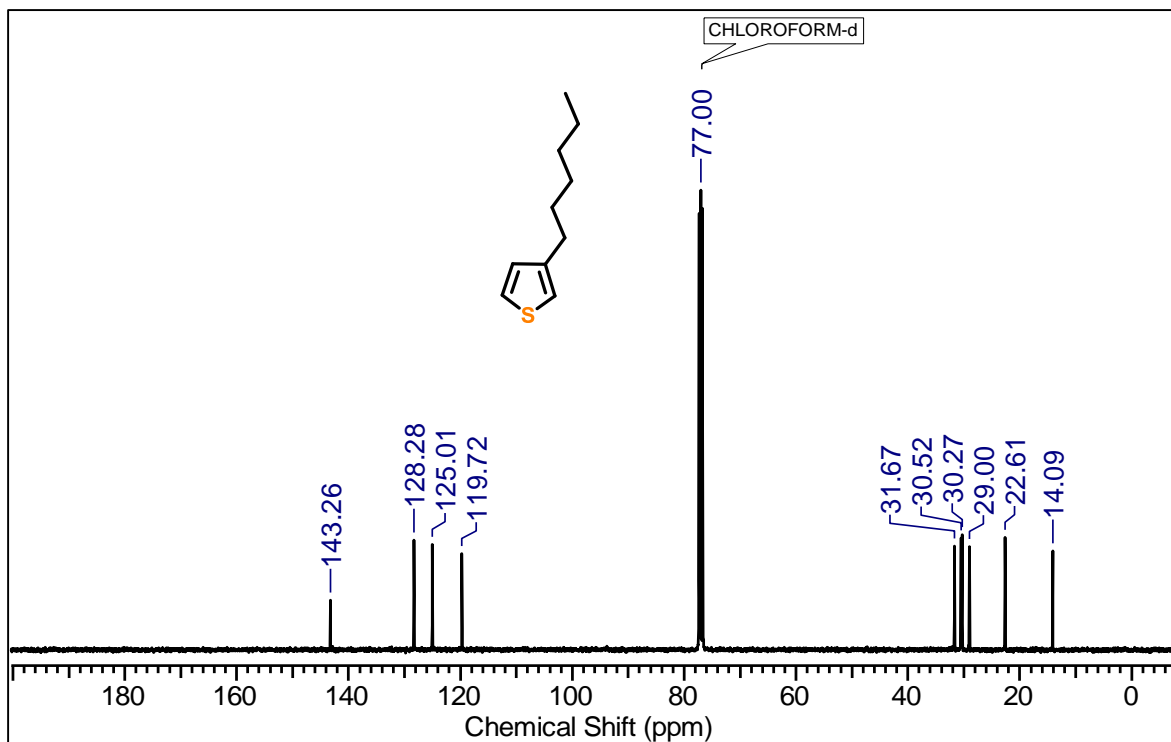
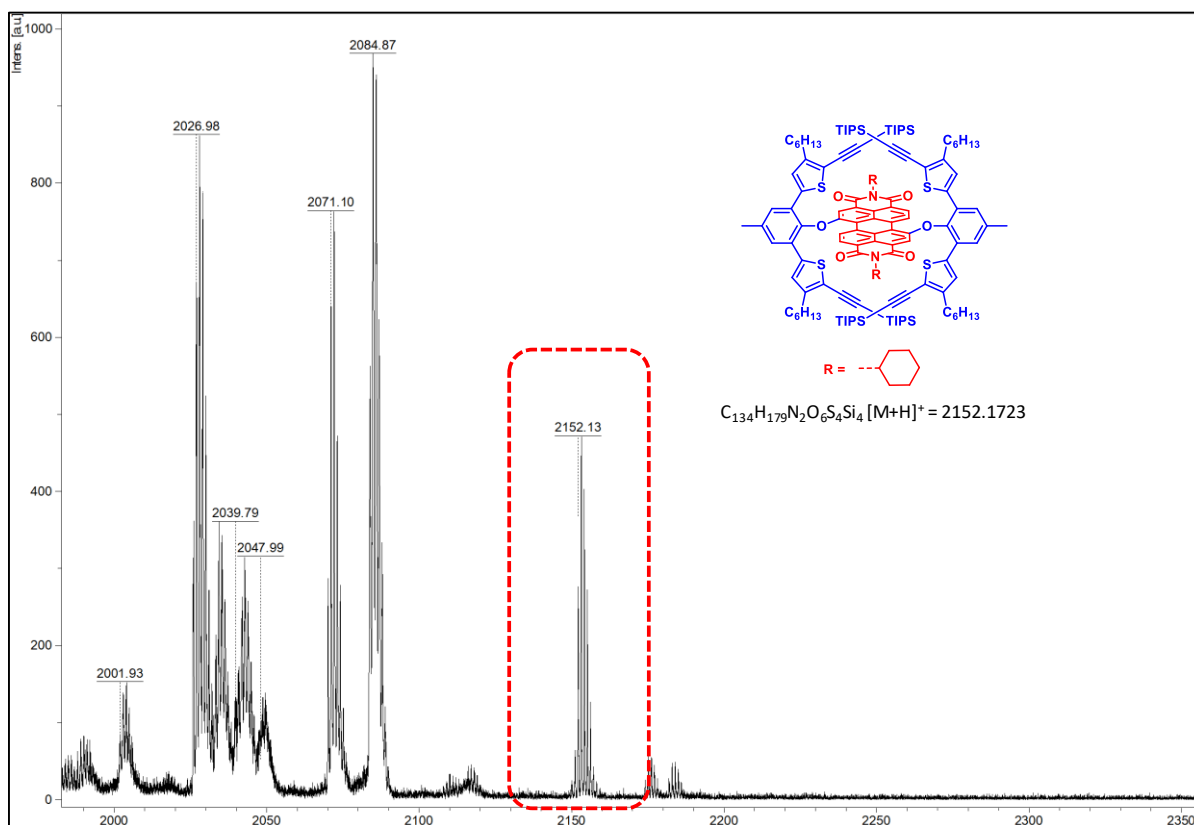**13C NMR** (125 MHz) spectrum of **T3** in CDCl$_3$ at 298 K.
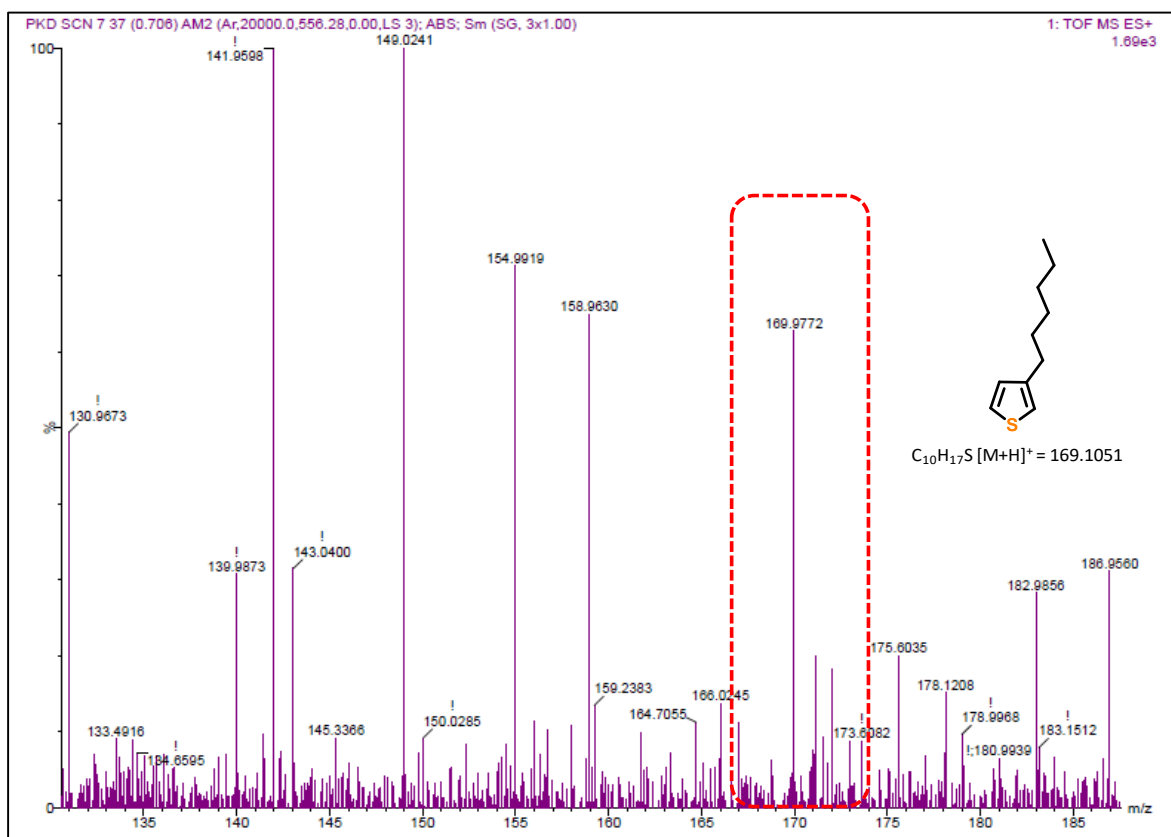


**HRMS** spectrum of 3-hexylthiophene (**T3**).

**¹H NMR** (400 MHz) spectrum of **T4** in CDCl₃ at 298 K.
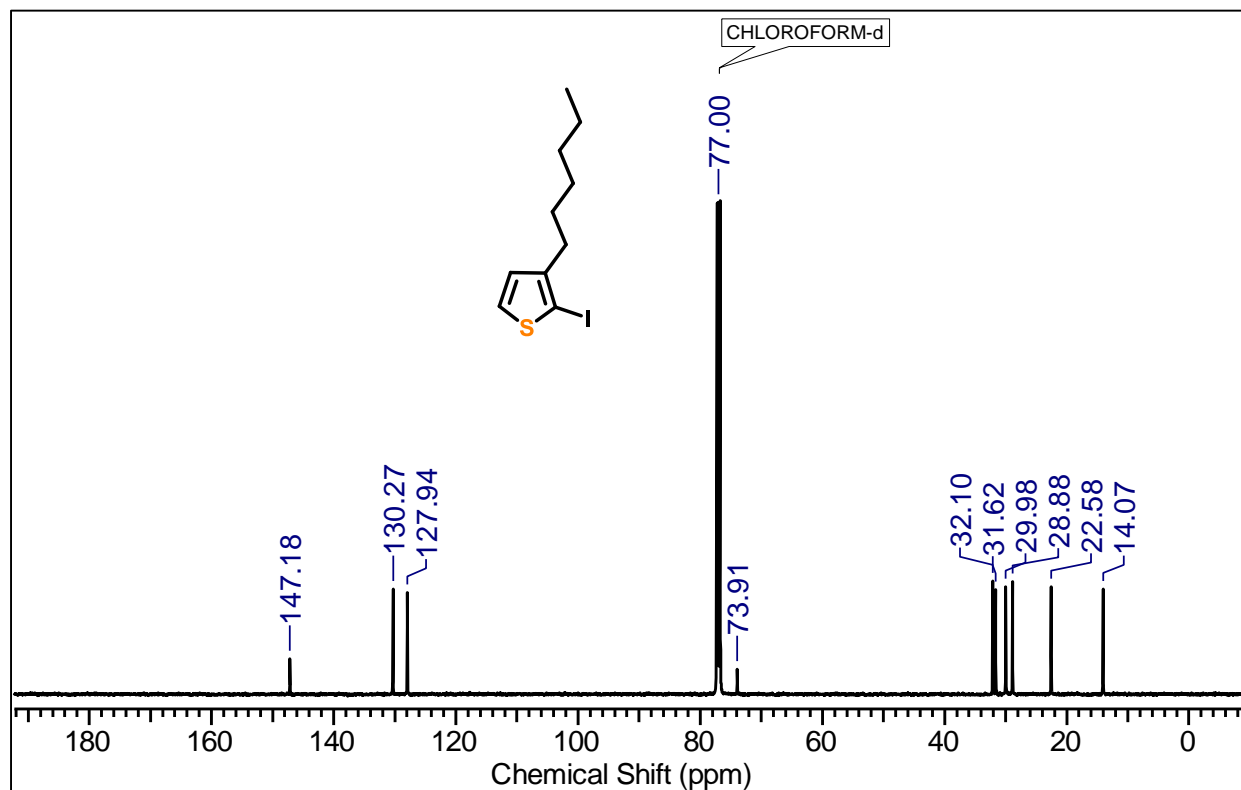


**¹³C NMR** (100 MHz) spectrum of **T4** in CDCl₃ at 298 K.

$C_{10}H_{15}IS [M]^+ = 293.1939$,
$C_{10}H_{16}IS [M+H]^+ = 295.0017$
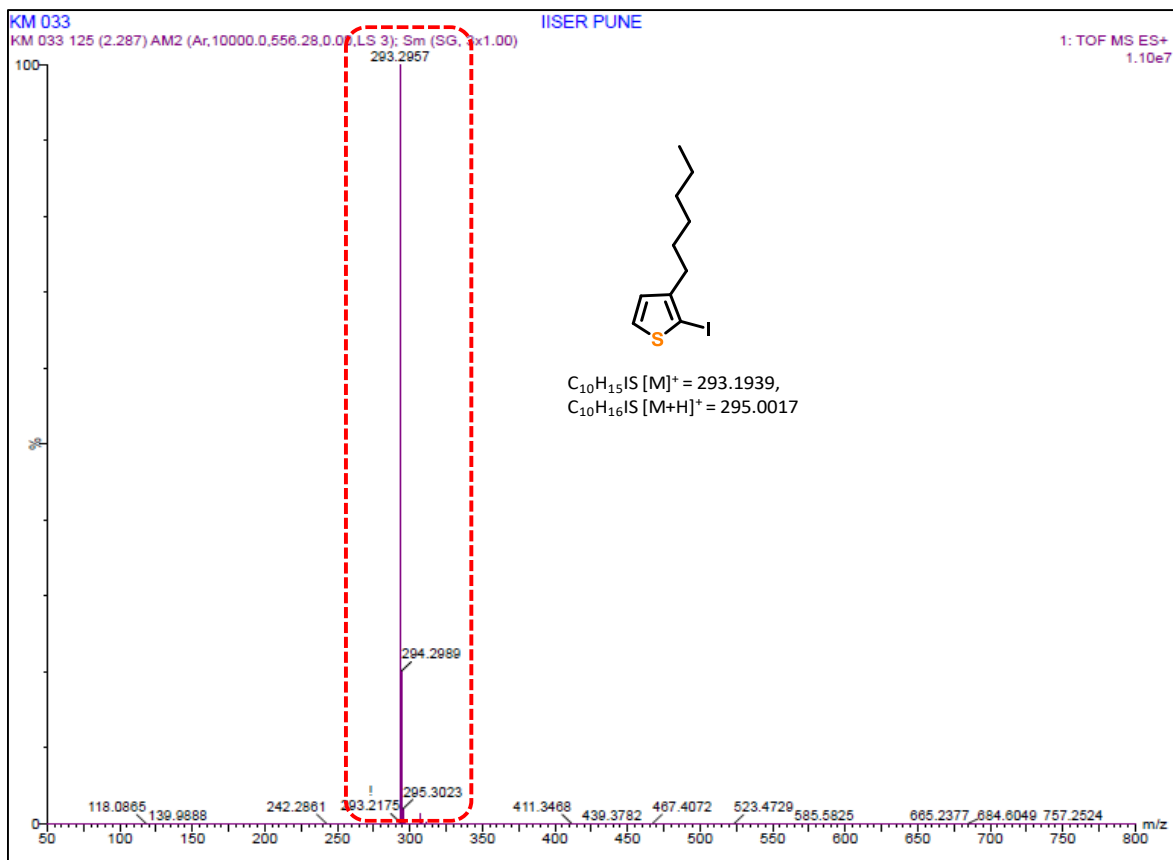
**HRMS** spectrum of 3-hexyl-2-iodothiophene (**T4**).
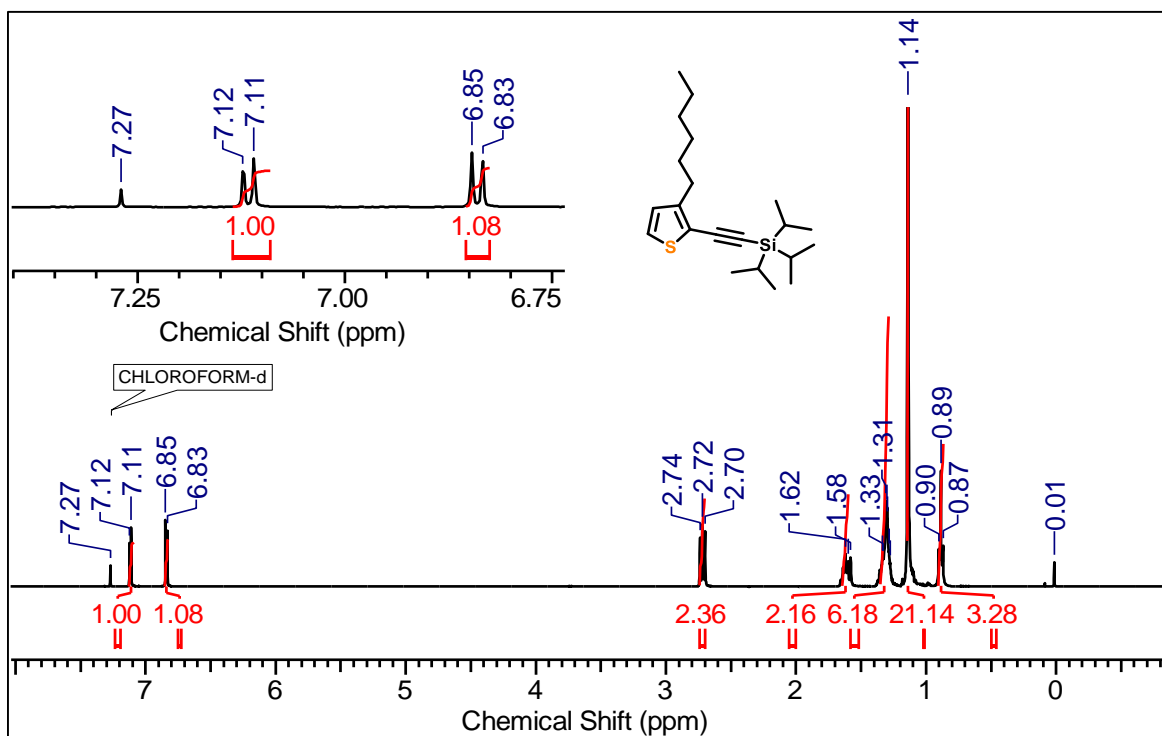


**$^1$H NMR** (500 MHz) spectrum of **T5** in CDCl$_3$ at 298 K.
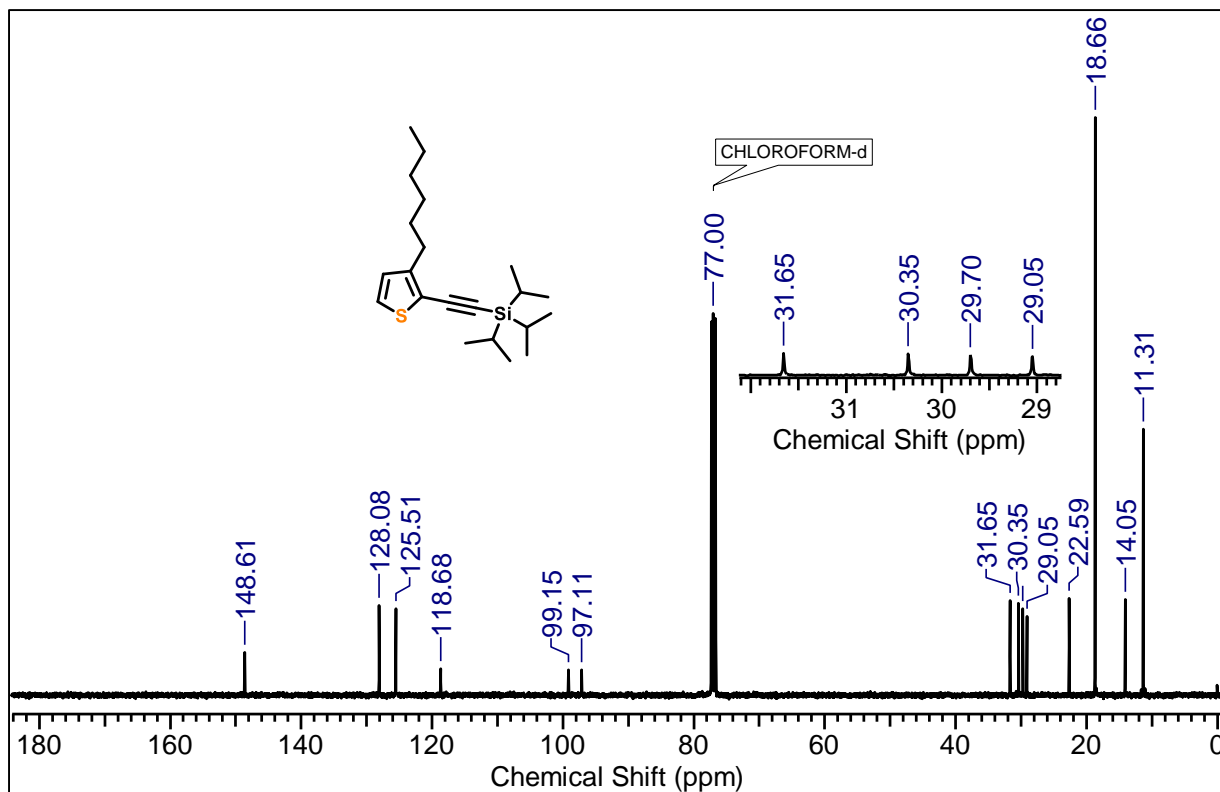
**¹³C NMR** (100 MHz) spectrum of **T5** in CDCl₃ at 298 K.
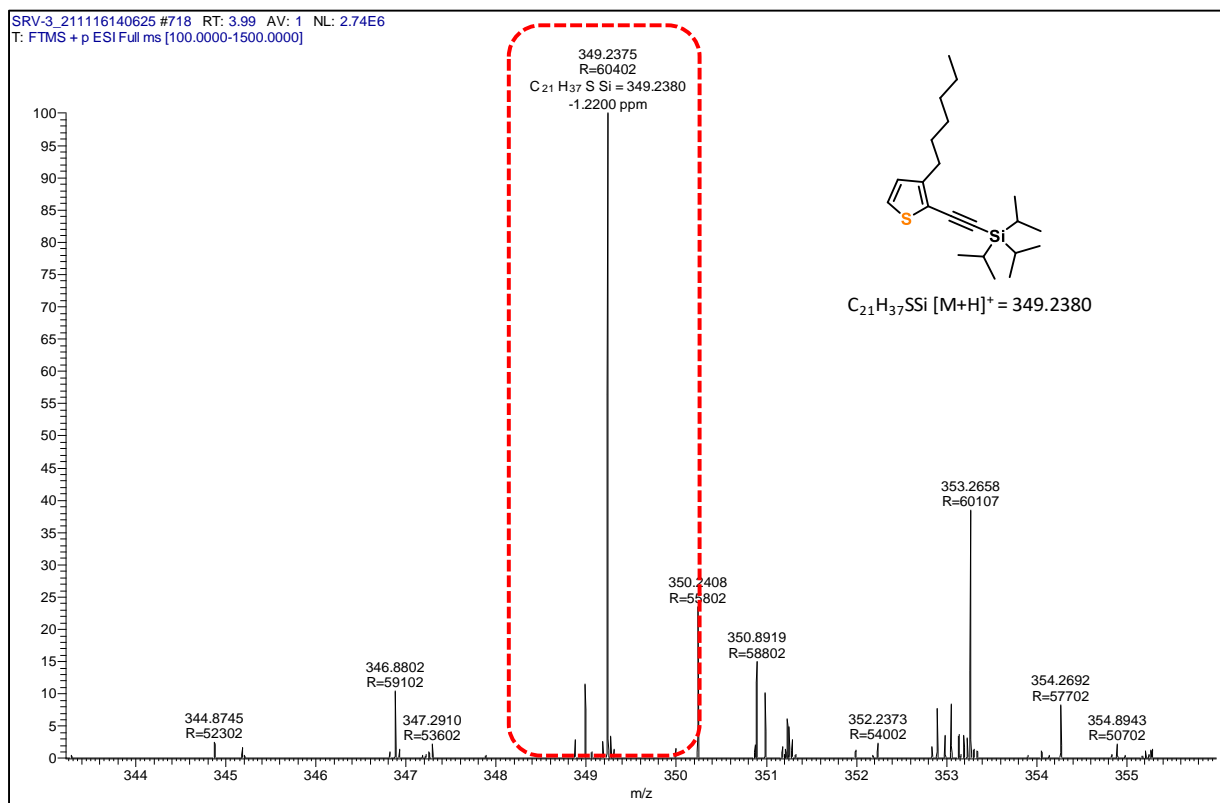


**HRMS** spectrum of ((3-hexylthiophen-2-yl)ethynyl)triisopropylsilane (**T5**).
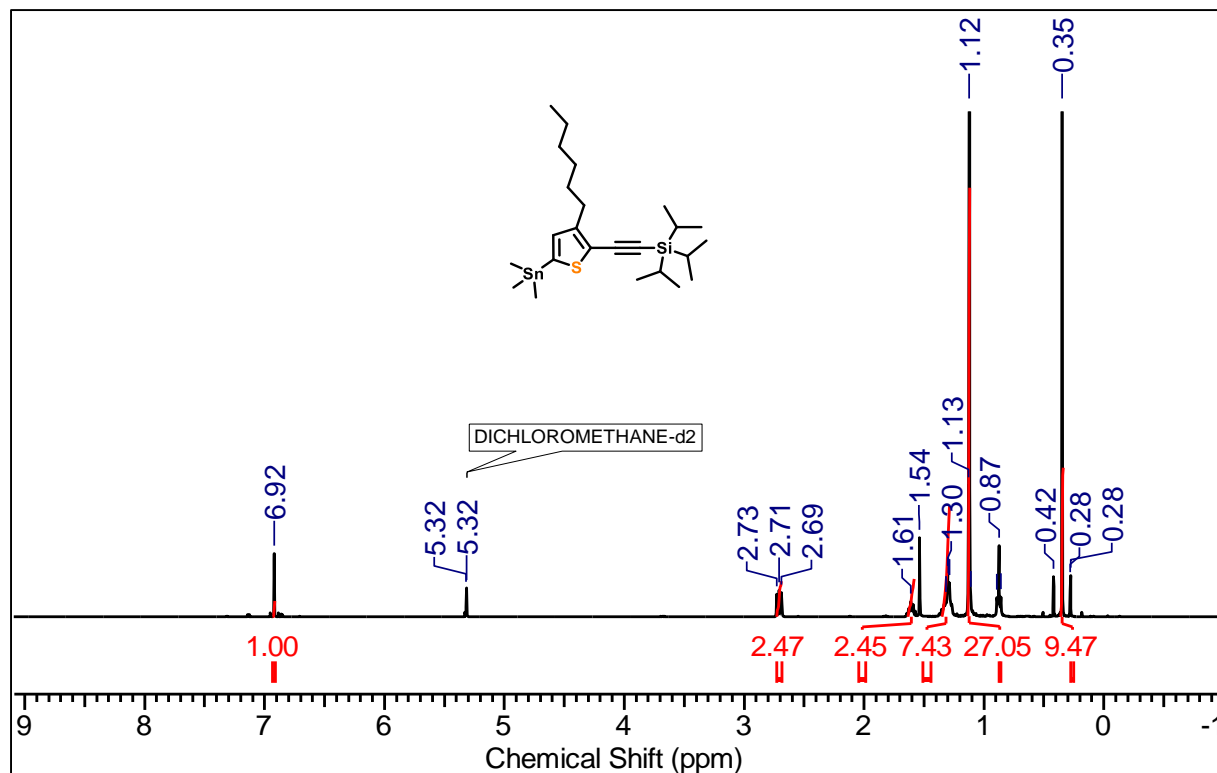
**¹H NMR** (400 MHz) spectrum of **T6** in CDCl₃ at 298 K.
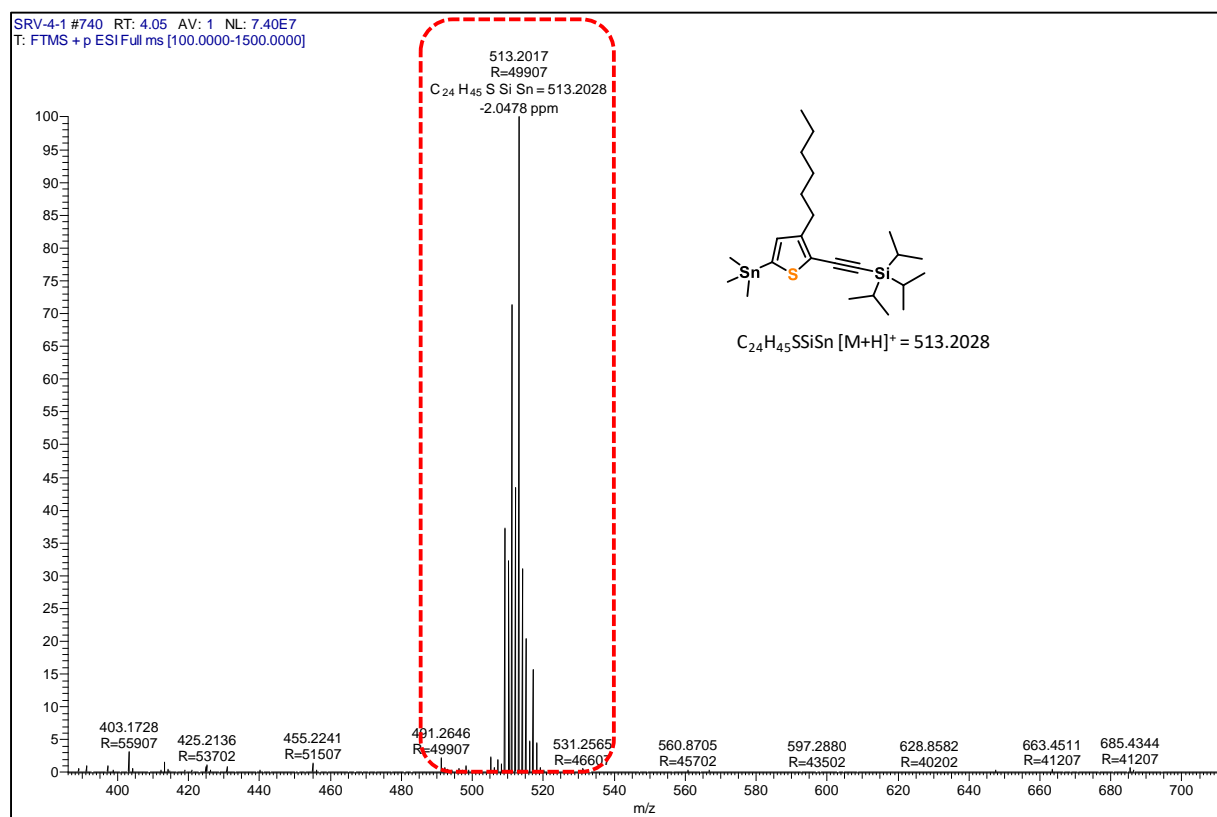


**HRMS** spectrum of ((3-hexyl-5-(trimethylstannyl)thiophen-2-yl)ethynyl)triisopropylsilane (**T6**).
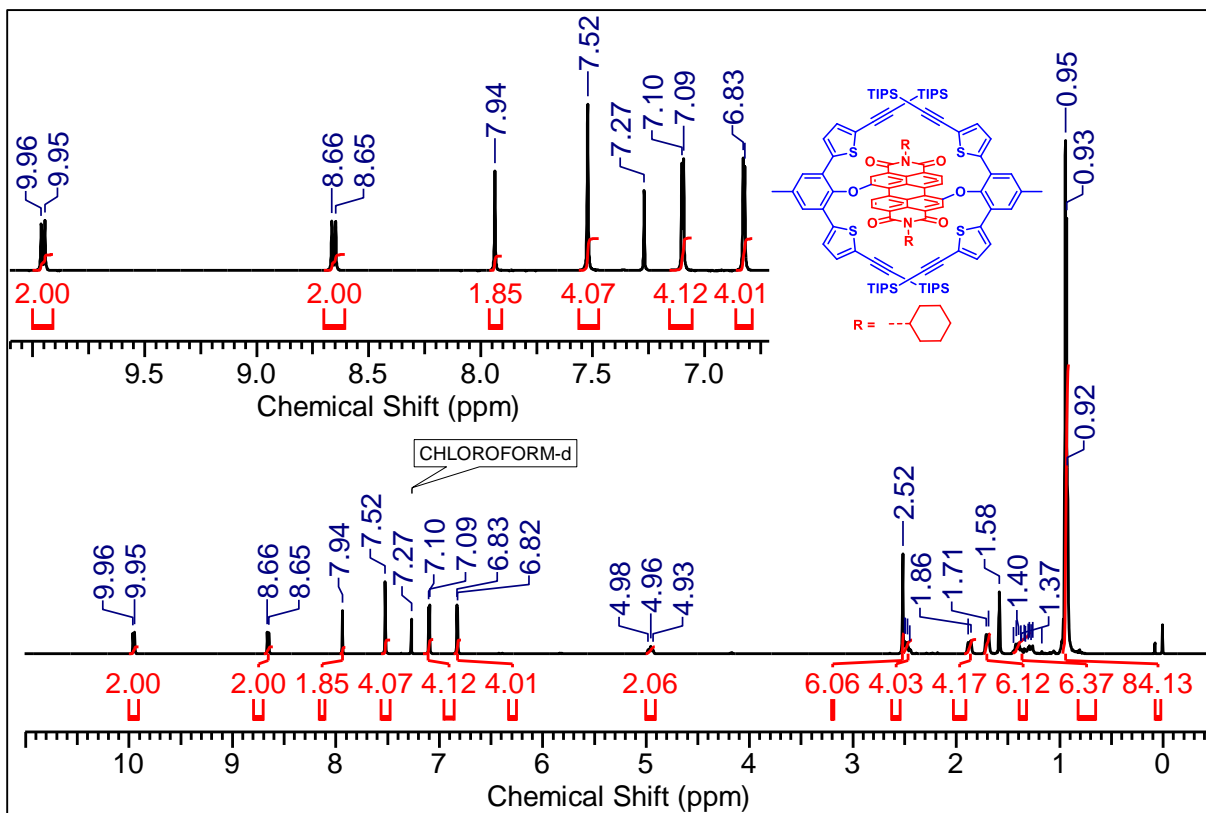
**$^1$H NMR** (500 MHz) spectrum of **4a** in CDCl$_3$ at 298 K.
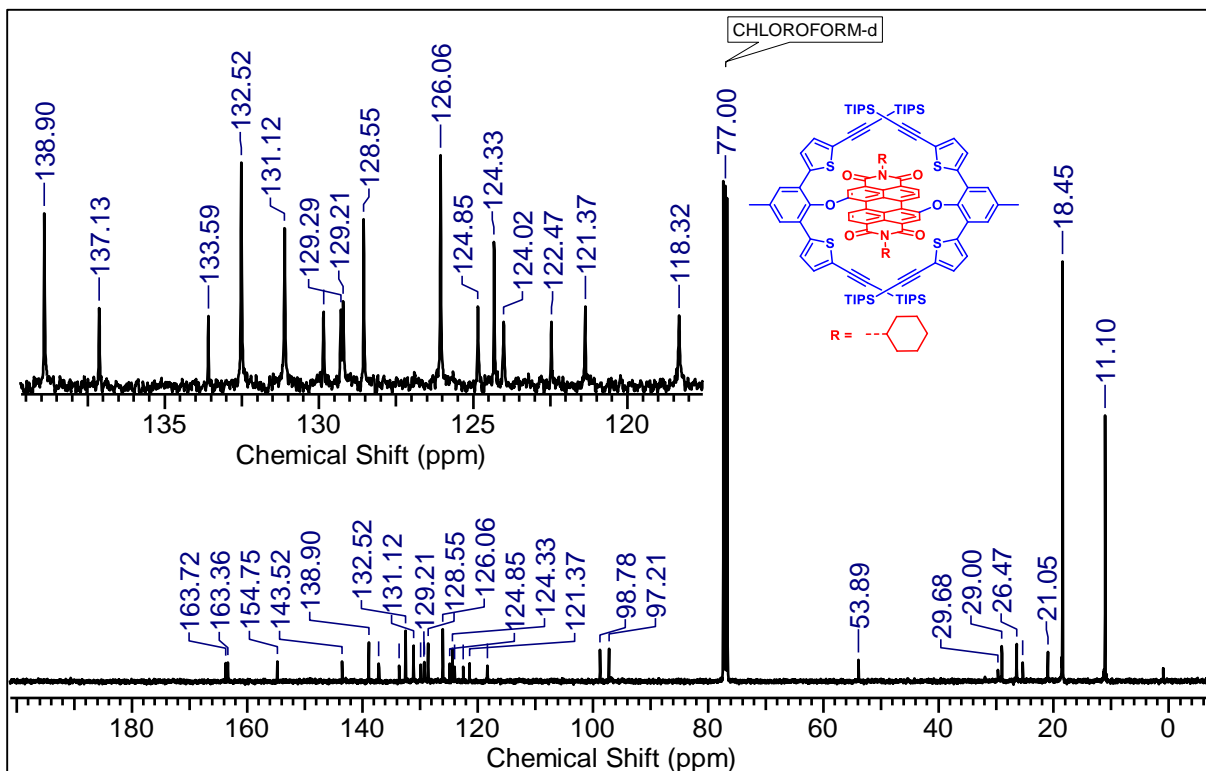


**$^{13}$C NMR** (125 MHz) spectrum of **4a** in CDCl$_3$ at 298 K.
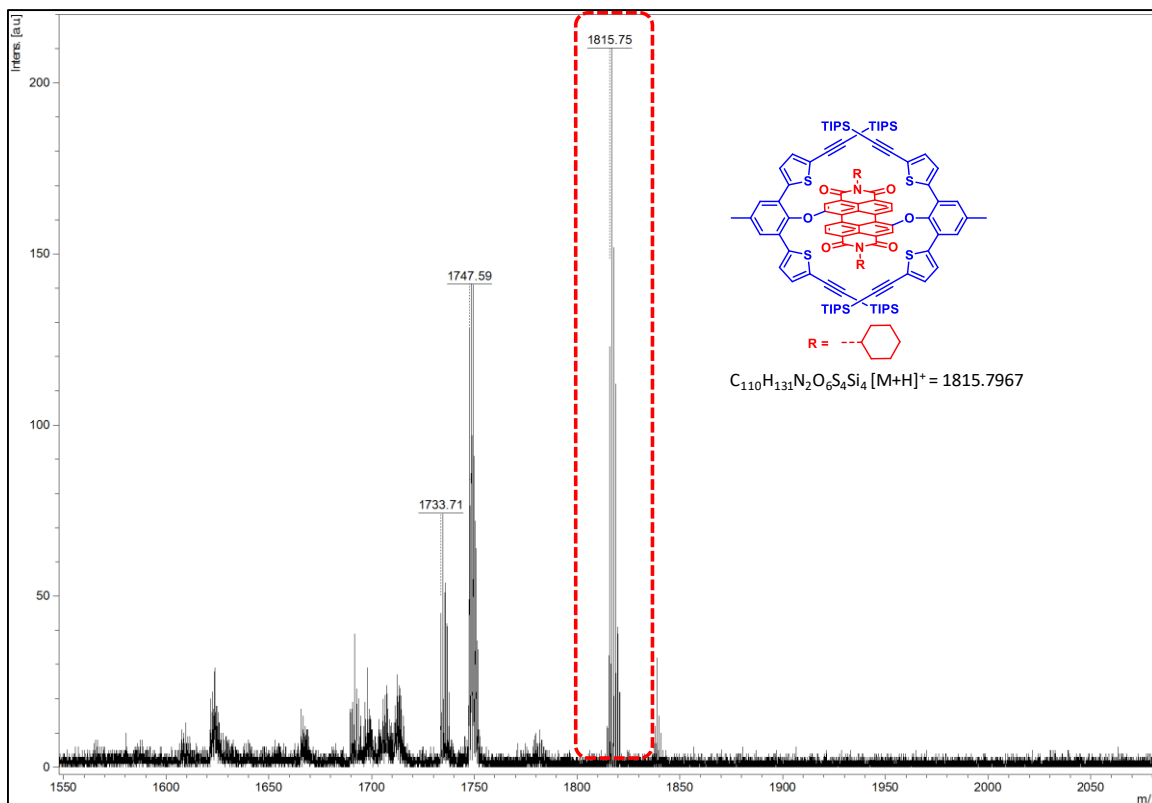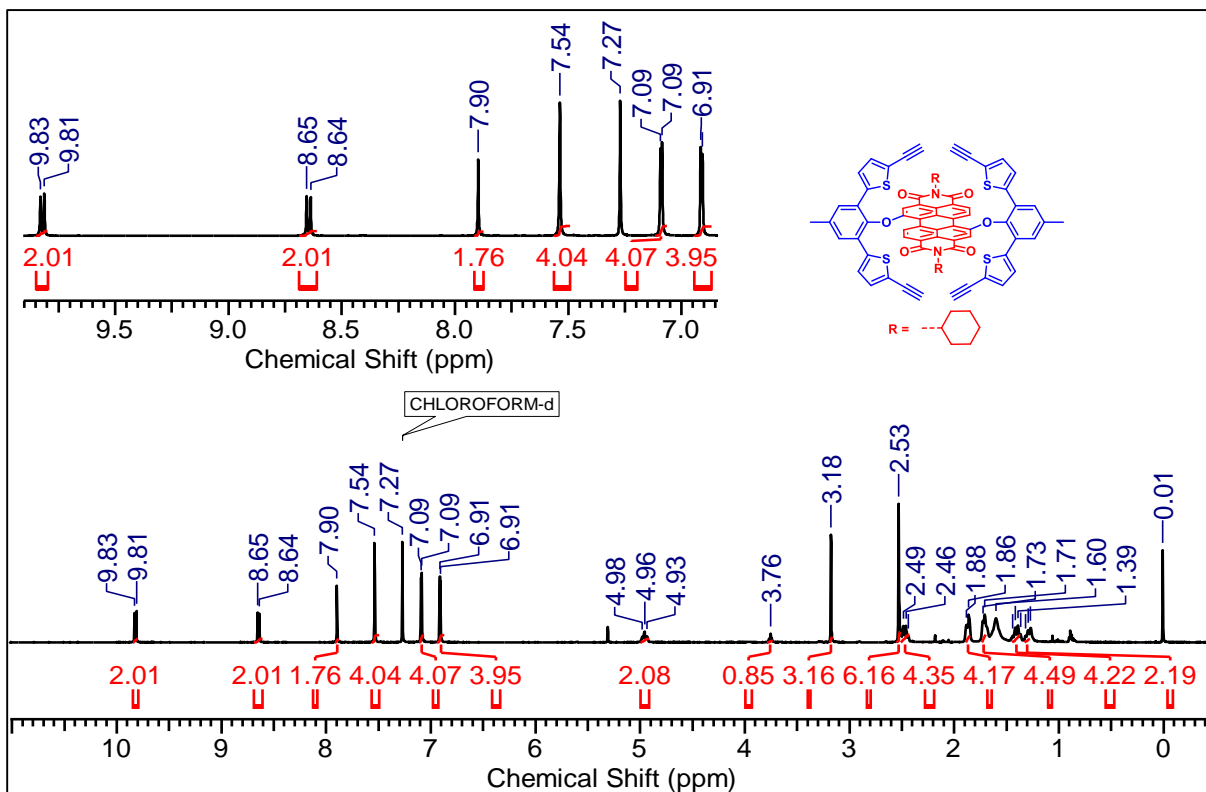
**MALDI-TOF** spectra of molecule **4a**.
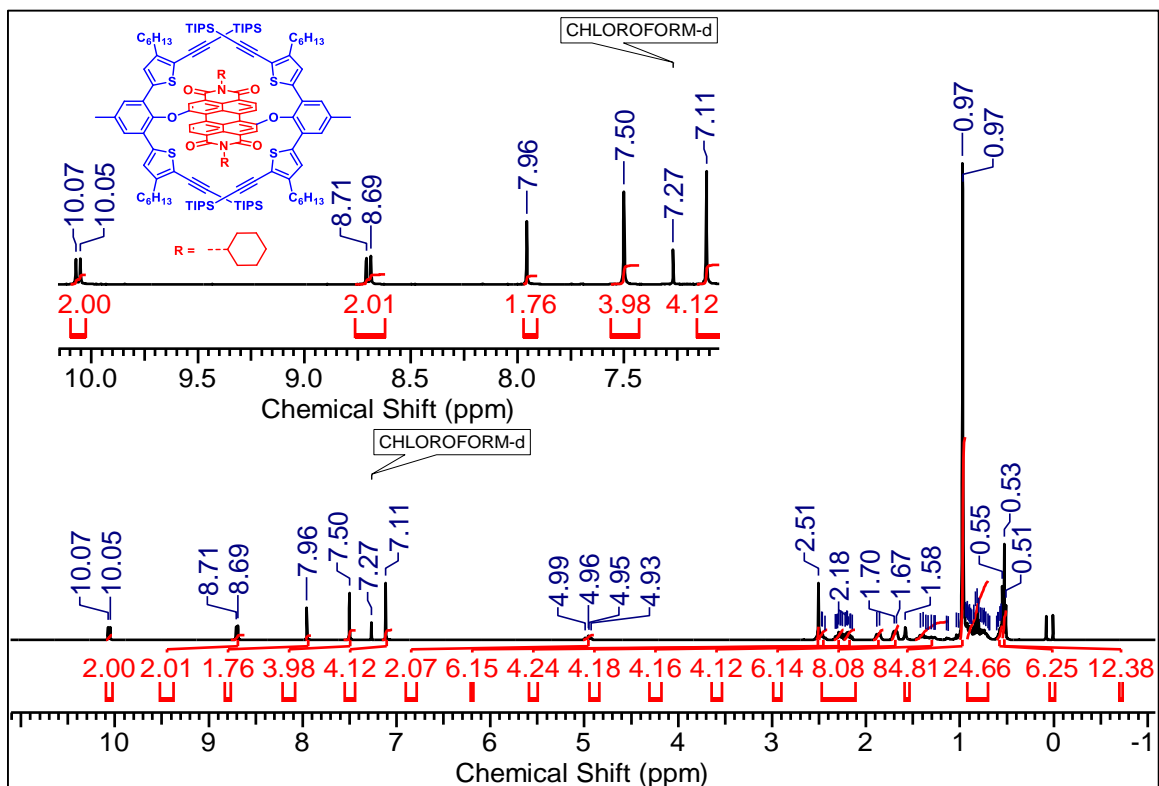


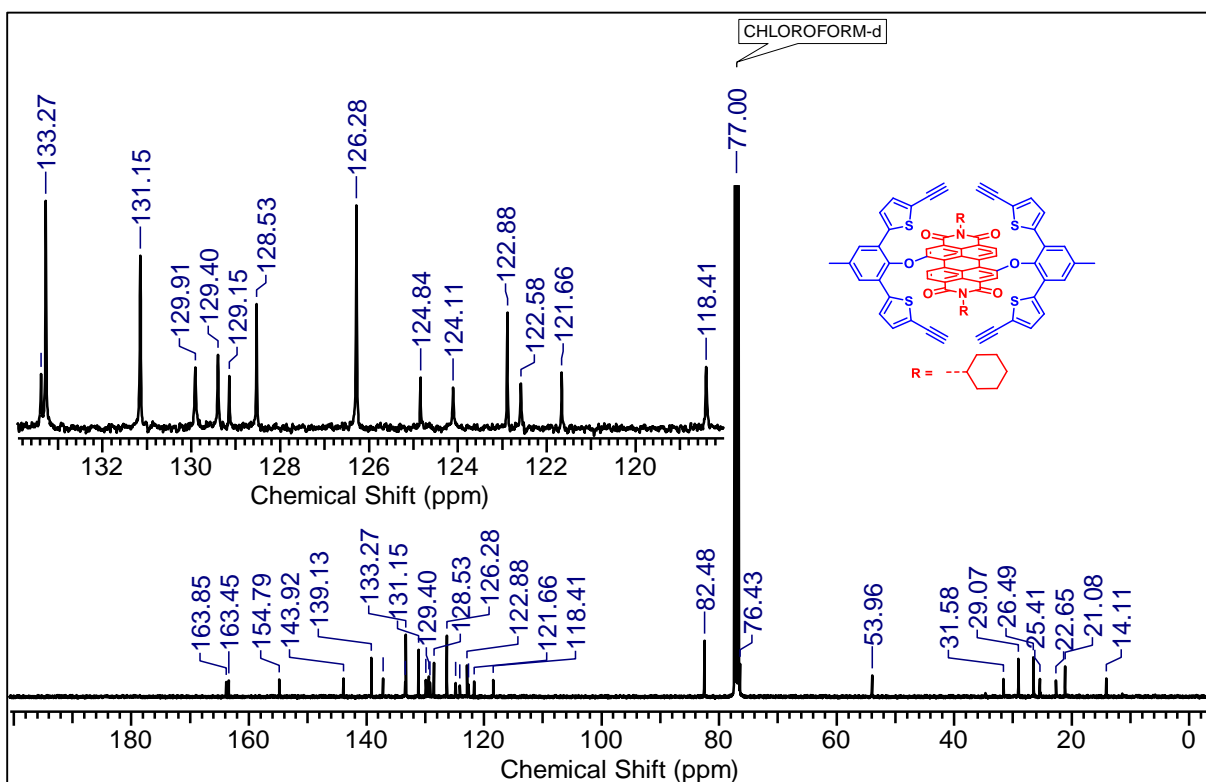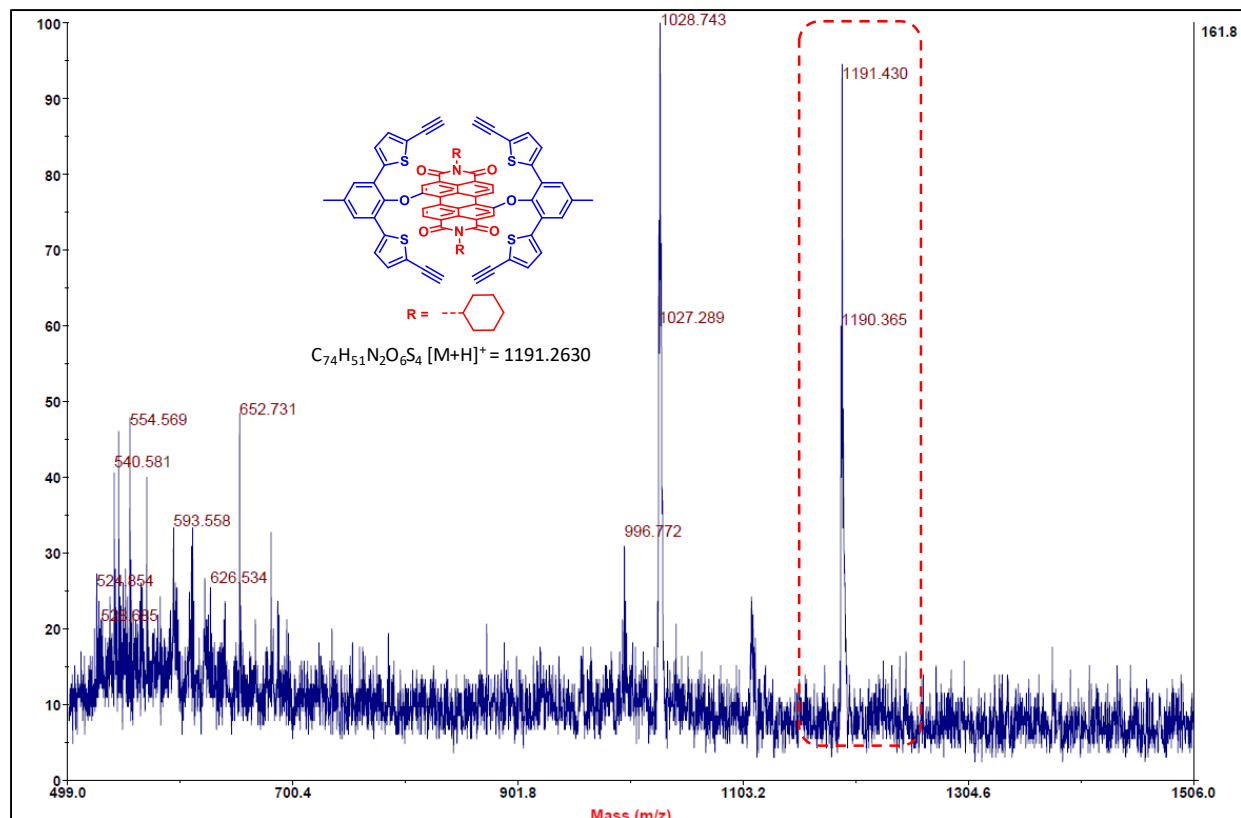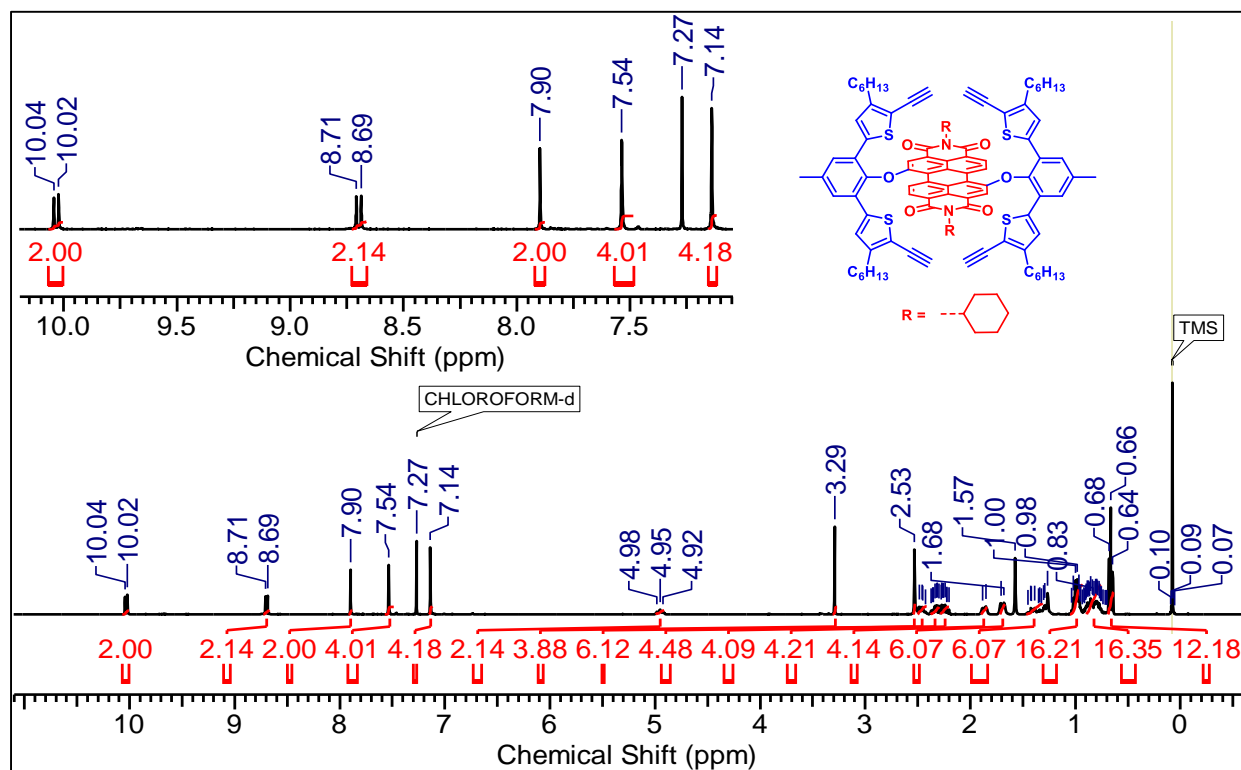**¹H NMR** (400 MHz) spectrum of **4b** in CDCl₃ at 298 K.

**13C NMR** (100 MHz) spectrum of **4b** in CDCl$_3$ at 298 K.



$C_{134}H_{179}N_2O_6S_4Si_4$ [M+H]$^+$ = 2152.1723
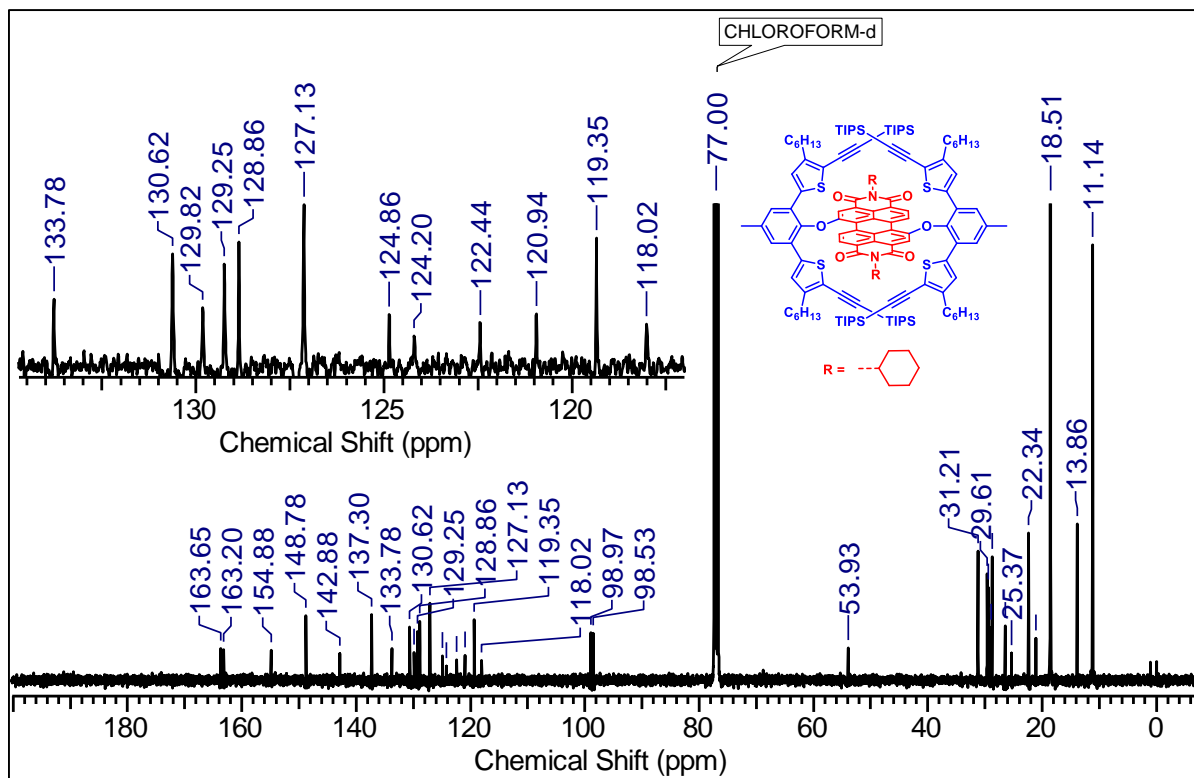
**MALDI-TOF** spectra of molecule **4b**.

**¹H NMR** (400 MHz) spectrum of **5a** in CDCl₃ at 298 K.



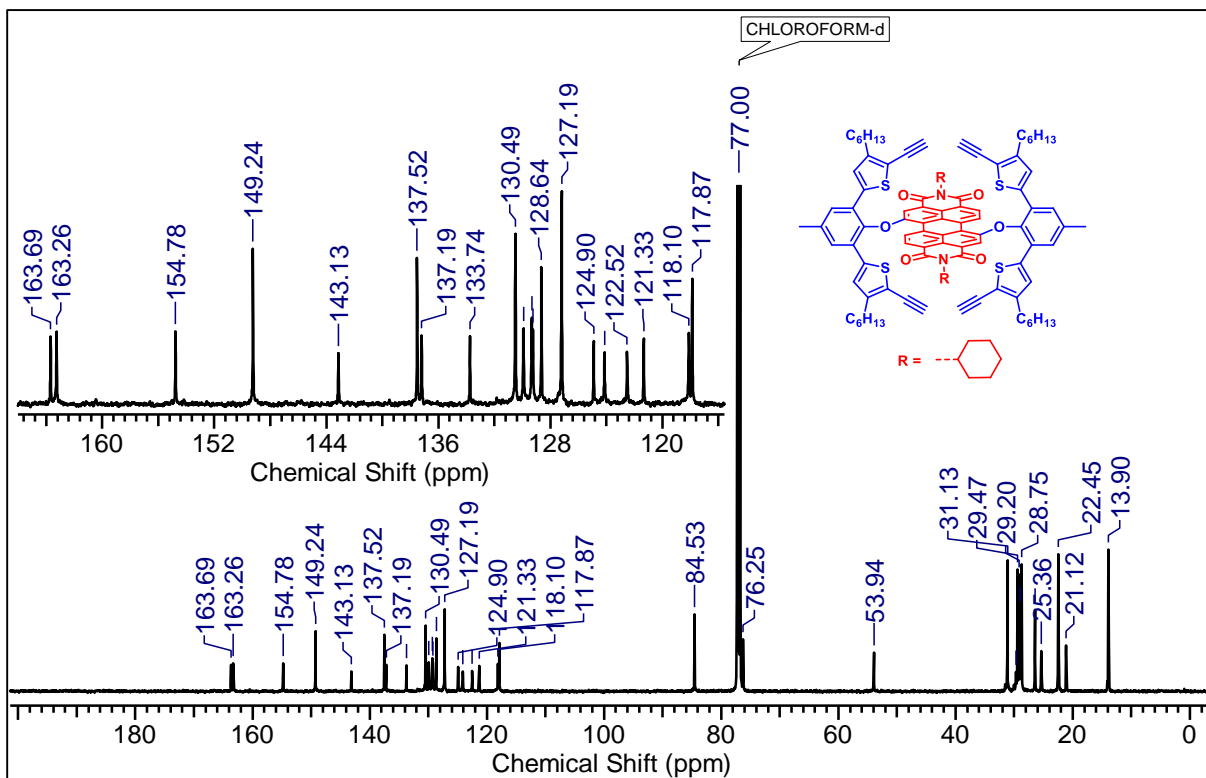**¹³C NMR** (100 MHz) spectrum of **5a** in CDCl₃ at 298 K.

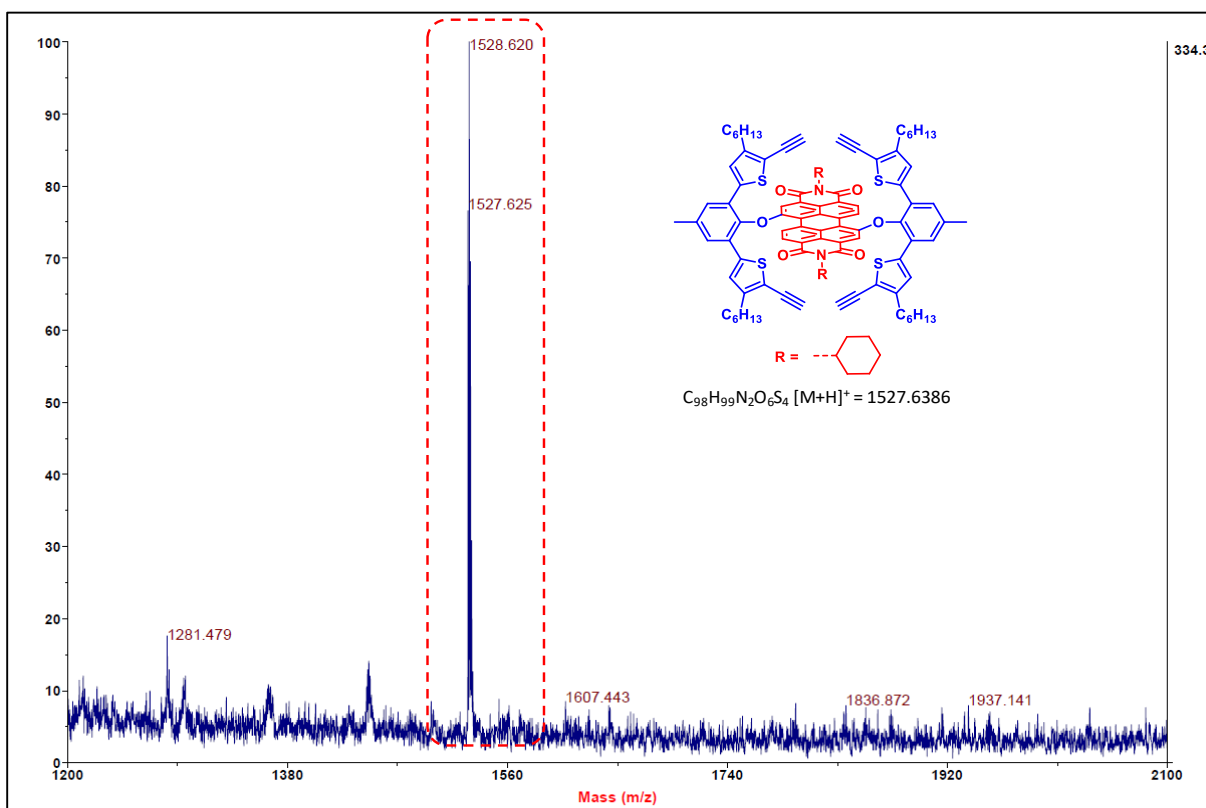**MALDI-TOF** spectra of molecule **5a**.



**¹H NMR** (400 MHz) spectrum of **5b** in CDCl₃ at 298 K.

$^{13}$C NMR (125 MHz) spectrum of 5b in CDCl$_3$ at 298 K.



MALDI-TOF spectra of molecule 5b.

**¹H NMR** (500 MHz) spectrum of **SP1** in CDCl₃ at 298 K.
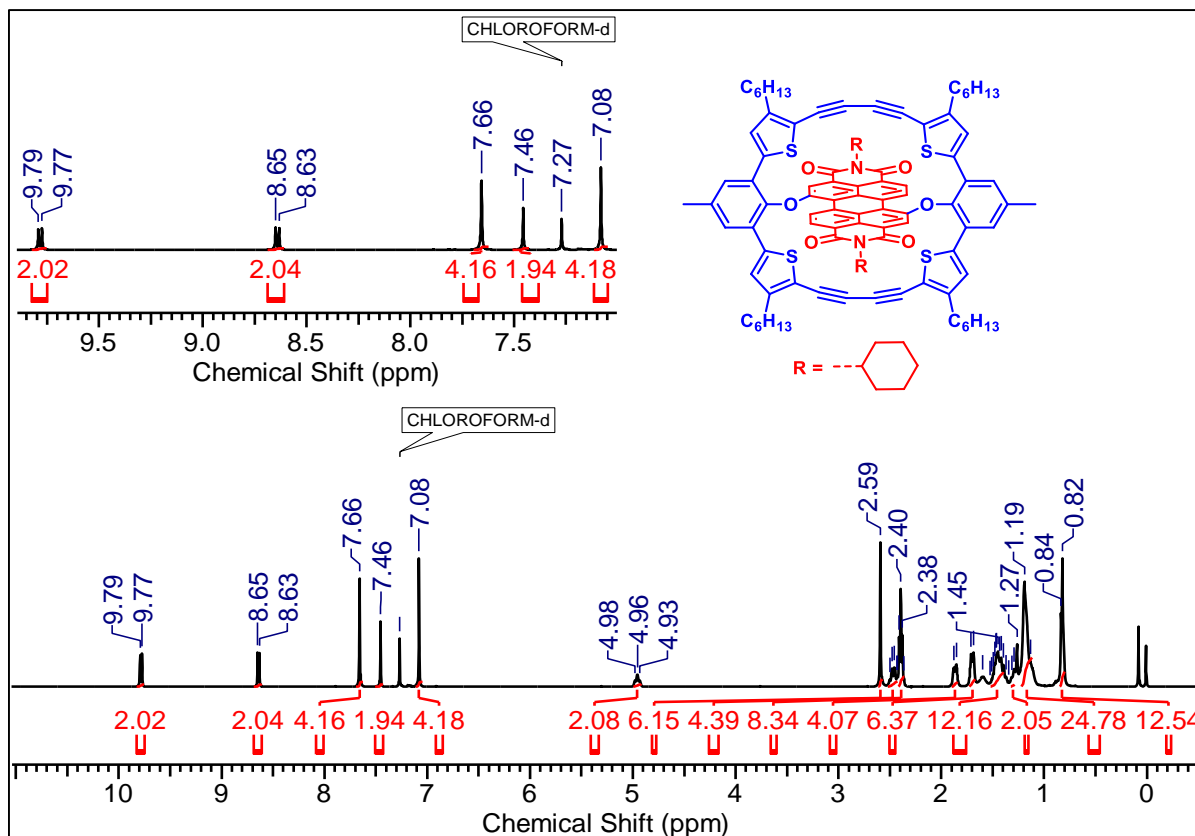


$C_{74}H_{47}N_2O_6S_4$ [M+H]⁺ = 1187.2317
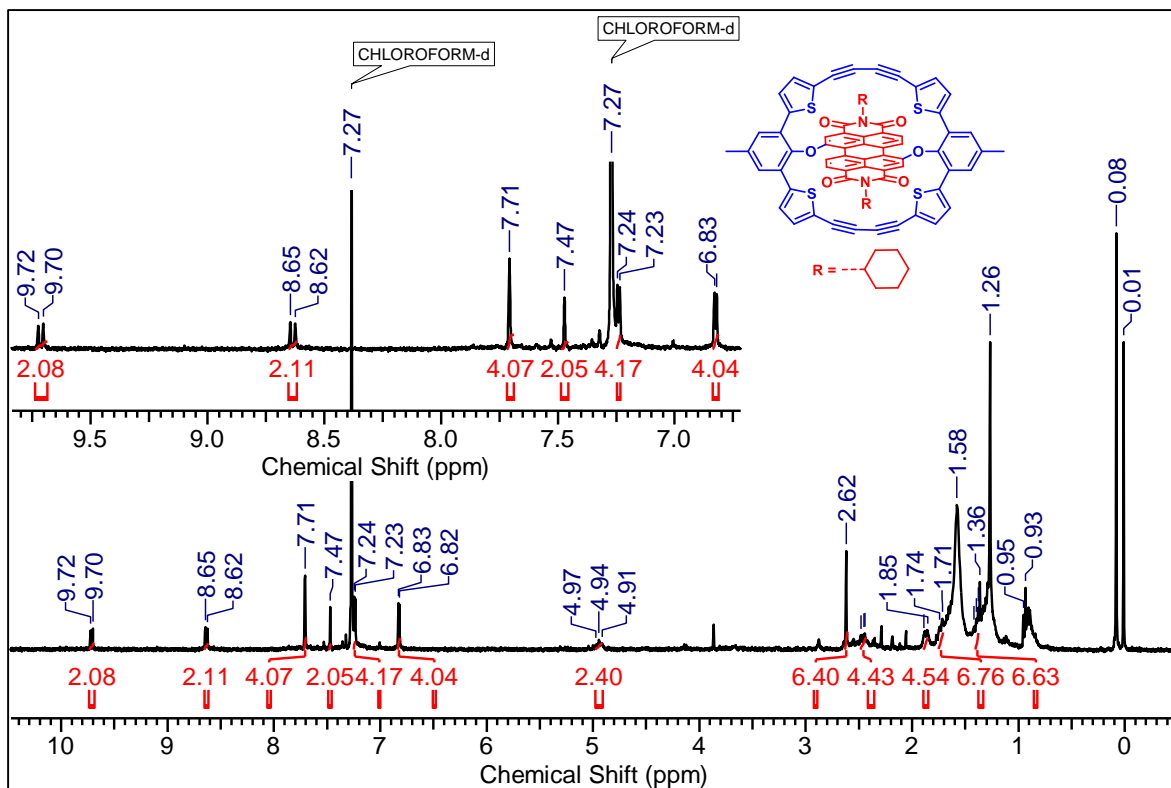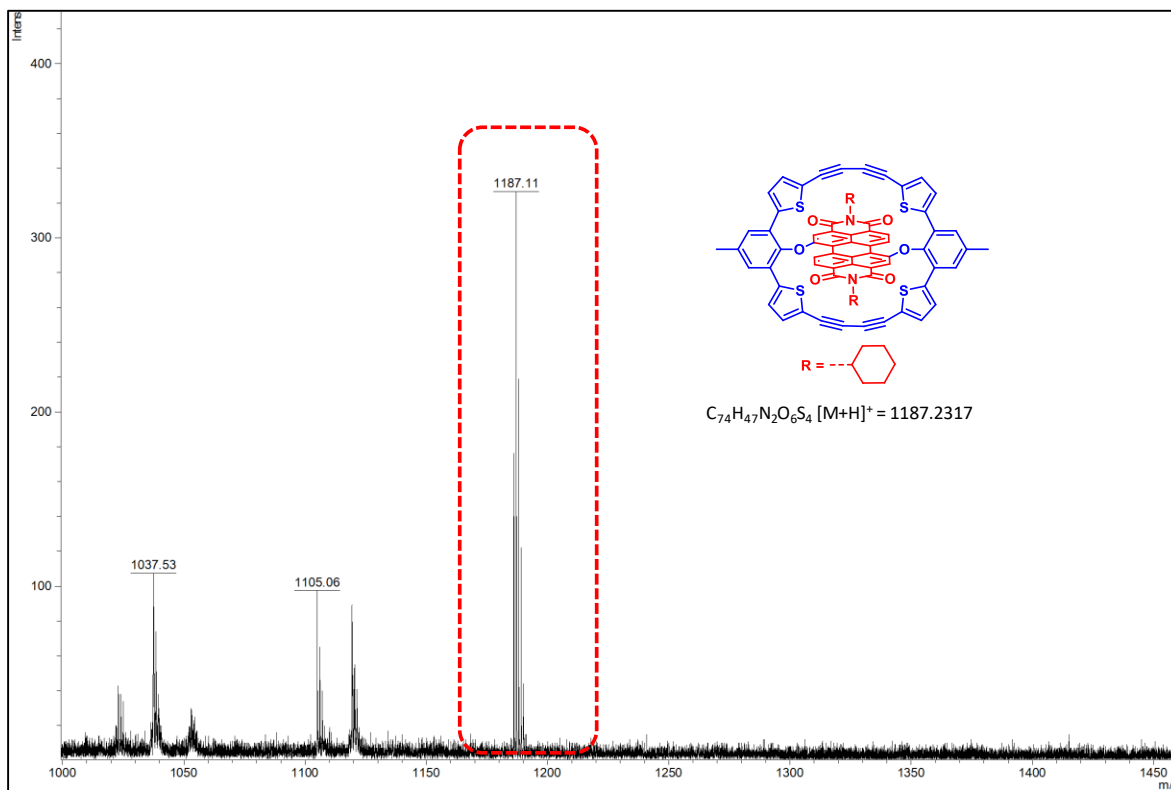
**MALDI-TOF** spectra of molecule **SP1**.

**¹H NMR** (500 MHz) spectrum of **SP2** in CDCl₃ at 298 K.



**¹³C NMR** (125 MHz) spectrum of **SP2** in CDCl₃ at 298 K.
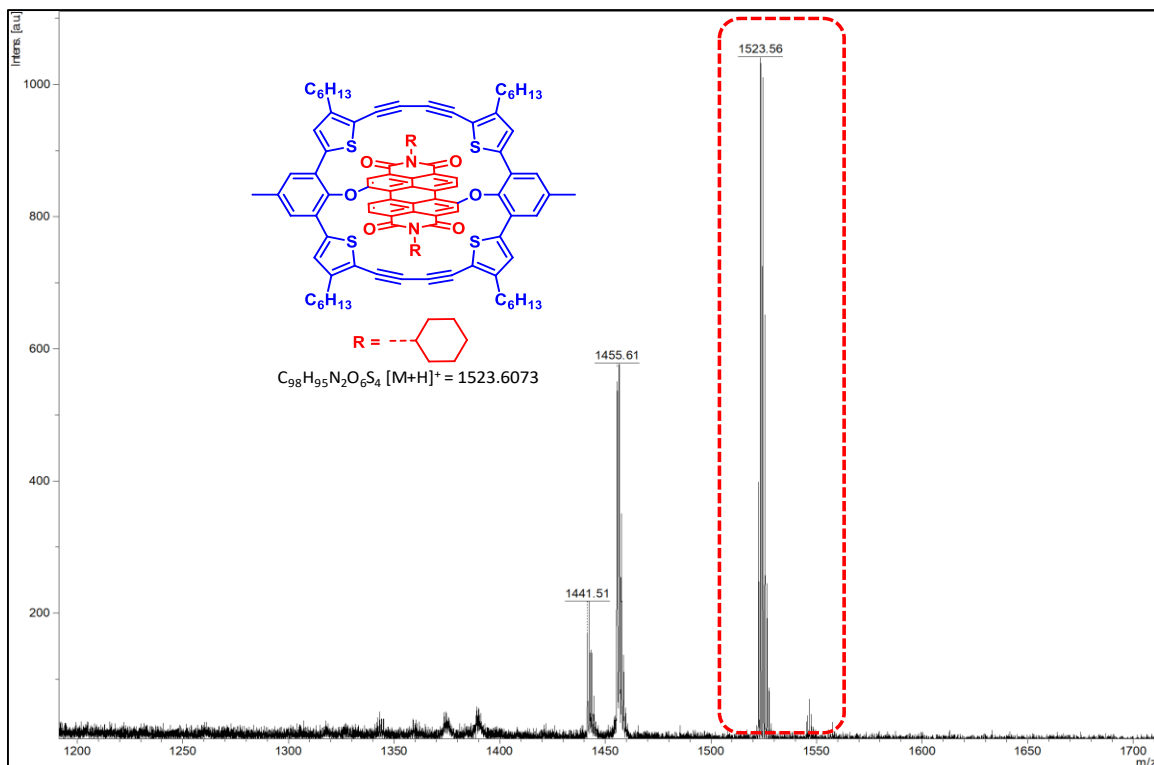
**MALDI-TOF** spectra of molecule **SP2**.



$^1$**H NMR** (400 MHz) spectrum of **SP2D** in CDCl$_3$ at 298 K.

**13C NMR** (125 MHz) spectrum of **SP2D** in CDCl$_3$ at 298 K.



$C_{196}H_{189}N_4O_{12}S_8$ [M+H]$^+$ = 3046.2067,
$C_{196}H_{188}N_4O_{12}S_8$ [M+Na]$^+$ = 3068.1887
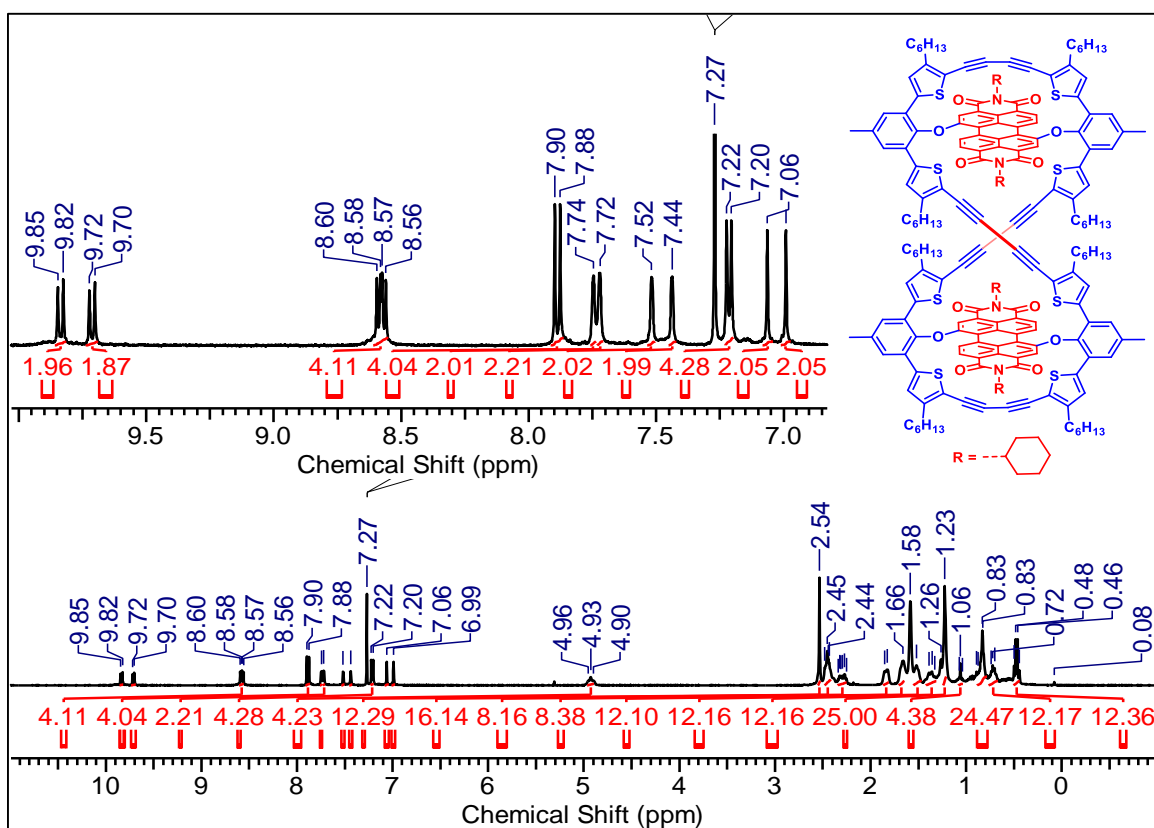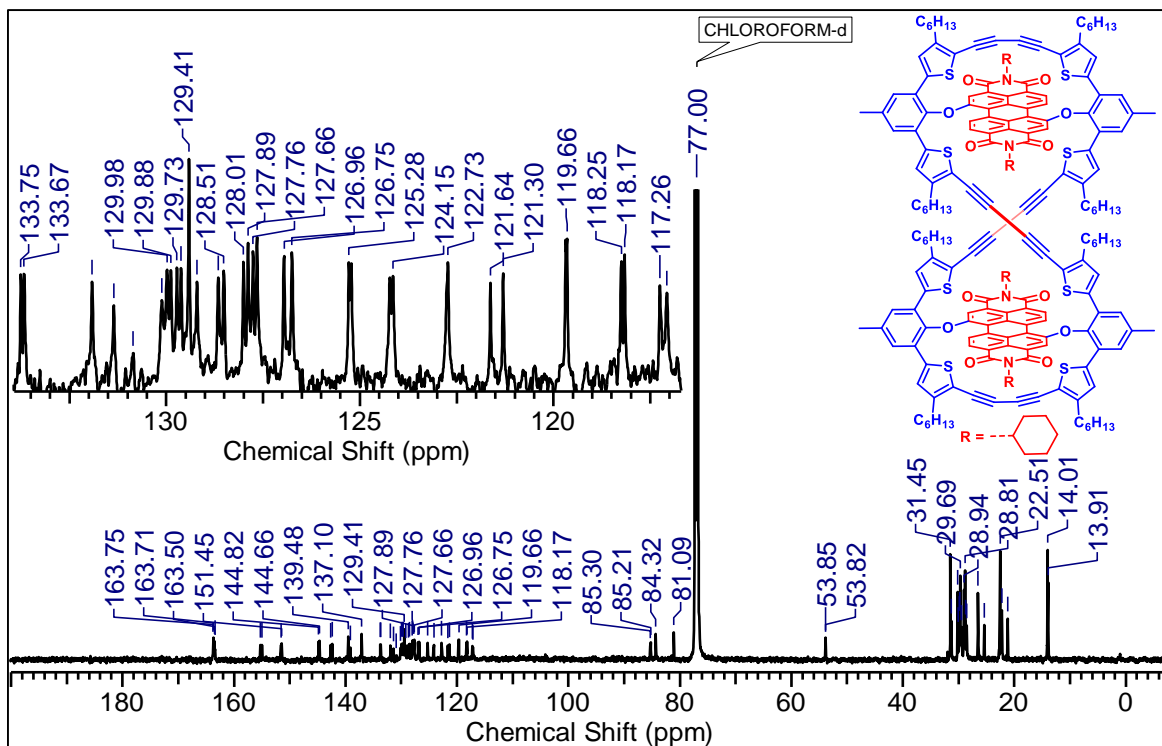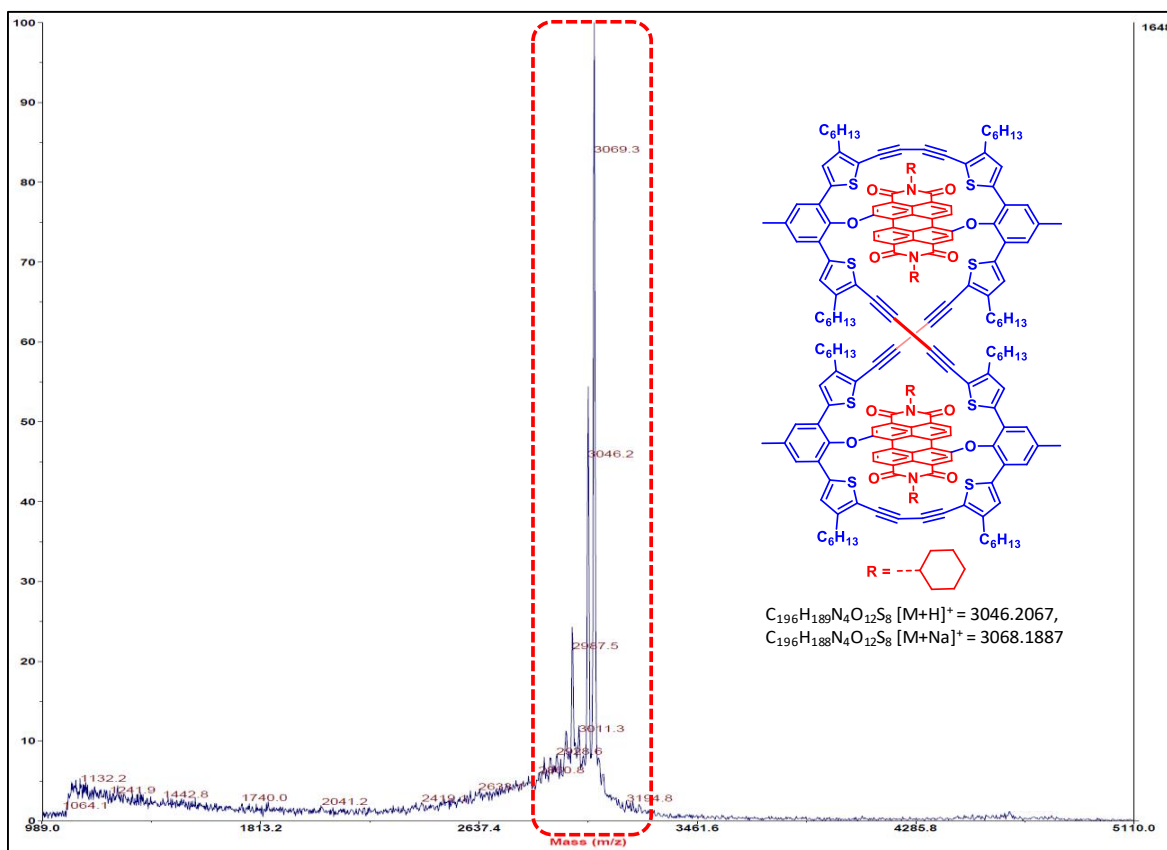
**MALDI-TOF** MS spectra of molecule **SP2D**.
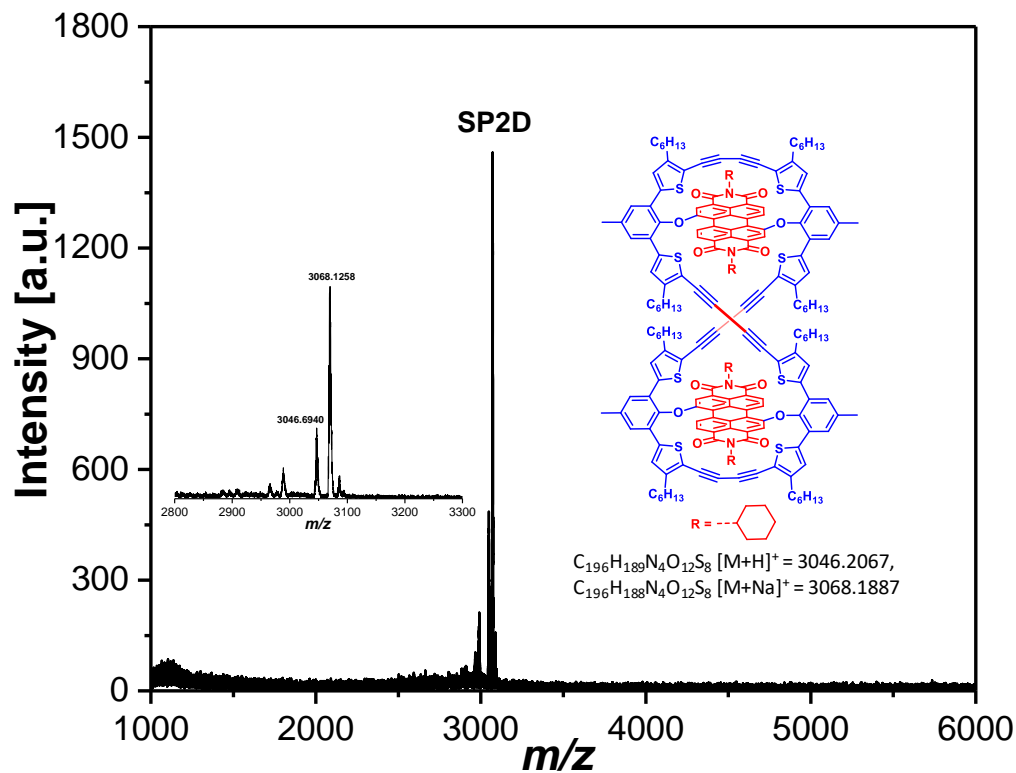
**MALDI-TOF** MS spectra of molecule **SP2D**.
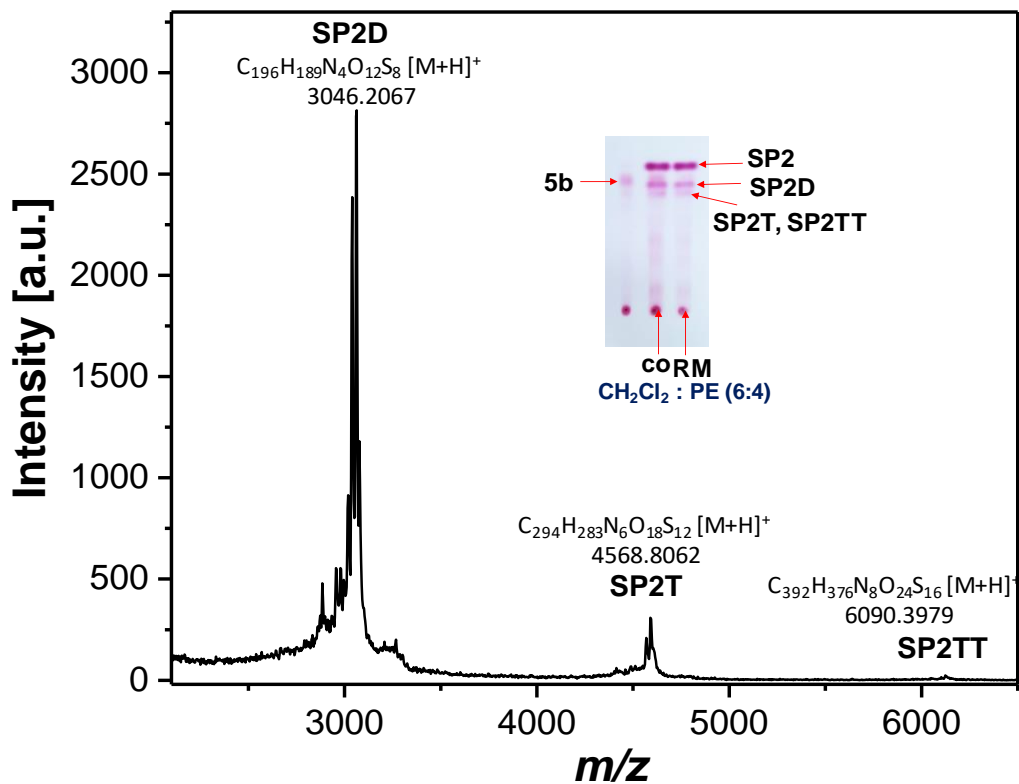


**MALDI-TOF** MS spectra of molecule **SP2D**.
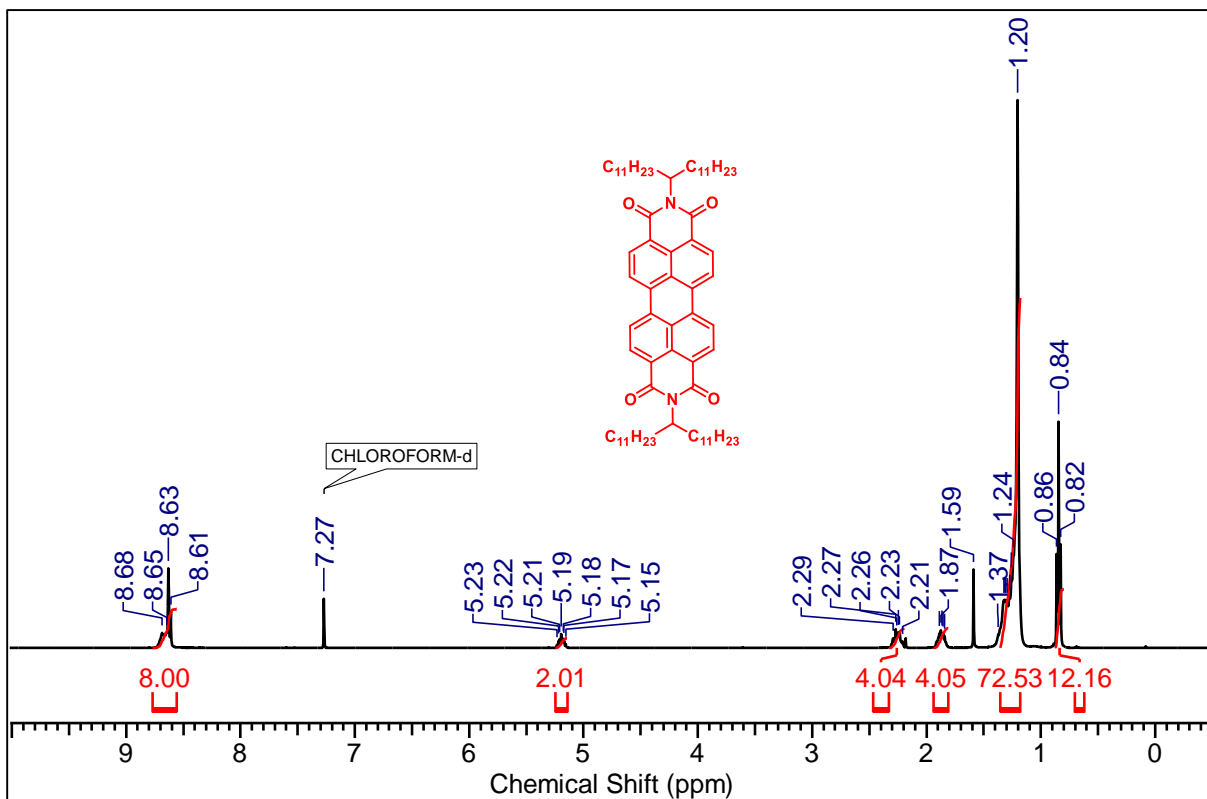
**¹H NMR** (500 MHz) spectrum of **Trico-PBI** in CDCl₃ at 298 K.
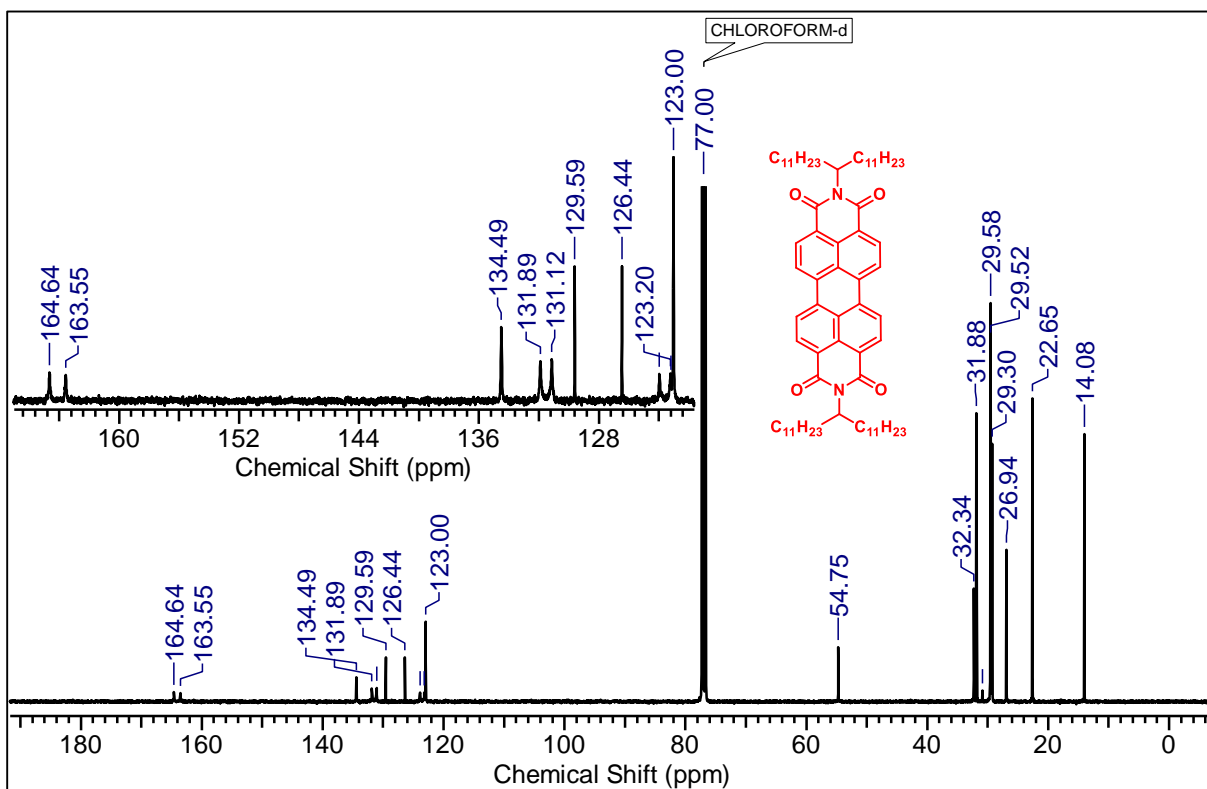


**¹³C NMR** (125 MHz) spectrum of **Trico-PBI** in CDCl₃ at 298 K.
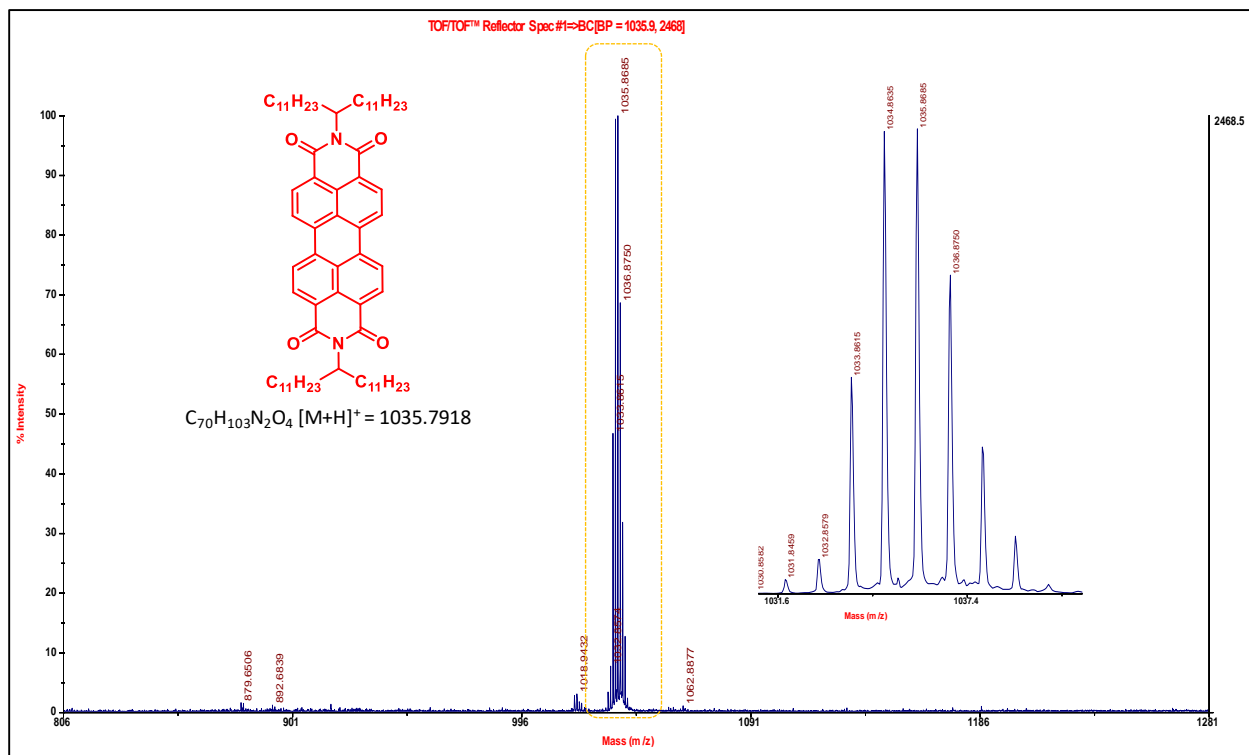
**MALDI-TOF** MS spectra of molecule **Trico-PBI**.
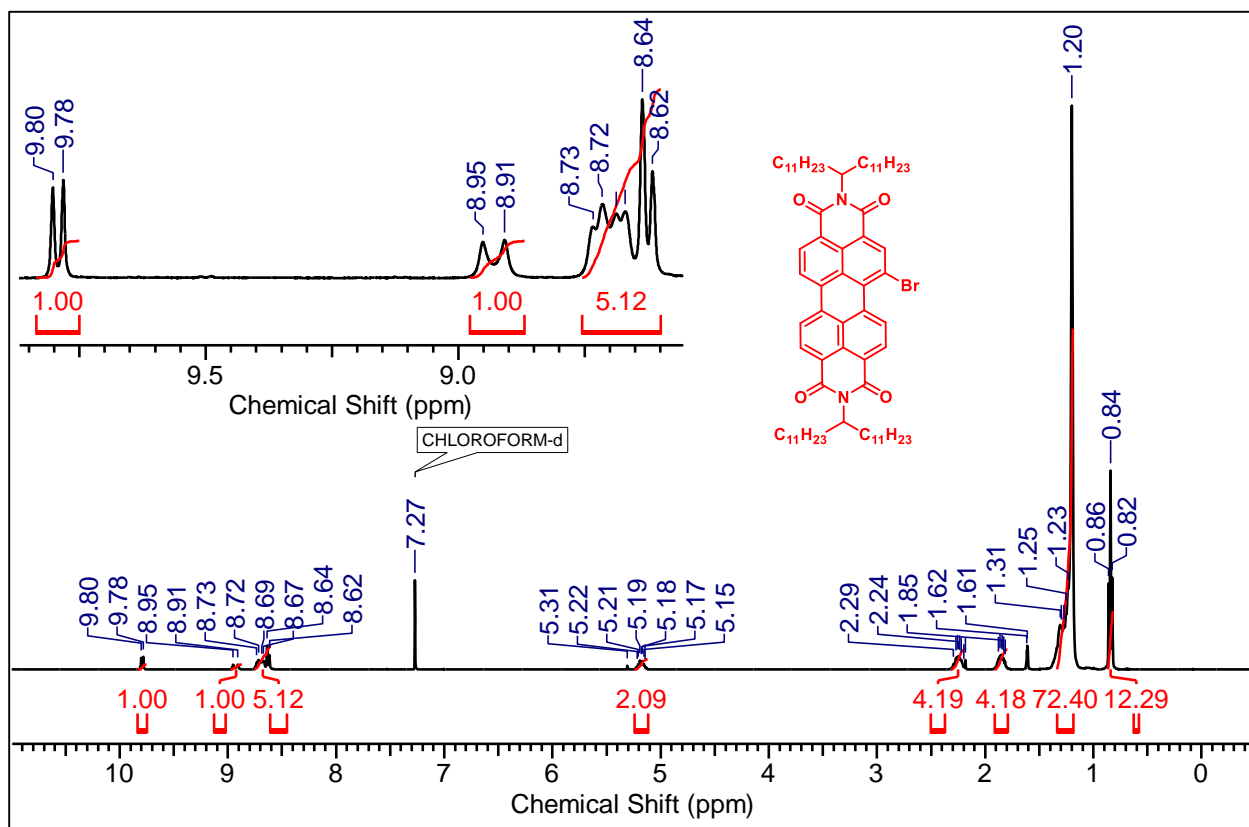


**1H NMR** (500 MHz) spectrum of **1a** in CDCl$_3$ at 298 K.
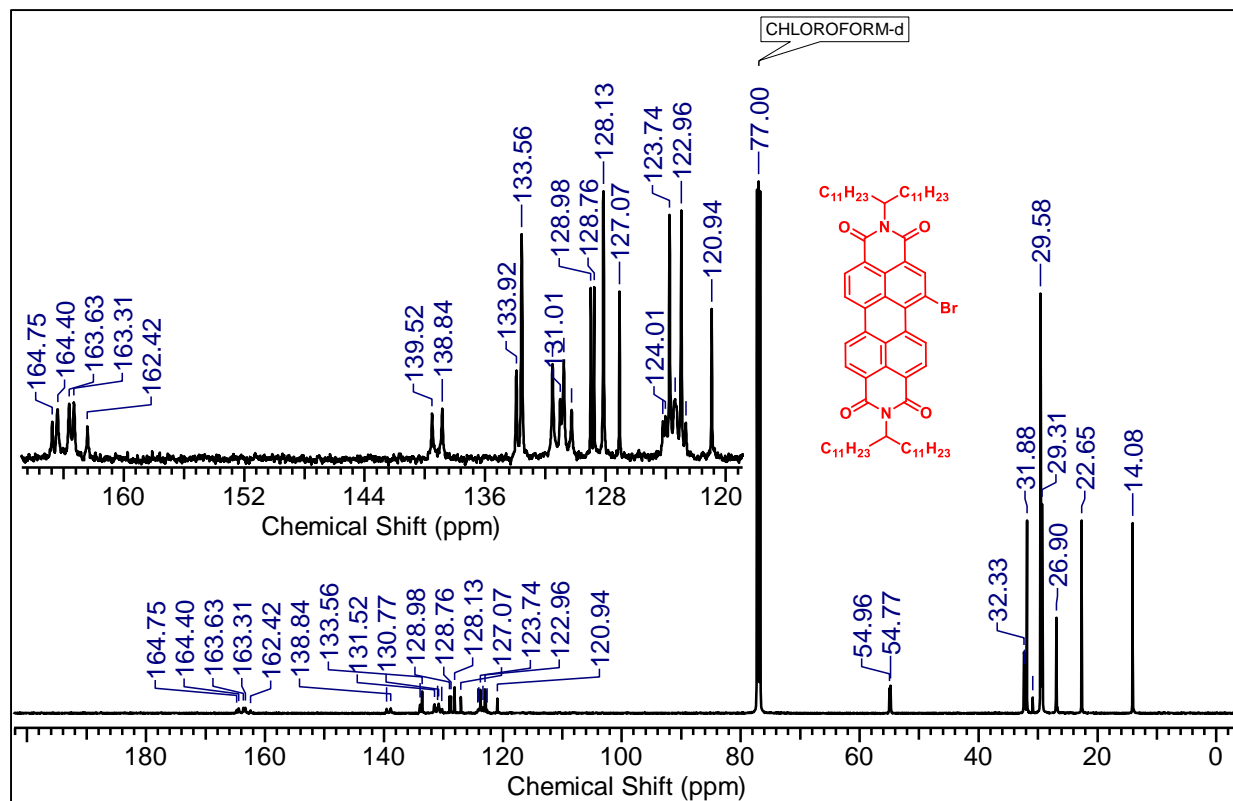
**¹³C NMR** (125 MHz) spectrum of **1a** in CDCl₃ at 298 K.
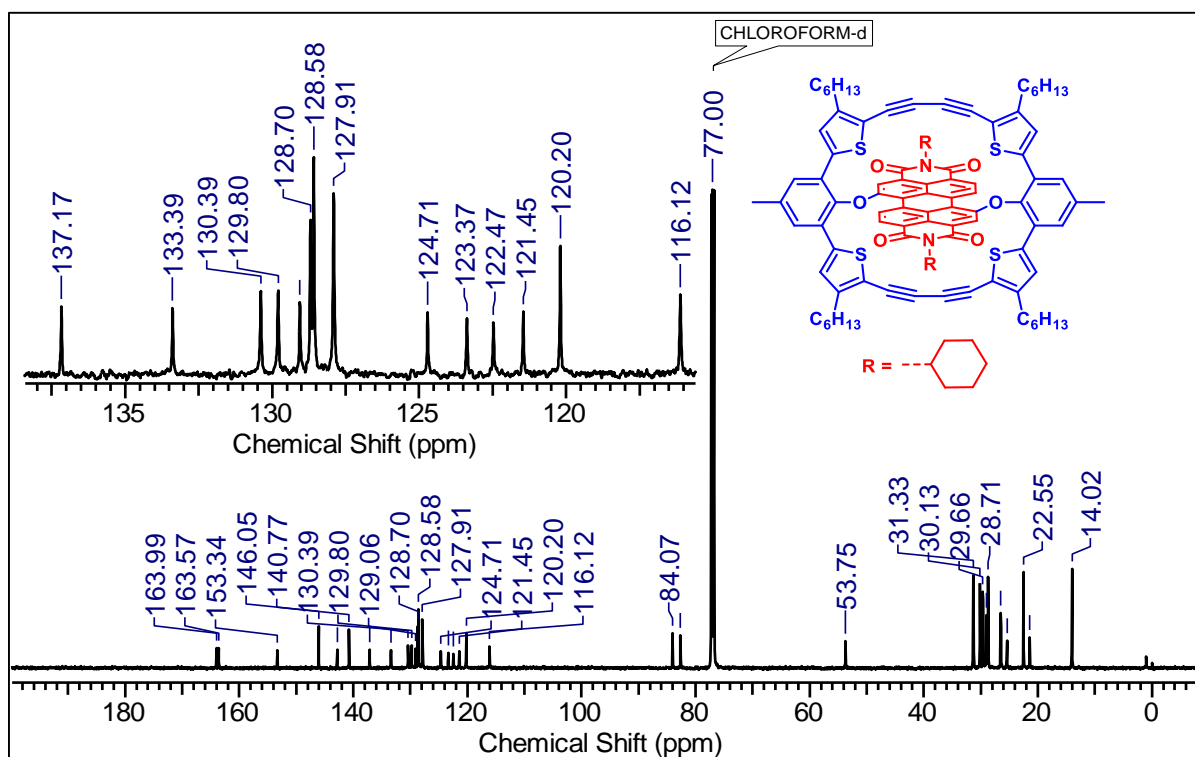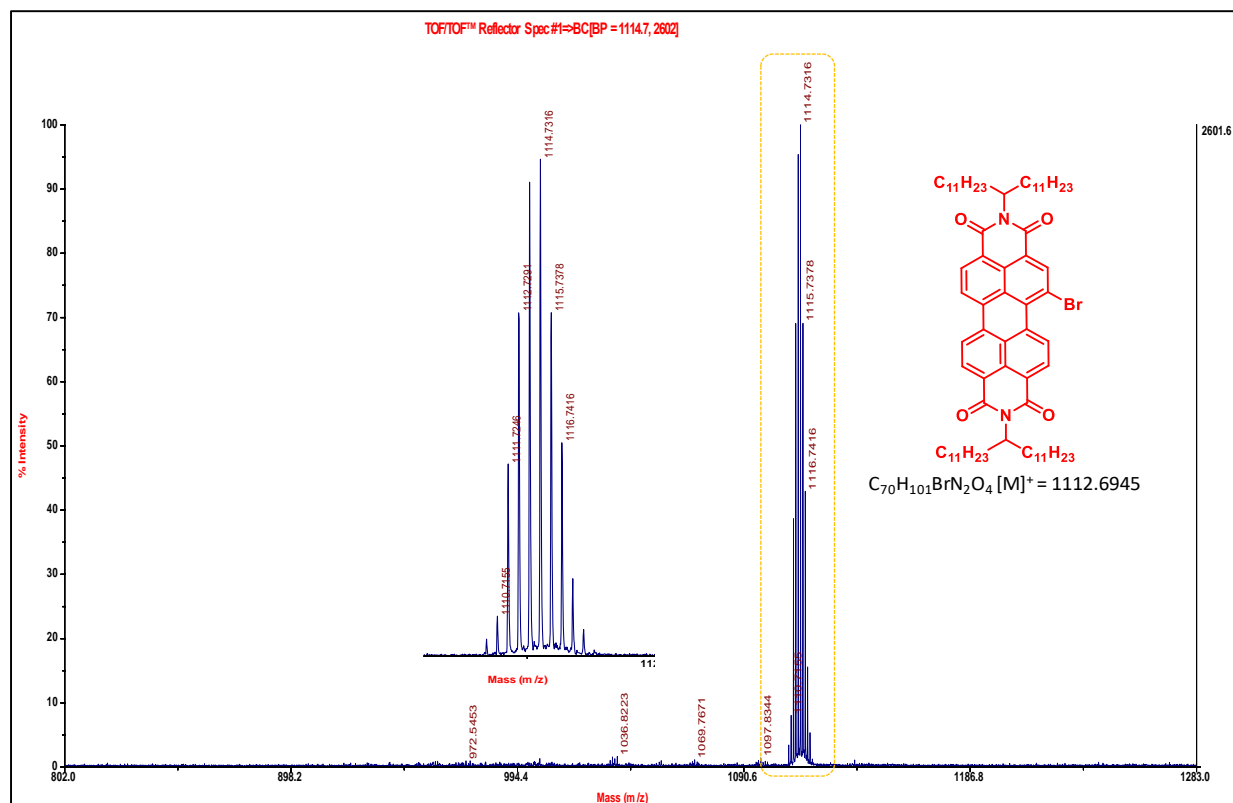


**MALDI-TOF** MS spectra of molecule **1a**.
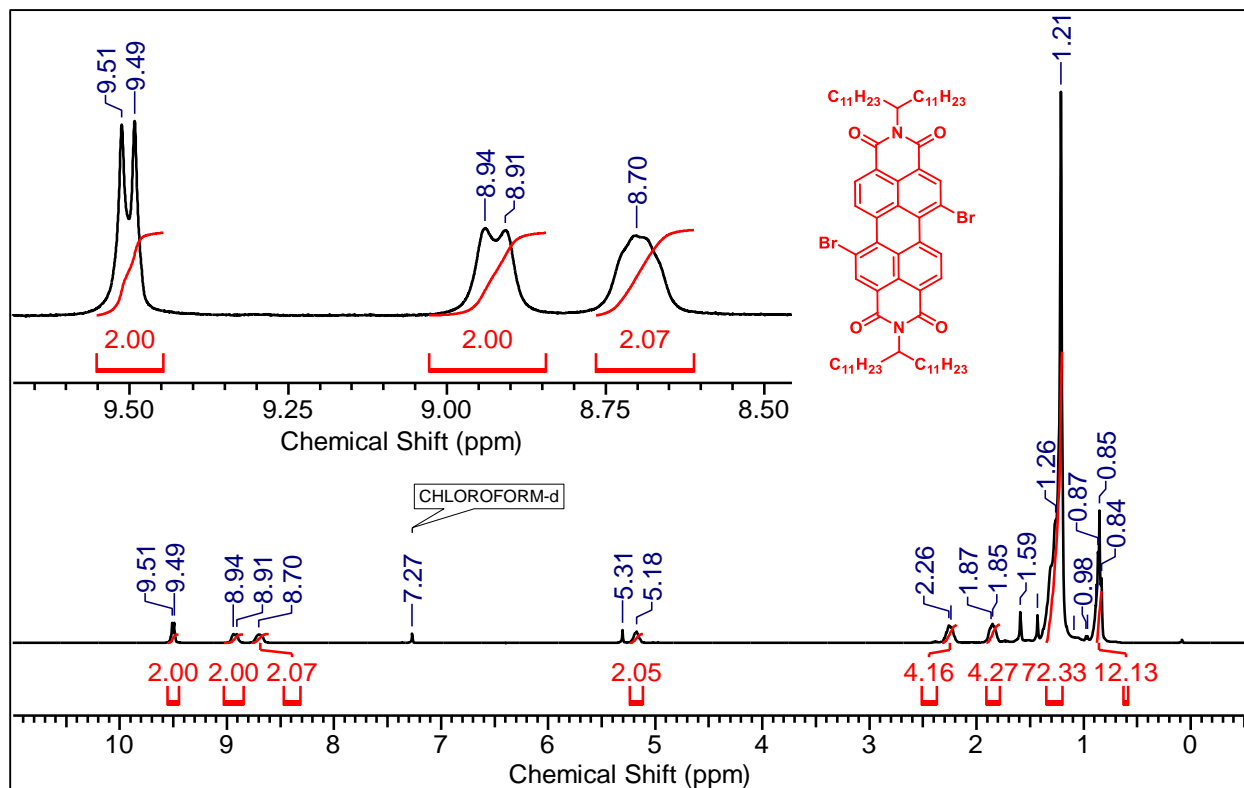
**¹H NMR** (500 MHz) spectrum of **1b** in CDCl₃ at 298 K.
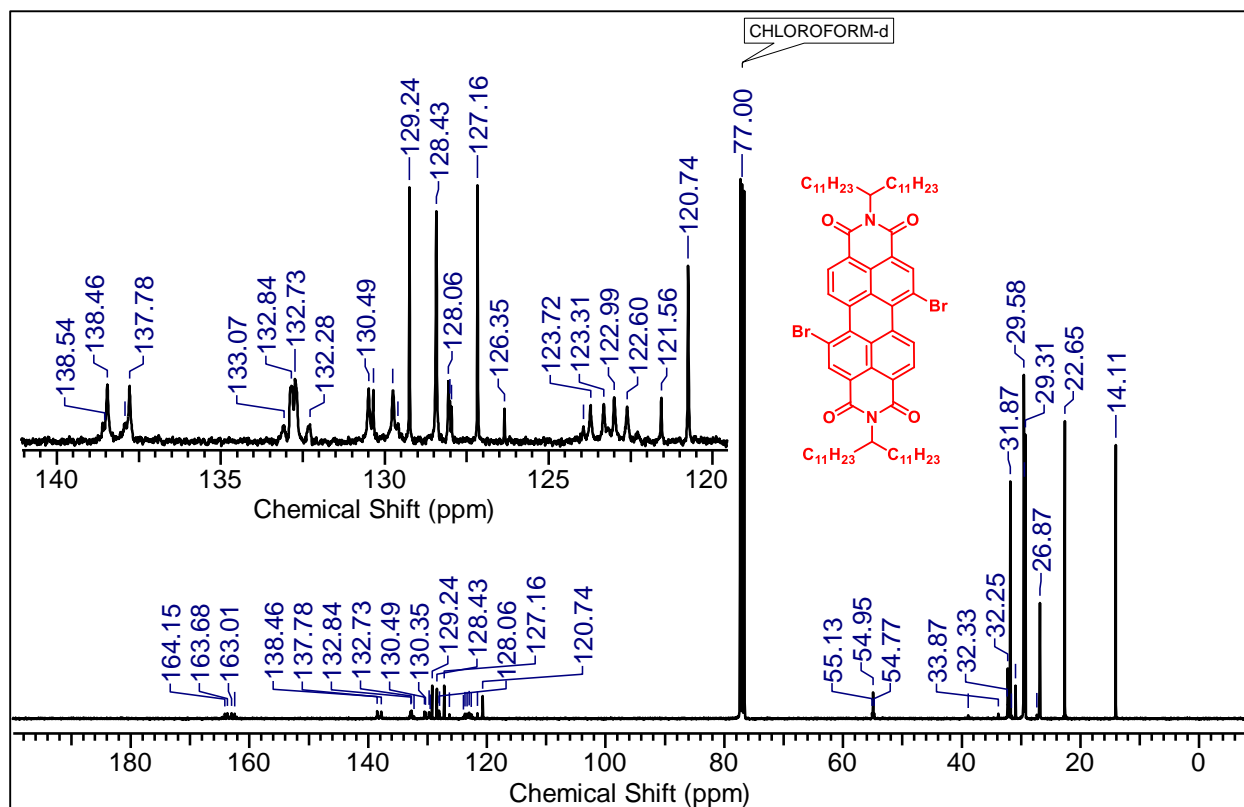


**¹³C NMR** (125 MHz) spectrum of **1b** in CDCl₃ at 298 K.
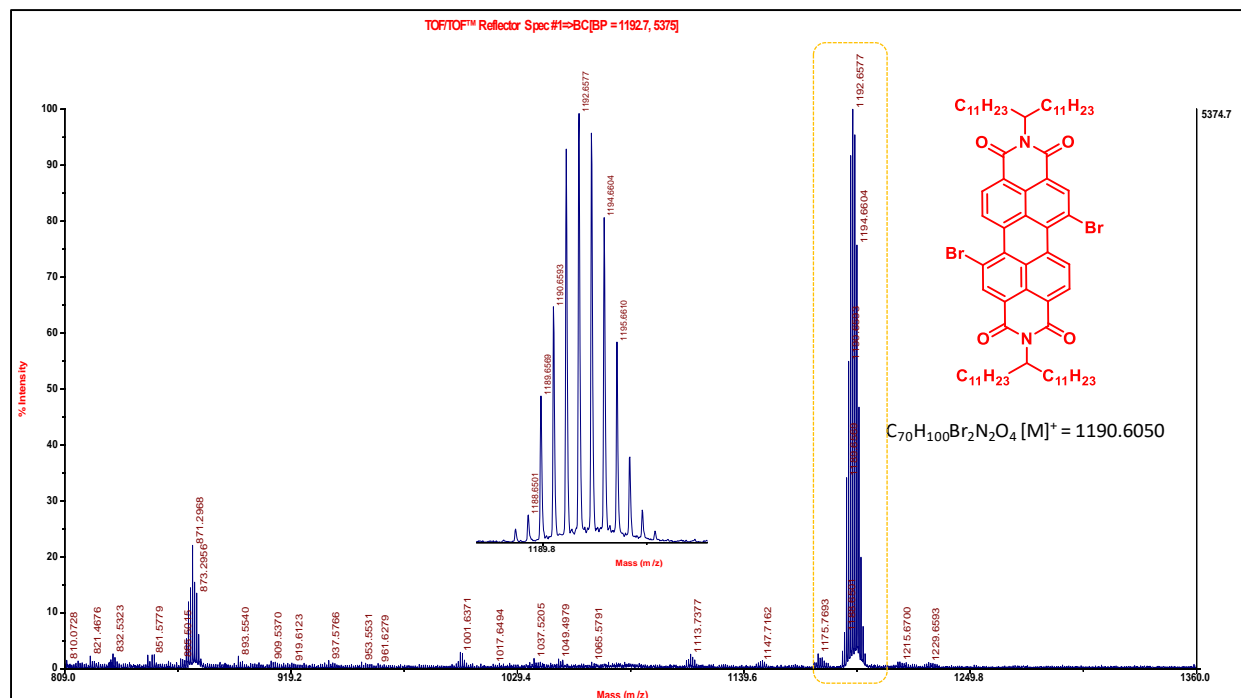
**MALDI-TOF** MS spectra of molecule **1b**.
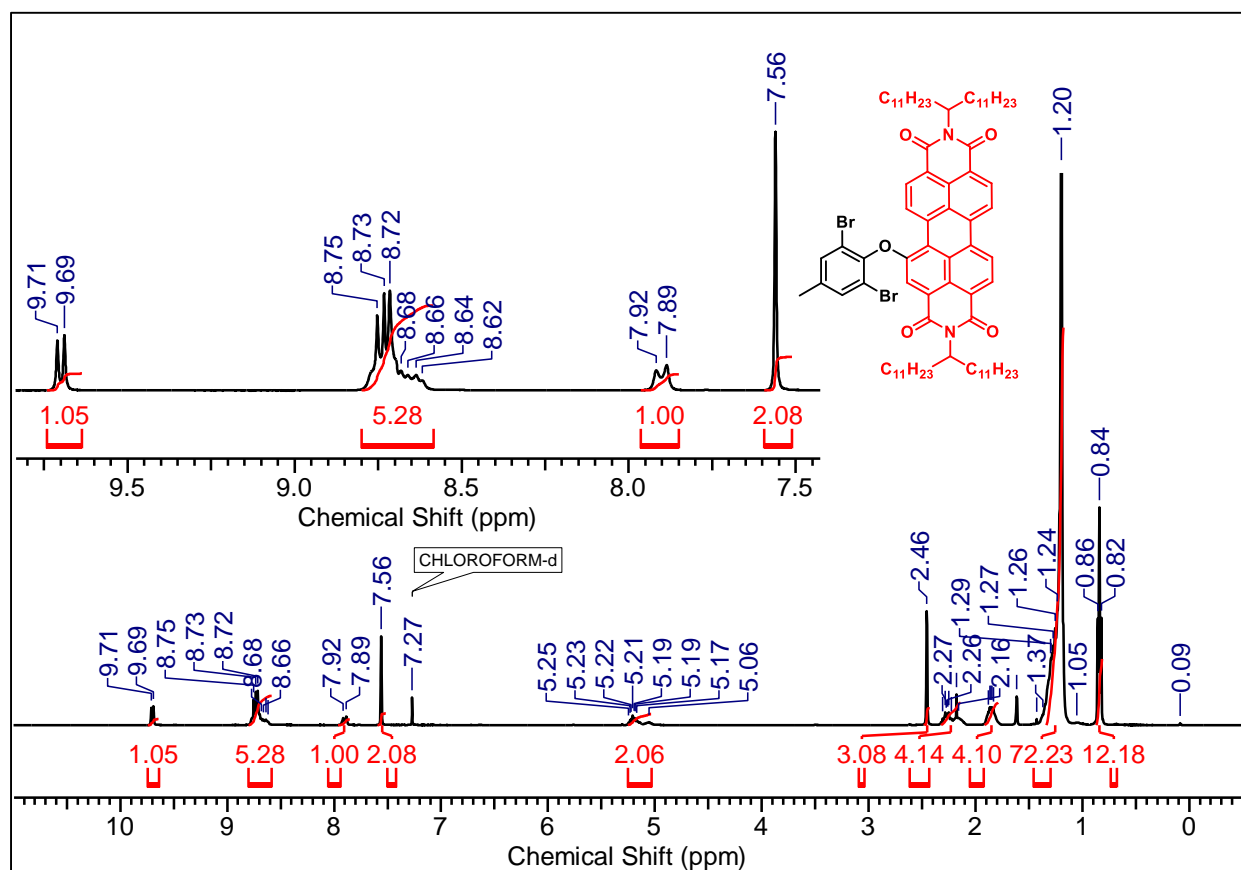


**$^1$H NMR** (500 MHz) spectrum of **2a** in CDCl$_3$ at 298 K.

**13C NMR** (125 MHz) spectrum of **2a** in CDCl₃ at 298 K.



$C_{77}H_{107}Br_2N_2O_5 \ [M+H]^+ = 1297.6547$
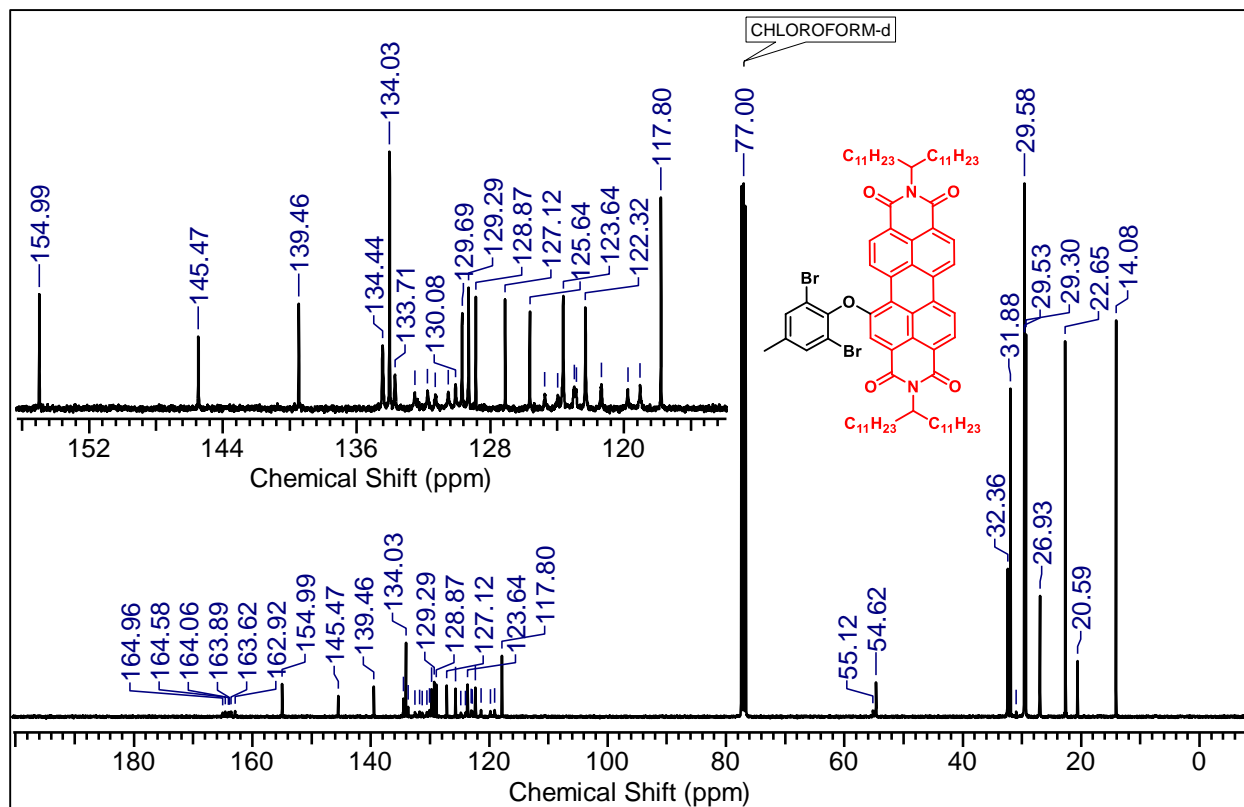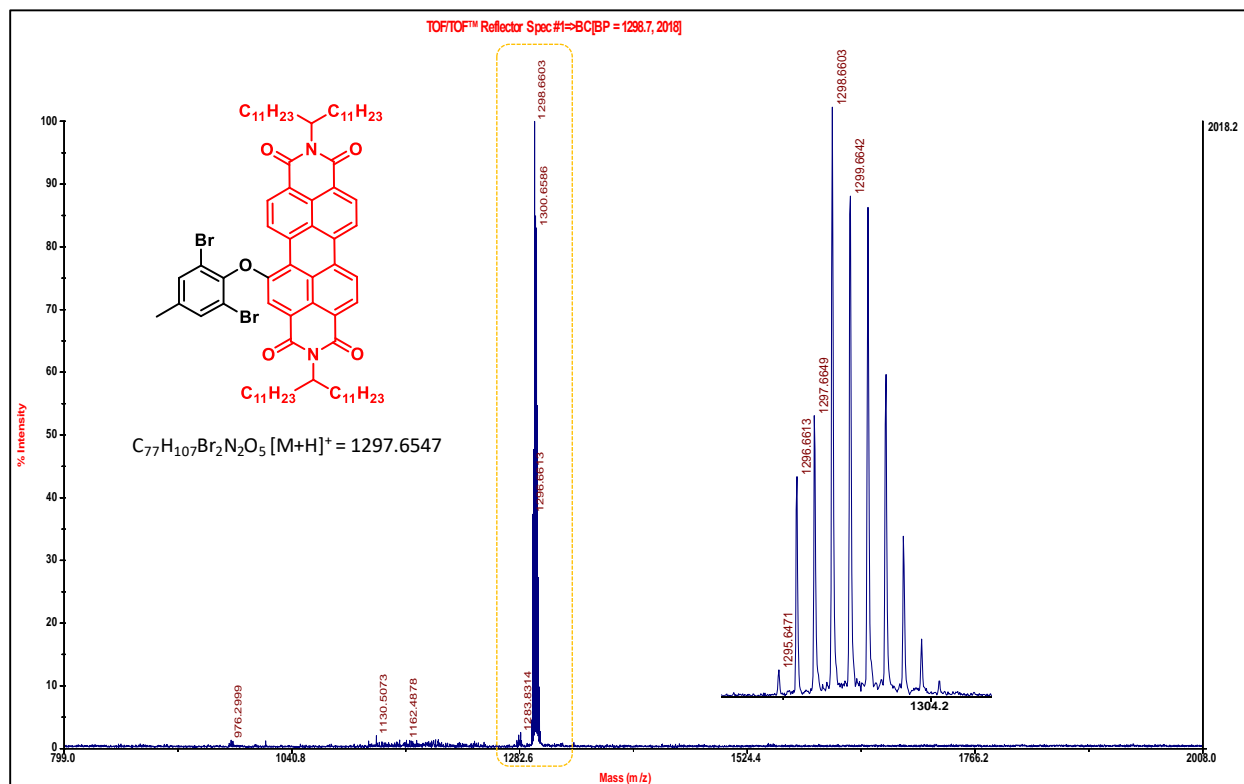
**MALDI-TOF** MS spectra of molecule **2a**.

**¹H NMR** (500 MHz) spectrum of **2b** in CDCl$_3$ at 298 K.



**¹³C NMR** (125 MHz) spectrum of **2b** in CDCl$_3$ at 298 K.

**MALDI-TOF** MS spectra of molecule **2b**.

$C_{82}H_{109}Br_2N_2O_6 [M+H]^+ = 1375.6652$



**¹H NMR** (500 MHz) spectrum of **3a** in CDCl₃ at 298 K.

**13C NMR** (125 MHz) spectrum of **3a** in CDCl3 at 298 K.



**1H NMR** (500 MHz) spectrum of **3b** in CDCl3 at 298 K.

**$^{13}$C NMR** (125 MHz) spectrum of **3b** in CDCl$_3$ at 298 K.



$C_{122}H_{166}N_2O_6S_4$ [M]$^+$ = 1883.1629
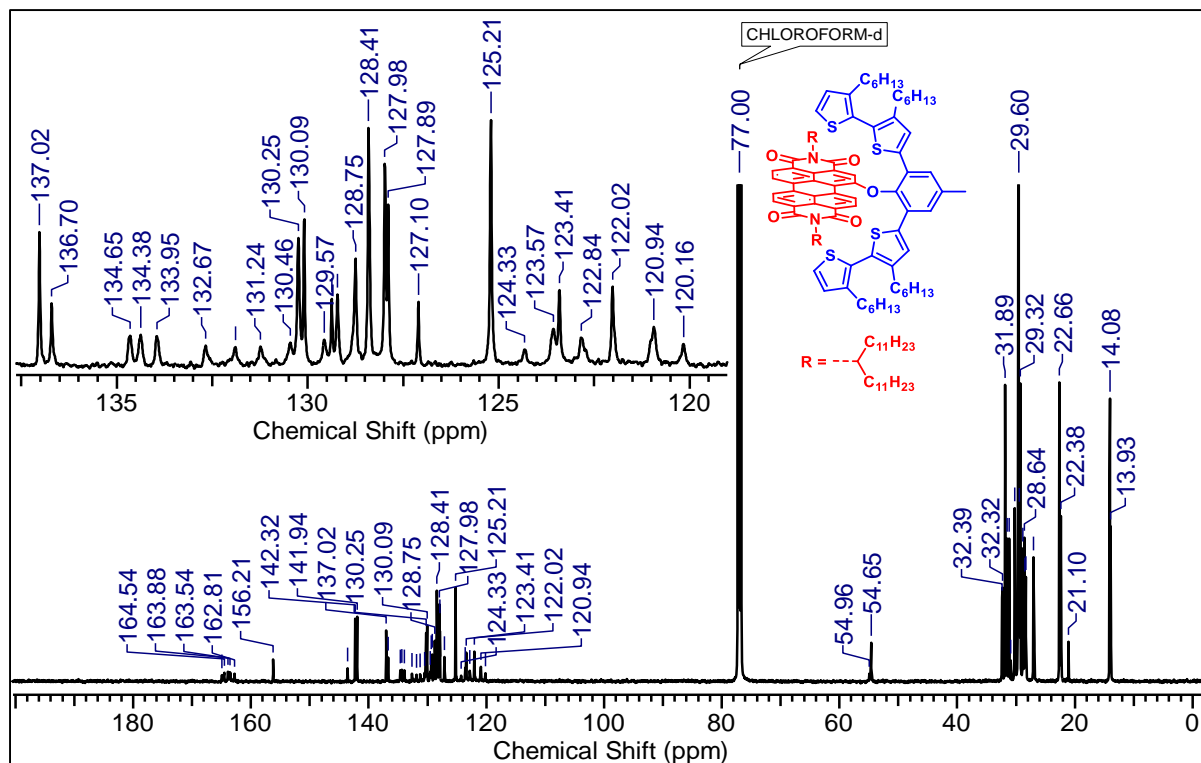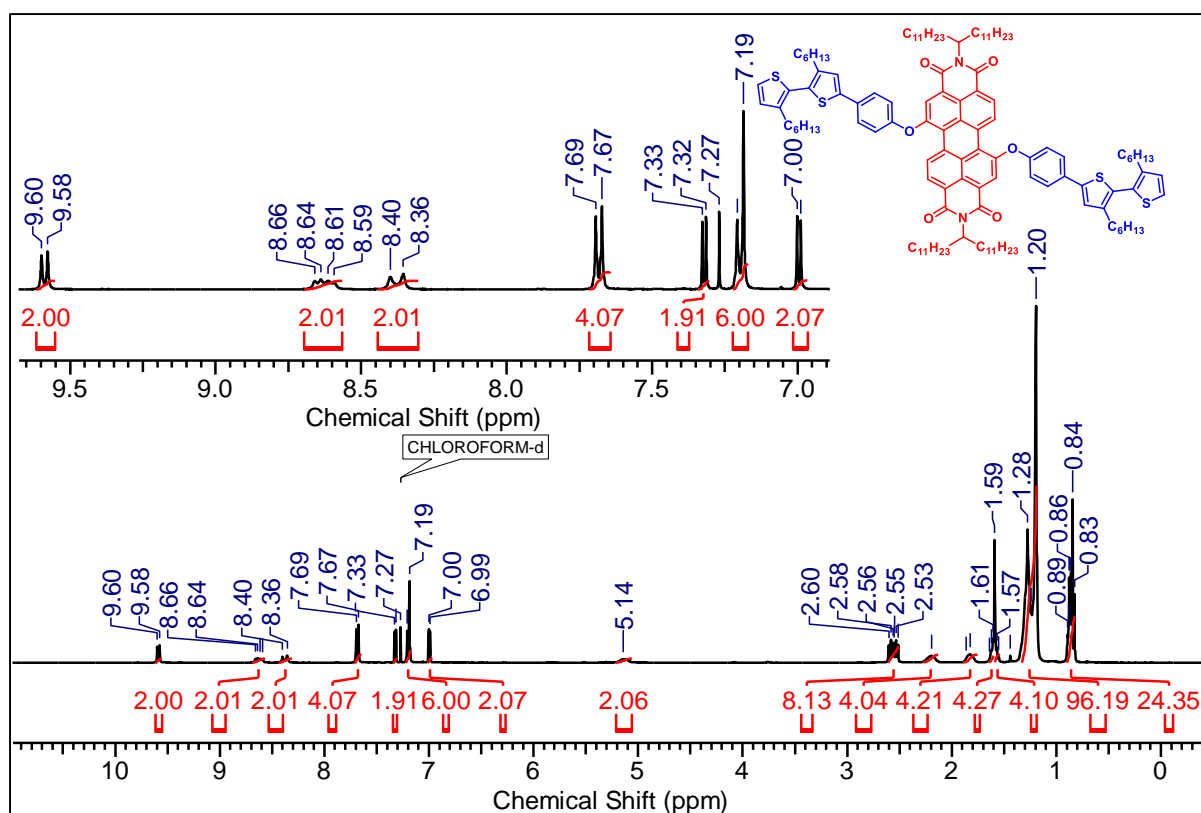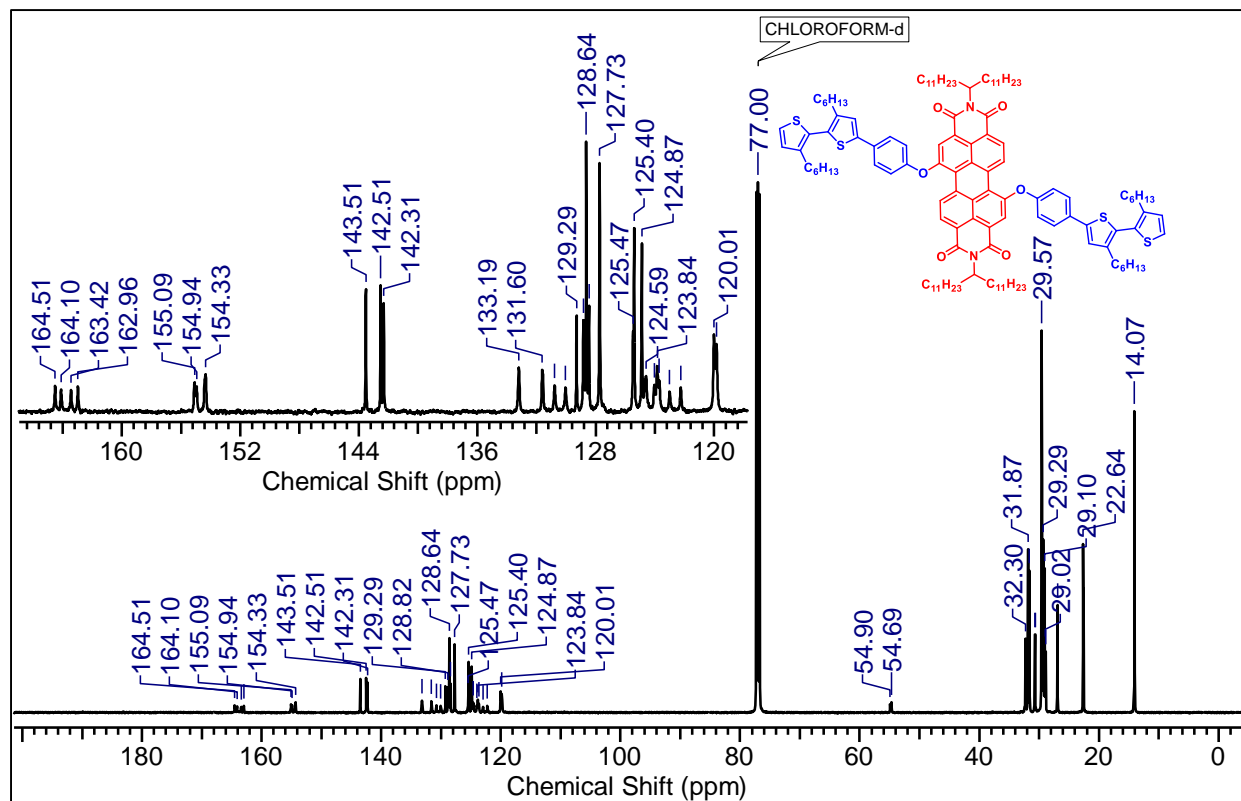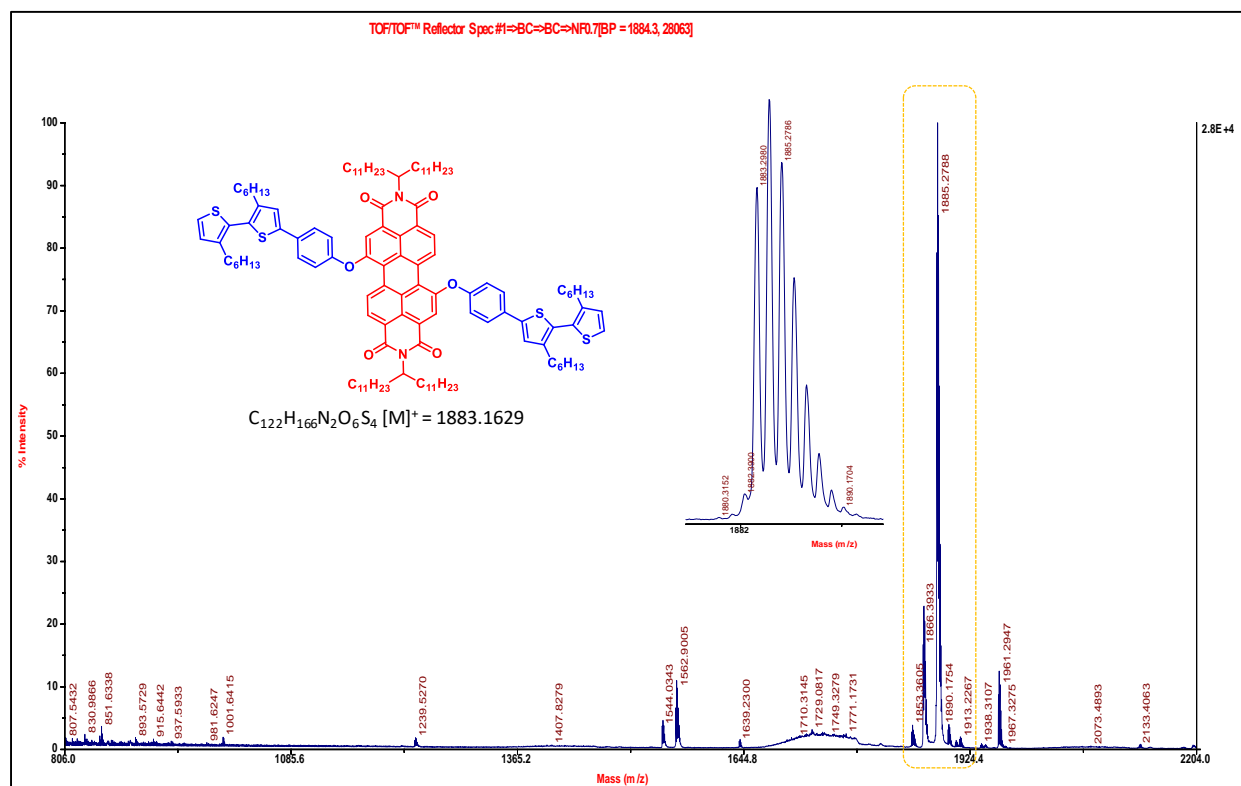
**MALDI-TOF** MS spectra of molecule 3**b**.
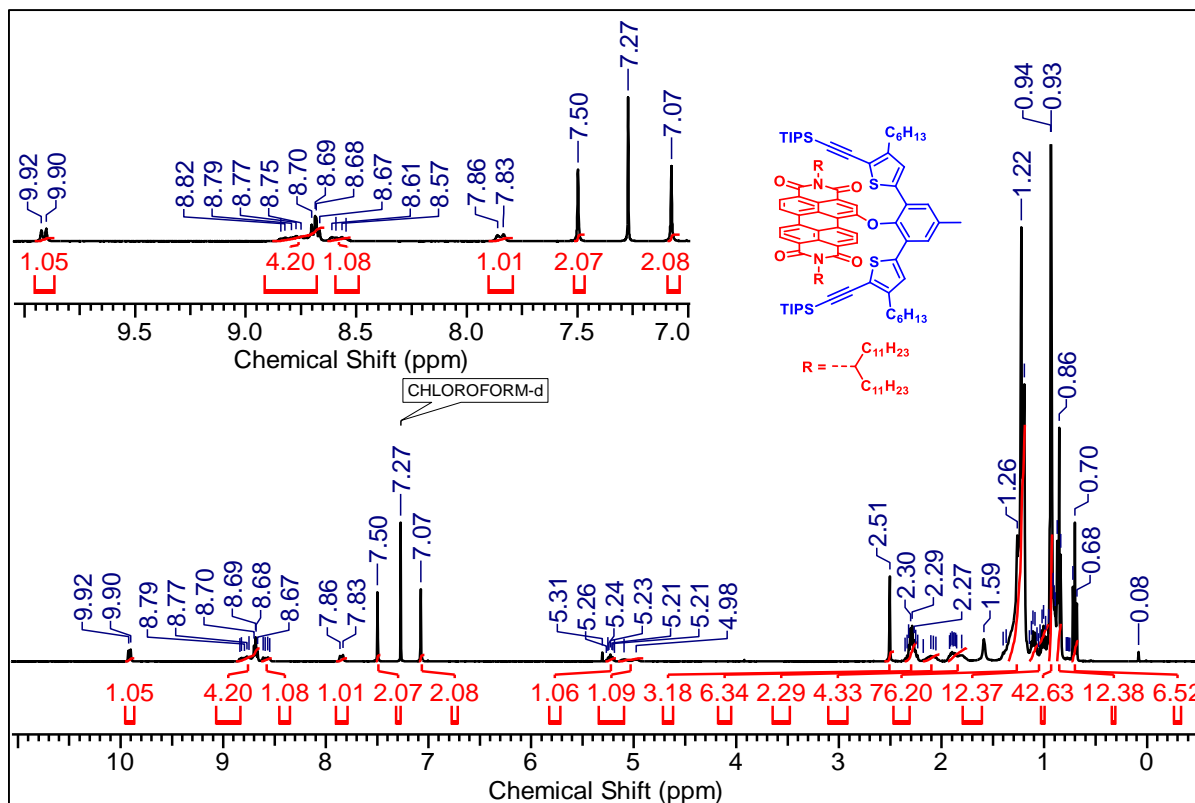
**¹H NMR** (500 MHz) spectrum of **4a** in CDCl₃ at 298 K.
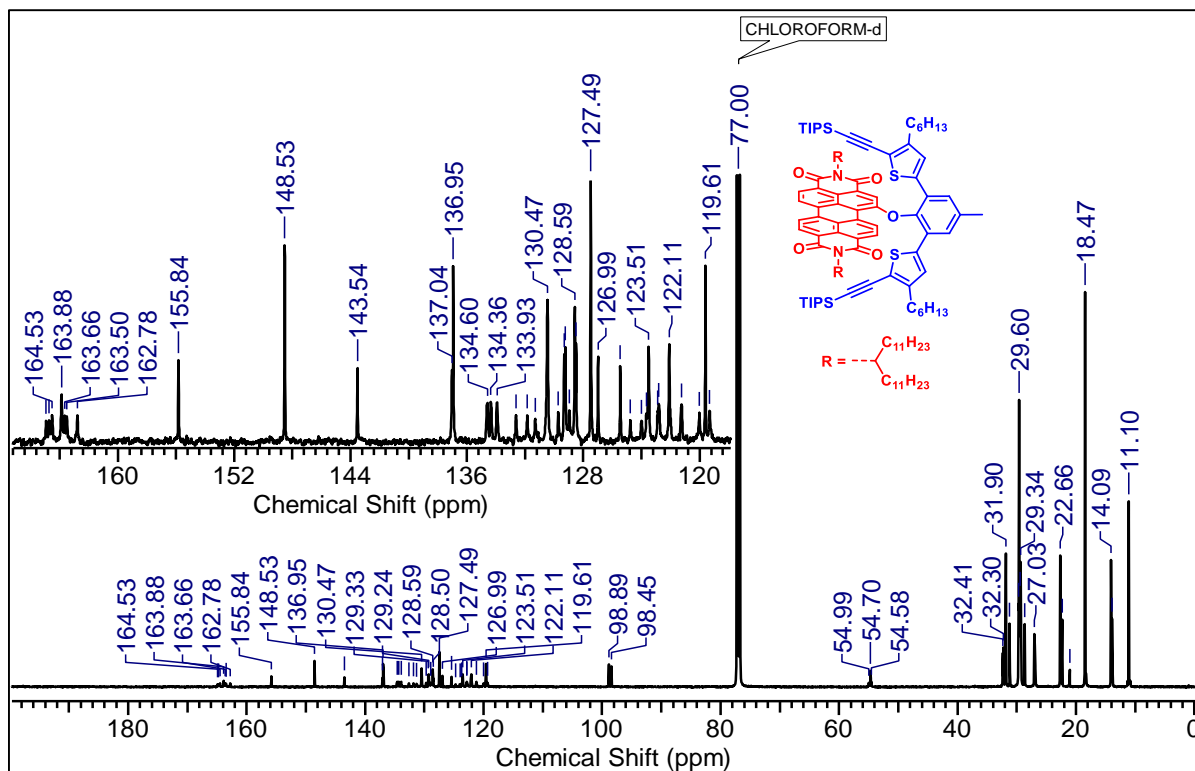


**¹³C NMR** (125 MHz) spectrum of **4a** in CDCl₃ at 298 K.

**¹H NMR** (500 MHz) spectrum of **4b** in CDCl₃ at 298 K.



**¹³C NMR** (125 MHz) spectrum of **4b** in CDCl₃ at 298 K.

**MALDI-TOF** MS spectra of molecule **4b**.



$^1$**H NMR** (500 MHz) spectrum of **5a** in CDCl$_3$ at 298 K
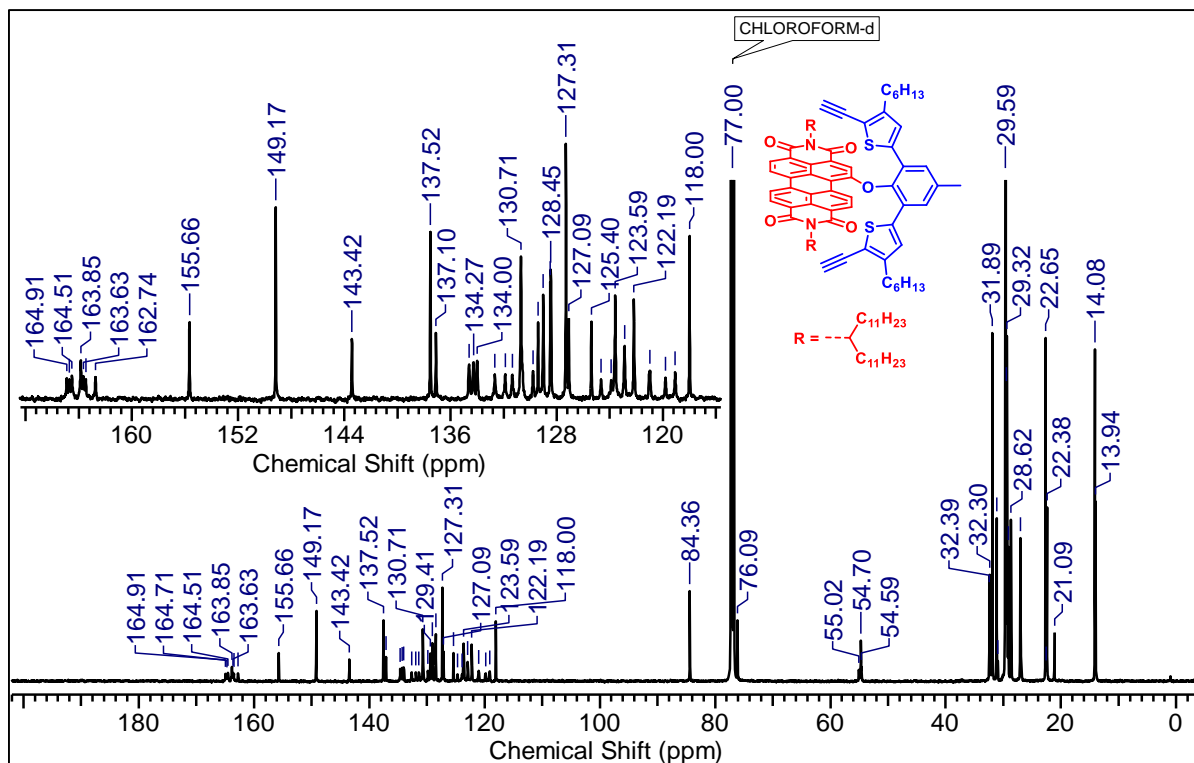
**13C NMR** (125 MHz) spectrum of **5a** in CDCl$_3$ at 298 K.
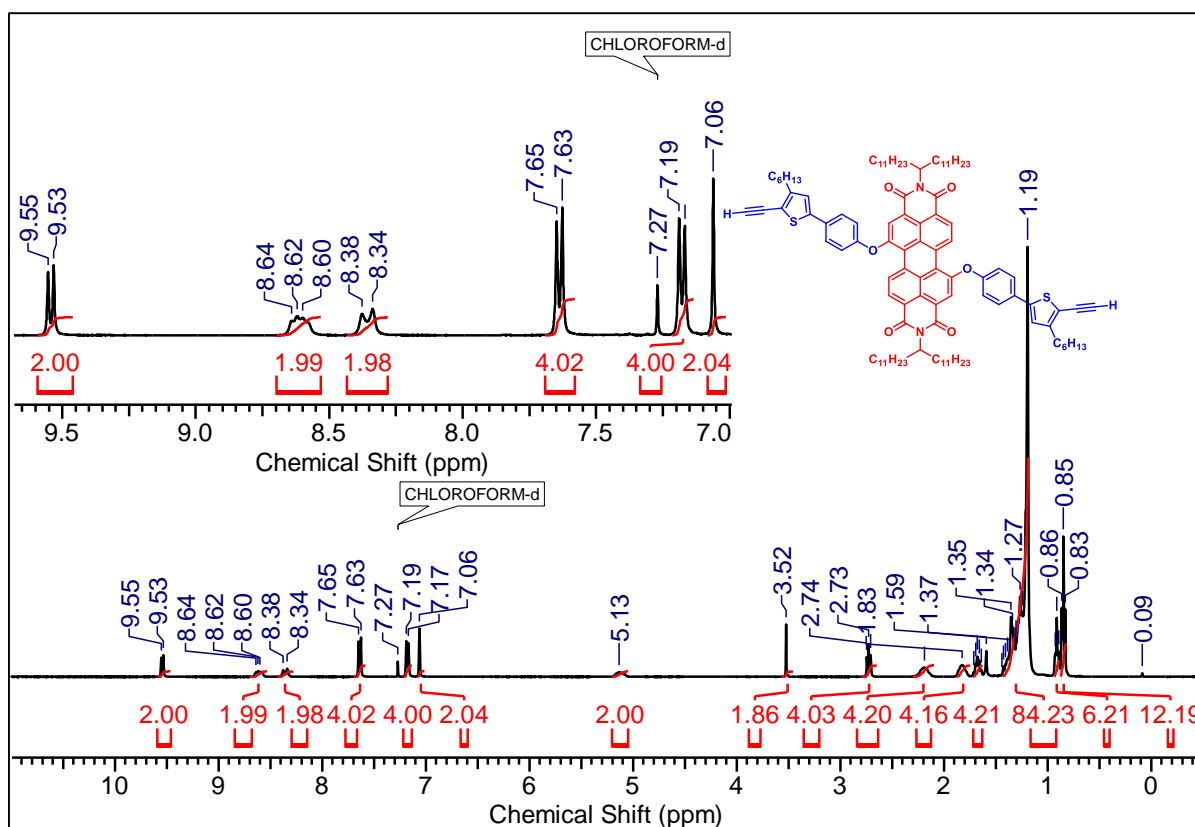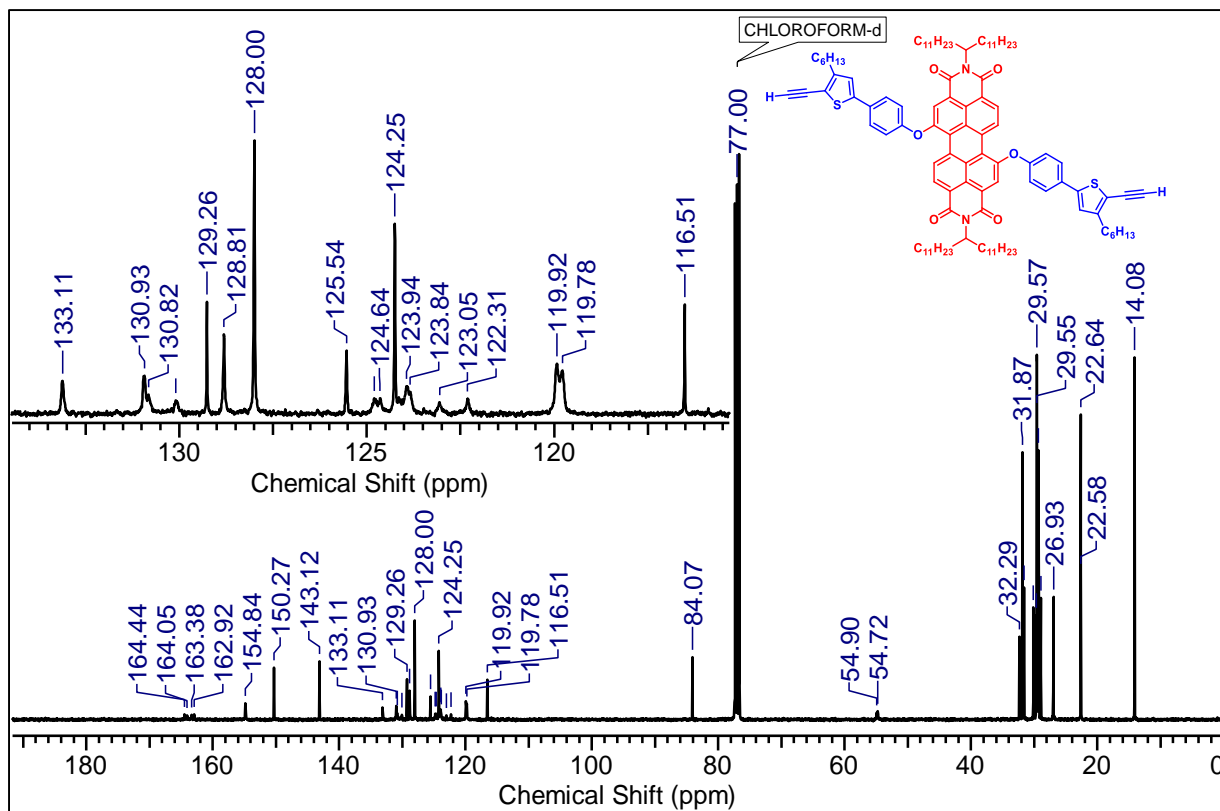


**1H NMR** (500 MHz) spectrum of **5b** in CDCl$_3$ at 298 K.

**13C NMR** (125 MHz) spectrum of **5b** in CDCl₃ at 298 K.
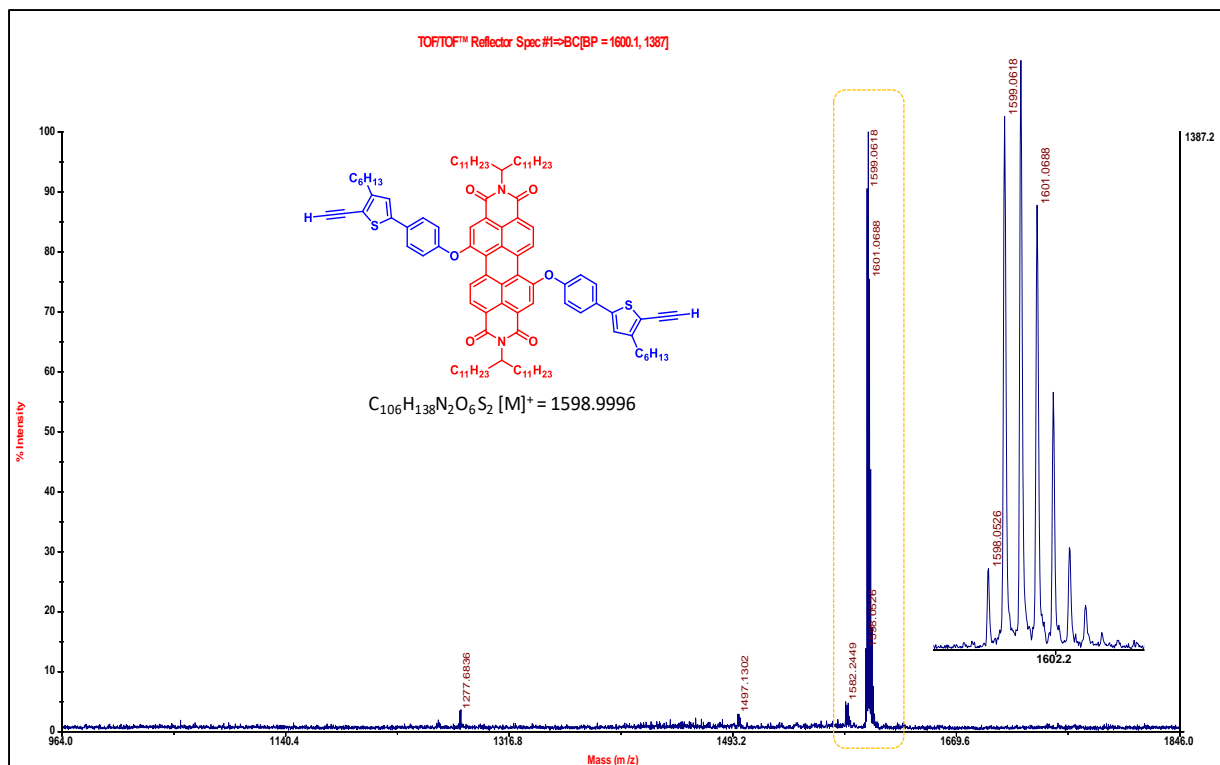


**MALDI-TOF** MS spectra of molecule **5b.**
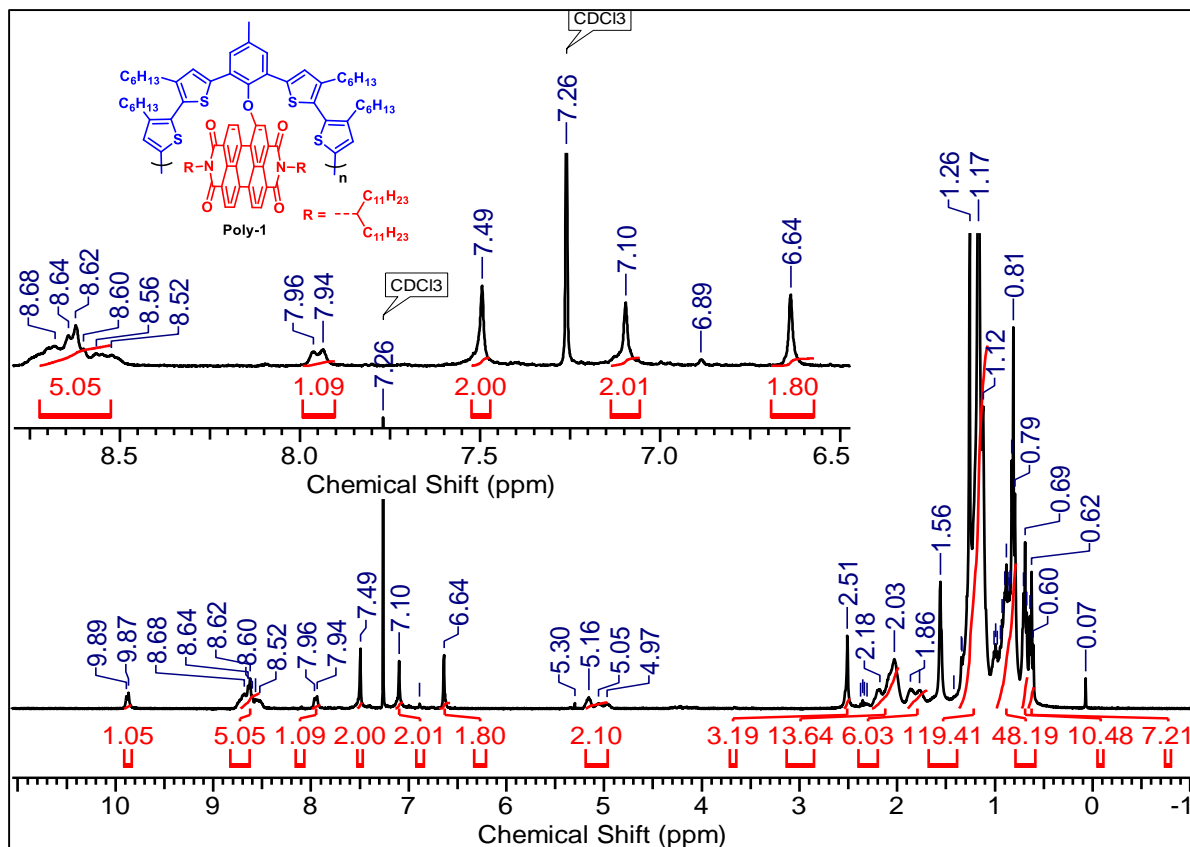
**¹H NMR** (500 MHz) spectrum of **Poly-1** in CDCl₃ at 298 K.
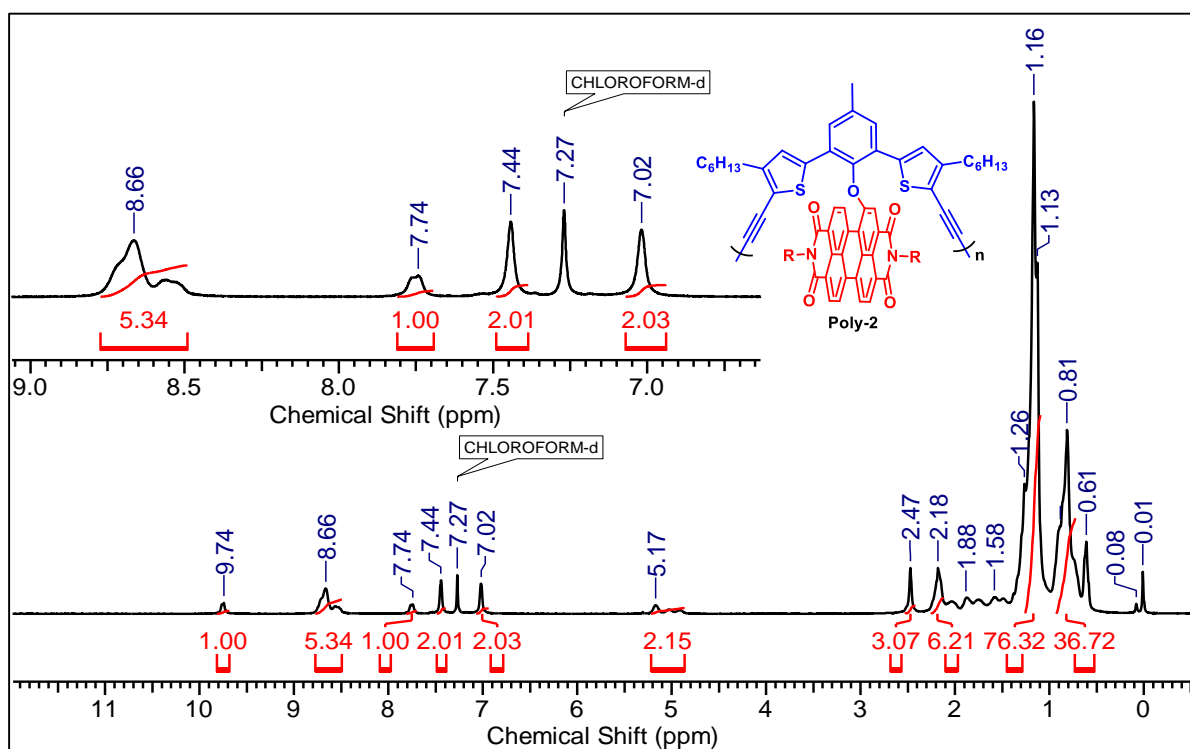


**¹H NMR** (500 MHz) spectrum of **Poly-2** in CDCl₃ at 298 K.
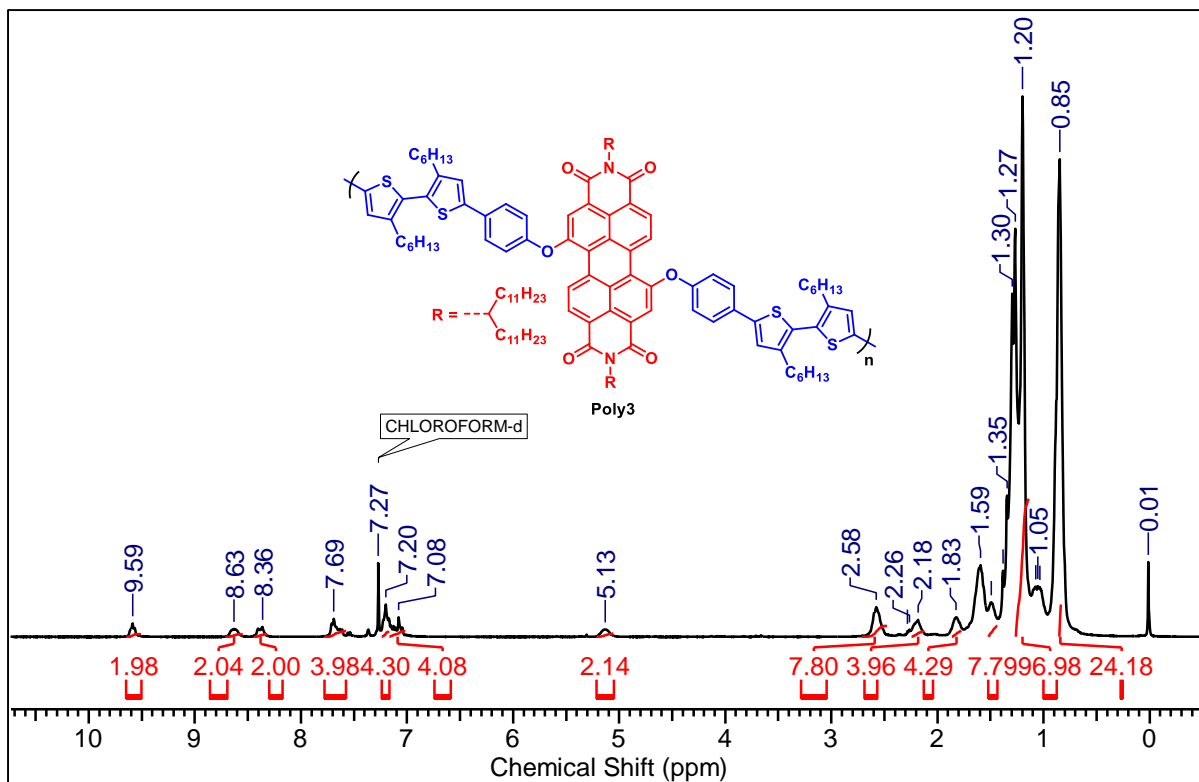
**¹H NMR** (500 MHz) spectrum of **Poly-3** in CDCl₃ at 298 K.
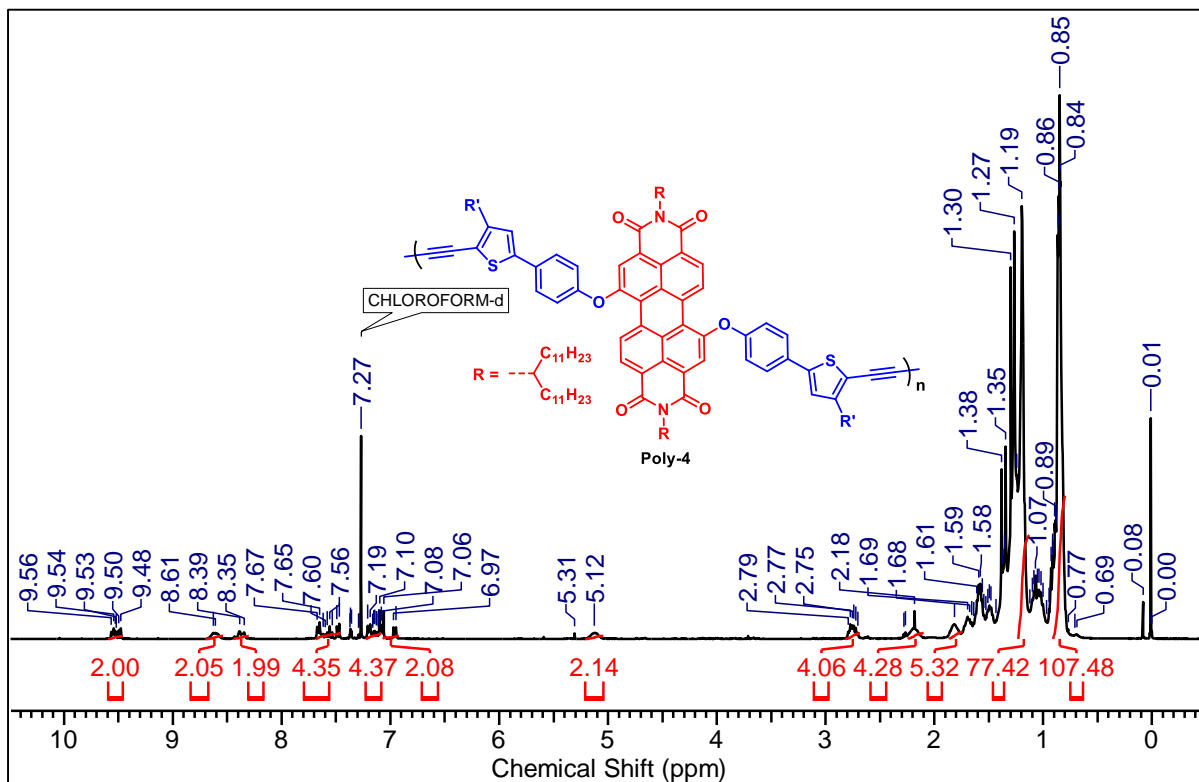


**¹H NMR** (500 MHz) spectrum of **Poly-4** in CDCl₃ at 298 K.
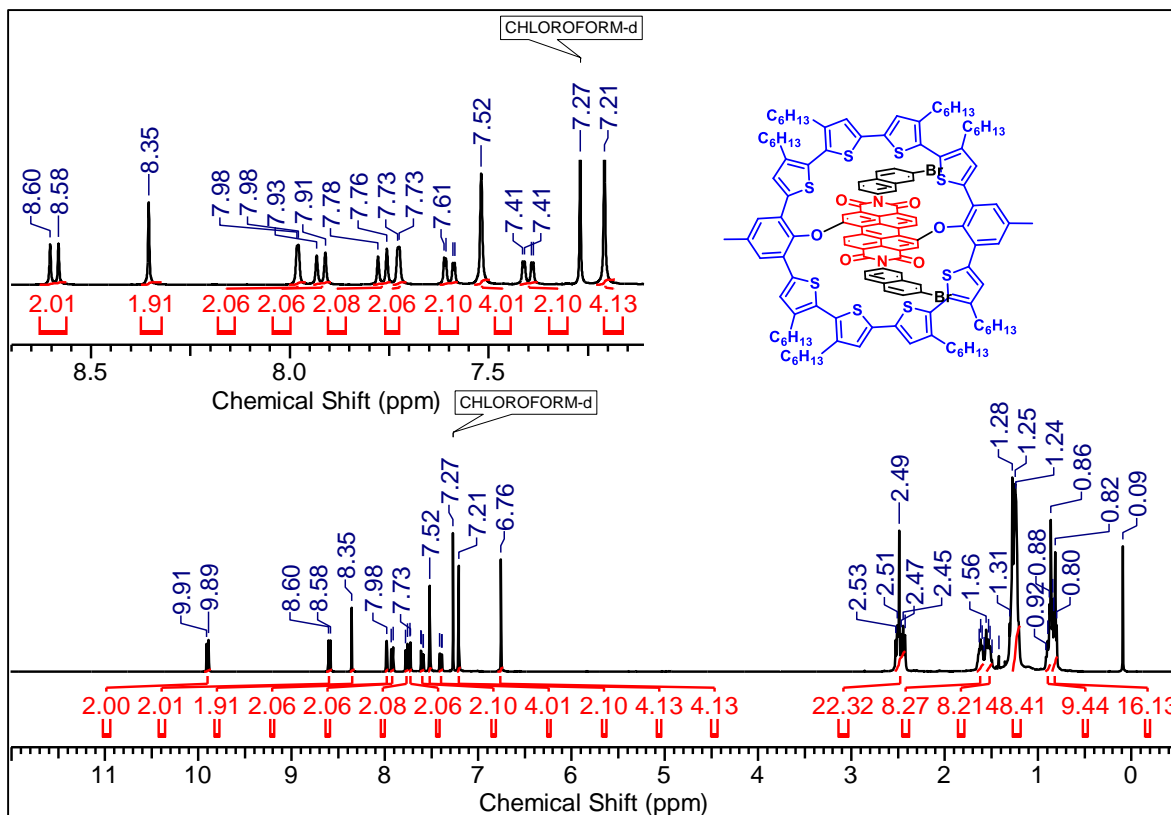
**¹H NMR** (400 MHz) spectrum of **TSP2Br** in CDCl₃ at 298 K.
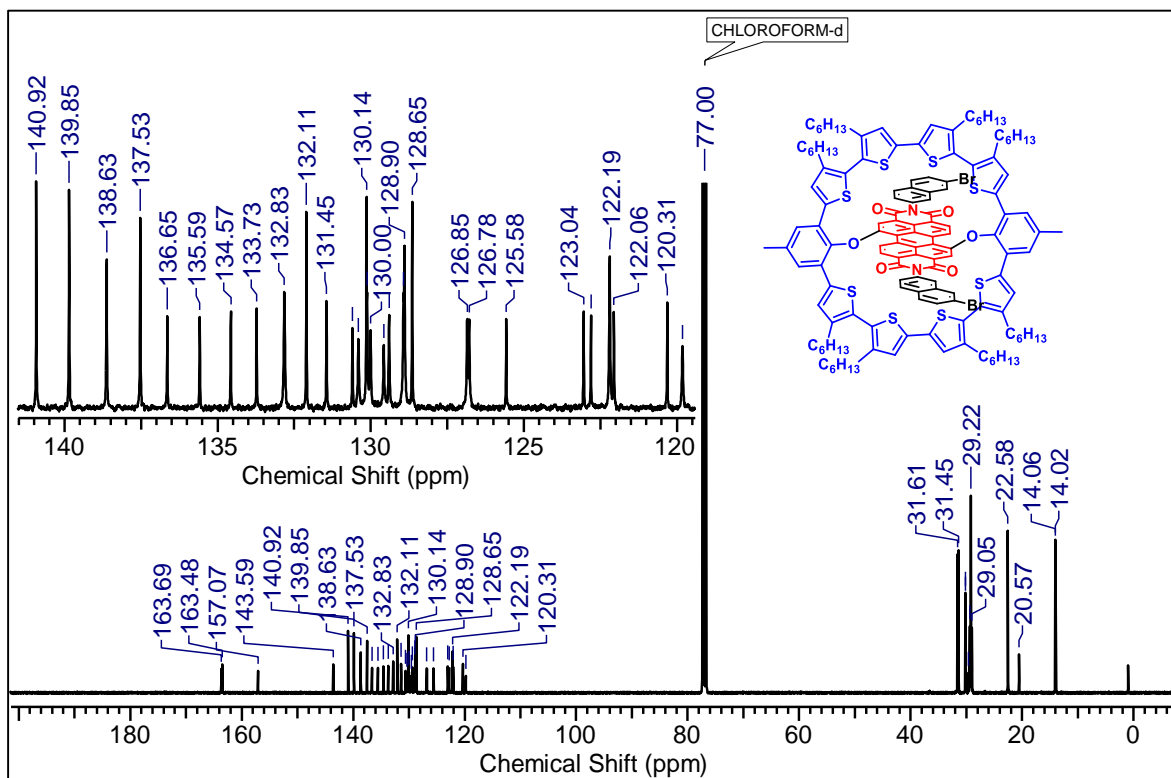


**¹³C NMR** (100 MHz) spectrum of **TSP2Br** in CDCl₃ at 298 K.
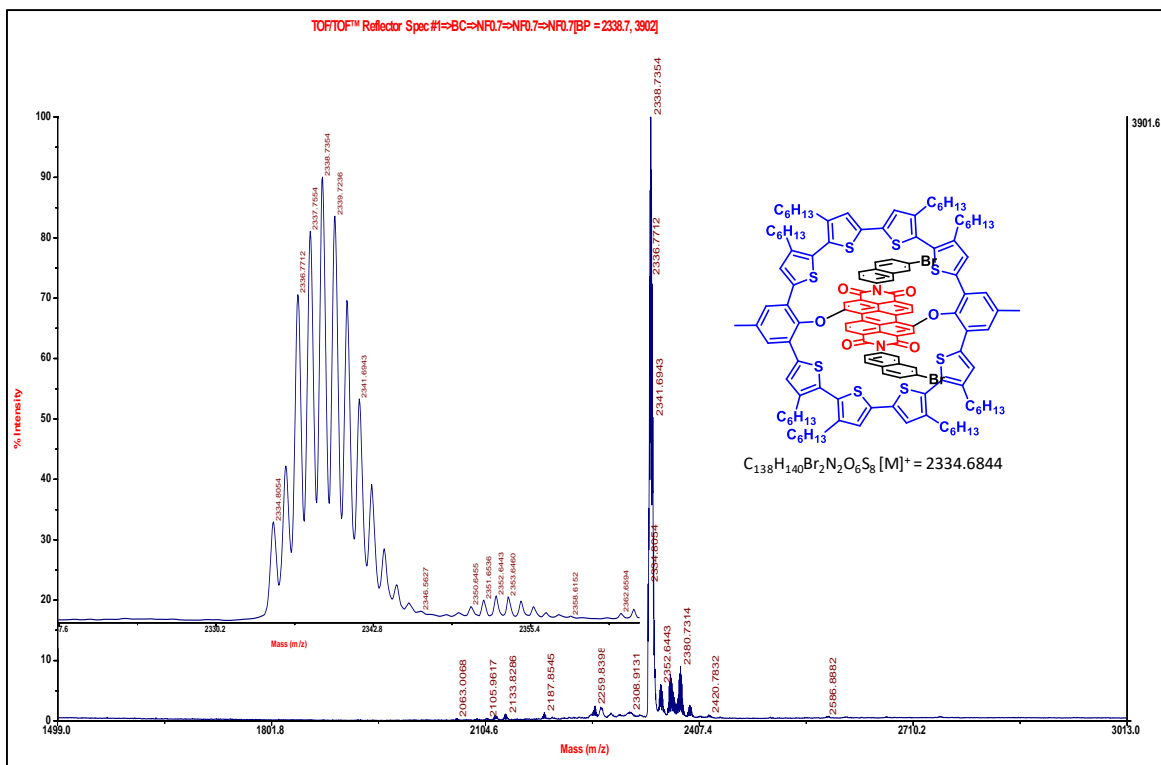
**MALDI-TOF** MS spectra of molecule **TSP2Br.**
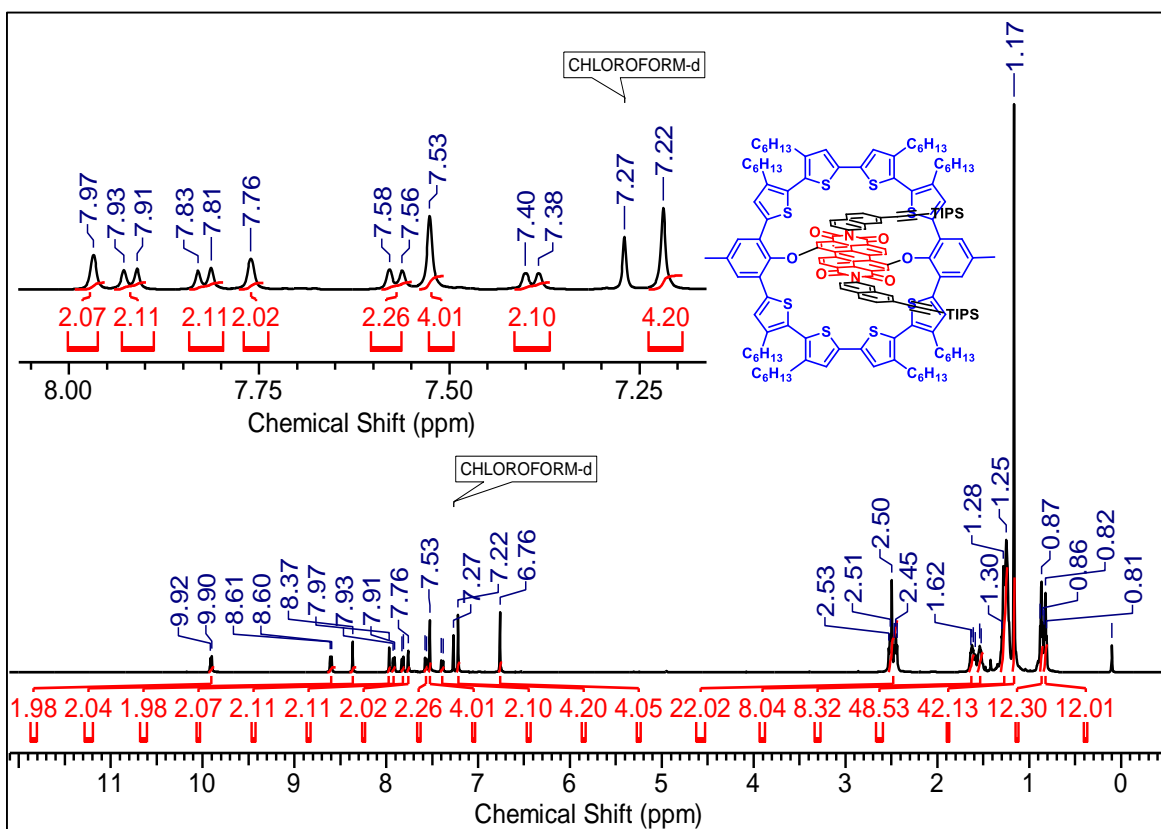


**¹H NMR** (400 MHz) spectrum of **TSP2TIPS** in CDCl₃ at 298 K.
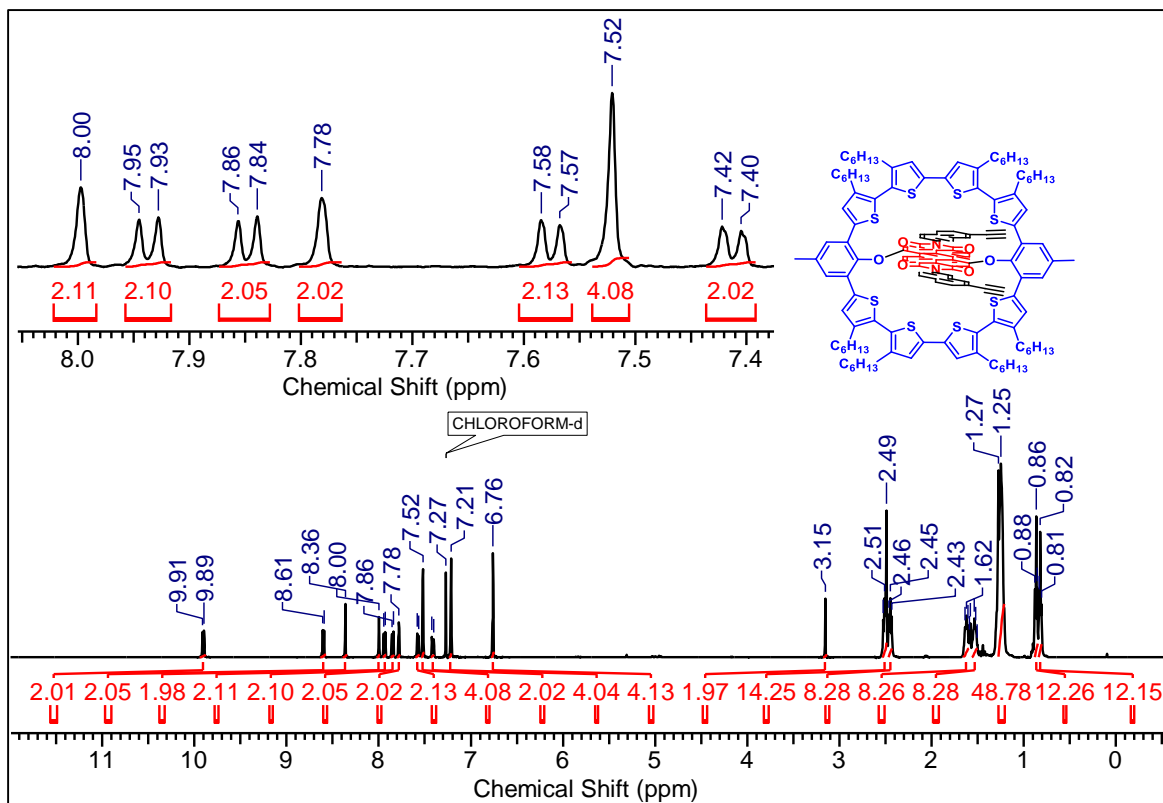
**<sup>13</sup>C NMR** (100 MHz) spectrum of **TSP2TIPS** in CDCl<sub>3</sub> at 298 K.
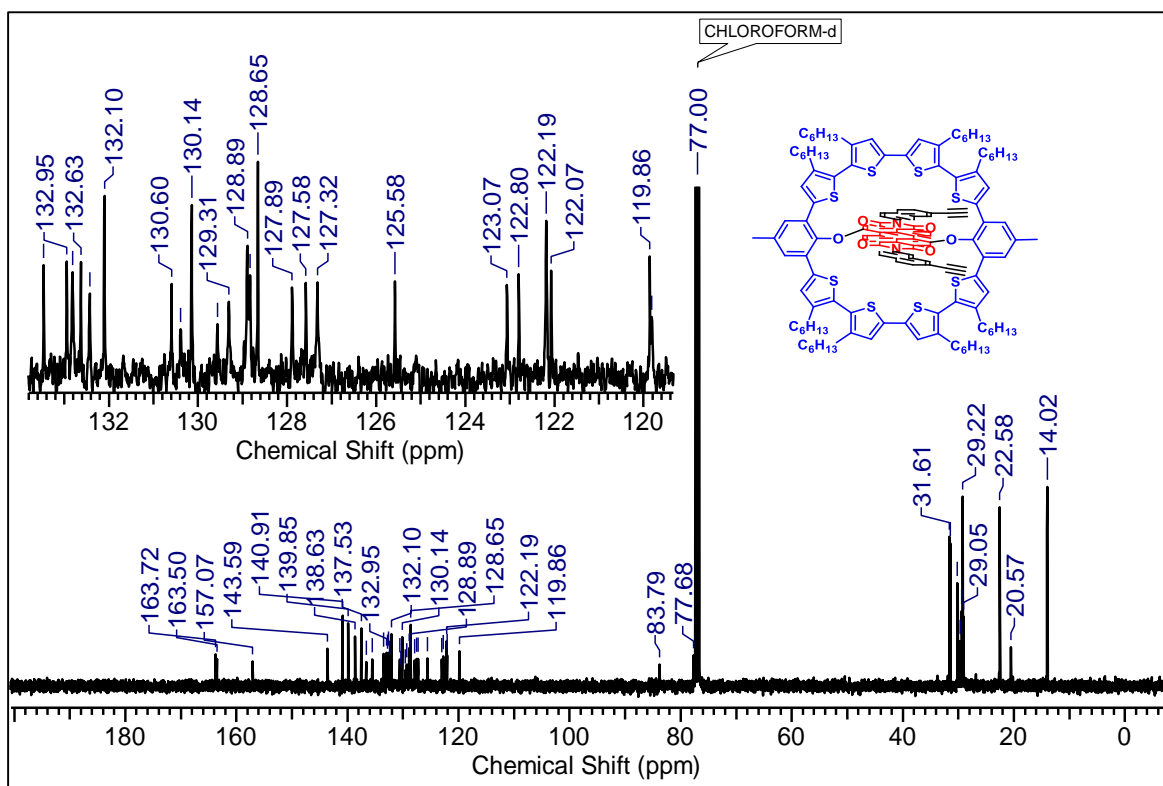


**MALDI-TOF** MS spectra of molecule **TSP2TIPS**.

**¹H NMR** (500 MHz) spectrum of **TSP2Acetylene** in CDCl₃ at 298 K.



**¹³C NMR** (100 MHz) spectrum of **TSP2Acetylene** in CDCl₃ at 298 K.
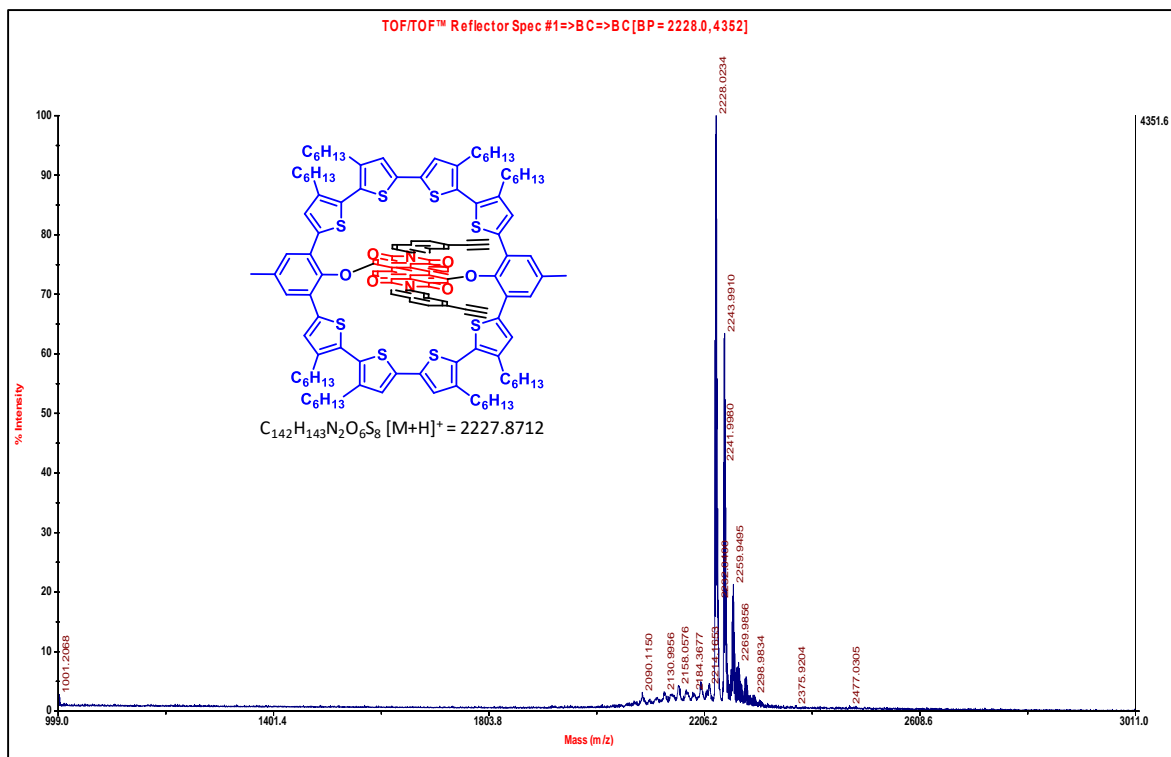
**MALDI-TOF** MS spectra of molecule **TSP2Acetylene**.
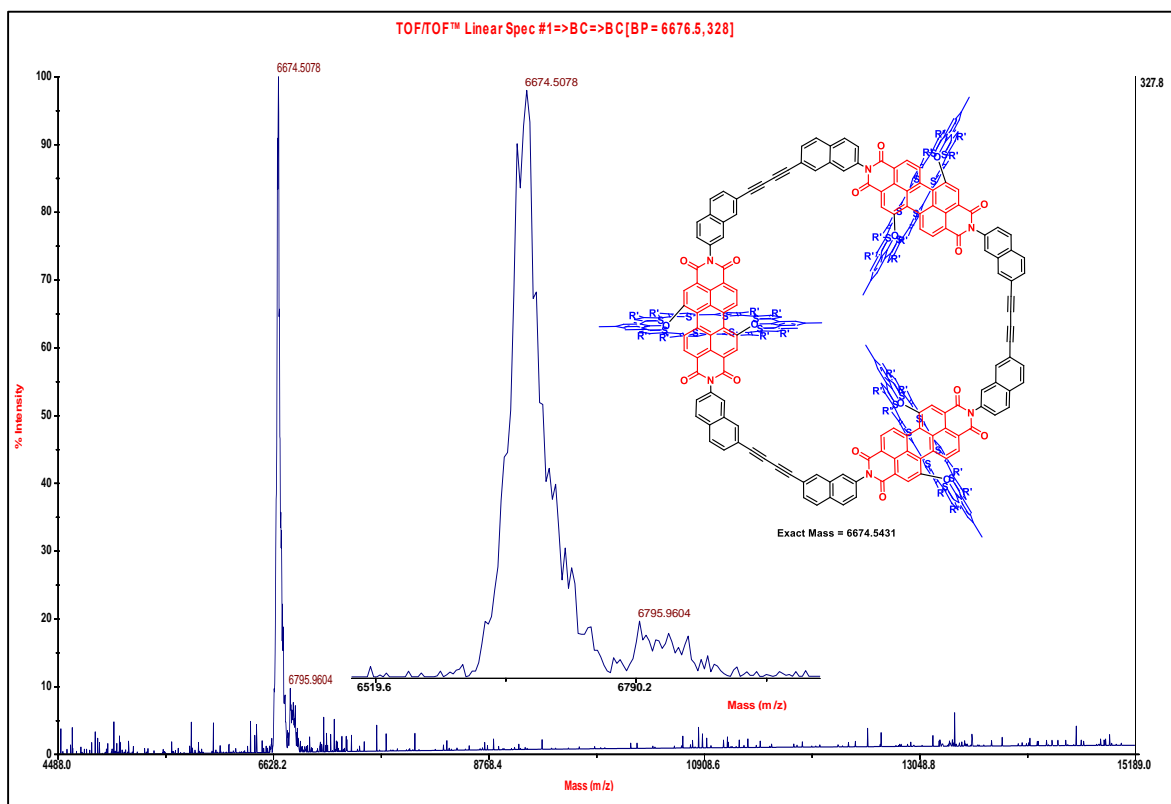


**MALDI-TOF** MS spectra of molecule **TSP2-Trimer**.

# *Abstract*

## ABSTRACT

--------------------------------------------------------------------------------------------------------

**Name of the Student:** Veer Sairam Dnyaneshwar     **Registration No.:** 10CC17J26015

**Faculty of Study:** Chemical Science     **Year of Submission:** 2023

**AcSIR academic centre/CSIR Lab:** CSIR-National Chemical Laboratory, Pune

**Name of the Supervisor(s):** Dr. Santhosh Babu Sukumaran

**Title of the thesis:** "New Molecular Designs for Donor-Acceptor Strapped Macromolecules and Polymers of Perylenebisimide"

--------------------------------------------------------------------------------------------------------

Perylene bisimide is one of the most distinctly studied fluorescent dyes among organic materials. Moreover, PBIs are indeed a preferred chromophore due to their excellent chemical and thermal stability, wide spectrum of visible light absorption, and distinctive electrochemical properties. The chemical functionalization of PBIs is possible at many positions, including the imide-, ortho-, and bay positions. However, since the imide nitrogen atoms of PBI act as the nodes of frontier orbitals, linking PBI units through these nitrogen atoms would not disrupt the PBI frontier orbitals. On the other hand, introducing new substituents at the bay position facilitate easy tuning of the optical and electrochemical properties, making them ideal for light harvesting, luminescent applications. PBI-based materials were primarily used as high-quality colorants in the pigment and textile industry, but they have recently found diverse applications in optoelectronic devices such as organic solar cells (OSCs), light-emitting diodes (OLEDs), transistors, energy storage devices, sensors, and lasers. Furthermore, well-defined π-conjugated donor-acceptor covalently bonded macrocycles are inspiring as modular building blocks for the development of novel materials (1D and 2D polymers) and supramolecular structures that allows both light harvesting and excitation energy transfer inside the molecule's core.

Two important classes of molecules, such as thiophene (donor) and perylene bisimide (PBIs) (acceptor), serve as the foundation for the current thesis. The thesis entitled "New Molecular Designs for Donor-Acceptor Strapped Macromolecules and Polymers of Perylene Bisimide" is divided into four different chapters. In chapter 1, we describe the nature of light harvesting, facts about the excited states, and intermolecular electronic interactions. Additionally, a general overview of perylene bisimide molecules is also discussed. Chapter 2 represent, Oligothiophene-Ring-Strapped Perylene Bisimides: Functionalizable Coaxial Donor-Acceptor Macrocycles. Our macrocycle design with a supportive spatial arrangement of the donor and acceptor units will urge more complex synthetic systems with exciting electron transfer and charge separation features. In the following Chapter 3, the challenge that persisted in Chapter 2 was addressed. The design and synthesis of Donor Strapped Perylene Bisimide Macrocycle and Lemniscate Dimer with Extended Charge Separation is covered in Chapter 3, the new macrocycle design enables the formation of higher analogs equally capable of stabilizing the charge-separated state. In Chapter 4, we continue the discussion from chapters 2 and 3 and focus on Perylene Bisimide Based Donor-Acceptor π-Conjugated Hanging and Linear Polymers.

## List of publication(s) in SCI Journal(s) emanating from the thesis work

1. **S. D. Veer**, V. C. Wakchaure, K. Asokan, R. Dixit, T. Goswami, R. Saha, R. Gonnade, H. N. Ghosh, S. S. Babu, Oligothiophene Ring Strapped Perylene bisimides: A Macrocycle Towards Co-axial Donor-Acceptor Design, *Angew. Chem. Int. Ed.* **2023**, e202212934.

2. **S. D. Veer**, T. Goswami, S. Ravindranathan, R. Gonnade, R. Dixit, H. N. Ghosh, S. S. Babu, Donor Strapped Perylene Bisimide Macrocycle and Lemniscate Dimer with Extended Charge Separation, *Org. Chem. Front.* **2023**, *DOI: 10.1039/d3qo01060k.*

3. **S. D. Veer**, Thanasekar C, T. Goswami, H. N. Ghosh, S. S. Babu, Donor-Strapped Perylene Bisimide Based Donor-Acceptor $\pi$-Conjugated Polymers, *(Manuscript Submitted)*

4. **S. D. Veer**, T. Goswami, H. N. Ghosh, S. S. Babu, Shape Controlled Synthesis of Oligothiophene-Ring-Strapped Pyrene Macrocycles. *(Manuscript Submitted)*

## List of publication(s) in SCI Journal(s) (published & accepted) other than thesis

1. K. C. Ranjeesh, R. Illathvalappil, **S. D. Veer**, J. Peter, V. C. Wakchaure, Goudappagouda, R. J. Vipin, S. Kurungot, S. S. Babu, Imidazole-Linked Crystalline Two-Dimensional Polymer with Ultrahigh Proton-Conductivity, *J. Am. Chem. Soc.* **2019**, *141*, 14950-14954.

2. V. C. Wakchaure, **S. D. Veer**, A. D. Nidhankar, Goudappagouda, R. A. Nayak, K. Asokan, S. Ravindranathan and S. S. Babu, Donor-acceptor based solvent-free organic liquid hybrids with exciplex emission and room temperature phosphorescence, *Chem. Commun.*, **2022**, *58*, 1998-2001.

3. V. C. Wakchaure, **S. D. Veer**, A. D. Nidhankar, V. Kumar, S. S. Babu, Polymerizable Solvent-free Organic Liquids: New Approach for Large Area Flexible and Foldable Luminescent Films, *Manuscript submitted*.

4. A. D. Nidhankar, Goudappagouda, P. Kothavade, S. D. Dongre, **S. D. Veer**, S. R. Dash, K. Rajeev, K. N. N. Unni, K. Shanmuganathan and S. S. Babu, Thermally Activated Delayed Fluorescent Solvent-free Organic Liquid Hybrids for Tunable Emission Applications, *Manuscript submitted*.

# List of National International Conference

1. Participated in the *"15th International Conference on Polymer Science and Technology"* (SPSI MACRO-2018), held during December 19-22, 2018 at Indian Institutes of Science Education and Research, Pune and CSIR- National Chemical Laboratory, Pune, India.

2. Participated in *"NCL-RF Annual Students conference 2018"*, held during November 29-30, 2018, at CSIR- National Chemical Laboratory, Pune, India.

3. Participated in *"NCL-RF Annual Students conference 2019"*, held during November 28-29, 2019, at CSIR- National Chemical Laboratory, Pune, India.

4. Participated in *"Basic Fire Safety & Emergency Preparedness"* on 18th November 2021, at CSIR- National Chemical Laboratory, Pune, India.

5. Participated in *"NCL-RF Annual Students conference 2021"*, held during November 29-30, 2021, at CSIR- National Chemical Laboratory, Pune, India.

6. Attended ACS Science Talk on Covalent Organic Frameworks and the Morphology [0-1-2-3] on, 29th January 2021.

## LIST OF ORAL AND POSTER PRESENTATION

1. Delivered an oral presentation for *Rajappa Award for Research Fellow (CSIR-NCL-RF*, the Best paper award for the paper published with the highest impact factor in material science in 2022), on National Science Day-2023, held on February 26, at CSIR- National Chemical Laboratory, Pune, India.

2. Presented poster in *"National Science Day-2023"*, held on February 24th-28th, 2023, at CSIR- National Chemical Laboratory, Pune, India.

3. Presented poster in *"National Science Day-2021"*, held on February 24th-25th, 2021, at CSIR- National Chemical Laboratory, Pune, India.

# Awards and Honours

1. Awarded for *"Rajappa Award for Research Fellow (CSIR-NCL-RF)"*, the Best paper award for the paper published with the highest impact factor in chemical science in 2023.

2. Best poster award in *"National Science Day-2021"*, held on February 24th-26th, 2021, at CSIR- National Chemical Laboratory, Pune, India.

# *General Remark*

- ✓ All the moisture and air sensitive reactions have been carried out in anhydrous solvents under argon atmosphere in oven-dried glassware. The anhydrous solvents were distilled prior to use: $CH_2Cl_2$, $CHCl_3$ and DMF from $CaH_2$; methanol from Mg cake; Toluene and THF on Na/benzophenone; triethylamine and diisopropylamine over KOH.

- ✓ $^1H$ NMR spectra were recorded on AV–200 MHz, AV–400 MHz, JEOL AL- 400 (400 MHz) and DRX–500 MHz spectrometer using tetramethylsilane (TMS) as an internal standard. Chemical shifts have been expressed in ppm units downfield from TMS.

- ✓ $^{13}C$ NMR spectra were recorded on AV–50 MHz, AV–100 MHz, JEOL AL- 100 (100 MHz) and DRX–125 MHz spectrometer.

- ✓ High-resolution mass spectra (HRMS) were recorded on a Thermo Scientific Q-Exactive, Accela 1250 pump and also EI Mass spectra were recorded on Finngan MAT–1020 spectrometer at 70 *eV* using a direct inlet system. The mass spectrometry experiments were conducted on Bruker ultraflex MALDI-TOF MS.

- ✓ FT-IR spectra were obtained on Perkin Elmer Spectrum Two spectrophotometer in 4000-400 cm-1 range with a resolution of 4 cm$^{-1}$.

- ✓ All reactions are monitored by Thin Layer Chromatography (TLC) carried out on 0.25 mm E-Merck silica gel plates (60F–254) with UV light, I2, and anisaldehyde in ethanol as developing agents.

- ✓ All evaporations were carried out under reduced pressure on Heidolph rotary evaporator below 50 °C unless otherwise specified.

- ✓ Silica gel (60–120), (100–200), and (230–400) mesh were used for column chromatography.

- ✓ HPLC analysis was performed on Agilent 1260, Infinity Series using normal (CHIRALPAK IA, 5 mm, 4.6 mm x 250 mmL) columns.

- ✓ Single Crystal X-ray Diffraction data were collected on a Bruker SMART APEX II CCD diffractometer with graphite-monochromatized (Mo Kα = 0.71073 Å) radiation at ambient temparature.

- ✓ UV-Vis absorption spectra were recorded with a Shimadzu 1800 spectrophotometer, while all emission spectra were performed using PTI Quanta Master™ Steady State Spectrofluorometer. CD spectra were recorded on a Jasco J-815 CD spectrometer equipped

with a Jasco PTC-424S/15 Peltier system. Solid state UV absorbance spectra were recorded on SHIMADZU UV-3600Plus spectrophotometer, ISR-603.

GDCh

**Research Articles**

*Angewandte*
*Chemie*
International Edition
www.angewandte.org

Donor-Acceptor Systems

# Oligothiophene-Ring-Strapped Perylene Bisimides: Functionalizable Coaxial Donor–Acceptor Macrocycles

*Sairam Dnyaneshwar Veer, Vivek Chandrakant Wakchaure, Kiran Asokan, Ruchi Dixit, Tanmay Goswami, Ramchandra Saha, Rajesh Gonnade, Hirendra N. Ghosh,\* and Sukumaran Santhosh Babu\**

**Abstract:** Aesthetic designs from nature enable new knowledge to be gained and, at the same time, inspire scientific models. In this context, multicomponent macrocycles embody the advantage of precisely positioning the structural units to achieve efficient communication between them. However, the construction of a functionalizable macrocycle for ultrafast charge separation and stabilization has not been attempted. Herein, we report the synthesis, crystal structure, and transient absorption of a new functionalizable macrocycle consisting of an oligothiophene-ring-strapped perylene bisimide. Transient absorption results point to a sequential improvement in charge separation and stabilization from the macrocycle to the corresponding linear dimer and 2D polymer due to the unique design. Our macrocycle design with a supportive spatial arrangement of the donor and acceptor units will inspire the development of more complex synthetic systems with exciting electron-transfer and charge-separation features.

## Introduction

Nature often inspires new molecular and supramolecular designs to solve many fundamental scientific challenges. For instance, the natural photosynthetic system with long-lived charge separation (CS) is still a fascinating concept to mimic and realize in a laboratory setting.[1–3] The presence of an ordered molecular unit with optimized energy characteristics leads to efficient energy and electron-transfer (ET) processes with relevance for the design of synthetic analogues. Detailed studies revealed that the preferred orientation of chromophores in donor–acceptor (D-A) assemblies supports long-lived CS.[4–6] Hence, many D-A-based coaxial designs have been trialed to achieve better CS.[7–10] Among those, a combination of perylene bisimides (PBIs) with various donor molecules exhibited faster ET and a long-lived CS state.[11]

PBIs are widely studied dyes for their fascinating optical and redox features, outstanding electron transport, and self-assembly to form diverse nanostructures.[11–23] Therefore, PBIs have found use in various applications, including organic solar cells, batteries, supercapacitors, sensors, and photocatalysis.[16,17,24–31] Synthetic manipulation through core functionalization of up to four bay positions (1,6,7,12) and four *ortho* positions (2,5,8,11) resulted in numerous derivatives and has made PBIs a favorite choice of organic materials chemists.[32–37] Many supramolecular assemblies of PBIs with carbon nanotubes (CNTs), carbon nanodots, and other structures have also been explored for ET studies.[38,39] Furthermore, many complex molecular architectures, polymers, and macromolecules composed of PBIs have been reported in combination with other functional molecules.[40–45] The most exploited electron D-A pair of PBIs and thiophenes has led to *p-n*-heterojunctions useful in energy harvesting and storage devices.[46–49] Many research groups were keenly involved in synthesizing PBI-based macrocycles, even using a D-A combination.[50–52] Ball et al. reported giant macrocycles of a fused PBI dimer or a PBI (acceptor) containing a bithiophene (donor) strap achieved through multinuclear metal (Pd/Pt) intermediates, and the former exhibited high electron mobility.[50,51] However, a completely donor-strapped PBI remained unexplored until Würthner and co-workers reported macrocyclic D-A dyads formed by imide functionalization of PBI with a cyclic oligothiophene through a platinum-mediated cross-coupling reaction.[52,53] In all these oligothiophene–PBI macrocycles,

[*] S. Dnyaneshwar Veer, V. Chandrakant Wakchaure, K. Asokan, S. Santhosh Babu
Organic Chemistry Division
National Chemical Laboratory (CSIR-NCL)
Dr. Homi Bhabha Road, Pune 411 008 (India)
E-mail: sb.sukumaran@ncl.res.in

S. Dnyaneshwar Veer, V. Chandrakant Wakchaure, R. Dixit, R. Gonnade, S. Santhosh Babu
Academy of Scientific and Innovative Research (AcSIR)
Ghaziabad 201 002 (India)

R. Dixit, R. Gonnade
Physical and Materials Chemistry Division, National Chemical Laboratory (CSIR-NCL)
Dr. Homi Bhabha Road, Pune 411 008 (India)

T. Goswami, R. Saha, H. N. Ghosh
Institute of Nanoscience and Nanotechnology (INST)
Sector 81, Mohali 411008, Punjab (India)
E-mail: hnghosh@inst.ac.in

H. N. Ghosh
Radiation and Photochemistry Division
Bhabha Atomic Research Centre
Mumbai 400085 (India)

the yield was only moderate.[50–53] Interestingly, the macrocyclic dyad exhibited ultrafast ET within approximately 1 ps from the donor oligothiophene to the acceptor PBI. Through suitable placement of the donor–acceptor units in the dyad, fast charge recombination within 8–12 ps was observed. Hence, alternate molecular designs involving high-yielding reactions might be considered to speed up the ET process and achieve a long-lived CS state.

In this study, we synthesized half- and full-oligothiophene-ring-strapped PBIs substituted at the bay position, resulting in a new D-A macrocycle dyad (Scheme 1). Moreover, the functionalization of the macrocycle delivered the corresponding linear dimer and two-dimensional (2D) polymer. Our approach focused on bay-substituted strapped PBIs with D-A units oriented nearly orthogonal to enhance the ET. Though many strapped or encapsulated molecular systems have been reported,[54,55] a combination of an electron-donating oligothiophene with electron-accepting PBIs may lead to exciting heterojunction materials.

## Results and Discussion

Half- and full-oligothiophene-ring-strapped PBI molecules **TSP1** and **TSP2** were synthesized through aromatic nucleophilic substitution, Stille coupling, and oxidative coupling



**Scheme 1.** Synthesis of oligothiophene-ring-strapped PBIs. a) Synthesis of macrocycles **TSP1** and **TSP2**: i) K$_2$CO$_3$, DMF, 120°C, 1 h; ii) Pd(PPh$_3$)$_2$Cl$_2$, toluene, 140°C, 12 h; iii) FeCl$_3$, CH$_3$NO$_2$, CH$_2$Cl$_2$, room temperature, 2–3 h. b) Synthesis of dimers **TSP1D** and **TSP2D**: i) t-BuOH, KOH, 60–65°C, 2.5–5 h; ii) imidazole, Zn(OAc)$_2$, 150°C, 7–10 h.

*Angew. Chem. Int. Ed.* **2023**, *62*, e202212934 (2 of 9)

© 2022 Wiley-VCH GmbH
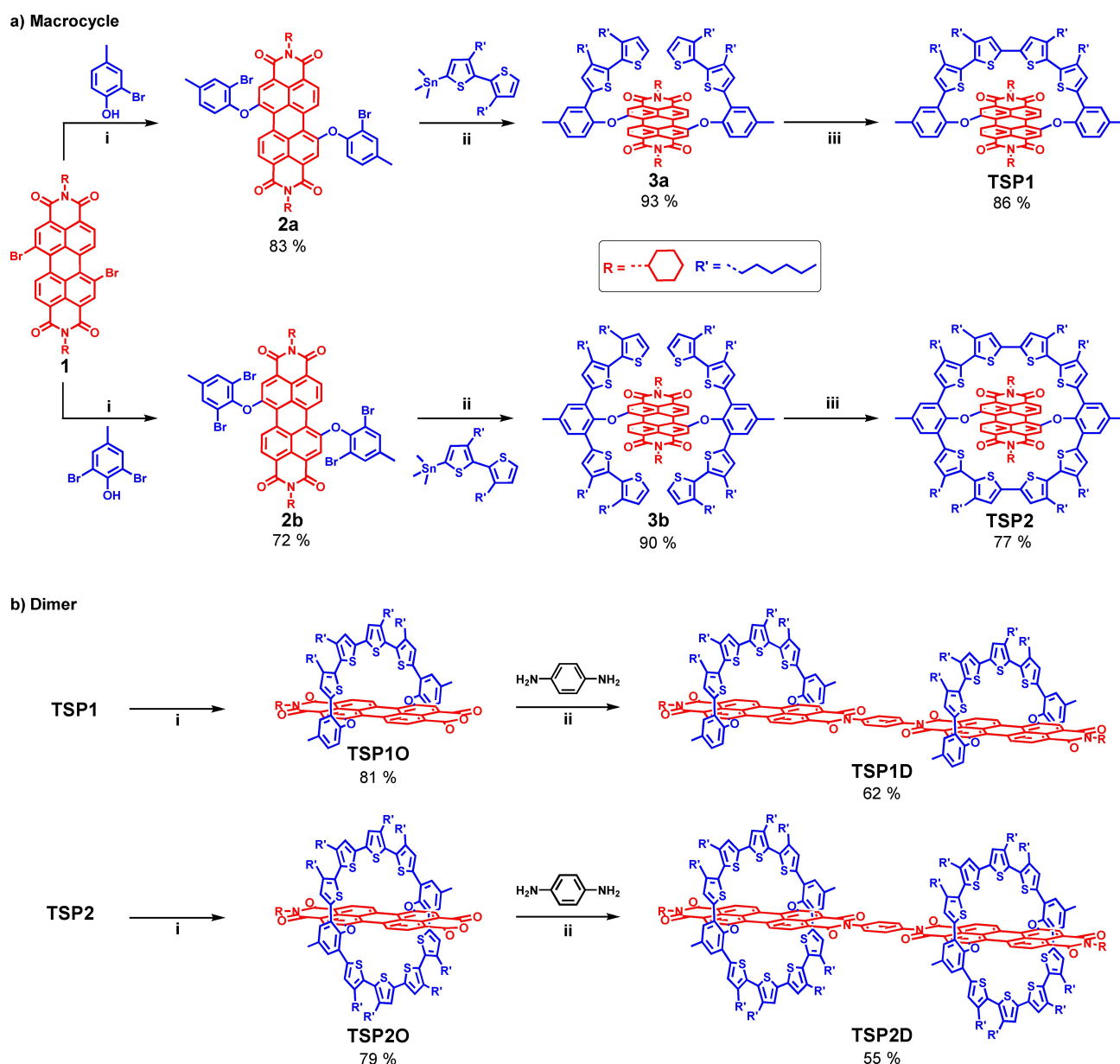
reactions in good yields (Scheme 1). The synthesis started with commercially available 1,7-dibromoperylene-3,4,9,10-tetracarboxylic dianhydride, which on treatment with cyclohexylamine in a mixture of DMF and ethanol (1:1), gave molecule **1** in 81 % yield. Upon heating with 2-bromo-4-methylphenol and 2,6-dibromo-4-methylphenol at 120 °C in the presence of $K_2CO_3$ in dimethylformamide, molecule **1** yielded **2a** (83 %) and **2b** (72 %), respectively. Stille coupling reaction of **2a** and **2b** with (3,3′-dihexyl-[2,2′-bithiophen]-5-yl)trimethylstannane delivered **3a** (93 %) and **3b** (90 %), respectively. Further, we optimized the oligothiophene ring closure using $FeCl_3$-mediated oxidative coupling to yield half- and full-oligothiophene-ring-strapped PBI molecules **TSP1** (86 %) and **TSP2** (77 %) in high isolated yields with 100 % conversion. As compared to other reported macrocycles, the yields of the present systems are significantly high.[50–53] All the synthesized molecules were characterized by $^1$H and $^{13}$C NMR spectroscopy and matrix-assisted laser desorption ionization time-of-flight mass spectrometry (MALDI-TOF MS). A detailed 2D NMR study sheds light on the possible cross-coupling between the various proton and nullifies any interaction between the hydrogen atoms of the thiophene ring and the PBI units (Figures S1–S8).

To study the effect of core isolation of PBI using oligothiophene rings, absorption and steady-state emission of reference molecule **rPBI** and **TSP1,2** were recorded in $CH_2Cl_2$ (Figure 1a,b). Normalized absorption spectra showed a clear red-shift of around 16 nm in the absorption maximum from **rPBI** to **TSP1** and **TSP2** (Figure S9). The emission intensity of **TSP1** and **TSP2** in the solution is negligibly low in $CH_2Cl_2$ (Figure 1b, S9). A comparison indicated no change in absorption or emission features upon oligothiophene ring closure (Figure S9). The variation observed in the visible and fluorescence color from **rPBI** to **TSP1** and **TSP2** is displayed in Figure 1c. To see the redox behavior of **TSP1** and **TSP2**, cyclic voltammetry (CV) and differential pulse voltammetry (DPV) were recorded. These experiments were carried out in $CH_2Cl_2$ ($C = 1$ mM) using $Bu_4NPF_6$ as the supporting electrolyte. Two reversible reduction waves at potentials of −1.22, −1.39 V for **TSP1** and −1.24, −1.47 V for **TSP2** (Figures 1d,e and S10–S12, Table S1) were observed. Two reversible reduction waves point to the first and the second one-electron stepwise reductive process leading to anion and dianion formation of the PBI core. The observed reduction potentials are slightly shifted to negative potential relative to **rPBI** (Figure S10 and Table S1). There are two reversible oxidation peaks at 0.54, 0.79 V for **TSP1**, and 0.57, 0.87 V for **TSP2** in the positive potential sweep due to the oxidation of oligothiophene rings. Though the donor and acceptor units are linked in the macrocycles, the redox features indicate that the electronic states are only slightly affected.

The energies and electronic wave function distributions for the frontier molecular orbitals (MOs) demonstrate predominant contributions of the oligothiophene unit in the highest occupied molecular orbital (HOMO) and those of the PBI blocks in the lowest unoccupied molecular orbital (LUMO; Figure 2a,b), validating the preferred photoin-
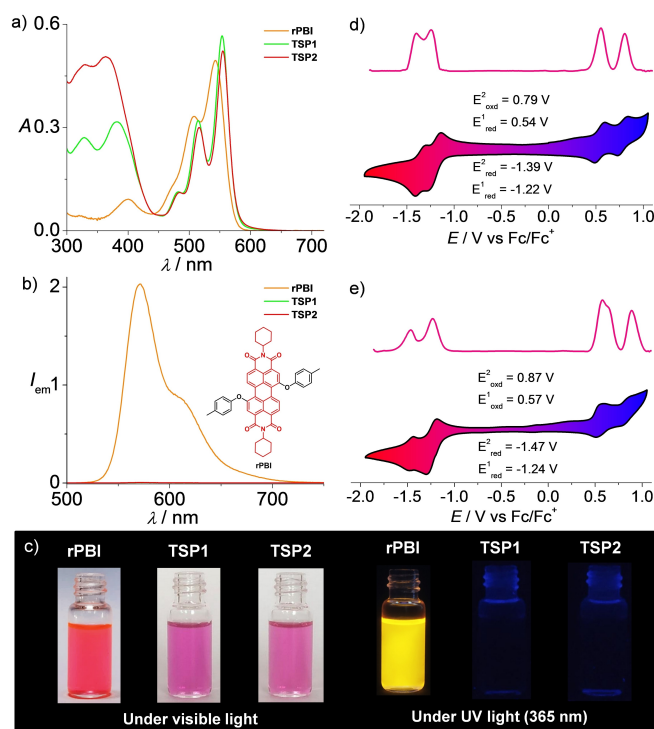


*Figure 1.* a) UV/Vis absorption and b) steady-state fluorescence spectra of **rPBI**, **TSP1**, and **TSP2** in $CH_2Cl_2$ ($\lambda_{ex} = 460$ nm for **rPBI**, 480 nm for **TSP1**, and 485 nm for **TSP2**); inset shows the chemical structure of **rPBI**. c) Photograph of **rPBI**, **TSP1**, and **TSP2** in $CH_2Cl_2$ under visible and UV (365 nm) light. d,e) CV and DPV measurements of **TSP1** (d) and **TSP2** (e) in $CH_2Cl_2$ ($C = 1$ mM) with $Bu_4NPF_6$ at 100 mV s$^{-1}$ scan rate.

duced ET direction from oligothiophene to PBI blocks mediated through the lowest energy excited states. The connection of the oligothiophene ring through oxygen to the PBI unit prevents electronic communication between the D-A units. Besides, the presence of two phenyl rings on PBI containing thiophene ring at the ortho position fails to delocalize the lobes all over the ring. The lack of CT bands in the absorption spectra (Figures 1a, S13) and the redox behavior of the macrocycles (Figure 1d,e) support the above observations.

To understand the orientation of the oligothiophene ring around the PBI, a single crystal of **TSP2** was grown from a $CH_2Cl_2$ : $CH_3OH$ mixture. The final structure of **TSP2** was confirmed by single-crystal X-ray analysis of the needle-like crystals (Figures 2c and S14–S16). The crystal structure of **TSP2** belongs to the triclinic $P\bar{1}$ space group containing one and a half molecules in the asymmetric unit.[56] Out of two molecules, one of them occupies a special position (inversion center; Figure S14). Most of the *n*-hexane moieties display thermal disorder due to conformational flexibility. The crystal structure shows that PBI is nearly perpendicular (ca. 80°) to the strapped oligothiophene ring. The thiophene core unit of the **TSP2** molecules, which occupies an inversion center, is more planar than the thiophene core unit of the other **TSP2** molecule, which is more twisted from the planarity. The crystal structure is stabilized by several
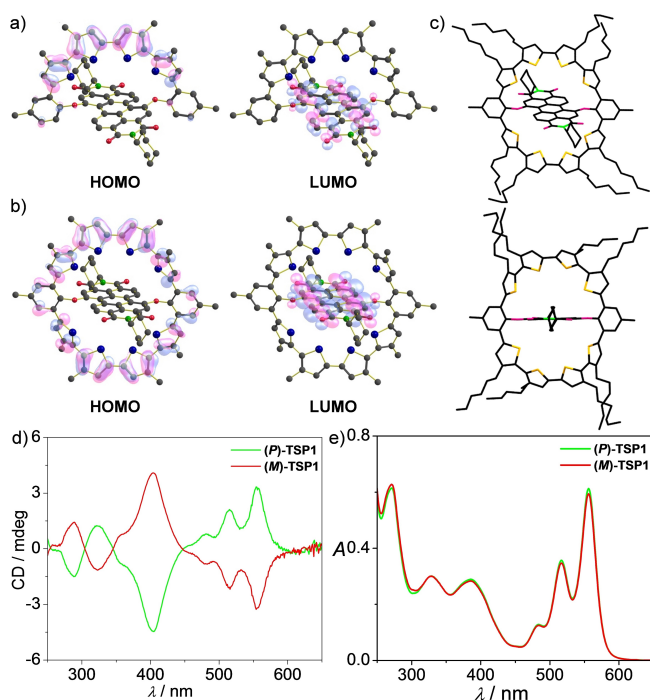
**Figure 2.** a,b) HOMO and LUMO of **TSP1** (a) and **TSP2** (b) based on geometry-optimized structures from DFT calculations; alkyl chains are replaced with methyl groups. c) Crystal structure of **TSP2** showing the individual molecule; hydrogen atoms are removed for clarity. d) CD and e) UV/Vis absorption spectra of **(P)-TSP1** and **(M)-TSP1** in CH$_2$Cl$_2$ ($C = 10^{-5}$ M).



**Figure 3.** a–c) Femtosecond transient absorption spectra of **TSP1** (a), **TSP2** (b), and **rPBI** (c) in CH$_2$Cl$_2$ after laser excitation at 460 nm. d) Comparative dynamic profiles of **TSP1** and **TSP2**, monitoring at 745 nm.

hydrogen-bonding interactions involving carbonyl groups of the PBI unit and H atoms of the thiophene unit (C–H⋯O, 2.474 Å, 144.5°; 2.573 Å, 167.9°). The crystal structure is also supported by several C–H⋯π contacts engaging alkyl chain C–H groups and the π-cloud of the thiophene moiety. The presence of these multiple noncovalent interactions was found to be the major driving force for extended molecular packing. As reported, strapped PBIs obtained through bay functionalization will result in *M* and *P* isomers,[36] as confirmed by the crystal structure of **TSP2**. Hence, enantiomer separation was attempted for both **TSP1** and **TSP2**. Only the racemic mixture of **(M)-TSP1** and **(P)-TSP1** isomers were successfully separated by semipreparative high-performance liquid chromatography (HPLC) on a chiral stationary phase using a mixture of *n*-hexane : isopropanol (95:5) as the eluent. The isomerically pure **(M)-TSP1** and **(P)-TSP1** were characterized by circular dichroism (CD) spectroscopy. The mirror image CD signals confirm the formation of atropisomers by **TSP1** (Figure 2d,e).

Transient absorption (TA) spectroscopy was employed to elucidate the excited-state dynamics in these systems. Figure 3a,b shows the TA spectra of **TSP1** and **TSP2**, respectively, following photoexcitation with 460 nm pump pulses probing in the visible region of the spectrum for a variety of pump–probe delay times ranging between 2.5 and 200 ps. Both spectra possess two closely placed photo-induced bleach features around 520 and 563 nm (Figure 3a–

c), resembling their peak positions in steady-state spectra. The 460 nm pump does not possess enough energy to excite the thiophene ring. Hence, these negative signatures must originate from the ground-state bleaching (GSB) of S$_0$–S$_n$ transitions in the PBI moiety of the macrocycle (**PBI***). Along with the presence of these GSB signatures, the spectra were dominated by the presence of a broad photo-induced absorption signal throughout the red regime peaking at around 750 nm. This spectrum is quite unique in nature and different from that of **rPBI** (Figure 3c). The TA spectra of **rPBI** are composed of a photoinduced bleach signal at 554 nm and a stimulated emission (SE) signature at 617 nm, along with a sharp positive feature at 705 nm. This positive signal necessarily arises from the photoinduced absorption of S$_1$ states. However, the positive features in **TSP1** and **TSP2** are quite broad and very different from the **rPBI** positive signature. This must originate from the formation of **PBI** radical anion in the macrocycle system (Figure S17).[57–60]

We monitored the dynamic profiles of these various features found in our systems to examine different plausible phenomena occurring in the macrocycle, such as photo-induced ET, separation of charge carriers, and formation of cationic/anionic species. These dynamic profiles were fitted with multiexponential time components (see Table S2). In Figure 3d, we have plotted the kinetic profiles of **TSP1** and **TSP2** monitoring at 745 nm (PBI radical anion position). The positive signal in the red region of the spectra may well be composed of excited state absorption of PBI*, but the signal would be primarily dominated by the PBI anion as the CS process is supposed to occur on a very fast time scale. On applying global fitting analysis, a short-lived SE signature appeared in the case of **TSP1** (Figure S18). It was associated with very fast decay (200 fs), and because of that, this feature was not noticed in the normal spectra plot. For

*Angew. Chem. Int. Ed.* **2023**, *62*, e202212934 (4 of 9)

© 2022 Wiley-VCH GmbH

**TSP2**, we could not locate any SE signature. These observations point to a very fast charge separation process in these macrocycles. In this case, the rise times were found to be enhanced from **TSP1** to **TSP2**, as well as their recovery dynamics. These growth time scales necessarily signify the charge separation process ($\tau_{CS}$).[52,57–60] From the multiexponential fitting, charge separation processes were found to be occurring on a time scale of 1.8 ps ($k_{CS} \approx 0.5 \times 10^{12}$ S$^{-1}$) and 3.1 ps ($k_{CS} \approx 0.3 \times 10^{12}$ S$^{-1}$) for **TSP1** and **TSP2**, respectively. The recovery of the radical anion in the **TSP2** system takes place at a much slower rate than that occurring in **TSP1**, indicating superior separation of charge in the closed cycle (Table S2). These data corroborate very well the dynamic change found in the case of GSB and confirm the separation of charge from **PBI*** (S1) to the **PBI** anionic state. The macrocyclic molecule, **TSP2**, allows extensive CS and would be a great contender for an organic photovoltaic material.

One of the attractions of the current design is the opportunity to functionalize the macrocycles further. The present oligothiophene-strapped PBI macrocycles **TSP1,2** can be used for the synthesis of monoimide–monoanhydride (**TSP1O** and **TSP2O**; Scheme 1) and dianhydride (**TSP2OO**) macrocycles (Scheme S2). Monoimide–monoanhydride macrocycles can be used to prepare linear dimer analogues, and dianhydride macrocycles can be used to make various types of 1D and 2D polymers (Schemes 1 and 2). To widen the scope of strapped PBIs, the corresponding monoimide–monoanhydrides were synthesized from **TSP1** and **TSP2** (Scheme 1). The formation of the anhydrides was characterized by $^1$H and $^{13}$C NMR spectroscopy, Fourier transform

infrared spectroscopy (FT-IR), and MALDI-TOF MS (Figure S19). The reaction of the monoimide–monoanhydride derivatives with benzene-1,4-diamine resulted in the corresponding dimers **TSP1D** and **TSP2D** (Scheme 1). The formation of dimers was confirmed by comparing the FT-IR spectra of the starting materials and the corresponding dimers (Figure S20). $^1$H NMR spectra of **TSP1,2** and the corresponding dimers showed marked differences and hence confirmed the formation of the latter (Figures 4a and S21). A singlet at 7.39 ppm corresponding to the middle phenyl ring connecting the two macrocycles pointed to the formation of **TSP2D** (Figure 4a). The structure of **TSP1D** and **TSP2D** was finally confirmed by extensive 2D NMR analysis (Figure S22–S29). Similar to **TSP1** and **TSP2**, the corresponding dimers also exhibit two reversible oxidation and reduction peaks in CV and DPV (Figures 4b,c, S30 and S31). Oxidation peaks at 0.52, 0.76 eV and 0.63, 0.96 eV and reduction peaks at −1.19, −1.40 eV and −1.22, −1.49 eV were observed, respectively, for **TSP1D** and **TSP2D**. Dimers exhibited only a slight red shift in absorption as compared to **TSP1,2**, and the emission remained quenched (Figures S32–S36). Such a coaxial D-A macrocycle dimer offers the possibility of one-dimensional polymers for efficient electron and hole transport.[7–10]

After noticing the importance of the full oligothiophene ring around the PBI unit to support ultrafast ET and stabilization of the CS state, a three-component 2D polymer **TSP-2DP** was synthesized using the dianhydride of **TSP2** (Scheme S2) and $N^I,N^I$-bis(4-aminophenyl)benzene-1,4-diamine (Scheme 2). Polymerization in the presence of Zn-
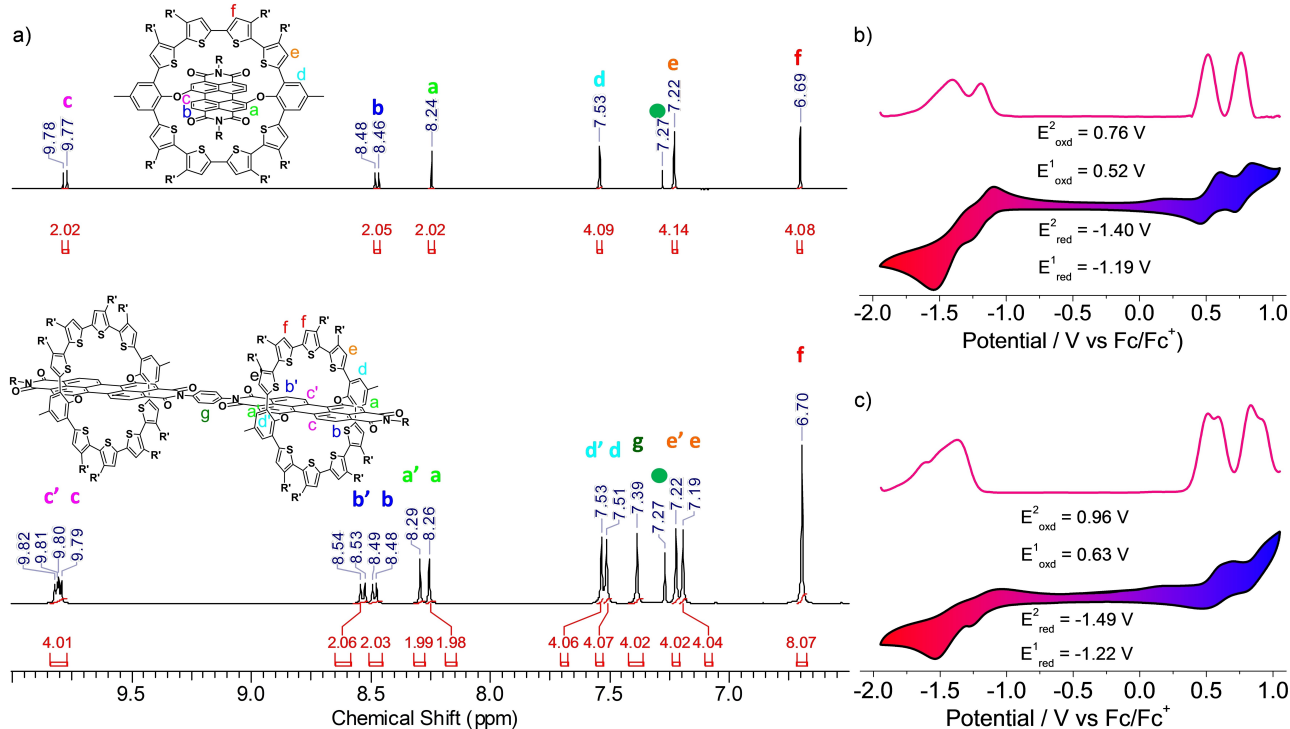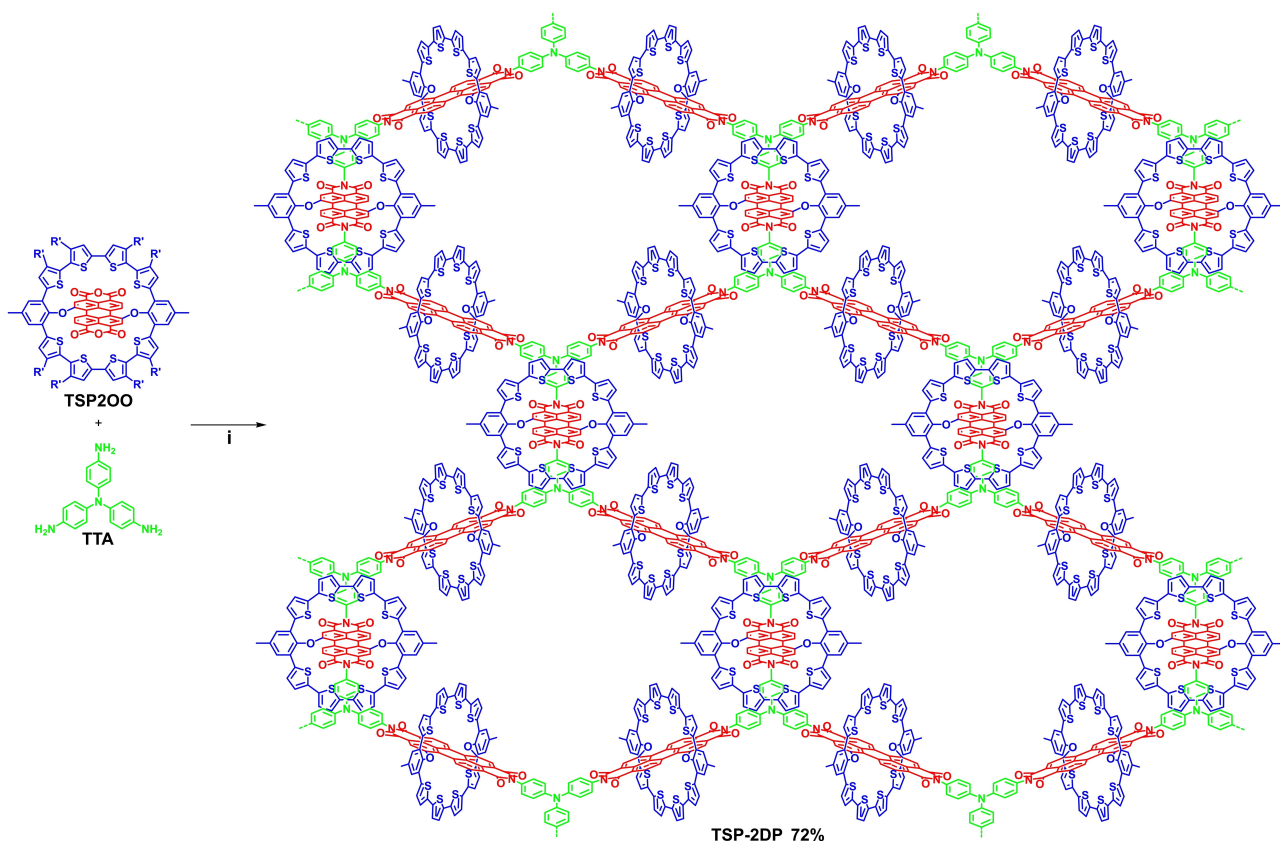


***Figure 4.*** a) Comparison of the $^1$H NMR spectra of **TSP2** and **TSP2D** in CDCl$_3$. b,c) CV and DPV measurements of **TSP1D** (b) and **TSP2D** (c) in CH$_2$Cl$_2$ ($C = 1$ mM) with Bu$_4$NPF$_6$ at 100 mV s$^{-1}$ scan rate.

**Scheme 2.** Synthesis of a 2D polymer of oligothiophene-ring-strapped PBI (alkyl chains of **TSP-2DP** have been removed for clarity): i) imidazole, Zn(OAc)₂, 160 °C, 48 h.

(OAc)₂ in imidazole started to precipitate **TSP-2DP** after 24 h, and the reaction was completed after 48 h. The formation of a 2D polymer was characterized by solid-state $^{13}$C cross-polarization magic angle spinning nuclear magnetic resonance ($^{13}$C CP-MAS NMR) spectroscopy, FT-IR, X-ray photoelectron spectroscopy (XPS), powder X-ray diffraction (PXRD), thermogravimetric analysis (TGA), CV, DPV, diffuse reflectance UV/Vis-NIR spectroscopy and morphological analyses (Figures 5a—c and S37–S45).[61] The formation of **TSP-2DP** was confirmed by the $^{13}$C CP-MAS NMR spectrum, which showed signals at 162.8 (C=O), 155.2 (C–O, carbon of PBI, and oxygen of phenyl ring), and 147.8 ppm (C–O/N, two different carbon atoms: one from (C–O) of the phenyl ring and another from (C–N) of triphenylamine) due to carbon atoms of PBI and triphenylamine (Figure 5a). Signals at 139.3, 129.9, and 122.7 ppm from the remaining aromatic rings and at 30.3, 23.1, and 14.1 ppm from the alkyl chains also substantiate the incorporation of both monomers in the 2D-polymer. A comparison of FT-IR spectra of **TSP-2DP** with the starting materials showed that the characteristic N–H stretching bands at 3410 and 3340 cm$^{-1}$ and N–H bending band at 3205 cm$^{-1}$ of $N^I,N^I$-bis(4-aminophenyl)benzene-1,4-diamine and C=O stretching bands at 1825, 1767, 1738 cm$^{-1}$ of the anhydride had disappeared, while intense new bands appeared at 1706 and 1671 cm$^{-1}$ (C=O), which can be assigned to vibrations of the imide carbonyl group (Figures 5b and S37). The disappear-ance of the characteristic peaks (marked in the box) suggested the complete consumption of monomers during 2D polymerization (Figure 5b). Transmission electron microscope (TEM) images of **TSP-2DP** suspended in CH₃OH revealed the presence of multilayer stacks of the 2D-polymer structure (Figures 5c and S42). This hints at extended 2D polymerization during the reaction and further stacking between the 2D-polymer layers.

Figure 5d presents the TA spectra of the polymeric **TSP-2DP** system, obtained following the photoexcitation by 460 nm pump pulses. The spectra resemble the signature of **TSP1** and **TSP2**. However, the GSB signals are now red-shifted, and the radical anion feature was also observed in the red wing of the spectra. The global fitting analysis revealed the presence of a short-lived SE signature for **TSP1D**, **TSP2D**, and **TSP-2DP** (Figure S46). In Figure 5e, we have compared the dynamic profile of this feature in three different macrocyclic systems, **TSP2**, **TSP2D**, and **TSP-2DP**. Interestingly, **TSP2** and **TSP2D** possess almost the same dynamics, and the only difference was the decreased growth time scale (Figure S47, Table S2). Hence, in the dimer system, the CS rate is increased. From multi-exponential fitting data, the CS time scales were calculated as $\tau_{CS} \approx 1.0$ ps ($k_{CS} \approx 1.0 \times 10^{12}$ S$^{-1}$) and 0.7 ps ($k_{CS} \approx 1.4 \times 10^{12}$ S$^{-1}$), respectively, for **TSP1D** and **TSP2D**. In the case of **TSP-2DP**, the CS rate was found to be highest ($\tau_{CS} \approx 0.1$ ps and $k_{CS} \approx 10 \times 10^{12}$ S$^{-1}$; Table S2). This high CS rate is

*Angew. Chem. Int. Ed.* **2023**, *62*, e202212934 (6 of 9)
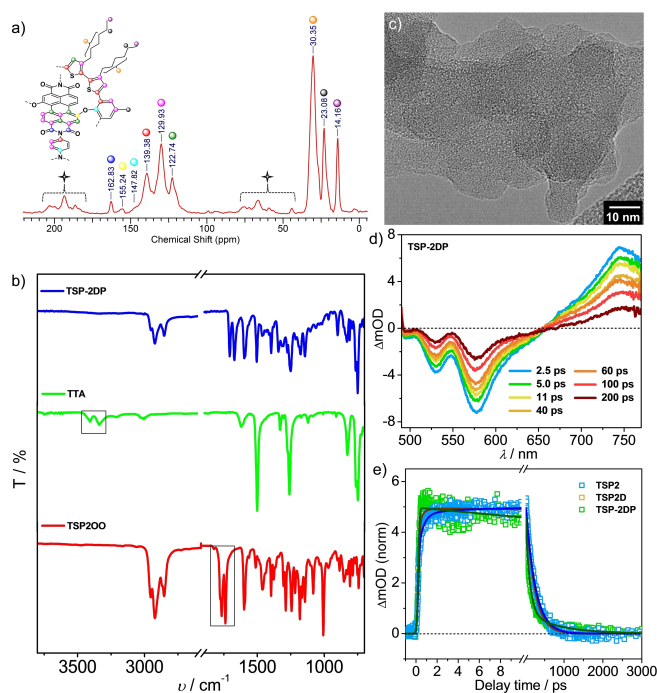
© 2022 Wiley-VCH GmbH

**Figure 5.** a) $^{13}$C CP-MAS NMR spectrum of **TSP-2DP**, asterisks denote spinning sidebands. b) Comparison of the FT-IR spectra of **TSP-2DP**, **TTA**, and **TSP2OO**. c) HR-TEM image of **TSP-2DP** suspended in CH$_3$OH. d) Femtosecond transient absorption spectra of **TSP-2DP** in CH$_3$OH after laser excitation at 460 nm. e) Comparative dynamic profiles of **TSP2**, **TSP2D**, and **TSP-2DP**, monitoring the PBI anionic signature at the red wing of the spectra.

attributed to the precise positioning of the D–A units and extreme interaction between donor and acceptor owing to close proximity. Interestingly, the recovery rate was found to be the slowest in this polymeric system. This **TSP-2DP** radical anion decays biexponentially with $\tau_{CR} \approx 105$ ps (87.9%) and 840 ps (12.1%) time components. Hence, **TSP-2DP** possesses not only the fastest CS but also the slowest recovery time among all macrocyclic systems (Figure 5d,e, Table S2). Figure S48 shows the correlation between the chemical structure of the macrocycles studied and the TA results.

As we moved from **TSP2** to **TSP2D** and to **TSP-2DP**, the CS time scale was changed from 3.1 to 0.7 and further to 0.1 ps, respectively, and recovery of the radical anion was significantly slowed down. This behavior can be attributed to the following factors: 1) The covalently linked donor–acceptor macrocycle in the dimer and 2D polymer converts the CS into an efficient intramolecular process in the individual macrocycle itself and thereby delays the charge recombination process. 2) The presence of spatially and electronically separated donor–acceptor units connected in series is most supportive in this process. 3) In the dimer and 2D polymer, the macrocycle connected by phenyl and triphenylamine units, respectively, imparts more rigidification than that of **TSP2**. The near-infrared part of the TA spectra supports radical cation formation (Figure S49) and

hence unambiguously confirms the reason for long-lived charge-separated states in TSP macrocyles (Table S2).[53,62]

The trends in the TA study indicate the vital supportive role of molecular design[63] in increasing the rate of the CS process and its stabilization as compared to similar dyads.[52,53] The macrocyclic dyad reported by Würthner and co-workers exhibited ultrafast ET within approximately 1 ps, however, with a fast charge recombination within 8–12 ps. The CS and charge recombination time scales of the TSP molecules were 3.1 and 0.1 ps, and 245.3 (100%) and 105 (87.9%), 840 ps (12.1%) for **TSP2** and **TSP-2DP**, respectively, when monitoring the radical anion peak of PBI (Table S2). Hence, a distinctly different photoinduced ET and stabilization of the CS state is displayed by the present TSP systems. The D–A macrocycle synthesized through bay functionalization of PBI using an oligothiophene ring connected through an electron-donating phenoxy group supersedes the similar one obtained through imide functionalization[52,53] in terms of fast electron transfer and long-lived CS.

## Conclusion

In conclusion, a new macrocycle with a PBI acceptor unit perpendicular to the strapped oligothiophene ring was synthesized and studied for its ET properties by TA. A nearly orthogonal orientation of the D–A units in the macrocycle, confirmed by single-crystal X-ray analysis, resulted in ultrafast ET and stabilization of the CS state for a longer duration than the previously reported oligothiophene ring strapped PBI through imide functionalization. The macrocycle design achieved by bay functionalization of PBI enabled the development of the corresponding linear dimer and 2D polymer. Precise positioning of the D–A units in the macrocycle prevents strong direct intermolecular interactions through π–π stacking and slows down the charge recombination process. Hence, the presence of a coaxial thiophene–PBI macrocycle along with a second triphenylamine donor in the three-component 2D polymer facilitates efficient CS and its stabilization. In short, molecular-design-assisted control over the excited-state CS and its stabilization was demonstrated. Such a nature-inspired synthetic route toward complex structures could lead to new materials for artificial photosynthesis and organic electronics.

## Acknowledgements

*Angew. Chem. Int. Ed.* **2023**, *62*, e202212934 (7 of 9)

© 2022 Wiley-VCH GmbH

## Conflict of Interest

The authors declare no conflict of interest.

## Data Availability Statement

The data that support the findings of this study are available in the Supporting Information of this article.

[1] R. J. Cogdell, A. Gall, J. Köhler, *Q. Rev. Biophys.* **2006**, *39*, 227–324.

[2] K. N. Ferreira, T. M. Iverson, K. Maghlaoui, J. Barber, S. Iwata, *Science* **2004**, *303*, 1831–1838.

[3] D. M. Guldi, *J. Phys. Chem. B* **2005**, *109*, 11432–11441.

[4] A. A. Bakulin, A. Rao, V. G. Pavelyev, P. H. M. van Loosdrecht, M. S. Pshenichnikov, D. Niedzialek, J. Cornil, D. Beljonne, R. H. Friend, *Science* **2012**, *335*, 1340–1344.

[5] L. Giribabu, A. A. Kumar, V. Neeraja, B. G. Maiya, *Angew. Chem. Int. Ed.* **2001**, *40*, 3621–3624; *Angew. Chem.* **2001**, *113*, 3733–3736.

[6] C. Wiebeler, F. Plasser, G. J. Hedley, A. Ruseckas, I. D. W. Samuel, S. Schumacher, *J. Phys. Chem. Lett.* **2017**, *8*, 1086–1092.

[7] S. Prasanthkumar, S. Ghosh, V. C. Nair, A. Saeki, S. Seki, A. Ajayaghosh, *Angew. Chem. Int. Ed.* **2015**, *54*, 946–950; *Angew. Chem.* **2015**, *127*, 960–964.

[8] J. López-Andarias, M. J. Rodriguez, C. Atienza, J. L. López, T. Mikie, S. Casado, S. Seki, J. L. Carrascosa, N. Martín, *J. Am. Chem. Soc.* **2015**, *137*, 893–897.

[9] D. Ley, C. X. Guzman, K. H. Adolfsson, A. M. Scott, A. B. Braunschweig, *J. Am. Chem. Soc.* **2014**, *136*, 7809–7812.

[10] Y.-L. Wu, K. E. Brown, M. R. Wasielewski, *J. Am. Chem. Soc.* **2013**, *135*, 13322–13325.

[11] M. R. Wasielewski, *Acc. Chem. Res.* **2009**, *42*, 1910–1921.

[12] E. Krieg, A. Niazov-Elkan, E. Cohen, Y. Tsarfati, B. Rybtchinski, *Acc. Chem. Res.* **2019**, *52*, 2634–2646.

[13] F. Würthner, C. R. Saha-Möller, B. Fimmel, S. Ogi, P. Leowanawat, D. Schmidt, *Chem. Rev.* **2016**, *116*, 962–1052.

[14] S. Chen, P. Slattum, C. Wang, L. Zang, *Chem. Rev.* **2015**, *115*, 11967–11998.

[15] T. Seki, X. Lin, S. Yagai, *Asian J. Org. Chem.* **2013**, *2*, 708–724.

[16] T. Weil, T. Vosch, J. Hofkens, K. Peneva, K. Müllen, *Angew. Chem. Int. Ed.* **2010**, *49*, 9068–9093; *Angew. Chem.* **2010**, *122*, 9252–9278.

[17] "Perylenes in Organic Photovoltaics": C. Li, K. Müllen in *Eco- and Renewable Energy Materials* (Ed.: Y. Zhou), Springer, Berlin, **2013**.

[18] M. Ogasawara, X. Lin, H. Kurata, H. Ouchi, M. Yamauchi, T. Ohba, T. Kajitani, T. Fukushima, M. Numata, R. Nogami, B. Adhikari, S. Yagai, *Mater. Chem. Front.* **2018**, *2*, 171–179.

[19] R. Sethy, J. Kumar, R. Métivier, M. Louis, K. Nakatani, N. M. T. Mecheri, A. Subhakumari, K. G. Thomas, T. Kawai, T. Nakashima, *Angew. Chem. Int. Ed.* **2017**, *56*, 15053–15057; *Angew. Chem.* **2017**, *129*, 15249–15253.

[20] W. Wagner, M. Wehner, V. Stepanenko, S. Ogi, F. Würthner, *Angew. Chem. Int. Ed.* **2017**, *56*, 16008–16012; *Angew. Chem.* **2017**, *129*, 16224–16228.

[21] C. Roche, H.-J. Sun, P. Leowanawat, F. Araoka, B. E. Partridge, M. Peterca, D. A. Wilson, M. E. Prendergast, P. A. Heiney, R. Graf, H. W. Spiess, X. Zeng, G. Ungar, V. A. Percec, *Nat. Chem.* **2016**, *8*, 80–89.

[22] X. Zhang, S. Rehm, M. M. Safont-Sempere, F. Würthner, *Nat. Chem.* **2009**, *1*, 623–629.

[23] S. Yagai, T. Seki, T. Karatsu, A. Kitamura, F. Würthner, *Angew. Chem. Int. Ed.* **2008**, *47*, 3367–3371; *Angew. Chem.* **2008**, *120*, 3415–3419.

[24] P. Cheng, G. Li, X. Zhan, Y. Yang, *Nat. Photonics* **2018**, *12*, 131–142.

[25] C. Wang, F. N. Miros, J. Mareda, N. Sakai, S. Matile, *Angew. Chem. Int. Ed.* **2016**, *55*, 14422–14426; *Angew. Chem.* **2016**, *128*, 14634–14638.

[26] D. Liu, J. Wang, X. Bai, R. Zong, Y. Zhu, *Adv. Mater.* **2016**, *28*, 7284–7290.

[27] S. Kaloyanova, Y. Zagranyarski, S. Ritz, M. Hanulová, K. Koynov, A. Vonderheit, K. Müllen, K. Peneva, *J. Am. Chem. Soc.* **2016**, *138*, 2881–2884.

[28] P. D. Frischmann, Y. Hwa, E. J. Cairns, B. A. Helms, *Chem. Mater.* **2016**, *28*, 7414–7421.

[29] J. M. Mativetsky, E. Orgiu, I. Lieberwirth, W. Pisula, P. Samorì, *Adv. Mater.* **2014**, *26*, 430–435.

[30] X. Zhan, A. Facchetti, S. Barlow, T. J. Marks, M. A. Ratner, M. R. Wasielewski, S. R. Marder, *Adv. Mater.* **2011**, *23*, 268–284.

[31] M. Bonchio, Z. Syrgiannis, M. Burian, N. Marino, E. Pizzolato, K. Dirian, F. Rigodanza, G. A. Volpato, G. L. Ganga, N. Demitri, S. Berardi, H. Amenitsch, D. M. Guldi, S. Caramori, C. A. Bignozzi, A. Sartorel, M. Prato, *Nat. Chem.* **2019**, *11*, 146–153.

[32] C. E. Ramirez, S. Chen, N. E. Powers-Riggs, I. Schlesinger, R. M. Young, M. R. Wasielewski, *J. Am. Chem. Soc.* **2020**, *142*, 18243–18250.

[33] D. Schmidt, M. Stolte, J. Süß, A. Liess, V. Stepanenko, F. Würthner, *Angew. Chem. Int. Ed.* **2019**, *58*, 13385–13389; *Angew. Chem.* **2019**, *131*, 13519–13523.

[34] B. Zhang, H. Soleimaninejad, D. J. Jones, J. M. White, K. P. Ghiggino, T. A. Smith, W. W. H. Wong, *Chem. Mater.* **2017**, *29*, 8395–8403.

[35] Á. J. Jiménez, M.-J. Lin, C. Burschka, J. Becker, V. Settels, B. Engels, F. Würthner, *Chem. Sci.* **2014**, *5*, 608–619.

[36] P. Osswald, F. Würthner, *Chem. Eur. J.* **2007**, *13*, 7395–7409.

[37] E. Sebastian, M. Hariharan, *J. Am. Chem. Soc.* **2021**, *143*, 13769–13781.

[38] V. Strauss, J. T. Margraf, K. Dirian, Z. Syrgiannis, M. Prato, C. Wessendorf, A. Hirsch, T. Clark, D. M. Guldi, *Angew. Chem. Int. Ed.* **2015**, *54*, 8292–8297; *Angew. Chem.* **2015**, *127*, 8410–8415.

[39] C. Schmidt, F. Hauke, M. Prato, A. Hirsch, D. M. Guldi, *J. Am. Chem. Soc.* **2011**, *133*, 4580–4586.

[40] M. Ball, B. Zhang, Y. Zhong, B. Fowler, S. Xiao, F. Ng, M. Steigerwald, C. Nuckolls, *Acc. Chem. Res.* **2019**, *52*, 1068–1078.

[41] M. Sapotta, A. Hofmann, D. Bialas, F. Würthner, *Angew. Chem. Int. Ed.* **2019**, *58*, 3516–3520; *Angew. Chem.* **2019**, *131*, 3554–3558.

[42] P. Spenst, R. M. Young, B. T. Phelan, M. Keller, J. Dostál, T. Brixner, M. R. Wasielewski, F. Würthner, *J. Am. Chem. Soc.* **2017**, *139*, 2014–2021.

[43] P. Spenst, F. Würthner, *Angew. Chem. Int. Ed.* **2015**, *54*, 10165–10168; *Angew. Chem.* **2015**, *127*, 10303–10306.

[44] Y. Wu, R. M. Young, M. Frasconi, S. T. Schneebeli, P. Spenst, D. M. Gardner, K. E. Brown, F. Würthner, J. F. Stoddart, M. R. Wasielewski, *J. Am. Chem. Soc.* **2015**, *137*, 13236–13239.

[45] F. Schlosser, J. Sung, P. Kim, D. Kim, F. Würthner, *Chem. Sci.* **2012**, *3*, 2778–2785.

[46] M. Hecht, T. Schlossarek, M. Stolte, M. Lehmann, F. Würthner, *Angew. Chem. Int. Ed.* **2019**, *58*, 12979–12983; *Angew. Chem.* **2019**, *131*, 13113–13117.

[47] J. L. Segura, H. Herrera, P. Bäuerle, *J. Mater. Chem.* **2012**, *22*, 8717–8733.

[48] H. Wonneberger, C.-Q. Ma, M. A. Gatys, C. Li, P. Bäuerle, K. Müllen, *J. Phys. Chem. B* **2010**, *114*, 14343–14347.

[49] C.-C. You, P. Espindola, C. Hippius, J. Heinze, F. Würthner, *Adv. Funct. Mater.* **2007**, *17*, 3764–3772.

[50] M. L. Ball, B. Zhang, Q. Xu, D. W. Paley, V. C. Ritter, F. Ng, M. L. Steigerwald, C. Nuckolls, *J. Am. Chem. Soc.* **2018**, *140*, 10135–10139.

[51] M. Ball, B. Fowler, P. Li, L. A. Joyce, F. Li, T. Liu, D. Paley, Y. Zhong, H. Li, S. Xiao, F. Ng, M. L. Steigerwald, C. Nuckolls, *J. Am. Chem. Soc.* **2015**, *137*, 9982–9987.

[52] K. Bold, M. Stolte, K. Shoyama, M. Holzapfel, A. Schmiedel, C. Lambert, F. Würthner, *Angew. Chem. Int. Ed.* **2022**, *61*, e202113598; *Angew. Chem.* **2022**, *134*, e202113598.

[53] K. Bold, M. Stolte, K. Shoyama, A.-M. Krause, A. Schmiedel, M. Holzapfel, C. Lambert, F. Würthner, *Chem. Eur. J.* **2022**, *28*, e202200355.

[54] C. Pan, C. Zhao, M. Takeuchi, K. Sugiyasu, *Chem. Asian J.* **2015**, *10*, 1820–1835.

[55] T. M. Swager, *Acc. Chem. Res.* **2008**, *41*, 1181–1189.

[56] Deposition Number 2166196 (for **TSP2**) contains the supplementary crystallographic data for this paper. These data are provided free of charge by the joint Cambridge Crystallographic Data Centre and Fachinformationszentrum Karlsruhe Access Structures service.

[57] N. Pearce, K. E. A. Reynolds, S. Kayal, X. Z. Sun, E. S. Davies, F. Malagreca, C. J. Schürmann, S. Ito, A. Yamano, S. P. Argent, M. W. George, N. R. Champness, *Nat. Commun.* **2022**, *13*, 415.

[58] T. W. Kim, S. Jun, Y. Ha, R. K. Yadav, A. Kumar, C.-Y. Yoo, I. Oh, H.-K. Lim, J. W. Shin, R. Ryoo, H. Kim, J. Kim, J.-O. Baeg, H. Ihee, *Nat. Commun.* **2019**, *10*, 1873.

[59] R. F. Kelley, W. S. Shin, B. Rybtchinski, L. E. Sinks, M. R. Wasielewski, *J. Am. Chem. Soc.* **2007**, *129*, 3173–3181.

[60] M. Fujitsuka, K. Harada, A. Sugimoto, T. Majima, *J. Phys. Chem. A* **2008**, *112*, 10193–10199.

[61] V. C. Wakchaure, A. Kottaichamy, A. Nidhankar, K. C. Ranjeesh, M. Nazrulla, M. Thotiyl, S. S. Babu, *ACS Appl. Energy Mater.* **2020**, *3*, 6352–6359.

[62] R. Renner, M. Stolte, J. Heitmüller, T. Brixner, C. Lambert, F. Würthner, *Mater. Horiz.* **2022**, *9*, 350–359.

[63] J. Sukegawa, C. Schubert, X. Zhu, H. Tsuji, D. M. Guldi, E. Nakamura, *Nat. Chem.* **2014**, *6*, 899–905.

CCS CHINESE CHEMICAL SOCIETY | SIOC 1950 | ROYAL SOCIETY OF CHEMISTRY

## RESEARCH ARTICLE

Check for updates

# A donor strapped perylene bisimide macrocycle and its lemniscate dimer with extended charge separation†

Sairam Dnyaneshwar Veer,[a,b] Tanmay Goswami,[e] Sapna Ravindranathan,[b,c] Rajesh Gonnade, [ID][b,d] Nitika Kharbanda,[e] Hirendra N. Ghosh [ID] *[e,f] and Sukumaran Santhosh Babu [ID] *[a,b]

Macrocyclic structures are fascinating due to their unique design and capability to place chromophores in specific orientations, resulting in exciting optoelectronic properties. However, the synthetic challenges limit the broad exploration of such systems. Herein, we report a thiophene–diacetylene-based ring strapped perylene bisimide macrocycle and its notably different electron transfer features. Single-crystal analysis of the macrocycle pointed to the nearly orthogonal placement of donor–acceptor units, facilitating better electronic communication between them. Interestingly, introduction of an alkyl substituent on the peripheral thiophene ring opened the possibility of forming a higher oligomer macrocycle consisting of two strapped perylene bisimide units. Diffusion and two-dimensional NMR experiments provided insight into the structure of the figure-eight-shaped lemniscate dimer. Transient absorption measurements showed faster electron transfer and extended stabilization of the charge-separated state. The thiophene–diacetylene-based ring is a better donor unit to facilitate rapid electron transfer and extended charge separation in the macrocycle and its lemniscate dimer. The new macrocycle design enables the formation of higher analogs equally capable of stabilizing the charge-separated state.

## Introduction

The natural photosynthetic system where chlorophyll molecules are organized in an orderly pattern to ensure effective light harvesting and redox reactions is a perfect example of light-harvesting complexes with multiprotein assemblies and macrocyclic structures.[1–5] Inspired by this ideal concept, researchers have attempted to create various multicomponent π-conjugated systems. Such macrocyclic arrays have attracted significant interest due to their promising capability to efficiently collect solar energy and transform it into chemical, electrical, or other forms of energy.[6–9] Although there have been many synthetic structural resemblances of light-harvesting assemblies, it has only rarely been thought of to use focused and channeled excitation energy.[10–12] In this direction, there has been a lot of interest in chromophores that can harvest light and create long-lived charge-separated states using molecular assemblies, particularly macrocycles consisting of suitably placed donor and acceptor units.[13,14] A variety of macrocyclic arrays based on porphyrins,[15,16] oligothiophenes,[17,18] BODIPY,[19,20] carbazoles,[21,22] and perylene bisimides (PBIs)[6,23] have been used as light-absorbing components in macrocycles.

PBI is one of the most distinctly studied fluorescent dyes among organic materials.[24,25] Moreover, PBIs are indeed preferred chromophores due to their excellent chemical and thermal stability, a wide spectrum of visible light absorption, and distinctive electrochemical properties.[7,26–28] The chemical functionalization of PBIs is possible at many positions, including the imide-, *ortho*-, and bay positions.[27,28] However, since the imide nitrogen atoms of PBI act as the nodes of frontier orbitals, linking PBI units through these nitrogen atoms would not disrupt the PBI frontier orbitals.[26–28] On the other hand, introducing new substituents at the bay positions of PBI has

*a Organic Chemistry Division, National Chemical Laboratory (CSIR-NCL), Dr Homi Bhabha Road, Pune-411 008, India. E-mail: sb.sukumaran@ncl.res.in*
*b Academy of Scientific and Innovative Research (AcSIR), Ghaziabad-201 002, India*
*c Central NMR Facility, National Chemical Laboratory (CSIR-NCL), Dr Homi Bhabha Road, Pune-411008, India*
*d Physical and Materials Chemistry Division, National Chemical Laboratory (CSIR-NCL), Dr Homi Bhabha Road, Pune-411 008, India*
*e Institute of Nanoscience and Nanotechnology (INST), Sector 81, Mohali-140306, Punjab, India*
*f Radiation and Photochemistry Division, Bhabha Atomic Research Centre, Mumbai 400085, India*
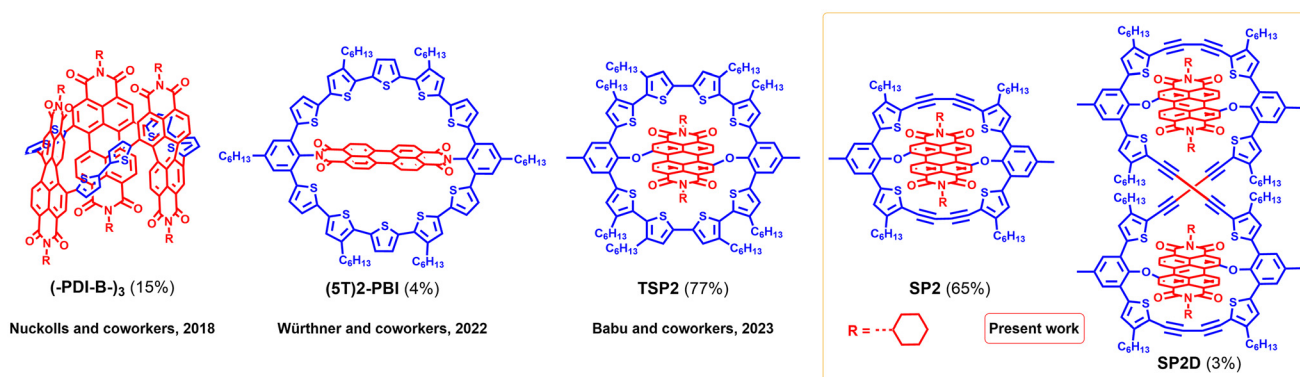
**Chart 1** Examples of thiophene and PBI-based donor–acceptor macrocycles such as a capsule-shaped bithiophene-PBI macrocycle (2018), an oligothiophene strapped PBI macrocycle functionalized *via* the imide position of PBI (2021), and an oligothiophene (2023), and the present work on diacetylene–thiophene strapped PBIs functionalized *via* the bay position of the PBI.

shown to be successful in changing the frontier orbital levels. Besides, specific substituents at the bay position facilitate easy tuning of the optoelectronic characteristics, making them ideal for light harvesting and luminescent applications.[29,30] Nuckolls and coworkers previously reported that PBI-based cyclic conjugated macrocycles generate substantially higher photocurrent than acyclic analogs (Chart 1).[31] In 2021, the research group of Würthner reported a completely strapped donor–acceptor PBI through the imide position exhibiting ultrafast electron transfer (Chart 1).[32] Moreover, a considerable number of α-conjugated macrocyclic oligothiophenes containing various cyclo(*n*)thiophenes have been reported through the thiophene–acetylene linkage developed by Bäuerle and coworkers.[17,18] Recently, our group also reported another oligothiophene strapped PBI, functionalized at the bay position

*via* an oxidative coupling reaction, along with the corresponding linear dimer and a 2D polymer (Chart 1).[33] We aimed to develop macrocyclic donor–acceptor systems with extended charge separation (CS) and stabilization. In this work, we demonstrate another straightforward approach with acetylene chemistry,[34] which allows easily achievable covalently bonded, rigid macrocyclic scaffolds. The unique design consists of rigid donor–acceptor units oriented nearly orthogonal to each other for improved CS. Most importantly, the Hay–Glaser coupling reaction yields diacetylene–thiophene-strapped PBIs (**SP1** and **2**) in good yields and opens up the possibility of generating a dimer (**SP2D**) and higher analogs (Chart 1, Scheme 1 and S3†). The present study describes the rational design, synthesis, and electron transfer properties of new donor–acceptor macrocycles.
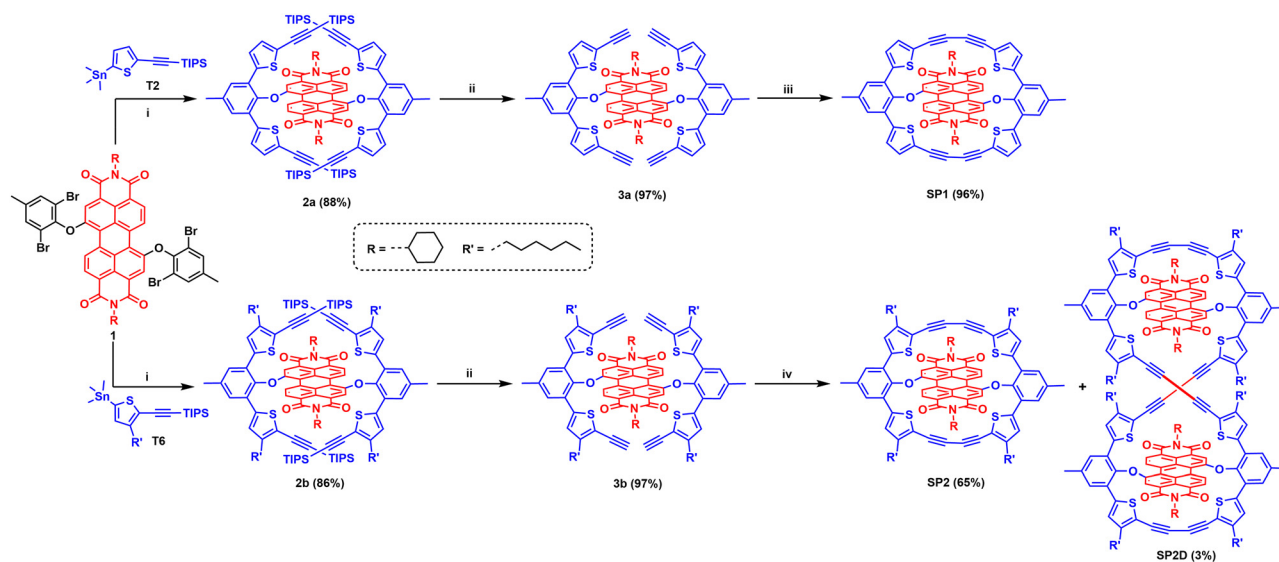


**Scheme 1** Synthesis of diacetylene–thiophene strapped PBIs. (i) Pd(PPh₃)₂Cl₂, toluene, 140 °C, 12 h, (ii) TBAF, THF, RT, 15 min, (iii) TMEDA, CuCl, THF, RT, 6 h, and (iv) TMEDA, CuCl, THF, RT, 12 h.

# Results and discussion

Strapped PBI molecules are synthesized through a series of reactions, including aromatic nucleophilic substitution and the Stille, Sonogashira, and Hay–Glaser coupling reactions (Scheme 1). *N,N′*-Dicyclohexyl-1,7-bis(2,6-dibromo-4-methyl-phenoxy)peril-ene-3,4:9,10-bisdicarboximide (**1**) was synthesized by adopting a previously reported procedure (72%).[33] The reaction of 1 with T2 (Scheme S1†) without an alkyl chain on the thiophene-delivered molecule **2a** in 88% yield (Scheme 1). Cleavage of the triisopropylsilyl group of **2a** using tetrabutylammonium fluoride delivered the free acetylene molecule **3a**, which is less stable under ambient conditions. Hence, we proceeded further with the crude product for the Hay–Glaser coupling reaction in the presence of CuCl and TMEDA in tetrahydrofuran in high dilution at room temperature resulting in the strapped PBI derivative **SP1** (Scheme 1).

The Hey–Glaser coupling reaction of **3a** exclusively yielded **SP1** in 96% yield within 6 h without purification. However, **SP1** is less soluble in common organic solvents, and the suspension obtained in many solvents after ultrasound sonication settles down immediately. Hence, we coupled **1** with the **T6** derivative (Scheme S2†) with an alkyl chain on the thiophene to yield product **2b** and, subsequently, product **3b**. In the case of **3b**, the subsequent reaction was slowed to 12 h for complete conversion to yield **SP2** in 65% (Scheme 1), whereas the rate of the reaction from **3a** to **SP1** seems faster than that from **3b** to **SP2** product formation. Interestingly, we also observed the formation of a dimer **SP2D** in a very low yield (3%), trimer **SP2T**, and tetramer **SP2TT** in trace amounts exclusively when **3b** was used (Scheme 1 and S4†). Both trimer **SP2T** and tetramer **SP2TT** were only characterized by MALDI-TOF-MS. Since dimer to tetramer formation is achieved only by **3b**, the presence of an alkyl chain on the thiophene ring plays a critical role in forming higher analogs.

We compared the infrared spectra of **SP1, 2,** and **SP2D** with those of **2a, 2b, 3a,** and **3b** to monitor the formation of diacetylene between the thiophene rings (Fig. S1 and 2†). The typical terminal alkyne (–C≡C–H) stretching frequency of **3a** and **3b** at 3103 cm$^{-1}$ and 3306 cm$^{-1}$, respectively, disappeared in **SP1, 2,** and **SP2D**. This indicates the complete consumption of terminal acetylene in **3a** and **3b**. The alkyne (–C≡C–) vibration of **3a** and **3b** was observed at 2203 cm$^{-1}$ and 2100 cm$^{-1}$, whereas the stretching frequency of the Hay–Glaser coupled symmetric and asymmetric alkynes (–C≡C–) was noticed at 2155 cm$^{-1}$ and 2108 cm$^{-1}$ for **SP1**, 2165 cm$^{-1}$ and 2130 cm$^{-1}$ for **SP2** and 2150 cm$^{-1}$ and 2102 cm$^{-1}$ for **SP2D**, respectively (Fig. S2†).[35] Furthermore, all the pure products were confirmed by $^1$H NMR, $^{13}$C NMR, and FT-IR spectroscopy, and MALDI-TOF spectrometry. Since **SP1** exhibits limited solubility in common organic solvents, we proceeded with **SP2** and **SP2D** for further detailed analysis.

Absorption and emission of molecules **SP2** and **SP2D** were recorded in CH$_2$Cl$_2$ (Fig. 1a, b, and Table S1†). Normalized absorption spectra showed an ∼19 nm red shift in the absorption maximum from **rPBI**[33] to **SP2** (Fig. 1a and S3†). A similar
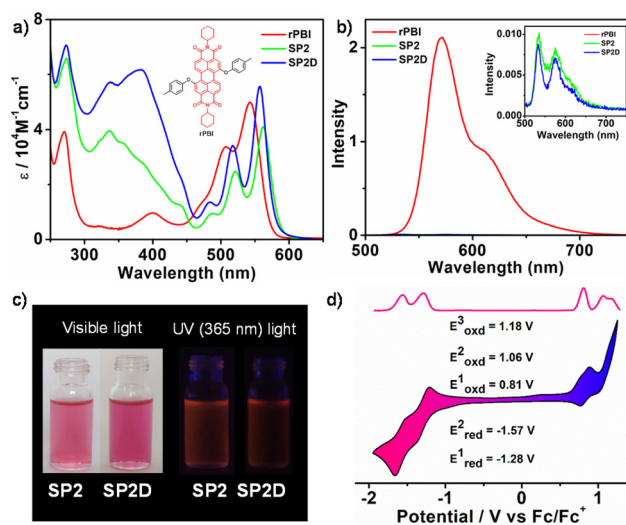


**Fig. 1** (a) Absorption and (b) normalized emission spectra of **rPBI**, **SP2**, and **SP2D** in CH$_2$Cl$_2$. Insets show (a) the chemical structure of **rPBI** and (b) the emission spectra of **SP2** and **SP2D** alone. (c) Photographs of **SP2** and **SP2D** in CH$_2$Cl$_2$ under visible (left) and UV (365 nm) (right) light. (d) CV of **SP2** in CH$_2$Cl$_2$ (*c* = 1 mM).

red shift was noticed in the case of molecule **TSP2** (Fig. 1) as well and is due to the bay functionalization of PBI.[33] The dimer **SP2D** also retained almost the same red shift (∼15 nm) in absorption maximum compared to **rPBI**. The emission of **SP2** and **SP2D** is completely quenched in CH$_2$Cl$_2$, and the intensity varies with solvent polarity (Fig. 1b and c and S4–7†). The emission quantum yield decreased from **rPBI** (74%) to **SP2** (11%) and **SP2D** (8%) in CH$_2$Cl$_2$ solution (Table S3†). **SP2** exhibited slightly higher emission intensity in CCl$_4$ and *p*-xylene, and emission was negligibly low in the rest of the solvents (Fig. S6†). The variation observed in the visible color and fluorescence intensity of **SP2** in different solvents is shown in Fig. S7.† The normalized spectra of **SP2** and **SP2D** showed no shift in emission maxima, indicating no noticeable spectral change upon dimer formation (Fig. 1b). When we monitored the fluorescence lifetime, the long-lived component was increased from **rPBI** (5.1 ns (100%)) to **SP2** (6.7 ns (30%) and 3.3 ns (70%)) and **SP2D** (8.7 ns (26%) and 3.2 ns (74%)) (Fig. S8 and Table S2†). The electrochemical property of **SP2** was investigated using cyclic voltammetry (CV) and differential pulse voltammetry (DPV). These experiments were carried out in CH$_2$Cl$_2$ (*c* = 1 mM) using Bu$_4$NPF$_6$ as the supporting electrolyte. CV and DPV of **SP2** and **SP2D** in CH$_2$Cl$_2$ displayed two reversible reduction and three reversible oxidation processes with half-wave reduction potentials ($E_{1/2}^{\text{red}}$) of −1.28/−1.57 V and −1.26/−1.53 V, respectively, and half-wave oxidation potentials ($E_{1/2}^{\text{ox}}$) of +0.81/+1.06/+1.18 V and +0.75/+1.07/+1.19 V, respectively (Fig. 1d, S9, S10, and Table S1†). The observed reduction potentials are slightly shifted to the negative potential compared to **rPBI**.[33] In order to understand the difference in the reactivity of **3a** and **3b**, crystallization of **2a** and **2b** was attempted from the solvent mixtures CH$_2$Cl$_2$ : MeOH (v/v;
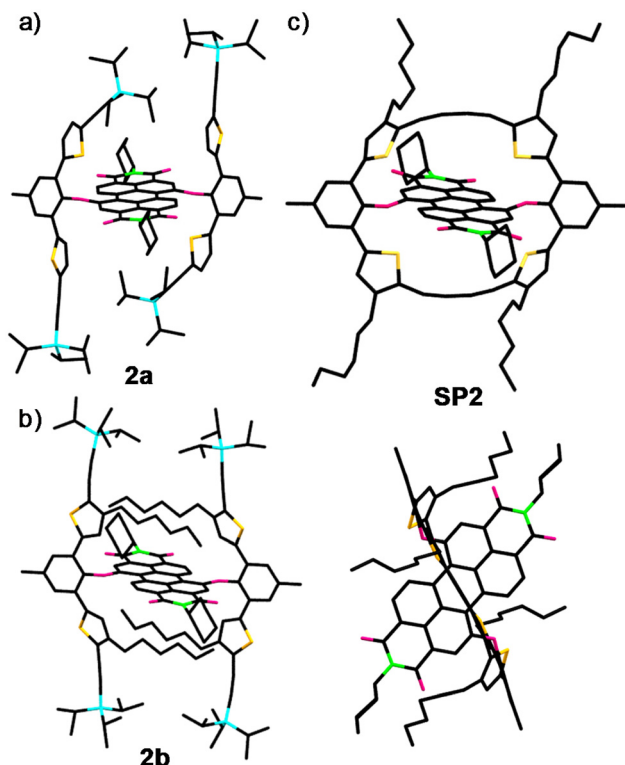
**Fig. 2** Crystal structure of (a) **2a**, (b) **2b**, and (c) **SP2**. Hydrogen atoms are removed for clarity.

50 : 50) and $CH_2Cl_2$ : $n$-hexane (v/v; 50 : 50), respectively. The single crystal structure of **2a** (CCDC 2247679†) and **2b** (CCDC 2247688†) showed a marked difference in the orientation of the thiophene arm containing TIPS acetylene moieties. In **2a**, the absence of an alkyl chain on the thiophene ring enabled the orientation of the arms in a supportive way for ring closure using a diacetylene linkage (Fig. 2a and S11†).

However, in **2b**, the presence of an additional $C_6$-alkyl chain on the thiophene moiety changed the orientation of the thiophene rings. Interestingly, all four thiophene rings protrude outwards (Fig. 2b and S12†). It could be due to the hydrophobic interactions between the alkyl chains, which are stacked over each other. The methylene groups on the alkyl chains also participate in a marginal C–H⋯π interaction involving the central PBI moiety. These supramolecular interactions seem to be stabilizing the crystal structure. Such outward orientation of thiophene moieties could slow the macrocyclization of **SP2**, resulting in the formation of the corresponding dimer **SP2D** and higher analogs, trimer **SP2T**, and tetramer **SP2TT**.

The crystal structure of **SP2** (CCDC 2247690†) is confirmed by single crystal structure analysis. Needles of **SP2** were grown from the mixture of solvents, $CHCl_3$ : MeOH (v/v, 50 : 50) (Fig. 2c). The intramolecular geometry of **SP2** revealed that the **PBI** unit is perpendicular (86.38°) to the strapped thiophene ring (Fig. 2c). The presence of hydrogen bonding, >C=O⋯H, between adjacent PBI units parallel to the $a$-axis generates a one-dimensional molecular string comprising **SP2** molecules (Fig. S13 and 14†). The adjacent 1D strings are connected along the $b$-axis using >C=O⋯H hydrogen bonds involving
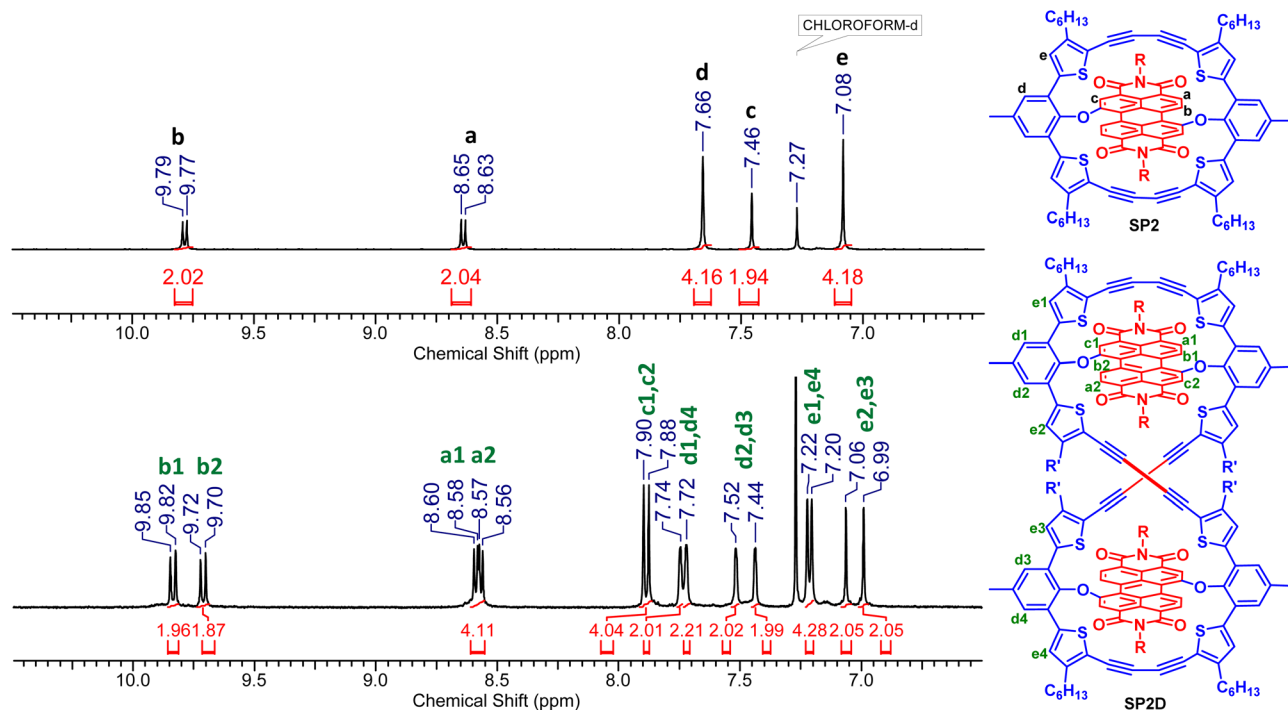


**Fig. 3** Comparison of the aromatic region of the $^1$H NMR spectra of **SP2** and **SP2D**.

>C=O of PBIs and H atoms of the macrocycle unit to form a compact packing on the *ab* plane.

A comparison of the $^1$H NMR spectra of **SP2** and **SP2D** showed a doubling of signals from the PBI unit in **SP2D** (Fig. 3, S15 and 16†). The aromatic signals from the thiophene–diacetylene unit showed further splitting of signals indicating molecular symmetry breaking during dimer formation. Extra signals resulting from dimerization were also observed in the $^{13}$C NMR spectra (Fig. S17–19†). Dimer formation was confirmed by comparing the diffusion-ordered

spectra of **SP2** and **SP2D** measured under identical conditions (Fig. 4a). The diffusion of **SP2D** is almost twice as slow as that of **SP2**, as expected for a dimer (Fig. 4a). On the other hand, the solvent diffusion coefficient did not change significantly, indicating identical conditions in the two measurements. Dimer formation results in distinct environments for both alkyl and aromatic protons. Correlations observed in total correlation spectroscopy (TOCSY) clearly showed distinct connectivities between protons belonging to different environments observed in the dimer (Fig. 4b, S20 and 21†). This was further
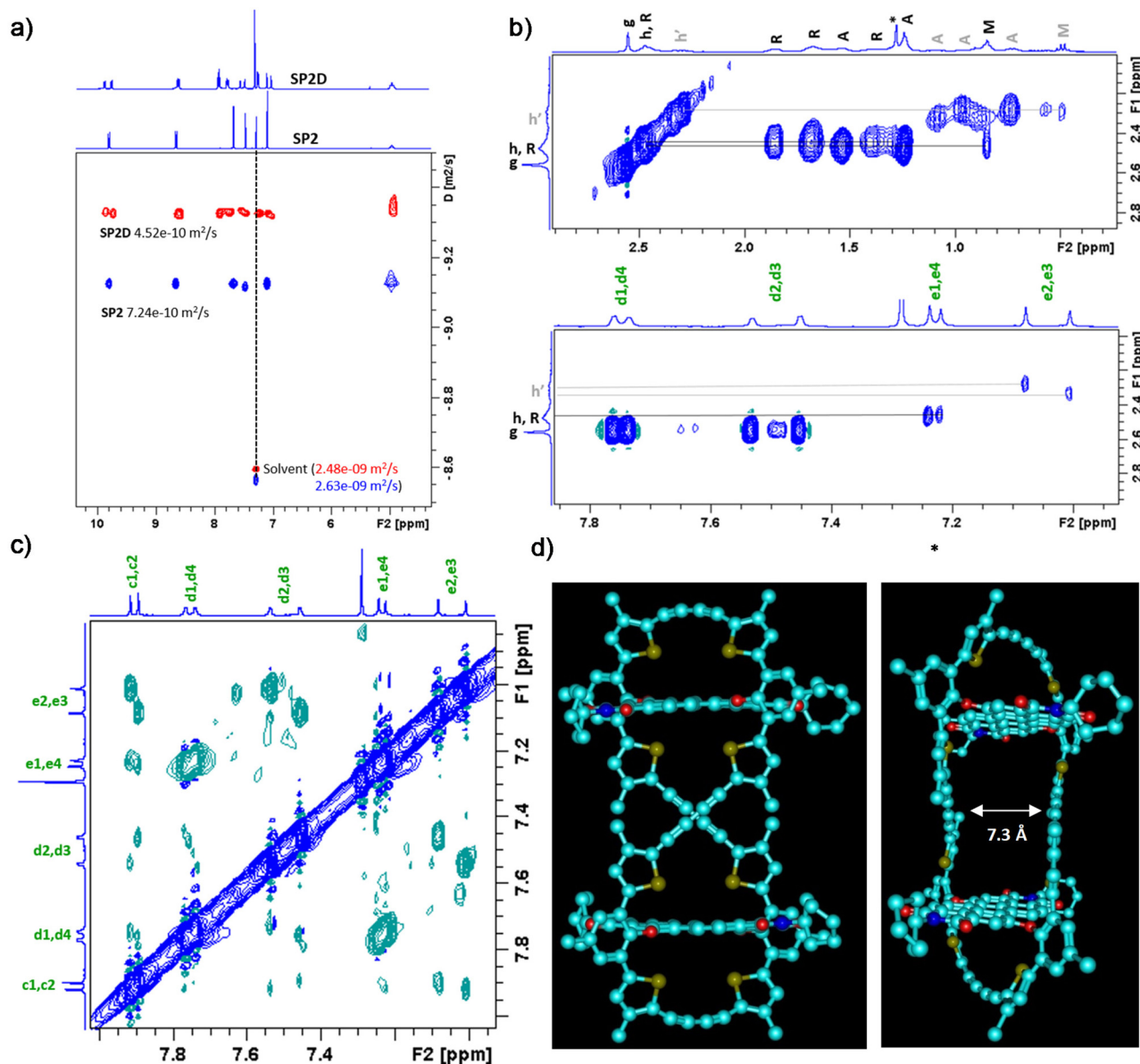


**Fig. 4** (a) Comparison of the aromatic region of the diffusion ordered spectra of **SP2** (blue) and **SP2D** (red) at 298 K with an overlay of $^1$H NMR spectra on top. (b) Regions from the TOCSY spectrum of **SP2D** showing distinct correlations between protons belonging to different environments. (c) Aromatic proton correlations in the ROESY spectrum of **SP2D**. Cyclohexyl ring protons and methyl/methylene protons of the alkyl chain are labeled R and M/A, respectively. Signal labeling is the same as in Fig. 2. Grey labels refer to additional alkyl proton environments arising from dimer formation, while additional aromatic proton signals are indicated explicitly by numerals. Residual solvent and water signals are marked by asterisks. (d) Optimized structure showing the geometry of **SP2D** by DFT calculations; the alkyl chain and hydrogens are excluded for clarity.

confirmed by $^1$H–$^{13}$C heteronuclear single quantum coherence (HSQC) and heteronuclear multiple bond correlation (HMBC) experiments (Fig. S22†). Signals from different environments showed unique correlations in 2D rotating frame Overhauser effect spectroscopy (ROESY) and nuclear Overhauser spectroscopy (NOESY) spectra (Fig. 4c, S23 and 24†).

For example, protons d1 and d4 correlate strongly with e1 and e4, indicating their mutual proximity, while the d2 and d3 protons are close to e2 and e3, thus representing distinct environments. While the loss of symmetry during dimerization results in non-degenerate signals for all protons in **SP2D**, the outer diacetylene–thiophene ring protons "d" and "e" show further chemical shift distinctions. This implies that the outer ring partially twists into a nearly "8" shape. The two halves of the diacetylene–thiophene ring are aligned at an angle with respect to each other to eliminate steric effects from the long alkyl chains. Dimerization and a tilt in the orientation of the two halves of the outer ring result in four distinct signals for "d" and "e". The structure of **SP2D** inferred on the basis of the NMR data (Fig. S15–24†) agrees with the optimal geometry determined from DFT calculations, as shown in Fig. 4d. Calculations show that the two halves of the diacetylene–thiophene ring are twisted with respect to each other, and the "dimer-forming" diacetylene links are separated by ~7.3 Å. Variable temperature $^1$H NMR spectra of **SP2D** revealed that signals corresponding to different environments arising from

dimerization do not undergo significant chemical shifts or linewidth changes, indicating that the dimer conformation is reasonably stable (Fig. S25†).

For a better understanding of the excited state electron transfer dynamics in these macromolecular systems, femtosecond transient absorption spectroscopy (FTAS) was employed in the $CH_2Cl_2$ solutions of **SP2** and **SP2D**. Fig. 5a and b represent the visible range FTAS spectra of these two systems after 420 nm pump excitation. Both spectra are very similar, having two ground-state bleach features at 525 and 565 nm and a broad photoinduced absorption signal at the red region peaking around 730 nm. These spectra are very different from the pristine **rPBI** system (Fig. S26†), where a sharp positive signal owing to S1–S$n$ transition dominates the spectra. In contrast, macrocycles have very different and broad positive signals, which must arise from the formation of the PBI radical anion.[36–38]

The dynamic profiles of **SP2** and **SP2D** are plotted in Fig. 5c, monitoring at the maximum peak position. These profiles were fitted with multiexponential time components and are listed in Table S4.† The rise time of **SP2** was found to be substantially enhanced in the **SP2D** system. As this positive signal signifies the formation of the PBI radical anion, we can assign this rise time as the CS time scale ($\tau_{CS}$) in these donor–acceptor systems.[36] From the fitting data, $\tau_{CS}$ was calculated to be 2.7 and 8.4 ps, corresponding to electron transfer rate con-
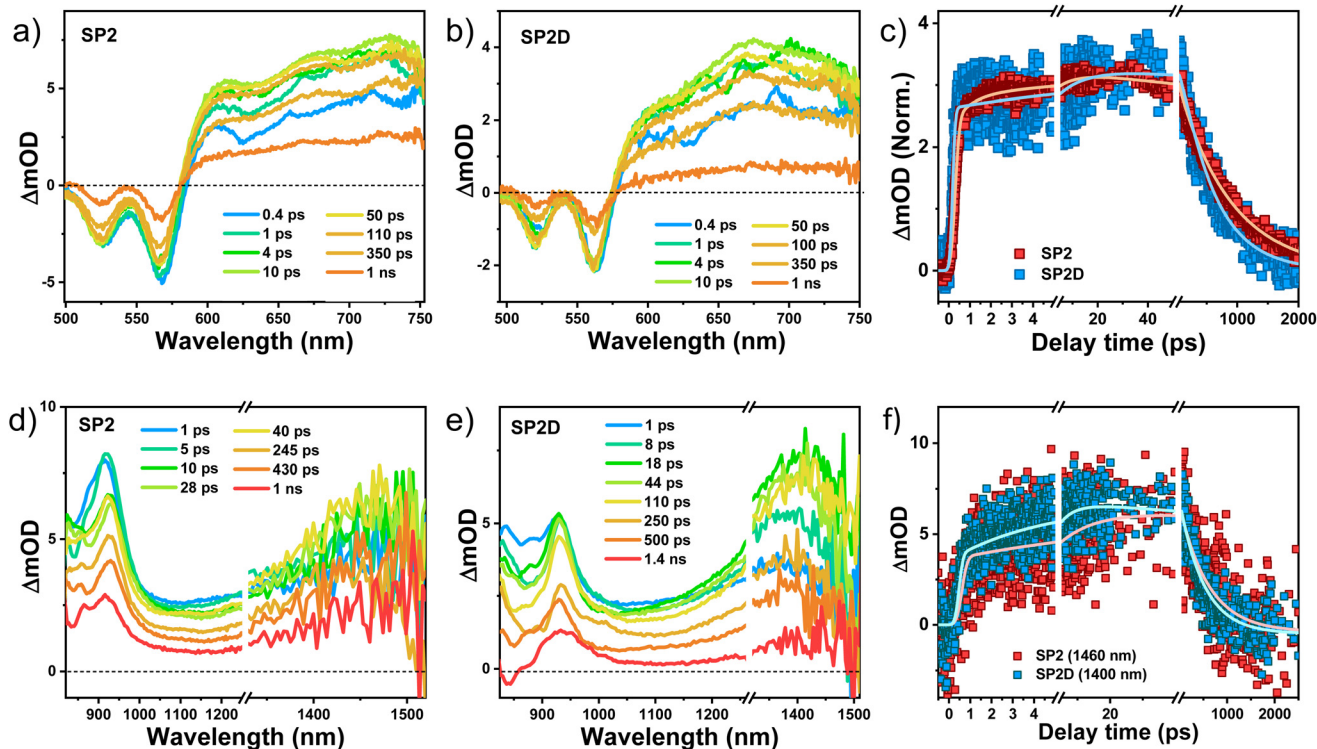


**Fig. 5** FTAS spectra of (a) **SP2** and (b) **SP2D** in $CH_2Cl_2$ in the visible region after laser excitation at 420 nm (left) and of (d) **SP2** and (e) **SP2D** in the NIR region after laser excitation at 420 nm (right). (c) Normalized kinetic profiles of the radical anions in **SP2** and **SP2D**, monitoring at 730 and 738 nm, respectively. (f) Normalized kinetic profiles of the oligothiophene radical cation in **SP2** and **SP2D**, monitoring at 1460 and 1400 nm, respectively.

stants of $0.4 \times 10^{12}$ s$^{-1}$ and $0.1 \times 10^{12}$ s$^{-1}$ for **SP2** and **SP2D**, respectively. Hence, the CS process is slower in **SP2D** than in **SP2**.

Next, we plotted the FTAS spectra of these two systems by monitoring the NIR region (820–1520 nm) after 420 nm photo-excitation (Fig. 5d and e). These spectra consisted of two distinct positive features, one around 930 nm and the other around 1400 nm. The 930 nm signature closely resembled the sharp positive signal observed in **rPBI** (Fig. S26†). As this signal appeared in the **rPBI** molecule, it could not be any radical or anionic signature; it must have originated from the excited state absorption from the S1 state of PBI.[38] On the other hand, the 1400 nm broad positive signal was observed only in the macrocycles. According to previous reports, oligothiophene radical cations have strong absorption in this region.[38] So, we assigned this signature as the formation of the oligothiophene radical cation. Observation of both the cationic and anionic species confirmed efficient charge separation in the macrocycle system. In Fig. 5f, we plotted the dynamic profile of the radical cation originating in **SP2** and **SP2D**. The multiexponential fitting parameters are listed in Table S4.† Both dynamics are very similar, with the only difference being the marginal increment in the growth time scale in **SP2** (11.8 ps) from that of **SP2D** (7.3 ps). This can be anticipated due to the similarity in the structural components of **SP2** and **SP2D**, leading to nearly identical optical properties. However, the spectral pattern of **SP2D** in the NIR region is more intense and distinguishable than that of **SP2**, indicating towards more prominent charge separation in **SP2D**.

The role of the acetylene bridged thiophene ring is critical in this molecular design. The CS process in the case of the previously reported oligothiophene ring strapped **TSP2** [33] and the present acetylene bridged thiophene ring strapped **SP2** was found to be occurring on a time scale of 2.7 ps ($k_{CS} \sim 0.4 \times 10^{12}$ s$^{-1}$) and 3.1 ps ($k_{CS} \sim 0.3 \times 10^{12}$ s$^{-1}$), respectively. However, a significant enhancement was observed in the charge recombination time scale of **SP2**, 545 ps (85.6%), >1 ns (14.4%), compared to that of **TSP2**, 245.3 ps (100%).[33] The charge separation process lasted longer than those of **(5T)$_2$-PBI** and **7T-PBI**, $\tau_{CS} = \sim 12$ ps.[32,38] This is attributed to the rigid structure in the donor unit due to the acetylene bridge that prevented the C–C (sp$^3$) bond rotation and eventually enhanced the effective conjugation of the donor unit.[39] Even the dimer **SP2D** also exhibited reasonably high stabilization of the charge-separated state supported by the rigid structure, as indicated by the temperature-dependent NMR experiments (Fig. S25†).

## Conclusions

In conclusion, we reported the synthesis, crystal structure, and transient absorption studies of new thiophene–diacetylene strapped perylene bisimide macrocycles. Single-crystal X-ray analysis showed the preferred perpendicular orientation of the planar perylene bisimide inside the thiophene diacetylene ring. The presence of an alkyl chain on the thiophene ring enabled the formation of higher oligomers, such as a dimer, trimer, and tetramer. Transient absorption studies pointed to stabilization of the charge-separated states due to the unique macrocycle design. Although the placement of chromophores in the preferred orientation in macrocycles is challenging, here, it was achieved through a unique molecular design. Hence, it supported the electronic communication between the donor–acceptor units in the molecule and enabled fast electron transfer. Besides, it formed a higher analogue, a figure-eight-shaped lemniscate dimer with similar electron transfer and stabilization of the charge-separated states. The concept of functionalizable macrocycles offers the inclusion of multiple donor–acceptor units in a single system and, at the same time, delivers exciting electron transfer features due to the unique positioning in the macrocycle. Such larger multi-component macrocyclic systems are of fundamental importance and pave the way for futuristic applications.

## Conflicts of interest

There are no conflicts to declare.

## Acknowledgements

## References

1 T. Pullerits and V. Sundström, Photosynthetic Light-Harvesting Pigment–Protein Complexes: Toward Understanding How and Why, *Acc. Chem. Res.*, 1996, **29**, 381–389.

2 A. W. Roszak, T. D. Howard, J. Southall, A. T. Gardiner, C. J. Law, N. W. Isaacs and R. J. Cogdell, Crystal Structure of the RC-LH1 Core Complex from Rhodopseudomonas Palustris, *Science*, 2003, **302**, 1969–1972.

3 S. Sengupta and F. Würthner, Chlorophyll J-Aggregates: From Bioinspired Dye Stacks to Nanotubes, Liquid Crystals, and Biosupramolecular Electronics, *Acc. Chem. Res.*, 2013, **46**, 2498–2512.

4 R. Bhosale, J. Míšek, N. Sakai and S. Matile, Supramolecular n/p-Heterojunction Photosystems with

Oriented Multicolored Antiparallel Redox Gradients, *Chem. Soc. Rev.*, 2010, **39**, 138–149.

5 B. Fimmel, M. Son, Y. M. Sung, M. Grüne, B. Engels, D. Kim and F. Würthner, Phenylene Ethynylene-Tethered Perylene Bisimide Folda-Dimer and Folda-Trimer: Investigations on Folding Features in Ground and Excited States, *Chem. – Eur. J.*, 2015, **21**, 615–630.

6 F. Schlosser, M. Moos, C. Lambert and F. Würthner, Redox-Switchable Intramolecular π−π -Stacking of Perylene Bisimide Dyes in a Cyclophane, *Adv. Mater.*, 2013, **25**, 410–414.

7 P. Spenst and F. Würthner, Photo- and redox functional cyclophanes, macrocycles, and catenanes based on aromatic bisimides, *J. Photochem. Photobiol., C*, 2017, **31**, 114–138.

8 A.-B. Bornhof, A. Bauzá, A. Aster, M. Pupier, A. Frontera, E. Vauthey, N. Sakai and S. Matile, Synergistic Anion–(π) n −π Catalysis on π-Stacked Foldamers, *J. Am. Chem. Soc.*, 2018, **140**, 4884–4892.

9 D. Gust, T. A. Moore and A. L. Moore, Mimicking Photosynthetic Solar Energy Transduction, *Acc. Chem. Res.*, 2001, **34**, 40–48.

10 A. Adronov and J. M. J. Fréchet, Light-Harvesting Dendrimers, *Chem. Commun.*, 2000, **18**, 1701–1710.

11 S. Setayesh, A. C. Grimsdale, T. Weil, V. Enkelmann, K. Müllen, F. Meghdadi, E. J. W. List and G. Leising, Polyfluorenes with Polyphenylene Dendron Side Chains: Toward Non-Aggregating, Light-Emitting Polymers, *J. Am. Chem. Soc.*, 2001, **123**, 946–953.

12 F. J. M. Hoeben, P. Jonkheijm, E. W. Meijer and A. P. H. J. Schenning, About Supramolecular Assemblies of π-Conjugated Systems, *Chem. Rev.*, 2005, **105**, 1491–1546.

13 Y. Tobe, N. Utsumi, K. Kawabata and K. Naemura, Synthesis and Self-Association Properties of Diethynylbenzene Macrocycles, *Tetrahedron Lett.*, 1996, **37**, 9325–9328.

14 M. C. O'Sullivan, J. K. Sprafke, D. V. Kondratuk, C. Rinfray, T. D. W. Claridge, A. Saywell, M. O. Blunt, J. N. O'Shea, P. H. Beton, M. Malfois and H. L. Anderson, Vernier Templating and Synthesis of a 12-Porphyrin Nano-Ring, *Nature*, 2011, **469**, 72–75.

15 P. S. Bols and H. L. Anderson, Template-Directed Synthesis of Molecular Nanorings and Cages, *Acc. Chem. Res.*, 2018, **51**, 2083–2092.

16 J. Krömer, I. Rios-Carreras, G. Fuhrmann, C. Musch, M. Wunderlin, T. Debaerdemaeker, E. Mena-Osteritz and P. Bäuerl, Synthesis of the First Fullya-Conjugated Macrocyclic Oligothiophenes:Cyclo[n]-thiophenes with Tunable Cavities in the Nanometer Regime, *Angew. Chem., Int. Ed.*, 2000, **39**, 3481–3486.

17 K. Nakao, M. Nishimura, T. Tamachi, Y. Kuwatani, H. Miyasaka, T. Nishinaga and M. Iyoda, Giant Macrocycles Composed of Thiophene, Acetylene, and Ethylene Building Blocks, *J. Am. Chem. Soc.*, 2006, **128**, 16740–16747.

18 J. E. Donehue, O. P. Varnavski, R. Cemborski, M. Iyoda and T. Goodson, Probing Coherence in Synthetic Cyclic Light-Harvesting Pigments, *J. Am. Chem. Soc.*, 2011, **133**, 4819–4828.

19 T. Sakida, S. Yamaguchi and H. Shinokubo, Metal-Mediated Synthesis of Antiaromatic Porphyrinoids from a BODIPY Precursor, *Angew. Chem., Int. Ed.*, 2011, **50**, 2280–2283.

20 Y. Qin, X. Liu, P.-P. Jia, L. Xu and H.-B. Yang, BODIPY-Based Macrocycles, *Chem. Soc. Rev.*, 2020, **49**, 5678–5703.

21 W. Zhang and J. S. Moore, Arylene Ethynylene Macrocycles Prepared by Precipitation-Driven Alkyne Metathesis, *J. Am. Chem. Soc.*, 2004, **126**, 12796–12796.

22 B. Schmaltz, A. Rouhanipour, H. J. Räder, W. Pisula and K. Müllen, Filling the Cavity of Conjugated Carbazole Macrocycles with Graphene Molecules: Monolayers Formed by Physisorption Serve as a Surface for Pulsed Laser Deposition, *Angew. Chem., Int. Ed.*, 2009, **48**, 720–724.

23 F. Schlosser, V. Stepanenko and F. Würthner, Perylene Bisimide Macrocycles and Their Self-Assembly on HOPG Surfaces, *Chem. Commun.*, 2010, **46**, 8350.

24 X. Guo, A. Facchetti and T. J. Marks, Imide- and Amide-Functionalized Polymer Semiconductors, *Chem. Rev.*, 2014, **114**, 8943–9021.

25 X. Zhan, A. Facchetti, S. Barlow, T. J. Marks, M. A. Ratner, M. R. Wasielewski and S. R. Marder, Rylene and Related Diimides for Organic Electronics, *Adv. Mater.*, 2011, **23**, 268–284.

26 F. Würthner, C. R. Saha-Möller, B. Fimmel, S. Ogi, P. Leowanawat and D. Schmidt, Perylene Bisimide Dye Assemblies as Archetype Functional Supramolecular Materials, *Chem. Rev.*, 2016, **116**, 962–1052.

27 F. Würthner, Perylene Bisimide Dyes as Versatile Building Blocks for Functional Supramolecular Architectures, *Chem. Commun.*, 2004, **14**, 1564–1579.

28 C. Huang, S. Barlow and S. R. Marder, Perylene-3,4,9,10-Tetracarboxylic Acid Diimides: Synthesis, Physical Properties, and Use in Organic Electronics, *J. Org. Chem.*, 2011, **76**, 2386–2407.

29 P. Osswald and F. Würthner, Conformational Effects of Bay Substituents on Optical, Electrochemical and Dynamic Properties of Perylene Bisimides: Macrocyclic Derivatives as Effective Probes, *Chem. – Eur. J.*, 2007, **13**, 7395–7409.

30 E. Ramirez, S. Chen, N. E. Powers-Riggs, I. Schlesinger, R. M. Young and M. R. Wasielewski, Symmetry-Breaking Charge Separation in the Solid State: Tetra(Phenoxy) Perylenediimide Polycrystalline Films, *J. Am. Chem. Soc.*, 2020, **142**, 18243–18250.

31 M. Ball, B. Zhang, Y. Zhong, B. Fowler, S. Xiao, F. Ng, M. Steigerwald and C. Nuckolls, Conjugated Macrocycles in Organic Electronics, *Acc. Chem. Res.*, 2019, **52**, 1068–1078.

32 K. Bold, M. Stolte, K. Shoyama, M. Holzapfel, A. Schmiedel, C. Lambert and F. Würthner, Macrocyclic Donor–Acceptor Dyads Composed of a Perylene Bisimide Dye Surrounded by Oligothiophene Bridges, *Angew. Chem., Int. Ed.*, 2022, **61**, e202113598.

33 S. D. Veer, V. C. Wakchaure, K. Asokan, R. Dixit, T. Goswami, R. Saha, R. Gonnade, H. N. Ghosh and

S. S. Babu, Oligothiophene-Ring-Strapped Perylene Bisimides: Functionalizable Coaxial Donor–Acceptor Macrocycles, *Angew. Chem., Int. Ed.*, 2023, **62**, e202212934.

34 P. Siemsen, R. C. Livingston and F. Diederich, Acetylenic Coupling: A Powerful Tool in Molecular Construction, *Angew. Chem., Int. Ed.*, 2000, **39**, 2632–2657.

35 G. Baranović, L. Colombo, K. Furić, J. R. Durig, J. F. Sullivan and J. Mink, Vibrational Assignment of 1,4-Diphenylbutadiyne, *J. Mol. Struct.*, 1986, **144**, 53–69.

36 R. F. Kelley, W. S. Shin, B. Rybtchinski, L. E. Sinks and M. R. Wasielewski, Photoinitiated Charge Transport in Supramolecular Assemblies of a 1,7, N,N '-Tetrakis(Zinc Porphyrin)-Perylene-3,4:9,10-Bis(Dicarboximide), *J. Am. Chem. Soc.*, 2007, **129**, 3173–3181.

37 M. Fujitsuka, K. Harada, A. Sugimoto and T. Majima, Excitation Energy Dependence of Photoinduced Processes in Pentathiophene–Perylene Bisimide Dyads with a Flexible Linker, *J. Phys. Chem. A*, 2008, **112**, 10193–10199.

38 K. Bold, M. Stolte, K. Shoyama, A. Krause, A. Schmiedel, M. Holzapfel, C. Lambert and F. Würthner, Macrocyclic Donor-Acceptor Dyads Composed of Oligothiophene Half-Cycles and Perylene Bisimides, *Chem. – Eur. J.*, 2022, **28**, e202200355.

39 P. Pachfule, A. Acharjya, J. Roeser, T. Langenhahn, M. Schwarze, R. Schomäcker, A. Thomas and J. Schmidt, Diacetylene Functionalized Covalent Organic Framework (COF) for Photocatalytic Hydrogen Generation, *J. Am. Chem. Soc.*, 2018, **140**, 1423–1427.